

ULTRA- REALISTIC IMAGING

ADVANCED TECHNIQUES IN
ANALOGUE AND DIGITAL
COLOUR HOLOGRAPHY

HANS BJELKHAGEN
DAVID BROTHERTON-RATCLIFFE



CRC Press
Taylor & Francis Group

ULTRA- REALISTIC IMAGING

**ADVANCED TECHNIQUES IN
ANALOGUE AND DIGITAL
COLOUR HOLOGRAPHY**

ULTRA- REALISTIC IMAGING

**ADVANCED TECHNIQUES IN
ANALOGUE AND DIGITAL
COLOUR HOLOGRAPHY**

**HANS BJELKHAGEN
DAVID BROTHERTON-RATCLIFFE**



CRC Press

Taylor & Francis Group

Boca Raton London New York

CRC Press is an imprint of the
Taylor & Francis Group, an **informa** business
A TAYLOR & FRANCIS BOOK

CRC Press
Taylor & Francis Group
6000 Broken Sound Parkway NW, Suite 300
Boca Raton, FL 33487-2742

© 2013 by Taylor & Francis Group, LLC
CRC Press is an imprint of Taylor & Francis Group, an Informa business

No claim to original U.S. Government works

Printed on acid-free paper
Version Date: 20130212

International Standard Book Number-13: 978-1-4398-2799-4 (Hardback)

This book contains information obtained from authentic and highly regarded sources. Reasonable efforts have been made to publish reliable data and information, but the author and publisher cannot assume responsibility for the validity of all materials or the consequences of their use. The authors and publishers have attempted to trace the copyright holders of all material reproduced in this publication and apologize to copyright holders if permission to publish in this form has not been obtained. If any copyright material has not been acknowledged please write and let us know so we may rectify in any future reprint.

Except as permitted under U.S. Copyright Law, no part of this book may be reprinted, reproduced, transmitted, or utilized in any form by any electronic, mechanical, or other means, now known or hereafter invented, including photocopying, microfilming, and recording, or in any information storage or retrieval system, without written permission from the publishers.

For permission to photocopy or use material electronically from this work, please access www.copyright.com (<http://www.copyright.com/>) or contact the Copyright Clearance Center, Inc. (CCC), 222 Rosewood Drive, Danvers, MA 01923, 978-750-8400. CCC is a not-for-profit organization that provides licenses and registration for a variety of users. For organizations that have been granted a photocopy license by the CCC, a separate system of payment has been arranged.

Trademark Notice: Product or corporate names may be trademarks or registered trademarks, and are used only for identification and explanation without intent to infringe.

Library of Congress Cataloging-in-Publication Data

Bjelkhagen, Hans I.
Ultra-realistic imaging : advanced techniques in analogue and digital colour holography / Hans Bjelkhagen, David Brotherton-Ratcliffe.
pages cm
Includes bibliographical references and index.
ISBN 978-1-4398-2799-4 (hardback)
1. Holography. 2. Image processing--Digital techniques. I. Brotherton-Ratcliffe, David. II. Title.

TA1540.B54 2012
621.36'75--dc23

2012044176

Visit the Taylor & Francis Web site at
<http://www.taylorandfrancis.com>

and the CRC Press Web site at
<http://www.crcpress.com>

Contents

Foreword	xvii
Preface	xix
Acknowledgments.....	xxiii
Authors.....	xxv
1. Ultra-Realistic Imaging and Its Historical Origin in Display Holography	1
1.1 Ultra-Realistic Imaging and Interferential Techniques	1
1.2 Before Holography	2
1.3 Early Holography	3
1.4 Display Holography Milestones.....	5
1.4.1 Full-Parallax Transmission Holograms	6
1.4.1.1 Earliest Work at Conductron Corporation.....	6
1.4.1.2 Early Work in France.....	7
1.4.1.3 Paula Dawson	8
1.4.1.4 Nick Phillips and John Webster.....	8
1.4.1.5 John Webster and Margaret Benyon.....	10
1.4.1.6 Ralph Wuerker.....	10
1.4.1.7 40 J Ruby Laser Facility at Fermilab	10
1.4.1.8 Hologram of Swedish Crown	11
1.4.1.9 Carl Fredrik Reuterswärd.....	12
1.4.1.10 Demise of Laser and Mercury Lamp Transmission Holograms	14
1.4.2 Pulsed Holographic Portraits	14
1.4.2.1 Use of Neodymium Lasers for Portraiture Applications.....	16
1.4.2.2 Reagan Portrait and Portraiture into the Future.....	17
1.4.3 Steven Benton's Rainbow Hologram	18
1.4.3.1 Transmission Pseudo-Colour Techniques	18
1.4.3.2 Large Rainbow Display Holograms and Embossed Holograms	19
1.4.3.3 US Rainbow Displays—Holographics North Inc.....	20
1.4.3.4 French Rainbow Displays—AP Holographie SARL	20
1.4.3.5 Australian Rainbow Displays—Australian Holographics Pty. Ltd.....	21
1.4.3.6 Parameswaran Hariharan	22
1.4.3.7 Günther Dausmann	22
1.4.3.8 Dieter Jung and Rudie Berkhouwt	22
1.4.4 Circular Transmission Holograms	24
1.4.5 Achromatic or Black-and-White Holograms	24
1.4.6 Monochrome Reflection Holograms.....	26
1.4.6.1 Sweden—Laserggruppen Holovision AB	27
1.4.6.2 Mass Production of Reflection Holograms.....	30
1.4.7 Pseudo-Colour Reflection Holograms	31
1.4.8 Holographic Movie Films	33
1.4.9 Multiplex and Stereographic Holograms	34
1.5 Digital and Analogue Full-Colour Holography.....	37
References	37
2. Lippmann Photography	41
2.1 Brief History of Interferential Colour Recordings	41
2.2 Examples of Interferential Structures in Nature.....	42

2.3	Lippmann Photography.....	43
2.4	Theory of the Lippmann Process	46
2.4.1	Treatment of Monochromatic Recording.....	46
2.4.2	Treatment of Monochromatic Replay	46
2.4.3	Treatment of Polychromatic Recording	47
2.4.4	Treatment of Polychromatic Replay.....	48
2.5	Early Lippmann Emulsions	49
2.5.1	Auguste (1862–1954) and Louis Lumière (1864–1948).....	49
2.5.2	Richard Neuhauss (1855–1915).....	50
2.5.3	Hans Lehmann (1875–1917)	51
2.5.4	Edmond Rothé (1873–1942).....	52
2.6	Recording of Early Lippmann Photographs	53
2.6.1	Recording Equipment	53
2.6.2	Processing Lippmann Silver Halide Emulsions	54
2.6.3	Viewing Lippmann Photographs	54
2.6.4	Early Investigations of Lippmann Emulsions.....	56
2.6.5	Museum Collections of Lippmann Photographs	57
2.7	Modern Lippmann Photography	57
2.7.1	Modern Lippmann Emulsions	58
2.7.2	Recording and Processing of Lippmann Photographs Today.....	58
2.7.3	Modern Lippmann Photographs Made with Different Modern Materials.....	58
2.7.3.1	Photopolymer Recording Materials	59
2.7.3.2	Silver Halide Recording Materials.....	60
2.8	Concluding Remarks.....	64
	References	65
3.	Continuous Wave Lasers for Colour Holography	71
3.1	Introduction.....	71
3.2	Gas Lasers.....	72
3.2.1	Helium–Neon Laser.....	72
3.2.2	Argon Ion Laser	73
3.2.3	Krypton Ion Laser.....	73
3.2.4	Helium–Cadmium Laser	74
3.2.5	Other Gas Lasers.....	75
3.2.5.1	Helium–Mercury Laser	75
3.2.5.2	Helium–Selenium Laser	75
3.2.5.3	Other Metal Vapour Ion Lasers.....	75
3.2.5.4	Copper and Gold Vapour Lasers	76
3.3	Dye Lasers	76
3.3.1	Liquid Dye Lasers.....	76
3.3.2	Solid-State Dye Lasers.....	77
3.4	Diode-Pumped Solid-State Lasers.....	77
3.4.1	Green Emission DPSS Lasers.....	78
3.4.1.1	Verdi 532 nm Laser	78
3.4.1.2	Other Green DPSS Lasers.....	78
3.4.2	Blue Emission DPSS Lasers	78
3.4.3	Red Emission DPSS Lasers	80
3.4.4	Yellow Emission DPSS Lasers	80
3.4.5	Orange Emission DPSS Lasers.....	80
3.4.6	Future DPSS Laser Technology	80
3.4.6.1	Praseodymium-Doped Lasers	80
3.4.6.2	Microchip Lasers.....	81
3.4.6.3	Chromium Forsterite	81

3.4.6.4	Optical Parametric Oscillators	81
3.5	Semiconductor Diode Lasers.....	82
3.5.1	Introduction.....	82
3.5.2	Operation and Construction.....	82
3.5.3	Mode Structure and Coherence	83
3.5.4	Operation at Single Longitudinal Mode	83
3.5.5	Amplification	84
3.5.6	Summary.....	85
3.6	Fibre Lasers.....	85
3.7	CW Laser Sources for Colour Holography Today.....	85
	References	86
4.	Recording Materials for Colour Holography	89
4.1	Introduction.....	89
4.1.1	Silver Halides	89
4.1.2	Dichromated Gelatin.....	90
4.1.3	Photopolymers	90
4.2	Holographic Recording.....	90
4.2.1	Sensitivity of Photographic and Holographic Materials.....	93
4.3	Holographic Emulsions.....	93
4.3.1	Demands on Recording Emulsion	93
4.3.2	Resolution of Holographic Image	94
4.3.3	Image Resolution Determined by Recording Material.....	95
4.4	Problems due to Short or Long Exposure	96
4.4.1	Pulsed Holography	96
4.4.2	Reciprocity Failure.....	97
4.4.3	Holographic Reciprocity Failure.....	99
4.5	Increasing Sensitivity by Hypersensitisation and Latensification	100
4.5.1	Hypersensitisation.....	100
4.5.1.1	Water Solution of TEA	100
4.5.1.2	Water Treatment	100
4.5.2	Latensification.....	100
4.5.3	Internal Latensification	101
4.6	Substrates for Holographic Emulsions.....	102
4.6.1	Glass Plates	103
4.6.2	Film Substrates	103
4.7	Commercial Recording Materials for Colour Holography	104
4.7.1	Manufacturing Companies	104
4.8	SilverCross Emulsion Research Project	105
4.8.1	Precipitation Stage	106
4.8.2	Washing Stage.....	107
4.8.3	Coating Stage	108
4.9	Additional Silver Halide Materials for Holography	109
4.10	DCG Materials.....	110
4.10.1	Preparing Gelatin Plates	110
4.10.2	Sensitising the DCG Emulsion	110
4.10.3	Exposure	111
4.10.4	Pulsed Laser Exposure of DCG.....	111
4.10.5	DCG Processing.....	111
4.10.6	Panchromatic DCG Emulsions	112
4.10.7	Commercial DCG Materials	115
4.11	Photopolymer Materials.....	115
4.11.1	Recording Photopolymer Holograms with Pulsed Lasers.....	116

4.11.2	Panchromatic Photopolymers	117
4.11.3	Commercial Photopolymer Materials.....	118
	References	119
5.	Analogue Colour Holography	123
5.1	Introduction.....	123
5.2	Origins in Monochromatic Holography	124
5.3	History of True Full-Colour Holography.....	126
5.3.1	Silver Halide-Sensitised Gelatin Technique	128
5.3.2	Colour Holograms in Single-Layer Silver Halide Emulsions.....	132
5.4	Colour Recording in Holography.....	134
5.4.1	Colour Theory and Colour Measurements	134
5.4.2	Selection of Laser Wavelengths	137
5.4.3	Illumination of Colour Holograms	142
5.4.4	Demands on Lasers Required	143
5.5	Setup for Recording Colour Holograms	143
5.5.1	Colour Transmission Holograms	143
5.5.2	Colour Reflection Holograms	143
5.5.3	Exposure of Colour Holograms	146
5.5.4	Processing Recorded Colour Holograms.....	148
5.5.5	Sealing of Colour Holograms	149
5.5.6	Recorded and Evaluated Holograms.....	150
5.6	Full-Colour Pulsed Portraiture	152
	References	153
6.	Pulsed Lasers for Holography.....	157
6.1	Introduction.....	157
6.2	Ruby Laser	158
6.2.1	Practical Design of Ruby Lasers Suitable for Holography	160
6.2.2	Pulse Lengthening in the Ruby Laser.....	161
6.3	Flashlamp-Pumped Lasers Based on Crystals Doped with Neodymium at 1 μm	162
6.3.1	Nd:YAG	163
6.3.2	Nd:YAP and Nd:YLF	164
6.3.3	Nd:Glass.....	164
6.3.4	Nd ³⁺ -Doped Ceramic YAG	165
6.3.5	Design of Commercial Neodymium Holography Lasers	165
6.3.5.1	Design and Operation of Master Oscillator	167
6.3.5.2	Amplification.....	167
6.3.5.3	Pump Electronics.....	169
6.3.5.4	Cooling	170
6.3.6	Towards Even Higher Energy	170
6.3.7	Applications	171
6.4	High-Energy Two-Colour Emission: Stimulated Raman Amplification.....	172
6.4.1	SRS Red–Green Pulsed Laser	173
6.5	Pulsed RGB Lasers—Neodymium Lasers at 1.3 μm	176
6.5.1	Dual-Ring Cavity Pulsed RGB Nd:YLF/Nd:YAG Laser.....	177
6.5.2	Dual Linear-Cavity Pulsed RGB Nd:YAG Laser	179
6.5.3	Short-Cavity Pulsed RGB Lasers	183
6.5.3.1	Green Lasers.....	183
6.5.3.2	Red and Blue Lasers	187
6.5.4	Amplification at 1.3 μm : Higher Energy Emissions in the Red and Blue	187
6.6	Pulsed Holography Lasers Based on Titanium Sapphire ($\text{Ti}:\text{Al}_2\text{O}_3$) and Cr:LiSAF.....	187
6.7	Chromium Forsterite.....	189

6.7.1	Injection Seeding	190
6.8	Pulsed Diode-Pumped Lasers for Holography and the Future.....	191
	References	193
7.	Digital Colour Holography.....	197
7.1	Introduction.....	197
7.2	Holographic Stereograms	197
7.3	One-Step Digital Holograms	198
7.4	A Simple DWDH Printer.....	199
7.4.1	Optical Scheme	199
7.4.2	Speckle Blur	200
7.4.3	Operation.....	200
7.4.4	Image Data	201
7.4.5	Deficiencies	201
7.5	Modern DWDH Printers.....	202
7.5.1	Use of Pulsed Lasers.....	202
7.5.1.1	Microsecond Pulsed Lasers.....	203
7.5.2	Lens-Based Printers.....	203
7.5.3	Speckle in Lens-Based Printers	205
7.5.4	Triple-Beam Printers.....	205
7.5.4.1	Hogel-Writing Sequence	205
7.5.4.2	Basic Systems in RGB-Pulsed Laser Triple-Beam Printers.....	206
7.5.5	Printers Based on Liquid Crystal on Silicon Displays	216
7.5.6	Printers Incorporating Variable Reference Beam Systems	217
7.5.7	HPO Printers.....	219
7.5.8	Single-Beam RGB Printers	223
7.5.8.1	Screen-Based Hogel Formation Systems	223
7.5.9	Ultra-Realistic Printers	226
7.5.9.1	3N-Objective Printers	228
7.5.10	DWDH Transmission Hologram Printers.....	228
7.6	MWDH Printers.....	230
7.7	Copying Full-Colour DWDH Holograms.....	232
	References	234
8.	Digital Holographic Printing: Data Preparation, Theory and Algorithms	237
8.1	Introduction.....	237
8.2	Basic Considerations.....	237
8.3	Coordinate Systems	238
8.4	Coordinate Meshes	241
8.5	Independent Primary Colours.....	242
8.6	Viewing Plane	242
8.7	Simple Cases.....	243
8.7.1	Full-Parallax DWDH “Denisyuk” Reflection Hologram	243
8.7.2	MWDH Master Hologram.....	245
8.8	Image-Planed DWDH HPO Holograms.....	245
8.8.1	Printer, Camera and Viewing Window Options	247
8.8.2	General Rectangular Viewing Window	248
8.8.2.1	Simple Translating Camera	248
8.8.3	Centred Camera Configuration	256
8.8.4	Centred SLM Configuration	260
8.8.5	Fundamental Integer Constraints.....	263
8.9	Rainbow and Achromatic Transmission Holograms	268
8.9.1	MWDH	268

8.9.1.1	Vertically Aligned RGB H ₁ Master	268
8.9.1.2	Component-Colour H ₁ Masters	271
8.9.1.3	Achromatically Tilted Component-Colour H ₁ Masters.....	275
8.9.1.4	Achromatically Tilted RGB H ₁ Master	276
8.9.2	MWDH Achromats.....	276
8.9.3	DWDH	276
8.9.3.1	Synthesis of the Vertical Slit	277
8.9.3.2	Transformations Required When Using an RGB Laser.....	278
8.9.3.3	Transformations for One-Colour Laser.....	281
8.10	Correcting for Inherent Distortion in Printer Optical Objectives	283
8.10.1	Setting up the Formalism.....	283
8.10.2	Data Predistortion	285
8.10.3	Non-Paraxial I-to-S Transformations	288
	References	292
9.	Digital Holographic Printing: Computational Methods for Full-Parallax Holograms	293
9.1	Introduction.....	293
9.2	Practical Strategies for Changing the Image Plane	294
9.2.1	Camera Definition.....	295
9.2.2	Changing the Image Plane—Two-Step I-to-S Transformations.....	296
9.2.3	General Full-Parallax Paraxial Objective Transformations	298
9.2.4	Non-Paraxial Printer Objectives	300
9.2.5	Larger Holograms	300
9.2.6	Rectangular Viewing Windows	301
9.2.6.1	General Astigmatic Rectangular Viewing Window.....	302
9.3	Resolution Requirements of DWDH Reflection Holograms	310
9.4	DWDH Transmission Holograms	311
9.5	MWDH Reflection Holograms	312
9.6	Full-Parallax and HPO DWDH	313
	References	315
10.	Image Data Creation and Acquisition for Digital Display Holograms	317
10.1	Introduction.....	317
10.2	Image Acquisition from a Physical Scene: HPO Holograms	317
10.2.1	Simple Translating Camera.....	318
10.2.2	Hybrid Translating/Rotating Camera with Fixed Target.....	319
10.2.3	Hybrid Translating/Rotating Camera with Optimised Target	326
10.2.4	Resolution Requirements	330
10.2.5	Image Reduction and Magnification.....	331
10.2.6	Commercial Holocam Systems.....	331
10.2.7	Alternative Strategies—Rotating the Object	334
10.3	Image Acquisition from a Physical Scene: Full-Parallax Digital Holograms.....	339
10.3.1	Horizontal Rotating Platform with Vertically Linear-Translating Camera.....	340
10.3.1.1	Calculation of a Centred Camera Data Set.....	340
10.3.1.2	Derivation of the I-to-S Transformation.....	344
10.3.2	3D Structured-Light Scanners	346
10.4	Images Derived from a Virtual Computer Model: HPO Holograms	348
10.4.1	Data Preparation	348
10.4.2	Creating a 20 cm × 30 cm Landscape Hologram	349
10.5	Images Derived from a Virtual Computer Model: Full-Parallax Holograms	357
10.5.1	Creating a MAXScript GUI.....	357
10.5.2	Function of Script	360
10.5.3	Global Variables.....	361

10.5.4	Writing the “Make Directories” Event Handler	362
10.5.5	Writing the “Calculate” Event Handler	363
10.5.6	Writing the “Make Camera” Event Handler.....	364
10.5.7	Writing the “Start Render” Event Handler	365
	Reference	368
11.	Theoretical Basis for High-Fidelity Display Holograms	369
11.1	Introduction.....	369
11.2	Three-Dimensional Paraxial Theory of the Thin Transmission Hologram.....	370
11.2.1	Collimated Reference and Object Beams	373
11.2.2	Source-Size Blurring	376
11.2.3	Chromatic Blurring.....	379
11.3	Laser Transmission Holograms and the Problem of Speckle.....	380
11.4	Three-Dimensional Theory of the Thick Transmission Hologram.....	381
11.4.1	Snell’s Law at the Air–Hologram Boundary	382
11.4.2	Blurring in the Ultra-Thick Transmission Hologram	383
11.5	Reflection Holograms	384
11.6	A Simple Model of the Thick Hologram: Parallel Stacked Mirrors	386
11.7	Holograms of Finite Thickness.....	390
11.8	Emulsion Swelling and Change in Refractive Index on Processing.....	393
11.9	Non-Paraxial Behaviour and Digital Image Predistortion	394
11.10	Solving the Helmholtz Equation in Volume Gratings: Coupled Wave Theory.....	394
11.10.1	One-Dimensional Coupled Wave Theory	394
11.10.2	Solution with Perfect Bragg Compliance	395
11.10.3	Boundary Conditions.....	397
11.10.4	Power Conservation.....	398
11.10.5	Diffraction Efficiency.....	398
11.10.6	Small Departure from Bragg Condition.....	399
11.10.6.1	Behaviour of the Lossless Transmission Hologram.....	401
11.10.6.2	Behaviour of the Lossless Reflection Hologram.....	405
11.10.7	Effect of Loss in the Dielectric	413
11.10.8	Recording of Complex Wave Fronts and Multiple Gratings	414
11.10.9	Multiple Gratings Generated by Many Object Points	414
11.10.10	Recording Multiple Colour Gratings.....	418
11.10.11	Dispersion Equation Theory	418
11.11	Blurring Revisited.....	419
11.11.1	Blurring in the Digital Hologram	420
11.12	Computational Methods of Calculating Diffractive Efficiency of Planar Gratings.....	421
11.12.1	Rigorous Coupled Wave Theory and Rigorous Modal Theory	421
11.12.2	Rigorous Chain Matrix Method.....	421
	References	423
12.	Diffraction Efficiency: An Alternative Approach Using the PSM Model	425
12.1	Introduction.....	425
12.2	Formulation of the Simplest Model—The Unslanted Reflection Grating at Normal Incidence	425
12.2.1	Comparison with a Numerical Solution of the Helmholtz Equation.....	429
12.3	Unslanted Multiple-Colour Gratings at Normal Incidence	430
12.3.1	Numerical Solution for Two-Colour Normal-Incidence Reflection Gratings.....	431
12.3.2	Numerical Solution for Three-Colour Normal-Incidence Reflection Gratings.....	433
12.4	Unslanted Reflection Grating at Oblique Incidence	435
12.4.1	σ -Polarisation	435
12.4.2	π -Polarisation	438

12.4.3	Simplification of PSM Equations to Ordinary Differential Equations.....	439
12.4.4	Analytic Solutions for Sinusoidal Gratings	440
12.4.5	Multiple Colour Gratings.....	442
12.4.6	Comparison of Kogelnik's Theory with the PSM Theory for Unslanted Gratings at Oblique Incidence	443
12.5	Slanted Reflection Gratings	445
12.5.1	Analytical Solutions for Single-Colour Gratings	446
12.6	Slanted Reflection Gratings in Three Dimensions	448
12.7	Transmission Gratings with Slanted Fringes.....	450
12.8	Comparison of the PSM Theory with Kogelnik's Theory for Slanted Gratings.....	450
12.9	Polychromatic Slanted Reflection Gratings.....	451
12.10	Extending PSM to Describe Spatially Multiplexed Monochromatic Gratings	451
12.11	Coupled Wave Theory, PSM and the Rigorous Coupled Wave Theory	455
12.12	Lippmann Photography.....	456
12.13	Discussion	458
	References	459
13.	Illumination of Colour Holograms	461
13.1	Introduction.....	461
13.1.1	Chromatic and Source-Size Blurring	461
13.1.2	Geometry Matching	464
13.1.3	Illumination of HPO Holograms	465
13.1.4	Illumination of Large Rainbow and Rainbow-Achromatic Displays	467
13.2	Illumination of Holograms by Laser Sources.....	467
13.2.1	Importance of Wavelength Matching	469
13.2.2	Illumination of Full-Colour Transmission Holograms.....	469
13.2.3	Gas Lasers.....	470
13.2.4	Semiconductor Laser Diodes and Solid-State CW Lasers	470
13.3	Non-Laser Light Sources Used for Hologram Illumination.....	471
13.3.1	Halogen Lights.....	472
13.3.2	Special Lamps.....	473
13.3.3	Mercury Lamps.....	473
13.3.4	Arc Lamps.....	473
13.3.5	Plasma Lamps	474
13.3.6	LEDs	475
13.3.6.1	Theory of LED Operation	476
13.3.6.2	Blue to Green LEDs: 450 to 530 nm	478
13.3.6.3	Yellow-Green to Red LEDs: 565 to 645 nm.....	478
13.3.6.4	LEDs and Hologram Illumination—Wavelength Matching	478
13.3.6.5	White Phosphor LEDs.....	478
13.3.6.6	Multicolour LEDs	479
13.3.6.7	LED Colour Rendering.....	479
13.3.6.8	Preferred LEDs for Colour Holography	481
13.3.6.9	Lenses for LED Spotlights	481
13.3.6.10	White LED Spotlights	482
13.3.6.11	Special LED Spotlights for Colour Holograms.....	483
13.3.6.12	LED and Lamp Safety	485
13.4	Exhibition Facilities and Galleries Suitable for Displaying Holograms	486
13.5	Edge-Lit Holograms	489
13.6	Illumination of Large Displays	490
	References	491

14. Applications of Ultra-Realistic Holographic Imaging.....	493
14.1 Introduction.....	493
14.2 Some Scientific Applications of Holographic Imaging	493
14.2.1 Bubble Chamber Holography.....	494
14.2.2 Holographic Microscopy.....	496
14.2.3 Holographic Endoscopy	497
14.3 Visual Applications of Full-Colour Holographic Imaging.....	499
14.3.1 Holographic Copies of Museum Artefacts	499
14.3.1.1 Virtual Museum Exhibitions.....	499
14.3.1.2 Museum Holography in Greece.....	501
14.3.1.3 Museum Holography in England.....	504
14.3.1.4 Holographic Reproduction of Oil Paintings	505
14.3.2 Digital Display Holograms for Advertising and Product Promotion	507
14.3.2.1 Introduction	507
14.3.2.2 Key Organisations	507
14.3.2.3 Zebra Imaging	507
14.3.2.4 XYZ, Geola and Sfera-S	507
14.3.3 Digital Display Holograms for Mapping and Architectural Design	511
14.3.3.1 Horizontally Mounted Overhead-Illuminated Holograms.....	511
14.3.4 Digital Holographic Colour Portraits.....	512
14.3.5 Digital Art Holograms	515
14.3.6 Smaller Full-Colour Holograms	515
14.3.7 Holographic Fuel-Effect Electric Fires.....	517
14.4 Future Applications.....	517
14.4.1 Holographic Windows and Super-Realistic 3D Static Displays	517
14.4.1.1 Creation of Space—High Virtual Volume Displays	518
14.4.1.2 Constraints on Digital Holograms.....	518
14.4.2 Updateable 3D Holographic Displays.....	521
14.4.3 Real-Time 3D Display Technologies Based on Holography	522
14.4.3.1 Simple Autostereoscopic Systems Based on Holographic Screens.....	522
14.4.3.2 Multiprojector Autostereoscopic Systems Based on Holographic Screens.....	522
14.4.4 Future Real-Time True Holographic Displays.....	523
References	525
15. Acronyms	529
Appendix 1: Historical Origins of Display Holography: Spreading Awareness	537
A1.1 Hologram Exhibitions.....	537
A1.2 Commercial and Educational Entities Involved in Holography	538
A1.2.1 Companies Producing Holograms	538
A1.2.2 Hologram Galleries.....	539
A1.2.3 Holographic Museums	540
A1.2.4 Educational Institutes.....	540
Appendix 2: History of the Geola Organisation	541
A2.1 The Beginning	541
A2.2 First Meeting in Vilnius.....	543
A2.3 Incorporation of Geola UAB	545
A2.4 First Romanian Exhibition of Large-Format Holography	547
A2.5 Start of XYZ	547
A2.6 Panchromatic Film and Sfera-S	549
A2.7 Vilnius Digital Printer	550
A2.8 Sale of XYZ	552

Appendix 3: Active Cavity Length Stabilisation in Pulsed Neodymium Lasers	553
A3.1 Introduction.....	553
A3.2 Example of Cavity Stabilisation System Using Heated Rear Mirror Holder	553
A3.3 Active Cavity Length Stabilisation by Piezo Element.....	557
A3.3.1 Statistical Optimisation Algorithm.....	558
A3.4 Extension to Other Lasers.....	559
References	559
Appendix 4: Aberration Correction by Image Predistortion in Digital Holograms	561
A4.1 Introduction.....	561
A4.2 Mathematical Model	561
A4.3 Calculation of Optimal Reference Replay Angle	562
A4.4 Compensation for Geometrical Distortion	564
A4.5 Compensation for Chromatic Aberration	566
A4.6 Other Corrections	568
Reference.....	568
Appendix 5: MAXScript Holocam Program	569
Appendix 6: Design Study of Compact RGB LED Hologram Illumination Source	573
A6.1 Introduction.....	573
A6.2 Monochromatic Light Source	574
A6.3 Polychromatic Light Source.....	575
A6.4 Design of the Main Lens Surface	577
A6.4.1 Monochromatic Light Source	577
A6.4.2 Mathematical Formulation.....	578
A6.4.3 Geometrical Ray Tracing in the Point-Source Approximation	580
A6.4.4 Ray Intersection with Target Plane	581
A6.4.5 Calculation of Power Density Distribution at Target Plane.....	582
A6.4.6 Numerical Solution	583
A6.4.7 Ray Tracing with Finite Source Size	583
A6.4.7.1 Method.....	584
A6.4.7.2 Spatial Coherence	585
A6.5 Selected Cases: Computational Results.....	586
A6.5.1 Case 1.....	586
A6.5.2 Case 2.....	589
A6.5.3 Case 3.....	591
A6.6 Commercial Design of Nine-Diode Framing Light Source	594
A6.7 Additional Considerations	595
A6.8 Reflective Light-Source	595
Appendix 7: Bilinear and Bicubic Interpolation.....	597
A7.1 Introduction.....	597
A7.2 Bilinear Interpolation.....	597
A7.3 Bicubic Interpolation	598
Appendix 8: Rigorous Coupled Wave Theory of Simple and Multiplexed Gratings	601
A8.1 Introduction.....	601
A8.2 Derivation of RCW Equations	601
A8.3 Simplification in the Case of Simple Non-Multiplexed Grating	602
A8.4 Derivation of Boundary Conditions.....	602
A8.5 Numerical Solution of RCW Equations.....	603
A8.5.1 Comparison of Kogelnik's Theory and PSM Theory with RCW Theory.....	604

A8.5.2 Comparison of N-PSM Theory with RCW Theory.....	604
A8.5.3 Comparison of N-PSM with RCW Theory for Multicolour Gratings.....	606
References	608
Appendix 9: Recent Developments.....	609
A9.1 New Equipment, Materials, Techniques and Applications	609
A9.2 Progress at Zebra Imaging.....	610
A9.3 The <i>Queen Elizabeth II</i> Portrait and the Jersey Postage Stamp.....	612
A9.3.1 Achromatic Portrait of the Queen.....	612
A9.3.2 Hologram Postage Stamp of the Queen.....	612
A9.4 Lasers for Colour Holography	614
A9.4.1 New Lasers from Cobolt	614
A9.4.2 New Lasers from Coherent	614
A9.4.3 New Lasers from Laser Quantum.....	614
A9.4.4 Progress in RGB Laser Technology at Geola	614
A9.5 Progress in Recording Materials and Recording Techniques	615
A9.5.1 Surface Plasmon Waves	615
A9.5.2 Anomalously High Pulsed Sensitivity of Photoresist	616
A9.6 Printers to Record Digital Colour Holograms	616
A9.6.1 CGH Composite Reflection Hologram Printer	616
A9.6.2 Pioneer's Compact Holographic Printer	617
A9.7 3D Display Systems	618
A9.7.1 HoloVizio from Holografika	618
A9.7.2 SeeReal Technologies' Holographic 3D Display	618
A9.8 New Holography Camera from the Hellenic Institute of Holography.....	621
A9.9 HoloKit from Liti Holographics	621
References	622
Index.....	623

Foreword

It is my pleasure to write the Foreword to this book. I have known the authors, as well as their professional accomplishments in this field, for three decades.

Hans I. Bjelkhagen has devoted his entire professional life to holography. He is most well known for advancing the fields of silver-halide materials and their processing, interferometry, pulsed portraiture, Lippmann photography, and ultrarealistic color holography. He taught annual summer workshops at Lake Forest College from 1982 to 1997 that included courses on color holography, photochemistry, and pulsed portraiture.

As leader and organizer, Bjelkhagen cochaired with me the triennial International Symposium on Display Holography (ISDH) until I retired in 1997. In 2005, he revived and chaired a successful ISDH in the United Kingdom. With this encouragement, we held an ISDH in China in 2008, where he was a cochairman. He also helped organize the 2012 ISDH at the Massachusetts Institute of Technology. He is the current chairman of the annual Practical Holography Conference in California sponsored by the International Society for Optical Engineers (SPIE). Less well known is that he is a meticulous collector of all information pertaining to holography, maintains a detailed directory on holographers past and present, and collects holographic postage stamps that have been issued internationally.

David Brotherton-Ratcliffe is a polymath whose career spans both theoretical and experimental sciences including plasma physics, magnetohydrodynamics, nuclear fusion, laser engineering, diffractive optics, holography, and advanced systems design for the recording and production of both analogue and digital large-format holograms. His recent work in pulsed laser portraiture systems and computer-generated full-color, full-parallax holograms as presented in this book is truly state-of-the-art.

An abundance of books and articles on holography at the elementary level have already been published over the years since the mid-1960s. It is not necessary to repeat their contents here. This book is a condensation at the highest level of the authors' collective knowledge and experience in the area of display holography that includes history, theory, practice, and detailed designs of industrial systems. It includes over 500 photographs, diagrams, and design schematics for the recording and production of ultrarealistic holographic images.

Tung H. Jeong

Preface

Ultra-Realistic Imaging may be defined as any imaging technique that is able to record and reconstruct the visible electromagnetic light field scattered from a real-world object or scene with a resolution better than or equal to that of the unaided human eye. This book is devoted to a discussion of how the goal of ultra-realistic imaging may be attained through the application of the interferential methods of modern analogue and digital holography—and in particular through volume phase holography.

Holography was discovered more than 60 years ago. With the discovery of the laser and the off-axis technique in the early 1960s, it very quickly became obvious that the method constituted a unique imaging principle with enormous possibilities. However, the quality of the holographic image depended intrinsically on many things—such as the photosensitive material, the chemical processing scheme, the recording laser and not least, the illumination source with which the recorded hologram had to be viewed. This innate dependence of holography on critical associated technologies has been responsible for the waves of great enthusiasm for the subject being followed by periods of equally great disillusionment.

Holography has of course had its successes. The embossed security hologram and packaging industries are testament to this, but the role of holography as a technique of true ultra-realistic imaging is only just now becoming possible. This has been due to great progress in the key associated technologies of photosensitive materials, recording lasers, light sources, spatial light modulator technology and computers.

Digital techniques in holography are particularly exciting. Very large, high-definition full-colour holograms can now be written as a matrix of tiny elementary holograms, rather like a modern high-definition television screen is made up of pixels. One of the applications becoming possible with this technology is the creation of high virtual volume (HVV) displays. These are full-colour, full-parallax holograms that can replay 3D scenes having volumes from tens of cubic metres to cubic kilometres. Well-known holographers such as Nick Phillips and Paula Dawson took the first steps towards this type of display in the 1970s and 1980s using analogue laser transmission holography. Virtual volumes of tens of cubic metres were realised, but the images were noisy, monochromatic and had to be illuminated by bulky lasers. The new digital HVV holographic displays will have none of these deficiencies. In their ultimate incarnation, HVV displays can be used to create virtual holographic windows—these are ultra-realistic displays that seek to mimic a real window with a virtual 3D scene. As “space with a view” becomes an ever more costly commodity within the context of humanity’s inextricable progression to increasingly high-density urban environments, holographic windows may well provide a valuable solution.

Such applications are of course simply light-years away from the conventional holography that most people are used to today. This radical transformation is only becoming possible now because of great progress in many associated fields. The information content of an HVV hologram is enormous—the required image processing has simply not been practical until recently. Likewise, the image data could not be written to a hologram at a sufficiently high resolution without the recent progress in HD spatial light modulator technology. Panchromatic photosensitive materials of sufficient resolution were not previously known. And compact narrowband laser and LED illumination technology was not available for the illumination of such displays.

This book is certainly not intended as a basic introduction to holography. There are already many excellent books fulfilling this need. Rather, it brings together a discussion of key methods that enable holography to be used as a technique of ultra-realistic imaging.

The book starts with a historical review of progress to date in holography. We felt that this was merited from a contextual point of view and we have also taken the liberty to document some of our personal work here. Chapter 2 is devoted to Lippmann photography. This 100-year-old interferential colour photographic technique is relatively unknown, but Lippmann photographs offer exceptional colour fidelity. When Lippmann photography was introduced by Gabriel Lippmann, the impression his type of colour

images made on photographers of the day was clearly expressed by Edward Steichen who wrote to Stieglitz in 1908:

Professor Lippmann has shown me slides of still-life subjects by projection, that were as perfect in colour as in an ordinary glass positive in the rendering of the image in monochrome. The rendering of white tones was astonishing, and a slide made by one of the Lumière brothers, at a time when they were trying to make the process commercially possible, a slide of a girl in a plaid dress on a brilliant sunlit lawn, was simply dazzling, and one would have to go to a good Renoir to find its equal in colour luminosity.

A discussion of CW recording lasers for holography is given in Chapter 3. This has been an area of great progress and there is every reason to expect that such progress will continue at an even greater rate into the future. Small DPSS and semiconductor lasers can now be integrated into portable full-colour holographic cameras. Such systems have potential for use in areas such as museum archives. Museums such as the British Museum in London and the Louvre in Paris have shown real interest here. Pulsed holography lasers are reviewed in Chapter 6. Recent progress in RGB pulsed laser design has been instrumental in achieving high-quality digital colour holograms; pulsed lasers constitute a crucial technology for HVV displays. Detailed optical designs are reviewed for many of the principal laser types with emphasis on attaining the parameters necessary for digital and analogue holography.

A full review of current photosensitive materials for colour holography is given in Chapter 4. Such materials are totally key to ultra-realistic holographic imaging. Some great materials are available today and there are indications that further progress will occur in the field. For example, processing-free photopolymers with index modulations approaching and even surpassing those observed in dichromated gelatin have been discovered. Modern methods of analogue holography are covered in Chapter 5; the latest work in this field has demonstrated the production of holograms that are almost indistinguishable from real objects. Work has underlined the importance of choosing the correct recording lasers here and progress in laser engineering has greatly helped this field.

Chapter 7 is devoted to the relatively new but extremely exciting field of digital holographic printing. Digital holographic printing is distinct from computer-generated holography (CGH). Here, we describe the detailed design of various types of digital holographic printers. We explain how ultra-realistic volume phase holograms may be printed as a matrix of elementary volume holograms using computer image data. Unlike CGH, each elementary volume hologram is created by an optical interference process. We discuss the generation of HVV displays and the design of HVV printers. The image processing algorithms required for the different types of digital holograms are developed in depth in Chapters 8 and 9. Chapter 8 introduces the mathematical and geometrical notation but is otherwise devoted mostly to horizontal parallax-only holograms. Chapter 9 deals with practical computational algorithms required for the full-parallax case.

3D image data acquisition systems must be used when digital holograms are to be printed of real-world objects or scenes. The most popular type of system is the *Holocam*—a camera on one or more motorised rails. These systems and the image processing algorithms required to convert the raw image data to the format required by digital printers are reviewed in Chapter 10. Other techniques such as structural light are also reviewed.

Chapters 11 and 12 are devoted to physical theory of the holographic grating and the hologram. Here, we develop various models from first principles. Paraxial and fully non-paraxial formulae are derived for image distortion, image blurring and chromatic aberration. Kogelnik's coupled wave theory is derived from first principles and expressions for diffractive efficiency are given. We also review N-coupled wave theory and discuss the question of diffuse holograms and polychromatic gratings. Of special interest is Chapter 12, which describes a new theory capable of treating the polychromatic grating as an infinity of parallel stacked mirrors. This theory lends a useful insight to the interpretation of Kogelnik's model—an issue which is not usually taken up in standard texts but which is nevertheless of some importance for a proper understanding of the process of holographic diffractive reflection and transmission.

Illumination sources are of fundamental importance to holography as they dictate how the holographic image replays. We give an up-to-date review of these sources in Chapter 13. Of particular importance are

the new LED and laser diode sources. These devices are characterised by a much smaller value of étendue, a high power and a narrower bandwidth. They may be expected to improve, in a rather fundamental way, the displayed image properties of the polychromatic volume reflection hologram.

Finally, Chapter 14 contains a review of some of the most important applications of ultra-realistic holography. We include a section on scientific imaging where holographic microscopy, holography endoscopy and bubble chamber holography are discussed. Sections are also included on how digital holography can be used in advertising and display, urban planning, military mapping and architecture. Analogue holography is discussed in relation to its increasing interest from museums as a vehicle for both archival and travelling exhibitions. The book ends with a section on updateable and real-time digital full-colour holographic displays.

We have included a number of (mostly technical) appendices that should be of interest to workers in the field. Wherever possible in the book, we have tried to include enough detail so that the experienced reader may actually start using the techniques described. It is the authors' hope that this book will fill a gap that currently exists in the technical literature by providing a comprehensive treatment of holography and its key associated fields in the context of ultrahigh-fidelity full-colour imaging. By necessity, familiarity with a number of relatively advanced topics is assumed. Some of the chapters are completely non-mathematical; others, such as Chapters 8 through 10, despite the apparent complexity of expressions, only require a basic knowledge of mathematics. Chapters 11 and 12 probably require a slightly deeper knowledge, but nothing more than the mathematics learnt at the second or third year of a typical undergraduate course in mathematical physics. The book is, however, designed to be relatively modular and omission of the more mathematical chapters should not, in general, preclude a reading of the less mathematical ones.

Finally, we should point out that we have included within the book a number of photographs of holograms. In many previous books, it has always been possible to discriminate between a photograph of an actual object and a photograph of the hologram of the object. However, as the field progresses and the quality of images increases, this discrimination becomes increasingly difficult. Various hologram images we present here, particularly those recorded recently using the technique of full-colour analogue holography, may therefore appear to simply be photographs—which, of course, is not the case!

**H. I. Bjelkhagen
D. Brotherton-Ratcliffe**
London, UK

Acknowledgments

This book would not have materialised without the inspiration and encouragement of many people. Various people and institutions have also helped in providing material, which has made the book more interesting and more complete. First and foremost, we would both like to thank John Navas of Taylor & Francis, CRC Press for his encouragement and support in writing this book. Thanks also to Rachel Holt and Amber Donley of Taylor & Francis.

DBR: I would like to especially thank Nicholas Phillips, even though, sadly Nick is no longer with us, for the interesting and penetrating discussions I had with him, for his never-waning enthusiasm, and most importantly for his amazing inspiration: it was Nick's work that inspired me to take up holography in the first place. I would also like to say a special thank you to Stanislovas Zacharovas for his continual support with Geola over the years. I would like to thank Mikhail Grichine and Alexej Rodin for their part in introducing me to pulsed laser photonics and for many years of invaluable discussions; thanks also to Marcin Lesniewski for his vitally important input in the area of high numerical aperture Fourier transform objective design. I would like to thank Ramunas Bakanas for our long discussions on all aspects of laser physics and on the optics of digital holographic printers—and also for his unwavering commitment to Geola. I would like to thank Lev Isacenkov, without whom the Geola organisation would never have existed, and Eric Bosco and Lynne Hryniw, the founders of XYZ Imaging Inc., for their constant enthusiasm and great contribution to the practical realisation of direct-write digital holography. Thanks also to Yuri Sazonov and Olga Gradova, without whom Geola's work in digital holography would not have gotten very far, through lack of a suitable photosensitive film. Many thanks also to Paula Dawson, Juyong Lee and Jesper Munch for their support, first of Australian Holographics Pty. Ltd., and then of the Geola organisation. I should also mention Peter Hering from the Caesar Institute and Rob Taylor of Forth Dimension Holographics Inc. I would like to thank Andrej Nikolskij, Julius Pileckas and Jevgenij Kuchin at Geola, not only for their help in checking my formulae in Chapters 8 and 9, but also for their commitment over the years to Geola. Thanks also to John Fleming, who worked with me on the design project that led to Appendix 6, and to Chris Chatwin and Rupert Young for our fruitful collaborations at the University of Sussex. Finally, I would like to thank key members of the teams at Australian Holographics Pty. Ltd., LMC France Instruments SARL, Geola Technologies Ltd. (GT) and at the Centre for Laser Photonics (CLP) in North Wales—Geoff Fox (AH), Svetlana Karaganov (AH), Simon Edhouse (AH), Yasmin Farquhar (AH), Vytas Serelis (AH), Florian Vergnes (LMC and later manager of Geola UAB), Jerzy Lelusz (GT/CLP), Nataly Vidmer (GT/CLP), Lishen Shi (GT/CLP), Junhua Lu (GT) and John Tapsell (GT).

HB: I would like to thank Nils Abramson at the Royal Institute of Technology in Stockholm, who introduced me to holography in 1968 and who was responsible for my decision to select holography as a professional career. My Swedish colleagues, Per Skande and Johnny Gustafsson were involved in many of the commercial display holography projects carried out at Holovision AB in the 1970s. I would also like to express my gratitude to Tung H. Jeong, Lake Forest College, Illinois, for his collaboration in several projects including the *Lake Forest International Display Holography Symposia* with which I have been involved since 1982. Ed Wesly, from Chicago, has collaborated in many of my projects, both at Fermilab, Northwestern University, and holography business activities in Chicago. Thanks also to Max Epstein and Michel Marhic, Northwestern University, who were involved in many of the research projects carried out when I was working at the University in Evanston as well as being my colleagues at Holicon Corp. and the Light Wave hologram galleries in the United States. I am particularly thankful to Nicholas Phillips who invited me in 1997 to join him at the Centre for Modern Optics (CMO) at De Montfort University in Leicester, UK. Together, we worked on improving silver halide materials and processing methods, even after CMO moved to Wales. In particular, Nick had a lot of input into the European *SilverCross* emulsion project. Ardie Osanlou, my long-time CMO colleague, is gratefully

acknowledged for working with me on many of our holography projects. Peter Crosby and Evangelos Mirlis, one of my PhD students, have both been particularly helpful in the emulsion and museum holography projects. In regard to my Lippmann photography research, I must acknowledge Darran Green's important contribution. Since the 1990s, one of my main interests in holography has been to develop ultra-realistic 3D images, which required recording high-quality colour holograms, in particular, of the Denisyuk single-beam reflection type. My very first such experiments were carried out in France together with Dalibor Vukičević, Strasbourg University, who devoted a lot of his time helping to record the first successful results. I had the honour to know and meet both Emmett Leith and Yuri Denisyuk many times. I am very thankful for the many valuable discussions I had with them and for the support they gave me in my research on holographic recording materials and display holography applications. I want to also mention Gennady and Svetlana Sobolev, Michael Shevtsov and Vladimir Markov, who for many years, have been very helpful, providing me with insights into ultrafine-grain silver halide emulsions. In addition, I would like to mention my Bulgarian colleague and friend, Ventseslav Sainov, who has worked with me on emulsions and colour holography projects. Last but not least, I would like to express my deep gratitude to Teresa Bjelkhagen, who provided me with translations of important Russian publications such as N. I. Kirillov's 1979 book on ultrahigh-resolution emulsions. She has also supported my work in holography from the beginning.

Authors



Dr Hans I. Bjelkhagen, Professor Emeritus of Interferential Imaging Sciences at Glyndŵr University, Centre for Modern Optics (CMO), located in North Wales, UK, was awarded his Doctoral Degree in 1978 by the Royal Institute of Technology in Stockholm, Sweden.

Over the last 15 years, Bjelkhagen has received much international recognition for his work in the field of colour holography and holographic recording materials. He has specialised in recording Denisyuk-type colour holograms. He has also researched and improved Lippmann photography over a period of many years.

In 1983, Bjelkhagen joined CERN in Geneva, Switzerland, where he was involved in the development of bubble chamber holography. A year later, he participated in an international team project, recording holograms in the 15-foot bubble chamber at Fermilab in Batavia, Illinois. Between 1985 and 1991, he was employed at Northwestern University, in Illinois, working on medical applications of holography.

In 1997, Bjelkhagen was invited by Professor Nick Phillips to join him at CMO at De Montfort University, Leicester, England. In 2004, CMO moved to the then newly established OptIC in Wales.

In addition to scientific applications, Bjelkhagen is a well-known holographer who has recorded many holograms for 3D display purposes. From his early years in the field, he has been involved in large-format, high-quality display holography, using both pulsed and CW lasers. He has recorded many unique art objects, such as the Swedish *Coronation Crown of Erik XIV* (the crown dates back to 1561), and the Chinese *Flying Horse from Kansu* (from 100 AD). Bjelkhagen has worked with a number of famous artists, for example, Carl Fredrik Reuterswärd, creating holograms exhibited in many art museums and galleries around the world.

Bjelkhagen has also used pulsed holography to record a number of holographic portraits. In 1989, he recorded a portrait of the inventor of single-beam reflection holography, Yuri Denisyuk. The most famous person recorded by Bjelkhagen was President Ronald Reagan. His portrait was recorded on 24 May 1991. This was the first and, so far, the only holographic portrait recorded of an American President. A copy of this holographic portrait is held in The National Portrait Gallery of the Smithsonian Institution in Washington, DC.

Bjelkhagen has published more than 100 papers in refereed journals and conference proceedings, and holds 14 international patents. His most important academic contribution is a book on *Silver-Halide Recording Materials for Holography and Their Processing* published by Springer. He is a member of the Optical Society of America and is a fellow of the International Society for Optical Engineering (SPIE). He is the Chairman of SPIE's Photonics West Practical Holography Conference and SPIE's Holography Technical Group. He is an Accredited Senior Imaging Scientist and Fellow of the Royal Photographic Society (RPS) as well as Chairman of the RPS 3D Imaging & Holography Group. In 2001, he received the RPS Saxby Award for his work in holography, and in 2011, the Denisyuk Medal, from the D.S. Rozhdestvensky Optical Society, Russia.



Dr David Brotherton-Ratcliffe is the founder and scientific director of the well-known laser physics and holography organisation, Geola. He obtained a BSc (Hons) in Physics and Astrophysics from Queen Mary College, London University, in 1981. In 1984, while still at London University but now seconded to the United Kingdom Atomic Energy Authority at Culham Laboratories, he received a PhD for his work in nuclear fusion and magnetohydrodynamics. From 1985 to 1989, he continued to work as a theoretical physicist at the Flinders University of South Australia.

Brotherton-Ratcliffe first started to work in holography in 1982 during his doctoral studies, but it was not until 1989 that he founded Australian Holographics Pty. Ltd. and began working full-time in the fields of holography, optics and laser physics. During the 1990s, Australian Holographics became well known for its large-format display holograms, which were successfully marketed in Australia and throughout the Asia-Pacific region, often attracting significant media coverage.

In 1992, Brotherton-Ratcliffe founded the Geola organisation in Lithuania and began working seriously on high-energy pulsed laser technology. He founded associated companies in Australia, France and Romania, and travelled frequently between these countries for several years.

In 1999, Brotherton-Ratcliffe patented a key idea that proved to be highly influential: the printing of full-colour digital holograms, dot by dot, using RGB pulsed lasers. Over the years since 1999, Brotherton-Ratcliffe has come to be recognised as one of the leading workers in the expanding field of digital holographic printing.

Brotherton-Ratcliffe is the author of more than 14 patent families and over 60 publications in refereed journals and conference proceedings. He has published in the fields of plasma physics, magnetohydrodynamics, nuclear fusion, theoretical physics, laser physics, optics, holography and aerodynamics.

1

Ultra-Realistic Imaging and Its Historical Origin in Display Holography

1.1 Ultra-Realistic Imaging and Interferential Techniques

Modern high-definition flat-screen television displays offer a realism simply unthinkable just 10 years ago. Many such televisions now even offer the possibility of displaying high-quality three-dimensional (3D) images when used in conjunction with special glasses. From a certain perspective, today's television technology might well be regarded as falling within the category of "ultra-realistic imaging". However, if one examines the intrinsic information content of today's high-definition televisions, it is in fact far inferior to that of interferometric displays such as holograms or Lippmann photographs.

This book is about the technology of such interferometric systems and, most notably, about holography. Although the technologies underpinning the current display revolution are relatively mature, these technologies are nevertheless subject to certain well-defined limits. This is particularly true with 3D display. In contrast, interferometric displays, although they must still be regarded as being in their infancy, offer a clear potential to overcome some of the most important limits.

Interferometric displays have the innate and critical ability to reconstruct, to a high degree of precision, the original distribution of light emanating from a given scene. In the case of Lippmann photography, the frequency spectrum of the light can be reproduced with extraordinary precision. In the case of holography, it is the spatial structure of the image that is reproduced to an accuracy that can potentially reach a resolution of less than 1 µm. New techniques in colour holography provide the best of both worlds, offering the possibility of both excellent spectral and structural recording.

We can illustrate the huge difference between current non-interferometric displays and interferometric displays by comparing a modern 3D-enabled high-definition television with a full-colour digital hologram. The television display typically comprises several million pixels, each of which can be viewed from one point of view. The hologram, on the other hand, comprises roughly the same number of "holographic pixels", or hogels, but here, each hogel itself projects several million different images depending on the angle of view! The static information in the digital hologram is therefore a factor of some millions of times greater than that of the high definition static television display. This situation is even more marked for analogue holographic displays.

This incredible capacity to encode information, inherent to interferometric or holographic displays, leads to possible applications of this technology that would be extremely difficult to realise using non-interferometric principles. One such application is the holographic window. This is a 3D static or animated digital full-colour holographic display of extreme clarity and depth. It can be viewed from any distance and behaves just like a window—it could for example portray the view out of a New York skyscraper or the view out of a mountaintop restaurant. Such displays, when available at the correct price, are likely to become ubiquitous.

A physical window is something that we all take for granted. However, the window is very different from a high-definition television display. The light field surrounding a window is generally extremely complex—simply because the light traversing the window emanates from 3D objects, which are themselves complex. As a viewer approaches a normal television screen, the picture rapidly defocuses, and upon closer inspection, we see the pixels rather than a picture. In a 3D-enabled television, as we approach the screen, the perspective becomes completely erroneous. However, as we approach a window's surface,

our eyes simply focus through the window to view, in perfect clarity, the objects behind it. We shall explore later on in this book the detailed physical requirements necessary for the construction of a full-colour holographic window. However, it is clear that the current techniques of digital holography known today are very close to the point of being able to realise such displays.

Large-format digital holographic windows are not the only application for ultra-realistic imaging as promised by interferometric techniques. Archival and the display of museum artefacts are, for example, growing problems that could be addressed by holography. High-definition full-colour holographic displays now have such a realism that it can be extremely difficult to tell whether the object in question is a hologram or indeed the real thing. Museums often cannot afford to display their collections due to insurance costs, and in addition, priceless items are all too often damaged when transported to exhibitions. Next-generation holographic technology promises to offer real solutions to these problems and to bring the realism of important and interesting museum collections to more people.

New techniques in analogue colour holography have recently been shown [1] to be capable of reproducing oil paintings with exceptional fidelity. Progress in this area promises to lead to a whole new industry of copying or reproducing paintings of significant value or cultural significance. Again, next-generation technologies are expected to produce such accurate reproductions that viewing the copy will be no different from viewing the original.

The basic idea behind what we mean by ultra-realistic imaging is then the reconstruction of totally realistic light distributions as viewed by the human eye. Eventually, we might hope to do this in real time, such as in true holographic television (see, for example, [2]), but the information content of such systems is so high that it is probable that many static applications of interferometric displays will precede this.

The interferometric science of holography is almost certainly set to become a key field in twenty-first-century display systems. In the remainder of this chapter, we shall review the historical development of display holography. Much of what has occurred in the past cannot be described as “ultra-realistic imaging” of course. However, in the 64 years since holography was invented, the field has made great progress. We find ourselves today at a stage in which holography can really start to seriously provide the promise of ultra-realistic imaging. This book is about the technological and scientific issues involved in transforming today’s holographic technology into tomorrow’s ultra-realistic display science. To set things into perspective, we shall start by retracing progress to date. Additional historical information is included in Appendix 1.

1.2 Before Holography

Long before holography came into being, there existed a colour photographic recording technique known as Lippmann photography, the roots of which can be traced back to the beginning of the twentieth century. During that period, Gabriel Lippmann began experimenting with colour photography in France. His work concerned optical wavefront reconstruction through the recording of standing waves in a volume medium. Lippmann’s photographic recording technique was similar to the then unknown technique of holography; but it was not terribly effective as a viable commercial solution to colour photography at the time, because very long exposure times were required for practical use. This was due to the requirement of high resolving power, which could only be provided by materials of very low light sensitivity.

Lippmann was awarded the Nobel Prize in Physics for his invention in 1908. His technique was remarkable for its capability to record colour in a photograph but also for the way in which this was accomplished: this was a brand new idea—the recording of spectral information interferometrically in an ultrafine-resolution material. It was this idea of recording interference fringes throughout the depth of the emulsion that Denisyuk used in the former Union of Soviet Socialist Republics (USSR) when he introduced the technique of recording reflection holograms in the early 1960s. The technique of storing information in a recording medium as a physical interference structure constitutes the basis of the science of *interferential imaging*. Lippmann photography was the first interferential imaging technique discovered; this will be described in detail in Chapter 2.

Before the holographic theory was formulated as a coherent and comprehensive whole, a number of scientists (W. L. Bragg, H. Broersch and F. Zernike) considered the possibilities of x-ray microscopy for recreating an image from the diffraction pattern of a crystal lattice [3]. In 1920, the Polish physicist Mieczyslaw Wolfke wrote, “If an x-ray diffraction pattern of a crystal is illuminated with monochromatic light, a new diffraction pattern is created. This diffraction pattern is identical with the image of the object” [4]. However, it would take another 28 years until this idea was developed properly.

1.3 Early Holography

The holographic theory was presented to the world for the first time in 1948 by a Hungarian-born physicist and Nobel Prize winner, Dennis Gabor (1900–1979) [5–7]. At that time, Gabor (Figure 1.1) was trying to improve the resolution of the electron microscope by overcoming the spherical aberration of the lenses. He asked himself, “Would it not be possible to take first a bad picture, but one which contains the whole information, and correct it afterwards by a light-optical process?” [8]. He found that, by adding a coherent background as a phase reference, the original object wave was contained in the resulting interferogram, which he later called a *hologram*. Gabor concentrated on experimentally verifying his theory, using visible light of the best possible coherence that he could achieve for recording his holograms, which were of the in-line transmission type. He was forced to use filtered light from a mercury lamp, which he focussed through a pinhole. The resulting low intensity required a fast recording material. However, the demand on the material’s resolving power was much more severe when the first off-axis transmission holograms were recorded in the early 1960s utilising laser light. This was even more pronounced for the first reflection holograms, which required an even higher resolving power.

Even if holography had already been invented in 1948, it was not until the early 1960s that the scientific community became properly aware of it. The reason for this was that the laser had only been invented in 1960 [9,10], and with this discovery, the quality of recordable holograms simply skyrocketed. Progress in holography immediately after the discovery of the laser occurred almost simultaneously in both the United States and in the former USSR. At the University of Michigan, Emmett Leith (1927–2005) and Juris Upatnieks (Figure 1.2) had been working on side-looking radar and communication theory. They applied the same principles to optical electromagnetic wavelengths and published their first articles on holography in the *Journal of the Optical Society of America* [11–13]. Their 1964 publication revealed the possibility of recording transmission holograms of 3D objects by introducing an off-axis reference beam [14]. This new technique was different from Gabor’s technique because it separated the recorded image from the reference beam, making the holographic image substantially easier to view. A hologram

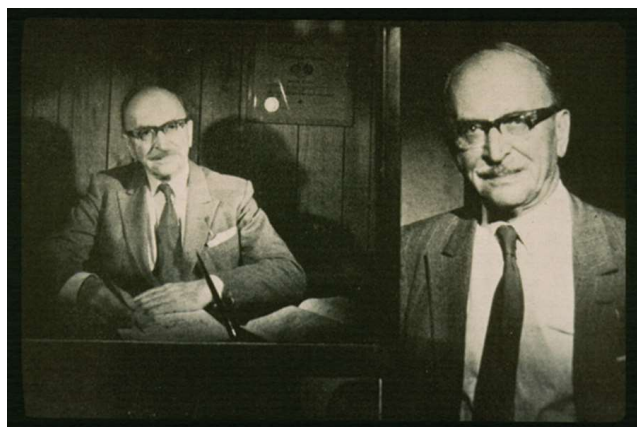


FIGURE 1.1 Gabor next to an off-axis transmission hologram portrait of himself. (Photo courtesy of the MIT MoH Collection.)



FIGURE 1.2 Upatnieks and Leith in the laboratory. (Photo courtesy of the MIT MoH Collection.)

of a model railroad engine (Figure 1.3) was put on display at the OSA spring meeting in Washington, D.C., in April 1964. At that time, Kodak produced the 649-F spectroscopic silver halide plates, which had a resolving power of 2000 line pairs per millimetre. This material was conveniently used by Leith and Upatnieks for their first laser-recorded transmission holograms, whose quality was remarkably good. The railroad engine hologram, illuminated by laser, displayed an extremely realistic 3D image and had a huge impact on the participants attending the meeting.

In principle, when a laser transmission hologram is illuminated using the same laser light used for the recording, the recorded holographic image is essentially identical to the light field emanating from the laser-illuminated object itself. The displayed hologram and its associated publication initiated tremendous

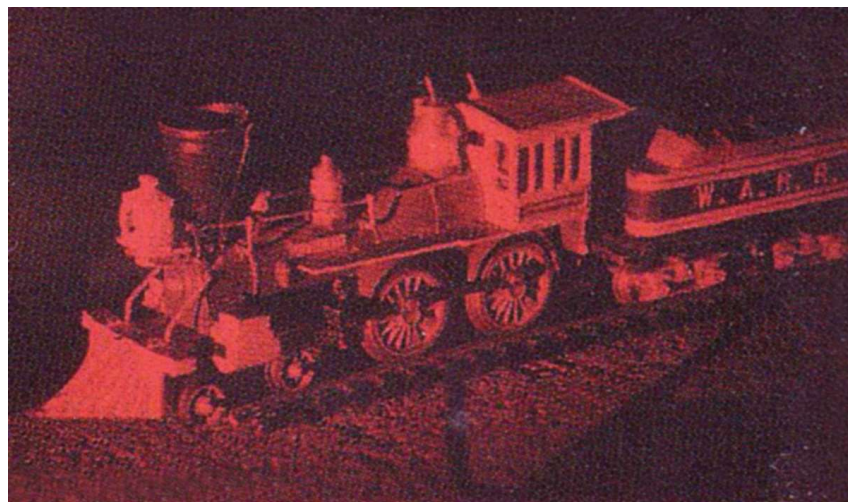


FIGURE 1.3 Leith and Upatnieks' off-axis transmission hologram, which was displayed in April 1964 at the OSA Spring meeting. (Photo courtesy of the MIT MoH Collection.)

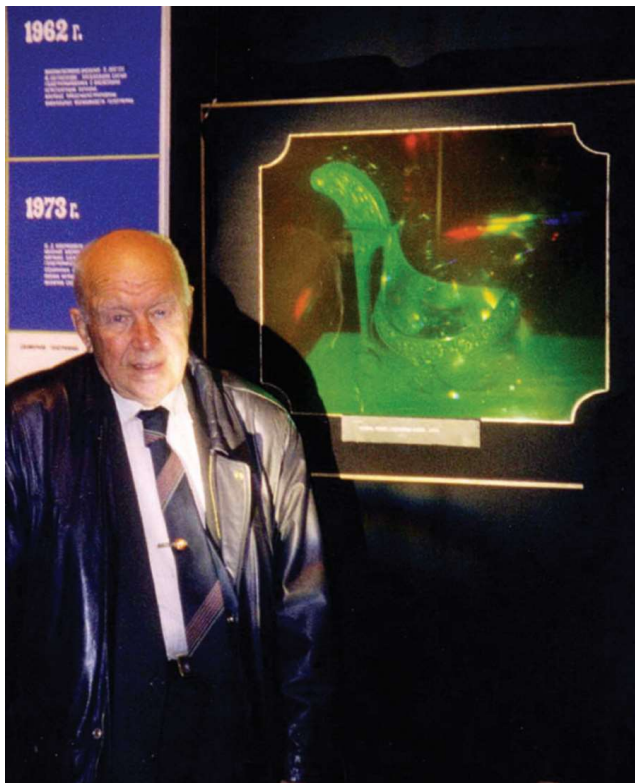


FIGURE 1.4 Yuri Denisyuk at the holographic museum in St. Petersburg next to an early, large single-beam reflection hologram.

worldwide interest in the new imaging technique of holography. The word *holography* was coined by Rogers; Gabor used the words *hologram* and *wavefront reconstruction* in his early articles [15].

Inspired by Lippmann's colour photographic technique, a different hologram-recording technique was invented in the former USSR by Yuri Denisyuk (1927–2006) [16,17] (Figure 1.4). For his first laser-recorded single-beam *reflection holograms*, he had to use a high-resolution emulsion made by him and Protas [18]. Like Gabor, both Leith and Denisyuk used mercury lamps for holographic recording experiments before they were able to use lasers.

1.4 Display Holography Milestones

As soon as the first laser-recorded holograms appeared, holography started to be promoted as a means of creating 3D images for display purposes. The interested reader is referred to a book by Johnston [19] on the detailed history of holography, including display holography. The reader new to holography may find it useful to also consult other books on holography to obtain information on the fundamental principles behind the different basic types of holograms and how they are recorded (see, for example, [20–27]). A recent book published in 2011 by Toal [28] gives a comprehensive discussion of most aspects of holography, including digital holograms and various modern applications, and is particularly recommended. In the following sections, we provide a brief historical review of the different types of hologram and how they were developed and promoted as a potential new 3D display medium. In addition to milestone achievements, some of the examples provided are also from the authors' own activities and projects in the field of display holography dating from the early 1970s until today.

1.4.1 Full-Parallax Transmission Holograms

The first type of hologram recording technique that could be used for display applications was the off-axis transmission hologram. Because only one laser wavelength was used for recording the first transmission holograms, only monochrome 3D images could be created. However, these off-axis transmission holograms provided remarkably realistic full-parallax 3D images. Lasers as well as yellow- or green-filtered mercury lamps were used for displaying the holograms. Lasers were used in public exhibitions until laser safety regulations were introduced. In 1972, two primary groups in the United States were developing laser standards; these resulted in the Z-136.1 (1973) standard. The American National Standards Institute created the concept of classifying lasers according to a scheme of graded risk of exposure and risk of injury involved. Later, laser safety regulations were introduced in Europe and other countries, mainly following the American regulations.

One of the main reasons why off-axis laser transmission holograms were able to provide such a realistic image was because the virtual image replayed in the same position that was occupied at the time of the recording by the object itself. This meant that the viewer's eyes focussed naturally on the exact location of the holographic image behind the plate. This was very different from the 3D display techniques in vogue at the time; with stereo photographs, one had to focus at the plane of the photograph independent of whether the image appeared behind or in front of this plane.

In addition to the accurate replay of the vertical and horizontal parallax, even the reflections contained in the first off-axis transmission holograms moved as in real life. The images were extremely sharp, and very soon, the analogy with looking through a window was coined. This analogy would become all the more appropriate as image quality and hologram size grew.

Lasers were found to produce the sharpest images on replay, but the phenomenon of speckle with lasers of too great a temporal coherence was disturbing. In the early days, filtered mercury lamps were therefore used; one could then no longer see the speckle, but the image was no longer as sharp as when using a laser, especially at larger image depths. The efficiency of the early transmission holograms was low and the noise high. Nonetheless, these early transmission holograms were received with surprise and appreciation; despite their imperfect images, these 3D "windows" constituted something simply never seen before.

1.4.1.1 Earliest Work at Conductron Corporation

In the beginning, most activities in display holography in the United States took place in and around Ann Arbor, Michigan. In the mid-1960s, the Conductron Corporation, which was owned by Keeve (Kip) Siegel, got involved in the field and started to develop and commercialise display holography. Gary Cochran and the staff at Conductron spent much time turning holography into a commercial 3D display technology. One of their first clients was General Motors, which ordered four large display holograms for the opening of the General Motors Building in New York. In 1966, Conductron was bought by McDonnell Douglas Electronics Co. in Missouri, but the research and production continued in Ann Arbor (not until 1970 was the operation moved to Missouri). The pulsed ruby laser, which had been developed at Conductron, was used for recording many large-format display holograms. Lawrence Siebert, who constructed the first pulsed laser at Conductron, recorded the first photographic portrait in 1967 (he was the subject) [29]. A picture of this first portrait hologram is shown in Figure 1.5.

The early pulsed hologram portraits produced very realistic images, but their monochrome appearance quickly led to them being regarded as "dead masks". One well-known McDonnell Douglas hologram was the 1972 *Hand in Jewel* hologram with a real image of a hand holding a bracelet. This image projected through Cartier's store window on Fifth Avenue in New York. The hologram was commissioned by Robert Schinella, who was marketing display holography applications at the time. Over the next few years, many display holograms were produced, some on square-metre plates. A well-known portrait hologram is the 50 cm × 60 cm hologram portrait of Dennis Gabor sitting behind a desk, which is shown in Figure 1.1. The hologram was recorded by Robert Rinehart at McDonnell Douglas to commemorate



FIGURE 1.5 Siebert in the first pulsed laser portrait. (Courtesy of the IEEE, 1968.)

the fact that Gabor was awarded the Nobel Prize in Physics in 1971. The hologram portrait was on display at the Royal Institute of Technology in Stockholm when Gabor received his Nobel Prize in December that year.

The first mass-produced hologram (500,000 copies) was a transmission hologram of chess pieces, which was included in the 1967 *World Book Encyclopaedia* and its *Science Year Annual*. A red filter was also provided to be used to illuminate the transmission film hologram with a white spotlight.

One of the first established artists to use the pulsed transmission hologram technique at Conductron was Bruce Nauman, who recorded a well-known series of holograms entitled *Making Faces* in 1968. His holograms were exhibited at the Castelli Gallery in New York. Another artist was Salvador Dalí, who made holograms with McDonnell Douglas and who also exhibited in New York at the Knoedler Gallery. Harriet Casdin-Silver (1925–2008) in the United States and Carl Fredrik Reuterswärd in Sweden are two other established artists who were attracted to lasers and holography, and created early holographic art pieces.

In 1973, McDonnell Douglas sadly closed its holography division because they had not achieved the marketing success they had hoped for. According to Kip Siegel's business philosophy, this may not have been a surprise. He had developed a reputation for believing that "What you have to do is to sell the *promise* of technology to investors", rather than a ready technology [30]. This idea was, and indeed continues to be, adopted by various display holography companies around the world; many start-up companies are still only able to sell the promise of technology to investors because even though holography has great potential, it is still currently a work in development. It is common that entrepreneurs promoting display holography and the investors who come into contact with the subject get very excited. Unfortunately, all too many underestimate the work required; there is a need to understand the technology and also its limitations as well as to develop a product that the market is willing to buy for a commercially profitable price.

1.4.1.2 Early Work in France

Soon after the world became aware of holography, universities and companies became involved in research and started to record display holograms. Early large-format transmission holograms were recorded in France at Viénot's Laboratoire d'Optique in Besançon. A very large and particularly impressive hologram was the $1\text{ m} \times 1.5\text{ m}$ *Venus de Milo* transmission hologram recorded by Jean-Marc Fournier and Louis Tribillon, which is shown in Figure 1.6.



FIGURE 1.6 Jean-Marc Fournier and the 1 m × 1.5 m *Venus de Milo* transmission hologram. (Courtesy of J.-M. Fournier.)

1.4.1.3 Paula Dawson

Paula Dawson from Australia was one of the first artists to take advantage of the very large image depths offered by laser transmission holograms. She recorded her first art holograms in Besançon, France. In 1980, she produced a large-format laser transmission hologram that was 95 cm × 150 cm in size entitled *There's No Place like Home*. In 1989, back in Australia and working at Heytesbury Holography Bell Resources Ltd., Melbourne, she created another 95 cm × 150 cm hologram entitled *To Absent Friends*; this piece, which was of a life-size bar decorated for New Year's Eve was recorded using a large-frame continuous wave (CW) laser and portrayed the bar after closure. Figure 1.7 shows Paula Dawson and the bar installation in the holographic laboratory. More about Dawson's art holograms can be found in [31].

1.4.1.4 Nick Phillips and John Webster

Nicholas (Nick) Phillips (1933–2009) and John Webster, both working in the United Kingdom, were the first scientists to use pulsed lasers for recording commercial display holograms. Both worked on improving the pulsed ruby laser for its use in holographic recording. Based on the modifications they made and on their advice, the JK ruby laser, manufactured in Rugby, United Kingdom, became the laser of choice for the recording of high-quality pulsed holograms around the world. Many large-format holograms were recorded by Phillips, both with CW and pulsed lasers. Some of these holograms were exhibited at two major hologram exhibitions in London at the Royal Academy of Arts (*Light Fantastic I* in 1977 and *Light Fantastic II* in 1978). These exhibitions were responsible for bringing many people into the field of holography, including one of the authors (DBR). Phillips also taught at the Royal College of Art in London, where art students now had access to a pulsed ruby laser recording facility.



FIGURE 1.7 (a) Paula Dawson showing how large her holograms are and (b) the bar installation for the hologram entitled *To Absent Friends*. (Panel b courtesy of P. McLean, 1989.)

1.4.1.5 John Webster and Margaret Benyon

John Webster, working at the Central Electricity Generating Board in Southampton, needed extremely high-quality, high-resolution holograms for nuclear fuel inspection [32,33]. In addition, he also worked with artists producing display holograms. Notably, he recorded pulsed holograms together with the artist Margaret Benyon, MBE [34]. He has also recorded display holograms for museums, for example, in Italy, as well as using holographic techniques to perform interferometric inspection of art objects. Later, he continued to work on pulsed holography, acting as a consultant in Canada and in the United States.

1.4.1.6 Ralph Wuerker

Ralph Wuerker at TRW Systems, Redondo Beach, California, was also a pioneer in pulsed lasers, double-pulsed display holography, and interferometric inspections. He was involved in recording holograms under zero-gravity conditions on the space shuttle (SL-3 mission) [35], as well as recording pulsed holograms of museum artefacts as early as 1969 and later in 1972 in Italy [36,37]. Wuerker's ruby laser was flown to Venice, where he recorded holograms of Donatello's *John the Baptist* and Pisano's *Mother and Child*.

1.4.1.7 40 J Ruby Laser Facility at Fermilab

When one of the authors (HB) worked on bubble chamber holography at Fermilab, Batavia, Illinois, in the early 1980s, a 40-J pulsed ruby laser (made by JK-Lumonics) was in operation. This laser was the most powerful ruby laser made by JK Lasers (we shall have more to say about this high-resolution imaging application in Chapter 14). Edward (Ed) Wesly, who was a member of the bubble chamber holography team at Fermilab, used the same laser in 1986 to record a very large-depth pulsed laser transmission hologram entitled *Man on the Motorbike*. A photo of this 30 cm × 40 cm hologram is shown in Figure 1.8.



FIGURE 1.8 Ed Wesly on his motorbike (1986; 30 cm × 40 cm laser transmission hologram shot with the 40-J JK ruby laser at Fermilab).

1.4.1.8 Hologram of Swedish Crown

An example of an early, highly publicised display holography project in Sweden was the transmission hologram of the *Coronation Crown of Erik XIV* (from 1561). The 20 cm × 25 cm off-axis transmission hologram was recorded by one of the authors (HB) in the cellar under the Royal Castle in Stockholm. The crown was moved from the treasury down to a room in the cellar on the night of 20 August 1974. Figure 1.9 shows HB next to the hologram recording setup with the crown. The CW He–Ne laser and photographic equipment were arranged directly on the floor. Note the Styrofoam panels surrounding the setup, which prevented air motion during the recording. The hologram (Figure 1.10) was installed in a special display case, where it was illuminated by a mercury-arc lamp equipped with a yellow filter (Figure 1.11). It was produced for the International Stamp Exhibition *STOCKHOLMIA'74* in Sweden. The Swedish Post had issued a series of five stamps featuring the Royal Treasures, including one of the



FIGURE 1.9 Recording of the *Crown* hologram in the cellar of the Royal Castle in Stockholm.

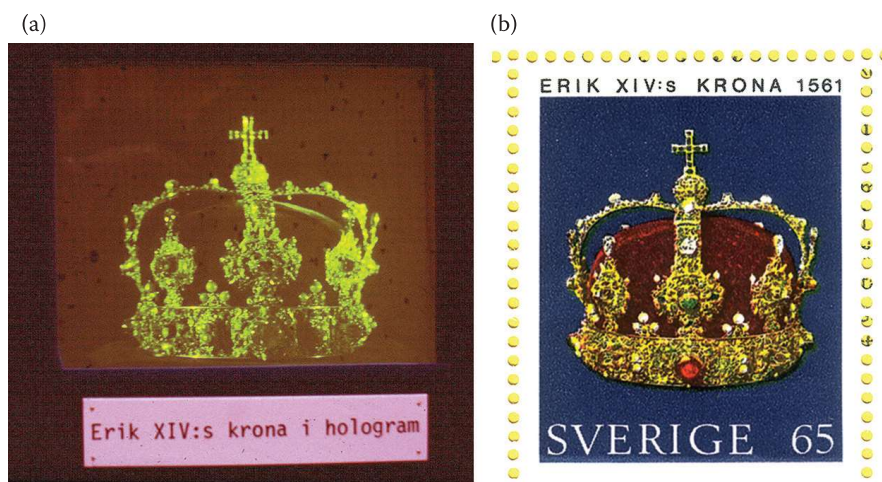


FIGURE 1.10 (a) The *Crown* hologram in the display case and (b) the Crown postage stamp.

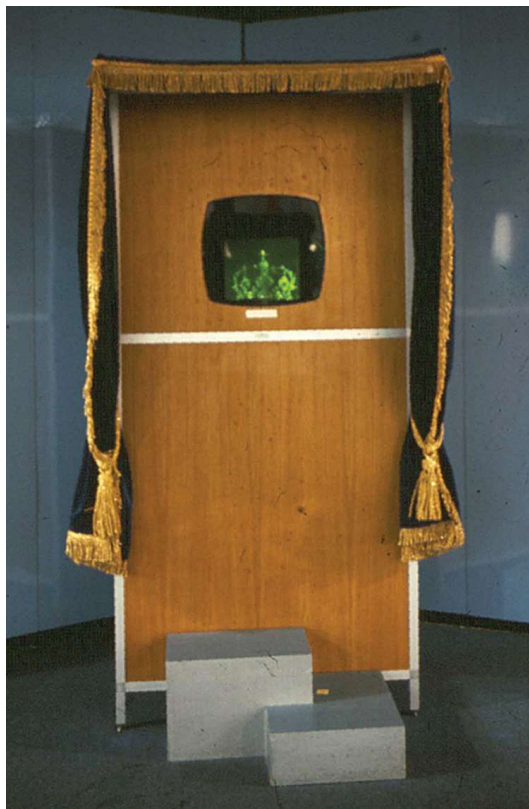


FIGURE 1.11 Crown hologram display case with a mercury lamp at the bottom.

Crown. Because it was not possible to show the real crown at the stamp exhibition, the hologram was ordered by the Swedish Post Authority as the next best thing. The stamp show took place between 21 and 29 September 1974 in Älvsjö, south of Stockholm. The hologram was a main attraction at the show, and people waited in long lines to be able to get a glimpse of the holographic crown. Many people came to the stamp exhibition only to see the hologram.

1.4.1.9 Carl Fredrik Reuterswärd

The Swedish artist Carl Fredrik Reuterswärd, who is better known for his *Non-Violence Sculpture* outside the United Nations Building in New York, recorded many early off-axis transmission holograms at holographic laboratories in Stockholm [38]. On 20 January 1963, he announced somewhat eccentrically in the *New York Herald Tribune* that he was going to be closed for holidays during the period 1963 to 1972 to devote his time to lasers and holography (Figure 1.12). As it turned out, his holidays extended until the end of the 1970s.

Reuterswärd created many large-format art holograms—one example was a piece entitled *Gateaux Gabor*, 50 cm × 60 cm, which he recorded in 1978 together with one of the authors (HB) at Lasergruppen Holovision AB. The hologram, which portrayed a burning cake, was made to celebrate the 30th anniversary of Gabor's 1948 article on holography. This was a nice example of how an interference pattern in a hologram could be used by an artist. One could visualise the heat from the burning candles, which created a tremendous 3D “smoke” pattern above the birthday cake (made of wood and with white silicon sealant serving as the whipped cream). During the recording exposure, the 30 candles were actually burning (Figure 1.13). The light emitted from the burning candles (mainly in the yellow–red region of the spectrum) did not fog the green-sensitive Agfa plate, which was exposed using a 514.5-nm argon-ion laser.



FIGURE 1.12 The *New York Herald Tribune* advertisement.

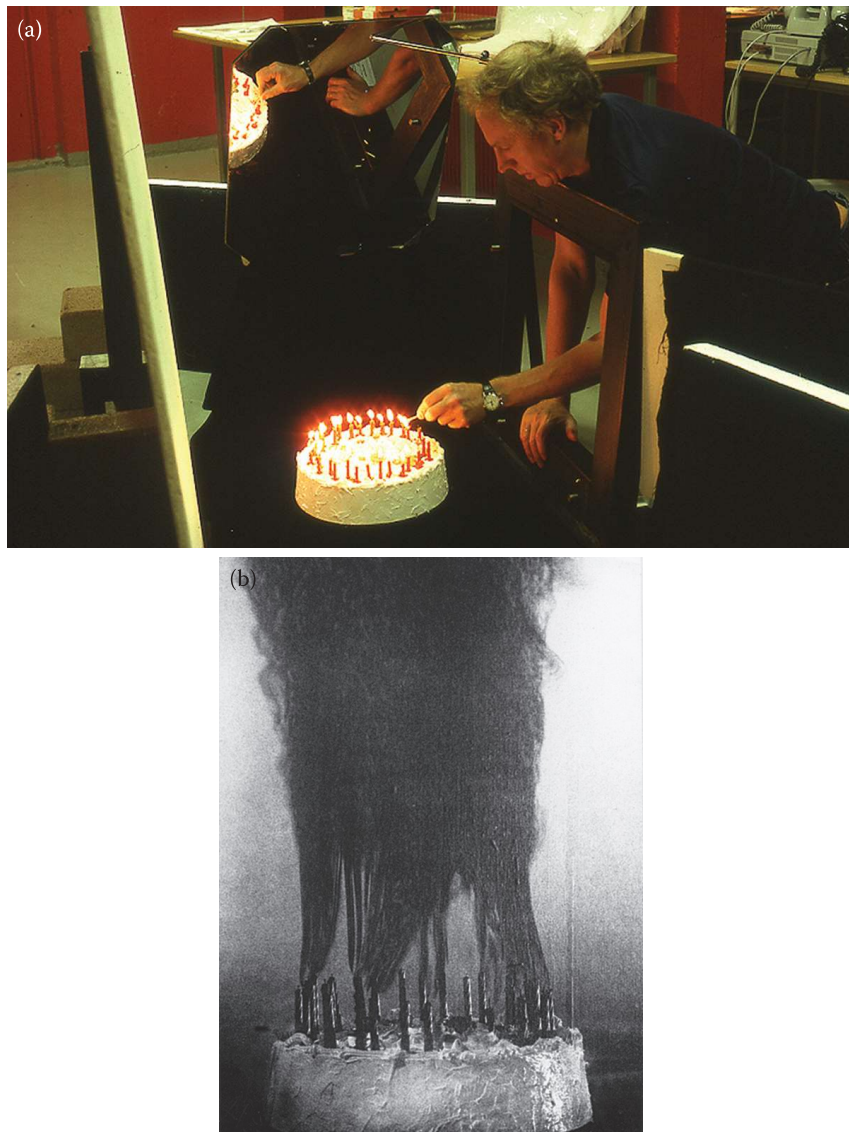


FIGURE 1.13 (a) Carl Fredrik Reuterswärd lights the candles through the holographic plate holder and (b) the *Gateaux Gabor* or *Smoke without Fire* hologram.

1.4.1.10 Demise of Laser and Mercury Lamp Transmission Holograms

By the end of the 1970s, despite their amazing ability to portray large 3D scenes, creating the illusion of a window into another world, large off-axis transmission holograms had more or less completely disappeared due to the practical problems of displaying them using either mercury lamps or lasers. Indeed, laser safety regulations now prevented powerful CW lasers from being used in public exhibitions, and this severely limited progress in the field. Off-axis transmission holograms continued to be produced, however, as master holograms or intermediate holograms. These are often referred to as H_1 holograms; rather than being themselves the final product, they simply serve to make white light-viewable hologram copies. These copied holograms are named H_2 holograms and can be of either the transmission or the reflection type. However, the H_2 is most often an image-planed reflection hologram in which a limited-depth monochromatic 3D image appears both behind and in front of the holographic plate. Most pulsed holographic portraits are nowadays transferred to such reflection copies.

1.4.2 Pulsed Holographic Portraits

Holographic portraits recorded using pulsed lasers were offered by several holographers and companies after Siebert recorded the first portrait in 1968. One of the authors (HB) has been involved in recording pulsed portraits since 1971, first in Sweden at the Royal Institute of Technology and at Lasergruppen Holovision AB and later in the United States at Holicon Corporation, Evanston, Illinois [39,40]. Unlike the earliest pulsed transmission holograms, the final hologram portraits were always reflection copies that could be illuminated using simple halogen spotlights. The downside to this convenience was that the image depth was severely limited in comparison with the laser-illuminated transmission hologram. Carl Fredrik Reuterswärd also created pulsed art holograms in cooperation with HB in Sweden. One example was a hologram entitled *Cross Reference* in which Reuterswärd posed as Salvador Dalí. His moustache was shaped to form the letters *C* and *R*, which are the initials both of the work and of Reuterswärd's first and last names (Figures 1.14 and 1.15).

In the former USSR, Vadim Bryskin recorded pulsed portraits using solid-state lasers developed in St. Petersburg. Among the holographers involved in the early recording of holographic portraits in the United States were Peter and Ana Maria Nicholson, who worked at the Center for Experimental Holography, Brookhaven National Laboratory in Long Island. Later, they moved to the University of Hawaii, where many portraits were recorded. Peter Nicholson gained access to the pulsed ruby laser from the McDonnell Douglas laboratories; McDonnell Douglas had donated their laser to the Smithsonian upon the closure of their laboratories. After returning from Hawaii, Ana Maria Nicholson continued recording portraits, first at the Museum of Holography in New York and then at the Center for the Holographic Arts located in Long Island City, New York (Figure 1.16).

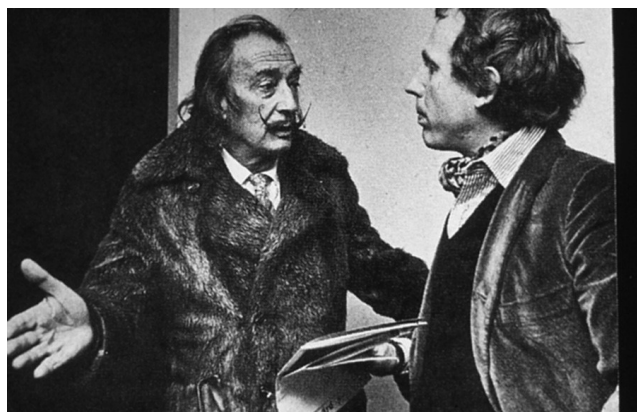


FIGURE 1.14 Salvador Dalí and Carl Fredrik Reuterswärd. (Courtesy of C. F. Reuterswärd.)

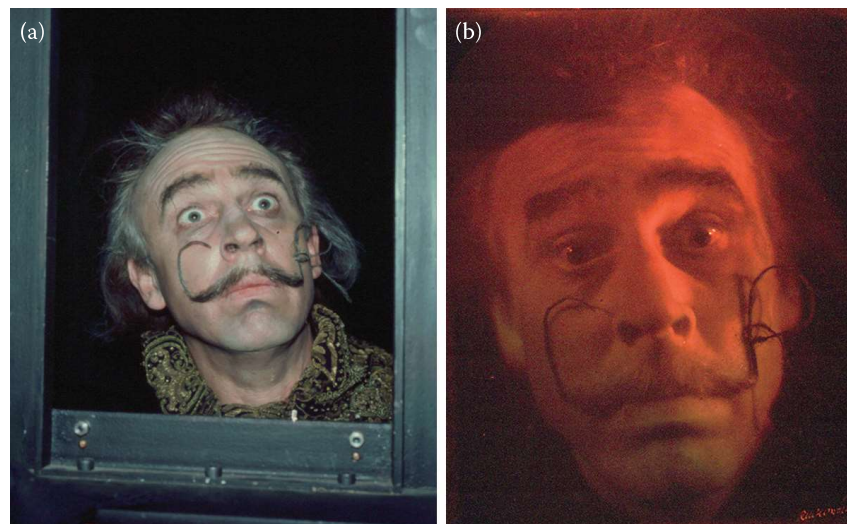


FIGURE 1.15 (a) Carl Fredrik Reuterswärd behind the plate holder. (b) *Cross Reference* hologram portrait.



FIGURE 1.16 Peter and Ana Maria Nicholson at the Long Island facility.



FIGURE 1.17 An example of combining a hologram and a gauche underpainting, carefully registered with the hologram entitled *Painted Margot* by Margaret Benyon.

Ron and Bernadette Olson operated a holographic studio in San Francisco, where they recorded many stunning pulsed portraits of people and animals using a neodymium YAG laser. Anaït Arutunoff Stephens (1922–1998) in California had her own in-house pulsed laser facility and created portraits and other art holograms.

As previously mentioned, Margaret Benyon, the first UK art holographer, active since the late 1960s, created many art pieces based on pulsed portraits. An example combining a hologram and a gauche underpainting, carefully registered with the hologram entitled *Painted Margot*, is shown in Figure 1.17 [41]. Regarding other portrait holographers from the United Kingdom, one should mention Edwina Orr and Martin Richardson, who both recorded portraits of famous people as well as creating pulsed art pieces. Martin Richardson's work has been documented in his book, *Space Bomb* [42]. Robert Munday is another holographer who started early on working at John Webster's laboratory and later with Nick Phillips at the Royal College of Art in London. In 1991, Munday started his own company, Spatial Imaging Ltd., where he recorded portraits of entertainment and sports celebrities. He has also pioneered the art of holographic stereography, a technique that he, together with Chris Levine, used to record the hologram portrait of Queen Elizabeth II.

There were also holographers in France who made early pulsed portraits. An interesting animated hologram portrait was recorded in 1978 at Laboratoire d'Optique in Besançon by Aebischer and Carguille [43]. A pulsed portrait studio existed in Paris in the 1980s and 1990s operated by Anne-Marie Christakis. Pulsed portraits were also recorded by Yves Gentet, who later became an expert in colour holography. On the border between Germany and France, Paul Smigielski and his team at the French–German Research Institute Saint Louis and HOLO 3 (both located in Saint Louis) recorded pulsed holograms (of the display type, including portraits) and interferometric holograms [44]. Michel Grosmann and Patrick Meyruies at the Louis Pasteur University in Strasbourg have also been involved with display holography since the early days.

1.4.2.1 Use of Neodymium Lasers for Portraiture Applications

Most of the pulsed holograms prior to the mid-1990s were recorded using ruby lasers. However, the deep red light of ruby led to rather waxy-looking portraits. The problem was that the topmost layer of human

skin was actually transparent to the ruby radiation. This meant that subjects had to be made-up heavily. The Olsons were one of a few to use neodymium YAG lasers as opposed to ruby lasers to circumvent this problem. One of the authors (DBR) worked with colleagues Mikhail Grichine and Alexey Rodin in Lithuania at the Geola Laboratories in the early 1990s to develop hybrid neodymium YLF/phosphate glass pulsed lasers suitable for holography [45–47]. Geola incorporated these pulsed lasers into semiautomated pulsed portraiture systems [48–54], which could also produce the H₂ copy. Many such systems were sold after the mid-1990s, and in fact, Geola continues to actively sell such systems today. Rob Taylor at Fourth Dimension Holographics, Inc. in the United States was one of the first clients for a Geola automated system. Taylor continues to produce holographic portraits today. The artist Juyong Lee in South Korea also currently operates a Geola system. Lee has made many large pulsed reflection holograms—for example, his 1999 *Dreaming History* series.

During the 1990s, as well as manufacturing pulsed lasers and automated pulsed laser holography systems, Geola also operated its own holographic portraiture studio in Vilnius, where holograms were produced of works by many artists, including the German artist H. R. Giger.

1.4.2.2 Reagan Portrait and Portraiture into the Future

Probably the most famous person to be recorded in a pulsed hologram portrait was President Ronald Reagan. One of the authors (HB) and a team from Holicon Corporation recorded the portrait (Figure 1.18) at the Brooks Institute of Photography in Santa Barbara, California, on 24 May 1991 [55].

Monochrome holographic portraits (often replaying as orange–yellow or green images) initially fascinated people, but their intrinsically waxy images and high prices always stifled sales. Even in the ex-Soviet Union, sales remain small today—Sergei Vorobyov continues to sell holographic portraits from his studios in Moscow, where he has done so for more than 25 years.

However, a new type of digital holographic portrait is available today. These holograms are fundamentally more appealing than the earlier pulsed portraits, and laser irradiation of the subject is not required. They can include limited animation, and the images from which they are made are derived using either modern structured light techniques or, in the case of horizontal parallax-only holograms, by a digital camera moving along a horizontal rail. We shall have a lot more to say about such modern digital techniques later on.



FIGURE 1.18 (a) The recording of the Ronald Reagan portrait—from left to right, Ronald Reagan, one of the authors (HB) and Ernest Brooks II; (b) the Ronald Reagan portrait.

1.4.3 Steven Benton's Rainbow Hologram

Among the articles on holography published toward the end of the 1960s, one particular publication is especially important. The article by Stephen Benton (1941–2003) described a white light-viewable transmission hologram—the so-called *Rainbow Hologram* or *Benton Hologram* [56]. Figure 1.19 shows Benton next to the 1977 *Crystal Beginnings*, a rainbow hologram recorded at Polaroid Corporation.

The rainbow hologram technique was an important improvement for recording transmission holograms because these holograms could be viewed using the white light from an ordinary halogen spotlight. The holograms were bright because they used the entire spectrum of the illuminating light and could represent much deeper images than the normal type of analogue reflection hologram. They were also extremely colourful, which again differentiated them from the intrinsically monochrome images of the laser transmission and white-light reflection holograms known before. The downside was that these new rainbow holograms did not encode the vertical parallax and exhibited a rather narrow viewing window in the vertical direction.

The rainbow technique is a two-step process in which the master H_1 is reduced to a horizontal section of the holographic plate (a slit with very little vertical extension) or to a narrow film strip. The transmission H_2 hologram is the final rainbow hologram that is generated from the strip master. When the rainbow hologram is illuminated with white light, a real image of the horizontal strip floats in front of the H_2 and acts to disperse the illuminating light into a rainbow spectrum. When the viewer's eye is coincident with the real image of the slit, a sharp image becomes visible. Depending on where the viewer's eyes are located in the vertical direction, the colour and magnification of the perceived image change.

1.4.3.1 Transmission Pseudo-Colour Techniques

It is also possible to generate rainbow holograms with mixed colours by using more than one slit. The *pseudo-colour transmission technique* is based on multiple white-light rainbow holograms in which different spectra are superimposed at the position of the observer's eyes. Often, these holograms are very impressive regarding both their colour composition and brightness. One problem though is that the colours and image magnification of any Benton-type hologram varies depending on the vertical position of the observer. The multicolour technique for rainbow holograms was introduced in 1977 by Tamura [57].

A slightly different type of transmission hologram, which produces a multicoloured image when illuminated by white light, was introduced by Hariharan [24]. Here, the hologram is made as a number of

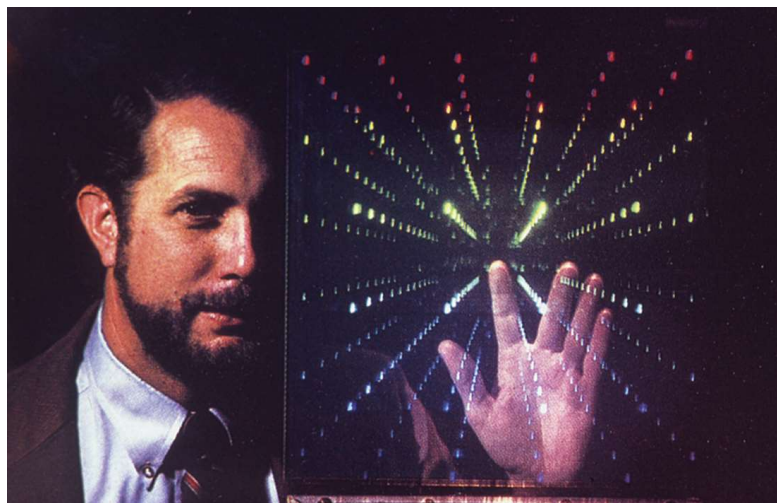


FIGURE 1.19 Stephen Benton with his rainbow hologram *Crystal Beginnings*. (Photo courtesy of the Jeanne Benton MIT MoH Collection, 1980.)

superimposed component holograms formed from optical images of a subject. These images are formed either by an optical imaging system or by separate primary holograms of the subject. Each primary (slit) hologram is formed using coherent light of a given wavelength and is designed to be reconstructed upon viewing of the final transmission hologram at that particular wavelength. The use of a sandwich of two photosensitive media, each containing at least one component hologram, to form the product transmission hologram was also described by Hariharan. Grover and Tremblay [58] also demonstrated the possibilities of creating natural-colour rainbow holograms.

1.4.3.2 Large Rainbow Display Holograms and Embossed Holograms

Rainbow holograms, being transmission holograms, must be illuminated from behind. This makes them uniquely suitable for shop window displays where images can actually project out in front of the window. Large rainbow holograms recorded on silver halide materials are often used as promotional 3D displays. Rainbows are well suited to such applications because of their superior brightness and because of their ability to portray large depths without defocusing. The holograms can also be laminated to a mirror if standard front illumination is required. The rainbow technique became popular among artists early on and it was also quickly adopted as the holographic technique of choice for the mass production of document security holograms (Figure 1.20). The first company to use holograms on credit cards was MasterCard



FIGURE 1.20 Embossed mirror-backed rainbow credit card holograms.

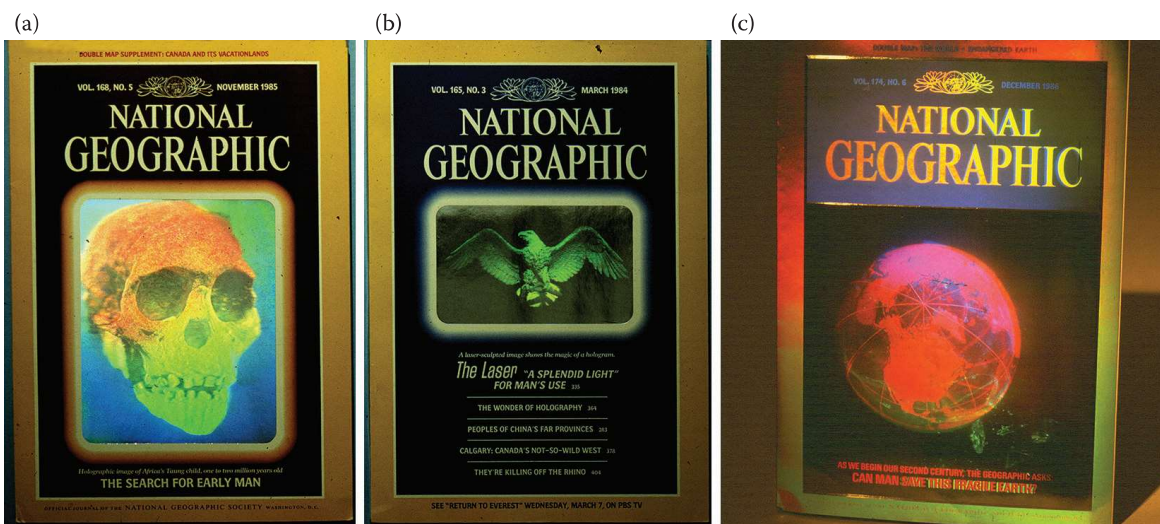


FIGURE 1.21 Three *National Geographic* covers with embossed holograms. (a) November 1985, (b) March 1984 and (c) December 1986.

towards the end of 1982. The holograms were produced by American Bank Note Holographics, Inc. Later, VISA also introduced holograms on their credit cards.

The mass-produced rainbow holograms used for security applications were produced on nickel shims using relief patterns; these relief patterns were then embossed onto plastic materials. The manufacturing of document security holograms remains today the main commercial application of holography. Such holograms or similar types of optical variable devices (OVDs) are not only used on credit cards but also on banknotes, passports and legal documents. Mirror-backing is almost always applied to security holograms, which explains why these optical variable devices always have a mirror-like appearance.

Another early application of mass-produced embossed holograms was the inclusion of holograms on journal covers. For example, there were three *National Geographic* covers in the 1980s that featured such holograms, 11 million copies being produced for each issue (Figure 1.21).

1.4.3.3 US Rainbow Displays—Holographics North Inc.

John Perry of Holographics North in the United States has been a driving force in the application of large-format rainbow holograms for display applications for many decades [59]. The size of such displays has reached several metres in width but has usually been constrained to a metre in height by the availability of the photographic material. Perry has worked with artists as well as recording holograms for advertising companies and trade shows. Most often, such large-format rainbow holograms were recorded on film. One example of Perry's work is the Tonka Toys hologram, mastered by Holicon Corporation and transferred by John Perry. In 1987, both Hasbro (*Visionaries*) and Tonka Toys (*SuperNaturals*) produced toys with holograms attached. To promote this new line of toys, Tonka Toys ordered a large-format hologram to be exhibited in a New York Toy Show. The hologram is shown in Figure 1.22. By using the pseudo-colour technique described above, the text at the top of the hologram appeared in a different colour.

1.4.3.4 French Rainbow Displays—AP Holographie SARL

In France, AP Holographie, located in Metz and run by Jacques Bousigné, François Mazzero and Jean-François Moreau, was also well known for their large-format rainbow holograms. They

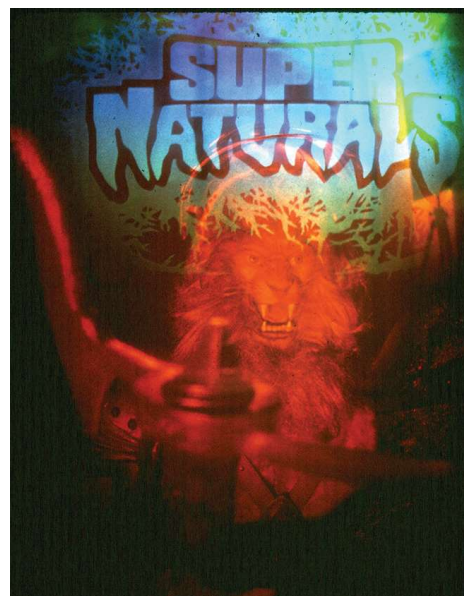


FIGURE 1.22 The Tonka Toys rainbow hologram.

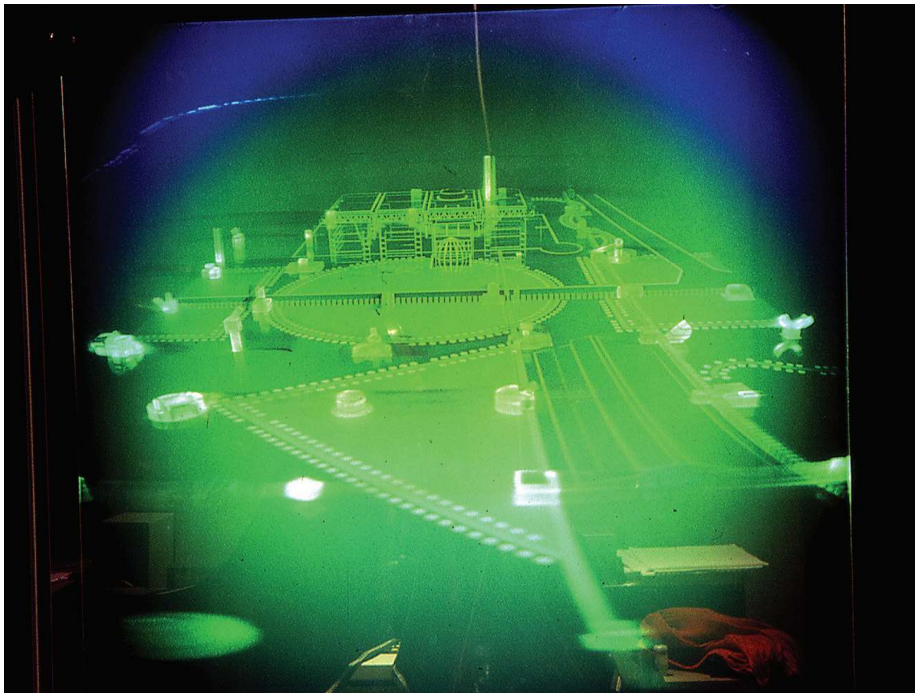


FIGURE 1.23 *La Villette* rainbow hologram by AP Holographie.

produced many holograms for the 1983 Geneva Car Show. Another famous AP rainbow hologram was the square-metre *Parc des Folies à la Villette* produced in 1983 and is shown in Figure 1.23. The hologram was recorded from an architect's model and produced to promote La Villette Science Park in Paris.

1.4.3.5 Australian Rainbow Displays—Australian Holographics Pty. Ltd.

From 1989 to the mid-1990s, Australian Holographics Pty. Ltd., based in Adelaide, South Australia, produced some extremely large rainbow holograms. The company was founded by one of the authors (DBR) and was later (circa 1993) managed by Simon Edhouse. The chief holographer was Geoff Fox. Yasmin Farquhar ran the company's two popular holographic galleries in Adelaide and Hahndorf. The large analogue pseudo-colour rainbow holograms produced by Australian Holographics were made on a floating 25 tonne optical table (Figure 1.24) measuring $5\text{ m} \times 6\text{ m}$ [60]. The recording laser was a Coherent Innova argon laser of 5 W, although large-frame krypton and argon-pumped dye lasers were later added for the production of metre-square reflection holograms.

One of the peculiarities of the Australian system was that the rainbow masters, which could be well over 2.3 m long, were all side-illuminated by a small spherical mirror and mounted in oil. Juyong Lee was one of the first artists to collaborate with Australian Holographics. Lee worked at the company's facilities in 1993 to produce a series of 10 pseudo-colour rainbow holograms measuring $2.2\text{ m} \times 1.1\text{ m}$, which formed part of the 1993 EXPO in South Korea. In 1994, Australian Holographics made a series of metre-square rainbow holograms for the Singapore Military, which were installed in the Singapore underground system; the installation was reported in newspapers and on Singapore national television like many of the company's higher profile projects. Paula Dawson was another artist to work at Australian Holographics, producing a hologram of a huge sculptured dome in 1995.

In 1994, Australian Holographics gained access to the large collection of artefacts owned by the museum of South Australia. The joint venture, the signing of which was again covered on national television and was even debated in the state parliament, led to the company producing some spectacular



FIGURE 1.24 Dmitry Konovalov (left), cofounder of General Optics Pty. Ltd., and Geoff Fox (right), chief holographer, sitting on the giant 25 tonne, 5 m × 6 m pneumatically suspended table at Australian Holographics.

large-format rainbow holograms of such items as the museum's T-rex skull (Figure 1.25) and its unique Thylacine exhibits. Some of these holograms, even though nearly 20 years old, still come onto the market today from time to time. When Australian Holographics closed in the late 1990s, its equipment was split between Adelaide University and the Geola Company in Lithuania.

1.4.3.6 Parameswaran Hariharan

Parameswaran Hariharan is an Indian-born scientist and a pioneer of holography in Australia. He worked at the Commonwealth Scientific and Industrial Research Organisation in Canberra. Hariharan's main research field was display holography and interferometry [24]. He introduced new processing techniques for holography and described how to produce pseudo-colour display holograms of both the transmission and reflection types, including sandwich techniques as well. He was the first to make a successful hologram in colour using three lasers and, for a time, collaborated with the artist Alexander in producing large holograms and surrealistic holographic stereograms.

1.4.3.7 Günther Dausmann

In Germany, Günther Dausmann has been involved in display holography since the beginning. His first company, Holtronic, offered both equipment and large-format CW and pulsed transmission and reflection holograms including stereograms. Later, he focussed on document security holograms, and in 2001, he produced the two-dimensional monochrome photopolymer hologram portraits for the German passport. His company, Holography Systems München GmbH, is now part of the successful document security company Hologram Industries in France, and his German operation has changed to Hologram Industries Research GmbH.

1.4.3.8 Dieter Jung and Rudie Berkhouwt

Among the established artists who have been attracted to rainbow holograms, one should mention Dieter Jung in Germany [61]. Jung created many large-format holograms—for example, the *Into the Rainbow*



FIGURE 1.25 (a) Monique Haan preparing a T-rex skull from the South Australian Museum in 1994. (b) Holographer Mark Trinne mounting the heavy skull on the optical table at Australian Holographics. (c) The mounted skull illuminated by argon laser light.

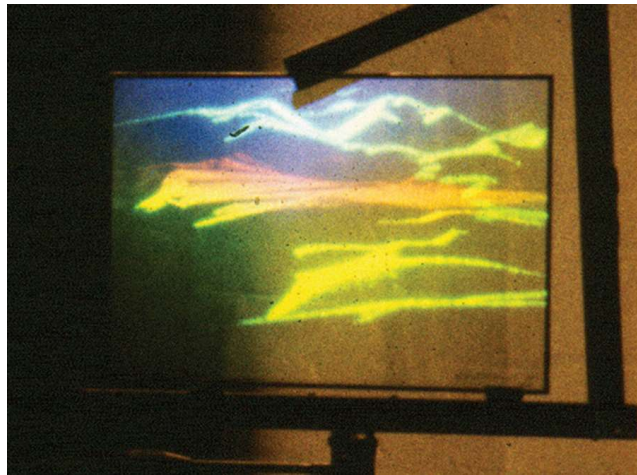


FIGURE 1.26 The 4-D *Landscape* hologram by Rudie Berkhouwt.

hologram series (one embossed version of *Into the Rainbow* is on the cover of the book made by Topac GmbH [61]). Rudie Berkhouwt (1946–2008) working in United States is also well known for his beautiful art rainbow holograms—an example is shown in Figure 1.26.

1.4.4 Circular Transmission Holograms

By surrounding an object with a film and adding a reference beam from above the object, it is possible to record a circular transmission hologram having a 360° image. This technique was first published in 1966 by Jeong et al. [62]. However, the technique has rarely been used to record display holograms. A large-diameter (120 cm) circular hologram of this type was recorded by Upatnieks and Embach in 1980 [63]. A special hologram viewer was constructed to rotate the hologram permitting it to be viewed from a stationary position. The project involved recording holograms of musical instruments and the hologram viewer had an associated audio tape to demonstrate the sound of the various instruments displayed.

1.4.5 Achromatic or Black-and-White Holograms

As a complement to rainbow and monochrome holograms, there has been interest in creating achromatic or black-and-white holographic images. With regard to rainbow holograms, Benton developed a technique to make an achromatic image hologram in 1978 [64]. His first such hologram was *Aphrodite*; later, he recorded a hologram of a mummy's skull, *Pum II*, which became part of a Smithsonian Institute programme to provide 3D copies of valuable artefacts in danger of decay or loss.

It should be mentioned that the emulsion thickness manipulation techniques for producing pseudo-colour reflection holograms can also be used to create black-and-white images. Orr and Trayner [65] produced impressive large-format black-and-white holograms using emulsion thickness manipulation in-between recordings. In this case, only two colours are necessary to create white. In the Commission Internationale de l'Eclairage (CIE) diagram, the colours should be chosen in such a way that a straight line drawn between them should pass right through the white region in the centre of the diagram. Obviously, there are many possibilities for choosing the primary colours that satisfy this condition. Orr and Trayner used yellow and blue, which they achieved by preswelling the emulsion with different concentrations of triethanolamine. The technique was used during the transfer process of the pulsed masters to the reflection copies. The 50 cm × 60 cm reflection hologram, *Kate McGougan & Stephen Jones Hat* (styled by Robin Beeche), made by Edwina Orr and David Trayner (Richmond Holographic Studios Ltd.) is an excellent example of a black-and-white hologram and is shown in Figure 1.27.

By producing an inverted rainbow spectrum using a diffraction grating, and using this to illuminate a transmission hologram, it is also possible to create achromatic images, a technique introduced by Kevin



FIGURE 1.27 *Kate McGougan & Stephen Jones Hat* black-and-white portrait hologram. (Courtesy of 1985 Edwina Orr and David Trayner. Richmond Holographic Studios.)

Bazargan in 1985 [66]. An important application of this technique is the holographic medical imaging application, which allows computerised tomography (CT) and magnetic resonance images (MRI) to be visualised as achromatic 3D holographic images. These multiplex holograms, developed and produced by Stephen Hart at Holorad LLC (former Voxel) Voxel in Salt Lake City, Utah, are still in use today. The image data is generated from a series of sequential slices of computerised tomographic or magnetic resonance imaging data [67]. A single piece of holographic film is then exposed multiple times to create the hologram by multiplexing these slices in depth. When the film is processed, the resulting hologram is referred to as a *Voxgram*. It must be examined on a special display unit called a *Voxbox*; it is this display device that produces the inverted rainbow spectrum required for illumination. Applications such as imaging brain tumours and related vasculature before surgery can be visualised in 3D and full parallax. A Voxgram hologram is shown in Figure 1.28.

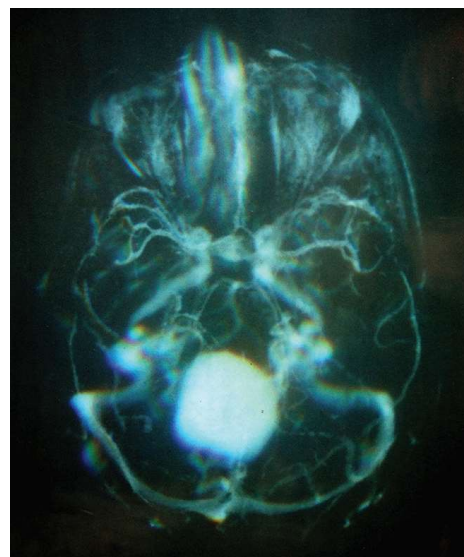


FIGURE 1.28 Achromatic Voxgram of a brain tumour.

1.4.6 Monochrome Reflection Holograms

In 1962, Denisyuk introduced the single-beam reflection recording technique; shortly after this period, such holograms started to be used for 3D displays. Because the technique was introduced in the former USSR, it is natural that such white-light holograms were mainly recorded in countries from the Soviet Union. Another reason was that the required ultrafine-grain silver halide emulsions already existed there. In Western countries, white-light holography was dominated by Benton's rainbow technique and this only changed when Agfa introduced their monochrome HD emulsions and when low-noise processing techniques had been developed. Nick Phillips (Figure 1.29) was able to record high-quality reflection

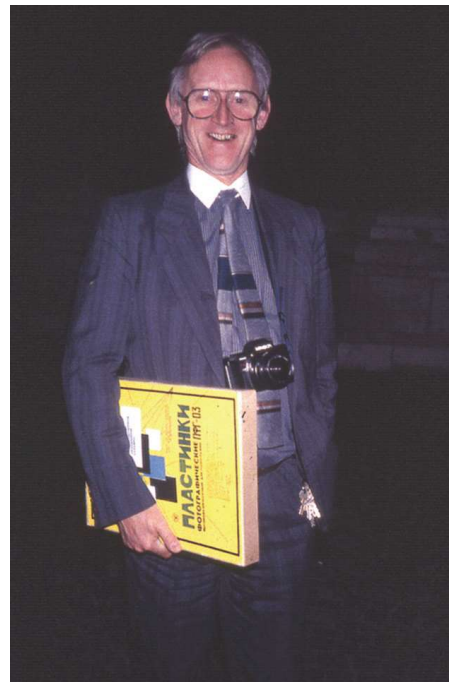


FIGURE 1.29 “Bridging the gap between Soviet and Western holography”, Nick Phillips with a box of Slavich PFG-03 holographic plates.

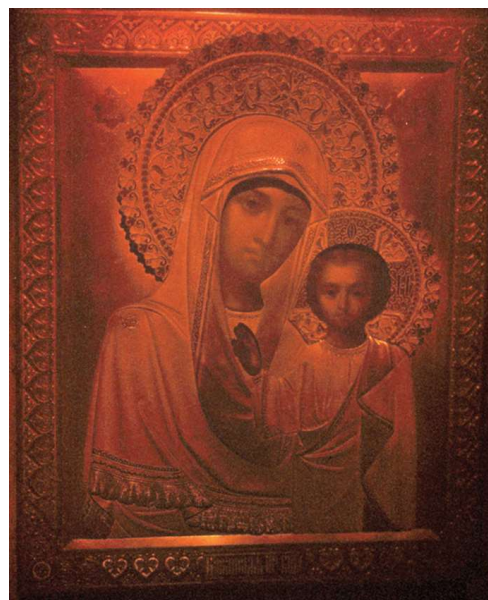


FIGURE 1.30 The *Icon* Denisyuk hologram by Vanin.

holograms based on his low-noise processing on Agfa and, later, on Ilford materials [68–70]. By the late 1970s, high-quality reflection holograms on Agfa and Ilford emulsions were being used to record museum artefacts and also for advertising and product promotion projects.

Early Denisyuk reflection holograms from the former USSR were very impressive. This was due principally to the ultrafine-grain emulsions, which ensured that the diffraction efficiency and signal-to-noise ratio of the holograms were very high. Holograms of many artefacts from museums, such as the Hermitage in St. Petersburg were recorded and used at exhibitions. An example of a typical Denisyuk hologram is the *19th Century Icon* hologram produced by Valery Vanin in 1981 and reproduced here in Figure 1.30.

1.4.6.1 Sweden—*Lasergruppen Holovision AB*

A hologram of a *Gold Collar* is an early example of how a monochrome Denisyuk reflection hologram was used in a museum display in place of the real artefact. The 30 cm × 40 cm hologram was recorded in 1980 by Lasergruppen Holovision AB in Stockholm, Sweden. The three-ringed gold collar with filigree, granulation and carved figures was found in 1827 in Sweden and is from AD 400 to 550. Because of its high value, the collar is kept in the National Historical Museum in Stockholm. A local museum located near the place where the gold collar was found, *Falbygdens Museum*, was not allowed to exhibit the real gold collar, so they decided to exhibit a hologram of it instead. The collar hologram and its display case are shown in Figure 1.31. Today, modern colour holography can offer something even more realistic than this stunning yellow monochrome hologram from 1980.

Another early example of a large Denisyuk hologram produced by Lasergruppen Holovision AB is the 50 cm × 60 cm *Alfred Nobel Bust* plate ordered by the Swedish Nobel Foundation. The recording took place in 1981; the hologram recording setup in the laboratory is shown in Figure 1.32. Figure 1.33 depicts a photograph of the finished yellow–orange tuned hologram. This hologram, on display in the Nobel Foundation Building in Stockholm (Figure 1.34), has a label next to it stating that the hologram is based on five Nobel prizes in physics.

Another example by Lasergruppen Holovision AB is a 30 cm × 40 cm advertising hologram, the *Martini* hologram. This hologram was on display at Stockholm's International Arlanda Airport. Alcoholic beverages could not be advertised using photographic advertising, but advertising using holograms was still acceptable at that time. The hologram display cabinet at the airport is shown in Figure 1.35.

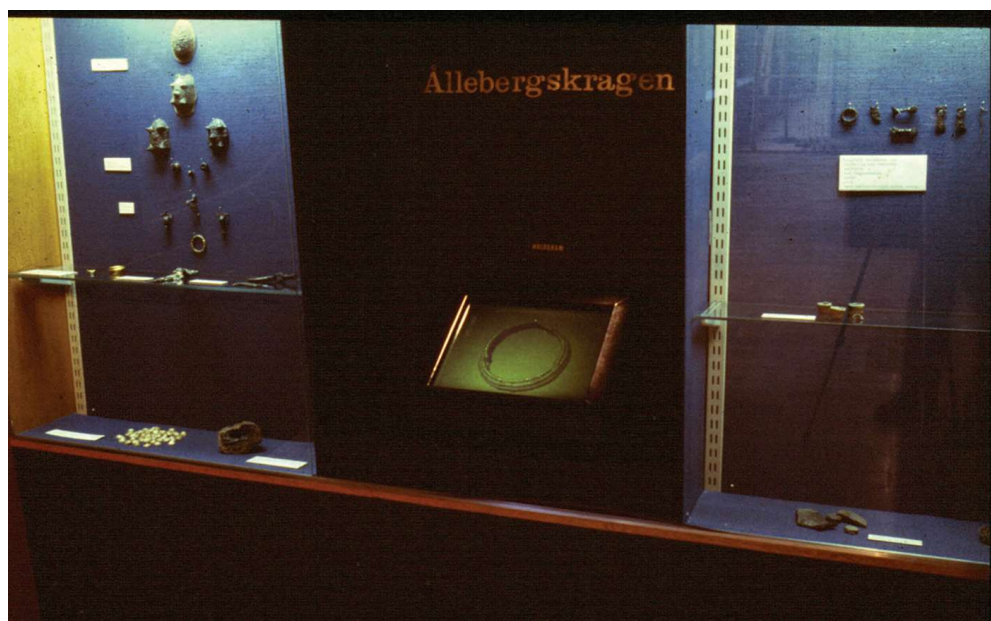


FIGURE 1.31 The *Gold Collar* hologram in the museum display.

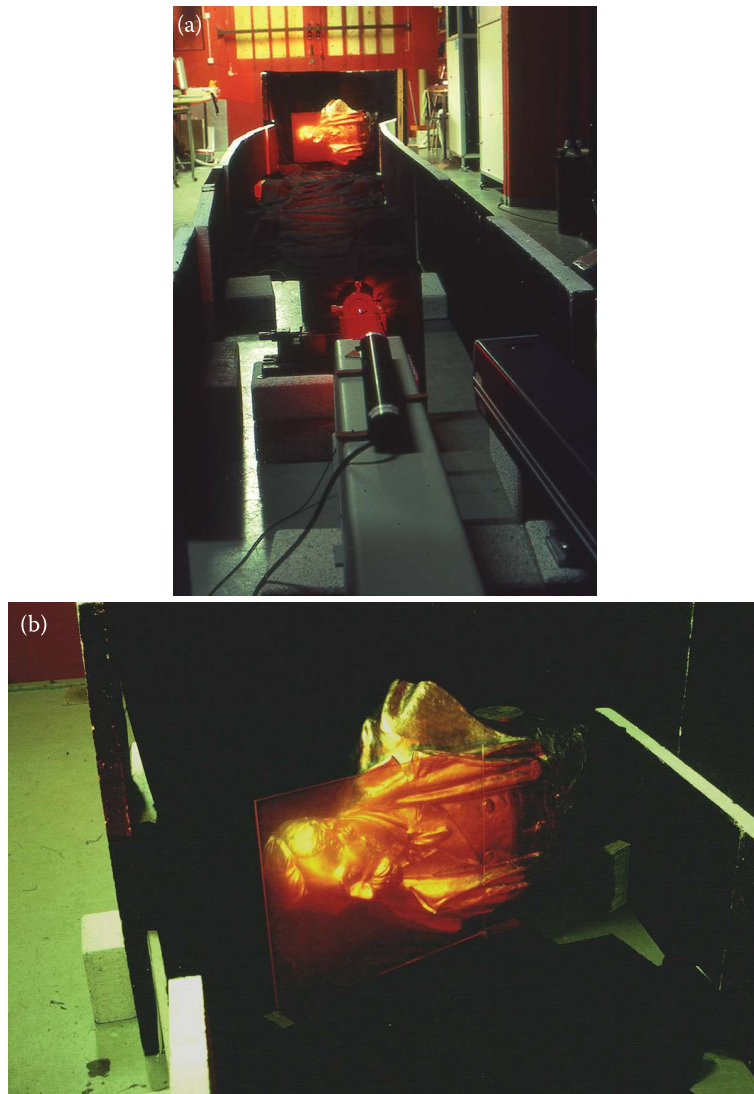


FIGURE 1.32 (a) Recording setup on the concrete floor showing the Alfred Nobel bust in the background and (b) the Nobel bust with the recording glass plate in front of it.



FIGURE 1.33 The *Alfred Nobel* hologram.



FIGURE 1.34 The hologram installed in the Nobel Foundation Building, Stockholm.

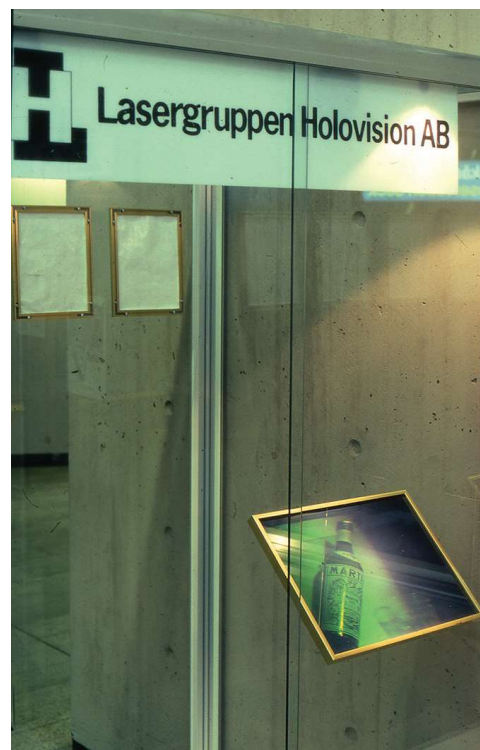


FIGURE 1.35 Hologram display cabinet at Arlanda Airport with the *Martini* hologram.

1.4.6.2 Mass Production of Reflection Holograms

A very early mass-produced reflection hologram was the *Marching Band Hologram*, a 10 cm × 12 cm silver halide Agfa film produced by McDonnell Douglas (Figure 1.36). It was included in two books, *Les Prix Nobel 1971* [71] and *Kosmos 49:1972* as well as in McDonnell Douglas's own promotional materials.

A project to produce large quantities of reflection holograms was undertaken as a joint effort between Applied Holographics PLC and Ilford Ltd. in the mid-1980s [72,73]. The idea was to use a pulsed ruby laser to record the holograms in an automatic fast-copying process. The *Holocopier AHS1* used a 240-mm-wide Ilford roll film (Holofilm 250 PAR) and a small JK ruby laser in the copier. Automatic processing of the film was performed in a machine from Hope Industries. Using the Holocopier, it was possible to produce reflection copies from reflection masters tuned at the 694 nm wavelength. It was also possible to directly record Denisyuk film holograms in the machine. According to Simon Brown,

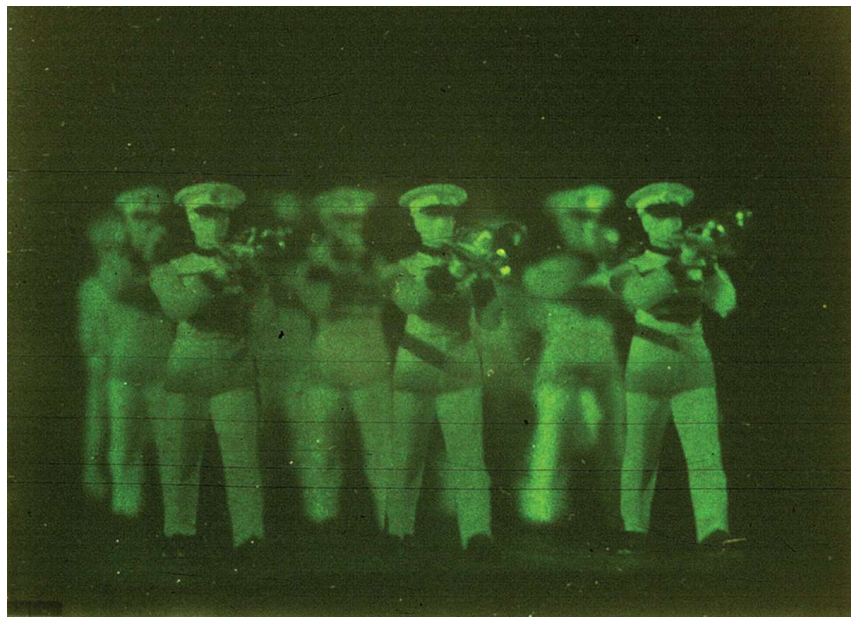


FIGURE 1.36 *The Marching Band* film hologram by McDonnell Douglas.



FIGURE 1.37 Tonka Toys figures with holograms.

it was possible to deliver high-quality copies in commercial quantities and at “realistic” prices. One of the first customers for the mass-produced holograms was Tonka Toys (Figure 1.37). Unfortunately, the toy hologram project turned out to be unique and eventually Applied Holographics gave up on display holography, turning to the more profitable document security market, trading as OpSEC both in the United Kingdom and in the United States.

In the mid-1990s, the Geola organisation in Lithuania used the concept of pulsed laser copying with its series of semiautomatic holographic portraiture systems based on neodymium glass lasers (initially the GP series, which was then followed by the more modern HS series). Geola offered versions of its systems with crystal amplifiers to achieve fast copy rates but few of these fast systems were sold.

1.4.7 Pseudo-Colour Reflection Holograms

Before true colour reflection holograms were developed, a pseudo-colour technique was used to create colour reflection holograms. Because it was difficult to produce such pseudo-colour reflection holograms on a large scale, they were produced mainly as artistic pieces in limited editions. The technique of creating different colours here was based on the fact that the colour in a reflection hologram is obtained by the diffraction of light from the recorded interference layers within the emulsion. The distance between these layers determines the colour. A certain distance between the interference fringes is generated during the recording of a reflection hologram depending on the laser wavelength used. However, this distance can be manipulated by various processing methods, with the result that different colours are obtained in the final hologram. Even using only a single-wavelength laser for the recording, such pseudo-colour reflection holograms were found to be able to display many different colours. Preswelling the emulsion before the recording resulted in shrinkage after processing, creating a colour of a shorter wavelength upon replay of the hologram compared to the colour of the laser light used. These methods were, however, very time consuming, and they were therefore mainly of interest for holographic art applications. The material most frequently used was the silver halide emulsion. The technique was introduced by Blyth in 1979 [74]. In an article by Hariharan [75], the pseudo-colour reflection process was described in greater detail. Normally the preswelling of the emulsion was performed by immersing the plates in various concentrations of triethanolamine solutions. Figure 1.38 shows an example of a pseudo-colour reflection hologram by John Kaufman [76]. Kaufman was one of the most experienced holographers who perfected this technique and who recorded many colourful art holograms. Other artists who produced many pseudo-colour holograms included Lon Moore and Larry Lieberman. At Holographic Images, Inc. in Florida, Lieberman developed a special step-rotation copying technique to produce large quantities of these types of holograms on film at more affordable prices.

For a long time, most reflection holograms were recorded on silver halide materials. This was definitely the case for the large-format holograms. However, other materials were also used. One material was the



FIGURE 1.38 4-Color Rock Rotation pseudo-colour reflection hologram by John Kaufman.

dichromated gelatin (DCG) emulsion, which was used from the very beginning for recording small reflection holograms—in particular, for pendants and jewellery items. Richard Rallison (1945–2010), Electric Umbrella and the International Dichromate Corporation, all located in Utah, produced large quantities of pendants for many years. An artist who has produced high-quality holographic jewellery and created beautiful art pieces recorded in DCG is August Muth (Figure 1.39) at Laserart Ltd., Santa Fe, New Mexico. Large and small DCG holograms were also produced in the Soviet Union. In 1987, Mike Medora established Raven Holographics Ltd. in the United Kingdom to record pseudo-colour DCG holograms. Richard Rallison was a partner in this company.

After DuPont and Polaroid started to manufacture photopolymers, this too became a material suitable for mass-produced monochrome reflection holograms. In 1987, a new monochrome photopolymer



FIGURE 1.39 DCG sculpture *Internal Reflections* by August Muth.

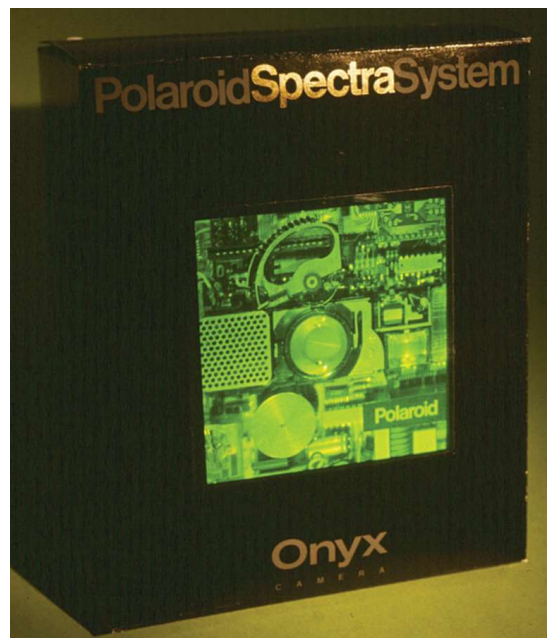


FIGURE 1.40 *Mirage* photopolymer hologram.

material (DMP-128) was introduced by Polaroid Corp. [77]. Their display holograms were produced in-house for clients, and were marketed under the name *Mirage*. One example of such a hologram attached to a Polaroid ONYX camera packaging is shown in Figure 1.40.

1.4.8 Holographic Movie Films

There have been several experiments reported whose aim was to record 3D holographic movies, but this has been an extremely difficult task thus far. The Conductron Corporation had already performed some tests recording moving holographic images in as early as 1966. A 70-mm animated holographic film of a merry-go-round was made and viewed using a strobbed laser source [78].

Gabor devoted a lot of time to designing a holographic projection screen for movie theatres [79]. The audience (in one plane or two) was covered by zones of vision having the width of the normal eye spacing, one for the right eye and one for the left with a blank space between the two pairs. The two eyes of the viewer had to see two different pictures: a stereoscopic pair. One of the movie projectors was used as the reference source and, for example, all the left viewing zones in the theatre as the object. The holographic screen, which was usually recorded as a reflection holographic optical element (HOE), became a very complicated optical system (when a picture was projected, it had to be seen only from all the left viewing zones). The recording process was repeated with the right projector as the reference and all the right viewing zones as the object beam. When viewing a 3D movie, the two projectors would then direct the left and right pictures to the two viewing zones in the theatre. Even if this worked in principle, it was found to be extremely difficult to create the large holographic projection screen with the required high-diffraction efficiency appropriate for a large audience. Gabor suggested that large screens should be made out of many smaller HOEs.

The most well-known experiments in the field of holographic movies were the ones performed by Victor Komar and his colleagues at the All-Union Cinema and Photographic Research Institute (NIKFI) in Moscow [80–82]. Figure 1.41 shows a photograph of a piece of 70-mm film strip with two different frames from recorded film scenes. The movies were rather short (only a few minutes) and it was only

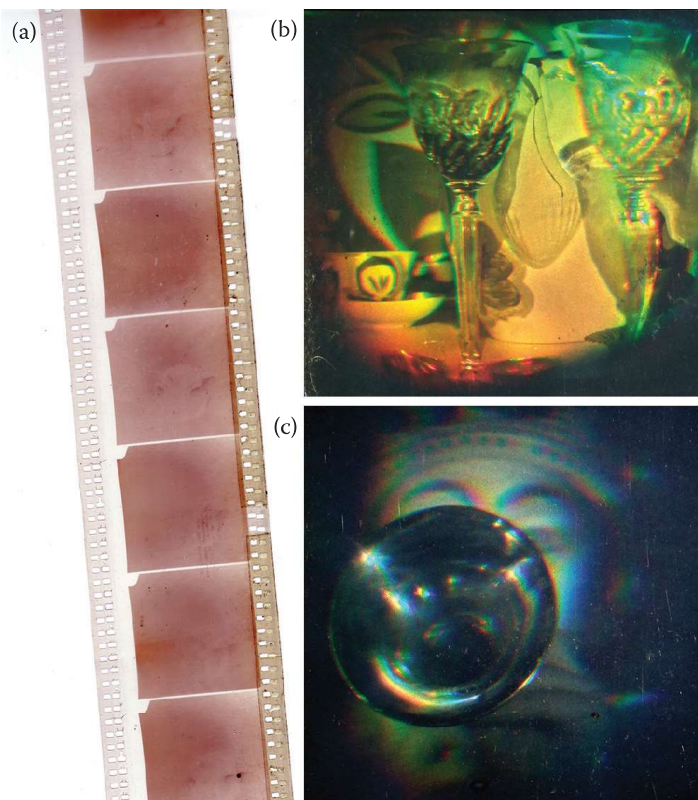


FIGURE 1.41 (a) Part of a 70-mm NIKFI holographic movie; (b) and (c) two different frames.

possible for four or five people to view them at the same time. The movies were projected on special HOE projection screens. Komar's first holographic colour film was produced in 1984 [83].

Paul Smigielski and colleagues at the Institute Saint Louis also made holographic movies [84]. Smigielski recorded short movies using a pulsed Nd:YAG laser—for example, a model train (*Holotrain* 1983) and a girl blowing soap bubbles (*Christiane et les Holobulles* 1985). The Australian artist Alexander worked with Smigielski at the Institute Saint Louis to make tests of holographic movies using a pulsed laser. Later in 1986, he created two movies: *Masks*, a 4-min movie, and *The Dream*, an 8-min movie. These movies were based on the multiplex technique and were recorded on a 25-cm-wide holographic film format [85].

1.4.9 Multiplex and Stereographic Holograms

The early multiplex technique produced display holograms from a combination of photographic or cinematographic recordings using special laser-copying techniques [86–88]. This made it possible to make holograms of people or objects as well as outdoor scenes without involving lasers in the first part of the process. One of the first holograms based on this method was a circular or semicircular hologram invented by Lloyd Cross [89]. This technique was similar to the rainbow hologram and was referred to as the *Integral* or *Multiplex* hologram; physically, this was a cylindrical 120° or 360° white light-viewable transmission hologram. The origination was done by recording the object or person on a rotating turntable using a conventional movie camera. Each movie frame was then converted to a vertical slit hologram on holographic film in a special printer. In this way, an animated holographic image could be recorded which appeared in the centre of the transparent cylindrical hologram when illuminated with a clear vertical-filament bulb positioned beneath the cylinder centre. Either the hologram rotated slowly, thus displaying a moving image, or the viewer walked around the stationary multiplex hologram to experience the animation. The best known multiplex hologram is Lloyd Cross' 120° hologram *Kiss II* from 1975. Three frames of this animated hologram are shown in Figure 1.42. Such holograms became popular in the mid-1970s and this situation lasted until the early 1980s. In addition to Cross, they were produced by Peter Claudio, Sharon McCormick and David Schmidt at the Multiplex Company in San Francisco, and by Hart Perry and Jason Sapan in New York. Jumpei Tsujuchi, a display holography scientist in Japan, was involved in display and medical holography and also recorded many multiplex holograms. Eventually, the interest in multiplex holograms disappeared and they are nowadays very rarely produced.

Flat transmission stereograms have been envisaged by King et al. [90] since the 1960s but became popular only in the late 1980s; these holograms were simpler to record and enabled a greater variety of objects to be used as subjects. Like rainbow holograms, they could also be made as pseudo-colour holograms. Large-format transmission stereograms were made by several companies, but the ones made at Advanced Dimensional Displays in California are particularly well known and were reported by Newswanger and Outwater [91]. One Advanced Dimensional Displays hologram is shown in Figure 1.43.



FIGURE 1.42 Lloyd Cross' hologram *Kiss II*. (Courtesy of L. Cross).



FIGURE 1.43 Craig Newswanger and one of the authors (HB) next to a large Advanced Dimensional Displays stereogram.



FIGURE 1.44 The *Dizzy Gillespie* large transmission stereogram.

Mark Diamond in Florida also recorded large stereograms—for example, the animated hologram of *Dizzy Gillespie*, shown in Figure 1.44. The recording was made at Advanced Dimensional Displays together with Craig Newswanger.

By the early 1990s, most large stereograms had started to be recorded as reflection holograms, these types of holograms being more practical to display.

Walter Spierings and his company, the Dutch Holographic Company B.V., introduced the first full-colour reflection stereograms [92]. A particularly stunning example of this technology was Dutch Holographics' 1991 three-colour reflection hologram of Ricky Henderson, the US baseball star (Figure 1.45). Spierings named the technology multiple photo-generated holography (MPGH) because the single-parallax reflection hologram produced by the technique required several hundred photos to be taken with a 35 mm camera on a linear track.* The photos were illuminated by laser light and projected in sequence

* In the case of the Ricky Henderson hologram, the photographs were actually taken with a static camera, the subject being located on a rotating platform. We shall study different types of camera geometries in Chapter 10.

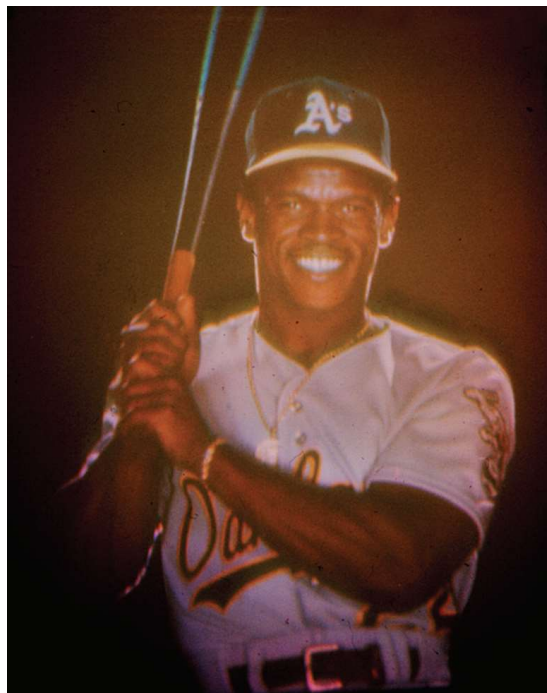


FIGURE 1.45 The first three-colour (multiple photo-generated holography) reflection holographic stereogram of US baseball star Ricky Henderson. (Courtesy of W. Spierings, 1991. Dutch Holographic Company B.V.)

onto a diffusion screen. Three separate H_1 transmission master holograms were produced using red, green and blue lasers. Each master was then transferred, one at a time, to a full-colour reflection H_2 on fine-grain silver halide emulsions. Spierings began working on the MPG H technique after being inspired by Steve Benton's work at MIT in the mid-1980s on computer-generated stereograms. At about the same time that Walter Spierings introduced his MPG H colour reflection holograms, another holographer, Rob Munday in the United Kingdom, was working on a similar (H_1/H_2) technique but with an important difference—this was the first of the digital stereogram systems. In 1991 Munday developed a system that he called the DI-HO (Digital Input–Holographic Output) to record H_1 photographic master stereograms and H_2 transfers using a modified high-resolution LCD screen. He used the Commodore Amiga 3000 Graphics Workstation with software that he had written himself named *Holomation*. The system could accept image input from sources such as a scanner or video as well as computer-generated artwork. The software also allowed for the planar separation of 2D graphic images which could then be combined with a 3D stereogram. Holograms up to a size $8'' \times 10''$ could be made with the system in both reflection and transmission format. Munday's first demonstration hologram was made in collaboration with MIT graduate Eric Krantz in 1992. It was a $7\frac{1}{2}'' \times 9''$ multi-colour H_2 reflection hologram of a *triceratops* dinosaur on a tiled surface (see Figure 1.46) made using multiple H_1 's produced from digital data (the *triceratops* was a computer-generated 3D model). The H_1 's were based on 70 slits, but Munday's technique allowed the number of slits to be increased to achieve better resolution if required.

Later in 1992 Munday also produced an embossed colour hologram called 'Z' using the above technique. The DI-HO system was used to record the stereogram frame by frame in three colour separations with each 'strip' colour separation contained on a single achromatic angled H_1 plate. The H_1 hologram was recorded on Agfa silver halide material using a Helium Cadmium laser. Munday then transferred the image to a surface relief photoresist H_2 before commissioning Applied Holographics plc to emboss the hologram. By the late 1990s, digital cameras and LCDs had largely replaced the old analogue techniques, giving birth to digital holographic printing.

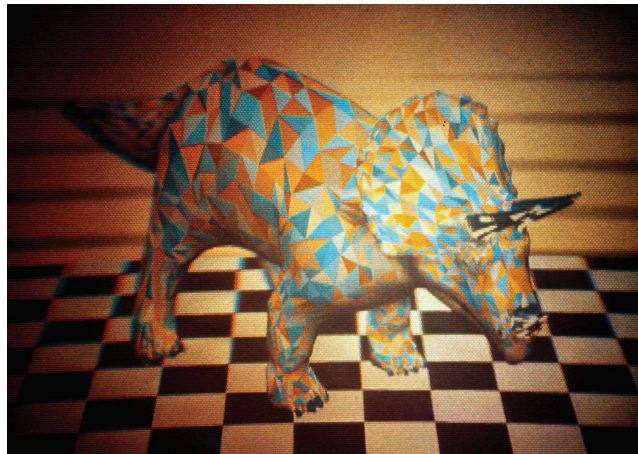


FIGURE 1.46 Triceratops hologram (courtesy of R. Munday).

1.5 Digital and Analogue Full-Colour Holography

Conventional display holography more or less disappeared in the 1990s because the easy-to-make monochrome 3D image was not able to sustain its role in displays and advertising. It was realised that colour was simply a “must” in any serious holographic display application; but at the same time, early colour reflection displays such as Dutch Holographics’ multiple photo-generated holograms were expensive, difficult to make and the quality was still somewhat lacking. Today, however, technology has appeared which holds definite promise of reversing this trend. Thanks to some crucial advances in areas such as holographic materials, lasers, electro-optics, image acquisition systems, computers and illumination technologies, full-colour holograms of both the digital and analogue type can now be produced with extraordinary realism. After a review of Lippmann photography in Chapter 2, we shall embark on a proper discussion of this new holography of ultra-realistic imaging.

REFERENCES

1. H. I. Bjelkhagen and D. Vukičević, “Color holography: a new technique for reproduction of paintings,” in *Practical Holography XVI and Holographic Materials VIII*, S. A. Benton, S. H. Stevenson, and T. J. Trout, eds., Proc. SPIE **4659**, 83–90 (2002).
2. P.-A. Blanche, A. Bablumian, R. Voorakaranam, C. Christenson, W. Lin, T. Gu, D. Flores, P. Wang, W.-Y. Hsieh, M. Kathaperumal, B. Rachwal, O. Siddiqui, J. Thomas, R. A. Norwood, M. Yamamoto and N. Peyghambarian, “Holographic three-dimensional telepresence using large-area photorefractive polymer,” *Nature*, **468**, 80–83, (4 Nov. 2010).
3. S. S. Shushurin, “On the history of holography,” *Soviet Phys. USPEKHI* **14**, 655–657 (1972).
4. M. Wolfke, “Über die Möglichkeit der optischen Abbildung von Molekulargittern,” [Transl.: On the possibility of the optical recording of a molecular lattice]” *Physik. Zeitschr.* **21**, 495–497 (1920).
5. D. Gabor, “A new microscopic principle,” *Nature* **161** (No.4098), 777–778 (1948).
6. D. Gabor, “Microscopy by reconstructed wave-fronts,” *Proc. Roy. Soc. (London)* **A197**, 454–487 (1949).
7. D. Gabor, “Microscopy by reconstructed wave-fronts: II,” *Proc. Phys. Soc. (London)* **64** (Pt. 6) No. 378 B, 449–469 (1951).
8. D. Gabor, “The outlook for holography,” *Optik* **28**, 437–441 (1968).
9. T. H. Maiman, “Stimulated optical radiation in ruby,” *Nature* **187**, 493–494 (6 Aug. 1960).
10. G. R. Gould, “The LASER, Light Amplification by Stimulated Emission of Radiation,” in *The Ann Arbor Conference on Optical Pumping*, P. A. Franken and R. H. Sands eds, Proc. The University of Michigan, (15 June – 18 June, 1959), p. 128.

11. E. N. Leith and J. Upatnieks, "Reconstructed wavefronts and communication theory," *J. Opt. Soc. Am.* **52**, 1123–1130 (1962).
12. E. N. Leith and J. Upatnieks, "Wavefront reconstruction with continuous-tone transparencies," *J. Opt. Soc. Am.* **53**, 522A (1963).
13. E. N. Leith and J. Upatnieks, "Wavefront reconstruction with continuous-tone objects," *J. Opt. Soc. Am.* **53**, 1377–1381 (1963).
14. E. N. Leith and J. Upatnieks, "Wavefront reconstruction with diffused illumination and three-dimensional objects," *J. Opt. Soc. Am.* **54**, 1295–1301 (1964).
15. P. Kirkpatrick, "History of holography," in *Holography*, B. J. Thompson ed., Proc. SPIE **15**, 9–12 (1968).
16. Y. N. Denisyuk, *Dokl. Akad. Nauk. (Academy of Sciences Reports, USSR)* **144** (No. 6), 1275–1278. [Transl.: Photographic reconstruction of the optical properties of an object in its own scattered radiation field]. *Sov. Phys. Doklady* **7**, 543–545 (1962).
17. Y. N. Denisyuk, "On the reproduction of the optical properties of an object by the wave field of its scattered radiation," *Opt. Spectrosc. (USSR)* **14**, 279–284 (1963).
18. Y. N. Denisyuk and I. R. Protas, "Improved Lippmann photographic plates for recording stationary light waves," *Opt. Spectrosc. (USSR)* **14**, 381–383 (1963).
19. S. F. Johnston, *Holographic Visions - A History of New Science*, Oxford University Press, New York (2006).
20. R. J. Collier, C. B. Burckhardt and L.H. Lin, *Optical Holography*, Academic Press, New York (1971).
21. H. J. Caulfield (ed.), *Handbook of Optical Holography*, Academic Press, New York (1979).
22. Y. N. Denisyuk, *Fundamentals of Holography*, Mir Publishers, Moscow (1984).
23. R. R. A. Syms, *Practical Volume Holography*, Oxford Engineering Science Series **24**, Oxford University Press, New York (1990).
24. P. Hariharan, *Basics of Holography*, Cambridge University Press, Cambridge (2002).
25. G. Saxby, *Practical Holography*, Third Edition, IOP Publishing Ltd, London (2004).
26. G. K. Ackermann and J. Eichler, *Holography - A Practical Approach*, Wiley-VCH Verlag GmbH & Co. KGaA, Weinheim (2007).
27. S. A. Benton and V. M. Bove Jr., *Holographic Imaging*, Wiley-Interscience, John Wiley & Sons Inc., Hoboken, NJ (2008).
28. V. Toal, *Introduction to Holography*, CRC Press, Boca Raton, FL (2011).
29. L. D. Siebert, "Large-scene front lighted hologram of a human subject," in Proc. IEEE **56** (No.7) 1242–1243 (1968).
30. S. F. Johnston, *Holographic Visions—A History of New Science*, Oxford University Press, New York (2006), p. 163.
31. P. Dawson, *Virtual Encounters; Paula Dawson Holograms*, Macquarie University and Newcastle Region Art Gallery, Australia (2010).
32. J. Webster and B. Tozer, "Holographic post irradiation examination of advanced gas cooled reactor fuel elements," in Proc. *J. Brit. Nuclear Energy Soc.*, (1980).
33. B. Tozer and J. Webster, "Holography as a measuring tool," *J. Photogr. Sci.* **28**, 93–98 (1980).
34. M. Benyon and J. Webster, "Pulsed holographic art practice," in *Practical Holography*, T. H. Jeong and J. E. Ludman eds., Proc. SPIE **615**, 36–42 (1986).
35. R. F. Wuerker, L. E. Hefflinger, J. V. Flannery and A. Kassel, "Holography on space shuttle," in *Recent Advances in Holography*, T.-C. Lee and P. N. Tamura eds., Proc. SPIE **215**, 76–84 (1980).
36. D. Westlake, R. F. Wuerker and J. F. Asmus, "The use of holography in the conservation, preservation and historical recording of art," in Society of Motion Picture & Television Engineers *SMPTE Journal*, **85**, 84–89 (1980).
37. R. F. Wuerker, "Holography of art objects," in *Recent Advances in Holography*, T.-C. Lee and P. N. Tamura eds., Proc. SPIE **215**, 167–174 (1980).
38. C. F. Reuterswärd, *25 Years in the Branch*, Benteli Verlag, Berne (1978).
39. H. I. Bjelkhagen, "Holographic portraits made by pulse lasers," *Leonardo* **25**, 443–448 (1992).
40. H. I. Bjelkhagen, "Holographic portraits," in *Holography, Commemorating the 90th Anniversary of the Birth of Dennis Gabor*, P. Greguss and T. H. Jeong eds., SPIE Institutes, Volume **IS 8**, 347–353 (1991).
41. M. Benyon, "Cosmetic series 1986–1987: a personal account," *Leonardo* **22**, 307–312 (1989).
42. M. Richardson, *Space Bomb – holograms & lenticulars: 1984–2004*, T.H.I.S. Limited, London (2004).

43. N. Aebischer and B. Cargquelle, "White light holographic portraits (still or animated)," *Appl. Opt.* **17**, 3698–3700 (1978).
44. P. Smigielski, H. Fagot, A. Stimpfling and J. Schwab, "Holographie ultra-rapide," *Nouv. Rev. d'Optique appliquée* **2**, 205–207 (1971).
45. A. M. Rodin and D. Brotherton-Ratcliffe, "Compact 16 Joule phase-conjugated SLM Nd:YLF/Nd:Phosphate glass laser", in *The XIV Lithuanian-Byelorussian workshop on Lasers and Optical Nonlinearity*, Proc., Preila, Lithuania (1999) pp. 51–52.
46. A. S. Dementjev, A. M. Rodin, M. V. Grichine and D. Brotherton-Ratcliffe, "High-energy phase-conjugated Nd:Glass laser for the pulsed holography," *Spinduliuotes ir medziagos saveika, Konferencijos pranesimu medziaga*, Kaunas, Technologija, (1999) pp. 249–252.
47. M. V. Grichine, D. Brotherton-Ratcliffe and A. M. Rodin, "Design of a family of advanced Nd:YLF/Phosphate glass lasers for pulsed holography," in *Sixth Int'l Symposium on Display Holography*, T. H. Jeong ed., Proc. SPIE **3358**, 194–202 (1998).
48. M. V. Grichine, D. Brotherton-Ratcliffe and G. R. Skokov, "An integrated pulsed-holography system for mastering and transferring onto AGFA or VR-P emulsions," in *Sixth Int'l Symposium on Display Holography*, T. H. Jeong ed., Proc. SPIE **3358**, 203–210 (1998).
49. A. M. Rodin, D. Brotherton-Ratcliffe and G. R. Skokov, "An automated system for the production of image-planed white-light-viewable holograms by pulsed laser," in *Practical Holography XIII*, S. A. Benton ed., Proc. SPIE **3637**, 141–147 (1999).
50. D. Brotherton-Ratcliffe, A. M. Rodin, and S. J. Zacharovas, "Evolution of automatic turn-key systems for the production of rainbow and reflection hologram runs by pulsed laser", in *Holography 2000*, T. H. Jeong and W. K. Sobotka eds., Proc. SPIE **4149**, 359–366 (2000).
51. A. M. Rodin, D. Brotherton-Ratcliffe and R. Rus, "Large-format automated pulsed holography camera System," in *Optical Organic and Inorganic Materials*, S. P. Asmontas and J. Gradauskas eds., Proc. SPIE **4415**, 39–43 (2001).
52. A. M. Rodin, D. Brotherton-Ratcliffe and R. Rus, "Large-format automated pulsed holography camera System," in *2nd International Conference Advanced Optical Materials and Devices*, Abstract Vilnius, Lithuania, 16–19 August, (2000) p. 60.
53. G. Gudaitus, S. J. Zacharovas, R. Bakanas, D. Brotherton-Ratcliffe, S. Hirsch, S. Frey, A. Thelen, L. Ladrière and P. Hering, "Portable holographic camera system HSF-MINI application for 3D measurement in medicine," in *2nd Int'l Conference "HOLOEXPO-2005, Science and Practice, Holography in Russia and Abroad*, Moscow (Russia) (2005) pp. 27–29.
54. R. Bakanas, G. A. Gudaitis, S. J. Zacharovas, D. Brotherton-Ratcliffe, S. Hirsch, S. Frey, A. Thelen, N. Ladrière and P. Hering, "Using a portable holographic camera in cosmetology," *J. Opt. Technol.* **73** 457–461 (2006).
55. H. I. Bjelkhagen, R. Deem, J. Landry, M. Marhic and F. Unterseher, "A holographic portrait of Ronald Reagan," in *Int'l Symposium on Display Holography*, T. H. Jeong, and H. I. Bjelkhagen eds., Proc. SPIE **1600**, 402–441 (1992).
56. S. A. Benton, "Hologram reconstructions with extended incoherent sources," *J. Opt. Soc. Am.* **59**, 1545–1546A (1969).
57. N. Tamura, "Pseudocolor encoding of holographic images using a single wavelength." *Appl. Opt.* **17**, 2532–2536 (1978).
58. P. Grover and R. Tremblay, "Multicolor wave front reconstruction in white light." *Appl. Opt.* **19**, 3044–3046 (1980).
59. J. F. W. Perry, "Design of large format commercial display holograms," in *Practical Holography III*, S. A. Benton ed., Proc. SPIE **1051**, 2–5, (1989).
60. D. Brotherton-Ratcliffe, "Large Format Holography," in *Sixth Int'l Symposium on Display Holography*, T. H. Jeong ed., Proc. SPIE **3358**, 368–379 (1998).
61. D. Jung, *Bilder · Zeichnungen · Hologramme*, Wienand Verlag, Cologne (1991).
62. T. H. Jeong, P. Rudolf and A. Luckett, "360° holography," *J. Opt. Soc. Am.* **54**, 1263–1264 (1966).
63. J. Upatnieks and J. T. Embach, "360-degree hologram displays," *Opt. Eng.* **19**, 696–704 (1980).
64. S. A. Benton, "Achromatic images from white light transmission holograms," *J. Opt. Soc. Am.* **68**, 1441A (1978).
65. E. Orr and D. Trayner, "Deep image reflection holograms in black and white and additional colours," in *Int'l Symposium on Display Holography*, T. H. Jeong ed., Vol. III, 379–388 (1989).

66. K. Bazargan, "A practical, portable system for white-light display of transmission holograms using dispersion compensation," in *Applications of Holography*, L. Huff ed., Proc SPIE **523**, 24–25 (1985).
67. S. J. Hart and M. N. Dalton, "Display holography for medical tomography," in *Practical Holography IV*, S. A. Benton ed., Proc. SPIE **1212**, 116–135 (1990).
68. N. J. Phillips and D. Porter, "An advance in the processing of holograms," *J. Phys. E: Sci. Instrum.* **9**, 631–634 (1976).
69. N. J. Phillips, A. A. Ward, R. Cullen and D. Porter, "Advances in holographic bleaches," *Phot. Sci. Eng.* **24**, 120–124 (1980).
70. N. J. Phillips, "Bridging the gap between Soviet and Western holography," in *Holography, Commemorating the 90th Anniversary of the Birth of Dennis Gabor*, P. Greguss and T. H. Jeong eds., SPIE Institute Volume **IS 8**, 206–214 (1991).
71. E. Ingelstam, *Les Prix Nobel en 1971*, The Nobel Foundation, Norstedt & Söner, Stockholm (1972).
72. S. J. S. Brown, "Automated holographic mass production," in *Practical Holography*, T. H. Jeong and J. E. Ludman eds., Proc. SPIE **615**, 46–49 (1986).
73. G. P. Wood, "New silver halide materials for mass production of holograms," in *Practical Holography*, T. H. Jeong and J. E. Ludman eds., Proc. SPIE **615**, 74–80 (1986).
74. J. Blyth, "Pseudoscopic moldmaking handy trick for Denisyuk holographers," *Holosphere* **8** (No.11), 5, (1979).
75. P. Hariharan, "Pseudocolour images with volume reflection holograms," *Opt. Commun.* **35**, 42–44 (1980).
76. J. A. Kaufman, "Previsualization and pseudo-color image plane reflection holograms," in Proc. *Int'l Symp. on Display Holography*, T. H. Jeong ed., Vol. I., 195–207 (1983).
77. R. T. Ingwall and M. Troll, "Mechanism of hologram formation in DMP-128 photopolymer." *Opt. Eng.* **28**, 586–591 (1989).
78. S. F. Johnston, *Holographic Visions—A History of New Science*, Oxford University Press, New York (2006), p. 166.
79. E. Ingelstam, *Les Prix Nobel en 1971*. The Nobel Foundation, Norstedt & Söner, Stockholm (1972) pp. 169–201
80. V. G. Komar, "Progress in the holographic movie process in the USSR," in *Three-Dimensional Imaging*, S. A. Benton ed., Proc. SPIE **120**, 127–144 (1977).
81. V. G. Komar, "Holographic motion picture systems compatible with both stereoscopic and conventional systems," *Tekhnika Kino i Televideniya*. No.10, 3–12 (1978).
82. V. G. Komar and O. I. Ioshin, "Motion pictures and holography," *SMPTE Journal* **89**, 927–930 (1980).
83. V. G. Komar and O. B. Serov, "Works on the holographic cinematography in the USSR," in *Holography'89*, Yu. N. Denisyuk and T. H. Jeong eds., Proc. SPIE **1183**, 170–182 (1989).
84. P. Smigelski, H. Fagot and F. Albe, "Holographic cinematography and its applications," in *Int'l Conference on Holography*, D. Wang and J. Ke eds., Proc. SPIE **673**, 22–27 (1987).
85. P. Alexander, "Development of integral holographic motion pictures," in *Fifth Int'l Symposium on Display Holography*, T. H. Jeong ed., Proc. SPIE **2333**, 187–197 (1995).
86. R. V. Pole, "3-D imagery and holograms of objects illuminated in white light," *Appl. Phys. Lett.* **12**, 20–23 (1967).
87. D. J. Debitetto, "Holographic panoramic stereograms synthesized from white light recordings," *Appl. Opt.* **8**, 1740–1741 (1969).
88. J. T. McCrickerd and N. George, "Holographic stereograms from sequential component photographs," *Appl. Phys. Lett.* **12**, 10–12 (1968).
89. L. Cross, "The Multiplex technique for cylindrical holographic stereograms," in SPIE San Diego August Seminar (1977). [Presented but not published]
90. M. C. King, A. M. Noll and D. H. Berry, "A new approach to computer-generated holography," *Appl. Opt.* **9**, 471–475 (1969). *See also:* Ref.[1.87]
91. C. Newswanger and C. Outwater, "Large format holographic stereograms and their applications," in *Applications of Holography*, L. Huff ed., Proc. SPIE **523**, 26–32 (1985).
92. W. Spierings and E. van Nuland, "Calculating the right perspectives for multiple photo-generated holograms," in *Int'l Symposium on Display Holography*, T. H. Jeong ed., Proc. SPIE 1600, 96–108 (1992).

2

Lippmann Photography

2.1 Brief History of Interferential Colour Recordings

Lippmann photography is an interferential colour photographic recording technique that is capable of reproducing colour images with extraordinary precision. Today, more than a century after its invention, many wonderful, perfectly preserved colour images exist from the turn of the century in this unique medium. Colours are recorded in Lippmann photography in a natural way without the use of dyes.

The interest in recording images that are as realistic as possible commenced with the invention of photography. After the invention of black-and-white photography in the nineteenth century, much research was devoted to the possibility of recording natural colour images. It is important to mention this work in the context of today's quest for ultra-realistic imaging. The issue here is how to accurately capture the reflected light from scenes and objects. What is extremely interesting is that it was possible to record the full-colour spectrum of a scene using one of the very first colour photography techniques discovered.

Even before photography was invented, Johann Wolfgang von Goethe (1749–1832) published a book on light and colour (*Zur Farbenlehre*), in which light and colour recordings were discussed [1]. The reader may be surprised to find the poet Goethe involved in light and colour theory. Actually, one scientist who took Goethe's colour philosophy seriously was Thomas Johann Seebeck (1770–1831). Although the collaboration between them did not really advance colour theory, it resulted in some observations that Goethe included as an appendix in his book [1]. This can be regarded as a very early (circa 1810) contribution to colour photography. Seebeck conducted experiments in which solar spectra were projected onto paper impregnated with silver chloride. The recordings showed colours that were induced by corresponding colours in the solar spectrum. The philosophical explanation for this observation was that "light chose to impress itself on material objects in its own colours." It therefore made sense to describe such a process as a natural colour-recording technique. In the recording material used somewhat later in Lippmann colour photography, the colours of the object were actually recorded according to the Goethe–Seebeck description. Sadly, the recordings by Seebeck were not permanent; they disappeared quickly when exposed to light.

Sir John Herschel (1792–1871) made a systematic investigation of solar spectra recorded in silver chloride paper [2]. Herschel could record colours but could not find a method to fix the image. This type of photographic recording technique is often referred to as *heliochromy* (sun colouring) and the images as *heliochromes*. A major contribution was made by Alexandre Edmond Becquerel (1820–1891) [3–8]. Instead of using paper as the material substrate, Becquerel coated a silver chloride (Ag_2Cl) emulsion onto a polished silver plate (applying chlorination by a galvanic process). Employing such plates, the colours of the recorded solar spectrum were much brighter than any previously recorded spectra. In addition to spectra, Becquerel succeeded in recording images of objects. He recorded some coloured engravings and brightly dressed dolls, which required between 10 and 12 h of exposure in bright sunlight. Similar experiments with silver plates coated with silver chloride were carried out by Abel Niepce de Saint-Victor (1805–1870) [9–14] and Alphonse-Louis Poitevin (1819–1882) [15]. Much research went into making the heliochromes permanent but without success. However, we know that Niepce de Saint-Victor was able to improve the technique considerably and recorded many beautiful heliochromes.

In Westkill, New York, Reverend Levi L. Hill (1816–1865) claimed that he had been able to record and fix heliochromes (hillotypes). Hill's technique has been described in a book [16], which he published in 1856. In 1987, Joseph Boudreau [17] of Paier College of Art in Hamden, Connecticut, was able to record hillotypes according to the complicated procedure described by Hill. In Germany, Wilhelm Zenker (1829–1899)

worked on the theory of colour photography and colour vision. His book on colour theory had the ancillary title *Photography in Natural Colours* [18]. He proposed an explanation for experiments that recorded spectral information in terms of standing waves of light, which formed within the light-sensitive layer and which were actually recorded. This structured layer, he maintained, would be able to selectively reflect different colours. Unaware of Zenker's theory, Lord Rayleigh (1842–1919) [19] suggested that "colour could be recorded as stationary luminous waves of nearly definite wavelength, the effect of which might be to impress upon the substance a periodic structure recurring at intervals equal to half the wavelength of the light." Lord Rayleigh maintained that the recording technique "produced just such a modification of the film as would cause it to reflect most copiously that particular kind of light." Lord Rayleigh never performed any experiments to verify his theory, but he mentioned, "I abstain at present from developing this suggestion, in the hope of soon finding an opportunity of making myself experimentally acquainted with the subject."

In 1889, in Strasbourg, Otto Wiener (1862–1927) investigated standing light waves and the polarisation of light. He was able to record such standing waves and thus prove that monochromatic light reflected off a mirror was recorded as a periodic interference pattern in an ultrahigh-resolution photographic emulsion [20]. In addition, he investigated the earlier experiments by Seebeck, Poitevin and Becquerel and explained the differences between them [21]. This work was done after Lippmann published his new technique of colour photography. The colours observed in the earlier experiments were obtained in two ways: by interference or by absorption and bleach-out. Zenker's theory was correct regarding Lippmann photography. However, it did not apply to the earlier colour recordings on chloride paper. There, a chemical bleaching process of pigments was behind the colours. The light-sensitive substances were bleached out only by those wavelengths of light that they absorbed, whereas they were not destroyed by light of their own colour.

In 1861, James Clerk Maxwell (1831–1879) demonstrated a colour photograph recorded according to the three-colour additive synthesis [22] that was based on the Young–Helmholtz three-colour theory of vision. An object (a tartan ribbon bow) was recorded on three separate black-and-white plates through three colour filters (red, green and blue). These plates were then projected separately through the same filters that were used for the recording. When the three projected images were registered with one another, the picture burst into colour.

2.2 Examples of Interferential Structures in Nature

It is interesting to mention that the principle of light reflection from periodic structures, upon which interferential colour-recording techniques is based, exists in nature. Opal, a sedimentary gem, gets its colours from tiny spheres of silica packed together. The sea mouse, *Aphrodita*, a marine worm, is named for its mouse-like appearance and behaviour. The spines, or *setae*, that emerge from the scaled back of the sea mouse are one of its unique features which can produce iridescence in a range of colours. Normally, these have a red sheen but when the light shines on them perpendicularly, they flush green and blue. These colours are believed to be a defence mechanism, giving warning to potential predators. The colours of moths, beetles and birds (peacock feathers) all possess light-reflecting structures creating

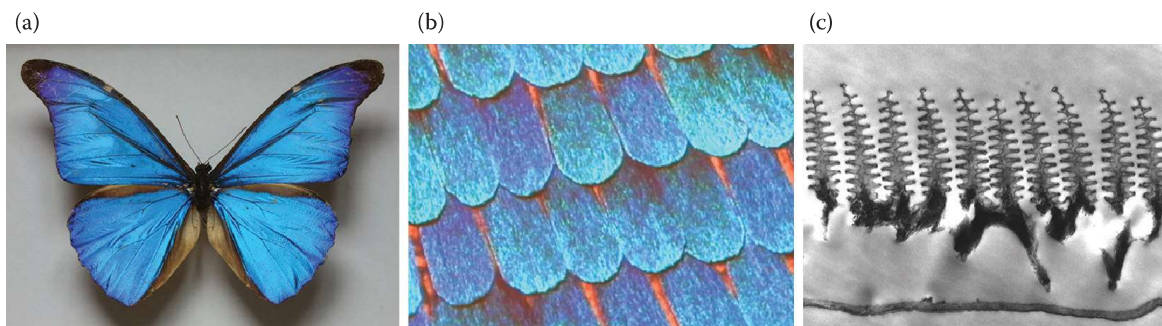


FIGURE 2.1 (a) *Papilio* butterfly, (b) wing scale and (c) wing structure. (Photos b and c courtesy of P. Vukusic, University of Exeter.)

iridescent bright colours. Perhaps, best known is the very bright coloured light reflected from some butterfly wings. The hue of this light changes with the viewing angle, and the colour appears highly saturated. The *Papilio achilles* butterfly of the *Morpho* type is shown in Figure 2.1. The reflection of the structured iridescent scales creates intense blue light. The colours are created by a tree-like structure of lamellae that are self-assembled from cuticles. Depending on the exact *Morpho* species, there are 6 to 10 branches on each side of the lamellae trunk with a density of 700 to 2000 lamellae per millimetre. More information about structural colours in nature can be found in several publications [23–31].

2.3 Lippmann Photography

Gabriel Jonas Lippmann (1845–1921) was born in Bonnevoie, Luxembourg, of French parents, on 16 August 1845. He entered the Normal School in 1867 and studied in Heidelberg, Germany, where he received the degree of Doctor of Philosophy in 1873. In 1875, he moved to Paris and became a professor of mathematical physics at the Sorbonne in 1883, a member of the Institute in 1886 and an Officer of the Legion of Honour in 1884. Previously, he had worked on thermodynamics, electricity and capillarity. At the Sorbonne, he was obliged to start teaching acoustics and optics, and it was in this way that he became interested in the theory of light and, in particular, colour theory. As early as 1886, he had developed a general theory of recording colours as standing waves in a light-sensitive emulsion. However, most of his time was devoted to perfecting a suitable recording emulsion for his experiments. This indicates that he had already developed the interference theory long before the result of the Wiener experiment [20] was published. Lippmann's work on what has come to be known as *interferential photography* or *interference colour photography* was published in several papers [32–35].

On 2 February 1891, Lippmann announced at the Académie de Sciences in Paris that he had succeeded in recording a true-colour spectrum [32]. In addition, the recording was permanent and could be observed in full daylight. A little more than one year later, on 25 April 1892, Lippmann gave a second presentation at the Académie de Sciences [33]. This time, he displayed four colour photographs of different objects: a stained glass window in several colours, a bunch of flags and a dish of oranges, a red poppy and a green parrot. Later, at a photographic exhibition in Paris, he displayed a landscape with a grey building surrounded with green foliage and blue sky. The size of these early photographs was 4 cm × 4 cm. Later, Lippmann used the format 6.5 cm × 9 cm for most of his colour photographs. He also recorded colour images in a dichromated gelatin emulsion [34], a material often used in holography today. Figure 2.2 shows two photographs by Lippmann.

Lippmann developed the first proper theory of the recording of monochromatic and polychromatic spectra [35]. He applied Fourier mathematics to optics, which was a new approach at that time. A bibliography on Lippmann and his inventions was published in 1911 by Lebon [36]. Although the new photographic colour-recording technique known as *Lippmann photography* was extremely interesting from a scientific point of view, it was not very effective for colour photography because the technique was complicated and the exposure times were too long for practical use. The difficulty in viewing the photographs was another contributing factor, in addition to the copying problem; this prevented Lippmann photography from becoming a practical photographic colour-recording method. Notwithstanding this, 100-year-old Lippmann photographs are extremely beautiful, and the fact that the colours are so well preserved in these photographs indicates something rather interesting about their archival properties.

The principle of Lippmann photography is illustrated in Figure 2.3. Owing to the demand for high resolving power in making Lippmann photographs, the material has to be a very fine-grain emulsion and consequently of very low sensitivity. The emulsion coating on the Lippmann plates must be brought into contact with a highly reflective surface, usually mercury. Light is thus reflected back into the emulsion and interferes with the incident light, producing a pattern of standing waves. These standing waves produce a very fine fringe pattern throughout the emulsion with a periodic spacing of $\lambda/(2n)$, which is recorded (here, λ is the wavelength of light in air, and n is the refractive index of the emulsion). The colour information is stored locally in this way. The larger the separation between the fringes, the longer the wavelength of the recorded image information. This picture is, however, only correct when fairly

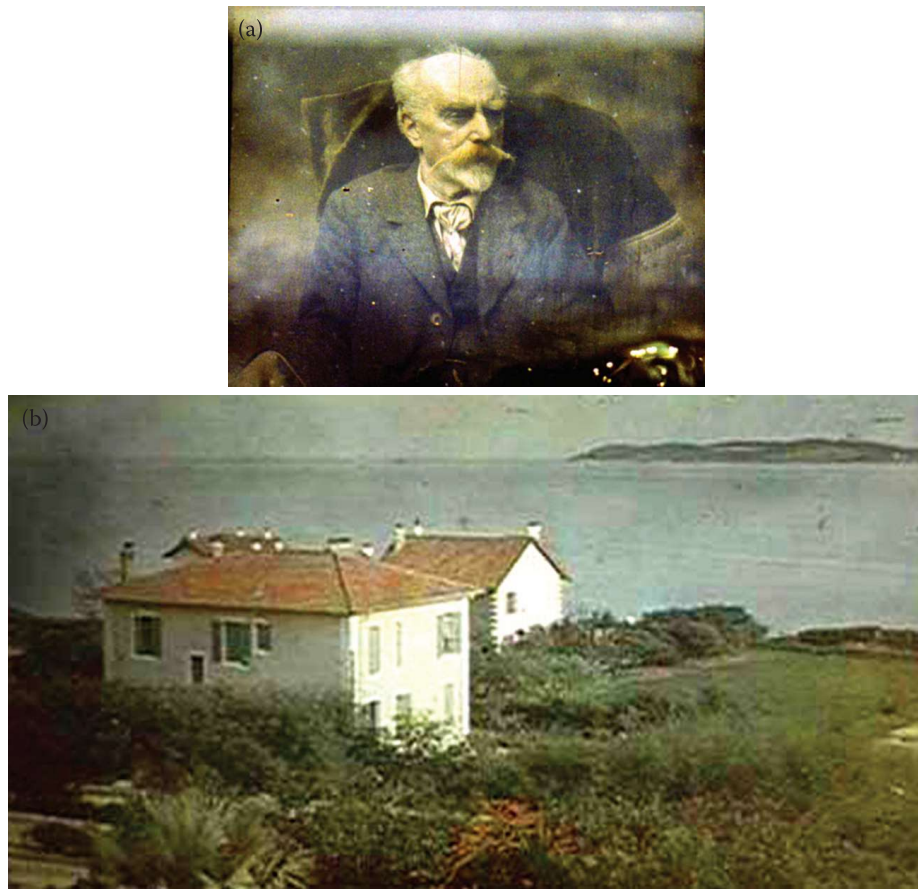


FIGURE 2.2 Two examples of colour photographs recorded by Gabriel Lippmann: (a) Lippmann Autoportrait and (b) Sainte Maxime, Var, France, 1913. (Courtesy of Musée de l'Elysée Collection, Lausanne. Inventory nos. 9079 and 9985.)

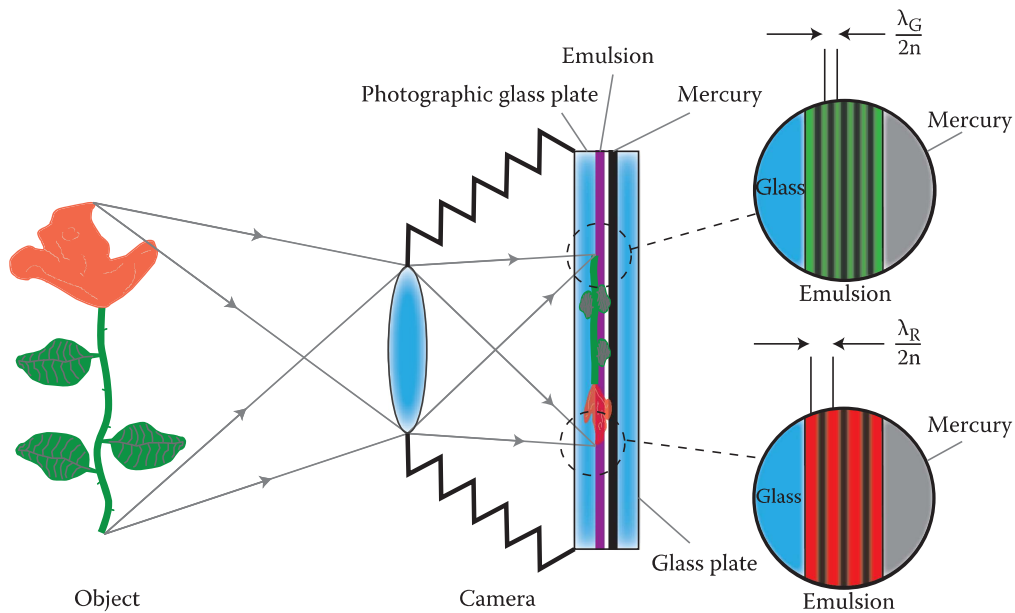


FIGURE 2.3 The principle of Lippmann photography.

monochromatic colours are recorded. A polychrome recording is actually rather more complex, but this was treated mathematically by Lippmann [35].

When the developed Lippmann photograph is viewed in white light, different parts of the recorded image produce different colours. This is due to the different spacings of the recorded fringes in the emulsion. The light is reflected from these fringes, creating precisely the colours that correspond to the original ones that had produced them during the recording. It is obvious that there must be a high demand on the resolving power of the recording material to record the fringes because the fringes are spaced at a distance of approximately half the wavelength of light. It is also clear that the processing of the photographic plates is critically important, as the separation between the fringes must not change because this would create erroneous colours on replay. In addition, one must find ways of obtaining high diffractive efficiency.

To observe the correct colours of a Lippmann photograph, the illumination and observation must be at normal incidence. When these angles change, the colour of the image changes. This change of colour with angle is called *iridescence* and is of the same type as found in peacock feathers and in mother of pearl. The image is recorded as a Bragg structure and is sensitive to the directions of illumination and observation. When a recorded Lippmann photograph is illuminated and observed perpendicularly, the correct colours are reproduced. However, when illuminated and viewed at oblique angles, the colours are tuned towards shorter wavelengths. Thus, red colours become orange, yellow or even green depending on the angles.

In the early 1890s, several scientists and researchers began to explore and further develop the new Lippmann photography technique. Among the most important contributions were those made by Auguste and Louis Lumière [37,38], Eduard Valenta [39], Richard Neuhauss [40], Herbert Ives [41] and Hans Lehmann [42]. There are several early books on Lippmann photography and colour photography [43–52]. An illustration of how a Lippmann photograph replays when illuminated in different ways is shown in Figure 2.4.

In 1908, Gabriel Lippmann (Figure 2.5) was awarded the Nobel Prize in physics for his invention. It was his idea of recording interference fringes throughout the depth of an emulsion that inspired Yuri Denisyuk in Russia in the early 1960s to introduce the technique of recording single-beam reflection holograms [53–55]. In recent years, there has been a revival of interest in Lippmann photography among scientists and holographers [56–83].



FIGURE 2.4 Lippmann photographic plate illuminated and observed in different ways: (a) negative reflected image seen when illumination and observation are not perpendicular, (b) positive red image seen in transmitted illumination caused by colloidal silver particles and (c) correct colour-reflected image seen when illumination and observation are perpendicular.

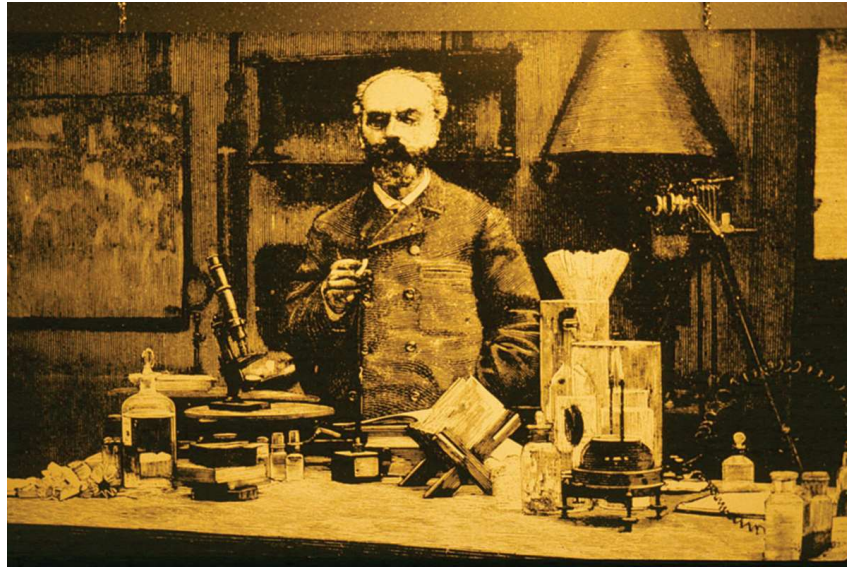


FIGURE 2.5 Gabriel Lippmann in his laboratory.

2.4 Theory of the Lippmann Process

2.4.1 Treatment of Monochromatic Recording

The transverse electric field of a monochromatic plane wave propagating in the $\hat{\mathbf{z}}$ direction and then reflected back on itself in the $-\hat{\mathbf{z}}$ direction can be expressed as

$$\mathbf{E}(z,t) = E_0 \cos 2\pi \left\{ \frac{nz}{\lambda} + vt \right\} \hat{\mathbf{x}} - E_0 \cos 2\pi \left\{ \frac{nz}{\lambda} - vt \right\} \hat{\mathbf{x}} \quad (2.1)$$

where λ is the wavelength in vacuum, v is the frequency, n is the refractive index of the emulsion, E_0 is the peak electric field amplitude and $\hat{\mathbf{x}}$ the unit vector in the direction orthogonal to z . The interference between the two components to this light field creates a standing wave with the following electric field distribution

$$\mathbf{E}(z,t) = 2E_0 \sin \left\{ 2\pi \frac{nz}{\lambda} \right\} \sin \{ 2\pi v t \} \hat{\mathbf{x}} \quad (2.2)$$

We can then define the intensity I associated with this standing wave as the time-averaged value of the squared electric field:

$$I = \langle E^2 \rangle = 2E_0^2 \sin^2 \left\{ \frac{2\pi nz}{\lambda} \right\} \quad (2.3)$$

A factor of 1/2 comes in here from the integration of the time dependence of Equation 2.2 over one period. The distance between two intensity maxima is $d = \lambda/(2n)$. During the recording of the Lippmann photograph, these intensity maxima are recorded in the emulsion. For example, for $\lambda = 400$ nm (blue light), the distance between these maxima is $d = 200$ nm (in air).

2.4.2 Treatment of Monochromatic Replay

To view the recorded Lippmann photograph, a diffuse light source emitting a white-light continuous spectrum is required to illuminate the plate. This white light is reflected off the recorded interference

fringes in the emulsion and, depending on the incident and reflected angles, the well-known Bragg condition will apply

$$\frac{m\lambda'}{n} = 2d \cos \alpha \quad \forall \quad m = 1, 2, 3, \dots \quad (2.4)$$

For the recorded fringe distance d , the reflected wavelength λ' is then given by

$$\lambda' = \frac{2dn \cos \alpha}{m} \quad (2.5)$$

If illumination and observation are both perpendicular to the plate ($\cos \alpha = 1$), then exactly the same wavelength is reflected on replay as the wavelength used for the recording.

2.4.3 Treatment of Polychromatic Recording

To record a more complex wave front, such as a landscape scene in natural colours, Lippmann introduced Fourier mathematics to show how such a recording could be theoretically described [35].

To see how this works, we first make the observation that most objects do not reflect pure spectral colours but rather a continuous spectrum $f(\lambda)$. Therefore, if an object is illuminated by a white spectrum, such as sunlight, which we shall denote by $F(\lambda)$, then an observer of the object will observe an intensity proportional to the product $F(\lambda)f(\lambda)$ reflected from every point of the object. As such, we must replace the expression for the electric field in the Lippmann photograph at recording (Equation 2.1) by the Fourier integral

$$E_x(z, t) = E_0 \int_{\lambda} \sqrt{F(\lambda)f(\lambda)} \cos 2\pi \left\{ \frac{nz}{\lambda} + vt \right\} d\lambda - E_0 \int_{\lambda} \sqrt{F(\lambda)f(\lambda)} \cos 2\pi \left\{ \frac{nz}{\lambda} - vt \right\} d\lambda \quad (2.6)$$

The intensity at the emulsion surface may then be written as before as the time average of the squared electric field:

$$I = 2E_0^2 \int_{\lambda} F(\lambda)f(\lambda) \sin^2 \left\{ \frac{2\pi nz}{\lambda} \right\} d\lambda \quad (2.7)$$

If we now denote the spectral sensitivity of the recording material as $O(\lambda)$ and we make the further assumption that the Lippmann emulsion inherits upon exposure and processing an effective reflectivity $R(z)$ proportional to the time averaged squared electric field intensity present at recording, then we may write down the following expression for the reflectivity of the Lippmann photograph:

$$R(z) = 2E_0^2 \int_{\lambda} F(\lambda)f(\lambda)O(\lambda) \sin^2 \left\{ \frac{2\pi nz}{\lambda} \right\} d\lambda \quad (2.8)$$

Assuming that the recording material is isochromatic (the response is equal for all wavelengths within the spectrum), then the product $F(\lambda)O(\lambda)$ is a constant, which, with appropriate normalisation, can be taken to be unity, whereupon the integral in Equation 2.8 simplifies to

$$\begin{aligned} R(z) &= 2E_0^2 \int_{\lambda} f(\lambda) \sin^2 \left\{ \frac{2\pi nz}{\lambda} \right\} d\lambda \\ &= E_0^2 \left\{ \int_{\lambda} f(\lambda) d\lambda - \int_{\lambda} f(\lambda) \cos \left\{ \frac{4\pi nz}{\lambda} \right\} d\lambda \right\} \end{aligned} \quad (2.9)$$

The second integral is very similar to the Fourier transform of the reflected spectrum. Note, however, the factor 2 here.

2.4.4 Treatment of Polychromatic Replay

When the recorded Lippmann photograph is illuminated with a diffuse white spectrum (the same as that used for the recording), each individual volume element in the emulsion reflects the incident waves according to Equation 2.9. We may therefore write down an approximate expression for the reflected electric field due to reflection at point z

$$dE_x(z, \lambda') = -E_0 \sqrt{F(\lambda')} R(z) \sin \left\{ 2\pi\nu't - \frac{4\pi n}{\lambda'} z \right\} \quad (2.10)$$

Note the phase term that is needed to account for the optical path length difference in the emulsion. Integrating all partial reflected waves, we obtain the total reflected field

$$\begin{aligned} E_x(\lambda') &= - \int_D E_0 \sqrt{F(\lambda')} R(z) \sin \left\{ 4\pi\nu't - \frac{4\pi n}{\lambda'} z \right\} dz \\ &= - \int_D E_0 \sqrt{F(\lambda')} R(z) \cos \left\{ \frac{4\pi n}{\lambda'} z \right\} \sin \{ 2\pi\nu't \} dz \\ &\quad + \int_D E_0 \sqrt{F(\lambda')} R(z) \sin \left\{ \frac{4\pi n}{\lambda'} z \right\} \cos \{ 2\pi\nu't \} dz \end{aligned} \quad (2.11)$$

where D is the thickness of the emulsion.

We may now use Equation 2.9 in Equation 2.11 to work out the reflected intensity as the time-averaged Poynting vector. In this calculation, we obtain several types of integral of which only one is non-zero due to simple orthogonality properties giving

$$I(\lambda') = \langle E_x(\lambda') H_y(\lambda') \rangle = \frac{nc\varepsilon_0}{2} F(\lambda) E_0^2 \left\{ \int_D R(z) \cos \left\{ \frac{4\pi n}{\lambda'} z \right\} dz \right\}^2 \quad (2.12)$$

where ε_0 is the electric field constant and c is the speed of light in vacuum.

The integral here is the inverse Fourier transform of the second term in $R(z)$. Its square determines the emulsion's reflectivity to the wavelength λ' .

From Equations 2.9 and 2.12, we can see that at a given image point, the reconstructed colour spectrum is proportional to the product $F(\lambda) f^2(\lambda)$. This means that the reflected spectrum of the recorded object is replayed by a Lippmann photograph as the square of the original spectrum (of course, this is under the assumption that the induced reflectivity is strictly proportional to the time averaged squared recording electric field intensity). In the field of digital image processing, this is referred to as a gamma correction of two. In practice, this can be compensated for by the γ curve of the recording material. This effect and the phase shift caused by using mercury (an optical medium of higher refractive index than gelatin) as the Lippmann reflector will be discussed later when we describe the possibility of recording Lippmann photographs without a reflector and using only the Fresnel reflection of air in contact with the emulsion gelatin.

Finally, a very pertinent question is whether the time coherence of white light is sufficiently long to record standing waves in a Lippmann emulsion at all. The expression relating the coherence time τ_c to the spectral bandwidth $\Delta\nu$ can be written as

$$\tau_c \Delta\nu \sim 1 \quad (2.13)$$

The coherence length L_c can likewise be defined as

$$L_c = \frac{c}{n} \tau_c \sim \frac{\lambda^2}{n \Delta\lambda} \quad (2.14)$$

Using monochromatic light from a laser, the coherence length can be very long. For white light (e.g., the sun's spectrum), the mean wavelength is approximately 550 nm and $\Delta\lambda \sim 300$ nm. This then equates to a coherence length of $L_c \sim 1 \mu\text{m}$! It is therefore remarkable that Lippmann photography works in practice and that it is capable of producing such wonderful and brilliant colour photographs.

2.5 Early Lippmann Emulsions

Let us look at how Lippmann plates were made and processed originally. The plates that Lippmann used were albumen emulsions containing potassium bromide. The plates were sensitised in a silver bath, washed, rinsed with cyanine solution and dried. The sensitivity was extremely low. Exposure times of 1 h or more were needed. When Auguste and Louis Lumière in Lyon, France introduced much finer-grained silver halide gelatin emulsions, these quickly became the recording material of choice for Lippmann photography [37,38]. Lippmann switched to the Lumière brothers' emulsions. These types of silver halide emulsions were much faster than the earlier albumen or collodion plates. Now the exposure time was only a few minutes rather than hours.

The most important contributions were made by Neuhauss and Lehmann; both were active in Germany. Neuhauss and Lehmann devoted a lot of time to the perfection of the Lippmann process. Many beautiful photographs were recorded by them, some of which have been preserved and are part of photographic collections in different museums around the world.

Almost all the research on Lippmann photography took place in Europe. Ives [41] is the only known scientist in the United States who was involved in the development of the technique. Most of the researchers of this time had their own way of preparing their silver halide emulsions. Later, at about the turn of the century, commercial Lippmann plates were produced by Kranseder & Cie A.G. in Munich and, after Kranseder's death, by Jahr's photographic company in Dresden. The recording procedure using the mercury plate holder was straightforward and more or less the same for all experimenters. As is the case in colour holography today, the recording material is the most important factor for recording high-quality Lippmann photographs as well as colour holograms. The preparation of the emulsion and its processing were absolutely critical to obtain good colour photographs. These emulsions were based on experience gained from making Lippmann photographs over several years.

2.5.1 Auguste (1862–1954) and Louis Lumière (1864–1948)

The Lumière brothers devoted several years to trying to commercialise the Lippmann technique. They were able to manufacture an ultrafine-grain panchromatic emulsion on which they recorded many beautiful colour photographs.

The Lumière brothers' first successful emulsion was published in 1893 [37] and later modified by them [38] as presented in Table 2.1. The Lumière brothers recorded several colour interference photographs. They recorded the first colour portrait in the summer of 1893. It was a photograph of a woman, resting her head on her arm at a table with a green background of grapes and a glass of red wine on the table. The exposure time was 4 min in bright sunlight. Louis Lumière was the one who was mainly responsible for these photographs. At the International Photographic Congress in Geneva in August 1893, he presented

TABLE 2.1

The Lumière Emulsion

Solution A	Solution B
Gelatin (10 g)	Gelatin (10 g)
KBr (3.5 g)	AgNO_3 (5 g)
Water (200 mL)	Water (200 mL)

Note: Sensitisers, such as erythrosine, cyanine, anisolin and methyl violet were used.

several colour portrait photographs and landscapes. These images ($3\text{ cm} \times 5\text{ cm}$) were projected on a $40\text{ cm} \times 70\text{ cm}$ screen with a projector designed by the Lumière brothers.

2.5.2 Richard Neuhauss (1855–1915)

Neuhauss, who was a physician from Berlin, was one of the most experienced experimenters. He made many beautiful Lippmann photographs. Between 1894 and 1908, he produced about 2500 plates and performed experiments in his home in Gross-Lichterfelde outside Berlin. The test object was most often a stuffed parrot that was installed on his balcony, but also landscapes and portraits. His book contains important information on emulsion making [40]. Neuhauss stressed the importance of gelatin quality for making successful emulsions. For the plates, he used gelatin primarily from Lautenschläger in Berlin. His recommended emulsion is found in Table 2.2.

To prepare the emulsion, the gelatin is first dissolved in cold distilled water; this takes about 10 min. Then, the gelatin–water solutions A and C are heated until the gelatin is completely melted, after which solution C is cooled down to 35°C and solution A to 37°C . The book stresses the fact that the temperature of the solutions *must not exceed* 40°C . Solution B is then mixed with solution A under vigorous stirring. This mixture is then poured *drop by drop* into solution C while stirring. When finished, sensitisers are added to the mixture:

- erythrosine–alcohol solution (1:500) 1 mL
- cyanine–alcohol solution (1:500) 2 mL

TABLE 2.2

Neuhauss' Emulsion

Solution A	Solution B	Solution C
Gelatin (2.5 g)	AgNO_3 (1.5 g)	Gelatin (5 g)
Water (70 mL)	Water (5 mL)	KBr (1.25 g)
		Water (75 mL)



FIGURE 2.6 Reproduction of one of Richard Neuhauss' stuffed parrot photographs from 1899. (Courtesy of the Royal Photographic Society Collection, Bradford, UK.)

The emulsion (which should now appear completely transparent) is now filtered in the coating bottle, which constitutes a part of the coating process. The preheated plates (previously cleaned in a 50% nitric acid solution for 24 h) are coated as soon as possible after the solution is ready. The emulsion is coated by letting it float over the surface of the levelled plates until the entire plate is completely covered. The amount of emulsion prepared in this way will be sufficient for 8 to 10 plates measuring 9 × 12 cm. The plates are then quickly cooled by placing them on a levelled marble table. It is important that the plates do not dry out completely after the cooling because there is a danger of potassium nitrate crystallising within the emulsion before they can be washed to remove the unwanted salt. The plates are then rinsed and placed in a tray filled with water for 15 min, during which time the water bath must be changed once. After the wash, the plates are dried. Neuhauss recommends the use of a centrifuge for this purpose to avoid leaving drop marks on the finished plates. The emulsion must appear completely clear, otherwise the plates will not perform well. He also mentions another important point concerning the mixing of the emulsion, which is the importance of mixing and then coating the plates without delay. Neuhauss used a stuffed parrot for many of his emulsion and recording tests. One such recording that has survived is shown in Figure 2.6.

2.5.3 Hans Lehmann (1875–1917)

The following recipe (Table 2.3) from Lehmann was used for manufacturing commercial plates at Richard Jahr's dry plate factory in Dresden. Not until 1925, long after Lehmann's death in 1917, was his formula revealed by Jahr [84].

The gelatin is dissolved at 35°C and then filtered. Solution B is added to 80 mL of solution A. Potassium bromide (3.2 g) is then added to and dissolved in the remaining solution A. When the potassium bromide has been completely dissolved, the solution is slowly poured into the gelatin–silver nitrate solution. Note that adding the KBr solution to the AgNO₃ solution is actually opposite to the way that the other emulsions are mixed. All solutions must be kept at 35°C. After precipitation is completed, stirring is required for 3.5 min. Then, the following sensitising dye solutions (warmed to 30°C) are added:

- pinacyanol–alcohol solution (1:1000) 4 mL
- orthochrom T–alcohol solution (1:1000) 4 mL
- acridine orange–alcohol solution (1:500) 4 mL

This should be done in approximately 45 s. No further heating of the emulsion is allowed. Well-cleaned glass plates are then coated and cooled. A 10 min wash is needed to remove the potassium nitrate. Finally, the plates are dried in a horizontal position. The main secret behind this recipe is the particular sensitising dyes used and their combination. Colour photographs recorded in this emulsion produced the best colour-correct sensitivity and colour balance ever achieved in Lippmann photography (Figure 2.7). If you want to try one of the old recipes today, this formula would definitely be the first choice.

Lehmann's improved emulsion possessed approximately 10 times higher sensitivity compared with previous Lippmann emulsions. In addition, the emulsion allowed a good colour balance, which meant that white was easily obtained. The colour sensitivity maxima peaked at the following wavelengths: 635, 585, 509 and 475 nm. Lehmann also provided exposure recommendations for the new emulsion, which were applicable to landscape photographs in bright sunlight (Table 2.4).

TABLE 2.3

Lehmann's Emulsion

Solution A	Solution B
Gelatin (20 g)	AgNO ₃ (4 g)
Water (390 mL)	Water (10 mL)



FIGURE 2.7 Reproduction of a *Still Life* 1908 Lippmann photograph by Hans Lehmann (Photo courtesy of Preus Photomuseum. Preus Photomuseum Collection, Norway.)

TABLE 2.4

Exposure Requirements for Lippmann Photographs using the Lehmann Emulsion

Aperture, F/number	F/3	F/3.5	F/4	F/4.5	F/5	F/6
Exposure time in seconds	6	8	11	14	17	25

For portraits, it was recommended that they not be made in direct sunlight but with a 20 s exposure time at F/3.5. Lehmann published articles on the practical aspects of recording Lippmann photographs and how to use the Zeiss equipment [85,86].

2.5.4 Edmond Rothé (1873–1942)

Edmond Rothé from Nancy University in France recorded Lippmann photographs without using the mercury reflector [87–91]. Instead, he used the light reflected at the gelatin–air interface only. Because of its simplicity, this technique is very interesting. The emulsion Rothé used for his experiments is given in Table 2.5. Rothé used the Lumière–Lippmann formula with minor modifications. We shall discuss the mercury-free, gelatin–air recording technique below.

Part A of Rothé's recipe is mixed at a high temperature. When cooled down to 40°C, the silver nitrate powder is added; this takes 1 to 2 min to dissolve under continuous agitation. Thereafter, the following sensitizers are added:

- cyanine–alcohol solution (1:500) 3 mL
- malachite green–alcohol solution (1:500) 2 mL
- gycin red–alcohol solution (1:500) 10 mL

The emulsion is then filtered. The plates should be coated, whirled and placed on a levelling table to set, then washed in running water for half an hour and dried. Both the demand for extremely high resolving power (very fine grains) and the colour sensitisation (isochromatism) of the Lippmann emulsion are

TABLE 2.5

Rothe's Emulsion

Part A	Part B
Gelatin (5 g)	AgNO ₃ (0.75 g, fine powder)
KBr (0.53 g)	
Water (100 mL)	

equally important. Today, the dyes used for the sensitisation of silver halide emulsions are mainly the cyanine and isocyanine dyes.

2.6 Recording of Early Lippmann Photographs

2.6.1 Recording Equipment

Many of the professional photographic cameras at the end of the 1900s were cameras for glass-plate negatives. The main additional piece of equipment required for the Lippmann photographer was the mercury dark slide. At first, the slide had to be made up by the person who wanted to record a colour photograph. However, after some time, it was possible to obtain the equipment from camera manufacturers. Carl Zeiss Kamerawerke in Jena manufactured mercury plate holders, filters and viewing and projection apparatae [86] (Figure 2.8). Equipment was also made by other German companies: Stegemann, Braun

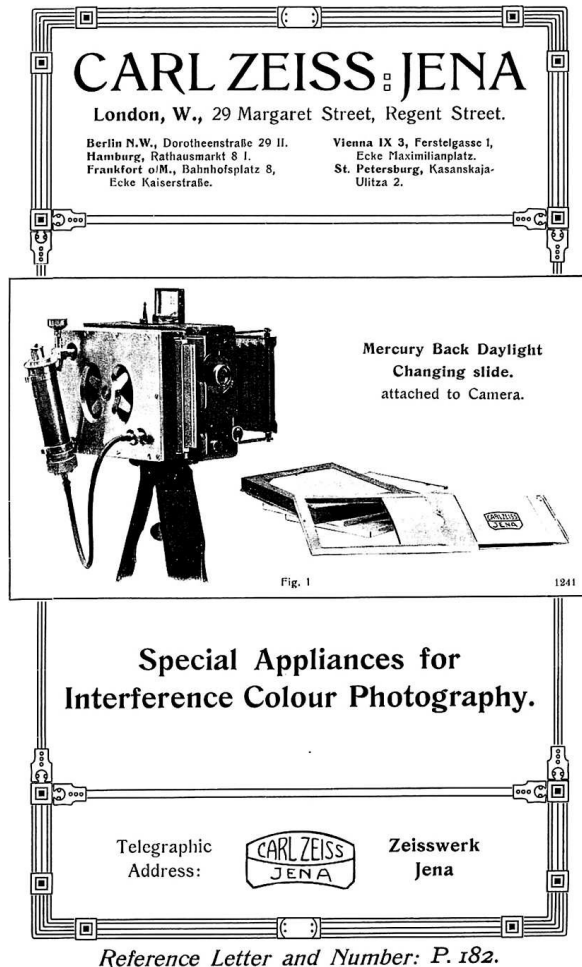


FIGURE 2.8 Zeiss interference colour photography catalogue.

and the plate manufacturer Kranseder & Cie. In England, dark slides were made by Watson & Sons and Penrose & Co.

Most Lippmann photographers used mercury for the required light reflection and phase locking. It worked rather well but involved both practical problems and safety concerns. Fog and streaks caused by mercury in contact with the silver halide emulsion was one such problem. A substitute for mercury was therefore of interest. As previously mentioned, Rothé recorded objects using the reflection off the gelatin–air interface only. Effectively, the reflection from this interface creates weak reflected light, which interferes with the (stronger) incoming light. Because lower modulation of the interference fringes was expected in this case, the efficiency of such an image was anticipated to be lower than when the mercury reflector was used. Notwithstanding this, Rothé reported good results and published several articles with details about his recording technique [87–91]. The main advantage was that an ordinary camera without special slides could be used and only Lippmann plates were needed for recording colour photographs. More about the difference between mercury–gelatin versus the air–gelatin interface later.

2.6.2 Processing Lippmann Silver Halide Emulsions

The processing of Lippmann colour photographs was more or less done in the same way by most experimenters. They used developers based on pyrogallol and ammonia, which were formulated to suit the particular emulsion. A surface developer will perform well because no image information is located deep inside the emulsion. In addition, the hardening effect on gelatin that pyrogallol provides is important. The Lumière developer was generally recommended. The recipe is given in Table 2.7. Development time was 1 to 3 min. Most often, the image was fixed by a 15 s immersion in a potassium cyanide bath (5%). However, the use of a safer sodium thiosulphate bath (15%–20%) was suggested by other Lippmann photographers. Rather later, fixing the developed image was not recommended because this would change the thickness of the emulsion and therefore change the colour of the image. The plate could be intensified by a bleaching and redeveloping process. Ives [41] tested other developers based on amidol and hydroquinone and used bleaching to create phase gratings which came out even more brilliant and with a narrower bandwidth when compared with those processed by pyrogallol. He was actually touching on modern processing methods that are now applied in holography.

2.6.3 Viewing Lippmann Photographs

There is one particular problem in viewing recorded Lippmann photographs. The reflection from the gelatin surface of the emulsion can cause colour distortion as a result of the phase shift in the gelatin–mercury interface during recording. Because the Lippmann photograph has to be viewed using perpendicular illumination, it is important to eliminate the specular surface reflection to see the image clearly. This can be accomplished by attaching a wedged glass plate (with an angle of ~10°) on top of the emulsion using an index-matching glue, most often Canada balsam ($n = 1.52$ – 1.54 ; Figure 2.9). The back of the photograph was usually painted black (Lippmann photographers often used asphaltum varnish mixed with machine oil for this purpose), covered with black paper and the edges sealed. Another possibility was to apply gum styrax ($n = 1.58$) which could be removed if desired after being slightly heated and the wedge plate reused for another Lippmann photograph. The refractive index of gum styrax is also a better match. Today, modern optical epoxy cements may be used as long as they do not affect the emulsion.

A good way to view a Lippmann photograph is by a small opening in a wall facing a brilliant white sky. If the observer stands with his back to the opening and holds the picture at arm's length, reflecting the sky, the image appears at its best. There were special viewing devices, such as the dioptric and the catoptric viewing apparatus, which facilitated the display of these beautiful colour photographs (Figure 2.10). The viewing difficulty inherent to Lippmann photographs resembles in some way today's difficulties in displaying and viewing holograms.

The photographs could also be viewed in an enlarged format by projecting the reflected image using a special projector. The image could not be projected like a modern slide however. Rather, the reflected image had to be projected by a projector of the aphengescope-type (Figure 2.11). Zeiss Works in Germany produced such viewing and projecting equipment for Lippmann photographs [86].

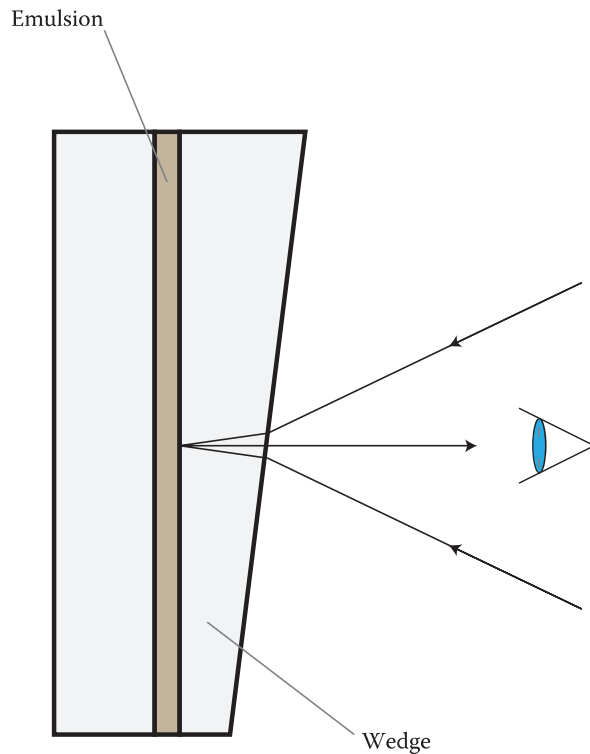


FIGURE 2.9 Wedged glass prism (Wiener prism) attached to a Lippmann photograph.

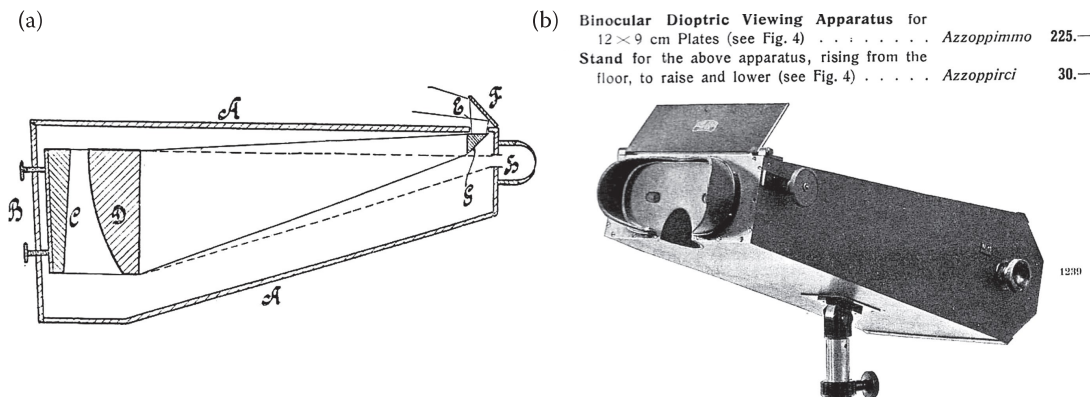


FIGURE 2.10 Zeiss viewing equipment for Lippmann photographs: (a) principle and (b) viewing apparatus.

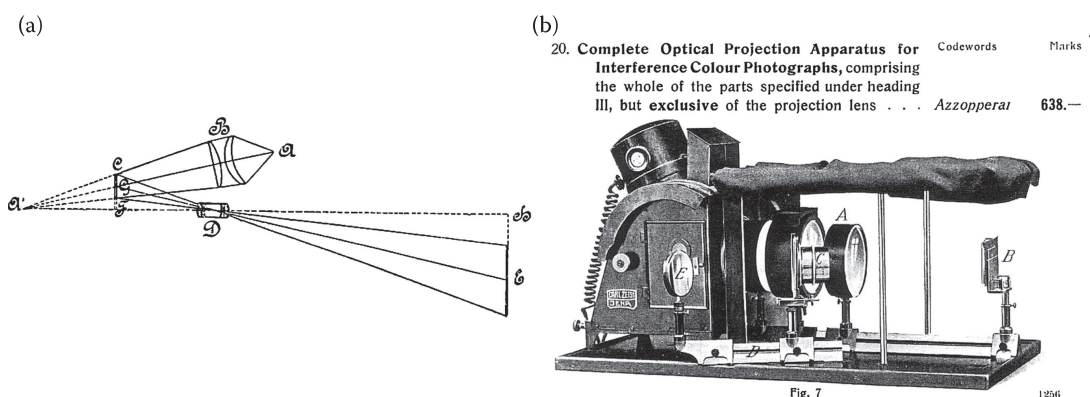


FIGURE 2.11 Zeiss projection equipment for Lippmann photographs: (a) principle and (b) projector.

2.6.4 Early Investigations of Lippmann Emulsions

The researchers working with Lippmann photography investigated the interference structure of the emulsion (Zenker's laminae) not only for the purpose of improving the colour-recording technique but also to prove Zenker's photochromic theory as applied to Lippmann photography. This theory, as previously mentioned, had convincingly been verified by Wiener's famous experiment on monochrome stationary light waves [20]. However, using optical microscopy to study the periodic silver grain structure in the emulsion pushed this technique to its very limits. Notwithstanding this, in 1897, Neuhauss succeeded in microscopically imaging the interference structure of red light recorded in a Lippmann emulsion [92] (Figure 2.12). He used a long wavelength recording in which the interference layers were most widely separated. In air, the distance between the interference layers was 330 to 380 nm, and in the emulsion, it was closer and depended on the refractive index of the emulsion. A fringe separation of 220 to 250 nm had to be microscopically resolvable to see the recorded structure in the emulsion. Neuhauss used different techniques for embedding the emulsion samples to be studied. He used paraffin, Canada balsam and glycerin, which slightly increased the separation of the layers in some cases. Flatau from the Anatomic Institute in Berlin helped him to prepare the thin emulsion layers (~2 µm in thickness) using a very fine microtome. The quality of the microscope lens was also considered to be very important, which is why the oil-immersion technique and a high-quality apochromatic lens (numerical aperture, 1.40) from Zeiss were used. Short-wavelength illumination also increased the resolution. Accordingly, Neuhauss used

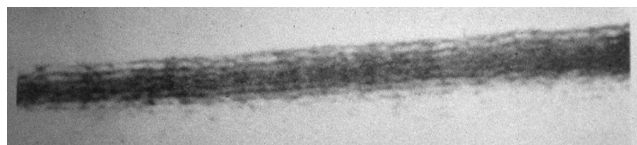


FIGURE 2.12 Neuhauss' first microrecording of a Lippmann emulsion revealing the interference fringes. (Courtesy of R. Neuhauss, 1898.)

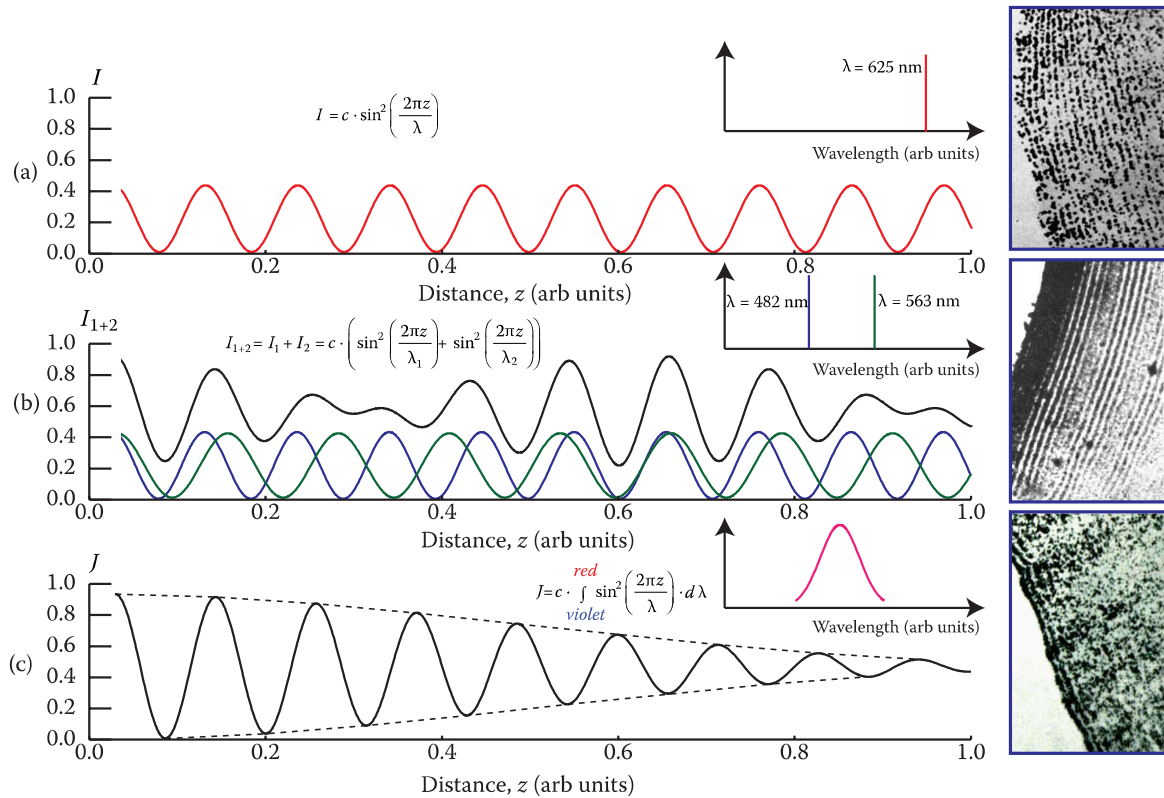


FIGURE 2.13 Lehmann's emulsion investigations.

sunlight passing through a dark blue dye to get a wavelength peaked at approximately 450 nm. Using these techniques, Neuhauss succeeded in recording photographs of the emulsion through a microscope having a linear magnification of approximately 4000 \times . The separation of interference layers was clearly visible and the distance between them could be measured. The results of the experiment were in good agreement with the theory. Thereafter, optical microscopy was often used by Lippmann photography scientists to study the influence of various recording and processing methods. Both Lehmann [42] and Cajal [93] made micrographs of Lippmann emulsions. Figure 2.13 shows the Lehman emulsion investigation.

The interest in Lippmann photography disappeared almost totally after 1907 when the Lumière brothers started to commercialise their autochrome plates for colour photography [94]. A much faster colour material was offered based on a different colour-recording principle with relative ease of handling. This became the first commercially successful colour photography technique and was used until the late 1930s when modern three-layer colour emulsions (with or without colour couplers) were introduced.

2.6.5 Museum Collections of Lippmann Photographs

Over a period of about 15 years, Lippmann photographs were recorded by a very limited number of scientists and photographers around the world. However, some of these photographs have been preserved and can be found in private and institutional collections. A rather large collection is in the Musée de l’Elysée Lausanne, Switzerland [95]. In France, Lippmann photographs are to be found at the following museums or institutes: Université Pierre et Marie Curie [96], Musée français de la Photographie [97], Société française de Photographie [98], all located in or near Paris, as well as in the Musée Nicéphore Niépce, Chalon-sur-Saône [99].

Preus Fotomuseum, Horten, Norway has some excellent photographs recorded by Neuhauss [100]. In England, the Royal Photographic Society has two Lippmann photographs. George Eastman House in Rochester, New York has several of Ives' photographs in their collection [101]. Museums of science and technology in a few countries may also have Lippmann photographs on display in their photographic exhibitions or in their collections.

2.7 Modern Lippmann Photography

Single-beam Denisyuk reflection holography [54,55] shows similarities with Lippmann photography. In both cases, an interference pattern is recorded in a high-resolution emulsion. For example, Kogelnik's theory [102] for the volume holographic grating is also applicable to Lippmann photography. The Bragg diffraction regime applies to both. The fundamental difference between a Lippmann photograph and a Denisyuk reflection hologram is that in the Lippmann case, there is no phase recording involved; the recorded interference structure is a result of the phase-locking of the light by the reflecting mirror. In holography, the phase information is actually recorded, being encoded as an interference pattern created between the light reflected from the object and a coherent reference beam. To some extent, a Lippmann photograph can be regarded as a reflection image-plane hologram recorded with light of very short temporal coherence. The reference wave is a diffuse complex wave front (the mirror image of the exit pupil of the recording lens).

The recording of monochromatic and polychromatic spectra has to be treated differently. The recording of monochromatic light in a Lippmann emulsion is easy to understand, and it is very similar to recording a volume reflection hologram. A broadband polychromatic spectrum such as a landscape image is very different. In this case, the recorded interference structure in the emulsion is located only very close to the surface of the emulsion that is in contact with the reflecting mirror. Thus, an emulsion thickness of only 1 to 2 μm is needed and actually preferred. A colour reflection hologram, on the other hand, is a result of the three colour process (red, green and blue) involving three monochrome recordings superimposed in the same emulsion. This can be done either by sequential or simultaneous exposure of the recording material when illuminated with the three primary laser wavelengths. In the case of the hologram, interference fringes are recorded throughout the whole depth of the emulsion. The thicker the emulsion is, then generally, the narrower the reconstruction band will be—which means that for the reconstruction of a colour hologram by a broadband white-light source, a compromise must be made between high image brightness and high colour saturation.

2.7.1 Modern Lippmann Emulsions

There was very little interest in making silver halide plates of the Lippmann type after interest in Lippmann photography disappeared. However, the need for such plates came back when holography started to become popular in the early 1960s. A full discussion of modern ultrafine-grain emulsions as used in holography, Lippmann photography and other high-resolution imaging applications will be presented in Chapter 4.

2.7.2 Recording and Processing of Lippmann Photographs Today

Recent progress in the development of colour holography has opened up new possibilities to investigate Lippmann photography. New and improved recording materials (silver halide and photopolymer) combined with special processing techniques developed for colour holograms may be expected to significantly improve Lippmann's interference photography. As mentioned in Section 2.3, a new interest in Lippmann's technology has been manifested by many recent publications [56–84]. Connes [61] published an excellent review of the history of standing light waves and colour interference photography. Nareid [62] and Fournier [64] both made contributions to the history of Lippmann photography. Nareid and Pedersen [63] have developed computer programs for modelling the Lippmann process. For monochromatic recording, Kogelnik's coupled wave theory [102] can be applied to Lippmann photography. For polychromatic recording, superposition of several frequencies in the recording light gives rise to aperiodic space gratings for which the Kogelnik theory cannot be applied. To treat such an aperiodic grating, Nareid and Pedersen [63] have, however, presented a treatment of wave propagation in a stratified medium where a first Born approximation is made. In addition, in Chapter 12, we shall discuss an alternative to Kogelnik's coupled wave theory in which a volume grating is treated as an infinite sum of infinitesimal discontinuities in the permittivity profile and the reflected signal wave is built up by summing the individual Fresnel reflections from such discontinuities in a consistent manner [103]. This model is able to naturally treat aperiodic (polychromatic) space gratings but at present has not been generalised to the diffuse images characteristic of Lippmann photographs.

Fournier and Burnett [66] describe colour rendition and archival properties of Lippmann photographs and compare Lippmann's technique with holography. They investigated old Lippmann photographs using modern electron microscopy. In addition, they recorded a monochromatic volume grating in DuPont photopolymer material using filtered light (520 nm, 10 nm bandwidth) from a slide projector. Marraud and Fournier [67] explained Lippmann's early introduction of Fourier mathematics in optics. A major contribution was made by Phillips et al. [69], comparing the theory of Lippmann photography and holography. Other important considerations, such as the influence of spatial coherence (camera lens aperture) and internal emulsion scattering were also treated in the article.

Rich and Dickerson [71] published results on recording Lippmann photographs on laboratory-made and commercial silver halide emulsions. Bjelkhagen [73] demonstrated the possibility of recording Lippmann photographs in DuPont panchromatic photopolymer materials. Bjelkhagen et al. [74] used the Slavich PFG-03C photographic emulsion to record Lippmann photographs using only the gelatin-air interface as the reflector. The history of Lippmann photography and modern recording techniques has been published by Bjelkhagen [75]. A potential modern application of Lippmann photography may appear in the document security field [76]. Optical variable devices (OVDs) such as holograms, are now common in this field. A Lippmann photograph can offer a new type of OVD, which belongs to the interference security image structures. It offers additional advantages over holograms for unique security documents.

2.7.3 Modern Lippmann Photographs Made with Different Modern Materials

One of the authors (HB) has spent considerable time recording modern Lippmann photographs on both photopolymer and silver halide materials. To record these photographs, the following camera was used:

- manufacturer: Eastman Kodak Co. (Folmer & Schwing Division)
- model: Auto Graflex Camera

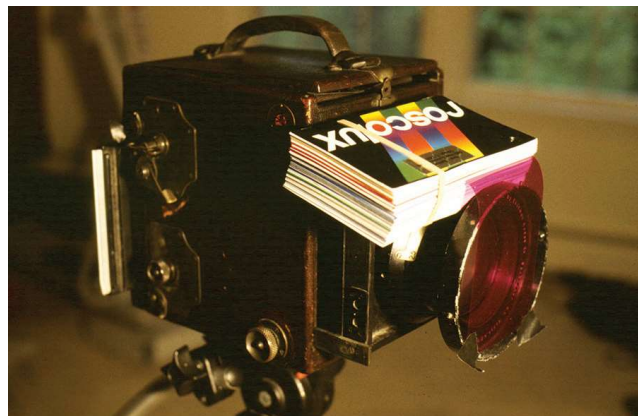


FIGURE 2.14 Graflex 4 in. \times 5 in. camera for Lippmann photography.

- format: 4 in. \times 5 in.
- lens: Kodak Aero Ektar F/2.5, 178 mm

A photograph of the camera is shown in Figure 2.14. It could accommodate both sheet film and glass plates.

2.7.3.1 Photopolymer Recording Materials

The first experiments on Lippmann photography were carried out on panchromatic photopolymer materials. The colour holography photopolymer material HRF-700X from E.I. du Pont de Nemours & Co. was used [104–107]. Although less sensitive than the silver halide emulsions (which are also slow, according to modern photographic standards), it has the special advantages of easy handling and dry processing (only UV-curing and baking).

The recording of a DuPont Lippmann photograph is relatively simple. Before the recording took place, a reflecting mirror foil was laminated to the polymer film. This was a silver-sputtered (800 Å) polyester film produced by Courtaulds Performance Films [107] without the standard anti-dust oxide (InO) top layer. The mirror foil was laminated to the photopolymer material under safelight and then loaded into a conventional sheet film holder. The film cassette was then attached to the back of the camera, which had to be mounted on a tripod. In front of the camera lens, a colour correction filter was used to compensate for the low red sensitivity and the high green sensitivity of the photopolymer material. After the exposure was finished, the film holder was removed from the camera and opened in full daylight. The mirror foil was detached from the photopolymer film which was then exposed to direct sunlight (or strong white or UV light) for developing. DuPont recommends an exposure of approximately 100 mJ/cm² at 350 to 380 nm. The photograph must then be put into an oven at a temperature of 100°C for 2 h to increase the brightness of the image. A still life (a bowl of fruit) and a stuffed parrot were recorded using the technique described. Two 500 W halogen lights illuminated the scene at a distance of half a metre. The exposure time was between 5 and 10 min at aperture F/4. After processing, the back of the film was laminated to a black foil. For better viewing of the image, the front of the film was laminated to a wedged glass plate.

A modern Lippmann photograph using the DuPont photopolymer is shown in Figure 2.15; the spectrum of the Lippmann photograph is also presented in Figure 2.16. For conventional photographic reproduction, the sky was used as the illuminating field and a 35-mm camera with a macro lens was used with standard negative colour film (Kodak Royal Gold 100 ASA). No wedge glass plate was attached to the polymer film, as it was easy to view the image without the wedge. Then again, using a wedge plate may be expected to improve the contrast of the photograph. Note that a small vibration of the object probably occurred during the long exposure, which caused the image of the parrot to blur slightly.



FIGURE 2.15 Modern photopolymer Lippmann photograph produced by one of the authors (HB).

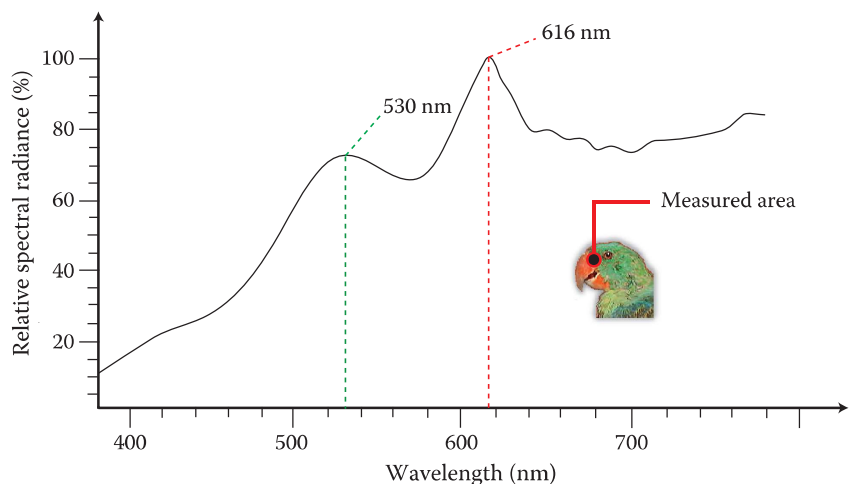


FIGURE 2.16 Spectrum recorded from Lippmann photograph of the parrot in Figure 2.15.

Figure 2.16 is interesting. The recording of a Lippmann photograph implies the recording of the entire reflected spectrum produced by the object rather than the common three-colour sampling used in most modern colour-recording techniques. This should be compared with the spectrograms produced by Fournier and Burnett [66] obtained from old Lippmann photographs.

2.7.3.2 Silver Halide Recording Materials

An easier solution than preparing one's own ultrahigh-resolution silver halide emulsions in the laboratory is to use the Slavich [108] commercial material designed for colour holography. Glass plates of a thickness of 1.5 mm and a size of 4 in. \times 5 in. coated with the Slavich emulsion were used by HB to record Lippmann photographs without a mercury reflector (Figure 2.17).

Recording a Lippmann photograph onto ultrafine-grain panchromatic silver halide emulsion was done in the following way: the plate was inserted into a conventional dark slide with the emulsion side facing away from the camera lens. A modified graphic film pack adapter was used, inside of which black velvet was attached to reduce scattered light (Figure 2.18). The plate holder was inserted into the camera, which was mounted on a tripod. Because the plate was exposed without mercury, the exposure time had to be increased compared with a recording with a mercury reflector. After the exposure was finished, the plate holder was removed from the camera and the plate processed in a darkroom.

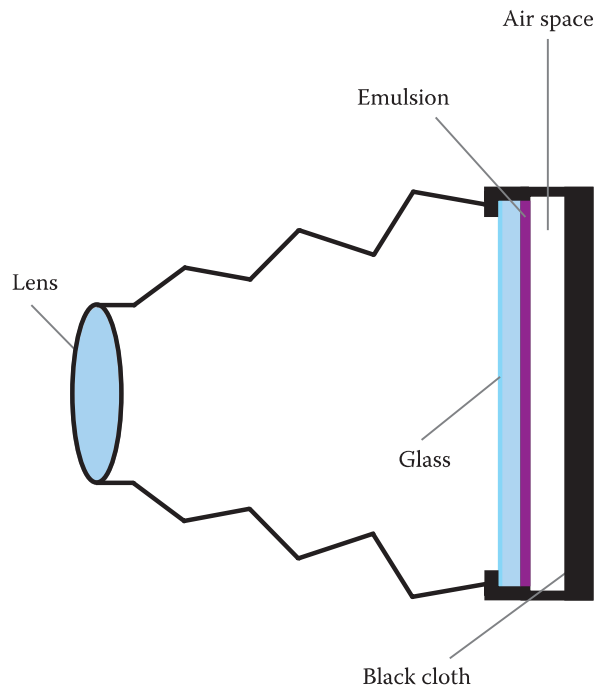


FIGURE 2.17 The principle of recording Lippmann photographs without mercury.

The reason why it is possible to obtain a Lippmann photograph without mercury can be explained in the following way. One must study the difference between reflections at the mercury surface and at the gelatin-air interface, as illustrated in Figure 2.19. A node is located at the mercury reflector (an optically thicker medium than gelatin), which is in contact with the gelatin surface. The phase shift there is π . On the contrary, an antinode is located at the gelatin-air surface when the reflection is obtained from a gelatin-air interface (an optically thinner medium than gelatin); in this case, because no phase shift occurs, a silver layer will be created at the emulsion surface after development. In the case of a mercury-gelatin interface, the first silver layer will be created at a distance from the interface of $\lambda/4$ inside the gelatin emulsion, whereas in the gelatin-air case, the second silver layer will be $\lambda/4$ closer to the gelatin-air interface surface compared with the same layer in the mercury-gelatin case. Because the coherence length of ordinary light is extremely short, this difference in distance from the gelatin-reflector surface is very important. The slightly increased modulation (caused by a higher degree of coherence) in the gelatin-air reflector case can somewhat compensate for the weaker reflection obtained. On the other



FIGURE 2.18 Modified Graphic Film Pack dark slide.

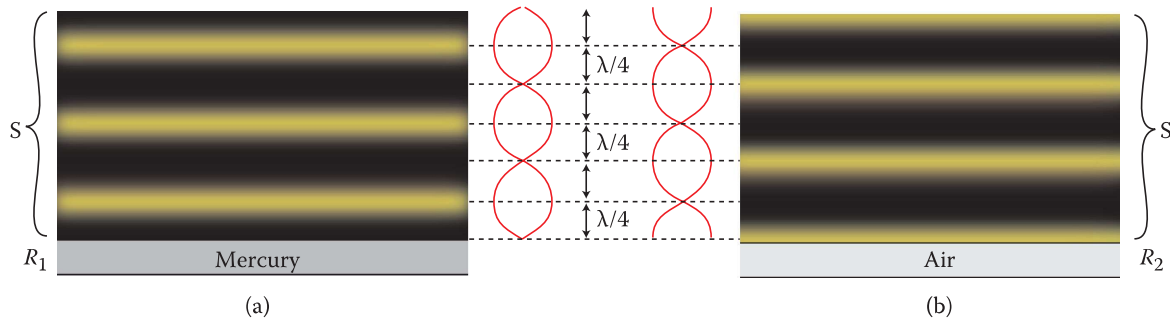


FIGURE 2.19 Light reflected at an optically thicker medium (mercury, R_1) and at an optically thinner medium (air, R_2). S is the gelatin emulsion. After development, the silver layers will be located at the antinodes.

hand, the exposure must be slightly increased to bring the recording up on the linear part of the Hurter–Driffield curve. During the development of the photograph, it is possible to also increase the interference fringe contrast using suitable developers. When using an air reflector, the surface reflection is in phase with the image. However, even in this case, it is recommended that a glass wedge be added to improve the image contrast.

The processing of the plates is critical. The Slavich emulsion is rather soft and it is important to harden the emulsion *before* the development takes place. Another fact is that the emulsion thickness is approximately 7 μm , which is much thicker than that necessary for Lippmann photography. The interference pattern is recorded only in a very thin volume at the top of the emulsion. This area has to be maintained intact after processing, another reason for the prehardening step. Emulsion shrinkage and other emulsion distortions caused by the developer must be avoided. The recommended bath to be used for this first processing step is listed in Table 2.6.

Among the old developers, the Lumière pyrogallol developer (Table 2.7) gave the best results and was used for all Lippmann photographs recorded by the author (HB). The development time was 90 s at approximately 18°C. The plates were not fixed to avoid shrinkage. After a 10 min wash, the plates were soaked in distilled water that contained a wetting agent. Finally, the photographs were slowly air-dried at room temperature.

TABLE 2.6

First Processing Bath for PFG03C

Distilled water	750 mL
Formaldehyde 37% (formalin)	10 mL (10.2 g)
Potassium bromide	2 g
Sodium carbonate (anhydrous)	5 g
Add distilled water to make	1 L
Processing time: 6 min	

TABLE 2.7

Lumière Developer

Solution A	Solution B
Pyrogallol (1 g)	Potassium bromide (30 g)
Distilled water (100 mL)	Distilled water (100 mL)

Note: Working solution: Mix 20 mL of Part A + 30 mL of Part B + 140 mL of distilled water. Add 10 mL of ammonia (s.w. 0.960) at 18°C just before using. Development time: 60 to 90 s.

Figure 2.20 shows a modern Lippmann photograph of one of the authors (HB) recorded on the PFG03C material using the simplified Lippmann technique without mercury. Figure 2.21 shows the recording setup. A colour correction filter was used in front of the camera lens to compensate for the fact that the Slavich material is not isochromatic. The aperture was F/4. The portrait was recorded on 2 July 1997 at 2:00 p.m. in direct sunlight. A diffusing screen was held above the subject's face to reduce the amount of glare off the face and a white screen was placed on the table to reflect additional soft light onto the face. The exposure time was 2 min.

After being processed, the back of the plate was painted black. For better viewing of the image, a wedged glass plate (Wiener prism) was cemented to the emulsion side of the plate—as previously done for the old Lippmann photographs.

It should be mentioned that Darran Green, Bury St. Edmunds in England, has devoted more than 10 years to perfecting the Lippmann technique. He makes his own silver halide emulsion and has recorded many beautiful Lippmann photographs, two of which are shown in Figures 2.22 and 2.23.



FIGURE 2.20 Lippmann photographic portrait of one of the authors (HB).



FIGURE 2.21 Recording of the Lippmann portrait—bright sunlight at 2 p.m., softened with diffuser; exposure time, 2 min; aperture F/4.

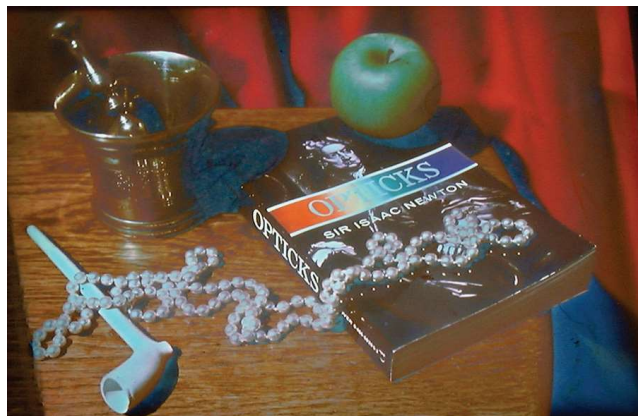


FIGURE 2.22 *Opticks*, a modern Lippmann photograph by Darran Green, Bury St. Edmunds, UK.



FIGURE 2.23 *Rose Garden*, another modern Lippmann photograph by Darran Green, Bury St. Edmunds, UK.

2.8 Concluding Remarks

There can be no doubt that the colours of Lippmann photographs are especially realistic. These photographs show extremely beautiful colours of a brightness and vividness that make today's conventional colour photographs seem almost bland in comparison. In particular, the colour reproduction of human skin is simply amazing when recorded with the Lippmann technique. Modern colour photography is certainly not bad, but it cannot reproduce the type of colours obtained in Lippmann photographs, as the Lippmann photograph records and reproduces the entire spectral data.

Modern Lippmann photography may have limited applications in photography but may also very well appeal to artists and art photographers. Lippmann photographs contain no dyes or pigments and their archival stability is very high. In addition, the new photopolymer Lippmann photographs are not sensitive to humidity variations, meaning that their colours will not vary according to environmental changes. Furthermore, a Lippmann photograph is fundamentally difficult to copy, making it attractive for security

applications. These features—unparalleled colour recording, great archival stability and resistance to copying—make Lippmann photography a unique photographic process.

Lippmann photography was the first interferometric imaging method to be discovered. It is capable of recording the spectral information of a two-dimensional scene to an exceptional precision. However, Lippmann photography led to another interferential method. This was the science of holography. Here, three-dimensional image data can be recorded to an exceptional precision—but at one wavelength only. The Lippmann photograph can, in some ways, be thought of as representing one extreme, with monochromatic holography as the other. In between these two extremes is polychromatic holography, in which the uncertainty in the recorded spectral data is roughly inversely proportional to the uncertainty in the geometrical data.

A discussion of Lippmann photography is therefore relevant in two ways. In itself, it constitutes a true technique of ultra-realistic imaging in the spectral domain and, as such, it may well have real applications. However, a discussion of Lippmann photography is also merited from the pedagogical and philosophical points of view due to its innate relationship to the wider field of holography.

REFERENCES

1. J. W. von Goethe, “Wirkung Farbige Beleuchtung,” in *Zur Farbenlehre*. Vol. II - Supplement, Cottasche Buchhandlung, Tübingen (1810) pp. 703–724.
2. J. F. W. Herschel, “On the chemical action of rays of the solar spectrum on preparations of silver and other substances, both metallic and non-metallic, and on some photographic processes,” *Phil. Trans.* **130**, 1–59 (1840).
3. A. E. Becquerel, “De l’image photographique colorée du spectre solaire,” *C. R. Acad. Sci.* **26**, 181–183 (1848).
4. A. E. Becquerel, “De l’image photochromatique du spectre solaire, et des images colorées obtenues dans la chambre obscure,” *C. R. Acad. Sci.* **27**, 483 (1848).
5. A. E. Becquerel, “De l’image photographique colorée du spectre solaire,” *Annal. Chim. Phys. (Paris)* **22**, 451–459 (1848).
6. A. E. Becquerel, “De l’image photochromatique du spectre solaire et des images colorées obtenues à la chambre obscure,” *Annal. Chim. Phys. (Paris)* **25**, 447–474 (1849).
7. A. E. Becquerel, “Nouvelles recherches sur les impressions colorées produites lors de l’action chimique de la lumière,” *Annal. Chim. Phys. (Paris)* **42**, 81–106 (1854).
8. A. E. Becquerel, *La lumière ses causes et ses effets* 2, (Chap.4) (F. Didot Frères, Fils et C^{IE}, Paris 1868) pp. 209–234.
9. C. F. A. Niepce de Saint-Victor, “Extrait d’un mémoire sur une relation existant entre la couleur de certaines flammes colorés, avec les images héliographiques colorées par la lumière,” *C. R. Acad. Sci.* **32**, 834–841 (1851).
10. C. F. A. Niepce de Saint-Victor, “Second mémoire sur l’héliochromie,” *C. R. Acad. Sci.* **34**, 215–218 (1852).
11. C. F. A. Niepce de Saint-Victor, “Troisième mémoire sur l’héliochromie,” *C. R. Acad. Sci.* **35**, 694–698 (1852).
12. C. F. A. Niepce de Saint-Victor, “Mémoire sur la gravure héliographique directement dans la chambre noire et sur quelques expériences scientifiques,” *C. R. Acad. Sci.* **41**, 549–553 (1855).
13. C. F. A. Niepce de Saint-Victor, “Quatrième mémoire sur l’héliochromie,” *C. R. Acad. Sci.* **54**, 281–284 (1862).
14. C. F. A. Niepce de Saint-Victor, “Cinquième mémoire sur l’héliochromie,” *C. R. Acad. Sci.* **56**, 90–93 (1863).
15. L.-A. Poitevin, “Action simultanée de la lumière et des sels oxygénés sur le souschlorure d’argent violet; application à l’obtention par la photographie des couleurs naturelles sur papier,” *C. R. Acad. Sci.* **61**, 1111–1113 (1865).
16. L. L. Hill, *A treatise on heliochromy; the production of pictures by means of light in natural colors*, Robinson & Caswell, New York (1856) [Reprinted by W. B. Becker, The Carnation Press 1972 State College, PA (1972)].
17. J. Boudreau, “Color daguerreotypes: hillotypes recreated,” in *Pioneers of Photography* (SPSE, Springfield, VA. 1987) Chapter 18, pp. 189–199.

18. W. Zenker, *Lehrbuch der Photochromie (Photographie der natürlichen Farben)*, Zenker, Berlin (1868) [Reprinted by B. Schwalbe, Verlag Friedrich Vieweg und Sohn, Braunschweig (1900)].
19. R. S. Lord Rayleigh, “On the maintenance of vibrations by forces of double frequency, and on the propagation of waves through a medium endowed with a periodic structure,” *Phil. Mag.* **24** (Ser. 5), 145–159 (1887).
20. O. Wiener, “Stehende Lichtwellen und die Schwingungsrichtung polarisierten Lichtes,” *Ann. d. Physik Chemie* **40**, 203–243 (1890).
21. O. Wiener, “Farbenphotographie durch Körperfarben und mechanische Farbenanpassung in der Natur,” *Ann. d. Physik Chemie* **55**, 225–281 (1895).
22. J. C. Maxwell, “Experiments on colour, as perceived by the eye, with remarks on colour-blindness,” *Trans. Roy. Soc. Edinburgh* **21**, 275–299 (1855).
23. H. Ghiradella, “Light and color on the wing: structured colors in butterflies and moths,” *Appl. Opt.* **30**, 3492–3500 (1991).
24. A. R. Parker, “515 million years of structural colour,” *J. Opt. A: Pure Appl. Opt.* **2**, R15-R28 (2000).
25. S. E. Mann, I. N. Miacoulis and P. Y. Wong, “Spectral imaging, reflectivity measurements, and modeling of iridescent butterfly scale structures,” *Opt. Eng.* **40**, 2061–2068 (2001).
26. P. Vukusic, R. Sambles, C. Lawrence and G. Wakely, “Sculpted-multilayer optical effects in two species of Papilio butterfly,” *Appl. Opt.* **40**, 1116–1125 (2001).
27. C. Lawrence, P. Vukusic and R. Sambles, “Grazing-incidence iridescence from a butterfly wing,” *Appl. Opt.* **41**, 437–441 (2002).
28. G. Tayeb, B. Gralak and S. Enoch, “Structural colors in nature,” *Optics and Photonics News*, **14** (2) 38–43 (2003).
29. L. I. Rugani, “Structural and photonic properties of butterfly wings replicated,” *Photonics Spectra* (No. 12) 18 (2006).
30. R. T. Lee and G. S. Smith, “Detailed electromagnetic simulation for the structural color of butterfly wings,” *Opt. Eng.* **48**, 4177–4190 (2009).
31. H. D. Wolpert, “Optical filters in nature,” *Optics and Photonics News* **20**, (2) 22–27 (2009).
32. G. Lippmann, “La photographie des couleurs,” *C. R. Acad. Sci.* **112**, 274–275 (1891).
33. G. Lippmann, “La photographie des couleurs [deuxième note],” *C. R. Acad. Sci.* **114**, 961–962 (1892).
34. G. Lippmann, “Photographies colorées du spectre, sur albumine et sur gélatine bichromatées,” *C. R. Acad. Sci.* **115**, 575 (1892).
35. G. Lippmann, “Sur la théorie de la photographie des couleurs simples et composées par la méthode interférentielle,” *J. Physique* **3** (No.3), 97–107 (1894).
36. E. Lebon, *Savants du jour: Gabriel Lippmann. Biographie, bibliographie analytique des écrits*, Gauthier-Villars, Paris (1911).
37. A. Lumière and L. Lumière, “Sur les procédés pour la photographie des couleurs d’après la méthode de M. Lippmann,” *Bull. Soc. franç. Phot. (2 série)* **9**, 249–251 (1893).
38. A. Lumière and L. Lumière, “Untersuchungen über die Herstellung einer lichtempfindlichen kornlosen Schicht,” *Eder’s Jahrbuch der Photographie und Reproductionstechnik* **11**, 27–30 (1897).
39. E. Valenta, *Die Photographie in natürlichen Farben mit besonderer Berücksichtigung des Lippmannschen Verfahrens sowie jener Methoden, welche bei einmaliger Belichtung ein Bild in Farben liefern*. Zweite vermehrte und erweiterte Auflage. Encyklopädie der Photographie, Heft 2, W. Knapp Verlag, Halle a.S (1912).
40. R. Neuhauss, *Die Farbenphotographie nach Lippmann’s Verfahren. Neue Untersuchungen und Ergebnisse*. Encyklopädie der Photographie, Heft 33, W. Knapp Verlag, Halle a.S (1898).
41. H. E. Ives, “An experimental study of the Lippmann color photograph,” *Astrophysical J.* **27**, 325–352 (1908).
42. H. Lehmann, *Beiträge zur Theorie und Praxis Direkten Farbenphotographie mittels Stehender Lichtwellen nach Lippmanns Methode*, Trömer, Freiburg i.Br. (1906).
43. A. Berthier, *Manuel de Photochromie Interférentielle. Procédés de Reproduction directe des Couleurs*, Gauthier-Villars et Fils, Paris (1895).
44. F. Drouin, *La photographie des couleurs*, C. Mendel, Paris (1896).
45. R. Child Bayley, *Photography in colours*, Iliffe, Sons & Sturmey Ltd., London (1900).
46. E. Senior, “Lippmann’s process of interference heliochromy,” in *A Handbook of Photography in Colours*, Section III, Marion & Co., London (1900) pp. 316–343.

47. A. Berget, *Photographie directe des couleurs par la méthode interférentielle de M. Lippmann*, Gauthier-Villars, Paris (1901).
48. L. Tranchant, *La photographie des couleurs simplifiée*, H. Desforges, Paris (1903).
49. E. König, *Die Farben-Photographie*, Gustav Schmidt Verlag, Berlin (1904) [2: English translation by E. J. Wall, *Natural-color photography*, Dawbarn & Ward, Ltd. London (1906)].
50. B. Donath, *Die Grundlagen der Farbenphotographie*, Verlag Freidrich Vieweg und Sohn, Braunschweig (1906).
51. S. R. y Cajal, *La fotografía de los colores. Fundamentos científicos y reglas prácticas*, Líbros Clan A. Gráficas S. L., Spain (1912) [Reprinted : Colección Técnicas Artísticas, Madrid (1994)].
52. E. J. Wall, “Die Praxis der Farbenphotographie: Das Lippmann-Verfahren,” in *Handbuch der wissenschaftlichen und angewandten Photographie*, ed. by A. Hay. Band VIII, Springer Verlag, Vienna (1929) pp. 219–230.
53. Y. N. Denisyuk, Dokl. Akad. Nauk. (Academy of Sciences Reports, USSR) **144** (No. 6), 1275–1278 (1962) [2: Transl.: Photographic reconstruction of the optical properties of an object in its own scattered radiation field]. *Sov. Phys. Doklady* **7**, 543–545 (1962).
54. Y. N. Denisyuk, “On the reproduction of the optical properties of an object by the wave field of its scattered radiation,” *Opt. Spectrosc. (USSR)* **14**, 279–284 (1963).
55. Y. N. Denisyuk and I. R. Protas, “Improved Lippmann photographic plates for recording stationary light waves,” *Opt. Spectrosc. (USSR)* **14**, 381–383 (1963).
56. K. F. Lindman, “Prüfung der Grundlagen der Theorie der Lippmannschen Farbenphotographie durch Versuche mit elektrischen Wellen,” in *Acta Academiae Aboensis X Sec.11.*, Åbo Akademi, Åbo (1937) pp. 1–62.
57. J.-L. Delcroix, “Utilisation des plaques Lippmann comme filtres,” *Revue d’Optique*. **27**, 493–509 (1948).
58. H. Fleisher, P. Pengelly, J. Reynolgs, R. Schools and G. Sincerbox, “An optically accessed memory using the Lippmann process for information storage,” in *Optical and Electro-Optical Information Processing* (MIT Press 1965) pp. 1–30.
59. R. E. Schwall and P. D. Zimmerman, “Lippmann color photography for the undergraduate laboratory,” *Am. J. Phys.* **38**, 1345–1349 (1970).
60. L. Lindegren and D. Dravins, “Holography at the telescope—an interferometric method for recording stellar spectra in thick photographic emulsions,” *Astron. Astrophys.* **67**, 241–255 (1978).
61. P. Connes, “Silver salts and standing waves: the history of interference color photography,” *J. Optics (Paris)* **18**, 147–166 (1987).
62. H. Nareid, “A review of the Lippmann color process,” *J. Photogr. Sci.* **36**, 140–147 (1988).
63. H. Nareid and H. M. Pedersen, “Modeling of the Lippmann color process,” *J. Opt. Soc. Am. A* **8**, 257–265 (1991).
64. J.-M. Fournier, “Le photographie en couleur de type Lippmann: cent ans de physique et de technologie,” *J. Optics (Paris)* **22**, 259–266 (1991).
65. J.-M. Fournier, “An investigation on Lippmann photographs: materials, processes, and color rendition,” in *Practical Holography VII*, S.A. Benton ed., Proc. SPIE **2176**, 144–152 (1994).
66. J.-M. Fournier and P. L. Burnett, “Color rendition and archival properties of Lippmann photographs,” *J. Imaging Sci. Technol.* **38**, 507–512 (1994).
67. A. Marraud and J.-M. Fournier, “Formation d’image accompagnée d’une analyse spectrale en champ complet: de J. Fourier à G. Lippmann,” *Microsc. Microanal. Microstruct.* **8**, 37–39 (1997).
68. J.-M. Fournier, B. J. Alexander, P. L. Burnett and S. E. Stamper, “Recent developments in Lippmann photography,” in *Sixth Int’l Symposium on Display Holography*, T. H. Jeong, H. I. Bjelkhagen eds., Proc. SPIE **3358**, 95–102 (1998).
69. N. J. Phillips, H. Heyworth and T. Hare, “On Lippmann’s photography,” *J. Photogr. Sci.* **32**, 158–169 (1984).
70. N. J. Phillips, “Links between photography and holography: the legacy of Gabriel Lippmann,” in *Applications of Holography*, L. Huff ed., Proc. SPIE **523**, 313–318 (1985).
71. C. C. Rich and L. Dickerson, “Lippmann photographic process put to practice with available materials,” in *Holographic Materials II*, T. J. Trout ed., Proc. SPIE **2688**, 88–95 (1996).
72. H. I. Bjelkhagen, “Silver halide emulsions for Lippmann photography and holography,” in *Int’l Symposium on Display Holography*, T. H. Jeong and H. I. Bjelkhagen eds., Proc. SPIE **1600**, 44–59 (1992).

73. H. I. Bjelkhagen, "Lippmann photographs recorded in DuPont color photopolymer material," in *Practical Holography XI and Holographic Materials III*, S. A. Benton and T. J. Trout ed., Proc. SPIE **3011**, 358–366 (1997).
74. H. I. Bjelkhagen, T. H. Jeong and R. J. Ro, "Old and modern Lippmann photography," in *Sixth Int'l Symposium on Display Holography*, T. H. Jeong, H. I. Bjelkhagen eds., Proc. SPIE **3358**, 72–83 (1998).
75. H. I. Bjelkhagen, "Lippmann photography: reviving an early colour process," *History of Photography* **23**, (No. 3), 274–280 (1999).
76. H. I. Bjelkhagen, "A new optical security device based on one-hundred-year-old photographic technique," *Opt. Eng.* **38**, 55–61 (1999).
77. H. I. Bjelkhagen and S. De Souza, "Computer simulation of the Lippmann photographic process and recording experiments using holographic materials," in *Practical Holography XV and Holographic Materials VII*, S. A. Benton, S. H. Stevenson and T. J. Trout eds., Proc. SPIE **4296**, 300–311 (2001).
78. H. I. Bjelkhagen, "Lippmann photography: its history and recent development," *The PhotoHistorian, Journal of the Historical Group of the Royal Photographic Society*, APIS 2002 Special double edition, PH.141–142, (2003) pp. 11–19.
79. A. Labeyrie, J. P. Huignard and B. Loiseaux, "Optical data storage in microfibers," *Opt. Lett.* **23**, 301–303 (1998).
80. P. Hariharan, "Lippmann photography or Lippmann holography?" *J. Mod. Optics* **45**, 1759–1762 (1998).
81. W. R. Alschuler, "On the physical and visual state of 100 year old Lippmann color photographs," in *Sixth Int'l Symposium on Display Holography*, T. H. Jeong and H. I. Bjelkhagen eds., Proc. SPIE **3358**, 84–94 (1998).
82. W. R. Alschuler, "Lippmann photography and the glory of frozen light: Eternal photographic color real and false," in Proc. IEEE *31st Applied Imagery Pattern Recognition Workshop* AIPR'02 (2002).
83. W. R. Alschuler, "Lippmann color process, the experience of amateurs in England," *The PhotoHistorian, Journal of the Historical Group of the Royal Photographic Society*, APIS 2002 Special double edition, PH.141–142, (2003) pp. 44–51.
84. R. Jahr, "Über die Herstellung sogenannter "kornloser" Platten für das Interferenz-Farben-Verfahren von Professor Lippmann nach Dr. Hans Lehmann," *Photographische Industrie* **23**, 1013–1014 (1925).
85. H. Lehmann, "Practical application of interference colour photography," *Brit. J. Phot. (Col. Suppl.)* (4 Nov. 1910) pp. 83–86, Practical application of interference colour photography. II. *Brit. J. Phot. (Col. Suppl.)* (2 Dec. 1910) pp. 92–95.
86. H. Lehmann, "Die Praxis der Interferenzfarbenphotographie, unter besonderer Berücksichtigung der in den Optischen Werkstätten von C. Zeiss in Jena konstruierten Specialapparaten," *Phot. Rundschau* **23**, 125–134 (1909) [English translation: "Practical application of interference colour photography," *Brit. J. Phot. (Col. Suppl.)* (4 Nov. 1910) pp. 83–86, "Practical application of interference colour photography II," *Brit. J. Phot. (Col. Suppl.)* (2 Dec. 1910) pp. 92–95.]
87. E. Rothé, "Photographies en couleurs obtenues par la méthode interférentielle sans miroir de mercure," *C. R. Acad. Sci.* **139**, 565–567 (1904).
88. E. Rothé, "Photographies en couleurs obtenues par la méthode interférentielle sans miroir de mercure," *Bull. Soc. Franç. Phot. (2 série)* **20**, 548–549 (1904).
89. E. Rothé, "Sur la photographie interférentielle," *La Photographie des Couleurs* **1**, (No.2), 97–108 (1906).
90. E. Rothé, "Franges d'interférences produites par les photographies en couleurs," *C. R. Acad. Sci.* **147**, 43–45 (1908).
91. E. Rothé, "Variations des franges des photochromies du spectre," *C. R. Acad. Sci.* **147**, 190–192 (1908).
92. R. Neuhauss, "Nachweis der dünnen Zenkerschen Blättchen in den nach Lippmann's Verfahren aufgenommenen Farbildern," *Ann. d. Physik Chemie* **65**, 164–172 (1898).
93. S.R. y Cajal, "Chromomicrophotographie par la méthode interférentielle," *La Photographie des Couleurs* **2**, (No.7), 97–101 (1907).
94. A. Lumière and L. Lumière, "Sur une nouvelle méthode d'obtention de photographies en couleur," *C. R. Acad. Sci.* **138**, 1337–1338 (1904).
95. Musée de l'Elysée Lausanne, 18, avenue de l'Elysée, CH-1014 Lausanne, Switzerland.
96. Université Pierre et Marie Curie, L.D.M.C., Tour 22, 4 place Jussieu, F-75252 Paris, France.
97. Musée français de la Photographie, 78, rue de Paris, F-91570 Bièvres, France.
98. Société française de Photographie, 71, rue de Richelieu, F-75002 Paris, France.
99. Musée Nicéphore Niépce, 28, quai des Messageries, F-71100 Chalon-sur-Saône, France.

100. Preus Fotomuseum - Norwegian Photographic Museum, PB 254, N-3192 Horten, Norway.
101. International Museum of Photography, George Eastman House, 900 East Avenue, Rochester, NY 14607, USA.
102. H. Kogelnik, "Coupled wave theory for thick hologram gratings," *Bell Sys. Tech. J.* **48**, 2909–2947 (1969).
103. D. Brotherton-Ratcliffe, "A treatment of the general volume holographic grating as an array of parallel stacked mirrors," *J. Mod. Optics* **59**, 1113–1132 (2012).
104. W. J. Gambogi, W. K. Smothers, K. W. Steijn, S. H. Stevenson and A. M. Weber, "Color holography using DuPont holographic recording film," in *Holographic Materials*, J. Trout ed., Proc. SPIE **2405**, 62–73 (1995).
105. T. J. Trout, W. J. Gambogi and S. H. Stevenson, "Photopolymer materials for color holography," in *Applications of Optical Holography*, T. Honda ed., Proc. SPIE **2577**, 94–105 (1995).
106. K. W. Steijn, "Multicolor holographic recording in Dupont holographic recording film: determination of exposure conditions for color balance," in *Holographic Materials II*, J. Trout ed., Proc. SPIE **2688**, 123–134 (1996).
107. Courtaulds Performance Films, POB 5068, Martinville, VA 24115, USA.
108. SLAVICH Joint Stock Co., Micron Branch Co., 2 pl. Mendeleeva, 152140 Pereslavl-Zalesky, Russia.

3

Continuous Wave Lasers for Colour Holography

3.1 Introduction

In this chapter, we shall review the most common types of continuous wave (CW) lasers that can be used in colour holography. The range of commercially available, off-the-shelf CW lasers that are suitable for holographic applications has grown significantly in the last few years. There is now a relatively large choice of laser wavelengths available—many offered by the extremely reliable diode-pumped solid-state (DPSS) laser technology.

CW laser sources of interest to holography may be broadly divided into five categories. These are gas lasers, semiconductor lasers, DPSS lasers, dye lasers and diode-pumped fibre lasers. Historically, gas lasers were the most popular source. This is now changing with semiconductor and DPSS lasers becoming increasingly popular. High-coherence visible fibre lasers are also starting to become commercially available and we can expect this sector to expand in the future. Narrow-line liquid dye lasers continue to represent a very flexible but rather inconvenient laser source for holography. Narrow-line solid-state dye lasers are not yet sufficiently developed to offer a sensible solution for holographic applications, but this could change as considerable progress continues to be made in the sector.

Many digital and analogue colour holographic applications can require high-power CW lasers. In analogue holography, this is because the new colour materials, as we shall see in Chapter 4, have intrinsically low sensitivity and as such necessitate high exposure energies. Because a relatively low exposure time is always recommended in analogue holography due to vibration and movement concerns, this translates into a minimum power requirement for the laser. Of course, such minimum power will scale with the intended hologram size—meaning that extremely small holograms can still require only small laser powers. Nevertheless, as a general rule, a suitable laser source for a full-colour analogue holography setup will usually need to be greater than several hundred milliwatts.

High power may also be desirable when CW lasers are used to print digital holograms. Because a single digital hologram can be composed of more than a million component holograms, or “hogels”, it is clear that one does not want to wait very long between exposures for the printing optics to settle to interferometric stability. As a result, one tries to use a very short exposure time—and this then leads directly to a requirement on the minimum laser power. The larger the power of the CW laser used, the faster one can print the hologram. Fringe-locking strategies can reduce the required power somewhat—but only to a certain point as, inevitably, the process of advancing optics from one hogel to the next induces vibrations over a wide spatial spectrum.

Digital holography and analogue holography impose differing requirements on the temporal coherence and power stability of CW laser sources. Because hogels are usually very small (typically 1 mm^2), one requires a coherence length of practically only a few centimetres, but because many such hogels must be printed, high power stability is vital. In contrast, analogue holography may require a coherence length of several metres if large depth scenes are to be recorded, but high power stability is not intrinsically necessary here, as exposure times may easily take into account a change in power.

Analogue colour holography usually requires the use of at least three laser frequencies, and these must be chosen carefully. In Chapter 5, we shall show how optimal wavelength sets can be defined from a colour model for three or more primary wavelengths. Digital holography has rather different constraints concerning the optimal wavelengths, as we shall see in Chapter 7. In Chapter 13, we shall discuss the

illumination of the hologram. Here again, modern narrow-band illumination sources can require the recording lasers to be “matched” to the illumination system.

The choice of the laser to be used in colour holography can therefore be quite complex. First, it will depend on whether the hologram is to be digitally printed or whether an analogue recording is to be used. In the case of analogue reflection holography, it will then depend on the format of the hologram. If the hologram is to be replayed by a narrow-band source, then the recording lasers (usually) must also be matched to the illumination source. Finally, the laser wavelengths will, for both analogue and digital applications, have to be chosen with reference to a given colour model.

The question of whether to employ CW lasers or pulsed lasers for a given holographic application will depend on many issues. In digital holography, pulsed lasers confer a complete immunity to vibrational dimming of the hologram. In addition, small and relatively cheap commercial pulsed DPSS lasers will undoubtedly become available for this application in the future. In analogue holography, there are situations in which the use of pulsed lasers is obligatory—such as when the objects to be recorded are physically unstable or when the recording must be performed in a noisy environment. On the other hand, some of the best new materials are not sensitive to fast pulses. In this chapter, we shall restrict ourselves to a discussion of CW laser sources. Pulsed laser sources will be discussed in Chapter 6.

3.2 Gas Lasers

3.2.1 Helium–Neon Laser

The helium–neon (HeNe) laser [1] is a neutral atom gas discharge laser operating with a mixture of helium and neon gas in a glass tube typically having a length of approximately 15 to 100 cm (Figure 3.1). A voltage of approximately 1 kV is applied to the two electrodes, producing a small direct current; this maintains an electric glow discharge. The glass tube incorporates Brewster windows and two laser mirrors, forming a resonant laser cavity with a typical loss of less than 1%. The Brewster windows ensure a linearly polarised emission.

In the gas discharge, helium atoms are excited into a metastable state from which they efficiently transfer energy to neon atoms (having similar excitation energy) via collisions. Neon atoms have a number of energy levels below the pump level, giving rise to various laser transitions. The transition at 632.8 nm is the most common, but other transitions of interest to holography are 543.5 nm (green emission), 594 nm (yellow emission) and 612 nm (orange emission). The emission wavelength is selected using selective resonator mirrors, which introduce high losses at the wavelengths of competing transitions. Additionally, an intracavity etalon can improve performance significantly. Figure 3.2 shows a photograph of a Russian LGN-222 laser with etalon producing a high coherence emission at 632.8 nm of more than 70 mW. Commercially available lasers producing green and yellow emissions are available but only at low powers (typically several milliwatts). Typical tube lifetimes are more than 20,000 h.

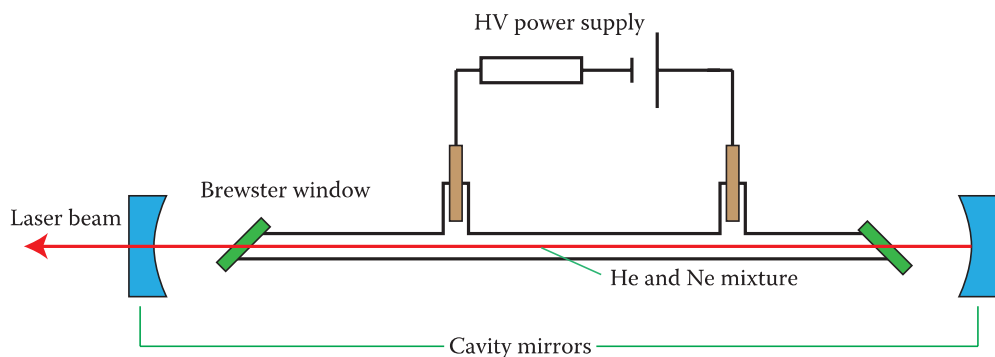


FIGURE 3.1 HeNe laser. An optional intracavity etalon can be used to improve the temporal coherence.



FIGURE 3.2 Picture of a Russian high-powered LGN-222 HeNe laser.

3.2.2 Argon Ion Laser

The argon laser [2] was invented in 1964 by William Bridges at Hughes Aircraft Corporation and is one of a family of ion lasers that use a noble gas as the active medium. Argon ion lasers are excellent sources of high-coherence green and blue light for use in colour holography (Figure 3.3). Optical powers from several watts to several tens of watts are common. The key component of this laser is the argon-filled tube, usually made from beryllium oxide ceramic. An intense electrical discharge between a hollow anode and a hollow cathode generates a high-density argon ion plasma. Unlike HeNe lasers, the energy level transitions that contribute to laser action come from ions. An optional solenoid wound around the tube can be used to generate an axial magnetic field that increases the output power by ensuring better plasma confinement. Typical CW plasma conditions in an argon laser discharge are characterised by current densities of 100 to 2000 Amps/cm², tube diameters of 1 to 10 mm, filling pressures of 0.1 to 1 torr and an axial magnetic field of the order of 1000 G.

Laser oscillation in the argon laser is restricted to a single line by an intracavity prism. High coherence is then attained by the use of an intracavity etalon. The laser is able to operate at a variety of wavelengths, the most useful of which for colour holography are (in order of decreasing power) the green line at 514.5 nm,* the blue-green lines at 488 nm (typically at 80% of the 514.5 nm power) and 496.5 nm (40% of 514.5 nm) and the blue emissions at 476.5 nm (30% of 514.5 nm) and 457.9 nm (15% of 514.5 nm). In addition to these lines, argon lasers also produce various weaker emissions at eight other wavelengths throughout the visible, ultraviolet and near-visible spectra, including 351.1, 363.8, 454.6, 465.8, 496.5, 501.7, 528.7 and 1092.3 nm.

A typical argon laser has a tube of approximately 1 m in length and can generate about 10 W of output power at 514.5 nm. The power consumption of such a laser is, however, several tens of kilowatts. The large amount of dissipated heat must be removed by water-cooling of the tube. Such water-cooling introduces significant vibration into the laser head; accordingly, an argon laser is best installed in a separate laser room and a beam tube used to deliver the beam to the holographic recording area.

3.2.3 Krypton Ion Laser

Krypton ion lasers are very similar to argon ion lasers. They provide a useful source of red radiation at 647.1 nm for colour holography. Generally, the emission at 647.1 nm is rather smaller than the 514.5 nm line for a given electrical power. For example, the single-frequency optical power available from a 2012 model Innova Sabre DBW25 argon laser manufactured by the company, Coherent, Inc., is approximately 6 W. The corresponding krypton laser generates 2.1 W at 647.1 nm.

In addition to the 647.1-nm line, krypton lasers can produce high powers in the violet at 413.1 nm (for example, the 2012 model Innova Sabre krypton laser from Coherent can produce an optical power at this

* An Innova Sabre argon laser, the largest commercially available laser from Coherent at the time of writing, produces 6 W of single frequency emission at 514.5 nm.

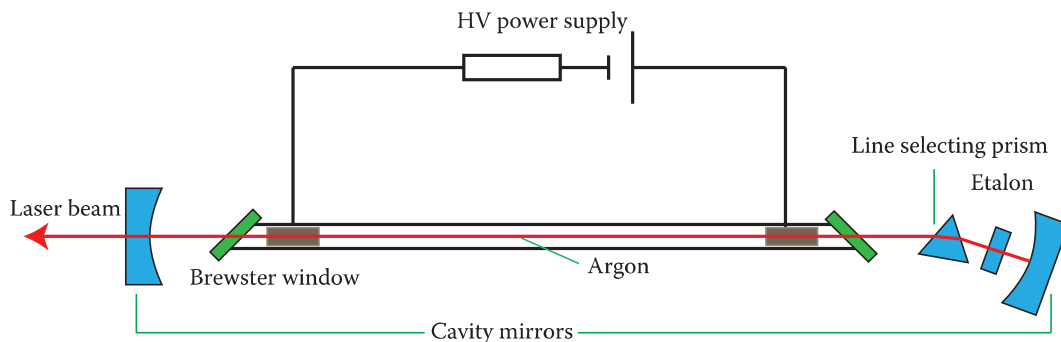


FIGURE 3.3 Basic schematic of an argon ion laser.

wavelength of 1.1 W). In addition to the two main lines, krypton lasers are able to generate weaker emissions at 406.7, 415.4, 468.0, 476.2, 482.5, 520.8, 530.9, 568.2 and 676.4 nm.

Like argon lasers, krypton lasers must be water-cooled and as such the laser is best installed in a separate laser room and a beam tube used to deliver the beam to the holographic recording area. Both argon and krypton laser tubes have a finite lifetime (usually somewhat greater than several thousand hours of operation). However, the tubes can break without warning if there is a problem with the cooling system or if, for example, the electricity supply fails inadvertently. The cost of the tubes in both these types of laser is a very large percentage of the total laser cost and, as such, manufacturers will often offer an automatic replacement service in return for a yearly service contract. The downside is that when one adds the annual service charge to the cost of the electricity required to run the laser, the bill can be very significant. Figure 5.25 in Chapter 5 shows a picture of two modern large-frame argon and krypton lasers.*

3.2.4 Helium–Cadmium Laser

The helium–cadmium (HeCd) laser [3] (see Figure 3.4) is one of a class of gas lasers using helium in conjunction with a metal that vaporises at a relatively low temperature. Both Penning and charge exchange collisions occur in the HeCd laser, and these two processes produce different laser transitions. The laser produces a blue-violet emission at 441.6 nm. Commercial (air-cooled) lasers are readily available with powers of up to approximately 130 mW. In addition to the 441.6-nm line, this laser may also produce a useful output at 325 nm. Typical coherence lengths available in commercial models today are usually no greater than 10 cm. The HeCd laser has been used extensively for recording holograms onto photoresists.

HeCd laser tubes are more complex than the tubes used in HeNe or ion lasers. They include a cadmium metal reservoir and a heater to control the cadmium vapour pressure. The vapour is propagated through the system through a process called cataphoresis. Outside the bore region of the tube, the cadmium vapour will coalesce on any cool surface. Cold traps and protective discharges are therefore required to prevent cadmium from being deposited onto the optical windows. A mechanism is also required to add helium to maintain an optimum pressure. Additionally, heaters to control tube temperature and various sensors inside the envelope for use in feedback control must be present. Typical tube lifetimes are approximately 5000 h. The power supplies are rather complex and must include power sequencing logic and multiple feedback loops.

* Mixed Argon-Krypton lasers exist, but it is not possible to individually adjust the output power of different wavelengths for simultaneous exposure of colour holograms.

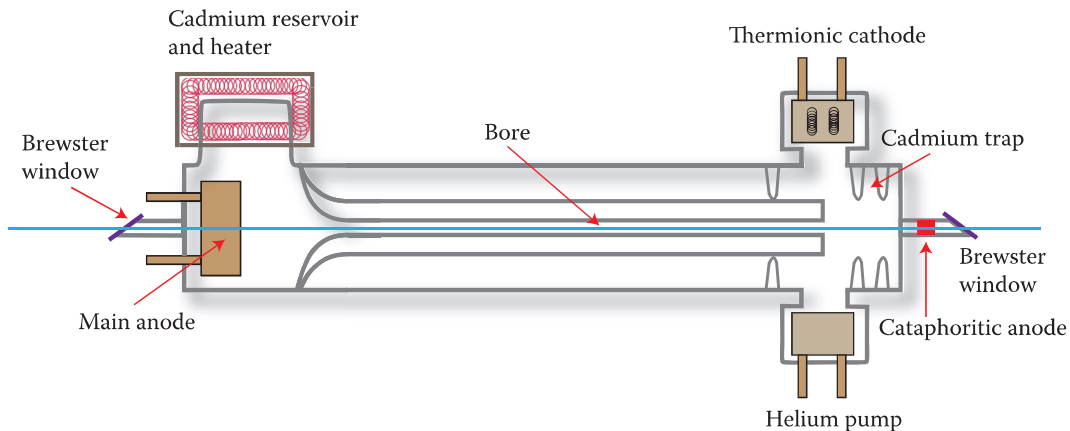


FIGURE 3.4 Basic tube design of a HeCd laser.

3.2.5 Other Gas Lasers

Various other gas lasers can, in principle, be used for holography. However, these lasers are certainly not popular. Some lend themselves to amateur fabrication, such as the helium–mercury laser and the helium–selenium laser. The high-power (>10 W) low-coherence 578.2-nm line of the copper vapour laser has been used as a very effective illumination source for large laser transmission holograms.

3.2.5.1 Helium–Mercury Laser

The helium–mercury (HeHg) laser is quite similar to the HeNe and Ar/Kr ion lasers in terms of operation. This laser operates through ion transitions of mercury. Another name for the HeHg laser is the “mercury vapour ion laser”. It emits in the green line at 567 nm and produces a less powerful output in the red–orange line at 615 nm. The typical multiline output power for a 1-m tube may exceed 20 mW. This laser is not currently available as a commercial product but does lend itself to amateur construction [4,5].

3.2.5.2 Helium–Selenium Laser

This laser is very similar to the HeHg laser. It has been observed to generate up to 46 lines [5], the six most powerful of which are 497.6, 499.3, 506.9, 517.6, 522.8 and 530.5 nm. Up to 30 mW* is typically obtained from a 1-m tube with a 4-mm bore at 200 mA discharge current and 4.5 torr helium filling pressure. Like the HeHg laser, this laser is not currently available as a commercial product but lends itself to amateur construction.

3.2.5.3 Other Metal Vapour Ion Lasers

In addition to the ion lasers discussed in this section, there are several other ions that exhibit laser oscillation from levels excited by either Penning or charge exchange ionisation. Lasers constructed from these ions contain possible holographic sources, but in practice, these lasers have not been used to date for holographic applications. Thermally produced metal vapours of Zn, Te, As, Mg, Tn, Tl and Be all exhibit laser emission when excited in He and Ne discharges.

* The highest recorded power is 250 mW.

3.2.5.4 Copper and Gold Vapour Lasers

The copper vapour laser is the most useful of this class of neutral metal vapour lasers. The primary emission lines for this laser are 510 and 578 nm at powers up to and exceeding 100 W. The copper vapour laser is unusual with respect to its high power and high efficiency; its normal operation is at pulse repetition rates of several tens of kilohertz.

In neutral metal vapour lasers, a fast electric discharge directly excites the metal atoms. High repetition rates then permit high average power output. The copper vapour is generated from copper placed in the discharge tube, where it is heated to approximately 1500°C and produces a vapour of approximately 0.1 mb. Several millibars of neon are added as a buffer gas to prevent window contamination and a loss of copper. The overall wall-plug efficiency of this type of laser is approximately 1%, which is the highest for any visible gas laser. Copper chloride and copper bromide lasers offer an alternative technology, having a lower temperature discharge.

Gold can also be substituted for copper, producing a powerful laser emission at 627 nm. Neutral metal vapour lasers are not usually useful for recording holograms due to their typically multimodal structure and low coherence character. However, the 578-nm line of copper is an extremely effective source for illuminating laser transmission holograms.

3.3 Dye Lasers

3.3.1 Liquid Dye Lasers

Liquid dye lasers constitute a coherent source of laser radiation with a wide tuning range and have applications in various fields including holography. These lasers are particularly pertinent to colour holography as they provide a source of tunable radiation at virtually any wavelength across the visible spectrum.

A liquid dye laser consists of an organic dye mixed with a solvent. The mixture is either circulated through a dye cell or formed into a dye jet. An external laser, often an argon ion laser, is used as the pump source.* The dye solution must be circulated at high speed to circumvent triplet absorption and consequent beam extinction, and also to decrease the degradation of the dye.

The pump light excites the dye molecules into their singlet state where they emit stimulated radiation. In the singlet state, the dye molecules emit light via fluorescence; the dye is now transparent to the lasing wavelength. Within approximately a microsecond, however, the dye molecules change to their triplet state in which light is emitted via phosphorescence; here, the molecules absorb the lasing wavelength, making the dye opaque.

A ring laser design is often chosen for CW operation. Frequency-selective elements such as prisms, gratings and etalons serve to select a given wavelength and to ensure good coherence. Typical dyes include rhodamine, fluorescein, coumarin, stilbene, umbelliferone, tetracene and malachite green. Typical solvents used are water, glycol, ethanol, methanol, hexane, cyclohexane and cyclodextrin. The first narrow line width dye laser was demonstrated by Hänsch [6]. Subsequently, grazing incidence grating designs [7,8] and multiple prism grating configurations were reported.

Liquid dye lasers having good spatial and temporal coherence characteristics may easily be constructed in the laboratory. Critical elements such as the dye jets are commercially available. Many laser models are also available commercially. Using a large-frame argon laser as the pump, several watts of useful power may be attained across the visible spectrum from a liquid dye laser.

The great disadvantage of the liquid dye laser is the need for large volumes of organic solvents. There are also significant cleaning and servicing issues. For use in colour holography, the inconvenience of the liquid dye laser must be balanced against the great advantage offered by its wide choice of wavelengths at high power.

* Fast flashlamps may also be used.

3.3.2 Solid-State Dye Lasers

We should mention that solid-state dye lasers that use dye-doped organic matrices as the gain medium have been reported. The first solid-state dye lasers were reported in the late 1960s by Soffer and McFarland [9] and Peterson and Snavely [10] who demonstrated stimulated emission from polymeric matrices doped with organic dyes. In recent years, significant breakthroughs have been achieved in the development of practical, tunable solid-state dye lasers. Stable CW output power of several watts over some hours of operation in solid-state dye lasers has been reported [11]. In addition, high coherence operation has also been reported [12]. As such, solid-state dye lasers may represent an interesting future choice for colour holography.

3.4 Diode-Pumped Solid-State Lasers

DPSS lasers employ semiconductor laser diodes to excite ions within a doped laser crystal. Laser transition occurs from the excited ion state to a lower state. The most commonly used laser crystals in commercial DPSS laser systems today are doped with the rare earth metal neodymium. We shall discuss the properties of neodymium-doped materials at length in Chapter 6 in the context of pulsed laser sources.

DPSS lasers may be generally constructed using two forms of pumping:

- End-pumping
- Side-pumping

Here, to illustrate how DPSS lasers work, we will briefly describe the simple end-pumped system shown in Figure 3.5 [13]. This laser is built using two crystals of Nd:YVO₄ in series-connected double Z resonators. Each of the four ends of the two crystals is pumped by separate 18-W 808-nm laser diode bars. The radiation from these bars is collected into fibre bundles and focussed into the Nd:YVO₄ crystals through their polished ends. Approximately 54 W of actual laser pumping power is delivered to the two crystals. The laser then produces 35 W of output power at 1064 nm. The electrical power consumed by the pumping diodes is only 180 W.

DPSS lasers have significant advantages over other types of lasers. Their efficiency means that little waste energy is injected into the system and this means that these types of lasers are often much more stable. Diode stacks also typically have operational lifetimes of more than 10,000 h. This, together with the high wall-plug efficiency, translates into very economical operation. Many CW DPSS lasers using

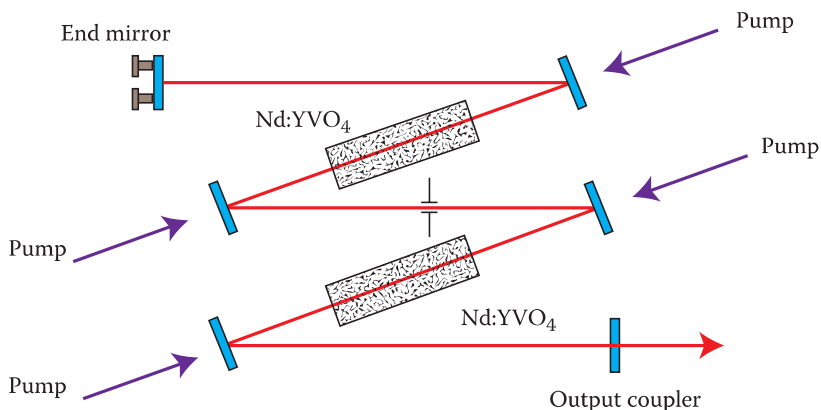


FIGURE 3.5 Simple DPSS laser built around two Nd:YVO₄ crystals in a Z cavity. Each crystal is pumped by separate diode bars through both its ends. The laser produces 35 W of optical power at 1064 nm for an absorbed pumping power of 54 W and a total electrical power consumption of 180 W.

neodymium-doped crystals have thus far been demonstrated. In addition, Ho-, Tm-, Yb- and Cr-doped crystals can be pumped using laser diodes.

3.4.1 Green Emission DPSS Lasers

The above example illustrates how DPSS laser technology can be used to construct extremely efficient and compact lasers. Single spatial and longitudinal mode operation can be ensured in DPSS lasers using an appropriate resonator design and frequency-selective elements. The 1064-nm line of Nd:YVO₄ can be doubled to produce a green emission at 532 nm by use of a non-linear frequency doubling crystal such as potassium dihydrogen phosphate (KTP). This may be internal or external to the resonator depending on the laser design. Q-switched operation may also be employed by the use of a passive Q-switch within the resonator. Today, many companies manufacture commercial laser systems operating at 532 nm. Perhaps the best known is the *Verdi* laser from Coherent.

3.4.1.1 *Verdi* 532 nm Laser

Figure 3.6 shows a basic optical scheme of the Verdi laser, which is manufactured by Coherent. A picture of the laser can be seen in Figure 5.25 in Chapter 5. The laser is capable of producing up to 18 W of highly stable single-frequency emission at 532 nm, with an estimated coherence length of more than 60 m. Maximum electrical power consumption is 1.3 kW. The Verdi is based on a single end-pumped Nd:YVO₄ crystal in a ring cavity.* Frequency doubling is internal via a lithium triborate (LBO) crystal. A Faraday rotator and waveplate ensure unidirectional lasing. This is an extremely good source for colour holography.

3.4.1.2 Other Green DPSS Lasers

The Nd:YVO₄^{4F_{3/2}-4I_{11/2}} transition has weaker Stark lines at 1074 and 1084 nm. Frequency-doubled emission at both of these lines (537 and 542 nm) has been reported in the literature. Commercial single-frequency lasers producing up to 50 mW at 542 nm were available at the time of writing. In addition to Nd:YVO₄, other neodymium crystals may be used in a DPSS laser. The most popular such lasers are based on either Nd:YAG (532 nm), Nd:YAP (539 nm) or Nd:YLF (523 and 527 nm). Yb:YAG can also produce a doubled emission at 515 nm (for example, Showa Optronics Company Ltd. produces a 50-mW single-frequency DPSS laser based on Yb:YAG at 515 nm).

3.4.2 Blue Emission DPSS Lasers

Nd:YAG has a transition at 946 nm, which can be doubled to 473 nm. Likewise, Nd:YVO₄ has a transition at 914 nm, which can be doubled to 457 nm. Examples of other less well-known materials are Nd:GSAG (943 nm) and Nd:YGG (935 nm). As early as 1997, more than 500 mW of single-frequency light at 473 nm was generated by a DPSS Nd:YAG ring cavity laser with frequency doubling using KNbO₃ [14]. Recently, Wang et al. have reported a highly stable single-frequency output power of 1 W at 473 nm from an end-pumped DPSS Nd:YAG laser using a ring resonator and intracavity frequency doubling with a periodically poled KTP (PPKTP) crystal [15]. Commercial, single-frequency DPSS lasers operating at 473 and 457 nm are available today. However, typical maximum output powers are currently limited to approximately 300 mW at 457 nm and 150 mW at 473 nm (for example, the 300 mW single-frequency BLSI model from CVI Melles Griot; Figure 3.7). Clearly, this can be expected to increase in the near future.

Neodymium-doped crystals have several transitions at approximately 1.3 μm. These may be tripled to produce a blue output using CW Q-switched operation. The most common include Nd:YVO₄ (447 nm), Nd:YAG (440 and 446 nm) and Nd:YLF (438 nm). The maximum output power currently available in

* A ring cavity is used to avoid the well-known “green problem”, which can occur when intracavity frequency doubling is used with a conventional linear cavity.

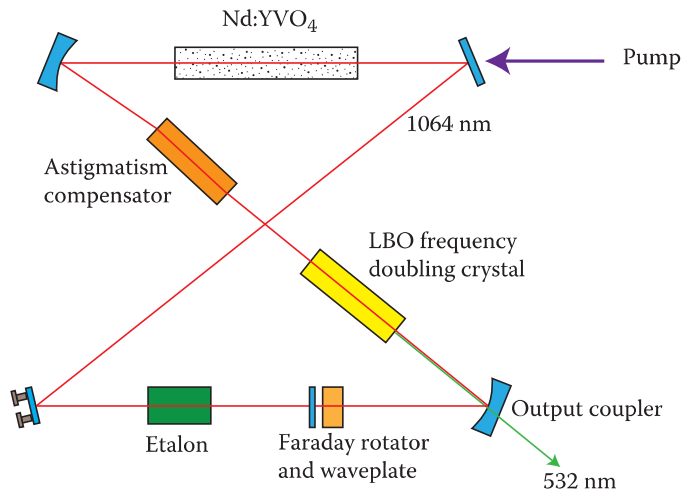


FIGURE 3.6 Simplified optical scheme of the DPSS *Verdi* laser from Coherent. The laser is capable of producing up to 18 W single frequency at 532 nm.



FIGURE 3.7 DPSS *BLS1* laser from Melles Griot, producing 300 mW of a single-frequency emission at 457 nm.

narrow-band commercial lasers is less than 50 mW. However, much higher outputs are certainly possible and again one can expect the maximum power offered by companies to increase in the coming years. We shall discuss similar lamp-pumped lasers in Chapter 6 in the context of pulsed operation.*

Yet another method to obtain a blue emission is sum-frequency mixing. Here, for example, an 808-nm diode is used to pump a Nd:YVO₄ crystal, which then emits at 914 nm. The 808-nm diode radiation is also used to pump a Nd:YLF crystal emitting at 1047 nm. Intracavity sum-frequency mixing at 914 and 1047 nm is then realised in an LBO crystal to produce an emission at 488 nm.

The Swedish company, Cobolt AB, use sum-frequency mixing of Nd:YVO₄ (914 nm) and Nd:YAG (1064 nm) in a PPKTP crystal to produce a single-frequency emission of 100 mW at 491.5 nm in their *Calypso* laser. The company also manufactures a version that produces a two-colour emission at 532 and 491.5 nm. A periodically poled crystal is the key component in such a multiline laser design. By placing multiple successive quasi-phase-matching gratings into a single crystal, it is possible to achieve multiple frequency conversion processes (in this case, doubling of 1064 to 532 nm and sum-frequency mixing of 914 and 1064 nm, giving 491.5 nm). Each grating has a different characteristic period along the direction of the propagation and is created in a lithographic process with subsequent exposure to a high electric

* The Lithuanian company, Geola, makes commercial lamp-pumped 50 Hz Nd:YAG Q-switched lasers giving average powers of more than 200 mJ at 440 nm. Nd:YLF and Nd:YAP lasers are also available for 438, 446 and 447 nm outputs.

field. Using two or more gratings in one crystal minimises the number of optical interfaces, reducing the complexity of the laser design and its production cost.

3.4.3 Red Emission DPSS Lasers

Red emission may be obtained by doubling one of the $1.3\text{ }\mu\text{m}$ lines in neodymium. Using a temperature-tuned PPKTP crystal, a record 1.3-W single-frequency red laser at 661 nm was achieved by intracavity second-harmonic generation in a Nd:YLiF₄ ring laser oscillating at the π -polarised transition ($\lambda \sim 1321\text{ nm}$) [16]. Intracavity second-harmonic generation of a diode-pumped Nd:YLiF₄ ring laser oscillating on the σ -polarised $^4\text{F}_{3/2}-^4\text{I}_{13/2}$ transition ($\lambda_{\omega} \sim 1314\text{ nm}$) with a temperature-tuned PPKTP crystal has also been reported, yielding up to 0.92 W of tunable ($\lambda_{2\omega} = 656-658\text{ nm}$) single-frequency output [17].

The Cobolt *Flamenco* is a commercial DPSS laser producing single-frequency emission of 400 mW at 660 nm (Figure 3.8). This laser is also based on frequency doubling of $1.3\text{ }\mu\text{m}$ in PPKTP. Using a type I critically phase-matched bismuth borate crystal, 620 mW of single-frequency emission at 671 nm has also been achieved using intracavity doubling of a π -polarised single end-pumped Nd:YVO₄ ring laser oscillating at the 1342-nm transition [18]. Various companies offer commercial CW DPSS Q-switched lasers using Nd:YAG, Nd:YVO₄ and Nd:YLF to generate up to 250-mW single-frequency emissions at 656.5, 660 or 671 nm.

3.4.4 Yellow Emission DPSS Lasers

Nd:YAG has a weak transition at 1123 nm. This can be doubled to produce an emission at 561 nm. In 2007, Zang et al. [19] reported single-frequency emission of up to 1.25 W at 1023 nm. Cobolt AB now produce a single-frequency laser (the *Jive*) capable of emitting up to 500 mW at the doubled wavelength (561 nm).

3.4.5 Orange Emission DPSS Lasers

Sum-frequency generation from the various infrared transitions of neodymium-doped crystals can produce emissions in the range 589 to 599 nm. For example, in 2008, Mimoun et al. [20] reported the generation of more than 800 mW of single-frequency emission at 589 nm by sum-frequency conversion of the 1319- and 1064-nm lines of Nd:YAG. However, few single-frequency orange DPSS sources were available at the time of writing.

3.4.6 Future DPSS Laser Technology

3.4.6.1 Praseodymium-Doped Lasers

Increasingly encouraging results have been reported recently concerning praseodymium (Pr³⁺)-doped crystal lasers. These lasers are extremely interesting due to their transitions in the visible spectrum. Unlike the Nd³⁺ ion, which has its transitions in the infrared and requires frequency conversion to

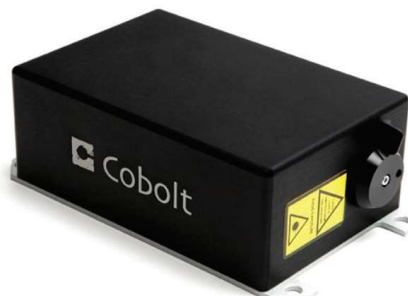


FIGURE 3.8 DPSS *Flamenco* laser from Cobolt AB, producing 400 mW of a single-frequency emission at 660 nm.

generate visible light, Pr^{3+} naturally lases at lines in the blue, green, orange and red. In addition, these transitions constitute four-level laser systems. In the past, however, a major difficulty with Pr^{3+} lasers has been how to pump the laser. The absorption transitions of Pr^{3+} are situated in the blue between 440 and 480 nm. The first experimental reports of Pr^{3+} lasers therefore used argon lasers [21,22], dye lasers [23] or an optically pumped semiconductor lasers [24].

Recent developments in high-power blue laser diodes emitting at approximately 445 nm have now enabled the construction of efficiently pumped Pr -doped lasers in compact setups. For example, Richter et al. [25,26] reported efficient CW lasing of praseodymium-doped LiYF_4 and LiLuF_4 crystals pumped either by an optically pumped semiconductor laser (at 479.5 nm) or a GaN laser diode (at 444 nm). Up to 600 mW (not single frequency) was obtained in the green at 523 nm, in the red at 640 nm and in the deep red at 720 nm. Additionally, more than 300 mW was obtained in the orange at 607 nm. Diode pumping of $\text{Pr:KY}_3\text{F}_{10}$, Pr:YAlO_3 , Pr:SrF_2 and $\text{Pr:SrAl}_{12}\text{O}_{19}$ crystals have also been reported [27–31].

Although no commercial DPSS Pr^{3+} laser systems were available at the time of writing, one should expect their appearance within the next few years.

3.4.6.2 Microchip Lasers

Microchip lasers are miniature (typically submillimetre) monolithic solid-state lasers comprising a laser crystal with integral mirrors. Other optical elements, such as a Q-switch or a frequency conversion crystal can also be included in the monolithic cavity. These types of lasers are most usually diode pumped. Because of their monolithic nature and their very small size, they are usually extremely stable and alignment-free. Very often, they naturally produce single-frequency emissions. For example, Sotor et al. [32] recently reported stable generation of 160 mW of 532-nm single-frequency radiation from a $\text{Nd:YVO}_4/\text{KTP}$ microchip laser. Work at the University of St Andrews in the late 1990s showed that single-frequency blue (33 mW at 473 nm) and red (10 mW at 671 nm) diode-pumped microchip lasers could also be produced using $\text{Nd:YAG}/\text{KNbO}_3$ and $\text{Nd:YVO}_4/\text{LBO}$, respectively [33]. Because of their small size, output power of DPSS microchip lasers is usually relatively small, but these lasers nevertheless constitute an interesting potential light source for colour holography.

3.4.6.3 Chromium Forsterite

The first reported lasing in a chromium-doped forsterite crystal was reported by Vladimir Petričević et al. in 1988 [34]. This vibronic laser has a broad range of transitions centred around 1.25 μm . Frequency doubling can potentially yield a useful red source, tunable over a wide range, although the thermal properties of forsterite are not good. Up to 1.1 W of emission has been reported at 1.2 μm [35], with pumping using a CW Nd:YAG laser. However, diode pumping of this material has proved difficult with very low efficiencies reported (only several milliwatts). We shall mention this laser system again in Chapter 6 when we talk about pulsed lasers. Narrow-band emission is possible when pumped with a Q-switched Nd:YAG laser—operation at 50 Hz with commercially available systems can deliver average powers of more than 50 mW at 627 nm.

3.4.6.4 Optical Parametric Oscillators

An optical parametric oscillator (OPO) is a parametric oscillator that oscillates at optical frequencies. It emits light not by stimulated emission, as in a true laser, but by a non-linear parametric process. Essentially, it converts an input laser beam (called the “pump”) into two output waves of lower frequency using a non-linear optical process. The sum of the two output frequencies (called the *signal** wave and the *idler* wave) is equal to the input wave frequency. Generally, narrow-band OPOs require an additional narrow-band pump laser, making them complex systems.

* The wave with a higher frequency is called the signal.

Green-pumped OPOs are potentially attractive because of their capability to generate emissions ranging from the visible to the mid-infrared region within a single device. However, the available non-linear materials required for green pumping are limited by the absorption of visible wavelengths and associated thermal lensing. A different approach, which has had some success, is intracavity frequency mixing of the pump, signal and idler waves in an OPO cavity.

At the time of writing, there were no commercial single-frequency CW sources of visible radiation produced by OPOs.

3.5 Semiconductor Diode Lasers

3.5.1 Introduction

There has been great progress in semiconductor diode lasers in recent years. The concept of the DPSS laser first originated principally because laser diodes themselves did not have the output characteristics and mode quality required for use as a laser source in many applications. This equation has, however, now changed and diode lasers are themselves being used today as useful high-coherence sources for applications such as holography.

3.5.2 Operation and Construction

Like a light-emitting diode, a semiconductor laser diode consists of a “*p–n*” junction, which is usually deposited onto a crystal wafer. On the *p* side of the junction, the semiconductor is heavily doped with acceptor atoms. These are atoms with a missing electron in the valence band (a “hole”). On the *n* side of the junction, the dopant atoms each have an extra electron in their conduction band. When an electrical voltage is applied across the junction, electrons migrate from the *n*-doped semiconductor to the *p*-doped semiconductor, where they combine with holes producing laser radiation. A laser cavity is created by simply polishing the ends of the diode (Figure 3.9). Laser diodes differ from LEDs in that their depletion layers are rather thinner and a larger forward current is used. Additionally, much more care is needed in regulating the current than in an LED. A popular packaging format for low-power (≤ 1 W) diodes incorporates a pin diode in-line with the rear facet, allowing current control by monitoring of the back-emitted laser radiation (Figure 3.10).

The efficiency of semiconductor laser diodes is extremely high, sometimes reaching 80%. Tremendous progress is also being made with increasing the power and quality of the diodes. At the time of writing, Mitsubishi had just released a 638-nm multilateral mode laser diode (ML501P73) producing an unprecedented 1 W of emission at this wavelength (equivalent to a luminosity of 120 lumens) in a 5.6-mm-diameter capless package.

TABLE 3.1

Current Semiconductor Lasers in the Visible and Near Infrared Spectra

Wavelength Range of Emission (nm)	Type of Semiconductor Diode
430–550	GaN/AlGaN
447–480	ZnSSe
490–525	ZnCdSe
620–680	AlGaInP/AlGaAs
670–686	GaInP/GaAs
750–870	AlGaAs/GaAs
904	GaAs/GaAs
870–1100	InGaAs/GaAs
1100–1650	InGaAsP/InP

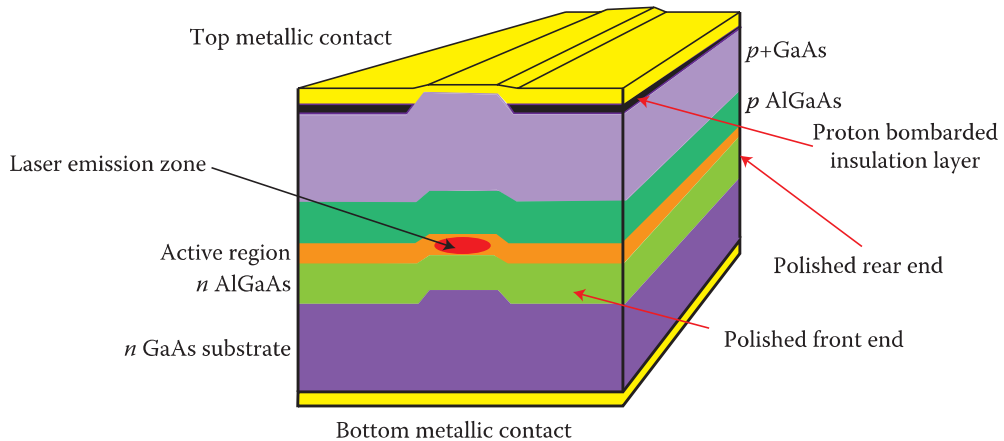


FIGURE 3.9 Typical structure of a double heterostructure edge-emitting laser diode. Dimensions of the active region are 200 μm in length, 2 to 10 μm in lateral width and 0.1 μm in transverse dimension.

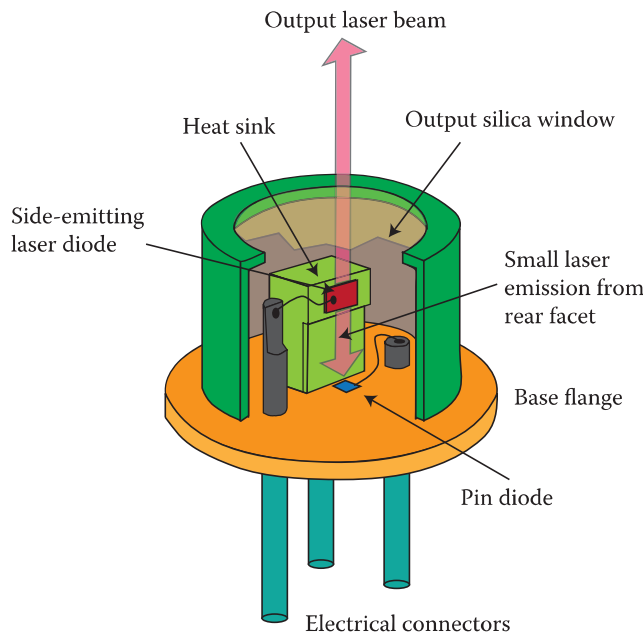


FIGURE 3.10 Typical mounting of a low-power laser diode ($\leq 1 \text{ W}$) in a TO-CAN style package (base either 5.6 or 9 mm) incorporating monitor pin diode.

3.5.3 Mode Structure and Coherence

Lower-power laser diodes often produce single lateral and transverse mode outputs because only one mode will fit into the small active volume. The output from these diodes can also be highly coherent as the very short $p-n$ junction acts as a stable etalon with a high free spectral range. Generally, the smaller, less powerful diodes can have long coherence lengths and can quite often be used successfully for holographic applications if their temperature is kept reasonably constant. The problem here is that increasing the temperature will create mode hops. High-power laser diodes are, however, often not single mode in either space or time.

3.5.4 Operation at Single Longitudinal Mode

Various techniques are nowadays employed to ensure stable single longitudinal mode operation, such as etching a diffraction grating onto the top surface of the diode (distributed feedback laser) or using twin



FIGURE 3.11 Laser diode stabilised by a volume holographic grating producing a single-frequency output of 40 mW at 405 nm for embossed holographic applications.



FIGURE 3.12 *Cyan* 488 laser from SpectraPhysics produces 150 mW of a single-frequency output at 488 nm from an external cavity-stabilised telecom diode. The laser head is just 12.5 cm long, and the unit consumes 6 W of electrical power.

semiconductor diode etalons (coupled cavity method). The US company Ondax uses a volume holographic element* to stabilise its laser diodes. It now offers a 640-nm diode laser producing up to 20 mW of highly coherent (>2 m coherence length) output power, which it advertises as a genuine “HeNe” replacement. Additionally, the company makes a full range of stabilised visible laser from 405 nm to 785 nm suitable for a wide range of holography applications (Figure 3.11). For example lasers, producing approximately 40 mW with good coherence at 405, 658, 685 and 690 nm—all in TO-CAN 5.6-mm packages were available at the time of writing. However, there have been reports in the scientific literature concerning much higher single-frequency powers. For example, more than 400-mW single frequency at 660 nm was obtained using an angled-grating structure in GaInP-AlInP [36].

Larger stabilised external cavities (often with piezo length control) can also be used very effectively to ensure very narrow band operation [37]. Again, the idea is to place the laser diode in a stabilised external cavity, dramatically improving the quality factor. The *Cyan* 488 laser from SpectraPhysics is one such laser producing 150 mW of output at 488 nm (Figure 3.12). It is based on a highly reliable telecom-grade diode laser in an external cavity configuration with a proprietary wavelength-locking scheme that ensures stable single-frequency operation. The unit only consumes 6 W of electricity and is barely 12 cm long.

3.5.5 Amplification

Another commercial semiconductor diode laser producing high-power narrow band emission is the *DL RFA SHG pro* laser from Toptica. This laser produces no less than 2 W at 589 nm with a line width of less than 1 MHz. The laser is based on a tunable external cavity diode laser operating at 1178 nm. The output

* These elements are relatively thick normal-incidence quasi-lossless reflection holographic gratings of low permittivity modulation written in glass using UV lasers. They are employed as the output coupler of the diode laser cavity and, being extremely angle and wavelength selective, strongly favour operation at a single longitudinal mode.

of the external cavity diode laser is amplified within a polarisation-maintaining Raman fibre-amplifier, which preserves the spectrum of the seed laser. The amplifier output is frequency-doubled in a resonator to the target wavelength of 589 nm.

Amplification of seed emissions by a tapered diode in a master oscillator power amplifier configuration is also possible. Tapered diodes are available in the red and infrared frequencies and doubling can offer emissions at blue and green frequencies. Toptica produce commercial narrow-band devices using tapered amplification from 396 to 495 nm, with up to 400 mW of power at 459 nm (*SYST TA SHG pro*).

3.5.6 Summary

There is now a significant choice of commercial, high-coherence semiconductor lasers available at relatively low power. The powers on offer are generally increasing as diodes become more efficient and as manufacturers improve their technologies. At the time of writing, CW semiconductor lasers suitable for holography (coherence length >5 m)* were available at 405 nm (~40 mW), 440 nm (~30 mW), 488 nm (150 mW), 633 nm (~50 mW), 645 nm (~50 mW), 660 nm (~80 mW), 685 nm (40 mW) and 690 nm (~40 mW).

3.6 Fibre Lasers

A fibre laser is a laser in which the active gain medium is an optical fibre doped with rare earth elements such as neodymium, praseodymium, erbium, ytterbium, dysprosium or thulium. It is also possible to construct doped fibre amplifiers that can provide light amplification without lasing. Non-linear processes in the fibre, such as stimulated Raman scattering or four-wave mixing, can also provide laser gain. High-power single-frequency fibre lasers have been developed in the 1.5 μm region, where they are used for applications such as LIDAR. As of the time of writing, high-coherence commercial fibre lasers in the visible band suitable for holography were still relatively rare. However, this is likely to change. We have already mentioned the *DL RFA SHG pro* laser from Toptica, which uses a polarisation-maintaining Raman fibre-amplifier to achieve 2 W of single-frequency emission at 589 nm from an external cavity diode seed. The Canadian company, MPB Communications Inc., offers a series of visible fibre lasers emitting at 514, 560, 580, 592.5, 628 and 640 nm. However, the company currently only produces a single-frequency version for 514 nm. Maximum power is 300 mW. The US company IPG Photonics produces single-frequency 532-nm green fibre lasers (the GLR series) suitable for holography to a staggering 100 W (Figure 3.13). Menlo Systems, Inc. has recently released the *Orange-One SHG*, a single-frequency fibre laser with second harmonic generation producing more than 200 mW at 510 to 560 nm.

3.7 CW Laser Sources for Colour Holography Today

For low-power (<50 mW) holographic applications, there is currently a large choice of commercial CW laser sources right across the spectrum (Figure 3.14). This alone represents tremendous progress when compared with the situation 10 or 20 years ago. This really renders obsolete such popular lasers as the HeNe and HeCd lasers. However, as the required power increases towards the 150-mW level, the number of available wavelengths thins out. At more than 400 mW, there are no blue lasers to compete with the ion gas lasers, and at more than 500 mW, there are no red lasers. Efficient commercial lasers offering high coherence and high power are certainly available in the green (532 nm) and yellow (589 nm) 9 spectral regions. However, the blue region of the spectrum and the lower-wavelength reds are particularly poorly served. Published scientific research clearly demonstrates that the technology is known today to fill these gaps, but it may be a few more years yet before such research makes its way to the commercial marketplace.

* Excluding fibre amplification.



FIGURE 3.13 100-W single-frequency 532-nm green fibre laser (the *GLR-100* from IPG Photonics).

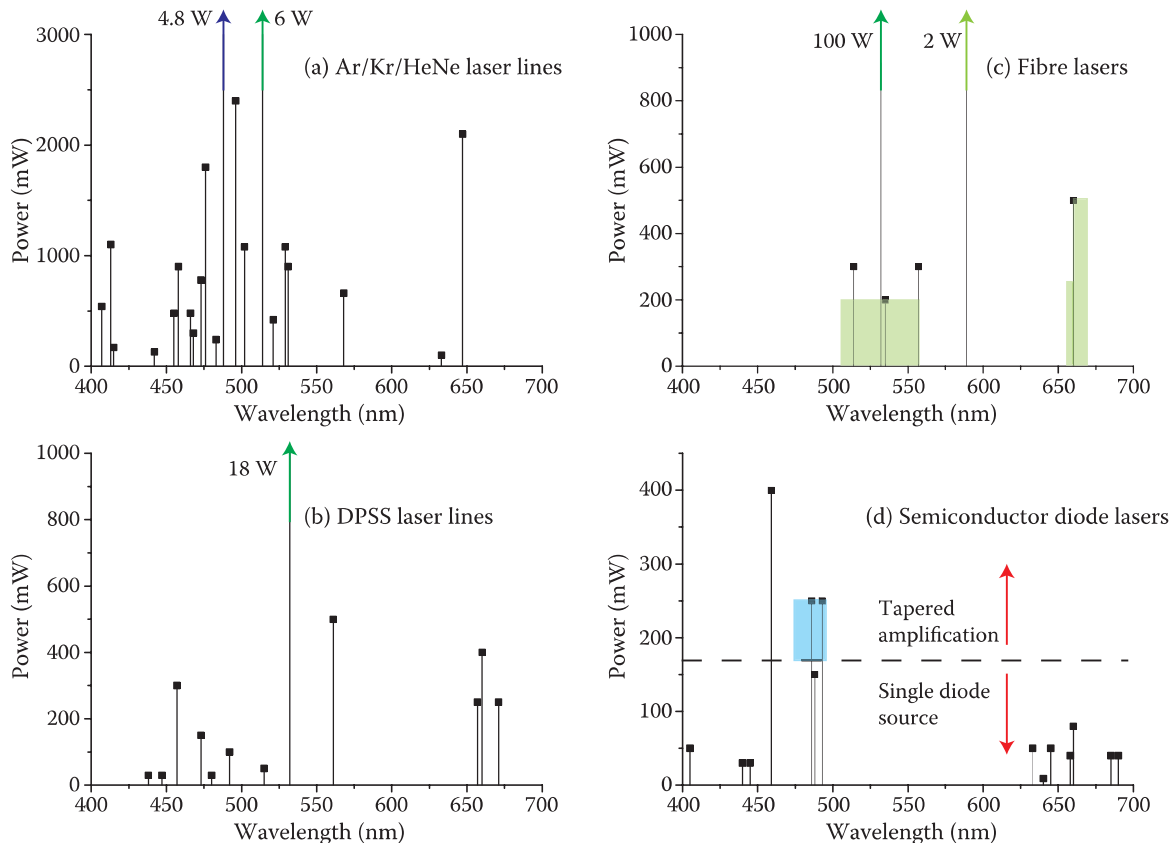


FIGURE 3.14 Commercial single-frequency laser frequencies available as of January 2012: (a) argon, krypton and HeNe lasers, (b) DPSS lasers, (c) fibre lasers and (d) semiconductor lasers.

REFERENCES

1. A. Javan, W. R. Bennett Jr. and D. R. Herriott, "Population inversion and continuous optical maser oscillation in a gas discharge containing a He–Ne mixture," *Phys. Rev. Lett.* **6**, 106–110 (1961).
2. W. B. Bridges, "Laser oscillation in singly ionized argon in the visible spectrum," *Appl. Phys. Lett.* **4**, 128 (1964); erratum: *Appl. Phys. Lett.* **5**, 39 (1964).
3. G. R. Fowles and W. R. Silfvast, "Laser action in the ionic spectra of Zn and Cd," *IEEE J. Quantum Elect.* **qe-1** 131 (1965).
4. D. C. Sinclair and W. E. Bell, *Gas Laser Technology*, Holt, Rinehart and Winston, New York (1969).
5. M. B. Klein and W. T. Silfvast, "New cw laser transitions in Se II," *Appl. Phys. Lett.* **18** 482–485 (1971).
6. T. W. Hansch, "Repetitively pulsed tunable dye laser for high resolution spectroscopy," *Appl. Opt.* **11**, 895–898 (1972).

7. I. Shoshan, N. N. Danon and U. P. Oppenheim, "Narrowband operation of a pulsed dye laser without intracavity beam expansion," *J. Appl. Phys.* **48**, 4495–4497 (1977).
8. M. G. Littman and H. J. Metcalf, "Spectrally narrow pulsed dye laser without beam expander," *Appl. Opt.* **17**, 2224–2227 (1978).
9. B. H. Soffer and B. B. McFarland, "Continuously tunable, narrow-band organic dye lasers," *Appl. Phys. Lett.* **10**, 266–267 (1967).
10. O. G. Peterson and B. B. Snavely, "Stimulated emission from flashlamp-excited organic dyes in polymethyl methacrylate," *Appl. Phys. Lett.* **12**, 238–240 (1968).
11. A. Bank, D. Donskoy and V. Nechitailo, "High-average-power quasi-cw tunable polymer laser," in *UV and Visible Lasers and Laser Crystal Growth*, R. Scheps and M. R. Kokta eds., Proc. SPIE **2380**, 292–297 (1995).
12. F. J. Duarte, "Multiple-prism grating solid-state dye laser oscillator: optimized architecture," *Appl. Opt.* **38**, 6347–6349 (1999).
13. W. L. Nighan, Jr, N. Hodgson, E. Cheng and D. Dudley, "Quantum-limited 35 W TEM₀₀ Nd:YVO₄ laser," in *Lasers and Electro-Optics*, CLEO'99 Tech Digest, OSA (1999) p. 1.
14. H. Welling, "Single-frequency source in the blue spectral region," *Opt. Lett.* **22**, 1220–1222 (1997).
15. Y. Wang, J. Liu, Q. Liu, Y. Li and K. Zhang, "Stable continuous-wave single-frequency Nd:YAG blue laser at 473 nm considering the influence of the energy-transfer up-conversion," *Opt. Expr.* **18**, 12044–12051 (2010).
16. F. Camargo, T. Zanon-Willette, R. Sarrouf, T. Badr, N. U. Wetter and J. Zondy, "1.3 Watt single-frequency Nd:YLF/ppKTP red laser," in *Conference on Lasers and Electro-Optics/International Quantum Electronics Conference*, OSA Technical Digest (CD), paper CThZ7 (2009).
17. R. Sarrouf, V. Sousa, T. Badr, G. Xu and J. -J. Zondy, "Watt-level single-frequency tunable Nd:YLF/periodically poled KTiOPO₄ red laser," *Opt. Lett.* **32**, 2732–2734 (2007).
18. F. Camargo, T. Zanon-Willette, T. Badr, N. U. Wetter and J. -J. Zondy, "620 mW single-frequency Nd:YVO₄/BiB₃O₆ red laser," in *Lasers and Electro-Optics, Conference on Quantum Electronics and Laser Science*, CLEO/QELS (2009) p. 1–2.
19. E. Jun Zang, J. Ping Cao, Y. Li, T. Yang and D. Mei Hong, "Single-frequency 1.25 W monolithic lasers at 1123 nm," *Opt. Lett.* **32**, 250–252 (2007).
20. E. Mimoun, L. De Sarlo, J. -J. Zondy, J. Dalibard, and F. Gerbier, "Sum-frequency generation of 589 nm light with near-unit efficiency," *Opt. Expr.* **16**, 18684–18691 (2008).
21. R. Smart, J. Carter, A. Tropper, D. Hanna, S. Davey, S. Carter and D. Szebesta, "CW room temperature operation of praseodymium-doped fluorozirconate glass fibre lasers in the blue-green, green and red spectral regions," *Opt. Commun.* **86**, 333–340 (1991).
22. T. Sandrock, T. Danger, E. Heumann, G. Huber and B. H. Chai, "Efficient Continuous Wave-laser emission of Pr³⁺-doped fluorides at room temperature," *Appl. Phys. B*, **58**, 149–151 (1994).
23. T. Danger, T. Sandrock, E. Heumann, G. Huber and B. H. Chai, "Pulsed laser action of Pr:GdLiF₄ at room temperature," *Appl. Phys. B-Photo* **57**, 239–241 (1993).
24. A. Richter, N. Pavel, E. Heumann, G. Huber, D. Parisi, A. Toncelli, M. Tonelli, A. Diening and W. Seelert, "Continuous-wave ultraviolet generation at 320 nm by intracavity frequency doubling of red-emitting praseodymium lasers," *Opt. Expr.* **14**, 3282–3287 (2006).
25. A. Richter, E. Heumann, E. Osiac, G. Huber, W. Seelert and A. Diening, "Diode pumping of a continuous-wave Pr³⁺-doped LiYF₄ laser," *Opt. Lett.* **29**, 2638–2640 (2004).
26. A. Richter, E. Heumann, G. Huber, V. Ostroumov and W. Seelert, "Power scaling of semiconductor laser pumped praseodymium-lasers," *Opt. Expr.* **15**, 5172–5178 (2007).
27. P. Camy, J. Doualan, R. Moncorge, J. Bengoechea and U. Weichmann, "Diode-pumped Pr³⁺:KY₃F₁₀ red laser," *Opt. Lett.* **32**, 1462–1464 (2007).
28. N. O. Hansen, A. R. Bellancourt, U. Weichmann and G. Huber, "Efficient green continuous-wave lasing of blue-diode-pumped solid-state lasers based on praseodymium-doped LiYF₄," *Appl. Opt.* **49**, 3864–3868 (2010).
29. M. Fibrich, H. Jelinkova, J. Šulc, K. Nejezchleb and V. Škoda, "Visible cw laser emission of GaN-diode pumped Pr:YAlO₃ crystal," *Appl. Phys. B*, **97**, 363–367 (2009).
30. T. Basiev, V. Konyushkin, D. Konyushkin, M. Doroshenko, G. Huber, F. Reichert, N. Hansen and M. Fechner, "First visible 639 nm SrF₂:Pr³⁺ ceramic laser," in *Lasers and Electro-Optics Europe (CLEO EUROPE/EQEC), 2011 Conference on and 12th European Quantum Electronics Conference*, OSA Technical Digest (CD) paper CA2-2 (2011) p. 1.

31. T. Calmano, J. Siebenmorgen, F. Reichert, M. Fechner, A.-G. Paschke, N.-O. Hansen, K. Petermann and G. Huber, "Crystalline Pr:SrAl₁₂O₁₉ waveguide laser in the visible spectral region," *Opt. Lett.* **36**, 4620–4622 (2011).
32. J. Z. Sotor, A. J. Arkadiusz and K. A. Abramski, "Single frequency monolithic solid state green laser as a potential source for vibrometry systems," *AIP Conf. Proc.* **1253**, 313–316 (2010).
33. R. Conroy, *Microchip lasers*, PhD Thesis, University of St Andrews, UK (1998).
34. V. Petričević, S. K. Gayen, R. R. Alfano, K. Yamagishi, H. Anzal and Y. Yamaguchi, "Laser action in chromium-doped forsterite," *Appl. Phys. Lett.* **52**, 1040–1042 (1988).
35. N. Zhavoronkov, A. Avtukh and V. Mikhailov, "Chromium-doped forsterite laser with 1.1 W of continuous-wave output power at room temperature," *Appl. Opt.* **36**, 8601–8605 (1997).
36. B. Pezeshki, M. Hagberg, M. Zelinski, S. D. DeMars, E. Kolev and R. J. Lang, "400-mW single-frequency 660-nm semiconductor laser," *IEEE Photonic Tech. L.* **11** (7), 791–793 (1999).
37. M. G. Boshier, D. Berkeland, E. A. Hinds and V. Sandoghdar, "External-cavity frequency-stabilization of visible and infrared semiconductor lasers for high resolution spectroscopy," *Opt. Commun.* **85**, 355–359 (1991).

4

Recording Materials for Colour Holography

4.1 Introduction

The recording materials used in modern polychromatic display holography are fundamental to achieving high image fidelity. It is perhaps not surprising that the earlier holographic recording materials used in holography are simply not suitable for recording full-colour holograms; polychromatic holograms put far higher demands on the recording material. Moreover, many of the earlier silver halide materials produced by commercial manufacturers such as Agfa and Kodak are no longer on the market. Additionally, these materials were not panchromatic, nor did they have sufficient resolving power to be used for recording colour holograms. The first commercial photopolymer materials did have sufficient resolving power, but many were only monochromatic. To record full-colour holograms, panchromatic materials with a resolving power of more than 10,000 line pairs/mm are required. In this chapter, we shall focus our attention on the materials required for recording ultra-realistic colour holograms and describe their characteristics and the demands put on them by this application.

The three main types of holographic recording materials that can be considered today are

- Silver halide materials
- Dichromated gelatin materials
- Photopolymer materials

4.1.1 Silver Halides

Silver halide recording materials are interesting for many reasons [1]. Historically, these emulsions were the first materials used for recording holograms; silver halide has, in the past, constituted the most important and most ubiquitous material employed in holography, particularly with respect to its numerous scientific and artistic applications. Most importantly, silver halide materials exhibit high sensitivity in comparison with many other alternative materials, they can be coated onto both film and glass and can cover very large formats. They can also be used to record both amplitude and phase holograms and are capable of a rather high resolving power.

Notwithstanding its advantages, silver halide does have various drawbacks: it is absorptive, has inherent noise and a limited linear response, it is irreversible and it needs wet processing. Phase holograms made with silver halide are also subject to printout problems. Agfa, Mortsel, Belgium; Ilford, Knutsford, UK; and Kodak, Rochester, NY all manufactured special holographic silver halide materials of a monochromatic form for a long time, but they no longer have any such materials on the market today. As a matter of fact, Ilford (now operating under the name Harman Technologies Ltd.) has started to manufacture holographic recording materials again, but these materials have too large a grain size for recording colour holograms. There are only very few commercial silver halide colour emulsion products on the market today. Among these are two Russian manufacturers and two European producers with rather limited production. However, it is difficult for such small commercial manufacturers to guarantee that each batch of material will possess exactly the same characteristics. As such, the serious worker in modern colour holography often needs to consider either sorting and calibrating commercial batches before use or, in many cases, actually producing the materials in-house.

4.1.2 Dichromated Gelatin

Dichromated gelatin (DCG) possesses a very high resolving power and a remarkable brightness due to a refractive index modulation of 0.08, which, until recently, was the largest known among holographic materials. Unfortunately, there are no commercial companies producing panchromatic DCG recording materials today, although the Russian company Slavich produces blue/green sensitive plates (PFG-04). Therefore, this is a material which one needs to make in-house if one wants to record colour holograms. In addition, until recently, the sensitivity of known panchromatic DCG materials was very low. Currently, the material is mainly used for producing holographic optical elements (HOEs)—for example, heads-up displays for aircraft. Recently, panchromatic DCG materials have been reported with greatly improved sensitivity. As such, DCG must be regarded as an interesting material for colour holography and in particular for digital techniques that write small elemental holograms, one at a time.

4.1.3 Photopolymers

Photopolymer materials can be used for recording phase holograms in which applications in the mass production of small (usually monochromatic) display holograms and optical elements currently constitute the main commercial interests. The sensitivity is not as high as with silver halide materials, but the advantages are a low light-scattering noise level as well as an innate suitability for the application of dry processing techniques. E. I. DuPont de Nemours & Co. Wilmington, DE, has been the main manufacturer of commercial photopolymer materials and has, for a long time, marketed these under the name of OmniDex. The DuPont material requires only a dry processing technique (exposure to UV light and heat treatment) to obtain a hologram. A new photopolymer material, Bayfol HX, suitable for colour holography, which requires even less postprocessing, has recently been introduced by Bayer Material Science AG in Germany.

One important application of colour photopolymer materials is document security. As a result, material manufacturers will often restrict sales to other users. At the time of writing, such a policy was in operation by both DuPont and Bayer, and with the best chemistries still under patent restriction, unlike silver halide and DCG, in-house fabrication of photopolymers cannot be regarded as a serious alternative for most workers. Although today's panchromatic photopolymer materials constitute an extremely interesting solution for colour display holography, from a purely practical point of view, there remains a sizeable question mark over whether these materials will be commercially applicable to display holography applications in the near-term. The only material freely available at the time of writing was the Polygramma DAROL photopolymer marketed by Lynx in Brazil.

4.2 Holographic Recording

Before a more detailed presentation of the materials suitable for recording ultra-realistic colour holograms is given, a general description is provided of how a holographic recording is made. In particular, we discuss how silver halide materials are able to store the interference patterns generated during the holographic recording process. What follows is therefore a short description of holographic recording theory with some definitions of common photographic properties that are of particular importance for recording colour holograms. For example, we shall explain how a latent image forms in ultrafine silver halide grains. The signal-to-noise ratio and diffraction efficiency in the holographic recording process will also be introduced. For more detailed information on the general principles governing the holographic recording process, and on silver halide materials in particular, the reader is referred to a book dedicated to this topic [1].

To record the entire light field scattered from an object, both the amplitude and phase of the electromagnetic waves involved must be stored in some way. There is, however, no material that can directly detect both the amplitude and the phase of a light wave. The practical solution is therefore to use the interferometric two-step process introduced by Gabor [2], in which phase information in an optical

signal is converted to an implicit amplitude variation through mixing with a coherent reference; this amplitude signal is then recorded as a density or index variation within a photographic emulsion. This is the holographic process. The hologram it produces constitutes a micropattern created in a light-sensitive material as the result of the coherent interference between the signal (the object beam) and its reference (the reference beam). The time of exposure for a given material depends on the sensitivity of the material used as well as on the intensity of the interference pattern. Silver halide materials must be processed after exposure in a very specific way so that the recorded latent image of the interference pattern is successfully converted to local variations in optical density, refractive index or thickness of the recording layer.

A silver halide photographic recording material is based either on a single type or on a combination of types of silver halide crystals embedded in a gelatin layer. This is commonly referred to as a photographic or photosensitive emulsion. Actually, this photosensitive emulsion is not really an "emulsion" at all but rather a thin film of silver halide microcrystals dispersed in a colloid (gelatin). However, the term emulsion is commonly used in photography for this type of perpetual suspension. The emulsion is coated on a flexible or stable substrate material such as glass or plastic film.

There are three types of silver halides: silver chloride (AgCl), silver bromide (AgBr) and silver iodide (AgI). Silver chloride is used for low-sensitivity emulsions. Chloride/bromide emulsions have high light sensitivity. However, the bromide/iodide emulsions have even higher sensitivity. Silver iodide is never used alone but is used in a mixture with silver bromide; it normally constitutes 5% or less of such a mixture. Adding some silver iodide to fine-grained emulsions at low concentrations gives a higher sensitivity and contrast as compared with pure silver bromide emulsions of the same grain size. Silver halide crystals are cubical in shape, and in each crystal, a silver ion (Ag^+) is surrounded by six halide ions. The crystal normally possesses an excess of halide ions that originate from the emulsion manufacturing process. Silver halide grain sizes vary from approximately 10 nm for the ultrafine-grained Lippmann and colour holography emulsions to a few micrometres for high-sensitivity photographic emulsions (Table 4.1). Only a silver halide emulsion of the ultrafine grain type can be used for colour holography. For more detailed definitions and the mathematical theory of conventional photographic silver halide materials, the reader is referred to various scientific books on photography [3–6].

The resolving power of a photographic material is a measure of its ability to record fine detail. It can be defined as "the ability of a photographic material to maintain in its developed image the separate identity of parallel bars when their relative displacement is small." Normally, the resolving power of a photographic material is tested by using a resolution test chart. The highest number of lines per millimetre that can be resolved in the emulsion corresponds to the resolving power of the tested material. A line in this definition is a line with its adjoining space and corresponds to "line pairs" in electronic images. The resolving power of the holographic material is a critical feature that must be taken into account when defining its characteristics.

The resolution capability of an image reproduction process is normally described by the optical transfer function (OTF). For a given test input, the OTF is defined as the complex response (amplitude and phase) of the reproduced image for each spatial frequency, v . Usually, in practice, only the modulus of the OTF is quoted, this being known as the modulation transfer function (MTF). The MTF is a good aid in demonstrating the quality of a particular photographic emulsion as well as constituting a means for comparing different emulsions. Briefly, a test pattern containing a sinusoidal variation in illuminance combined with a slow continuous and linear variation in spatial frequency along one direction is recorded. The modulation M of the pattern in the test target can then be defined as

$$M = (H_{\text{MAX}} - H_{\text{MIN}})/(H_{\text{MAX}} + H_{\text{MIN}}) \quad (4.1)$$

where H is the exposure* incident on the photographic material. When this pattern is recorded in the material, light scattering will take place in the emulsion, which will reduce the original contrast of

* See Section 4.2.1 for the definition of "exposure".

TABLE 4.1

Emulsion Grain Sizes

Type of Emulsion	Average Grain Diameter (nm)
Ultrafine-grain holographic emulsion	10–20
Fine-grain holographic emulsion	20–50
Fast holographic emulsion	50–100
Chlorobromide paper emulsion	200
Lithographic emulsion	200–350
Fine-grain photographic emulsion	350–700
Fast photographic emulsion	1000–2000
Fast medical x-ray emulsion	2500

the pattern. In this way, the modulation of the pattern will be decreased, in particular at high spatial frequencies. The effective recorded exposure modulation M' will then be given as

$$M' = (H'_{\text{MAX}} - H'_{\text{MIN}}) / (H'_{\text{MAX}} + H'_{\text{MIN}}) \quad (4.2)$$

where H' is the exposure within the emulsion.

The original modulation M is constant and accurately known; it is also independent of the spatial frequency. After the tested emulsion has been processed, the corresponding “exposed” modulation is obtained from observing the density variation. The ratio between the modulation M' in the emulsion and modulation M of the incident exposure is called the *modulation transfer factor*, also called the *response*

$$R = M/M' \quad (4.3)$$

If the response is plotted as a function of spatial frequency, this curve will then be the MTF of the material (Figure 4.1). The Fourier transform of the MTF is the line spread function of the emulsion, which indicates the width of a line image recorded in the emulsion.

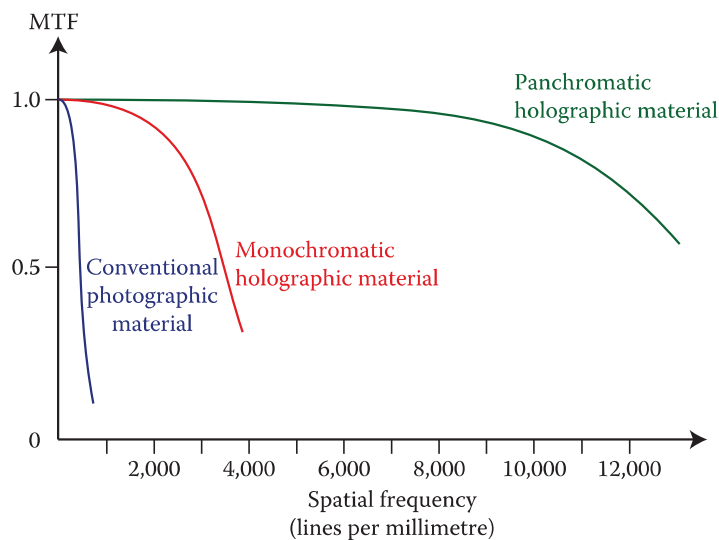


FIGURE 4.1 MTF for conventional photographic materials, for fine-grained holographic materials and for the ultrafine grain materials required for colour holography.

4.2.1 Sensitivity of Photographic and Holographic Materials

The time of exposure for a given material will depend on the sensitivity of the material used as well as on the intensity of the interference pattern. Some holographic materials must be processed after exposure in a specific way to obtain a hologram. The recorded intensity variations are converted during this processing step to local variations in optical density, to refractive index variations or to thickness variations of the recording layer.

The exposure of the recording material, H , is defined as the incident intensity, E , times the time of exposure, t . If the intensity is constant during the whole exposure time, which is usually the case, then

$$H = E t \quad (4.4)$$

Holographic materials are usually characterised using radiometric units. The radiometric equivalent of illuminance is irradiance. The unit of irradiance is Wm^{-2} and the exposure will then be expressed in Jm^{-2} . The sensitivity of a holographic emulsion is most often expressed in μJcm^{-2} or mJcm^{-2} . Knowing the sensitivity of the material used and having measured the irradiance at the position of the holographic plate, the exposure time can be found by dividing sensitivity by irradiance. Colour holographic materials must be sensitised in such a way that they are optimised for the laser wavelengths commonly used in holography.

4.3 Holographic Emulsions

The final quality of a holographic image will be a function of a number of factors such as the geometry and stability of the recording setup, the coherence of the laser light, the reference and object beam ratio, the type of hologram produced, the size of the object and its distance from the recording material and the recording material and the emulsion substrate used. It will also depend on the processing technique applied as well as the reconstruction conditions. We know that, if during the reconstruction of the hologram, the reference replay beam has identical characteristics to the recording reference beam, then no image aberration will occur.* This also applies when the reconstruction reference beam constitutes an exact conjugate of the original reference beam (time reversed). Theoretically, the holographic technique is the most perfect imaging technique in existence because both the amplitude and the phase of the light wave scattered from the object are recorded. However, in practice, the holographic image is subject to certain limitations imposed by the recording material. In fact, three main factors will determine the resolution of a holographic image: the recording wavelength, the numerical aperture and the properties of the recording material itself.

Of course, ideally, the ultimate resolution of a hologram should be independent of the properties of the recording material and should depend only on the wavelength that was used for the recording, on the size of the recorded area of the material (the aperture) and on the object distance. However, in practice, the limit on resolution may be set by the recording material. This is the case when the material cannot record spatial frequencies above a certain limit.

Additionally, even if we arrange for the replay reference beam to have identical characteristics as the recording beam, aberrations in the holographic image can be induced directly by the recording material. This is the case, for instance, when the refractive index of the recording material changes upon processing.

4.3.1 Demands on Recording Emulsion

A silver halide emulsion must comply with certain requirements to be suitable for the recording of colour holograms. The most important of these demands concerns the resolving power of the material. The recording material must be able to resolve the highest spatial frequencies of the interference pattern created by the maximal angle, θ , between the reference and the object beams in the recording setup

* The reader is referred to Chapter 11 for a discussion of the basic optical principles of holography.

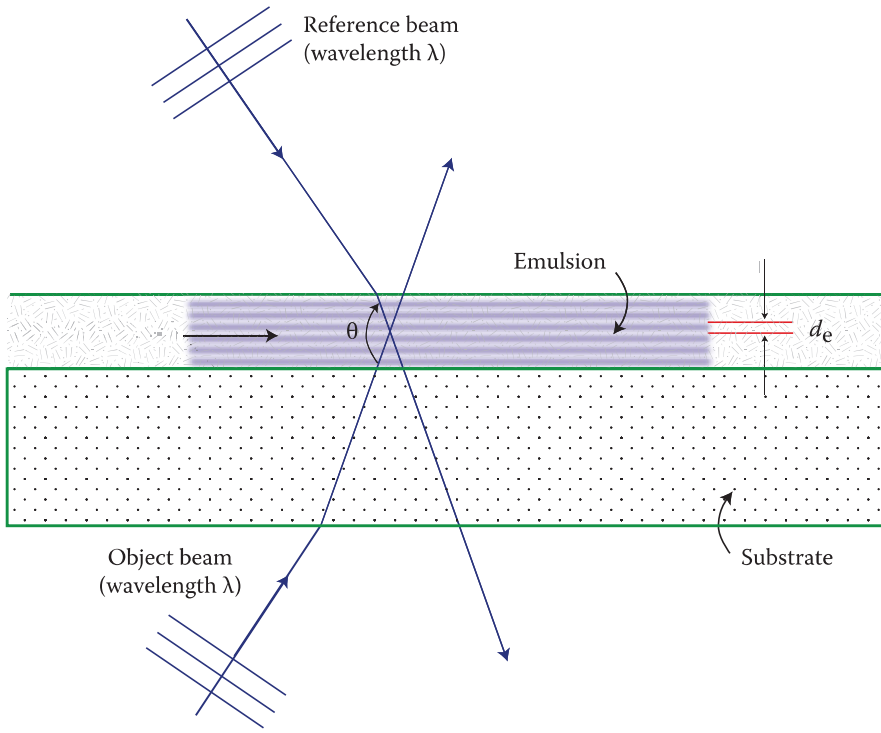


FIGURE 4.2 Demand on the resolving power from a material for recording a reflection hologram. The recording material must resolve the highest spatial frequencies of the interference pattern created by the maximal angle θ between the reference and the object beams in the recording setup.

(Figure 4.2). If λ is the wavelength of the laser light used for the recording of a hologram, then the closest separation d_a between the fringes in the interference pattern (in air) is given by

$$d_a = \frac{\lambda}{2 \sin(\theta/2)} \quad (4.5)$$

In the recording layer, the fringe spacing d_e will depend on the refractive index n of the emulsion and is given by

$$d_e = \frac{\lambda}{2n \sin(\theta/2)} \quad (4.6)$$

We can use these formulae to find the resolving power needed to record a colour reflection hologram with blue laser light at $\lambda = 440$ nm. Assuming an emulsion having a refractive index of $n = 1.62$ and a maximal angle of 180° between the beams, Equation 4.6 shows that a minimum resolving power of 7360 lines/mm is required. This is the minimum resolving power needed to record the information. Close to its resolution limit, the material will exhibit a lower MTF and will thus make a low-quality hologram with poor fringe contrast and low signal-to-noise ratio. For high-quality colour holograms, the resolution limit of the material must be much higher than the minimum value obtained according to the above formula.

4.3.2 Resolution of Holographic Image

In holography, the resolution of the holographic image and the resolving power of the recording material are not directly related in the way they are in photography. Equation 4.6 determines the minimum resolving power required to actually record a reflection hologram. This figure is not directly related to the resolution of the image recorded in or reconstructed by a hologram. If no lenses are involved in the holographic image formation process, the theoretical resolution of the image will be limited by diffraction

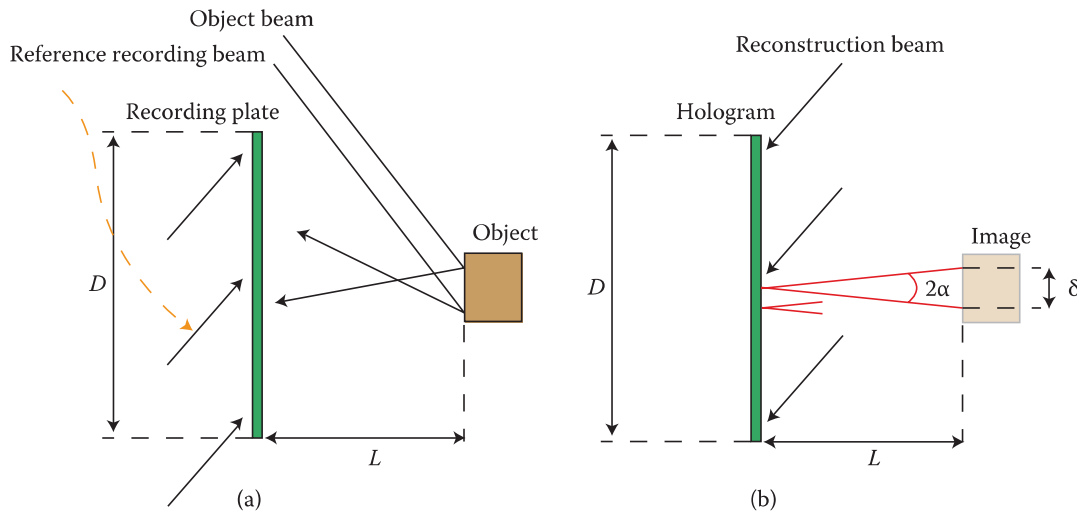


FIGURE 4.3 Diffraction-limited ideal resolution of the reconstructed image of a reflection hologram: (a) recording the hologram of an object and (b) replay of the recorded hologram showing that image detail is reconstructed with a characteristic length scale δ determined by L and D . This in turn is related to the angle of diffraction (2α).

and as such will be dependent on the area of the recording material, the recording laser wavelength and the distance between the recording material and the object (Figure 4.3). The image resolution δ is then

$$\begin{aligned}\delta &\sim \frac{\lambda}{2\sin\alpha} \\ &\sim \frac{\lambda L}{D} \quad \text{if } L \gg D\end{aligned}\tag{4.7}$$

where α is the angle indicated in Figure 4.3. Of course, if a limiting aperture is part of the system, diffraction will occur, causing the resolution to be slightly smaller than it would be if no aperture was present. For a circular aperture in incoherent light, the diffraction-limited resolution is given by

$$\begin{aligned}\delta &\sim 0.61 \frac{\lambda}{\sin\alpha} \\ &\sim 1.22 \frac{\lambda L}{D} \quad \text{if } L \gg D\end{aligned}\tag{4.8}$$

In a reflection hologram reconstructed using a broadband white-light source, the image resolution is mainly affected by the white-light source size, which has a much larger influence than the diffraction-limited resolution. More information about the illumination of colour reflection holograms and the influence on the image resolution and chromatic aberration using white-light sources will be provided in Chapter 11.

4.3.3 Image Resolution Determined by Recording Material

Theoretically, the resolution of the holographic image should be the true diffraction-limited resolution that can be obtained when the information is collected over an aperture equal to the size of the recording holographic plate. If the resolving power of the recording material is sufficient, the diffraction-limited resolution can be obtained under the assumption that the high-resolution recording material is also perfect in that the position of the recorded interference fringes will not be changed during the processing of the material. In practice, a stable support for the emulsion (such as a glass plate) is needed and the

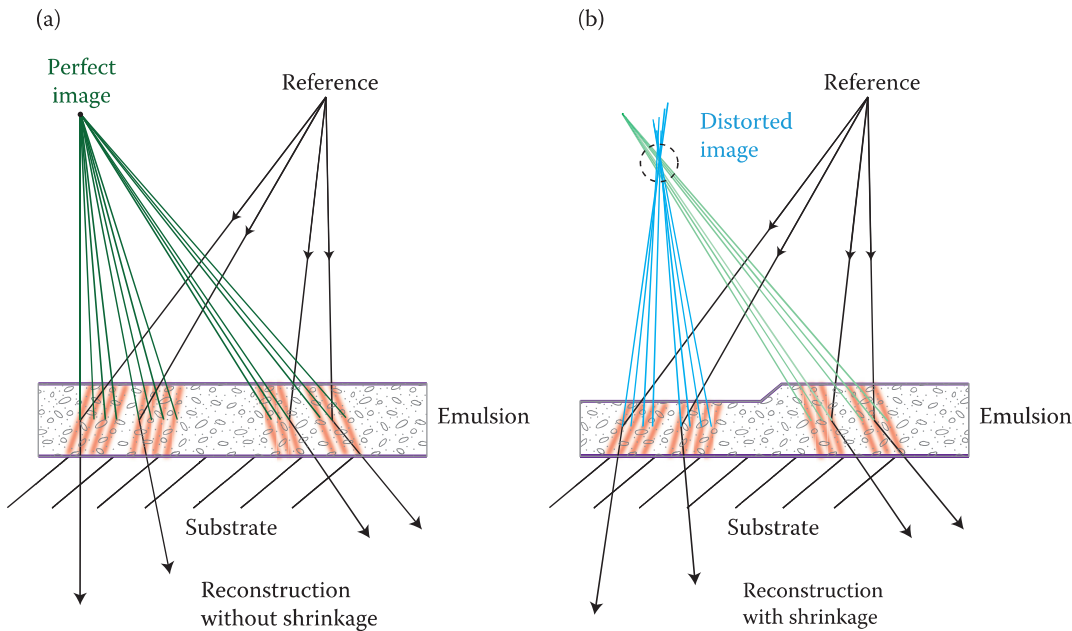


FIGURE 4.4 Illustration of how image distortion is introduced in an off-axis transmission hologram when the emulsion thickness changes. (a) shows the case with no change in thickness: here, a unique recording point produces image rays that coincide at the same unique point. (b) illustrates what happens when the emulsion shrinks (or expands). Now the image rays do not converge to a unique point.

processing methods applied must not affect the recorded fringe position in the emulsion, that is, no fixing. The most limiting factor controlling the resolution of a holographic image comes from distortions appearing in the emulsion. These aberrations, illustrated in Figure 4.4, are introduced by

1. Variations in the thickness of the recording medium before processing
2. Variations in the thickness of the recording medium during processing
3. Variation in the refractive index of the recording medium during processing
4. Deformation of the recording medium occurring between recording and reconstruction.

An ideal holographic recording plate should consist of a uniformly thick emulsion coated onto a perfectly flat plate of homogeneous glass having uniform thickness. In practice, the recording plate must be treated as one of the optical elements in the holographic system that can eventually affect the image quality.

4.4 Problems due to Short or Long Exposure

4.4.1 Pulsed Holography

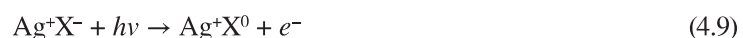
RGB pulsed lasers are nowadays being used more and more frequently to record digital colour holograms. We shall discuss such lasers in depth in Chapter 6 and the digital hologram printers employing these lasers in Chapter 7. The main reason for the use of pulsed lasers as compared with CW lasers is that their short pulses confer complete immunity to environmental vibration at recording. For holographic applications, solid-state lasers today are operated mainly in the Q-switched regime, with associated pulse lengths of approximately 10 to 60 ns. From the photographic point of view, these exposure times can all be regarded as "short".

4.4.2 Reciprocity Failure

In Q-switched operation, laser energy is released during a very short time, producing a very high peak output power. For a 10 J pulse at 20 ns, the peak power is 500 MW. Such high power is certainly desirable when exposing holographic materials of relatively low sensitivity. However, short exposure times are associated with the problem of reciprocity failure or more precisely, the failure of the reciprocity law. In general, the exposure H of the photographic material is given by Equation 4.4. The reciprocity law was originally formulated by Bunsen and Roscoe [7]; it states that a given exposure H is independent of the two factors, E and t , separately. However, this is not true for extreme values of E and t , and this phenomenon can also affect hologram recordings at very long exposure times and low light levels (the Schwarzschild effect). In particular, using low-power CW lasers for recording colour holograms over long exposure times can also create problems for the ultrafine-grain emulsions.

Curves showing the reciprocity law (or its failure) are often plotted as $\log(Et)$ versus $\log(E)$ for a fixed optical density. A typical reciprocity law–failure curve is shown in Figure 4.5. Between any two points on a horizontal part of the curve, there is no reciprocity failure. However, if the two points of the curve are not on a horizontal part of the curve, then the reciprocity law does not hold between the corresponding exposure times. In reality, the exposure necessary for obtaining a certain density in the developed material is not constant but depends on the exposure time t . For very short exposures at high intensities E , as well as for very long exposures at low intensities, H has to be strongly increased to get the same density as the one required for the optimal values of E and t . These effects are called *high-intensity reciprocity failure* (HIRF) and *low-intensity reciprocity failure* (LIRF), respectively. The HIRF becomes of importance even for pulses much longer than those from a conventional Q-switched laser and the effect is roughly constant for times less than 10^{-5} s for conventional silver halide photographic materials.

To better understand these phenomena and how we might increase the sensitivity of an ultrafine grain emulsion, we must study the formation of the latent image. The silver halide crystal is an n -type photoconductor with a valence band of electrons and with a conduction band in which injected electrons are free to migrate throughout the crystal until trapped by a lattice defect. During the exposure of an emulsion, photons are absorbed by the crystals. When a photon of sufficient energy is absorbed, an electron from the silver halide crystal Ag^+X^- is promoted to the conduction band, leaving behind a positive hole that constitutes a free halogen atom:



The silver ion will then attract the photogenerated electron to form a silver atom, the so-called *prespeck*



The free electron is first trapped by a positively charged surface lattice defect. Once trapped, the electron will attract an interstitial silver ion, Ag^+ to the sensitivity site to form the silver atom prespeck, Ag^0 .

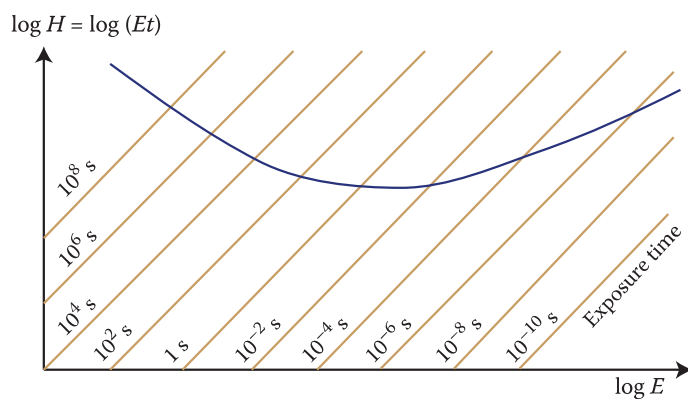


FIGURE 4.5 Typical reciprocity–law failure curve. Curves showing the reciprocity law (or its failure) are often plotted $\log(Et)$ versus $\log(E)$ for a fixed optical density. A material without reciprocity failure is a horizontal line for all exposure times.

Statistically, an isolated silver atom has an average lifetime of approximately 1 s. This lifetime can be calculated knowing the binding energy for the electron within the prespeck that has been experimentally measured to be approximately 0.7 eV. The Boltzmann statistical lifetime is then given by the standard formula

$$t = \tau e^{E_0/kT} \quad (4.11)$$

where $\tau = 10^{-12}$ s is the estimated electron collision period, E_0 is the binding energy, k is Boltzmann's constant (1.3805×10^{-23} J/K) and T the temperature in Kelvin. For $T = 300$ K and for $E_0 = 0.7$ eV, Equation 4.11 tells us that $t \sim 1$ s.

To create a sublatent image speck in the silver halide crystal where a diatomic silver molecule is formed by the process of nucleation, a second silver atom is required at the site of the first silver atom during its lifetime:



A subspeck of two atoms is stable at room temperature ($E_0 = 1.74$ eV giving $t = 1.7 \times 10^{17}$ s). The sublatent image speck grows larger with further photon absorption, resulting in photogenerated electrons. The latent image is usually regarded as a collection of a few silver atoms at one site produced by the reduction of silver ions in the process of photolysis. Silver formed in this way is known as *photolytic silver*. A latent image of at least three to four silver atoms is needed for developability. Developability means the formation of a latent image that has the catalytic property of increasing the development rate of silver halide grains reduced to metallic silver by the reducing agent called a *developer*. For all the exposed grains, chemical development will then reduce the entire silver halide grains to metallic silver.

The chemical sensitisation of an emulsion is similar to the doping process of a semiconductor. The introduction of such impurities as sulphur, gold, or silver, alone or in combination, into the emulsion increases the grain's sensitivity (finishing). Chemical reduction is induced by raising the temperature. Depending on the impurities which have been introduced into the emulsion, the emulsion is called *sulphur sensitised*, *gold sensitised*, *sulphur plus gold sensitised*, or, at times, *reduction sensitised*. The sensitivity of a grain is defined as the reciprocal of the number of absorbed photons necessary to produce the developability of the grain. A highly sensitised grain requires fewer photons than a less sensitised grain to be developable. Grain size is, however, even more important for sensitivity: the larger the grain, the higher the sensitivity of the material. A typical large silver halide grain with the volume of $1 \mu\text{m}^3$ ($= 10^{-12} \text{ cm}^3$) contains about 2×10^{10} silver ions. In such a grain, just a few photons are expected to produce a stable latent image, which can later be used to trigger off the process of converting the entire grain to silver atoms. The overall amplification, from the quanta absorbed to the silver atoms produced, can be greater than 10^9 in this process. For a typical conventional holographic emulsion with the grain size of approximately 50 nm, the amount of silver ions in the grain is approximately 2.6×10^6 , which translates to an amplification of about one million. However, note that this constitutes only approximately 1/1000 of the sensitivity of a conventional high-speed photographic film. The problem with ultrafine-grain colour holography emulsions is that it is impossible to make them very light sensitive.

Using pulsed lasers to record holograms with ultrafine-grain emulsions, one encounters the problem of HIRF. As the intensity increases, more absorbed photons are required per grain to produce the same density in the developed material as compared with exposures at lower intensity levels. HIRF is caused by the silver ions' motion and their concentration in the emulsion. The exposure time of about 1 s is sufficient for a mobile, interstitial silver ion to neutralise a trapped electron before another arrives. At high intensities, electrons are produced at such a rate that there is not enough time for the mobile silver ions to neutralise the trapped electrons. Because of electrostatic repulsion, the second electron is not trapped at the same site as the first electron. Recombination of holes and electrons may occur instead at an increasing rate or trapping of electrons may take place at some other site. In each case, the process of latent-image formation becomes inefficient.

It should be mentioned that LIRF can also affect the recording of large-format colour holograms on ultrafine grain emulsions using CW lasers. LIRF depends on the thermal stability of an isolated silver atom which, if not stabilised by combination with another silver atom within its lifetime (~ 2 s) will decompose into an electron and a silver ion again. This, of course, means that long exposure at a low light level becomes a very inefficient process in forming the latent image.

Another result of short exposure is the localisation of the latent image within the silver halide crystal. At exposure times longer than 10^{-2} s, the latent image is almost entirely localised on the surface of the silver halide crystals. At shorter exposure times, it is also formed inside the grains. Therefore, to develop the internal latent image specks as well, it is necessary to use the correct developing technique. A surface developer acts only on the latent image on the surface of the silver halide crystal. Internal development is performed on the internal latent image after the surface latent image has been bleached off. Total development is performed with an internal developer but without bleaching off the latent surface image. This type of development technique is definitely preferable for holograms exposed with a pulsed laser.

4.4.3 Holographic Reciprocity Failure

Early investigations on holographic reciprocity failure regarding fine-grain materials were performed by Vorzobova and Staselko [8,9]. They noted that there was a reduction in the γ value of holographic materials exposed with pulsed lasers. The diffraction efficiency for a Q-switched hologram decreased to 10% compared with that of a hologram recorded using a free-lasing mode. They concluded that the observed drop in diffraction efficiency of pulsed holograms was caused by a change in the optical characteristics of the photographic layer when the illumination time was reduced. In another Russian investigation, Benken and Staselko [10] studied the latent-image formation process in the Russian holographic materials LOI, PE-2 and IAE. They were particularly interested in the influence of the exposure time on the obtainable diffraction efficiencies. A dramatic difference in the diffraction efficiency of the PE-2 material was found when the material was exposed to a 20 ns pulse (Q-switched) as compared with a 300 μ s pulse (free lasing): the longer pulse produced a 100 times higher diffraction efficiency. Using a special scattering technique, the authors could measure the diffraction efficiency of the dynamic latent-image grating as well as the efficiency of the static grating (the developed grating). The former was divided by the latter and the ratios compared. The ratio that was obtained was approximately 10 to 20 for free-lasing pulses, whereas for Q-switched pulses, it could sometimes be as high as 1000. This difference was due to some extent to latent-image fading, which will be discussed later in this chapter. Pantcheva et al. [11] discussed emulsion-manufacturing methods to reduce HIRF for silver halide materials for pulsed holography. In particular, HIRF can be reduced by:

- Creating hole traps by introducing reducing agents
- Increasing electron lifetime by introducing shallow traps for electrons using, for example, metal ions
- Formation of a few stable and active sensitivity-specks on the microcrystal's surface by chemical sensitisation.

The different methods listed above were tested using emulsions with a grain size of approximately 30 nm. The best reducing agent seems to have been ascorbic acid, which means that a pretreatment of the holographic emulsion in an ascorbic acid solution before exposure can improve pulsed hologram recordings. Introducing metal ions into the emulsion at the preparatory stage increases the lifetime of the latent-image speck. The best results were obtained using lead ions, but cadmium ions also gave fairly good results. Gold sensitisation using, for example, HAuCl_4 also reduces HIRF. This confirms similar results obtained for conventional photographic emulsions [12]. Johnson et al. [13] discussed a slightly different aspect of reciprocity failure. It concerned the decrease in diffraction efficiency of the reconstructed images in multiple-exposure holograms recorded with equal energy per exposure. The authors call this phenomenon *holographic reciprocity law failure*.

4.5 Increasing Sensitivity by Hypersensitisation and Latensification

A photographic material can be treated in different ways before exposure to increase its sensitivity. The technique of increasing the material's sensitivity is referred to as *hypersensitisation*. If the treatment is performed after exposure but before development, it is called *latensification* (latent image intensification). The total increase in the holographic material's sensitivity that can be obtained with the help of these methods depends on the material used, the manufacturing method, the ripening and finishing, etc.

4.5.1 Hypersensitisation

Here, we will only discuss triethanolamine (TEA) and water treatments. TEA is the technique recommended by the UK company Colour Holographic Ltd. for their colour emulsion before recording.

4.5.1.1 Water Solution of TEA

TEA $[(\text{HOCH}_2\text{CH}_2)_3\text{N}]$ has been used extensively in holography to increase the sensitivity of recording materials [14–17]. The treatment of the material is performed in a bath with a TEA concentration of 0.7% to 2%, which provides an increased sensitivity factor of about 2. Higher concentrations (up to 10%) are recommended for materials intended for pulsed laser exposures according to Russian investigations. It is also recommended to use a bath at the temperature of 10°C to 15°C and not to dry the material in hot air. This method produces quite stable results, but it is advisable to expose the material soon after the treatment to keep the fog level low. Storing the material at low temperatures (-18°C) ensures better stability than storing it at room temperature. Kirillov [16] shows that the grain size in the emulsion is slightly reduced during TEA treatment, resulting in a holographic image of a higher quality. It should be mentioned that the TEA solution is also a swelling agent, which means that a TEA-treated emulsion of a recorded colour hologram may shrink after processing, which creates an erroneous colour replay.

4.5.1.2 Water Treatment

To avoid shrinkage caused by TEA hypersensitisation, it is possible to increase the sensitivity by simply treating the emulsion in water. Soaking the material in distilled water to which a few drops of a wetting agent have been added will remove excessive bromide and increase the concentration of silver ions, which in turn increases the material's sensitivity. The bath temperature should be 10°C to 12°C, and drying should take place in a low ambient temperature (13°C – 15°C). The durability achieved by this method is low and the material must therefore be exposed directly after treatment. If this is not done, the fog level will increase.

4.5.2 Latensification

Latensification leads to the acceleration of the development process, giving an apparent speed increase at short development times. The methods used for latensification are very similar to the ones used for hypersensitisation. Primarily, only dry methods are of interest. Latensification using low-intensity light offers a possibility of true speed increase by actually using the LIRF mechanism. Postexposure can be made at a suitable wavelength depending on the spectral sensitivity of the material used. A very low light intensity must be used for a long time. The latensification exposure takes between 15 min and 2 h for normal photographic materials. The Geola organisation sometimes use light latensification for the Russian ultrafine emulsions. After the holographic image recording has been performed, an additional exposure of the material is performed using incandescent light. The incoherent light wavelength band used for latensification should be located in a part of the spectrum in which the material has low sensitivity. For example, an ordinary, safe-light lamp with a suitable dark colour filter can be used. The material is exposed at a distance from the lamp of one to two metres. The power density of between 2.0 and 5.0 $\mu\text{W}/\text{cm}^2$ at the film level is recommended depending on the emulsion's sensitivity. The exposure time can be varied between 10 min and 1 hour. At optimal conditions, an increased sensitivity of a factor of about 2.5 can be obtained.

4.5.3 Internal Latensification

The most important aspect of processing pulsed holograms is the process of internal latensification, which takes place when a certain type of developing agent is used to develop the recorded hologram. Electron injection methods using developing agents for latensification of the internal image have been reported by James [18]. Some developing agents, such as phenidone (1-phenyl-3-pyrazolidone) for example, can latensify the internal latent image. It has been suggested that latensification depends here on the initial formation of isolated silver atoms, which subsequently lose electrons to the conduction band of the crystal. Conduction electrons formed in this way act to build up latent subimage centres in the same way as the photoelectrons formed by the exposure act. If such an action occurs between the developer and the latent subcentres or the very small latent-image centres, as suggested, this action should also lead to latensification of the internal image. At any rate, this effect can be obtained by adding 1 to 2 g/L of phenidone to a metol-hydroquinone developer. The reason why developers containing phenidone work so well with holograms exposed with Q-switched pulsed lasers is that internal image latensification takes place in combination with the superadditive effect with another developing agent. Figure 4.6 illustrates the practical action of the Kodak D-19 developer with and without phenidone for a hologram recorded on the former Agfa 10E75 material exposed using a 13 ns ruby pulse at 694 nm [15]. The figure shows that sensitivity increases dramatically when using phenidone in the developer. Latensification taking place in the developer is, however, not directly recognised as a separate method for hologram treatment. Binfield et al. [19] found that the type of developer used also has an effect on holographic reciprocity when recording holograms exposed with CW lasers.

A special developer for pulsed holograms was formulated based on the earlier tests using phenidone. The developer SM-6 (Salim's mistake) was found more or less by a mistake. Salim, a student of one of the authors (HB), was asked to add 0.6 g of phenidone to a certain developer but instead added 6 g, which is a rather high concentration as compared with photographic developers based on phenidone. Nonetheless, after trying many other concentrations, 6 g turned out to be the optimal concentration for pulsed holograms when using fine-grain materials. The developer SM-6 is now widely used for printed digital colour holograms recorded with RGB pulsed lasers (Table 4.2).

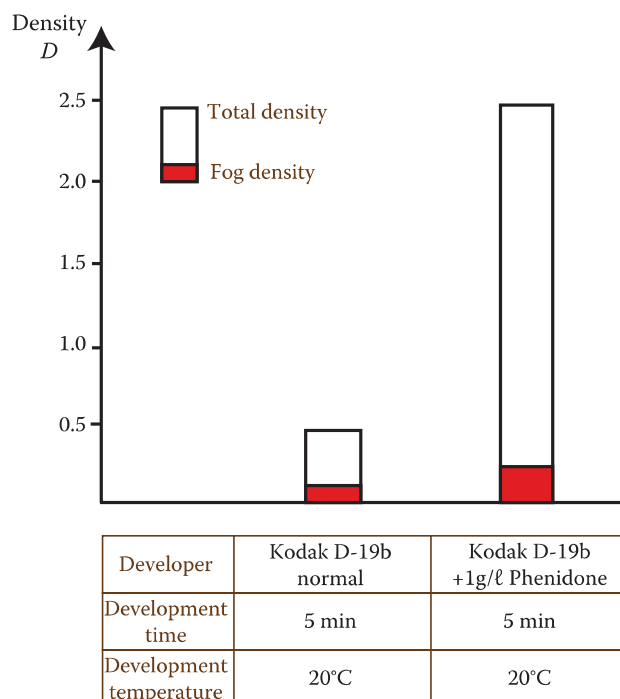


FIGURE 4.6 Density obtained on Agfa 10E75 material for a fixed short exposure (13 ns pulse at $\lambda = 694$ nm) using the Kodak D-19b developer with and without phenidone.

TABLE 4.2**SM-6**

Phenidone	6 g
Ascorbic acid	18 g
Sodium hydroxide	12 g
Sodium phosphate (dibasic)	28.4 g
Distilled water	1 L

Note: Developing time: 2–3 min at 20°C

4.6 Substrates for Holographic Emulsions

The material on which the emulsion is coated has a strong bearing on the final quality of the hologram. The best choice is often a glass plate as it is mechanically stable and optically inactive. Also, the light-scattering noise level in clear glass is very low. In many applications of holography, glass is actually the only possible support material. High-resolution imaging, hologram interferometry, HOEs and spatial filters are a few examples where a very stable emulsion support is important. In display holography, it is also often convenient to use glass plates, mainly because of the need for stability when using CW lasers. Producing master plates for hologram copying is another example suited to glass plates. Yet another example is the use of glass in the recording of expensive art holograms, where it is important to protect the emulsion well (if sealed with another glass plate after processing) against detrimental environmental effects (humidity, air pollution, etc.).

The use of film substrates has been growing steadily in recent years, especially in display holography for large-format colour holograms. In many cases, the use of film has many advantages as compared with that of glass (breakage, weight, cost, size, etc.). For example, for many display holography applications, film substrates are often sufficient and more economical than glass. Hologram copying in larger quantities is done mainly on film (sometimes the copies are laminated to a stable substrate after processing). The increased use of pulsed lasers has made hologram recording simpler when using film substrates. In Figure 4.7, the difference between holographic emulsions coated onto glass or film substrates is illustrated.

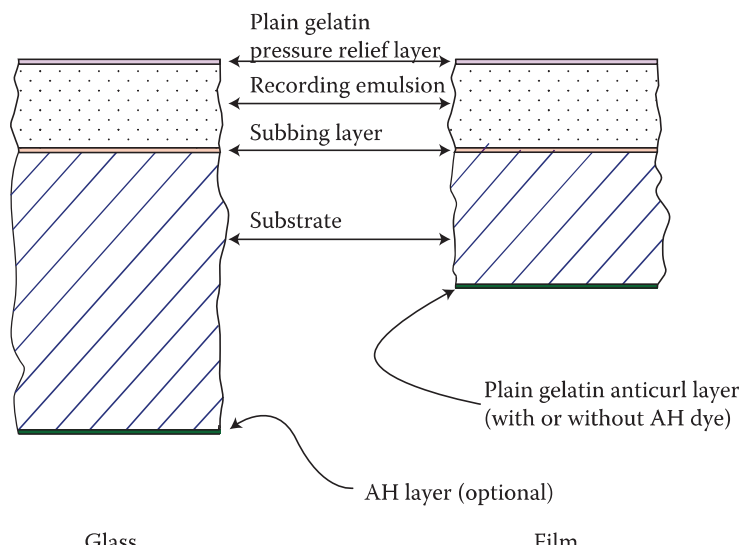


FIGURE 4.7 Holographic silver halide emulsion coated onto glass and film substrates, including additional layers used in holographic materials.

4.6.1 Glass Plates

Holographic glass plates are commonly made of soda-lime glass of high quality (free from graininess and molecular orientation) produced with the help of the flat-drawn sheet or the float process method. The refractive index (refractive dispersion) of glass varies depending on the light wavelength and is approximately 1.516 for $\lambda \sim 600$ nm. Good optical quality and high mechanical and thermal stability of glass are the main advantages when glass is used as a substrate for holograms. Young's modulus for glass is $70 \times 10^9 \text{ Nm}^{-2}$ and the thermal coefficient of expansion is only $8.1 \times 10^{-6} \text{ }^\circ\text{C}^{-1}$.

Glass thickness varies depending on the plate format and is typically between 1 and 6 mm. The emulsion coated onto untreated glass plates tends to peel off when dry, or frill off when it is wet. Therefore, a well-cleaned glass plate is often precoated with an extremely thin substratum of gelatin hardened with chrome alum—or sometimes with a layer of chrome alum solution alone—making the underlayer of the subsequently applied emulsion very hard. This process is referred to as *subbing*.

4.6.2 Film Substrates

Film substrates are of two main types: polyester (polyethylenterephthalate, PET) and a cellulose ester, commonly triacetate (cellulose triacetate) or acetate-butyrate. In addition to the light-sensitive emulsion coating (and the necessary subcoating), curl control and antihalation coating are often added here. The film may curl badly due to the variations in gelatin concentration caused by humidity. Therefore, a coating of pure gelatin is often applied to the back of the substrate to counteract the curl of the emulsion. If an absorbing dye is added to such gelatin coating it can serve as an antihalation layer at the same time. It should be mentioned that an antihalation cannot be used when a material is used for recording (Denisyuk) reflection holograms.

A film can also receive coating for static protection. The coating can be in the form of a layer containing matte particles that prevents close surface-to-surface contact and static electricity generation upon separation. The matting layer (coated on both sides of the substrate) also prevents individual film sheets from sticking together due to humidity variations during storage. In holographic materials these coatings are sources of noise explaining why the quality of a film hologram (especially on a polyester base) is not always as good as a hologram recorded on glass. As a matter of fact, a thin layer of pure gelatin is often coated over the light-sensitive emulsion (super coating). The reason for this is that if this layer is not applied, the emulsion grains affected by, for example, pressure marks could produce image defects during development.

Various important aspects must be considered when choosing a film base material for a given holographic application. The mechanical behaviour of the base material, with or without the emulsion, is strongly viscoelastic. Polyester is mechanically more stable (Young's modulus, $4.5 \times 10^9 \text{ Nm}^{-2}$) than triacetate (Young's modulus, $3.8 \times 10^9 \text{ Nm}^{-2}$) and it is also less sensitive to humidity. Because of the higher tensile strength, the polyester film can be made thinner than the triacetate film. On the other hand, this is birefringent and can cause many problems when recording reflection holograms (where the reference beam has to pass through the substrate). Polyester also has a higher inherent scattering level. During the manufacture of polyester, the polymer is biaxially oriented when it is drawn and tendered so that it has different refractive indices for each of the three orthogonal directions (α, β, γ). Polyester shows larger wavelength-dependent variations in refractive dispersion than triacetate does. For polarised light entering the polyester material at normal incidence, the refractive index for light at $\lambda \sim 600$ nm is $n_\gamma = 1.66$ and $n_\beta = 1.65$, respectively, depending on whether the electric field vector is oriented parallel or perpendicularly to the major axis. For polarised light propagating in the plane of the support, the effective refractive index is typically $n_\alpha = 1.5$. The refractive index for triacetate is approximately 1.48 at $\lambda \sim 600$ nm. This material is optically inactive and has a low inherent scattering level.

In general, polyester is recommended for transmission holograms in cases when a mechanically stable base is important, whereas triacetate is more suitable for reflection holograms, where birefringence causes severe problems if polyester is used. The inherent scattering levels in polyester may cause problems when recording colour holograms. The thickness of commercial film substrates for holography varies between 64 and 200 μm . Thinner film substrates apply to polyester materials only.

4.7 Commercial Recording Materials for Colour Holography

4.7.1 Manufacturing Companies

The market offers a very limited choice of silver halide recording materials for colour holography. In the past, Agfa-Gevaert, Ilford and Kodak manufactured materials for monochrome hologram recording. None of these companies have holographic materials on the market now. Recently, Harman Technologies (formerly Ilford) started limited production of a new holographic emulsion but with a silver halide grain size not suitable for colour holography. Kodak materials were used for the very first laser-produced holograms in the United States as well as for some early colour holography tests. The Kodak 649-F spectroscopic plate, often used in the early days, was actually panchromatic but had a rather low resolving power (only ~2000 lines/mm). In the following sections, materials from different manufacturers of colour holographic materials are presented. In general, the sensitivity of an emulsion depends on many factors, for example, the laser wavelength, the exposure time (reciprocity failure), the development (developer type, processing time, temperature, agitation, etc.) and storage conditions. Holographic sensitivity often varies from batch to batch, which is rare with conventional photographic materials. It is consequently recommended to make exposure and processing tests each time an important holographic recording is to be performed. It needs to be emphasised that, while it is nice to have high sensitivity for recording materials for colour holograms, it is not acceptable if it comes with an increased grain size. Unfortunately, it is much better to accept a longer exposure time (or to use a higher energy laser) and to obtain a scatter-free recording.

In Russia today, most of the manufacturing of holographic emulsions suitable for colour holography takes place in two companies, the Slavich Joint Stock Company [20] and Sfera-S AO [21]. Both are located in Pereslavl, a few hours' drive from Moscow. Slavich manufactures different types of silver halide materials for holographic purposes. The two main differences between these and previous western materials are the grain size and the silver content in the emulsion. The Russian emulsions have grain sizes as small as 10 nm, and the silver content is usually one-half (~0.25 g/cm³) of the normal silver content present in western materials. Materials such as the old Soviet PE-2 and LOI-2 also possessed these characteristics. The LOI-2 materials were developed by Protas and are now manufactured under the name of PFG-02. The PE materials were developed by Kirillov and are of the highest quality—their grain sizes for the best materials do not exceed 10 nm. Panchromatic materials for colour holograms are now manufactured by Slavich under the name of PFG-03C.

Sfera-S was formed by Yuri Sazonov in 2004. Sazonov was earlier responsible for holographic plate manufacturing as director of the Micron plant at Slavich. In his new company, Sfera-S, which is located in a former Slavich building, he is now responsible for manufacturing a high-quality emulsion for colour holography which is available coated both onto glass plates as well as onto film. The main customer is the Geola organisation in Vilnius, Lithuania [22], where these films are used for the production of digital colour holograms (more about digital printing in Chapter 7). The Sfera-S emulsion is currently the highest-quality commercial panchromatic colour holography material available. It is sensitive to the short laser-pulse recording primarily utilised in the pulsed RGB digital holographic printers used by Geola. Both the Slavich and Sfera-S materials are available from Geola or from their international network of distributors.

Colour Holographic [23] is the primary manufacturer of ultrafine-grain holographic emulsions in the United Kingdom. Their emulsion is based on the material that Richard Birenheide manufactured in Germany. This type of emulsion (BB emulsion) was launched in 1996. Mike Medora of Colour Holographic acquired the rights to the BB products in 2001. Initially, these emulsions were monochromatic and later a panchromatic emulsion, the BBVPan, was introduced. Ulibarrena et al. [24,25] published reports concerning this new panchromatic ultrafine grain emulsion, which has a mean grain size of 20 nm. The shrinkage or swelling of the emulsion after the plate is processed is one concern because the emulsion requires TEA pretreatment to increase its sensitivity. In colour reflection holography, a change in emulsion thickness is directly related to the wavelength of reconstruction and so affects the final replay spectrum and the colour reproduction of the image. Ulibarrena is now working at Colour

TABLE 4.3

Commercial Silver Halide Holographic Recording Materials for Colour Holograms

Material	Spectral Sensitivity (nm)	Resolving Power (line pairs/mm)	Grain Size (nm)	Substrate
Colour Holographic				
RGB, BB-PAN	440–650	4,000	20–25	glass
Slavich				
Pan, PFG-03C	450–700	5,000	10	glass/film
Sfera-S Ltd.				
Pan, PFG-03CN	435–665	6,000	9	glass/film
Ultimate				
08-COLOR	460–650	10,000	8	glass/film

Holographics and is responsible for emulsion manufacturing, including the panchromatic emulsion, which is now called RGB BBPAN. The company's production facility is based in Maldon, Essex, UK.

The other European manufacturer of colour emulsion is Ultimate Holography in France. This emulsion is based on the work by Yves Gentet [26,27]. The company produces a panchromatic colour emulsion with an 8 nm grain size. However, the production capacity of such plates is limited. Ultrafine-grain monochromatic red- and green-sensitive emulsions are also manufactured. Table 4.3 lists current commercial silver halide materials suitable for colour holograms.

At the time of writing, both Colour Holographics and Ultimate could not guarantee the commercial supply of panchromatic silver halide holographic plates to all customers. Both companies cited quality control difficulties for the limited volumes involved.

4.8 SilverCross Emulsion Research Project

A recent two-year European research project (EC FP6 CRAFT project 005901) SilverCross [28] produced an ultrafine-grain panchromatic (isochromatic) emulsion (grain size of ~10 nm) intended for full-colour reflection holograms and HOEs. Holograms recorded with the SilverCross emulsion exhibit very little blue light scattering; extremely realistic looking bright three-dimensional colour holographic images have been recorded with the emulsion. The project was successful in demonstrating the feasibility of the materials' technology and the intention was to start manufacturing this type of emulsion coated on glass plates and eventually also on film if there was a market for such colour holograms. However, substantial funding was required for setting up a factory for such plate/film manufacturing and to date this has not been accomplished. Because there are currently so few colour hologram-recording facilities around the world, it is of course difficult to justify an investment in large-scale manufacturing of ultrafine-grain emulsions.

To understand the principles of making an ultrafine-grain silver halide emulsion suitable for colour holography in a small-scale operation, a short summary of the SilverCross project is provided here. The research project was carried out by the following European partners:

- The Centre for Modern Optics, NEWI, (now Glyndŵr University), UK
- THIS Ltd., UK
- CLOSPi-BAS, Bulgaria
- Université de Liège, Belgium
- Cristo Stojanoff, Germany
- Vivid Components Ltd., UK
- Geola UAB, Lithuania

TABLE 4.4

The SilverCross Emulsion

Making Step	Chemical	Mixing Method
Basic chemicals	A: Gelatin solution B: AgNO ₃ solution B1: Gelatin solution C: KBr and KI solution C1: Gelatin solution	440 mL of 0.57% at 35°C 30 mL of 0.29 M at 19°C 0 15 mL of 0.59 M KBr [†] 15 mL of 0.029 M KI at 19°C 0
Precipitation		Jet B and C into A with stirring in <1 min
Preparation for freezing		Pour the precipitant into cells for freezing
Freezing		12–16 h at –20°C
Thawing		6–7 h at 20°C–24°C
Second freeze for storage		>12 h at –20°C
Coating preparation		Melt to 38°C
Dye addition		1.5 mL of 0.0026 M pinacyanol chloride, 1.5 mL of 0.0023 M quinaldine red
Coating		Apply 630 mL of emulsion/m ²
Drying		>12 h at 20°C–24°C
Packing		Place plates in light tight storage boxes and store between 0°C and 24°C
Sensitisation		Hypersensitise immediately before use, 1 min in 0.025 mL ascorbic acid sodium salt at 18°C ±1°C

Note: Recommended dyes: green, 2-(4-dimethylaminostyryl)-1-ethylquinolinium iodide (quinaldine red); red, 1,1'-diethyl-2',2'-carbocyanine chloride (pinacyanol chloride).

The task was to devise a new nanoparticle, panchromatic, silver halide/gelatin emulsion suitable for making full-colour holographic recordings using primarily CW laser exposure. It was possible to make an emulsion with particles close to the target size of 5 to 10 nm. The SilverCross emulsions all have grain sizes of between 8 and 15 nm. The hypersensitised emulsion is very close to the target sensitivity of less than 2 mJ/cm². The emulsion (frozen) and the coated plates (refrigerated) have good conservation characteristics as well as coping with easy storage conditions. Thus far, only plates of dimensions up to 30 cm × 40 cm have been manufactured.

The SilverCross emulsion is an ultrafine-grain emulsion utilising the important technique of freeze-drying by Kirillov et al. [29]. One of the many difficulties to solve in producing an ultrafine-grain emulsion is crystal grain growth restriction, which Kirillov was able to achieve for recording reflection holograms. In essence, Kirillov's technique is the removal of the precipitation by-products by freezing and thawing the emulsion. The technique Kirillov used involved a number of freeze/thaw cycles plus showering of the emulsion with very cold water as well as additions of gelatin and other chemicals.

There are three main stages that take place during the fabrication of the SilverCross emulsion:

- The precipitation stage
- The washing stage
- The coating stage

Table 4.4 summarises the recommended manufacturing process.

4.8.1 Precipitation Stage

Four main ingredients are used for the holographic emulsion: silver nitrate (AgNO₃), potassium bromide (KBr), potassium iodide (KI) and photographic gelatin. The mixing of the chemicals is achieved by the method of “double jet precipitation” (Figure 4.8).



FIGURE 4.8 Production of the SilverCross silver halide emulsion in the laboratory. Double-jet mixing of the silver nitrate and potassium bromide solutions with the gelatin solution in the beaker. (a) Emulsion mixing equipment. (b) Simultaneous addition of the two solutions. (c) Solutions mixed at different levels in the beaker.

4.8.2 Washing Stage

The mixed silver halide gelatin solution is then placed in a container, where it is kept at a temperature of -25°C for 30 min. The next step involves cutting the emulsion into cubes and detaching it from the container. The container with the frozen, cut emulsion is then kept at the low temperature of -25°C for 24 h, after which it is placed in deionised water at a temperature of 8°C for washing. The washing stage involves three cycles of 5 min each with agitation (Figures 4.9 and 4.10).

The emulsion is turned into liquid form by placing it in warm water and by continuous stirring. A small amount of methanol is added to assist the melting. Once the emulsion is fully dissolved, spectral sensitisation and hardening takes place. The dyes and the hardener are added to the emulsion, one by one, with continuous stirring (400 rpm).

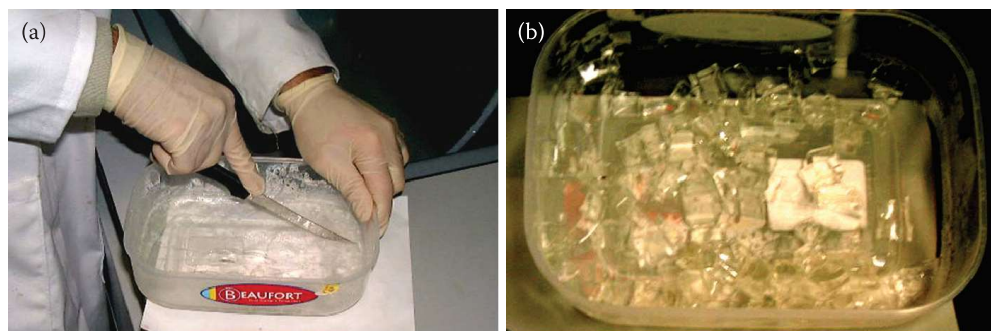


FIGURE 4.9 Frozen emulsion is cut into small cubes. (a) Cutting the frozen emulsion. (b) Frozen emulsion cubes.



FIGURE 4.10 Frozen emulsion treated in 8°C deionised water. (a) Frozen emulsion and beaker with water. (b) Breaking up the frozen emulsion cubes.

4.8.3 Coating Stage

For making 10 cm × 12 cm test plates, manual coating can be performed. The coating is achieved using glass syringes. Eight millilitres of the emulsion is required for each test plate (Figure 4.11–4.13). The larger SilverCross plates were coated by Stojanoff at Holotech in Germany using a special high-quality glass plate coating apparatus.

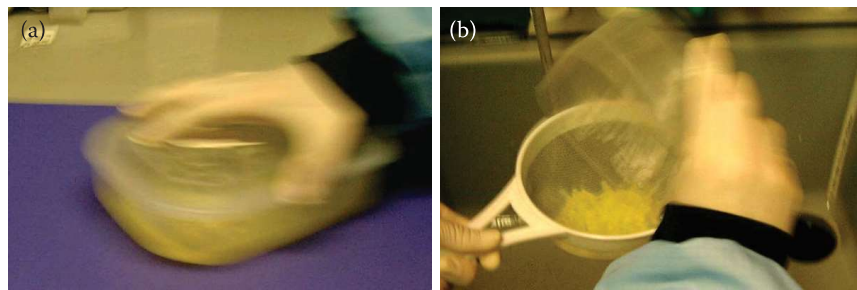


FIGURE 4.11 (a) Washing of the emulsion. (b) The by-products are removed using a sieve.

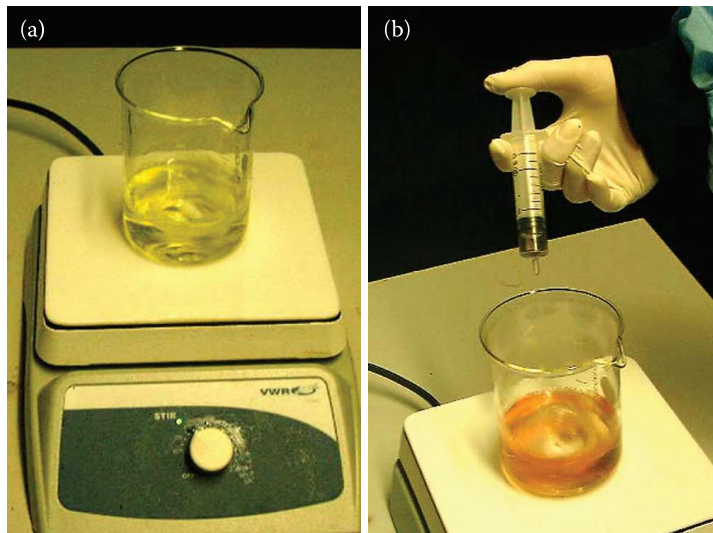


FIGURE 4.12 Hardener and sensitising dyes are added to the melted emulsion. (a) Beaker with the emulsion. (b) Dyes are added using a syringe.

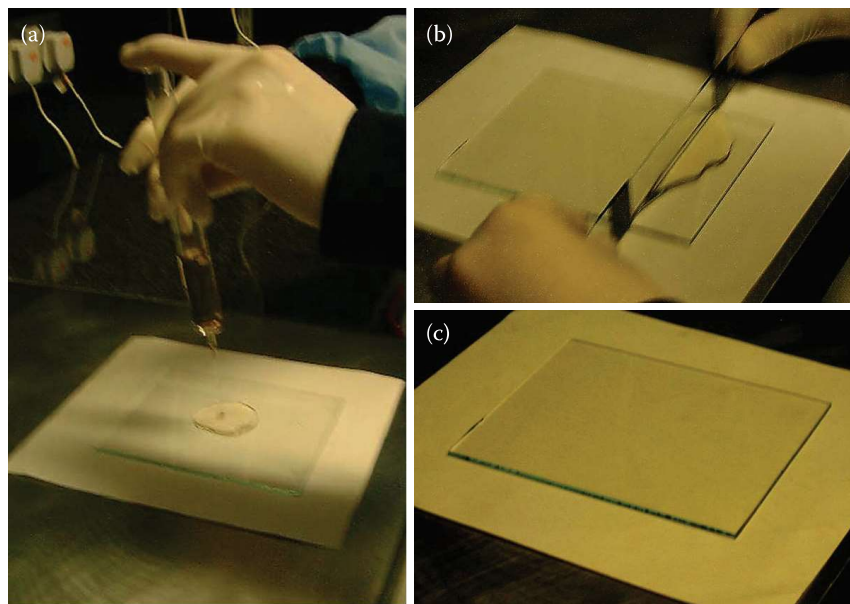


FIGURE 4.13 Manual coating of test plates. (a) Pouring emulsion on the glassplate. (b) Spreading the emulsion. (c) Coated plate.

4.9 Additional Silver Halide Materials for Holography

There are several other companies manufacturing silver halide materials for holography. These companies [30–32] have materials for applications other than colour holography—for example, products for recording transmission holograms and reflection holograms of the monochrome type. Microchrome [32] in California makes silver halide plates for the lithographic industry (similar to Agfa's former Millimask plates). These plates are used to image photomasks and patterns for microelectronics and holography use. The AGHD High Definition Plate is a blue–green sensitive emulsion coated on precision flat soda-lime glass. With an emulsion thickness of approximately 1.5 to 2 µm, it will resolve 2000 line pairs/mm. The other silver halide emulsion is the K1A Plate, which is on standard soda-lime glass that is extremely flat. The K180B high-resolution plate is an extremely high-contrast silver halide high-resolution plate that is used to image photomasks, patterns for microelectronics, holography and many other uses. This emulsion is coated on soda-lime glass that is extremely flat. It provides a more delineated “hard edge” and minimal background fog with good clear area density. These plates are primarily used to record transmission holograms from holographic companies making masters for embossed holograms. A high-resolution (2000 line pairs/mm) blue/green-sensitive film is also manufactured by the company.

Harman Technologies [31] manufactures the HOLO FX fine-grain holographic plates, which are coated with a fine grain holographic emulsion and are available in both red- and green-sensitive versions. With crystal sizes typically 30 to 40 nm, these plates are mainly intended for monochrome red and green holograms. The HOLO FX red-sensitive plates are sensitive from 600 to 694 nm, with a peak sensitivity at 660 nm. The HOLO FX green-sensitive plates are sensitive from 488 to 560 nm with a peak sensitivity at 532 nm.

ORWO FilmoTec GmbH [30] is a German company manufacturing ORWO holographic materials. The ORWO Holographic Film HF 53 is a silver halide recording material with highest resolution and low speed for holographic applications. It is green sensitised. The other green sensitive material is the HF 55 film, which is a material with lower resolution but higher speed for holographic applications. The holographic film HF 65 is a red-sensitised material. The ORWO film substrate is a clear triacetate of a thickness of 135 or 190 µm. The emulsion thickness is 6 µm.

Although the materials from these additional manufacturers are not suitable for full-colour reflection holograms, they can be used very successfully for either multicolour Benton-type transmission holograms or monochromatic laser transmission holograms.

4.10 DCG Materials

DCG is an excellent recording material for volume phase holograms and HOEs [33]. This grainless material has its highest sensitivity in the UV region but also extends into the blue and green parts of the spectrum. Recently, a panchromatic DCG material having useful sensitivity in the red, green and blue regions was reported. DCG is, however, still most often exposed with blue laser wavelengths. Depending on the processing parameters, diffraction efficiency and bandwidth can be controlled. It is easy to obtain high diffraction efficiency combined with a large signal-to-noise ratio. During the exposure of a DCG emulsion to UV or blue light, the hexavalent chromium ion (Cr^{6+}) is photoinduced to a trivalent chromium ion (Cr^{3+}), which causes cross-linking between neighbouring gelatin molecules. The areas exposed to light are hardened and become less soluble than the unexposed areas. Developing consists of a water wash, which removes the residual or unreacted chemical compounds. Dehydration of the swollen gelatin follows after the material has been immersed in isopropanol, which causes rapid shrinkage resulting in voids and cracks in the emulsion, thus creating a large refractive index modulation. The underlying mechanism is not completely understood because high modulation can also be caused by the binding of isopropanol molecules to chromium atoms at the cross-linked sites. Typical DCG material has a rather low sensitivity in the range of 100 mJ/cm².

There are very few commercial DCG recording materials on the market. Therefore, laboratories working on recording holograms and HOEs in DCG materials must usually prepare and coat their own emulsions. HOE manufacturers almost always prefer to produce their own emulsions. It does, however, take some time to learn how to make high-quality DCG plates.

4.10.1 Preparing Gelatin Plates

Often, it is convenient to use existing silver halide plates or film that can be easily fixed to remove the silver halide crystals. The diffraction efficiency of the final DCG hologram will depend on the initial hardness of the AgX plate used. The hardness can be decreased by soaking the plate in warm water, although too small a final hardness will lead to loss of the gelatin layer. The following steps should be employed (under standard lighting conditions):

- Soak in Kodak Rapid Fixer without hardener for 10 min at 20°C
- Soak in warm water at 40°C for 5 min
- Wash in running water at 20°C
- Soak in Kodak Rapid Fixer with 3.25% hardener for 10 min at 20°C
- Wash in running water at 20°C
- Dip in a bath with distilled water and photoflow at 20°C
- Drying

4.10.2 Sensitising the DCG Emulsion

The gelatin layer can be sensitised under dim red light conditions using the following steps. Note that some authors recommend omitting the drying step listed previously and proceeding directly to sensitisation:

- Soak the plate in a solution of ammonium dichromate (usually 5 g of ammonium dichromate in 100 mL of distilled water with some drops of wetting agent added) for 5 min
- Dry the plates on a hot plate or in an oven at 70°C
- Let the plates cool to room temperature for 1 h

Although the use of an AgX plate is the simplest technique, it is also possible to coat a 10- μm -thick emulsion directly onto an 8 in. \times 10 in. glass plate using 1 g of ammonium dichromate mixed with 3 g of photographic grade gelatin dissolved in 25 mL of distilled water. The emulsion must be spin-coated onto the glass substrate or applied by the doctor blade-coating technique. Note that the sensitising solution and the sensitised emulsion should only be handled in red safelight illumination. The concentration of ammonium dichromate controls the exposure time.

4.10.3 Exposure

The required CW exposure can range from approximately 50 to 1000 mJ/cm² at 514.6 nm depending on the sensitisation (ammonium concentration and drying method) and the gelatin hardening.

4.10.4 Pulsed Laser Exposure of DCG

There are very few publications about DCG holograms made using pulsed lasers. The possibility of using a pulsed laser has been reported by Krylov et al. [34] and Blyth et al. [35]. However, this technique is not really recommended. Blyth succeeded in recording a weak holographic image using a 6 ns pulse emitted from a 532 nm Nd:YAG laser, requiring 12 mJ/cm². To obtain an acceptable image, 10 such pulses emitted over 1 s were needed. By turning off the Q-switch (using free-lasing operation), better holograms were produced. However, it would seem logical that to get sufficient cross-linking, a train of nanosecond pulses would be needed over a few microseconds. Nevertheless, this technique should not be completely discounted for applications in digital holography, where hogels of only fractions of a square millimetre are written using pulsed lasers. We shall take up this discussion again in Chapter 7, when we talk about the basic constraints placed on the pulse length in a digital pulsed-laser holographic printer. It is also worth mentioning that the SHSG processing method for silver halide holograms, which will be discussed in detail in Chapter 5, provides a method for recording pulsed laser holograms in a panchromatic silver halide material and then converting this material into a material with the same properties as DCG.

4.10.5 DCG Processing

Table 4.5 lists the recommended DCG processing. Depending on the required hologram/HOE characteristics, one has to carefully control the propanol/water mixtures as well as the temperature of the different baths. Cold baths produce better uniformity and lower noise. Warm baths can yield high index modulation but often with increased noise. The bandwidth can be controlled by the processing temperature and the ratio of propanol/water mixtures. The drying of the plates is critical. The relative humidity in the laboratory has to be low (<40%). Moisture will degrade DCG holograms that are hydroscopic. It is therefore necessary to cover the final hologram emulsion with a glass plate, which is cemented using an optical adhesive. Before sealing the plates, it is recommended to bake the plates for 2 h in a vacuum oven at 100°C temperature. To be able to record colour holograms in a DCG emulsion,

TABLE 4.5

DCG Processing

-
1. Wash in a 0.5% ammonium dichromate solution—5 min at 20°C
 2. Wash in a Rapid Fixer solution—5 min at 20°C
 3. Wash in running water
 4. Wash under agitation in a 50:50 solution of isopropyl alcohol and water—3 min at 20°C
 5. Wash under agitation in a 100% isopropyl alcohol bath—3 min at 20°C
 6. Optional: dip plate in boiling 100% isopropyl alcohol bath
 7. Drying
-

the spectral sensitivity of the material that is usually only sensitive in the UV and blue/green part of the spectrum must be modified by a dye. To obtain red sensitivity, it is common to use a methylene blue (MB) dye [36–42].

4.10.6 Panchromatic DCG Emulsions

The DCG material can be used for recording colour reflection holograms. It is possible to record high-quality bright-colour holograms using DCG. Kubota and Ose [43] recorded colour holograms in a glass plate using a fixed Kodak 649F plate, which was red-sensitised using the MB dye. Normally, the DCG emulsion swells during processing, something which should be avoided when recording colour holograms. The swelling causes a colour shift of the reconstructed image towards longer wavelengths for reflection holograms—for example, reconstructing at wavelengths of 520 to 530 nm when the hologram was recorded at the 488 nm wavelength. The swelling must be corrected without permitting the deterioration of the reconstructed image. One method of reducing the thickness is to bake the hologram at temperatures of approximately 150°C. Another possible method is to swell the gelatin layer before exposure with a suitable liquid, such as TEA, glycerin or ethylene glycol. Kubota and Ose used ethylene glycol, which was added into the sensitising solution. In addition, they baked the hologram at 150°C after processing. The thickness was reduced gradually by this method without affecting the diffraction efficiency. The recording wavelengths they used were 458, 514.5 and 633 nm. Their technique to obtain high-quality colour DCG holograms is listed in Table 4.6.

Later, Kubota [44] used a DCG plate to make a sandwich hologram in which the green and blue images were recorded in the DCG plate, and the red image in a silver halide plate (Agfa 8E75 HD). Because the red sensitivity of the DCG is rather low and the author wanted to record a large (8 in. × 10 in.) Denisuk colour hologram using a 50 mW HeNe laser, he decided to make a sandwich. Employing the sandwich

TABLE 4.6

Production and Processing of MB-Sensitised DCG Plates

A. Preparation of the Sensitised Gelatin Plate from a Kodak 649F Plate

1. 15-min fix in Kodak Rapid Fixer with hardener
2. 15-min wash in running water (25°C)
3. 5 min in methyl alcohol
4. 5 min in clean methyl alcohol
5. 10-min soak in sensitising solution $[(\text{NH}_4)_2\text{-Cr}_2\text{O}_7; 3\%; \text{MB: } 6 \times 10^{-4} \text{ mol/L; ethylene glycol: } 3\%]$
6. Dry for more than 4 h in a desiccator with 28% aqueous ammonia solution and silica gel

B. Exposure

C. Heating

1. 24 h at room temperature, then 3 h at 60°C

D. Development

1. 30-s soak in mixture of one part Kodak fixer, two parts distilled water
2. 15-min wash in running water (25°C)
3. 3-min soak in hot water (47°C)
4. 3-min soak in mixture of 70% isopropyl alcohol and 30% distilled water (47°C)
5. 3-min soak in 100% isopropyl alcohol
6. 3-min dry in hot-air flow

E. Baking

1. Bake at 150°C until the colour shift is corrected

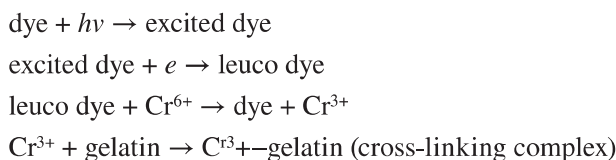
Source: From Kubota, T., and T. Ose. Lippmann color holograms recorded in methylene-blue-sensitised dichromated gelatine. *Opt. Lett.* 4, 289–291, 1979. With permission.

technique, one avoids the scattering problem* caused by sending blue laser light through a silver halide emulsion during recording. Since Kuboto's publication, there have been only a few articles on recording colour holograms in panchromatic DCG emulsions. However, these few articles clearly demonstrate that DCG must be regarded as an extremely useful material for full-colour holography.

Zhu et al. [45,46] recorded high-quality bright-colour holograms in a single-layer panchromatic DCG material, by using new types of multicolour photosensitisers and photochemical promoters for gelatin cross-linking. Using a red, green and blue laser, full-colour reflection holograms were successfully recorded at exposure levels of approximately 30 mJ/cm^2 . An even lower exposure level of 15 mJ/cm^2 was observed in the case of a monochromatic grating of 80% diffractive efficiency recorded at 514.6 nm. The water-soluble dye rhodamine 6G (R6G) was used to achieve the green-blue photosensitivity. This dye has good compatibility with the red sensitiser MB and other chemical reagents in the photosensitive DCG layer. The laser wavelengths used for the colour hologram recording were

- 633 nm (He–Ne laser) or 647 nm (Kr–Ion laser)
- 514.5 (Ar–Ion laser) or 532 nm (CW Nd:YAG laser)
- 488 nm (Ar–Ion laser) or 442 nm (He–Cd laser).

The chemical reagent, potassium chromate, was used in the photosensitive layer as the cross-linking reagent. Under laser radiation (i.e., red laser for MB, green and blue lasers for R6G), the photochemical reactions of MB and R6G molecules are both photobleaching reactions. The photochemical reactions of the panchromatic gelatin material can be proposed as follows:



When the dye (e.g., MB) is irradiated with a specific monochromatic laser line, its molecule absorbs a photon and passes to the excited state, whereupon the dye is reduced to its leuco (colourless) form by absorbing an electron from the surrounding medium. The leuco dye acts as an active reducing agent; it reacts with Cr^{6+} in the potassium chromate, and then Cr^{6+} is reduced to Cr^{3+} , whereas the dye then returns to its unexcited state. Cr^{3+} reacts with adjacent gelatin molecules to form a cross-linking complex and increases the refractive index of the exposed gelatin. Finally, a volume phase hologram based on the modulation of the refractive index is produced after the common DCG postprocessing procedures. To accelerate the photochemical reaction, a chemical reagent, 1,1,3,3-tetramethylguanidine (TMG), proposed by Blyth [47] is used in the photosensitive layer as a photochemical promoter. TMG has four methyl groups, which can donate additional electrons and the resonating structure of guanidine allows easier electron donation than other types of electron donors. The introduction of TMG as a strong electron donor can efficiently improve the photoreduction speed of the chromium ion and the sensitivity of the photosensitive system. Table 4.7 describes the production and postprocessing of the panchromatic DCG material.

Zhu et al. recorded both reflection gratings and full-colour Lippmann holograms in the new DCG material. The depth of the DCG layer was measured to be approximately $18\text{ }\mu\text{m}$; they cite required exposures as 60 mJ/cm^2 at 633 nm, 30 mJ/cm^2 at 514.5 nm and 40 mJ/cm^2 at 442 nm. The reflection gratings clearly showed that the central playback wavelength was very close to the original recording laser wavelength, demonstrating that this new material can indeed replay the natural colours of an object. A $7\text{ cm} \times 7\text{ cm}$ colour reflection hologram of a ceramic mask was recorded with the following wavelengths: 633, 514.5 and 488 nm; the exposures were performed sequentially, starting from the red component, followed by

* The grains in a standard red or green photographic emulsion will produce strong Rayleigh scattering when illuminated by blue light simply because the wavelength dependence of Rayleigh scattering scales as λ^{-4} .

TABLE 4.7

Preparation and Processing of Panchromatic Gelatin DCG Plates

A. Preparation of the Plates

1. Soak 2 g of French inert gelatin in 40 mL of deionised water at 25°C for 12 h
2. Heat the suspension in a thermostatic water bath to approximately 45°C, then maintain the temperature and stir the mixed solution slowly for 15 min
3. Add 2.5 mL of 0.5% potassium chromate solution at 45°C while stirring for 2 min
4. Add 0.6 mL of 25% TMG solution at 45°C while stirring for 2 min
5. Adjust the pH value to 9.18 with TMG or acetic acid solution (45°C, 2 min)
6. Add 0.3 mL of 0.4% MB solution to the suspension while stirring (45°C, 5 min)
7. Add 0.3 mL of 0.2% R6G solution to the suspension while stirring (45°C, 5 min)
8. Pipette out 8 mL of the mixed solution and spread it over an 8 × 24 cm² optical glass, keeping the coated plate horizontal in a dry location and in the dark

B. Postprocessing Procedure

1. Soak in Kodak F-5 Hardening Fixer solution at 25°C for 1 min
2. Wash holographic plate in running water at 25°C for 30 s
3. Swell holographic plate in warm water at 31°C for 1.5 min
4. Dehydrate in 60% isopropyl alcohol bath at 25°C for 1 min
5. Dehydrate in 90% isopropyl alcohol bath at 25°C for 1 min
6. Dehydrate in 100% isopropyl alcohol bath at 25°C for 2 min
7. Dry hologram rapidly with flowing hot air

Source: From Zhu, J. et al. True-color reflection holograms recorded in a single-layer panchromatic dichromated gelatin material. In *Holography, in Diffractive Optics, and Applications II*, edited by Sheng, Y., D. Hsu, C. Yu, and B. Lee. *Proceedings of SPIE* 5636, 245–253, 2005. With permission.

the green and blue components. The white-light replay of the DCG colour hologram demonstrated high colour saturation, low noise and high diffraction efficiency.

Artemjev et al. [48] have reported on how to record colour holograms using the Slavich PFG-04 DCG emulsion. In 1998, Wang et al. [49] explained how to avoid the problem of swelling of the DCG emulsion after processing colour holograms recorded in DCG emulsions. This problem has also been investigated by Kubota [50], who recommended that the reconstruction wavelength can be shifted to shorter wavelengths and controlled freely to a certain extent by using two different kinds of gelatin. No treatment is needed after the hologram is finished. More recently, Jiang et al. [51] have found a method for the wide-range quantitative adjustment of the playback wavelength of colour reflection holograms recorded in DCG. The main feature of this technique is to introduce a water-soluble organic reagent acrylamide into the DCG layer as a preswelling agent. Acrylamide will not react with the other chemical agents in the DCG emulsion. It will completely dissolve during the processing of the exposed DCG emulsion and result in a uniform emulsion shrinkage throughout the thickness of the emulsion. The shrinkage means that the image is reconstructed at shorter wavelengths after the dehydration process in isopropyl alcohol. By changing the concentration of preswelling, the final playback wavelength can be adjusted widely and quantitatively from red to green, and to blue, almost covering all the visible spectral range. A quantitative investigation to derive the relationship between the wavelength shift and the concentration of acrylamide added to the emulsion was presented. Because the problem of emulsion shrinkage after processing can make it difficult to record colour holograms in DCG materials, this new method was used to record high-quality colour holograms. By introducing new types of multicolour photosensitisers and photochemical promoters to conventional photo-cross-linking DCG systems, a single-layer panchromatic DCG material was fabricated in the laboratory. Its holographic recording characteristics, such as spectral response, photosensitivity to three primary colours and the angular and spectral selectivity of recorded volume holograms, were studied in detail. With this material, it was possible to obtain high diffraction efficiency (up to 85%) as well as high photosensitivity (as low as 20 mJ/cm²) for three primary colour laser wavelengths. Colour reflection holograms with high colour saturation and brightness were recorded at the exposure level of 30 mJ/cm² using RGB lasers.

4.10.7 Commercial DCG Materials

At the time of writing, there were no manufacturers of panchromatic DCG materials. Below are listed several companies which supply blue/green-sensitive DCG.

Slavich [20] in Russia is one manufacturer of presensitised dichromated plates for holography. The DCG emulsion is marked PFG-04. Plates up to a size of 30 by 40 cm can be ordered. These plates must be red-sensitised before recording colour holograms.

ORWO FilmoTec GmbH [30] in Germany produces the ORWO Holographic Film GF 40DCG emulsion, which is only available on 125- μm triacetate film, 104 cm wide, in 10- and 30-m lengths. Emulsion thickness of 6 or 20 μm . Film sheets measuring 50 cm \times 60 cm can also be ordered. Note that the film needs to be sensitised in dichromate solution as well as being red-sensitised before recording colour holograms. In fact, the GF 40DCG emulsion is actually a gelatin-coated film.

Holotec GmbH [52] is a German-based company that offers custom-made presensitised DCG emulsions coated on both plates and film. The Holotec emulsion is based on the high-quality DCG materials developed by Stojanoff in Aachen. The company can supply large-format DCG glass plates (square metre size) or film (PET), presensitised—but not red sensitised.

4.11 Photopolymer Materials

Photopolymer materials have become popular for recording phase holograms and HOEs [53–61]. This is particularly true for the mass production of holograms because some photopolymer materials do not require any postexposure processing or, at worse, they only require dry processing techniques. Companies like Bell Laboratories, DuPont, Polaroid and Hughes produced photopolymer materials for recording holograms at a very early stage. A review of photopolymer materials was published by Lessard [62]. A SPIE Milestone publication was also produced by Bjelkhagen [63] covering a selection of articles on holographic recording materials for holography including photopolymers and DCG.

The main advantages of photopolymer materials for recording holograms are:

- Fast dry processing method
- High diffraction efficiency
- Relatively low material cost
- High stability of the recorded hologram

Its disadvantages are a rather low sensitivity and the short shelf life of the prepared material. Since the time Hughes started to make photopolymer materials, there have been a lot of different materials experimented with at various universities and research centres. In particular, there are several types of photopolymer systems that have been developed:

- Acrylamide-based systems
- Acrylate-based systems
- Polymethyl methacrylate systems
- Polyvinyl alcohol and poly-acrylic acid systems
- Polyvinyl carbazole systems

To increase the sensitivity, it is important to decrease the inhibition period of the system. The cause of the inhibition period, which results in a loss of sensitivity in the photopolymers, is the presence of oxygen in the sample. There are different ways of reducing the inhibition period by, for example, pre-exposure and including a second sensitising agent in the polymer material. Special self-developing materials exist

which are intended for real-time hologram interferometry. Polaroid and DuPont are the main companies that have developed practical photopolymers for holographic applications. The Polaroid DMP-128 material was developed in the mid-1980s and, for many years, this material provided an excellent recording solution for HOEs and display holograms [64–66]. However, in 1998, Polaroid stopped producing holographic materials.

A photopolymer recording material, such as the DuPont material [67–69] consists of three parts:

- A photopolymerisable monomer
- An initiator system (initiates polymerisation upon exposure to light)
- A polymer (the binder)

To record a hologram in a photopolymer material, one starts with the exposure to the information-carrying interference pattern. This exposure polymerises a part of the monomer. Monomer concentration gradients, formed by variation in the amount of polymerisation due to the variation in exposure, give rise to the diffusion of monomer molecules from regions of high concentration to regions of lower concentration. The material is then exposed to regular light of uniform intensity until the remaining monomer is polymerised. A difference in the refractive index within the material is thereby obtained. The DuPont material requires only a dry processing technique (exposure to UV light and a heat treatment) to obtain a hologram.

The recording of a hologram on polymer is rather simple. The film has to be laminated to a piece of clean glass or attached to a glass plate using an index-matching liquid. Holograms can be recorded manually, but to produce large quantities of holograms, it is preferable to use a special machine. For hologram replication, laser line scanning techniques can provide the highest production rate. The photopolymer material needs an exposure of approximately 10 to 20 mJ/cm².

After exposure is finished, the DuPont film has to be exposed to strong white or UV light. DuPont recommends approximately 100 mJ/cm² exposure at 350 to 380 nm. After that, the hologram is put in an oven at a temperature of 120°C for 2 h to increase the brightness of the image. The process is suitable for machine processing using, for example, a baking scroll oven.

4.11.1 Recording Photopolymer Holograms with Pulsed Lasers

During the recording of an interference pattern in a photopolymer layer, a relatively slow diffusion process takes place; this makes use of the CW lasers most suitable for recording polymer holograms. However, there is a strong interest in using pulsed lasers to record holograms in photopolymer materials because these lasers confer a complete immunity to environmental vibration and stability problems. The question is how this can be accomplished. Weitzel et al. [70] and Mikhailov et al. [71] reported the recording of reflection holograms in DuPont HRF-800X071-20 photopolymer films. A pulsed laser with a pulse length of 25 ns was used to record holograms of a mirror. It was shown that the expected weak reflectance of the mirror holograms could be significantly increased by preillumination. Although pulsed preillumination enhanced only the reflectance, continuous incoherent preillumination significantly increased both the diffraction efficiency (which reached 80%) and the sensitivity (which increased 100 times), thus approaching the sensitivity of CW recording. The incoherent preillumination was provided by a broadband green-filtered light source that peaked at 500 nm. The results are comparable with those of hologram recordings obtained with CW exposure under the same processing conditions. The main reason for this reported behaviour of holograms recorded on DuPont photopolymer films is related to the kinetics of film components during exposure.

To better understand the behaviour of the photopolymer material under pulsed exposure, the reader is referred to the experimental results on polymerisation kinetics reported by Hoyle et al. [72]. A high level of polymerisation was observed in this article, even under a single high-intensity laser pulse. The rate of polymerisation depended on the type of polymerisable monomer as well as on the type of photoinitiator. In these experiments, the weak polymerisation ability was also significantly improved by accurate pre-illumination (prepolymerisation).

More details of recording pulsed holograms in DuPont photopolymers were published by Mikhailov et al. [73]. The preillumination technique should also apply to the recording of colour holograms using pulsed RGB lasers. This means that it might well be possible to record digital colour holograms using printers equipped with pulsed RGB lasers.

4.11.2 Panchromatic Photopolymers

Panchromatic photopolymer materials are suitable for recording colour holograms. This material is of interest for both recording one-off colour holograms, but most often, it is a suitable material for producing multiple copies from colour master holograms. DuPont introduced their panchromatic material in 1995 [74,75]. The new holographic photopolymer film was capable of producing high diffraction efficiency in colour volume holograms and HOEs. The properties of this panchromatic film allowed for a greater range of applications than had previously been considered feasible for colour holograms.

Since photopolymer materials became available, there have been several reports on using them for recording colour holograms [76–80]. In the earlier articles, the sandwich technique was used by combining two photopolymer sheets to create the colour hologram. Zhang et al. [76] recorded reflection gratings with red (647 nm), green (514 nm) and blue (488 nm) laser wavelengths using a quasipanchromatic photopolymer material prepared by the authors. The curves of percentage transmission versus wavelength and reconstructed wavelength versus exposure for the gratings were given. Using subtractive filters, colour reflection holograms were recorded employing red, green and blue laser wavelengths with simultaneous exposure.

Hubel and Klug [77] recorded colour holographic stereograms using multiple layers of the DuPont OmniDex photopolymer. Red, green and blue colour separations were reproduced at optimum replay wavelengths by exposing in blue and postswelling using monomer colour-tuning films. A theoretical analysis of the colour-reproduction was provided and the technique was compared with results using other materials. The signal-to-noise ratio, colour rendering and colour gamut area properties were shown to be comparable with those found when using DCG materials.

Kawabata et al. [78] introduced a new type of photopolymer system for recording reflection colour holograms. The photopolymer system using radical and cationic photopolymerisation controlled by the wavelength of light gave enhanced diffraction efficiencies and a balanced recording sensitivity (approximately 20–60 mJ/cm²) in the blue to red region of the spectrum. In colour hologram recordings, diffraction efficiencies of approximately 60% were obtained when using a photopolymer film composed of different spectral-sensitive photopolymer layers.

In another article, Kawabata et al. [79] recorded colour reflection holograms on a specially prepared photopolymer material. Here, a suitable red–green sensitive dye and a blue–green sensitive dye were selected as the photosensitisers. Colour holograms recorded in a single-layered panchromatic photopolymer material containing these mixed dyes resulted in diffraction efficiencies of only 20% because of the multiple-exposure technique. The decrease in diffraction efficiency for the triple recording, as compared with a single wavelength recording, resulted from a change in the monomer form caused by the diffusion of monomers. To improve the recording properties, a photopolymer film that was composed of two parts was prepared: a red–green sensitive layer and a blue–green sensitive layer. A polyethylene film was positioned between the two polymer layers to prevent them from mixing. The dual recordings in each layer resulted in a colour reflection hologram with enhanced diffraction efficiency in comparison with that of the triple recording. In this case, they achieved a diffraction efficiency of 64% in red, 65% in green and 53% in blue. Here, the exposures of the red and green components were carried out simultaneously followed by the exposure of the blue component. It was found that simultaneous exposure gave an enhanced diffraction efficiency compared with separate exposures.

At the Dublin Institute of Technology, full-colour reflection holograms have been recorded by Meka et al. [80] using a new panchromatic acrylamide-based photopolymer layer. The recording laser wavelengths were 633, 532 and 473 nm. The reflection holograms, recorded using a combined single beam of RGB wavelengths, were spectrally characterised and compared with the recording wavelengths. An object having an additive colour diagram was recorded. The shrinkage effect of this new recording material on reconstructed wavelengths was also discussed.

4.11.3 Commercial Photopolymer Materials

Currently, the main manufacturer of holographic photopolymer materials is E.I. DuPont de Nemours & Co. DuPont manufactures the Omnidex 706 monochromatic film (blue/green sensitive) which is a polymer that only needs dry processing (as described in the previous section). The material has a coated compound polymer layer thickness of 20 µm. The photopolymer film is generally coated in a 12.5 in. width on a 14 in. wide Mylar polyester base which is 50.8 µm thick.

The panchromatic material, however, is not a fully commercial product. DuPont has restricted the distribution of this material due to concerns from its security customers; it is not on the general market—and with the exception of their in-house hologram production and a few selected customers, the material is not commercially available. Zebra Imaging Inc. in the United States records its holograms on the DuPont colour material. In Japan, Dai Nippon also uses the DuPont material. Dai Nippon has a domestic photopolymer product that it uses for its own security applications.

Bayer MaterialScience AG in Leverkusen, Germany [81] has developed a new panchromatic photopolymer material that was recently introduced to the market under the name Bayfol HX [82–84], although sales are restricted. The material has many advantages, such as long lifetime, stability, almost no shrinkage and no postprocessing (thermal or wet). It comes in rolls of up to 1.2 m wide. Besides creating fascinating optical effects, this material can also be used to make ID cards and other documents that are forgery-proof. The current holographic performance of the material is as follows:

- Refractive index modulation (δn), 0.03 in reflection holograms*
- Diffraction efficiency, 98%
- Colour sensitivity, 450 to 650 nm
- Suitable for both reflection and transmission holograms
- Sensitivity for reflection holograms, 100 µW/cm² to 50 mW/cm²
- Photopolymer thickness, 10 to 25 µm
- Substrates PET or PC in roll format
- Environmentally stable (UV, heat and humidity)

Because the Bayer photopolymer film requires no subsequent chemical or thermal treatment, it is exceptionally suitable for cost-effective mass production of volume holograms. The Bayer photopolymer has real potential to become a leading material for light management within a variety of new technologies—for example, in improved three-dimensional digital and analogue holographic displays or for diffusers required in energy-efficient lighting technologies such as light-emitting diodes. However, like DuPont, Bayer has decided, at least for the moment, to restrict sales of its holographic materials to protect the value chain to the security industry.

Polygrama [85] in Brazil is another manufacturer of holographic photopolymer materials. Polygrama DAROL photopolymer is a dry film for holography, which is provided with adequate resolution, high contrast and low scatter. It is designed for use with blue-green lasers (488–535 nm) and red lasers (610–660 nm). It records a reflection hologram that must be thermally developed in a single process to deliver a hologram with high diffraction efficiency. It is totally moisture-resistant and stable. DAROL films are available as 20 cm × 10 cm sheets with a 30- to 40-µm-thick photopolymer onto optically clear polyester with laminated thin PET or HDPE cover. Colour sensitivity: 488 to 532 nm, 635 to 670 nm with a sensitivity of 5 to 30 mJ/cm², $\delta n \leq 0.100$ on thermally developed reflection holograms. Lynx in Brazil is distributing the DAROL film [86].

Finally, it should be mentioned that, for 10 years, the Dai Nippon Printing Co., Ltd. has produced TRUE IMAGE colour reflection holograms and security labels [87,88]. Initially, these images were recorded on DuPont's panchromatic photopolymer material. More recently, Dai Nippon Printing, in conjunction with Nippon Paint Co., Ltd., has developed a new photopolymer material that is now used for manufacturing mass-produced volume reflection holograms. Nippon Paint is responsible for materials development, whereas Dai Nippon Printing is responsible for the development of the production technology.

* At the time of writing, the best results obtained by Bayer had increased δn in their experimental materials to 0.06.

REFERENCES

1. H. I. Bjelkhagen, *Silver Halide Recording Materials for Holography and Their Processing*, Springer Series in Optical Sciences, Vol. **66**, Springer-Verlag, Heidelberg, New York (1993).
2. D. Gabor, "A new microscopic principle," *Nature* **161** (No. 4098) 777–778 (1948).
3. C. E. K. Mees, *The Theory of The Photographic Process*, 2nd Edn. Macmillan, New York (1959).
4. C. B. Neblette, *Photography, its Materials and Processes*, 6th Edn. Van Nostrand, New York (1962).
5. M. Sturge (ed.), *Neblette's Handbook of Photography and Reprography*, 7th Edn. Van Nostrand Reinhold, New York (1977).
6. T. H. James (ed.), *The Theory of The Photographic Process*, 4th Edn. Macmillan, New York (1977).
7. R. Bunsen and H. Roscoe, "Photochemische Untersuchungen," *Ann. der Physik Chemie* **117**, 529–562 (1862).
8. N. D. Vorzobova and D.I. Staselko, "Exposure characteristics of high-resolution silver-halide photographic materials for recording three-dimensional holograms by means of a pulsed laser," *Sov. J. Opt. Technol.* **44**, 249–250 (1977).
9. N. D. Vorzobova and D. I. Staselko, "Diffraction efficiency of 3-D holograms recorded with short exposures," *Opt. Spectrosc. (USSR)* **45**, 90–93 (1978).
10. A. A. Benken and D. I. Staselko, "Light scattering in the formation of a latent image by pulsed laser radiation," *Sov. Phys. Tech. Phys.* **27**, 896–898 (1982).
11. M. Pantcheva, T. Petrova, N. Pangelova and A. Katsev, "Chemical sensitization of fine-grain silver halide emulsions for holographic recording," in *Holography'89. International Conference on Holography, Optical Recording and Processing of Information*, Y. N. Denisyuk and T. H. Jeong eds. Proc. SPIE **1183**, 128–130 (1990).
12. A. Hautot, "Reciprocity characteristics of silver bromide and silver chloride emulsions," *Photogr. Sci. Eng.* **4**, 254–256 (1960).
13. K. M. Johnson, L. Hesselink and J. W. Goodman, "Holographic reciprocity law failure," *Appl. Opt.* **23**, 218–227 (1984).
14. K. Biedermann, "Attempts to increase the holographic exposure index of photographic materials," *Appl. Opt.* **10**, 584–595 (1971).
15. H. I. Bjelkhagen, "Holographic recording materials and the possibility to increase their sensitivity," CERN, Geneva, Switzerland, EF-report 84-7 (1984).
16. N. I. Kirillov, [Transl.: *High Resolution Photographic Materials for Holography and Their Processing Methods* [in Russian]] NAUKA, Moscow (1979).
17. Yu. N. Denisyuk and I. R. Protas, "Improved Lippmann photographic plates for recording stationary light waves," *Opt. Spectrosc. (USSR)* **14**, 381–383 (1963).
18. T. H. James, "Electron injection by developing agents - Latensification of internal image," *Photogr. Sci. Eng.* **10**, 344–349 (1966).
19. P. Binfield, R. Galloway and J. Watson, "Reciprocity failure in continuous wave holography," *Appl. Opt.* **32**, 4337–4343 (1993).
20. SLAVICH Joint Stock Company, Russia; www.slavich.com (Sept. 2012).
21. Sfera-S Ltd, Russia; www.geola.com (Sept. 2012).
22. Geola, Lithuania; www.geola.com (Sept. 2012).
23. Colourholographic Ltd, UK; www.colourholographic.com
24. M. Ulibarrena, L. Caretero, R. Madrigal, S. Blaya, and A. Fimia, "Multiple band holographic reflection gratings recorded in new ultra-fine emulsion BBVPan," *Opt. Expr.* **11**, 3385–3392 (2003).
25. M. Ulibarrena, "A new panchromatic silver halide emulsion for recording color holograms," *Holographer.org*, 1–12 (Jan. 2004). www.holographer.org (Sept. 2012).
26. Y. Gentet and P. Gentet, "Ultimate emulsion and its applications: a laboratory-made silver halide emulsion of optimised quality for monochromatic pulsed and full color holography," in *HOLOGRAPHY 2000*, T. H. Jeong, and W. K. Sobotka eds., Proc. SPIE **4149**, 56–62 (2000).
27. The Ultimate Holography, France; www.ultimate-holography.com (Sept. 2012).
28. H. I. Bjelkhagen, P. G. Crosby, D. P. M. Green, E. Mirlis and N. J. Phillips, "Fabrication of ultra-fine-grain silver halide recording material for color holography," in *Practical Holography XXII: Materials and Applications*, H. I. Bjelkhagen and R. K. Kostuk eds., Proc. SPIE **6912**, 09-1–14 (2008).

29. N. V. Kirillov, N. V. Vasilieva and V. L. Zielikman, "Preparation of concentrated photographic emulsions by means of their successive freezing and thawing" [in Russian], *Zh. Nauchn. Prikl. Fotogr. Kinematogr.* **15**, 441–443 (1970).
30. ORWO FilmoTec GmbH, Germany; www.filmotec.de (Sept. 2012).
31. Harman Technologies, UK (former ILFORD); www.ilfordphoto.com/holofx/holofx.asp (Sept. 2012).
32. Microchrome Technology Inc. USA; www.microchrometechnology.com (Sept. 2012).
33. L. H. Lin, "Hologram formation in hardened dichromated gelatin films," *Appl. Opt.* **8**, 963–966 (1969).
34. V. N. Krylov, V. N. Sizov, G. A. Sobolev, S. B. Soboleva, D. I. Staselko and M. K. Shevtsov, "Study of nontanned dichromated-gelatin layers for hologram recording by cw and pulsed laser radiation," *Opt. Spectrosc. (USSR)* **69**, 115–116 (1990).
35. J. Blyth, C. R. Lowe and J. F. Pecora, "Improving the remarkable photosensitivity of dichromated gelatin for hologram recording in green laser light," in *Advances in Display Holography*. H. I. Bjelkhagen ed., Proc. *7th International Symposium on Display Holography*, River Valley Press. UK (2006), pp. 78–83.
36. A. Graube, "Holograms recorded with red light in dye sensitized dichromated gelatin," *Opt. Commun.* **8**, 251–253 (1973).
37. M. Akagi, "Spectral sensitization of dichromated gelatin," *Photogr. Sci. Eng.* **18**, 248–250 (1974).
38. T. Kubota, T. Ose, M. Sasaki and K. Honda, "Hologram formation with red light in methylene blue sensitized dichromated gelatin," *Appl. Opt.* **15**, 556–558 (1976).
39. T. Kubota and T. Ose, "Methods of increasing the sensitivity of methylene blue sensitized dichromated gelatin," *Appl. Opt.* **18**, 2538–2539 (1979).
40. C. Solano, R. A. Lessard and P. C. Roberge, "Red sensitivity of dichromated gelatin films," *Appl. Opt.* **24**, 1189–1192 (1985).
41. N. Capolla and R. A. Lessard, "Processing of holograms recorded in methylene blue sensitized gelatin," *Appl. Opt.* **27**, 3008–3012 (1988).
42. R. Changkakoti and S. V. Pappu, "Towards optimum diffraction efficiency for methylene blue sensitized dichromated gelatin holograms," *Opt. Laser Technol.* **21**, 259–263 (1989).
43. T. Kubota and T. Ose, "Lippmann color holograms recorded in methylene-blue-sensitized dichromated gelatine," *Opt. Lett.* **4**, 289–291 (1979).
44. T. Kubota, "Recording of high quality color holograms," *Appl. Opt.* **25**, 4141–4145 (1986).
45. J. Zhu, Y. Zhang, G. Dong, Y. Guo and L. Guo, "Single-layer panchromatic dichromated gelatin material for Lippmann color holography," *Opt. Commun.* **241**, 17–21 (2004).
46. J. Zhu, J. Li, L. Chen, L. Wan and G. Dong, "True-color reflection holograms recorded in a single-layer panchromatic dichromated gelatin material," in *Diffractive Optics, and Applications II*, Y. Sheng, D. Hsu, C. Yu and B. Lee eds., Proc. SPIE **5636**, 245–253 (2005).
47. J. Blyth, "Methylene blue sensitized dichromated gelatin holograms: a new electron donor for their improved photosensitivity," *Appl. Opt.*, **30**, 1598–1602 (1991).
48. S. V. Artemjev, G.I. Koval, I. E. Obyknovennaja, A. S. Cherkasov and M. K. Shevtsov, "PFG-04 photographic plates based on the nonhardened dichromated gelatin for recording color reflection holograms," in *Three-Dimensional Holography: Science, Culture, Education*, T. H. Jeong and V. B. Markov eds., Proc. SPIE **1238**, 206–210 (1991).
49. J. Wang, R. Zheng and P. Liu, "A novel method to make Lippmann color holograms recorded in DCG," in *Holographic Displays and Optical Elements II*, D. Xu and J. H. Hong eds., Proc. SPIE **3559**, 30–34 (1998).
50. T. Kubota, "Control of the reconstruction wavelength of Lippmann holograms recorded in dichromated gelatin," *Appl. Opt.* **28**, 1845–1849 (1989).
51. M. Jiang, J. Zhu, Y. Hao, Y. Guo, and L. Guo, "Color holographic display based on single-layer and panchromatic dichromatic gelatin materials," in *Holography—Culture, Art, and Information Technology*. Proc. *8th International Symposium on Display Holography*, T. H. Jeong, F. Fan, H. I. Bjelkhagen and D. Wang eds., (2009) Tsinghua Univ. Press, China (2011), pp. 393–402.
52. Holotec GmbH, Germany; www.holotec.de (Sept. 2012).
53. W. S. Colburn and K. A. Haines, "Volume hologram formation in photopolymer materials," *Appl. Opt.* **10**, 1636–1641 (1971).
54. R. L. van Renesse, "Photopolymers in holography," *Opt. Laser Technol.* **4**, 24–27 (1972).
55. R. H. Wopschall and T. R. Pampalone, "Dry photopolymer film for recording holograms," *Appl. Opt.* **11**, 2096–2097 (1972).

56. B. L. Booth, "Photopolymer material for holography," *Appl. Opt.* **11**, 2994–2995 (1972).
57. E. S. Gyulnazarov, V. V. Obukhovskii and T. N. Smirnov, "Theory of holographic recording on a photopolymerized material," *Opt. and Spectrosc. (USSR)* **67**, 109–111 (1990).
58. C. Carré and D.-J. Lougnot, "Photopolymers for holographic recording: from standard to self-processing materials," *J. Physique III, France* **3**, 1445–1460 (1993).
59. A. Fimia, N. López, F. Mateos, R. Sastre, J. Pineda and F. Amat-Guerri, "New photopolymer used as a holographic recording material," *Appl. Opt.* **32**, 3706–3707 (1993).
60. S. Martin, P. E. Leclère, Y. L. M. Renotte, V. Toal and Y. F. Lion, "Characterization of an acrylamide-based dry photopolymer holographic recording material," *Opt. Eng.* **33**, 3942–3946 (1994).
61. S. Bartkiewicz and A. Miniewicz, "Methylene blue sensitized poly(methyl methacrylate) matrix: a novel holographic material," *Appl. Opt.* **34**, 5175–5178 (1995).
62. R. A. Lessard ed., *Selected papers on Photopolymers, Physics, Chemistry, and Applications*. SPIE Milestone Series, **MS114**, Bellingham, WA, USA (1995).
63. H. I. Bjelkhagen ed., *Selected papers on Holographic Recording Materials*. SPIE Milestone Series, **MS130**, Bellingham, WA, USA (1996).
64. R. T. Ingwall and H. L. Fielding, "Hologram recording with a new photopolymer system," *Opt. Eng.* **24**, 808–811 (1985).
65. W. C. Hay and B. D. Guenther, "Characterization of Polaroid's DMP-128 holographic recording photopolymer," in *Holographic Optics: Design and Applications*, I. Cindrich ed., Proc. SPIE **883**, 102–105, (1988).
66. R. T. Ingwall and M. Troll, "Mechanism of holograms formation in DMP-128 photopolymer," *Opt. Eng.* **28**, 586–591 (1989).
67. W. K. Smothers, B. M. Monroe, A. M. Weber and D. E. Keys, "Photopolymers for holography," in *Practical Holography IV*, S. A. Benton ed., Proc. SPIE **1212**, 20–29 (1990).
68. D. Tipton, M. Armstrong and S. Stevenson, "Improved process of reflection holography replication and heat processing," in *Practical Holography VII*. S. A. Benton ed., Proc. SPIE **2176**, 172–183, (1994).
69. S. H. Stevenson, M. L. Armstrong, P. J. O'Connor and D. F. Tipton, "Advances in photopolymer films for display holography," in *Fifth International Symposium on Display Holography*, T. H. Jeong ed., Proc. SPIE **2333**, 60–70 (1995).
70. K. T. Weitzel, U. P. Wild, V. N. Mikhailov and V. N. Krylov, "Hologram recording in DuPont photopolymer films by use of pulse exposure," *Opt. Lett.* **22**, 1899–1901 (1997)
71. V. N. Mikhailov, K. T. Weitzel, V. N. Krylov and U. P. Wild, "Pulse hologram recording in DuPont's photopolymer films," in *Practical Holography XI and Holographic Materials III*, S. A. Benton and T. J. Trout eds., Proc. SPIE **3011**, 200–202 (1997).
72. C. E. Hoyle, P. E. Sundell, M. Trapp, D. M. Kang, D. Sheng and R. Nagarajan, "Polymerization kinetics of mono- and multifunctional monomers initiated by high-intensity laser pulses: dependence of rate on peak-pulse intensity and chemical structure," in *Photopolymer Device Physics, Chemistry, and Applications II*, R. A. Lessard ed., Proc. SPIE **1559**, 202–213 (1991).
73. V. N. Mikhailov, V. N. Krylov, K. T. Vaitsel and U. P. Wild, "Recording of pulsed holograms in photopolymer materials," *Opt. and Spectrosc. (USSR)* **84**, 589–596 (1998).
74. W. J. Gambogi, W. K. Smothers, K. W. Steijn, S. H. Stevenson and A. M. Weber, "Color holography using DuPont holographic recording film," in *Holographic Materials*, J. Trout ed., Proc. SPIE **2405**, 62–73 (1995).
75. T. J. Trout, W. J. Gambogi and S. H. Stevenson, "Photopolymer materials for color holography," in *Applications of Optical Holography*, T. Honda ed., Proc. SPIE **2577**, 94–105 (1995).
76. J. F. Zhang, C. R. Ma and H. Y. Lang, "Colour reflection holograms with photopolymer plates," in *Three-Dimensional Holography: Science, Culture, Education*, T. H. Jeong and V. B. Markov eds., Proc. SPIE **1238**, 306–310 (1991).
77. P. M. Hubel and M. A. Klug, "Color holography using multiple layers of DuPont photopolymer," in *Practical Holography VI*, S. A. Benton ed., Proc. SPIE **1667**, 215–224 (1992).
78. M. Kawabata, A. Sato, I. Sumiyoshi and T. Kubota, "Novel photopolymer system and its application to color hologram," in *Practical Holography VII: Imaging and Materials*, S. A. Benton ed., Proc. SPIE **1914**, 66–74 (1993).
79. M. Kawabata, A. Sato, I. Sumiyoshi and T. Kubota, "Photopolymer system and its application to a color hologram," *Appl. Opt.* **33**, 2152–2156 (1994).

80. C. Meka, R. Jallapuram, I. Nayedenova, S. Martin and V. Toal, "Acrylamide based photopolymer for multicolor recording," in *Holography-Culture, Art, and Information Technology. Proc. 8th International Symposium on Display Holography*, T.H. Jeong, F. Fan, H.I. Bjelkhagen, D. Wang eds. (2009) Tsinghua Univ. Press, China (2011). pp. 410–416.
81. Bayer MaterialScience AG, Germany; www.bayermaterialsience.com (Sept. 2012).
82. F.-K. Bruder, F. Deuber, T. Fäcke, R. Hagen, D. Hönel, D. Jurbergs, M. Kogure, T. Rölle and M.-S. Weiser, "Full-color self-processing holographic photopolymers with high sensitivity in red – the first class of instant holographic photopolymers," *J. Photopolym. Sci. Technol.* **22** (2), 257–260 (2009).
83. F.-K. Bruder, F. Deuber, T. Fäcke, R. Hagen, D. Honel, D. Jurbergs, M. Kogure, T. Rolle and M.-S. Weiser, "Reaction-diffusion model applied to high resolution Bayfol HX photopolymer," in *Practical Holography XXIV: Materials and Applications*, H. I. Bjelkhagen and R. K. Kostuk eds., Proc. SPIE **7919**, 0I-1–15 (2010).
84. H. Berneth, F.-K. Bruder, T. Fäcke, R. Hagen, D. Hönel, D. Jurbergs, T. Rölle and M.-S. Weiser, "Holographic recording aspects of high-resolution Bayfol®HX photopolymer," in *Practical Holography XXV: Materials and Applications*, H. I. Bjelkhagen ed., Proc. SPIE **7957**, 0H-1–15 (2011).
85. Polygrama, Brazil; www.polygrama.com (Sept. 2012).
86. Lynx Comercio Importaco Ltd; www.lynx-us.com (Sept. 2012).
87. M. Watanabe, T. Matsuyama, D. Kodama and T. Hotta, "Mass-produced color graphic arts holograms," in *Practical Holography XIII*, S. A. Benton ed., Proc. SPIE **3637**, 204–212 (1999).
88. D. Kodama, M. Watanabe and K. Ueda, "Mastering process for color graphic arts holograms," in *Practical Holography XV and Holographic Materials VII*, S. A. Benton, S. H. Stevenson and T. J. Trout eds., Proc. SPIE **4296**, 196–205 (2001).

5

Analogue Colour Holography

5.1 Introduction

Colour holography is concerned with accurately capturing not only the three-dimensional (3D) shape information of an object but also the object's colour information. If the hologram produced is to be categorised as "ultra-realistic", the error in recording such shape and colour should be below the limits of human perception. Additionally, the field of view of such holograms should be as large as possible and both the vertical and horizontal parallax should be properly encoded. In this chapter, we shall discuss the problem of making holograms of real objects. In Chapters 7 through 10, we shall enlarge the discussion to computer-generated objects.

The most successful technique used to date to record ultra-realistic colour holographic images of real objects has been Denisyuk's reflection holography (Figure 5.1). Denisyuk's original holograms were of course monochromatic, but the technique can be extended by using three or more primary laser wavelengths, which are then used to create an achromatic laser beam. This "white" beam is used in place of the more usual monochromatic beam, characteristic of a conventional Denisyuk setup, and a Denisyuk colour hologram is recorded using a panchromatic photosensitive plate. The image replayed by a full-colour Denisyuk hologram constitutes a 1:1 scale representation of the object. As we shall see, the realism attainable today with the Denisyuk colour technique can properly be categorised as ultra-realistic because a viewer can really find it difficult to discriminate between the hologram and the real object. The most obvious disadvantage of the Denisyuk colour technique is that the final image appears completely behind the hologram surface. Although it is possible to copy a Denisyuk colour hologram to an H_2 hologram possessing a different plane, the price paid for this is a much smaller viewing angle. We shall return to this problem in Chapter 9 in which a solution is available using full-parallax digital techniques.

In general, Denisyuk colour holograms of real objects can be produced using either continuous wave (CW) or pulsed lasers. For the most part, CW lasers are used for their convenience—notably their larger available energies and the greater ease with which their beams can be spatially filtered and aligned. However, this is not a hard-and-fast rule and indeed some potential applications of colour holography, such as pulsed colour portraiture or the reproduction of interferometrically unstable objects, explicitly require the use of pulsed lasers.

Often, white light-viewable reflection holograms recorded with a single laser wavelength are referred to as *Lippmann holograms*. However, it would be more accurate to attribute the term Lippmann holography to Denisyuk colour holography because Lippmann photographs are, after all, intrinsically polychromatic. The Denisyuk colour holograms described in this chapter may therefore be properly termed Lippmann colour holograms.

In the following section, we shall present a brief history of full-colour analogue holography. What we actually mean by a *colour hologram* is an exact analogy with colour photography—in other words, a recorded holographic image with an accurate rendering of the object's colour. However, it needs to be pointed out that there are some colours that are impossible to record holographically. Holograms can only reproduce laser light that scatters off an object's surface without suffering a change in wavelength. However, in nature, we sometimes see colours that result from fluorescence. This process does not conserve wavelength and, as such, there is no coherence between the illuminating and scattered light. For example, some dyed and plastic objects achieve their bright saturated colours precisely by fluorescence. Using the techniques of photographic image acquisition (Chapter 10) and digital holographic printing (Chapters 7–9), one can nonetheless get around this limitation.

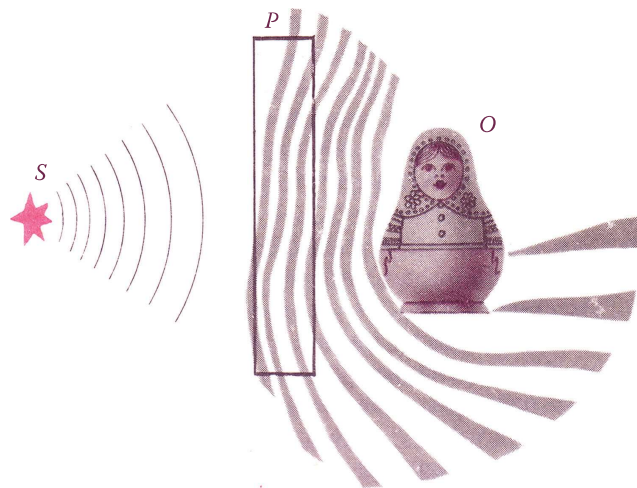


FIGURE 5.1 Denisyuk single-beam reflection hologram recording setup. S is the expanded laser beam illuminating the object O through the recording plate P and also acting as the reference beam. (From Denisyuk, *Fundamentals of Holography*, 1984. With the permission of Mir Publishers, Moscow.)

5.2 Origins in Monochromatic Holography

The field of display holography started in 1964 when Leith and Upatnieks [1] presented the possibility of recording transmission holograms of 3D objects by introducing the off-axis reference beam technique. Their hologram of a model railroad engine was on display at the OSA spring meeting in Washington, D.C. in April 1964 (Figure 1.3). This laser-illuminated hologram displayed a very realistic-looking 3D image; it had a huge impact on the participants at the meeting.

In principle, when the object is illuminated in a dark room with the same laser wavelength as that used for an off-axis transmission recording, it is not possible to see any difference between the recorded holographic image on display and the laser-illuminated object itself. In both cases, however, the viewer experiences speckle patterns covering the image or the object, as illustrated in Figure 5.2, which shows a painted egg and its associated laser transmission hologram. The size of the speckles depends on the observing aperture; the smaller the aperture diameter, the larger the speckles. It should be noted here

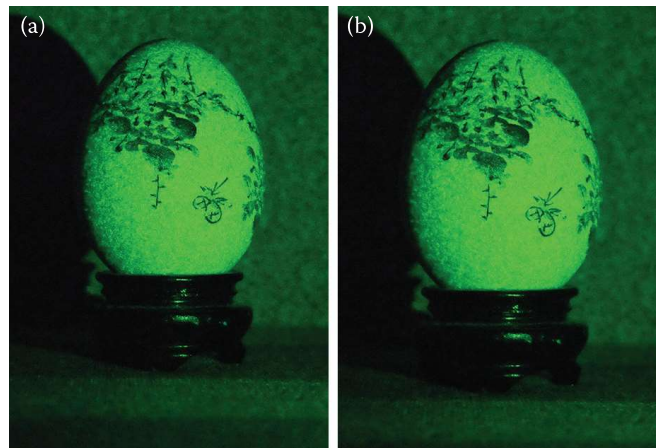


FIGURE 5.2 (a) A painted egg is illuminated with a green laser and (b) its holographic image is reconstructed from an off-axis transmission hologram with the same green laser. In both cases, the viewer sees a speckle pattern, which is caused by the viewer's eye aperture (iris) or, in the case of a photograph, the camera aperture. It is not possible to determine which one is the laser-illuminated object and which one is the image.

that speckle is a potential problem for ultra-realistic holographic imaging, particularly in high-light conditions when the aperture of the human eye is small. We shall see in Chapter 11 that one of the main effects that limit the perceivable depth in a hologram is the temporal coherence of the illuminating light source. However, too great a temporal coherence means that we start to see speckle degrade the image. This is the same problem encountered in the design of RGB lasers for projection televisions. However, the more wavelengths used to record a hologram, the less the speckle effect. For three laser wavelengths, it turns out that an illumination source with a bandwidth of approximately 2 nm is fairly ideal—at this bandwidth, both speckle noise and chromatic blurring fall below human sensitivities for normal ambient lighting conditions. This means that, from a fundamental point of view, it is easier to attain an ultra-realistic colour holographic image than a monochromatic one!

Another potential problem is human perception of colour. Humans easily compensate for different types of illumination. For example, a white surface in daylight also appears white in artificial illumination but is actually yellow. This means that there are some intrinsic problems with how exactly to record colour holographic images. The best solution is to record a hologram for a defined illuminating light source. However, one must realise that this has limitations: if the hologram and its designed light source are placed in strong ambient illumination, there is always the danger that the human eye will then perceive the holographic image incorrectly. Of course, this is exactly the same problem as a properly colour-calibrated high-definition television display being placed in high ambient illumination—here, the human observer will make erroneous colour corrections based on the presence of the strong ambient light source giving the impression of a bad image.

The displayed toy train hologram at the 1964 OSA spring meeting and Leith and Upatniek's article generated a tremendous interest in holography. As only one laser wavelength was used to record and display the hologram, the 3D image was, of course, monochromatic. However, multicolour wave front reconstruction was introduced in their article; the authors mentioned that it should be possible to illuminate a scene with coherent light of three primary colours (red, green and blue; RGB). Transmission holograms were the main topic of the article and therefore the three reference beams proposed for recording such a colour hologram had to come from three different directions to avoid cross-talk when the recorded hologram was viewed. The hologram would then comprise three incoherently superimposed R, G and B holograms, showing a full-colour 3D scene upon reconstruction. Leith and Upatnieks also pointed out that holography is related to the photographic Lippmann colour process described in Chapter 2. It is most likely that this off-axis transmission colour recording technique will appear in the future. Even if the recording setup (with CW RGB or pulsed RGB lasers) is rather complex, the display of such a hologram is more feasible thanks to small, cheap solid-state lasers or LEDs currently on the market. So far, no such colour hologram has been recorded according to the authors' knowledge, but it is only a question of time until we will see these displays.

Another type of transmission hologram that can be used to produce holograms that display images in different colours is the well-known rainbow or Benton hologram. This is an early technique that, in particular, appealed to artists who created beautiful pseudo-colour holograms. A true-colour variant of the rainbow hologram is also possible to attain using the holographic stereogram technique (using multiple sets of colour-separated photographs) and more recently using the direct write digital holography (DWDH) and master write digital holography (MWDH) techniques. As we shall see in Chapter 11, however, a true-colour image is only available at a certain vertical position in front of the hologram. As soon as the viewer moves up or down in front of the hologram, the colour of the image changes. Strictly speaking, this means that such holograms cannot be included in the category of ultra-realistic colour displays. Nevertheless, such holograms can produce stunning large depth scenes. Using direct write digital holography techniques with hogel sizes of as small as 250 µm, Stanislovas Zacharovas at the Geola organisation is producing wonderful full-colour images for applications such as postcards, first as silver halide masters and then as embossed shims for stamping (more about this application in Chapter 14).

It should also be mentioned that there is a reflection version of the pseudo-colour hologram that artists have used over many years to make beautiful multicoloured reflection holograms. Using this technique, it is possible to make reflection holograms using a single-wavelength laser and multiple exposures; at each exposure, the emulsion thickness is chemically changed and the objects being recorded are repainted. The final holographic image shows a multicoloured object; however, the colours are essentially fake.

5.3 History of True Full-Colour Holography

As already mentioned, the first principles for recording colour holograms were established a long time ago by Leith and Upatnieks [1]. Mandel [2] pointed out that it might be possible to record colour holograms directly using a polychromatic laser source and an off-axis setup. Lohmann [3] included polarisation as an extension of the suggested technique. These first methods concerned mainly transmission holograms recorded with three different laser wavelengths with substantially different reference beam directions to avoid cross-talk; we shall see in Chapter 11 that from fundamental considerations, the transmission hologram actually possesses a better reference beam angle discrimination than the corresponding reflection hologram. The recorded hologram must be reconstructed using the same three laser wavelengths from the corresponding reference directions. Colour holograms can be made this way, but at that time, the complicated and expensive reconstruction setup prevented this technique from becoming popular. The first transmission colour hologram was made by Pennington and Lin [4]. They used the 15- μm -thick Kodak 649-F emulsion with a spectral bandwidth of approximately 10 nm. This narrow bandwidth essentially eliminated cross-talk between the two colours (633 and 488 nm) at the reconstruction. In general, the cross-talk problem was solved by Collier and Pennington [5], who used spatial multiplexing and coded reference beams, which made it possible to record colour holograms in thin media.

The technique by which colour reflection holograms could be made is rather obvious because white light can be used for viewing such holograms. The problem here is the severe demand on the recording materials (Chapter 4). The lack of any suitable material in the early days resulted in early colour reflection holograms being of rather poor quality. Lin et al. [6] made the first two-colour reflection hologram that could be reconstructed in white light. They recorded a reflection hologram of a colour transparency illuminated with two wavelengths (633 and 488 nm; Figure 5.3). The material used here was the panchromatic spectroscopic Kodak 649-F plate, which was processed without fixing to avoid emulsion shrinkage.

Very few improvements in colour holography were made during the 1960s and practical progress did not occur until much later. Nevertheless, some important articles on colour holography were published during this period [7–11]. In 1979, a high-quality colour reflection hologram was recorded by Kubota and Ose [12]. They avoided the problem of using coarse-grain commercial holographic silver halide materials. Instead, they used a panchromatic dichromated gelatin (DCG) plate in which a much higher-quality colour hologram could be recorded (Figure 5.4). However, it was not until 1986, when Kubota [13] recorded a



FIGURE 5.3 First two-colour reflection hologram, recorded in 1965 by Lin et al. [6].



FIGURE 5.4 Example of one of Kubota's colour holograms recorded in a DCG emulsion.

20 cm × 25 cm sandwich colour hologram, that it was possible to demonstrate the true potential of colour display holography and the possibility of attaining ultra-realistic 3D images. This was one of the first really good Denisyuk colour reflection holograms recorded and is reproduced in Figure 5.5. Kubota used a DCG plate for the recording of the green (515 nm) and the blue (488 nm) components, and an Agfa 8E75 plate for the red (633 nm) component of the image. Because the DCG plate is completely transparent to red light, the silver halide plate (containing the red image) was mounted behind the DCG plate in relation to the observer.

In the former USSR, where finer-grain silver halide emulsions existed, some early colour holograms were recorded. The problem with these holograms was the brownish stain in the emulsion, which did not render good colour images. The processing technique used in the former USSR was mostly based on colloidal or pyrogallol-based developers. These techniques work very well when recording monochrome (red or green) holograms. However, a developed and bleached colour hologram has to be absolutely clear to obtain a colour-correct image. This is the reason why the early DCG colour holograms have much better colour rendering than early silver halide colour holograms.

The sandwich technique to record colour reflection holograms was also used by Sobolev and Serov [14]. For some time, the sandwich technique became the primary method of recording improved quality colour reflection holograms. Smaev et al. [15] and Sainov et al. [16] used this technique as well.

A 1983 review of various transmission and reflection techniques for colour holography can be found in a publication by Hariharan [17]. Regarding reflection colour holography, an extensive contribution was



FIGURE 5.5 Kubota's 1986 Japanese doll sandwich hologram *Dojo*.

made in the early 1990s by Hubel and Solymar [18]. In their publication, they gave a quantitative and exact definition (according to their opinion) of what a colour hologram was. They maintained that “A holographic technique is said to reproduce ‘true’ colours if the average vector length of a standard set of coloured surfaces is less than 0.015 chromaticity coordinate units, and the gamut area obtained by these surfaces is within 40% of the reference gamut.” In addition “the average vector length and gamut area should both be computed using a suitable white-light standard reference illuminant.” More about this definition and the subject of colour rendering will be discussed below. Hubel and Ward [19] and Hubel [20] recorded colour reflection holograms in Ilford emulsions. However, due to the emulsion’s 40-nm grain size, the recorded holograms suffered from blue-light scattering noise. The sandwich technique was used by Hubel and Ward, combining the green/blue and red Ilford emulsions (SP 672T for blue and green and SP 673T for red) with the recording laser wavelengths at 458, 528 and 647 nm.

5.3.1 Silver Halide-Sensitised Gelatin Technique

An interesting processing technique for silver halide colour holograms is the silver halide-sensitised gelatin (SHSG) technique, which is used to convert a silver halide-recorded hologram into a DCG type hologram. The advantage of the SHSG hologram over the DCG type is the high sensitivity of the panchromatic silver halide emulsion. A SHSG-processed hologram does not suffer from the printout associated with bleached holograms. SHSG processing was first introduced by Pennington et al. [21]. There are many publications on this technique, although most of them describe the processing of the old type of western monochrome holographic silver halide emulsions. This technique works best for the ultrafine-grain emulsions. During the recording of a colour hologram, any light scattering in the silver halide emulsion will be recorded as well. This means that even if one converts a silver halide hologram into a DCG type hologram (by removing the silver halide grains) the hologram will still show the recorded scattered light. Only the ultrafine-grain silver halide emulsions can therefore be used for successful SHSG processing of recorded full-colour holograms.

The SHSG technique of generating reflection holograms exposes the silver halide emulsion and then processes it in such a way that local tanning occurs within the emulsion. Then the material is fixed to remove all the silver halide grains from the emulsion, leaving only the gelatin. The last step of the processing is to dehydrate the material in a hydrophilic solvent similar to the usual DCG processing. This method for recording colour holograms was first developed by Usanov and Shevtsov [22–24], who introduced the SHSG method, which is based on the formation of a microcavity structure. The Russian technique can be explained in the following way. The gelatin in a photographic emulsion is adsorbed on the silver halide grains. In fact, only part of the gelatin molecules are adsorbed. The molecular chains are also linked within the gelatin mass of the emulsion. The thickness of the adsorbed layer in a dry emulsion is 2.5 to 4 nm. Each silver halide grain is surrounded by gelatin molecules linked at different points by active groups that are able to form complex compounds with the silver grains produced during development. The Russian method is based on the hypothesis that these adsorbed layers are less active and will be more difficult to harden than the surrounding gelatin mass. Variations in hardening between exposed and unexposed areas will therefore occur. After the silver and silver halide grains are removed from the emulsion, and the hologram is dehydrated, microcavities remain causing refractive index variation. One important point here is that the material needs additional hardening before the fixing step. After this, it is dehydrated with graded isopropanol solutions. Because a fixing step is applied in SHSG processing, which means that material is removed from the emulsion, the preferred method for obtaining reflection HOEs is the rehalogenating method.

There are different techniques for obtaining reflection phase silver halide holograms as explained in Figure 5.6. Emulsion shrinkage must be avoided when recording colour holograms. Conventional rehalogenating bleaching (a) is not recommended in this case. The fixation-free rehalogenating bleaching process (b) is the preferred technique for all types of hologram processing with regard to bleached colour reflection holograms. Because the SHSG processing requires fixation, which normally results in emulsion shrinkage, one has to try to avoid this by extensive hardening of the emulsion before fixation. The reversal (solvent) bleaching technique (c), which results in emulsion shrinkage, is not suitable for colour holograms. This bleaching process was popular for recording monochrome reflection holograms with red lasers, which resulted in orange/yellow images.

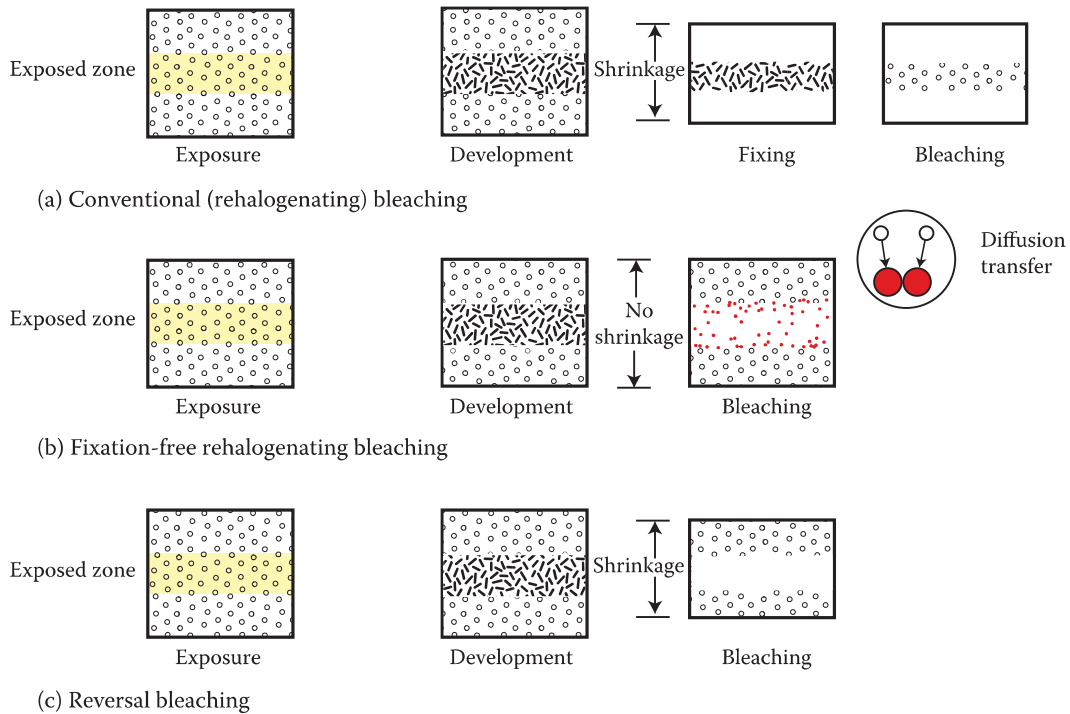


FIGURE 5.6 Different bleaching techniques for obtaining phase holograms with silver halide emulsions.

To solve the problem of SHSG emulsion shrinkage, selective hardening of the emulsion after bleaching and general emulsion hardening are the most important parts of the SHSG processing. After the two-step bleach and selective hardening process is completed, additional surface emulsion hardening is required. This can be performed by drying the emulsion in ethanol and then exposing the dry emulsion to formaldehyde vapour in a heated, sealed container, according to the method recommended by Usanov and Shevtsov. In this case, the hardening process can be performed in 15 to 30 min. Extensive hardening of the emulsion surface occurs during the dry-hardening step. The hard emulsion surface allows a high vapour pressure to build up inside the microcavities during the final dehydration step. Under this pressure, the microvoids expand and isopropanol is replaced by air, thus providing high-refractive index variations in the emulsion without any significant emulsion shrinkage. An example of a small Russian SHSG colour hologram is shown in Figure 5.7.

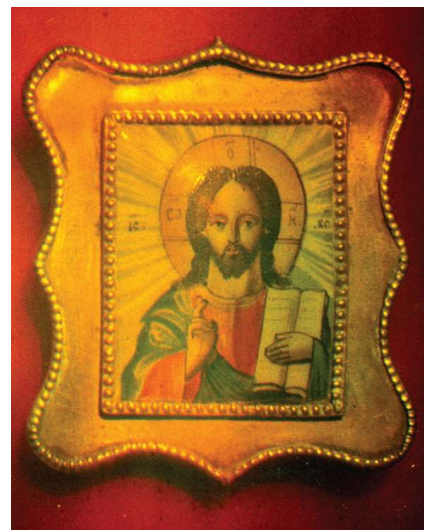


FIGURE 5.7 Russian SHSG-processed colour hologram.

In the early 1990s, an extensive research project to understand and further develop the SHSG processing technique was undertaken by one of the authors (HB) and his coworkers at the Centre for Modern Optics at De Montfort University, Leicester, United Kingdom. SHSG constitutes an important technique for processing colour reflection holograms and HOEs. By better understanding the gelatin hardening process and its role in SHSG processing, a recommended SHSG process was established for the ultra-fine-grain Slavich PFG-03C emulsion (Table 5.1). The effect of selective hardening was investigated to establish the optimum hardening condition. A chrome hardener was added to a modified rehalogenating bleach solution, and a warm-water bath was introduced for efficient gelatin cross-linking to occur; this was followed by an additional surface hardening in a sealed chamber with glutaraldehyde vapour which was found to work better than formaldehyde vapour. The dried hologram was placed in the chamber for a certain time; a slow-acting fixing solution was applied and then followed by conventional DCG

TABLE 5.1

Main SHSG Processing Steps

Processing Step	Time (minutes)
1. Prehardening in a formaldehyde solution	6
2. Develop in Agfa G282c developer at 22°C (diluted 1+5)	3
3. Bleach in the PBU-metol SHSG bleach at 22°C (diluted 1+1)	15
4. Treat in warm deionised water solution at 60°C (in safelight)	10
5. Dehydration in:	
50% water/50% industrial methylated spirits	3
100% industrial methylated spirits	3
6. Dry in oven at 45°C	5
7. Harden in chamber with glutaraldehyde vapour	25
8. Fix in SHSG fixing solution	2
9. Wash and dehydrate in	
50% water/50% isopropyl alcohol	10
100% isopropyl alcohol at 20°C	10
100% isopropyl alcohol at 70°C	2
10. Dry in oven at 45°C	
The following bath is used for the first prehardening step:	
Formaldehyde 37% (formalin)	10 mL (10.2 g)
Potassium bromide	2 g
Sodium carbonate (anhydrous)	5 g
Deionised water	1 L
The SHSG fix is mixed in the following way:	
Ammonium thiosulphate (anhydrous)	10 g
Sodium sulphate (anhydrous)	20 g
Deionised water	1 L
The SHSG bleach was based on the rehalogenating PBU-metol bleach, and the modified version is mixed in the following way (stock solution):	
Cupric bromide	1 g
Potassium persulphate	10 g
Citric acid	50 g
Potassium bromide	20 g
Borax	30 g
Deionised water	1 L
Add 1 g metol (<i>p</i> -methylaminophenol sulphate) after the other constituents are mixed.	

Note: To make this bleach for operations at a pH ~ 5, borax sodium tetraborate decahydrate was added to obtain the optimal condition for SHSG processing. A hardening compound is needed as well. Cr³⁺ ions were introduced into this bleach by adding 2% chromium (III) potassium sulphate.

isopropanol dehydration. Using this process, high-efficiency HOEs were obtained. The results of the CMO research project were published by Kim et al. [25–27] (Figure 5.8). Note that it is possible to obtain high diffraction efficiency (>95%) with no emulsion shrinkage after processing.

To investigate the microstructure of SHSG-processed emulsions, scanning electron microscopy of the Slavich PFG-03C plates was performed. To show the importance of sufficient emulsion surface hardening in a correctly hardened plate, microvoids located along the interference fringe pattern, and propagating through the emulsion, are shown in Figure 5.9. At a magnification of 80,000 \times (Figure 5.10), where a cross-section of 1 μm of the emulsion is depicted, microvoids are clearly visible. The size of the voids is approximately 100 nm.

The SHSG processing technique is rather time-consuming and complicated, and as such is mainly recommended for obtaining colour hologram masters or HOEs for contact copying in photopolymer film materials.

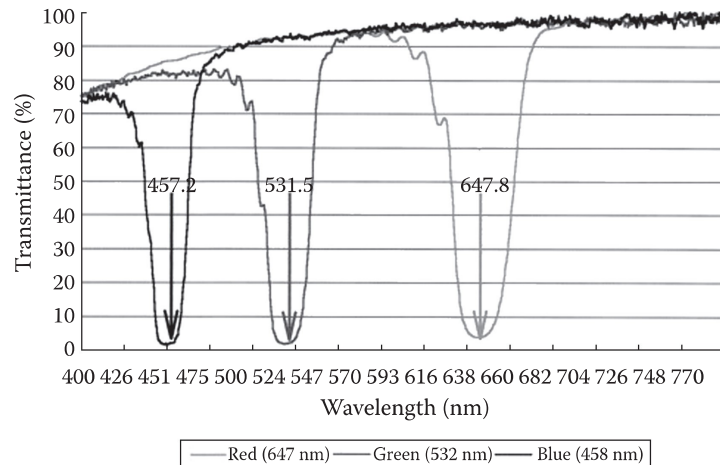


FIGURE 5.8 Recorded red, green and blue mirrors in SHSG-processed Slavich PFG-03C plates.

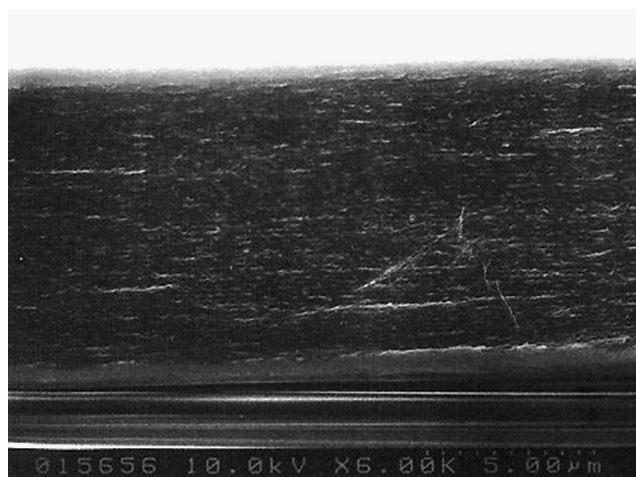


FIGURE 5.9 Microvoids in this SHSG-processed PFG-03C emulsion are visible and located along the interference fringes within the 7- μm emulsion cross-section (magnification, $\times 6000$). (From Kim, J.K. et al. *Appl. Opt.* 41, 1522–1533, 2002. With the permission of the Optical Society of America.)

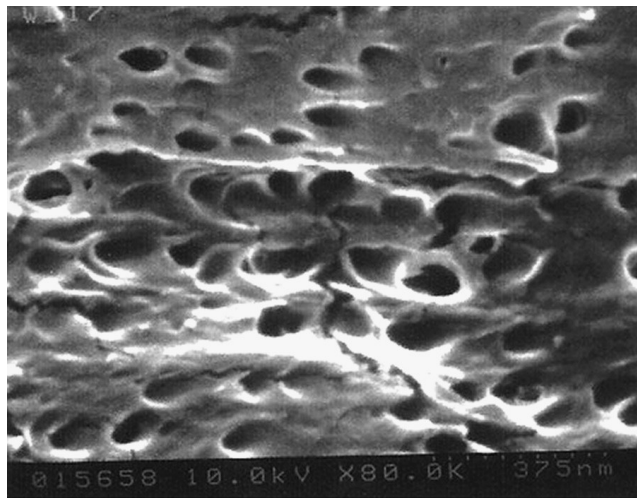


FIGURE 5.10 Scanning electron microscopy investigation of the SHSG-processed emulsion at 80,000 \times magnification. Microvoids (100 nm) are visible; 1-μm emulsion cross-section. (From Kim, J.K. et al. *Appl. Opt.* 41, 1522–1533, 2002. With the permission of the Optical Society of America.)

5.3.2 Colour Holograms in Single-Layer Silver Halide Emulsions

The sandwich technique served to demonstrate the potential of colour holography, but it was not really a simple technique for recording colour holograms. DCG emulsions are also difficult to use because of the necessity of preparing the panchromatic emulsion, which then requires a long exposure for the production of anything but the smallest colour holograms. In Russia, however, there was a different type of experimental silver halide emulsion for the recording of colour holograms.

In the mid-1990s, special panchromatic plates of the highest possible resolving power were prepared by Slavich for one of the authors (HB). These plates were prepared by Sergey Polyakov and his Slavich emulsion team and quickly hand-delivered by Henryk Kasprzak after they were finished. The first colour holograms on these plates were recorded in the laboratory by HB together with Dalibor Vukičević at the Louis Pasteur University in Strasbourg, France. The possibility of recording colour holograms in a single-layer ultrafine-grain panchromatic silver halide emulsion was published by Bjelkhagen and Vukičević [28] and later by Bjelkhagen et al. [29]. Their very first recorded colour holograms are shown in Figures 5.11 and 5.12a. These full-colour Denisyuk holograms were recorded with the following laser wavelengths: 633, 532 and 488 nm. The holograms were recorded with sequential exposures—first the blue exposure, then the green and finally the red exposure. Using sliding mirrors in the Denisyuk setup, the mixed RGB laser-light illumination of the object was not possible to observe. The red, green and blue beams were adjusted one at a time. The exposure time for each of the colour exposures was determined according to the sensitivity of the corresponding colour. Although the plates were panchromatic, they were not isochromatic, which translates to a different exposure for each colour. Therefore, the first time the mixed colours could be seen was after wet processing and after the recorded holograms had dried. The quality and colour rendering in these very first colour holograms were surprisingly good, thanks mostly to the ultrafine grains and the very high quality of the specially prepared Slavich emulsion. As already mentioned in Chapter 4, the key to success in recording analogue colour holograms is having access to suitable recording materials. The Denisyuk recording setup is straightforward and, apart from having access to stable output lasers with long coherence lengths and a vibration-free environment, there are no other requirements.

By about 2000, the Gentet brothers [30] in France, who had teamed up with Shevtsov from St. Petersburg, demonstrated high-quality colour reflection holograms recorded in the Ultimate ultrafine-grain silver halide emulsion manufactured in their laboratory. Their holograms were presented at the Holographic Millennium Conference in Austria. The most well-known Gentet holograms are the 30 cm × 40 cm holograms of butterflies and a toy fireman, which are reproduced here in Figure 5.13.

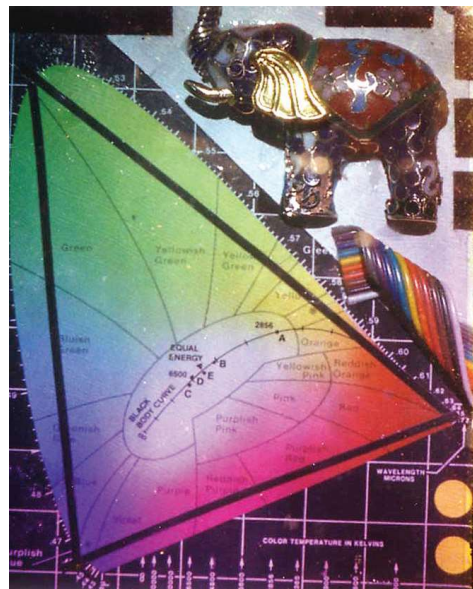


FIGURE 5.11 CIE test target hologram—this was the first hologram recorded in the special panchromatic Slavich emulsion.



FIGURE 5.12 (a) Colour hologram of a ceramic mask with blue background; (b) monochrome hologram of the same mask.



FIGURE 5.13 Two 30 cm × 40 cm Denisyuk colour reflection holograms produced by Yves Gentet and exhibited at the Holographic Millennium Conference in Austria.

The first Gentet holograms had a rather low blue component and the selected objects were mainly red or green. For example, the butterflies are mounted on a red background rather than a white one. Avoiding too much of the blue component means almost no blue light scattering in the emulsion, which results in extremely high contrast colour holograms. The problem with this approach is that white is reproduced more of a yellow colour. More recent holograms by Gentet have included blue objects and blue backgrounds.

5.4 Colour Recording in Holography

Methods for recording colour transmission holograms are based mainly on the geometry of the recording setup and are less affected by the material used for the recording. However, the original idea by Leith and Upatnieks [1] of using three different RGB reference directions to record an off-axis three-colour transmission hologram is now feasible. To display such a hologram today, one can use small, inexpensive lasers or LEDs. However, as we have already mentioned, it seems that there is no publication yet about the practical application of this colour transmission hologram technique.

Colour reflection holography presents few problems with regard to the geometry of the recording setup, but the final result is highly dependent on the recording material used and the processing techniques applied. The single-beam Denisyuk recording scheme has produced the best results so far and is the only one that can provide both 180° horizontal and vertical parallax. In addition to silver halide and DCG plates, photopolymer recording materials have also been used for recording colour reflection holograms.

There are at least five fundamental problems associated with the recording of colour reflection holograms in silver halide emulsions, which are the most convenient materials for large-format colour holograms because of their high sensitivity:

- Scattering occurring in the blue part of the spectrum during recording of a colour hologram requires a panchromatic ultrafine-grain silver halide material.
- Multiple exposures of a single emulsion may affect the diffraction efficiency of each individual recording [31,32]. Here, there is a difference between how many holograms can be recorded in an emulsion using the same laser wavelength and holograms recorded with different wavelengths, which is the case for colour holograms.
- Depending on the bandwidth of the light source used for the illumination of a colour hologram, the efficiency can be affected. White light-illuminated reflection holograms also normally show an increased bandwidth upon reconstruction, thus affecting the colour rendition.
- Shrinkage of the emulsion can often take place during processing, causing a wavelength shift.
- A set of laser recording wavelengths must be chosen to obtain the best possible colour rendition of the object.

5.4.1 Colour Theory and Colour Measurements

The problem of choosing the optimal primary laser wavelengths for colour holography is illustrated in the 1931 CIE (*Commission Internationale de l'Eclairage*) chromaticity diagram (Figure 5.14) and in the 1976 CIE version (Figure 5.15). The diagrams are useful devices for predicting the colours that can be matched by additively mixing a set of primary colours. Spectral colours are located along the horseshoe-shaped curve in the diagram. All visible colours are represented by points situated inside the diagram. Fully saturated colours are located along the periphery of the curve. The straight line joining the extremities of the curve (extreme red and blue) is the locus of purple. White is located in the centre of the area. The colours along the curve between the white point and the red region represent colours generated by a black body radiator, such as a hot filament at a certain temperature (K). By mixing different spectral colours, all possible colours can be synthesised.

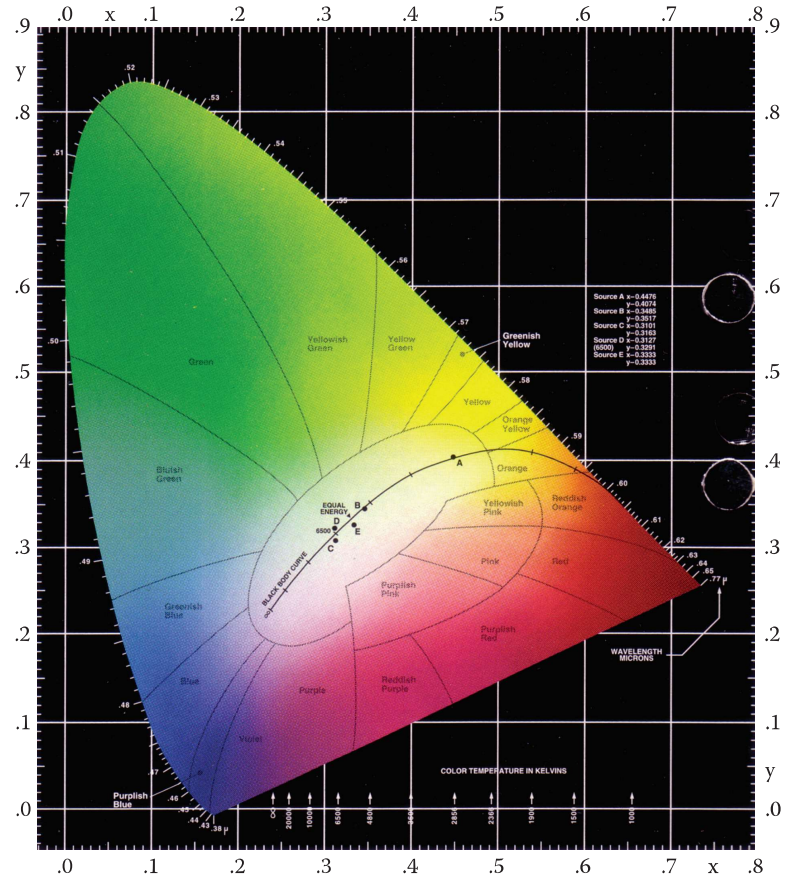


FIGURE 5.14 1931 CIE chromaticity diagram.

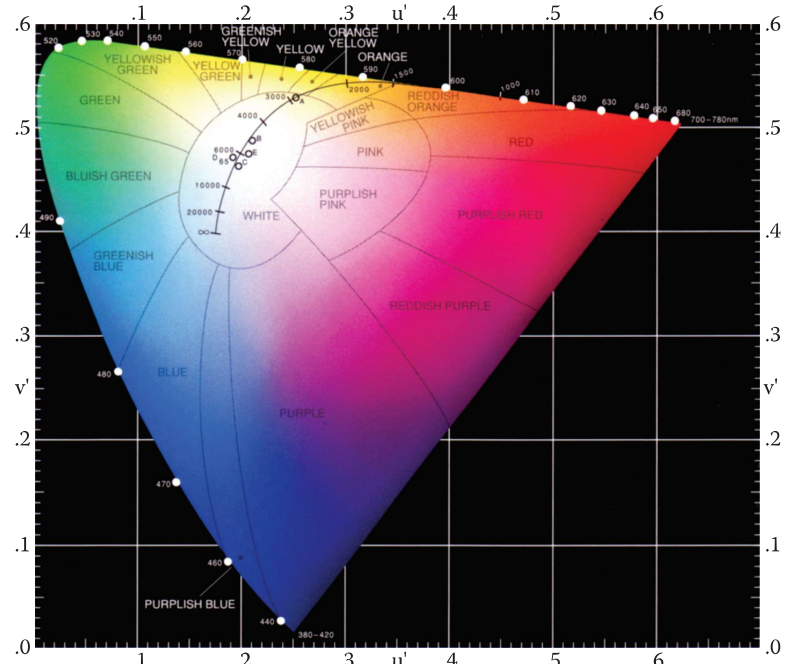


FIGURE 5.15 1976 CIE chromaticity diagram.

Some definitions used in discussions of colour can be useful to know:

Hue is that attribute of visual sensation that has given rise to colour names, for example, blue, green, yellow, and red.

Saturation, which is also referred to as the purity of colour, can be understood as the degree of purity in a given colour.

Brightness (or luminosity) is the attribute of a visual sensation according to which a given area appears to emit, or transmit, or reflect more or less light.

Lightness (or relative brightness) is the achromatic (colourless) continuum that goes from white, through gray, to black.

Luminance factor is the ratio of the luminance of a reflecting or transmitting surface, viewed from a given direction, to that of a perfect diffuser receiving the same illumination.

Chromaticity coordinates are the ratios of each of the three tristimulus values of a sample colour to the sum of the tristimulus values.

Colorimetry is the numerical expression of colours.

Primary colours are three colours of constant chromaticity used to specify an unknown colour by such amounts that are required in an additive mixture to match the unknown colour. Any three colours can serve as primary colours provided none of them can be matched by additive mixture of the other two.

Tristimulus values are the amounts of the primaries required to establish a match with a sample.

This is done either by the addition to the sample of all three primaries, or of only one primary to the sample to match any pair of primaries, or alternatively by the addition of any pair of primaries to the sample to match the remaining primary.

Chromaticity coordinates for any given colour are computed from the tristimulus values X , Y , Z as follows:

$$x = \frac{X}{X + Y + Z} = \frac{\text{red}}{\text{red} + \text{green} + \text{blue}} \quad (5.1)$$

$$y = \frac{Y}{X + Y + Z} = \frac{\text{green}}{\text{red} + \text{green} + \text{blue}} \quad (5.2)$$

$$z = \frac{Z}{X + Y + Z} = \frac{\text{blue}}{\text{red} + \text{green} + \text{blue}} \quad (5.3)$$

Chromaticity is defined as a point in a two-dimensional rectangular coordinate space, with x and y denoting ordinate and abscissa, respectively. Two of the three primaries (corresponding to X and Y) are selected in such a way that their luminance factors are zero. Accordingly, the luminance factor of any colour is given directly by its Y -tristimulus value. The coordinate z is normally not plotted because $z = 1 - (x + y)$. Colour is approximately specified in the CIE system by x , y and Y .

After the three different primary spectral colours have been selected, a triangle is made by joining the three points corresponding to the spectral colours in the diagram. The colours within the area covered by the triangle correspond to all the colours that can be produced by an appropriate mixture of the chosen spectral colours. It may seem that the main aim in choosing the recording wavelengths for colour holograms is to cover the maximum area of the chromaticity diagram. However, there are many other considerations to be taken into account when choosing the recording laser wavelengths for colour holograms as discussed by Buimistryuk and Dmitriev [33], Bazargan [34,35], Kubota and Nishimura [36,37] and Hubel [20]. It is useful to be aware of Wintringham's [38] gamut of surface colours. Surface colours refer to colours of natural and man-made objects. Normally, these colours are of low saturation.

Such colours are also found in many of the objects considered for display colour holography. Pointer [39] has extended the gamut of surface colours to include some of the highly saturated fabric dyes that were introduced after Wintringham's publication. In early colour hologram tests, the recording wavelengths were 476.5, 514.5 and 632.8 nm, mainly because these wavelengths were available in common CW lasers of that time. These wavelengths cover the Wintringham data sufficiently well. However, as will be explained in later sections, using very narrow band laser wavelengths, it is not sufficient to select three laser wavelengths within the Wintringham area of the diagram. Another important factor to consider is the reflectivity of the object at the selected laser wavelengths. Thornton [40] has shown that the reflectivity of an object at three wavelength bands, peaked at 450, 540 and 610 nm, has a very high bearing on colour reconstruction in conventional colour imaging. In this case, it is assumed that the primary RGB colours are rather broadband. The luminosity of the colour image is affected by the drop in luminous efficiency with very short or very long recording wavelengths. According to Hubel's [20] colour rendering analysis, the wavelengths required to maximise the gamut area are 456, 532 and 624 nm. Kubota and Nishimura [36,37] approached the wavelength problem from a slightly different point of view. They calculated the optimal trio of wavelengths based on a reconstructing light source at 3400 K, a 6- μm -thick emulsion with a refractive index of 1.63 and an angle of 30° between the object and the reference beam. Kubota and Nishimura obtained the following wavelengths: 466.0, 540.9 and 606.6 nm. Bazargan [35] found the ideal wavelengths to be 450, 540 and 610 nm. In the next section, the wavelength selection problem will be described and its influence on colour rendering discussed.

A practical factor to consider is the availability of wavelengths in common CW lasers. In the early days of colour holography, the main CW lasers were argon ion, krypton ion, helium–neon and helium–cadmium lasers. Today, as we discussed in Chapter 3, there are a variety of solid-state lasers having many different wavelengths within the visible electromagnetic spectrum. With regard to pulsed RGB lasers, the reader is referred to Chapter 6.

5.4.2 Selection of Laser Wavelengths

Choosing the correct recording laser wavelengths is a key issue where accurate colour rendition is a primary concern. So far, most colour holograms have been recorded using three RGB primary laser wavelengths, resulting in rather good colour rendition. However, the colours recorded are not identical to the original colours and colour desaturation may sometimes constitute a problem.

As a starting point to understanding the selection of laser wavelengths, the minimum requirement is three RGB laser wavelengths. This follows from the tristimulus theory of colour vision, which implies that any colour can, for the human observer, be matched as a linear superposition of three primaries. The tristimulus values of an object define the colour appearance of the object as illuminated by a certain light source and for an average human observer:

$$X = \int_{\lambda} \bar{x}(\lambda)S(\lambda)E(\lambda)d\lambda \quad (5.4)$$

$$Y = \int_{\lambda} \bar{y}(\lambda)S(\lambda)E(\lambda)d\lambda \quad (5.5)$$

$$Z = \int_{\lambda} \bar{z}(\lambda)S(\lambda)E(\lambda)d\lambda \quad (5.6)$$

In the above equations, \bar{x} , \bar{y} and \bar{z} represent the colour-matching functions of the average observer, $E(\lambda)$ represents the power output of the illuminant over the visible spectrum and $S(\lambda)$ is the spectral reflectance curve of the object. Each colour has a different spectral curve. The nature of the illuminant in colour holography plays a most important role regarding colour reproduction. The reason is the

fundamental difference between white light produced by narrow-band monochromatic laser wavelengths and the broadband light of a common illuminant such as daylight. Due to the narrow-band response of the laser illumination sources, the tristimulus values of a hologram are given by:

$$X^h = \sum_{i=1}^N E(\lambda_i) S(\lambda_i) \bar{x}_i(\lambda_i) \quad (5.7)$$

$$Y^h = \sum_{i=1}^N E(\lambda_i) S(\lambda_i) \bar{y}_i(\lambda_i) \quad (5.8)$$

$$Z^h = \sum_{i=1}^N E(\lambda_i) S(\lambda_i) \bar{z}_i(\lambda_i) \quad (5.9)$$

where i counts the laser wavelengths from 1 to N that are used during the recording of the hologram. There is a fundamental difference between the tristimulus values of the object given by Equations 5.4 through 5.6, and the tristimulus values of the hologram given by Equations 5.7 through 5.9. For the calculations of the tristimulus values of the object, all the components of the spectral curve are taken into account. For the hologram though, the only information within the spectral curves that is preserved is that located at the points corresponding to the recording wavelengths. It is apparent from Equations 5.7 through 5.9 that the monochromatic laser light introduces a sampling of the spectral properties of the object. Undersampling can lead to significant differences between the tristimulus values of the hologram and the tristimulus values of the object and hence an overall difference in colour. To demonstrate the effect of undersampling in colour holography, an example given by Peercy and Hesselink [41] is employed. In Figure 5.16, we plot the spectral reflectance curves of two different objects: A and B. Object A has a grey colour and B has a bluish-purple colour. At the wavelengths 477, 514 and 633 nm, both objects have the same value for spectral reflectance. Assuming a holographic recording of objects A and B with these laser wavelengths, the holographic images of both objects will appear to have the *same* colour because the hologram of the scene preserves only the surface-reflectance sampling of the wavelength information. The colour reproduction problem in this example is caused by under-sampling in the wavelength domain, which leads to aliasing.

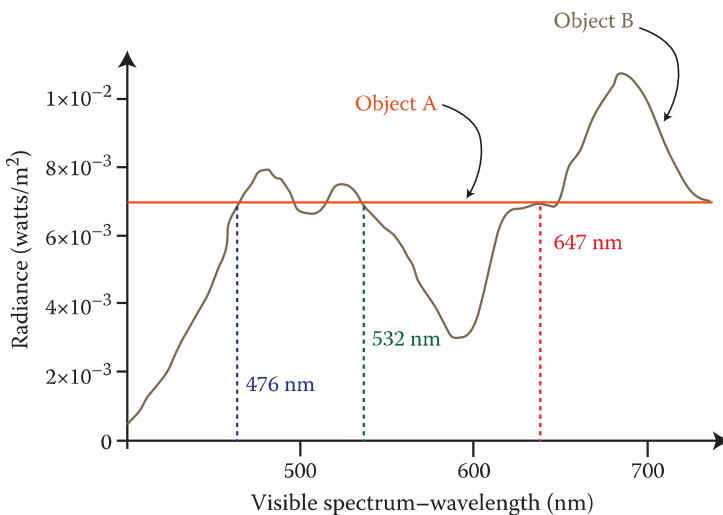


FIGURE 5.16 Aliasing due to undersampling of two objects A and B. (Modified from Peercy, M. S., and L. Hesselink. *Applied Optics* 33, 6811–6817, 1994).

It is important to ensure that a sufficient number of laser wavelengths are employed to avoid undersampling, but it is also critical to define the minimum number of laser wavelengths to produce a hologram that demonstrates a visibly acceptable error in colour rendering. Increasing the number of recording laser wavelengths will improve colour rendition, but, at the same time, it will considerably increase the complexity and cost of the recording setup.

There have been theoretical investigations carried out which have studied the minimum number of laser wavelengths needed to give an error in colour rendition that is small enough to be undetectable by an observer. Peercy and Hesselink [41] as well as Kubota et al. [42] obtained results which indicated that more than three laser wavelengths are needed to reduce the colour error.

Laser wavelength selection is very important to be able to record holograms with the best possible colour rendition. A computer simulation study was performed at the Centre for Modern Optics, De Montfort University. Mirlis et al. [43] and Bjelkhagen and Mirlis [44] presented the results of these computer simulations based on Equations 5.4 through 5.9. Error values were calculated for different numbers of laser wavelengths, taking into account all possible combinations of wavelengths between 400 and 700 nm. In this way, sets of optimal wavelengths were defined. It was also found that once above seven laser wavelengths, further improvement in colour rendition was minimal; four or five can be considered the optimum number for practical high-quality colour holography (Figure 5.17). In Table 5.2, the average colour rendering error for three to seven optimal laser wavelengths is listed. The Macbeth ColorChecker target (Figure 5.18) was used to illustrate the improved colour rendering. In Figures 5.19 through 5.22, the error for each Macbeth colour is illustrated, as calculated in the computer simulations. Figure 5.19 shows the average colour error for holograms recorded with the laser wavelengths 476, 532 and 647 nm.

If, instead of the actual three wavelengths used for recording of the colour holograms in our laboratory, the three optimal laser wavelengths defined by the computer simulation were used (Table 5.2), the colour error decreases as shown in Figure 5.20. It is obvious that to produce the best colour reproduction, one should try and find lasers that emit as close as possible to these optimal wavelengths. In Figures 5.21 and 5.22, the colour error is plotted for the optimal sets of four and five wavelengths, respectively.

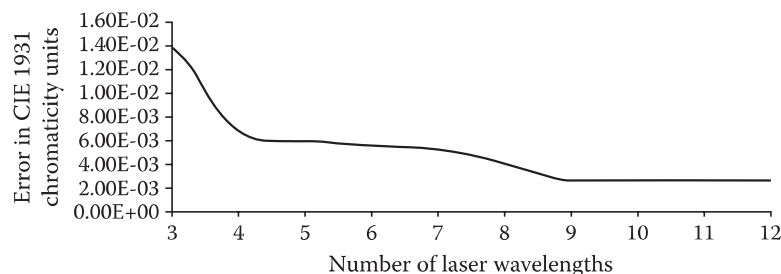


FIGURE 5.17 Total average colour error versus the number of laser wavelengths which are used in the recording of a colour hologram.

TABLE 5.2

Total Average Colour Error for Three to Seven Optimal Wavelengths

Number of Wavelengths	Optimal Laser Wavelengths (nm)	Colour Error
3	466, 545, 610	0.0137
4	459, 518, 571, 620	0.0064
5	452, 504, 549, 595, 643	0.0059
6	451, 496, 544, 590, 645, 655	0.0040
7	445, 482, 522, 560, 599, 645, 655	0.0026

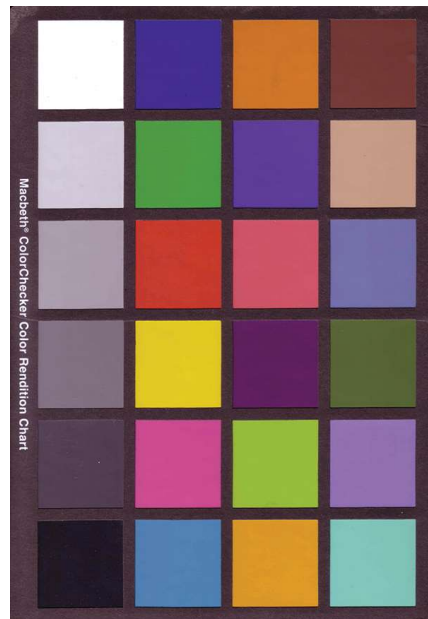


FIGURE 5.18 Macbeth ColorChecker target.

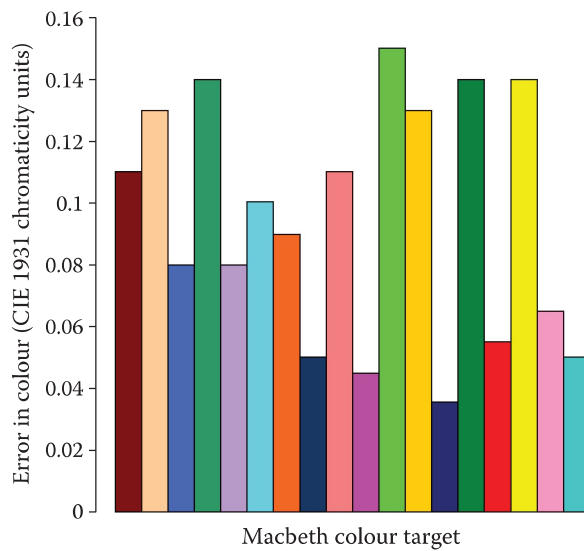


FIGURE 5.19 Computer simulation bar graph that displays the error for each Macbeth colour patch recorded in a hologram with three actual laser wavelengths at 476, 532 and 647 nm. (From Bjelkhagen, H. I., and E. Mirlis. *Applied Optics* 47, A123–A133, 2008. With permission of the Optical Society of America.)

By comparing the error graphs with each other, it is apparent that colour reproduction will be enhanced dramatically by employing one of the optimal sets. Optimal wavelength sets obtained in earlier publications are set out in Table 5.3.

We should underline that the optimal wavelength sets are a product of simulation and there is no guarantee that they correspond to easily existing or commercially available lasers suitable for holography. More work needs to be done in this area to define the best possible set of wavelengths for $n = 3, 4$ and 5 among current commercial laser emissions. Of course, high-power tunable lasers such as dye lasers

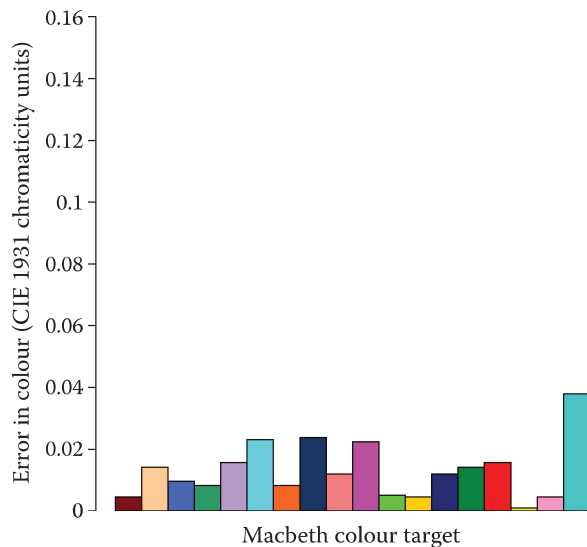


FIGURE 5.20 Computer simulation bar graph that displays the error for each Macbeth colour patch recorded in a hologram with three optimal laser wavelengths at 466, 545 and 610 nm. (From Bjelkhagen, H. I., and E. Mirlis. *Applied Optics* 47, A123–A133, 2008. With permission of the Optical Society of America.)

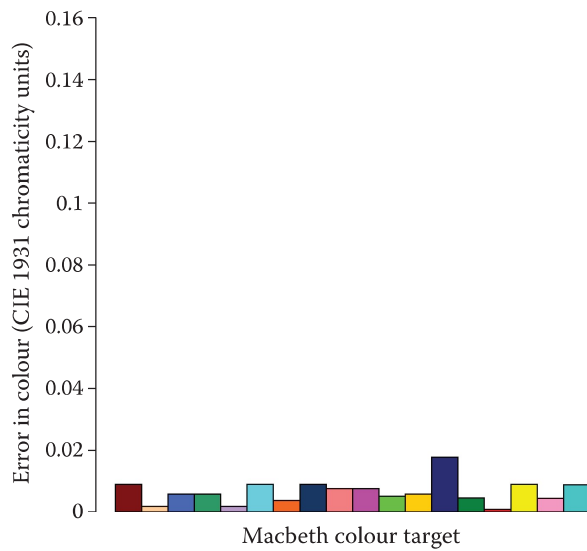


FIGURE 5.21 Computer simulation bar graph that displays the error for each Macbeth colour patch recorded in a hologram with four optimal laser wavelengths at 459, 518, 571 and 620 nm. (From Bjelkhagen, H. I., and E. Mirlis. *Applied Optics* 47, A123–A133, 2008. With permission of the Optical Society of America.)

might be used to match exactly the optimum set, but the technology becomes rather messy. Solid-state tunable lasers exist, but currently, the larger temporal coherence required for display holography can usually only be attained at the price of a very significant reduction in power.

We have already pointed out that the problem of speckle improves in a colour hologram and this has a beneficial influence on image resolution: there is an averaging of the speckle effect between different wavelengths when recording a colour hologram—this averaging effect is more pronounced when the number of recording laser wavelengths is increased [45]. Another improvement implicit to colour holography is lower susceptibility to moiré patterns, which may appear on the surface of the glass plate when

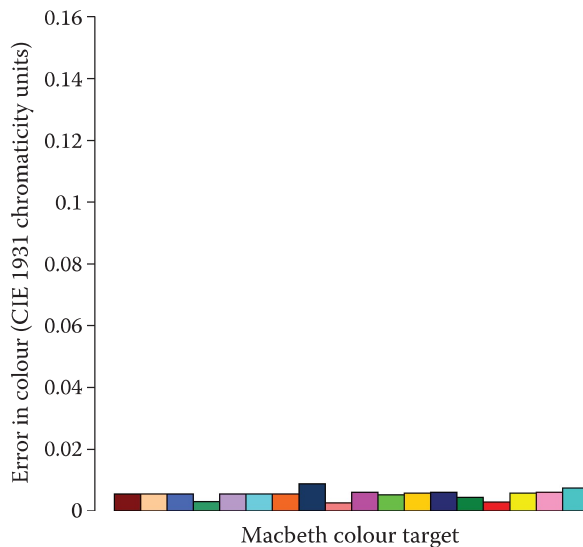


FIGURE 5.22 Computer simulation bar graph that displays the error for each Macbeth colour patch recorded in a hologram with five optimal laser wavelengths at 452, 504, 549, 595 and 643 nm. (From Bjelkhagen, H. I., and E. Mirlis. *Applied Optics* 47, A123–A133, 2008. With permission of the Optical Society of America.)

TABLE 5.3

Optimal Laser Wavelengths According to Different Investigations

Publication	Three Wavelengths	Four Wavelengths	Five Wavelengths
Mirlis et al. [43]	466, 545, 610	459, 518, 571, 620	452, 504, 549, 595, 643
Thornton [40]	475, 550, 625	460, 520, 580, 640	450, 500, 550, 600, 650
Peersey and Hesselink [41]	466, 541, 607	459, 515, 587, 663	
Kubota and Nishimura [37]	457, 532, 624		

recording a monochrome reflection hologram. The patterns are caused by interference between the two surfaces of the glass substrate. The multiple wavelengths present during the recording of a colour hologram causes individual moiré patterns corresponding to the different wavelengths to be superimposed, resulting in an almost moiré-free plate.

5.4.3 Illumination of Colour Holograms

The human observer will only correctly perceive colour and structural information in a colour hologram if the hologram is illuminated by the illuminant with which it was designed to be replayed. In addition, the intensity of diffracted light must be rather greater than the intensity of ambient light. The subject of illumination will be discussed at length in Chapter 13, but for now, we should underline the fact that a colour hologram can only be expected to replay properly if it is illuminated correctly. In Chapter 11, we shall derive expressions for the blurring in a general hologram and we shall see that the angular size of the light-source is critical to preserving structural information. Up until now, most colour reflection holograms have been illuminated with white-light halogen sources, but LED lighting is a strong candidate for the colour holograms of the future. However, narrow-band sources will bring their own problems—although more efficient, they will place higher demands on emulsion swelling and shrinkage at processing. High-power RGB laser sources are also being designed for projection televisions and are expected to provide a more expensive solution for super large depth digital colour holographic displays such as holographic windows—more about this in Chapter 14.

5.4.4 Demands on Lasers Required

To be able to record high-quality colour holograms, a minimum of three laser wavelengths (RGB) are needed. Each laser emission must be very stable.* From the experimenter's point of view, it is very difficult to obtain white, as variation in the output power in any of the lasers will result in a colour shift and thus a colour error in the recorded image. Generally, panchromatic emulsions are much less sensitive than their monochromatic cousins—as such, larger power CW lasers are required to record even quite small objects. As with any form of analogue holography, each laser must have good temporal coherence—at least several times the scene depth.

5.5 Setup for Recording Colour Holograms

5.5.1 Colour Transmission Holograms

Off-axis transmission colour holograms may soon be a reality. The main problems are a suitable laser illumination source (small red, green and blue solid-state sources ideally having a bandwidth of several nanometres) and the complex arrangement required to display such a hologram to avoid cross-talk. The laser safety aspect of the display system must be considered as well—that is, it is essential that the observer avoids looking directly into the reconstructing laser reference beams. However, the quality of a deep-scene hologram illuminated with the required amount of laser wavelengths would be very impressive. One should remember that a transmission hologram places far less demand on the recording material and, as a result, one needs less laser power for a given scene depth.

One variant of the colour transmission hologram is where the reference illuminating beams are brought in from three sides of a thick plastic block. The three-colour laser transmission hologram is optically mounted to the front of this block. The result is that each reference beam is internally reflected and dumped on the blackened black surface of the block. This type of hologram, which is really more suited to digital data due to implicit distortions, would be expected to have very good image contrast and, of course, no laser eye safety problems.

5.5.2 Colour Reflection Holograms

A typical recording setup for a three-colour Denisuk reflection hologram utilising red, green and blue CW lasers is illustrated in Figure 5.23. The three laser beams are combined using two dichroic mirrors and pass through the same beam expander and spatial filter. The resulting white laser beam illuminates both the holographic plate and the object itself through the plate. Each of the three primary laser wavelengths forms its own individual interference pattern in the emulsion; all these patterns are recorded simultaneously during the exposure. In this way, three holographic images (red, green and blue) are effectively superimposed in the emulsion. For most of the colour holograms recorded by one of the authors (HB), the following three primary laser wavelengths were employed:

- 476 nm (provided by an argon ion laser)
- 532 nm (provided by a CW frequency-doubled Nd:YAG laser)
- 647 nm (provided by a krypton ion laser)

By using dichroic beam combiners, simultaneous exposure of the holographic plate can be performed. This makes it possible to independently control the RGB ratio and the overall exposure energy in the emulsion. The RGB ratio can be varied by individually changing the output power of the lasers, whereas the overall exposure energy is controlled solely by the exposure time.

* From an absolute point of view one could compensate for power variations by using different shutter exposure times for each colour, but from a purely practical point of view it is much easier to have stable power emission at each colour.

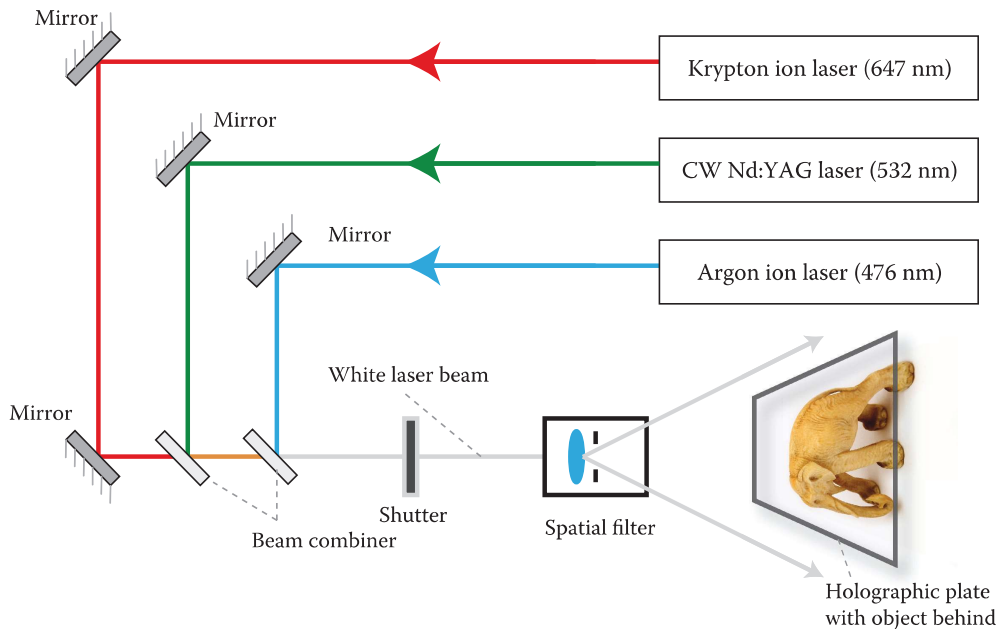


FIGURE 5.23 Denisyuk single-beam setup for recording colour reflection holograms.

In Figure 5.23, the object is shown positioned upside down. This is usual practice for holographers—working on an optical table with the beams running parallel with the table surface makes it easy to create the 45° overhead reference beam suitable for displaying the finished hologram. Of course, this can also be accomplished by introducing an overhead front-silvered mirror and installing the object in a normal position on the table surface. Every optical element (such as a mirror for example) introduced in the reference beam after the spatial filter is a source of noise. For example, dust particles on the mirror surface appear as disturbing dots on the hologram surface. Therefore, if possible, it is recommended to avoid using any optical elements in the reference beam after the spatial filter. In Figure 5.24, a *Russian Egg* is shown installed under the recording glass plate.



FIGURE 5.24 *Russian Egg* positioned upside-down on the recording table with the recording glass plate in front of it.

It is highly recommended to separate the room in which the lasers are located with their power supplies and the colour hologram recording room. The recording of analogue colour holograms is very sensitive to vibrations, air turbulence and noise sources (like from water-cooled ion lasers, for example). It is therefore best if the recording room is completely “silent” and during the recording, any existing air-conditioning in the room must be switched off. In Figures 5.25 through 5.29, two colour recording facilities are depicted. The Centre for Modern Optics’ laboratory at Glyndŵr University in Wales (now closed) and the HOLOS facility in Fitzwilliam, New Hampshire (also now closed).



FIGURE 5.25 Laser room at the CMO laboratory with the author (HB) behind the laser table.

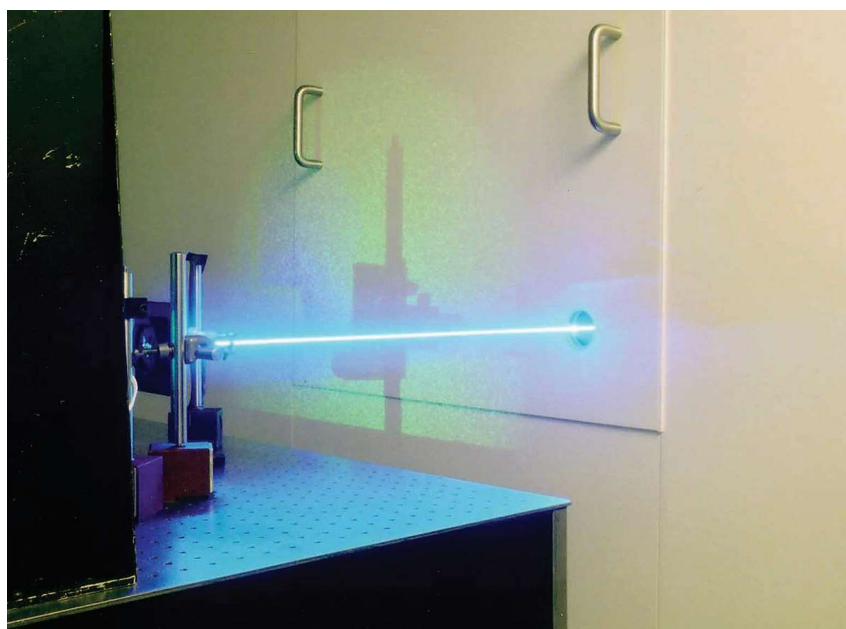


FIGURE 5.26 White laser beam passing through a hole in the wall between the CMO laser and recording rooms.



FIGURE 5.27 CMO recording room with the vibration-isolated table and the air-turbulence Styrofoam isolation sheets surrounding the recording setup.



FIGURE 5.28 HOLOS laser room with Qiang Huang behind the laser table.

5.5.3 Exposure of Colour Holograms

To determine the correct exposure time, it is necessary to know the sensitivity of the recording material. Because most of the panchromatic holographic recording materials are not isochromatic, one needs to establish the sensitivity at the three recording wavelengths. As an example, one particular batch number of the Slavich PFG-03C plates were determined to have the following sensitivity values:

- Blue (476 nm) $1480 \mu\text{J}/\text{cm}^2$
- Green (532 nm) $1410 \mu\text{J}/\text{cm}^2$
- Red (632 nm) $1084 \mu\text{J}/\text{cm}^2$

These values pertain to a particular processing technique, which will be described later. Very often, the PFG-03C emulsion has a higher red sensitivity as compared with the green and blue sensitivities.

To find the correct ratios between the recording wavelengths, the following technique can be used: Set the lasers to the same output power density as measured at the hologram recording position (this can be



FIGURE 5.29 Large recording table in the HOLOS recording room. The table is made of I-beams with 2-in. iron sheet metal slabs forming the table surface. Passive vibration isolation is provided between the I-beams with heavy-duty rubber inner tubes. This table was made for recording Denisyuk colour holograms of up to 1 m².

done using a laser power meter). Without recording a hologram, expose a third of the plate to be tested (cover the other two-thirds of the plate with black cardboard). Expose the test plate using one of the laser beams (red) for a given time (often a few seconds) slightly moving the sample during the recording. Make sure that this area of the plate has a mark (e.g., **R**). After this, the procedure is repeated with the second laser beam (green) exposing one of the previously covered areas (mask this with a **G** mark) of the test plate using *the same* exposure time as for the red. The red exposed area has to be covered not to be affected by the green exposure. Finally, the third area of the test plate is exposed with the third laser beam (blue) using the third, previously covered part (mask this with a **B** mark), again using the same exposure time. The red and green areas have to be covered during this third exposure. The test plate is then developed in a black-and-white developer and fixed. The exposure time should be chosen so that the optical density of this plate can easily be measured using a densitometer. If the recording material is isochromatic, of course, all three fields will have the same optical density after processing. However, in most cases, the **R**, **G** and **B** fields will have different optical densities. The test is repeated with the same exposure time, but now the laser power is increased for the colour regions (**R**, **G** or **B**) having lower optical density. After several such iterations, all three areas will have the same optical density after exposure.

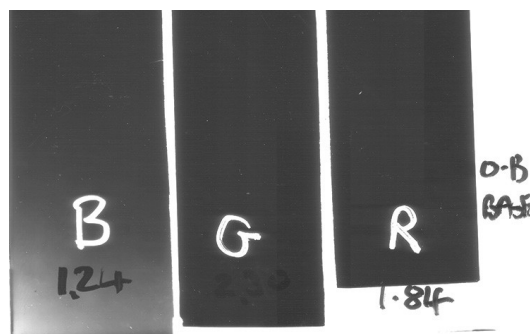


FIGURE 5.30 Emulsion colour sensitivity test plate marked with optical density values.

and processing (Figure 5.30) and the output power of the three lasers will be set for the material in question such that the correct white balance is obtained in a recorded colour hologram. Small adjustments of the laser output power may however be required to obtain the correct white colour balance. Nevertheless, this test procedure is the fastest way to set the lasers for recording colour holograms and to ensure that the exposure time is the same for all three laser wavelengths. What remains to be done is to find the overall correct exposure time to obtain the highest diffraction efficiency in the final colour hologram using simultaneous exposure. This requires a few test holograms with different exposure times.

5.5.4 Processing Recorded Colour Holograms

For colour holograms recorded on the Slavich PFG-03C emulsion, the processing set out in Table 5.4 is recommended. The final colour of the emulsion is completely clear (no stain caused by the developer or the bleach bath) and no emulsion shrinkage—these are both critical items for colour rendition. The processing consists of a prehardening step, a developing step and a rehalogenating bleach step.

The bleach can be used a few minutes after being mixed (enough oxidation of the developing agent metol must take place). Dilute 1 + 2 parts distilled water for use. More details on processing silver halide holograms and the chemicals used can be found in Bjelkhagen [46]. The prehardening bath is used to make sure the emulsion in the dried hologram after processing is very hard. One could suggest using a tanning developer such as a pyrogallol. The problem here is that the emulsion inherits a brown stain that

TABLE 5.4

Processing Colour Holograms

Formaldehyde hardener, 19°C ± 1°C	6 min
Rinse in a cold-water bath 10°C–15°C	10–20 s
CWC2 developer, 19°C ± 1°C	3 min
Wash in cold running water, 10°C–15°C	5 min
PBU-metol bleach, 19°C ± 1°C	5 min
Wash in cold running water, 10°C–15°C	10 min
Gently shower in deionised water	10–30 s
Kodak Photoflo (~1 + 200), 19°C ± 1°C	1 min

Allow to air-dry for 2 to 4 h with a good flow of cool (~20°C), clean air passing over the emulsion side of the plate.

The recipes for the hardener, the developer and bleach solutions are listed here:

Hardener:

Formaldehyde 37% (formalin)	10 mL (10.2 g)
Potassium bromide	2 g
Sodium carbonate (anhydrous)	5 g
Distilled water	1 L

Developer CWC2

Catechol	10 g
Ascorbic acid	5 g
Sodium sulphite (anhydrous)	5 g
Urea	50 g
Sodium carbonate (anhydrous)	30 g
Distilled water	1 L

Bleach solution PBU-metol

Cupric bromide	1 g
Potassium persulphate	10 g
Citric acid	50 g
Potassium bromide	20 g
Distilled water	1 L

Add 1 g metol [*p*-methylaminophenol sulphate]



FIGURE 5.31 The upper part of this Sfera-S plate was not prehardened before development which caused the emulsion to shrink and deform.

is very difficult to get rid of without affecting the emulsion thickness. The reader may recall having seen early colour holograms looking rather brownish rather than being absolutely clear. One could also suggest making the emulsion very hard during manufacturing. The problem here is that if it is already hard before processing, it is not possible for the developer to penetrate the emulsion and only the upper part of the emulsion is developed, resulting in very low diffraction efficiency. Some readers may remember what happened when John Webster asked Agfa to increase the hardness of their holographic emulsion for his nuclear fuel element inspection transmission holograms; this made it impossible to record reflection holograms on these emulsions. For colour holograms, one needs an emulsion that is rather soft; then, by using the prehardening step before development, high diffraction efficiency can be achieved combined with a very hard emulsion in the finished hologram free of any emulsion shrinkage. Figure 5.31 demonstrates what happens when part of a Sfera-S emulsion is not hardened before development.

5.5.5 Sealing of Colour Holograms

It is important to protect colour holograms recorded in silver halide emulsions. To prevent any emulsion thickness variations occurring (mainly shrinkage), which may affect colour rendition of the holographic image, the emulsion needs to be protected. Similarly, like DCG holograms, humidity variations affect the silver halide emulsion as well, even when the final colour hologram emulsion is highly hardened during processing. A further problem is that holograms on display get heated by the spotlights illuminating them and this can cause the emulsion to shrink as well. This effect will, however, be less pronounced using the new LED lights as explained in Chapter 13.

A colour reflection hologram can be protected by a clean glass plate cemented to the emulsion of the hologram using an optical cement or epoxy. It is important to use an optical cement that does not affect the emulsion—for example, by causing shrinkage or swelling. The first stage of the process is, when the plate is still wet, to completely scrape off 5 to 6 mm of the emulsion around the edges. The purpose here is to prevent moisture from penetrating through the thin gelatin layer around the edges when it has been sealed to the cover glass. The hologram is then laminated to a clean glass cover with, for example, the VITRALIT 6127 optical cement from Eurobond Adhesives Ltd. [47]. VITRALIT 6127 needs UV curing to harden. To avoid strong UV exposure (which can cause printout of the bleached silver halide emulsion), it is sufficient to expose the hologram with the cover plate to sunlight or strong white light.

The hardening takes place in less than 1 min. With such a short exposure time, using a UV lamp is also possible. Colour holograms sealed with VITRALIT 6127 have been on display for very long periods without any deterioration of the holographic image.

Often, it is desirable to blacken the backside of a colour reflection hologram. The most common way of doing this is to cover the emulsion with black paint. There are various spray paints that can be used for this purpose, but caution must be exercised when choosing a particular paint, as some paints will react with the emulsion. Instead of using spray paint, one can employ the silk screen coating technique with acrylic screen printing black ink—this gives a very uniform and thick protective layer. However, because colour holograms on glass substrates should really be protected with a cover glass plate, it is not advisable to attach any black coating to the emulsion. Instead, the black coating can then be applied to the cover plate and this means that the selection of the black coating is no longer critical.

Lamination of a colour reflection hologram recorded on film substrate can be done by using black Plexiglas with a clear adhesive from MACTac, for example, or the clear adhesive from 3M—the R948312P product. Sealing film holograms to black Plexiglas is a convenient way of combining blackening and mounting of film colour holograms. In particular, large-format film holograms need to be attached to a flat solid support for proper illumination. It needs to be pointed out that if colour film holograms are not perfectly sealed in this way, they may change colour due to large humidity variations or excessive heating. The film substrate (triacetate or polyester) does not provide a hermetic seal.

5.5.6 Recorded and Evaluated Holograms

Colour reflection holograms were recorded in the new panchromatic SilverCross emulsion [48]. The holograms were recorded in the same Denisyuk setup as previously described at the CMO laboratories with the same three RGB laser wavelengths. The processing method of Table 5.4 was used. It is important to point out that due to the ultrafine grains of the recording material, the holograms demonstrate very low light scattering in the blue region of the spectrum. An important aspect of the hologram is its ability to retain the spectral information of the image recorded. To retain this information, the processed photographic emulsion must not introduce changes to the interference pattern. If the emulsion shrinks or swells during the processing of the recorded hologram, it will distort the spectral information and it will introduce a colour shift. The spectral stability of the hologram is mainly dependent on the material that is used during the recording. The SilverCross emulsion is designed to provide high spectral stability and thus minimal colour distortion. Figure 5.32 shows a spectrogram taken by a spectrophotometer from the hologram of an elephant model. The model (left) and the hologram (right) are shown in the figure. It can be observed that the hologram, when illuminated by white halogen light, replays the spectral information of the recorded image, at the exact wavelengths used to record it (476, 532 and 647 nm). This indicates that no shrinkage of the emulsion has taken place during the recording.

In Figure 5.32, the measured white balance point coordinates at the elephant object are:

- $x = 0.42$
- $y = 0.40$

The corresponding measured white balance point coordinates at the hologram image are:

- $x = 0.38$
- $y = 0.42$

Many colour holograms have been recorded on the SilverCross emulsion to demonstrate its capabilities. Illustrated in Figure 5.33 is a photograph of a colour hologram of a blue object that can only be recorded in an ultrafine-grain emulsion. The recorded object is of the Franklin Mint decorative plate *Princess of the Iris* by M. Nolte.

One of the problems in colour analogue holography is the difficulty in obtaining an acceptable white colour in a hologram recorded of white objects. Very small variations in any of the red, green or blue

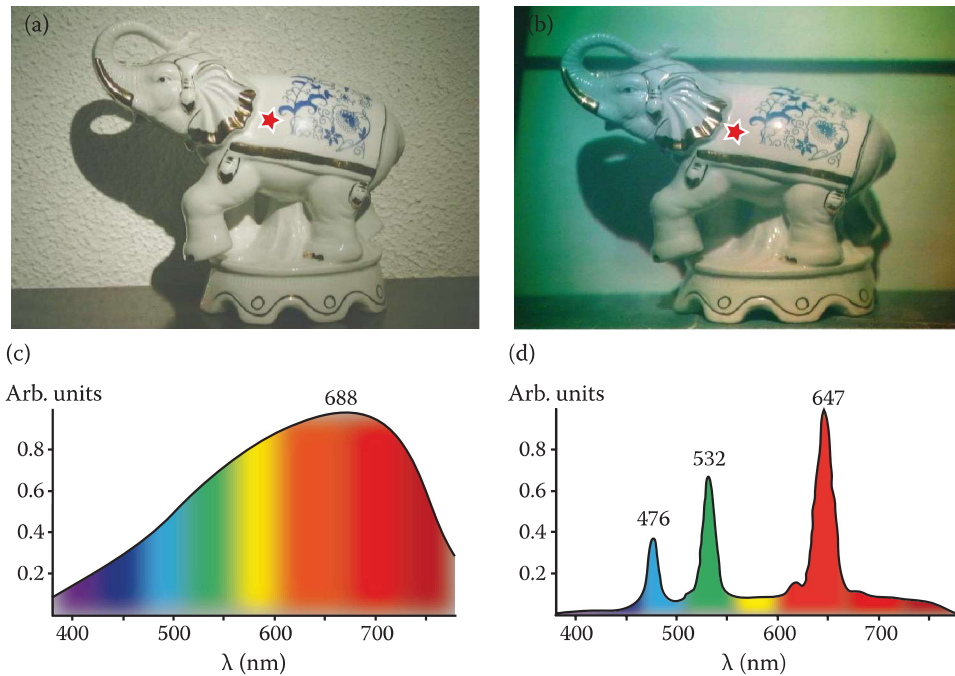


FIGURE 5.32 Evaluation demonstration of a colour hologram made using the SilverCross emulsion: the spectrum is measured at the white part of the elephant object (a) marked with a red star and the spectrum (c) is shown under the photo of the elephant. The spectrum (d) is measured at the corresponding point at the holographic image (b) of the elephant, also marked with a red star and is shown under the photo of the hologram image.

laser powers make the image turn slightly reddish or greenish. With the technique described previously (the RGB optical density test method), combined with extremely stable output powers from the RGB lasers, it is possible to get a white object to actually appear white in the recorded colour hologram (Figure 5.34).

Another problem that affects the possibility of obtaining a true white colour is connected to the processing of the hologram. If, for example, a developer containing pyrogallol is used, it is common to



FIGURE 5.33 SilverCross colour hologram of the decorative plate *Princess of the Iris*. The Franklin Mint Royal Doulton plate by M. Nolte.



FIGURE 5.34 Colour hologram showing the possibility of recording true white objects.

observe a brownish tint caused by the stained emulsion. Colloidal developing techniques also cause a reddish or brownish tint, as observed in many early Russian colour holograms. It is absolutely necessary that the developed and bleached emulsion is stain-free, which means that the hologram plate should be absolutely clear on processing.

5.6 Full-Colour Pulsed Portraiture

We have concentrated on the use of mostly CW lasers in this chapter to generate colour reflection holograms of real-world objects. One application of colour holography that requires pulsed lasers, however, is portraiture. The Geola organisation still manufactures monochrome holographic portraiture systems based on neodymium lasers. These machines can make large pulsed hologram masters as well as the final white light-viewable H₂ reflection copies. There is continuing mild interest in such systems from portrait holographers, artists, archaeologists and even medical scientists.

Very often, you will hear the comment that monochrome pulsed portraits are too “waxy” or give the impression of “ghosts”. A large part of this is due to the monochrome nature of these reflection holograms. However, what if one could use RGB pulsed lasers to record true-colour reflection portraits? Surely, this would resolve many of the criticisms. Geola actually set out to do precisely this in the early 1990s [49] but dropped the project after several years in favour of digital colour holography. Nevertheless, they succeeded in developing a high-energy two-colour Raman laser and recorded some two-colour holograms—it had been hoped that a three-colour RGB laser would have been possible using the Raman concept, but Geola never managed to attain an adequate beam distribution in the blue.

One of the complicating factors of colour reflection portraiture is that colour cross-talk in the H₁ master hologram must be controlled either by using a reflection master or by using substantially different reference beam angles for the three colours in a transmission geometry. The H₂ reflection master requires an ultrafine grain emulsion and so necessitates much larger exposure energies—not only does this push the energies required for a suitable RGB pulsed laser to approximately 3×10 J, but this also means that the human subject is irradiated with approximately 30 times the laser energy as compared with a conventional monochrome portraiture scenario. It is possible to achieve such exposure within ocular safety standards, but the larger and more numerous diffusers severely complicate the system. The transmission master has the great advantage that a fine-grain emulsion can be used with an antihalation coating to control scattering. This means that one only irradiates the human subject with around three times the energy used in monochrome portraiture ($\sim 3 \times 1$ J). However, the H₂ copy is now rather more complicated

and great care must be used to register the different colour images by producing exactly conjugate beams to the three original transmission reference beams. Additionally, an ultrafine grain emulsion is required for the final reflection H_2 if it is not to suffer from undue scattering. This means that several joules of energy in each colour are required to produce a $30\text{ cm} \times 40\text{ cm}$ colour H_2 . True-colour reflection holographic portraiture therefore looks extremely costly whichever way it is done! Geola dropped the project in the 1990s not because it could not make the lasers but because such systems would clearly not be commercial.

We shall see in Chapters 6 through 10 that the alternative technique of digital holography can in fact offer a rather better solution to full-colour portraiture. High-end structured-light quasi-real-time image acquisition systems combined with RGB pulsed-laser digital holographic printers can now print large holograms point by point; these holograms are at a stage where they are starting to become indistinguishable from full-colour analogue holograms. Of course, the great advantage here is that the image data is collected without laser illumination of the subject.

REFERENCES

1. E. N. Leith and J. Upatnieks, "Wavefront reconstruction with diffused illumination and three-dimensional objects," *J. Opt. Soc. Am.* **54**, 1295–1301 (1964).
2. L. Mandel, "Color imagery by wavefront reconstruction," *J. Opt. Soc. Am.* **55**, 1697–1698 (1965).
3. A. W. Lohmann, "Reconstruction of vectorial wavefronts," *Appl. Opt.* **4**, 1667–1668 (1965).
4. K. S. Pennington and L. H. Lin, "Multicolor wavefront reconstruction," *Appl. Phys. Lett.* **7**, 56–57 (1965).
5. R. J. Collier and K. S. Pennington, "Multicolor imaging from holograms formed on two-dimensional media," *Appl. Opt.* **6**, 1091–1095 (1967).
6. L. H. Lin, K. S. Pennington, G. W. Stroke, and A. E. Labeyrie, "Multicolor holographic image reconstruction with white-light illumination," *Bell Syst. Tech. J.* **45**, 659–661 (1966).
7. A. A. Friesem and R. J. Fedorowicz, "Recent advances in multicolor wavefront reconstruction," *Appl. Opt.* **5**, 1085–1086 (1966).
8. J. Upatnieks, J. Marks and R. Fedorowicz, "Color holograms for white light reconstruction," *Appl. Phys. Lett.* **8**, 286–287 (1966).
9. G. W. Stroke and R. G. Zech, "White-light reconstruction of color images from black-and-white volume holograms recorded on sheet film," *Appl. Phys. Lett.* **9**, 215–217 (1966).
10. E. Marom, "Color imagery by wavefront reconstruction," *J. Opt. Soc. Am.* **57**, 101–102 (1967).
11. A. A. Friesem and R. J. Fedorowicz, "Multicolor wavefront reconstruction," *Appl. Opt.* **6**, 529–536 (1967).
12. T. Kubota and T. Ose, "Lippmann color holograms recorded in methylene-blue-sensitized dichromated gelatin," *Opt. Lett.* **4**, 289–201 (1979).
13. T. Kubota, "Recording of high quality color holograms," *Appl. Opt.* **25**, 4141–4145 (1986).
14. G. A. Sobolev and O. B. Serov, "Recording color reflection holograms," *Sov. Tech. Phys. Lett.* **6**, 314–315 (1980).
15. V. P. Smaev, V. Z. Bryskin, E. M. Znamenskaya, A. M. Kursakova and I. B. Shakhova, "Features of the recording of holograms on a two-layer photographic material," *Sov. J. Opt. Technol.* **53**, 287–290 (1986).
16. V. Sainov, S. Sainov and H. Bjelkhagen, "Color reflection holography," in *Practical Holography*, T. H. Jeong and J. E. Ludman eds., Proc. SPIE **615**, 88–91 (1986).
17. P. Hariharan, "Colour holography," in *Progress in Optics* **20**, 263–324 North-Holland, Amsterdam (1983).
18. P. M. Hubel and L. Solymar, "Color reflection holography: theory and experiment," *Appl. Opt.* **30**, 4190–4203 (1991).
19. P. M. Hubel and A. A. Ward, "Color reflection holography," in *Practical Holography III*, S. A. Benton. Proc. SPIE **1051**, 18–24 (1989).
20. P. M. Hubel, "Recent advances in color reflection holography," in *Practical Holography V*, S. A. Benton ed., Proc. SPIE **1461**, 167–174 (1991).
21. K. S. Pennington, J. S. Harper and F. P. Laming, "New phototechnology suitable for recording phase holograms and similar information in hardened gelatin," *Appl. Phys. Lett.* **18**, 80–84 (1971).
22. Yu. E. Usanov and M. K. Shevtsov, "Principles of fabricating micropore silver-halide-gelatin holograms," *Opt. Spectrosc. (USSR)* **69**, 112–114 (1990).

23. Yu. E. Usanov, M. K. Shevtsov, N. L. Kosobokova and E. A. Kirienko, "Mechanism for forming a microvoid structure and methods for obtaining silver-halide gelatin holograms," *Opt. Spectrosc. (USSR)* **71**, 375–379 (1991).
24. Yu. E. Usanov and M. K. Shevtsov, "The volume reflection SHG holograms: principles and mechanism of microcavity structure formation," in *Holographic Imaging and Materials*, T. H. Jeong ed., Proc. SPIE **2043**, 52–56, (1994).
25. J. M. Kim, B. Choi, Y. Choi, S. I. Kim, J. M. Kim, H. I. Bjelkhagen and N. J. Phillips, "Transmission and reflection SHSG holograms," in *Practical Holography XV and Holographic Materials VII*, S. A. Benton, S. H. Stevenson and T. J. Trout eds., Proc. SPIE **4296**, 213–225 (2001).
26. J. M. Kim, B. S. Choi, S. I. Kim, H. I. Bjelkhagen and N. J. Phillips, "Holographic optical elements recorded in silver halide sensitized gelatin emulsions: Part 1. Transmission holographic optical elements," *Appl. Opt.* **40**, 622–632 (2001).
27. J. M. Kim, B. S. Choi, Y. S. Choi, J. M. Kim, H. I. Bjelkhagen and N. J. Phillips, "Holographic optical elements recorded in silver halide sensitized gelatin emulsions: Part 2. Reflection holographic optical elements," *App. Opt.* **41**, 1522–1533 (2002).
28. H. I. Bjelkhagen and D. Vukičević, "Lippmann color holography in a single-layer silver-halide emulsion," in *Fifth Int'l Symposium on Display Holography*, T. H. Jeong ed., Proc. SPIE **2333**, 34–48 (1995).
29. H. I. Bjelkhagen, T. H. Jeong, and D. Vukičević, "Color reflection holograms recorded in an ultrahigh-resolution single-layer silver halide emulsion," *J. Imaging Sci. Technol.* **40**, 134–146 (1996).
30. Y. Gentet and P. Gentet, "“Ultimate” emulsion and its applications: a laboratory-made silver halide emulsion of optimized quality for monochromatic pulsed and full color holography," in *HOLOGRAPHY 2000*, T. H. Jeong and W. K. Sobotka eds., Proc. SPIE **4149**, 56–62 (2000).
31. M. K. Shevtsov, "Diffraction efficiency of phase holograms for exposure superposition," *Sov. J. Opt. Technol.* **52**, 1–3 (1985).
32. D. Brotherton-Ratcliffe, "A treatment of the general volume holographic grating as an array of stacked mirrors," *J. Mod. Opt.* **59**, 1113–1132 (2012).
33. G. Ya. Buimistryuk and A. Ya. Dmitriev, "Selection of laser emission wavelengths to obtain color holographic images (in Russian)" *Izv. VUZ Priborostro. (USSR)*, **25**, 79–82 (1982).
34. K. Bazargan, "Choice of laser wavelengths for recording true-colour holograms," in *Holographic Systems, Components and Applications*, J. S. Dainty ed., Proc. IEE, No. 311, 49–50 (1989).
35. K. Bazargan, "Factors affecting the choice of optimum recording wavelengths in true-color holography," in *Int'l Symposium on Display Holography*, T. H. Jeong ed., Proc. SPIE **1600**, 178–181 (1992).
36. T. Kubota and M. Nishimura, "Recording and demonstration of cultural assets by color holography (I) - Analysis for the optimum color reproduction," *J. Soc. Photogr. Sci. Tech. Jpn.* **53**, 291–296 (1990).
37. T. Kubota and M. Nishimura, "Recording and demonstration of cultural assets by color holography (II) - Recording method of hologram for optimizing the color reproduction," *J. Soc. Photogr. Sci. Tech. Jpn.* **53**, 297–302 (1990).
38. W. T. Wintringham, "Color television and colorimetry," in Proc. IRE **39**, 1135–1172 (1951).
39. M. R. Pointer, "The gamut of real surface colours," *Color Res. Appl.* **5** (No.3), 145–155 (1980).
40. W.A. Thornton, "Luminosity and color-rendering capability of white light," *J. Opt. Soc. Am.* **61**, 1155–1163 (1971).
41. M. S. Peercy and L. Hesselink, "Wavelength selection for true-color holography," *Appl. Opt.* **33**, 6811–6817 (1994).
42. Kubota, E. Takabayashi, T. Kashiwagi, M. Watanabe and K. Ueda, "Color reflection holography using four recording wavelengths," in *Practical Holography XV and Holographic Materials VII*, S. A. Benton, S. H. Stevenson and T. J. Trout eds., Proc. SPIE **4296**, 126–133 (2001).
43. E. Mirlis, H. I. Bjelkhagen and M. Turner, "Selection of optimum wavelength for holography recording," in *Practical Holography XIX: Materials and Applications*, T. H. Jeong, and H. I. Bjelkhagen eds., Proc. SPIE **5742**, 113–118 (2005).
44. H. I. Bjelkhagen and E. Mirlis, "Color holography to produce highly realistic three-dimensional images," *Appl. Opt.* **47**, A123–A133 (2008).
45. J. Hartong, J. Sadi, M. Torzynski and D. Vukičević, "Speckle phase averaging in high-resolution color holography," *J. Opt. Soc. Am. A* **14**, 405–410 (1997).
46. H. I. Bjelkhagen, *Silver Halide Recording Materials for Holography and Their Processing*, Springer Series in Optical Sciences, Vol. **66**, Springer-Verlag, Heidelberg, New York (1993).

47. Eurobond Adhesives Ltd., UK; www.eurobond-adhesives.co.uk. (Sept. 2012)
48. H. I. Bjelkhagen, P. G. Crosby, D. P. M. Green, E. Mirlis and N. J. Phillips, "Fabrication of ultra-fine-grain silver halide recording material for color holography," in *Practical Holography XXII: Materials and Applications*, H. I. Bjelkhagen and R. K. Kostuk eds., Proc. SPIE **6912**, 09-1–14 (2008).
49. D. Ratcliffe, "New pulsed laser systems," in *Holography Marketplace*, Eight Edition, A. Rhody, and F. Ross eds., Ross Books, Berkely, CA (1999) pp. 98–102.

6

Pulsed Lasers for Holography

6.1 Introduction

Pulsed lasers were employed in holography from very early on. Their ability to capture holograms of human subjects and to “freeze” time fascinated people. Nevertheless, as we have seen in Chapters 3 to 5, historically, the continuous wave (CW) laser proved extremely convenient to use: more wavelengths were available in CW, there were fewer ocular safety risks, it was easier to obtain an acceptable spatial beam distribution, photosensitive materials worked better and you could see what was happening in real time! But with time, this bias towards CW lasers has changed. There has been great progress in the field of pulsed lasers. Most importantly, there is now a far larger range of wavelengths available. Higher pulse energies, greater coherence, better pulse stability and higher repetition rates are all now possible. In the future, compact diode pumping can be expected to totally replace the older and bulky flash pumping that is still in use in most pulsed holography lasers today.

A typical pulsed Q-switched laser possesses a laser emission that lasts several nanoseconds. The use of such light to record a hologram therefore implies implicit interferometric stability. An object moving at velocity v will move a distance $s = vt$ in a time τ . If one assumes that during a holographic exposure, objects may only move less than one-tenth of a wavelength of light, then the maximum tolerable velocity of an object in a pulsed holographic recording is given by

$$v < \frac{\lambda}{10\tau} \quad (6.1)$$

If one assumes a typical pulse length of $\tau = 30$ ns and a wavelength of $\lambda \sim 532$ nm, this tells us that the object's velocity must be less than 1.8 m/s. Clearly, this means that all normal objects and scenes, including humans, can be captured as pulsed holograms without concern as to movement or vibration.

The essential freedom from vibration and movement conferred by the use of a pulsed laser is the principal reason that pulsed lasers are so interesting to holography. Picosecond pulsed lasers can even be used to record a bullet in flight: we can turn Equation 6.1 around to write an expression for the maximum pulse duration acceptable for a given velocity. Accordingly, a bullet travelling at 300 m/s requires a maximum pulse length of 180 ps.

Besides being critical in human portraiture, immunity from vibration and movement are also critical for applications such as recording holograms of delicate museum objects, paintings or biological samples. Full-colour analogue holography (see Chapter 5) has made significant improvements over the last few decades and, as such, applications requiring the use of pulsed lasers have become significantly more pertinent—all the more so because large improvements have also occurred in the illumination sources required to display full-colour holograms (see Chapter 13).

Perhaps the most important application of pulsed lasers, however, is in the new field of ultra-realistic digital holographic printing. In the direct-write digital holography method, first introduced by Yamaguchi et al. [1] in the early 1990s, a reflection hologram is recorded as a rectangular matrix of abutting, usually square, microholograms known as hogels [2] or holopixels [3]. These hogels are generated by a conventional object beam and reference beam. Digital data is encoded onto the object beam by passing it through a spatial light modulator connected to a computer. Typical hogel sizes are approximately 0.5 to

1 mm². Zebra Imaging Inc. [4] was the first to extend Yamaguchi's work to three-colour reflection holograms using CW lasers. Zebra Imaging produced direct-write digital holograms, which fundamentally changed the way people thought about holograms. However, writing more than one million microholograms was nevertheless problematic with CW lasers because of the fundamental sensitivity to motion. In 1999, the Geola organisation solved these problems with the introduction of a direct-write digital holography scheme using a compact RGB pulsed laser [5,6]. By using 40 ns pulses each of around only 1 mJ, much less average laser power was required, meaning that the Geola printer could be quite compact. The lack of implicit sensitivity to vibration made the pulsed laser printers clearly much more suitable for commercial exploitation and allowed much higher print speeds. However, Geola had to design and produce its own RGB pulsed lasers that would be suitable for digital holography. The main issue here was to achieve critical pulse-to-pulse stability in all three colour channels over many tens of millions of pulses—one wrong pulse in a million meant that the hologram had to be scrapped. This was a significantly complicated task.

There is an important difference between CW and pulsed holography lasers. Today, there are many commercial manufacturers of CW lasers suitable for holography. The holographer therefore seldom finds it necessary to make such lasers himself or to have a detailed knowledge of their construction—it is rather easier to simply select an appropriate commercial model. With pulsed lasers, however, by far the greatest commercial application is industrial processing. All too often, commercial companies will not offer the specifications (most notably temporal coherence, spatial distribution, pulse-to-pulse stability and beam pointing stability) required in holographic applications. When contracting a company either to make a customised pulsed laser or to actually build the laser yourself, it is extremely useful to possess knowledge of the fundamental design issues. In Chapter 3, we simply reviewed the available CW laser types and the basic physics behind their operation without going into deeper discussion. In this chapter, however, we will delve much deeper into the design and construction of the most important types of pulsed lasers. Most often, we will concentrate on the optical schemes required to assure parameters suitable for holography. However, where appropriate, we will also briefly introduce the basic atomic physics behind the different active materials used. A more in-depth discussion of the atomic and quantum physics of relevant materials can be found in various textbooks [7–9]. More details on laser engineering and pumping technology can also be found in the excellent book by Walter Koechner [10].

6.2 Ruby Laser

Ruby, Cr³⁺:Al₂O₃, is a naturally occurring crystal. It is a variant of the mineral corundum, Al₂O₃—or sapphire—in which some of the Al³⁺ ions have been replaced by Cr³⁺. Ruby crystals suitable for use in lasers are usually produced artificially, however. This is done by adding small amounts of Cr₂O₃ to a highly purified melt of Al₂O₃. The crystal is then grown using the Czochralski method.

The ruby laser is a three-level system. Figure 6.1 shows an energy level diagram of the important features. The ground state of Cr³⁺ is ⁴A₂. A population inversion is created by pumping the Cr³⁺ ions from the ground state to the broad pump bands, ⁴T₂ and ⁴T₁. From here, the ions decay extremely rapidly to the metastable state, ²E, which has a fluorescent lifetime of 3 ms. ²E is in fact a doublet, and as such, there are actually two transitions to the ground state from the metastable state. These are the R₁ and R₂ emission lines of ruby and correspond to 592.9 and 694.3 nm. At room temperature, the R₁ attains lasing threshold before R₂; R₂ population transfer then occurs very rapidly from the upper to lower metastable level, which effectively leads to the entire population inversion decaying through R₁ at 694.3 nm.

The width of R₁ is 330 GHz at room temperature and is homogeneously broadened by interaction of the Cr³⁺ ions with lattice vibrations. Because of the fundamental degeneracy of the ground state, laser amplification only occurs if the R₁ level is at least half as densely populated as the ground state. This leads to a quite severe and fundamental constraint on the laser pumping power to achieve transparency; as a result, care must be taken to ensure that the laser crystal is uniformly illuminated by the pump, as any area in shadow will fall below the transparency condition and induce high optical absorption.

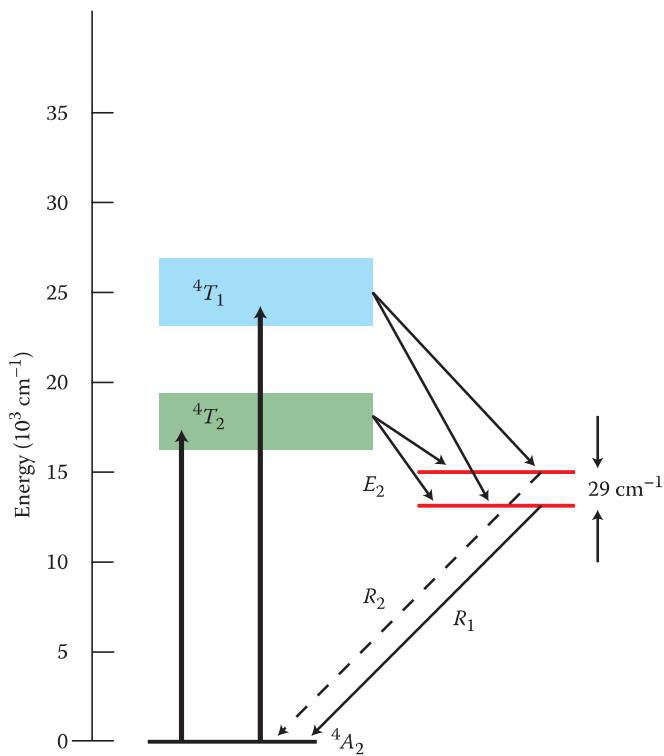


FIGURE 6.1 Energy level diagram of ruby.

Aside from being an innately three-level system and, as a consequence, requiring large optical pumping levels, the ruby laser benefits from its wide pumping bands; this makes pumping by xenon flashlamp relatively straightforward. Q-switching, which is usually arranged using a Pockels cell or (in older lasers) a Kerr cell, can produce large energies at some tens of nanoseconds. A master oscillator power amplifier (MOPA) architecture is often adopted. Figure 6.2 shows a photograph of a modern commercial ruby laser comprising a linear oscillator and an amplifier. Output energy at 694.3 nm is typically 3 J at 35 ns. The ruby laser also lends itself to a double pulsed output.

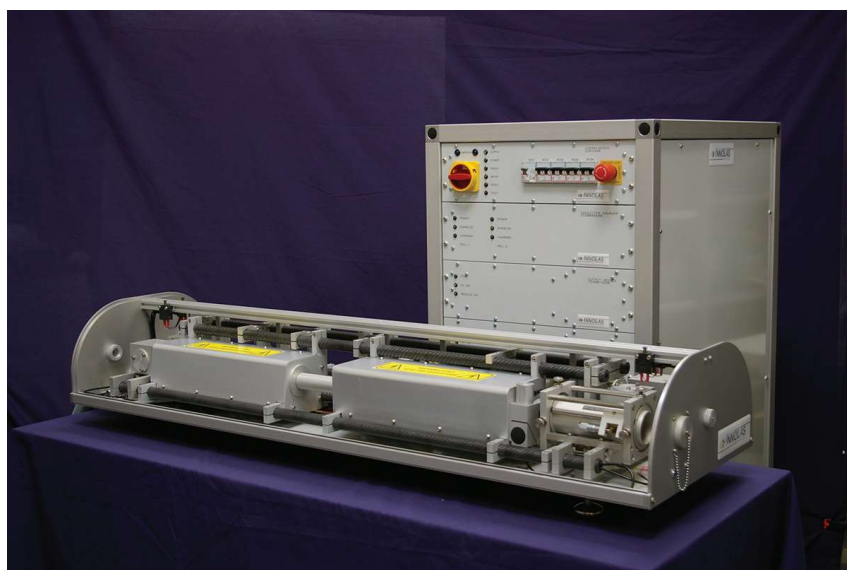


FIGURE 6.2 Modern commercial ruby laser (model HLSR-30 from InnoLas (UK)).

6.2.1 Practical Design of Ruby Lasers Suitable for Holography

Figure 6.3 illustrates Theodore “Ted” H. Maiman’s first ruby laser [11]. This used a pink ruby rod (1 cm × 1.5 cm) and a helical xenon flashlamp from General Electric, Cleveland, OH. JK Lasers, Rugby, UK (founded in 1971) was the first company to offer a range of commercial ruby lasers suitable for holography. We review here the design of the System 2000 laser, which JK made in the 1980s. This was a laser producing up to 30 J of energy in a single pulse using an oscillator and three amplifiers. JK also made lasers with fewer or no amplifiers giving outputs of approximately 50 mJ, 1 J and 10 J. Today, lasers similar to these are produced by InnoLas (UK) Ltd., Rugby, UK (Table 6.1).

Figure 6.4 shows the basic optical scheme of the System 2000 ruby laser from JK. The heart of the laser is a linear cavity oscillator built around a 4 in. × 1/4 in. ruby crystal from Union Carbide, Piscataway, NJ. The ruby crystal is pumped by multiple linear xenon flashlamps within a ceramic reflector. This was a significant advance over the previous helical flashlamps. Large currents flowing in the helical lamps led to plasma instabilities, which stressed the glass tubes significantly, reducing their lifetime compared with the linear tubes.

The oscillator cavity is approximately 40 cm in length and has a planoconcave configuration with a rear mirror of 100% reflectivity and an output coupler with a transmission of 20%. The oscillator contains a 1.7 mm brass aperture to assure the generation of TEM₀₀ only, a linear polariser, two etalons and a KDP Pockels Q-switch. The solid etalons, which assure good temporal coherence (>1 m), are 10 mm thick with 65% reflective coatings and 2.25 mm thick with 40% reflective coatings, respectively. The oscillator produces approximately 50 mJ of TEM₀₀ single frequency light at 694.3 nm in a 20 to 30 ns pulse. Note that the ruby rod is cut at a slight angle to stop laser oscillation from its ends.

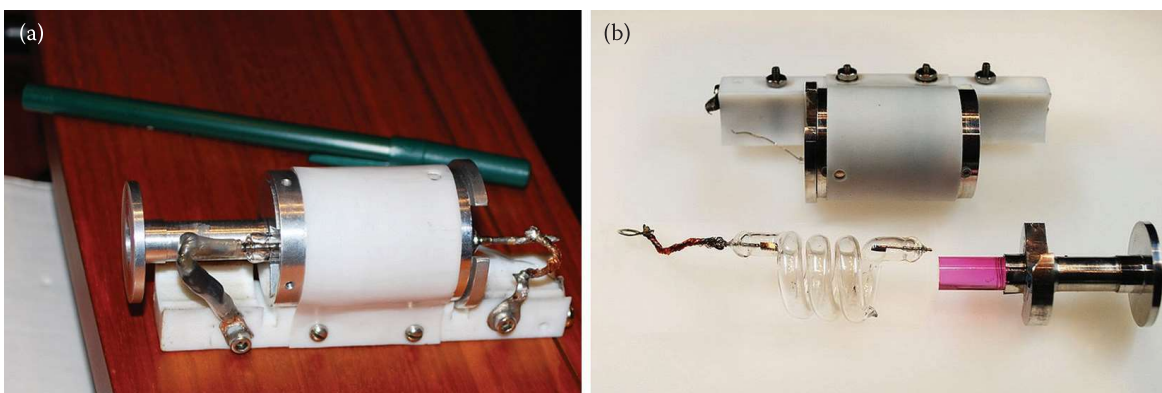


FIGURE 6.3 (a) Maiman’s original 1960 ruby laser outside (b) and disassembled.

TABLE 6.1

Main Parameters of Modern Commercial Ruby Lasers for Holography Applications from InnoLas (UK) Ltd.

	HLS-R20	HLS-R30	HLS-R40
Max. energy of single pulse	1 J	3 J	10 J
Laser head (H × W × L)	26 × 44 × 97 cm	26 × 44 × 137 cm	26 × 44 × 137 cm
Power supply (W × D × H)	60 × 80 × 130 cm	60 × 80 × 130 cm	60 × 80 × 150 cm
Wavelength		694.3 nm	
Pulse repetition rate		4 pulses/min	
Pulse duration		25 ns	
Coherence length		>1 m for 90% of shots	
Electrical supply		90–255VAC 50–60 Hz	
Max. power consumption		5 kW	

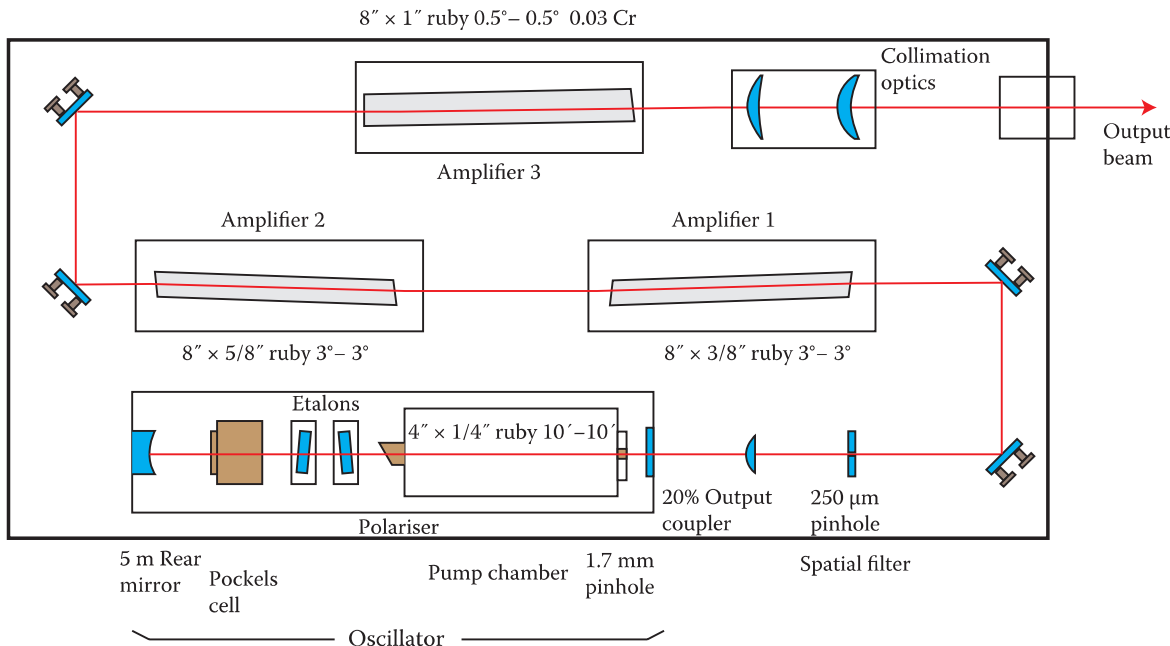


FIGURE 6.4 Optical scheme of a JK System 2000 ruby laser producing 30 J of output energy at 694.3 nm.

The System 2000 laser has three amplifiers in addition to the laser oscillator. The oscillator output beam is first cleaned by spatial filtering. This comprises a small positive lens ($f = +150$ mm) and a 250 μm diamond pinhole. Three single-pass amplifiers are then used to further increase the energy of the pulse. The first amplifier is 8 in. \times 3/8 in., and brings the pulse energy up to approximately 1 J. The second amplifier is 8 in. \times 5/8 in. producing 10 J, and the third is 8 in. \times 1 in. producing up to 30 J.

6.2.2 Pulse Lengthening in the Ruby Laser

Most Q-switched ruby lasers produce output pulses of approximately 20 to 30 ns duration. Some applications, however, require much longer pulses. As we pointed out at the start of this chapter, a 30 ns pulse length means that one can tolerate object speeds within a holographic setup of several metres per second. There are, however, many occasions in which the maximum object speeds are much slower than this. Reciprocity failure in silver halides is an important issue for finer grain emulsions and some materials, such as photopolymer and dichromated gelatin, are also much more sensitive to longer pulses. In addition, fibre optics can be used to carry coherent laser pulses at longer pulse durations. In the 1980s, one particular application focussed exceptional interest on generating longer pulses from a high-energy ruby laser. This was the application of bubble chamber holography, which was used for a time to record elementary particle tracks at Fermilab, Batavia, IL [12–14]. We shall discuss this application in Chapter 14, but for now, we shall briefly review the technique that was successfully implemented on a JK System 2000 laser whereby significantly longer pulses were generated [15].

Longer pulse lengths can be achieved in a variety of ways in pulsed lasers [16]. However, the most successful has been through fast feedback control of the Pockels Q-switch. The Fermilab team modified their JK System 2000 laser by replacing the rear oscillator mirror with one having 20% transmittance. They also replaced the standard Q-switch with a LaserMetrics model 1042 Pockels cell, which comprised two KDP crystals in parallel. This model was characterised by the relatively low quarter-wave voltage of 1200 V, which was important for designing the fast electronics.

The Fermilab pulse-stretching circuit is shown in Figure 6.5. It is composed of two parts

- fast feedback
- clamping

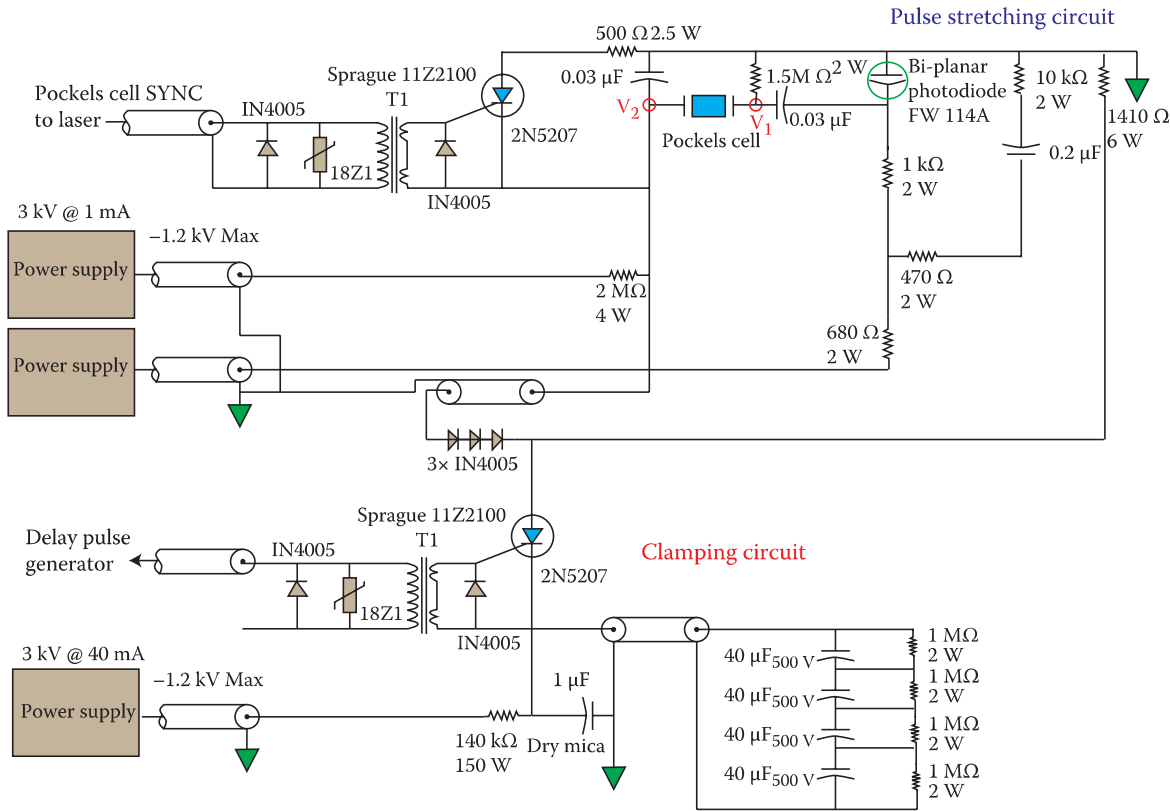


FIGURE 6.5 Fermilab pulse stretching circuit implemented on a JK System 2000 laser by the bubble chamber holography team [15].

Operation starts with the quarter-wave voltage being applied at V_2 and zero at V_1 . At a predetermined time after the oscillator flashlamp ignition, the System 2000 generates a CMOS signal that triggers the feedback Silicon Controlled Rectifier (SCR) (2N5207) changing the potential of V_2 to zero and opening the Q-switch. Up until now, this is just the standard operation of the laser. However, a fast photodiode (ITT FW114A) now measures the light escaping from the 80% oscillator rear mirror and produces a voltage at V_1 , which follows the instantaneous output power. In this way, the output power is controlled to a predefined value by the time-varying voltage at V_1 .

The desired laser pulse length is programmed into a LeCroy 222 delay generator. When time is up, this generator produces a TTL pulse which activates the clamp SCR (2N5207), bringing the V_2 voltage back to the quarter-wave voltage. Lasing then ends within $\sim 2 \mu\text{s}$, with V_1 returning to zero. Within approximately 3 ms, the current in both SCRs decreases to lower than holding values, turning them off.

The Fermilab team observed that for $40 \mu\text{s}$ pulses, an amplitude modulation of less than 5% was produced. The pulses could be successfully amplified to approximately 8 J. Coherence lengths of as long as 11 m for $2.5 \mu\text{s}$ pulses were measured. Similar fast-feedback schemes have since been used in a variety of holography lasers to control Pockels cells. The Geola organisation, for example, routinely uses very fast prelasing control in neodymium lasers at a variety of wavelengths (1 and $1.3 \mu\text{m}$) to ensure that the correct mode is present in the laser cavity at very low levels before opening the Q-switch properly. This technique guarantees stable pulses on demand with extremely small jitter.

6.3 Flashlamp-Pumped Lasers Based on Crystals Doped with Neodymium at $1 \mu\text{m}$

Another common lasing material is made by doping either glass or one of several crystals with the rare earth metal neodymium. In each case, the active ions are Nd^{3+} . The most common crystals used for pulsed lasers

suitable for holography are yttrium aluminium garnet (YAG or $\text{Y}_3\text{Al}_5\text{O}_{12}$), yttrium lithium fluoride (YLF or YLiF_4) and yttrium aluminium perovskite (YAP, YALO or Nd:YAlO_3). Both silicate and phosphate glasses are also routinely used. All these materials are available today in relatively large sizes and can be lamp-pumped using xenon discharge lamps. Yttrium vanadate (YVO_4) is often the preferred crystal for diode-pumped CW systems, but this material cannot be grown efficiently to sizes required for lamp pumping.

6.3.1 Nd:YAG

An energy level diagram of the Nd:YAG system is shown in Figure 6.6. The diagrams applicable to other crystal and glass hosts are extremely similar. However, the exact energy levels depend on the host's structure. The crystal field of the host splits each manifold into $(J + 1/2)$ levels, where J is the principal quantum number of the manifold. Therefore, the $^4I_{9/2}$ manifold is split into five Stark levels, which we label Z_1 to Z_5 . Likewise, the $^4I_{11/2}$ manifold is split into six Stark levels, Y_1 to Y_6 . Because each crystal host generates a slightly different field, the Stark splitting varies from host to host.

An important consequence of this multiplicity of states is that the fluorescence line shape is inhomogeneously broadened and exhibits significant asymmetry. This is even more apparent in glass, being an amorphous material; here, each site is different, and as a consequence, each of the energy levels is slightly different. The linewidth of the $1.06 \mu\text{m}$ YAG transition ($\delta\lambda_{\text{YAG}} \sim 7 \text{ nm}$) is therefore much smaller than the corresponding linewidth in silicate ($\delta\lambda_{\text{S,GLASS}} \sim 30 \text{ nm}$) or phosphate ($\delta\lambda_{\text{P,GLASS}} \sim 20 \text{ nm}$) glass.

In the crystal hosts, laser transitions occur between the $^4F_{3/2}$ manifold and the $^4I_{13/2}$, $^4I_{11/2}$ or $^4I_{9/2}$ manifolds. In glass, only $^4F_{3/2} \rightarrow ^4I_{11/2}$ occurs. The main laser transition of Nd:YAG occurs between the upper Stark level R_2 of $^4F_{3/2}$ and the third Stark level, Y_3 of $^4I_{11/2}$. This gives rise to an emission at 1064 nm . At

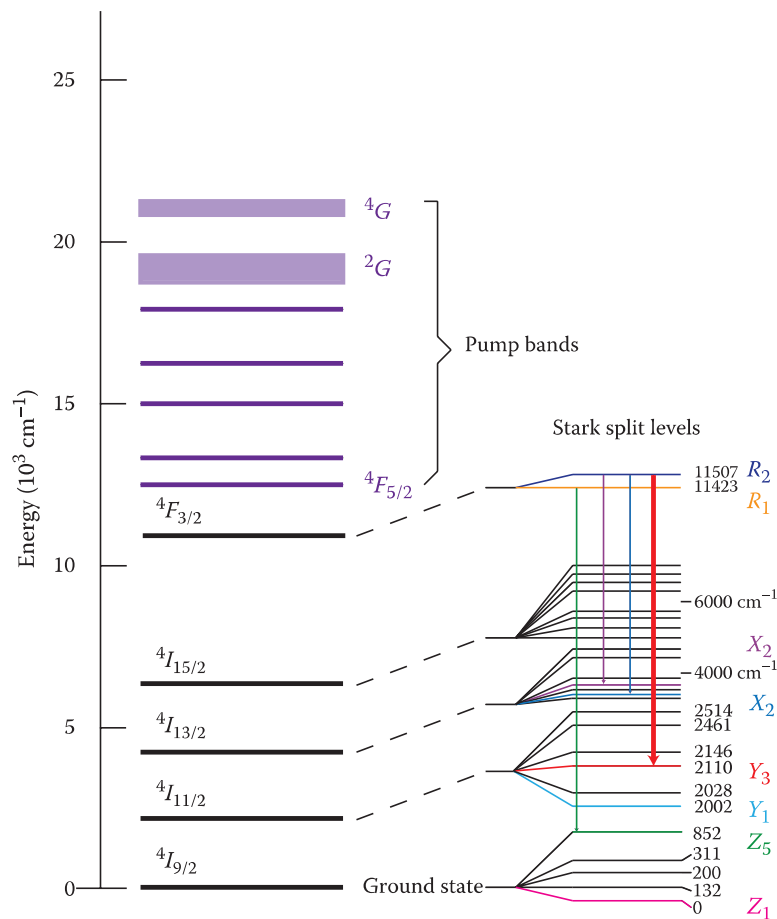


FIGURE 6.6 Energy level diagram of Nd:YAG.

room temperature, only 40% of the population inversion is in R_2 , but as lasing occurs, this is constantly replenished by thermal transitions from the lower Stark level R_1 .

The ground state of Nd:YAG is the $^4I_{9/2}$ level. Because the terminal level of the 1064 nm transition is $^4I_{11/2}(Y_3)$ and this is 2110 cm⁻¹ above the ground state, the population of $^4I_{11/2}(Y_3)$ through thermal transitions from the ground state is effectively zero [as the Boltzmann factor $\exp(\Delta E/kT) \sim \exp(-10)$]. Nd:YAG at 1064 nm is therefore an intrinsically four-level laser and, unlike the ruby laser, lasing threshold can easily be achieved at modest pumping.

The pump bands for Nd:YAG start at $^4F_{5/2}$ and continue upwards. They are unfortunately not intrinsically broad as in the ruby laser, and as a result, one has to work hard with flashlamp pumping to match the pump to the laser absorption. Nevertheless, the fact that Nd:YAG is a four-level laser system means that much less power is required to create a population inversion and this greatly mitigates the pumping issue. The fluorescence lifetime of the $^4F_{3/2}$ manifold in YAG is approximately 230 μ s, meaning that a variety of pump methods can be used, including flashlamps and semiconductor diodes. Once excited to any of the pump levels, ions decay efficiently to the upper lasing level.

6.3.2 Nd:YAP and Nd:YLF

Nd:YLF and Nd:YAP share principally the same features as Nd:YAG. As we have already mentioned, the main laser transitions are, however, a little shifted due to the effect of the different host. YLF emits at 1047 nm (π)/1053 nm (σ) and YAP at 1079.6 nm. YLF has a natural birefringence [which is why the main line is split into the ordinary (σ) and extraordinary (π) components] that dominates any thermally induced birefringence; its polarised output eliminates thermal depolarisation losses characteristic of YAG. Diode pumping is easier with YLF as its fluorescence lifetime of 485 μ s is more than twice that of YAG. Although the gain is lower in YLF, energy storage is rather better. As a result, large-energy Q-switched output can be attained with YLF (up to 0.5 J from a single oscillator). Finally, YLF has a weaker thermal lens than YAG, making it sometimes preferable as a lasing material compared with YAG when the laser oscillator must work at different repetition rates. However, the material properties of YAG are clearly superior to YLF; YLF is a softer crystal than YAG and has a lower thermal conductivity.

YAP shows similar mechanical properties to YAG but does not suffer from the stress birefringence of YAG. It is a good material for high average powers, having a similar slope efficiency to YAG at 1 μ m. Its fluorescence lifetime is only a little smaller than YAG at 170 μ s. Like YLF, YAP has different refractive and thermal/mechanical properties in different directions. As with YAG and YLF, YAP has a transition, $^4F_{3/2} \rightarrow ^4I_{13/2}$, producing emission near 1.3 μ m. We shall discuss such emissions in relation to red and blue lasers in the next section.

6.3.3 Nd:Glass

Nd:glass has advantages and disadvantages when compared with the crystal hosts. The major advantage is that it can be doped at high concentrations with excellent uniformity and it can be produced in extremely large sizes to diffraction-limited quality. As we have seen, the linewidth of glass is much wider than in crystal hosts. Although this increases the lasing threshold, it permits larger energy storage for a given linear amplification coefficient and also allows the efficient amplification of shorter pulses. As a consequence, extremely high-energy pulsed emissions can be created with a glass laser and indeed such lasers are used for nuclear fusion applications [17]. The main disadvantage of glass is that its thermal conductivity is poor (around five to six times smaller than YLF for example), and as a consequence of this, only small laser repetition rates can be achieved at high energy.

Glass and crystal lasers complement each other in a very real way. As we have mentioned previously, the thermal conductivity of glass is much smaller than YAG, YLF or YAP. The crystal hosts are therefore far superior to glass for the generation of high repetition rate emissions. In addition, the crystal hosts, having a narrower linewidth, require lower pumping to threshold. The laser transition wavelength in glass and the crystals differs by up to 6 nm, but this is well within the typical 20 to 30 nm linewidth of glass. As we shall see below, a familiar configuration is the hybrid MOPA scheme, in which a crystal host is used as the laser oscillator and glass amplifiers are then employed to boost the energy. Both silicate

TABLE 6.2
Parameters of Neodymium-Doped Glasses

	Silicate Glass (Q-246, KIGRE)	Phosphate Glass (Q-88, KIGRE)
Peak wavelength (nm)	1062	1054
Cross-section ($\times 10^{-20}$ cm $^{-2}$)	2.9	4.0
Fluorescence lifetime (μ s)	340	330
Linewidth (nm)	27.7	21.9
Thermal conductivity (W/m°C)	1.30	0.84
Thermal expansion ($10^{-7}/^{\circ}\text{C}$)	90	104
Young's modulus (kg/mm 2)	8570	7123

and phosphate glasses are routinely used. Table 6.2 summarises the important optical parameters of typical commercial glasses. As a general rule, silicate glass (1062 nm) seems better matched to Nd:YAG at 1064 nm. Conversely, phosphate glass at 1054 nm would seem better matched to Nd:YLF at 1053 nm. However, in practice, phosphate glass is often the most energy-efficient choice for both crystals.

6.3.4 Nd³⁺-Doped Ceramic YAG

Another material, Nd³⁺-doped ceramic YAG, is becoming increasingly popular. These laser rods have very similar properties to Nd:YAG crystals but, like glass, can be made in much larger sizes. Having good thermal properties, neodymium ceramic YAG may be used in place of glass amplifiers to allow high repetition rates. Nanocrystalline technology and the vacuum sintering method are used to fabricate such “synthetic” Nd:YAG crystals. Nd³⁺-doped ceramic YAG is probably the most important innovation in the field of laser material fabrication technology in the last decade. Such ceramic laser crystals exhibit several key advantages over conventional single crystal growth technologies. Most importantly, the possibility of growing large samples quickly and at a low cost means that the mass production of this material is possible. On the other hand, the possibility of increasing the neodymium doping concentration (>4% doping is possible) compared with melt-grown technologies makes it possible to miniaturise the laser materials and points the way to new applications, such as single-mode microchip lasers.

6.3.5 Design of Commercial Neodymium Holography Lasers

Commercial neodymium pulsed lasers, oscillating at 1 μ m and frequency-doubled to the green, were first used in holography to provide a more efficient* and more appropriate source of laser radiation for human and animal portraiture; previously, such applications had been catered for by the deep red emission of the ruby laser. Using glass amplifiers and a neodymium crystal oscillator, both pumped by liquid-cooled xenon flashlamps, a high pulse energy with excellent beam parameters can be efficiently obtained. The lasers are typically passively Q-switched for holographic applications. With electro-optic Q-switching and injection seeding [18–21], twin oscillator–amplifier configurations can produce the controllable mutually coherent double pulse emissions required by applications such as interferometry and holographic particle image velocimetry [22].

We describe here the construction of a family of Nd:YLF/Nd:phosphate glass lasers [23–25], which were designed especially for display holography by the Geola organisation. These lasers, which were first produced commercially in 1997, are currently in use by many holographers throughout the world and are still manufactured by Geola.

Each of the lasers is based on a high-stability single transverse and longitudinal mode ring cavity master oscillator and, depending on the model, can produce output energies from 1 to 5 J at the second harmonic wavelength of $\lambda = 526.5$ nm. The lasers incorporate a fast repetition mode, which can be used

* Frequency-doubled Nd:YLF/phosphate glass lasers are roughly four to five times more efficient than ruby in terms of electrical energy used per optical joule generated.

for the alignment of external optical elements. This mode only activates the oscillator and, at an adjustable frequency of up to 2 Hz, produces a bright green beam that has identical propagation characteristics to the main high-energy beam. This feature is a great improvement over the more common technique (often used with ruby lasers, for example) of using an additional CW alignment laser that inevitably is of a different wavelength and has different beam parameters compared with the main laser emission.

The lasers are built on a honeycomb stainless optical base that is mounted inside a separate laser case on a floating three-point suspension system. The master oscillator optical scheme is designed using a vertical cavity to minimise the influence of thermal bending. A breadboard thermosensor permits precise temperature equalisation of the liquid lamp coolant to the temperature of the optical breadboard. This

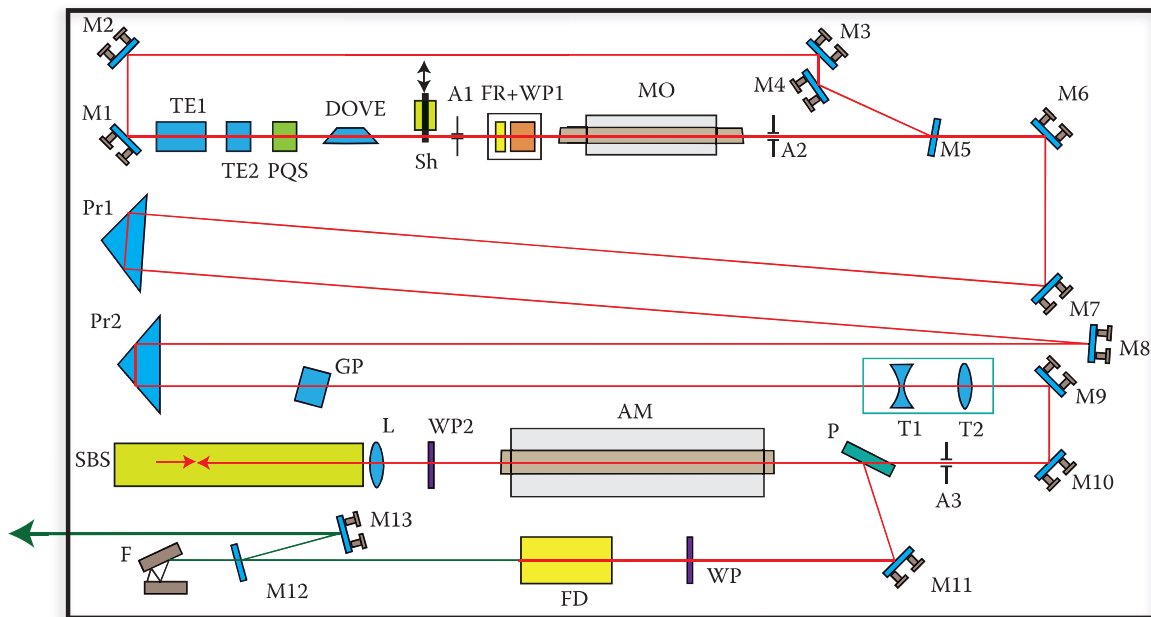


FIGURE 6.7 Optical schematic of the G2J Laser, a 2 J hybrid Nd:YLF/phosphate glass laser made by the Geola organisation.



FIGURE 6.8 Photograph of the G2J holography Laser. The laser produces 2 J at 527 nm. (Courtesy of Geola Digital UAB.)

reduces the influence of local heating of the breadboard by the pump chambers and preserves the laser scheme from thermal bending. The thermal walk-off of all adjustable optical mounts is designed to be minimal and each mount is tested in an interferometer before assembly.

Figure 6.7 shows the optical scheme of a G2J Laser. A photograph of its external appearance is shown in Figure 6.8. This laser produces up to 2 J of laser emission at 526.5 nm using a single Nd:YLF oscillator and a single double-pass Nd:phosphate glass amplifier with stimulated Brillouin scattering (SBS)* mirror.

6.3.5.1 Design and Operation of Master Oscillator

The ring master oscillator is defined by the output coupler (M5) and the four high-reflection mirrors (M1–M4). The resonator incorporates a Dove prism (mounted horizontally) and has an optical path length of 1.6 m. The Dove prism is used to reduce the sensitivity of the master oscillator to detuning of the cavity mirrors. A Nd:YLF laser rod (doped at 1.1%) measuring $\varnothing 5 \times 80$ mm is mounted in a stainless steel pump chamber incorporating a diffuse ceramic reflector. The rod is pumped by a linear flashlamp (5 × 76 XFP CFQ from Heraeus Noblelight, Great Britain). The close-coupled diffuse reflector design provides uniform rod pumping and ultraviolet (UV) filtration. The laser rod must be tuned rotationally in such a way that the polarisation of transmitted radiation remains invariant. This is the best way to suppress polarisation losses in the birefringent YLF crystal. An intracavity Faraday rotator (FR), together with a half-wave plate (WP1) totally suppress the generation of the parasitic reversed ring cavity mode.

Single longitudinal mode (SLM) generation is achieved with the use of a ring cavity, a LiF:F₂⁻ passive Q-switch and two tilted intracavity etalons (TE1 and TE2). A travelling-wave oscillator eliminates “spatial hole burning” caused by standing waves in a conventional linear oscillator. The passive Q-switch has frequency-selective properties due to its comparatively slow rate of change in transmission (i.e., its slow opening characteristics). The tilted etalons (TE1 and TE2) then provide final suppression of any satellite longitudinal modes.

Transverse mode selection is provided by two intracavity apertures (A1 and A2). A spherical mirror is used as the output mirror (M5). The master oscillator produces polarised pulses of single longitudinal and transverse mode with smooth temporal and spatial shapes. The output energy of these pulses exceeds 60 mJ at a wavelength of $\lambda = 1053$ nm; the pulse duration (full-width half-maximum, FWHM) is $\tau = 35$ ns. The intracavity beam shutter provides reliable blocking of the laser beam.

6.3.5.2 Amplification

A beam delivery scheme improves the oscillator output beam quality by natural “diffractive cleaning”. The output beam from the master oscillator is reflected by the mirrors M6 and M7. It is then reflected by Pr1, M8 and Pr2 before striking the parallel glass plate (GP). The glass plate provides a smooth beam translation in the x and y axes, and so allows fine beam adjustment at the phosphate glass laser rod in the amplifier pump chamber (AM). The total beam pass distance is approximately 4.5 m.

After cleaning, the beam expansion telescope (lenses T1 and T2) expands the oscillator beam to optimally fill the Nd:phosphate glass amplifier (AM). This leads to efficient energy extraction and preserves good beam quality. The telescope T1 and T2 employs precision x–y translation lens mounts and a precision collimation adjustment.

The broadened laser beam is directed by the mirrors M9 and M10 to the amplifier scheme, which consists of a polariser (P), the amplifier pump chamber (AM), a quarter-wave plate (WP), a positive lens (L) and a liquid mirror (SBS). An apodising aperture (A3) cuts off any remaining wings present in the transverse beam distribution at the input to the phosphate glass amplifier.

High-quality spatial and temporal distributions (Figure 6.9) are assured by a two-pass phosphate-glass amplifier (AM) design incorporating phase-conjugation by stimulated Brillouin scattering (SBS).

The high-efficiency glazed Al-ceramic reflector in the amplifier pump chamber has a common channel for lamp and rod cooling, ensuring extremely uniform pumping from a single flashlamp. The G2J model uses a $\varnothing 12 \times 300$ mm GLS32 phosphate glass rod in the amplifier pump chamber. A xenon filled linear flashlamp INP13-250 (Zenit Company, Moscow) provides UV cut-off to increase the lifetime of the laser rod.

* SBS mirrors are liquid mirrors that reflect a phase-conjugate of the incident beam.

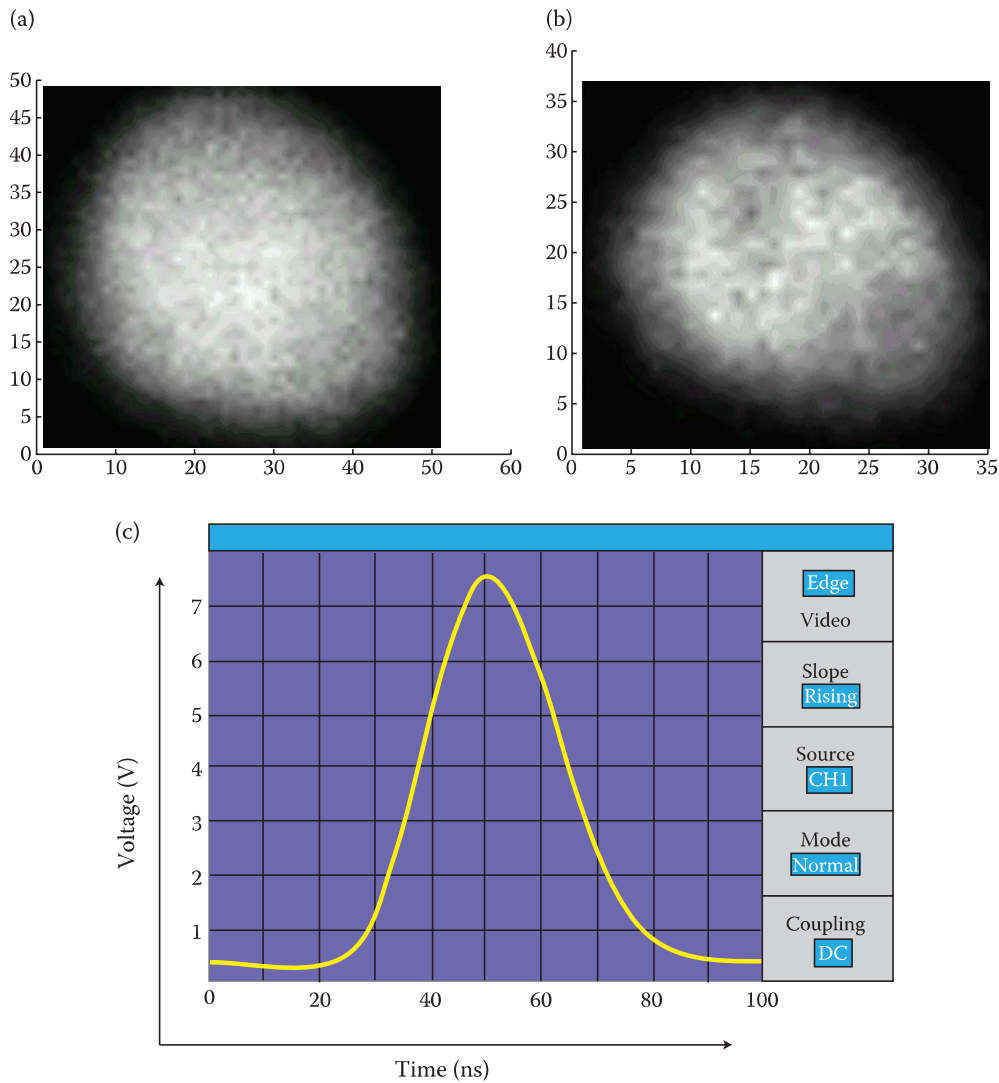


FIGURE 6.9 (a) Spatial beam distribution of the G2J Laser in near-field and (b) at 10 m from the laser head; (c) temporal distribution of the pulse.

The quarter-wave plate (WP2) and thin-film polariser (P) together form an optical separator which ensures that the second-pass (backwardly travelling) beam through the amplifier is diverted into the output channel (at P) and not back into the master oscillator. The quarter-wave plate ensures exact 90° polarisation rotation after the second pass. This suppresses any radiation going back into the master oscillator scheme. The use of a Brillouin cell (SBS) is very important for two reasons. First, SBS allows the formation of a diffraction-limited beam by compensation of the aberrations in the wave front, which are produced by the hot Nd:phosphate glass rod. This assures identical beam divergence and propagation direction in both the high-repetition low-energy alignment mode and in the usual high-energy, low-repetition mode. The second reason is the greater energy extraction possible with a double-pass scheme without self-excitation. Here, the Brillouin mirror serves as a selective reflector that reflects only a coherent signal and not the noise from any amplified spontaneous emission. As a result, around half of the stored energy in the Nd:phosphate glass rod is depleted.

The rotated second-pass radiation is reflected at the polariser (P) and directed to the mirror (M11). After the quarter-wave plate (WP), the radiation is converted to the second harmonic by a frequency doubler (FD). A deuterated potassium dihydrogen phosphate (DKDP) crystal is usually employed as the harmonic generator. This crystal must be sealed in a temperature-controlled dry cell because it is hydroscopic. A precision-engineered angle-tuning mechanism based on a simple mechanical design ensures excellent long-term stability of the harmonic output. This technique permits an energy conversion

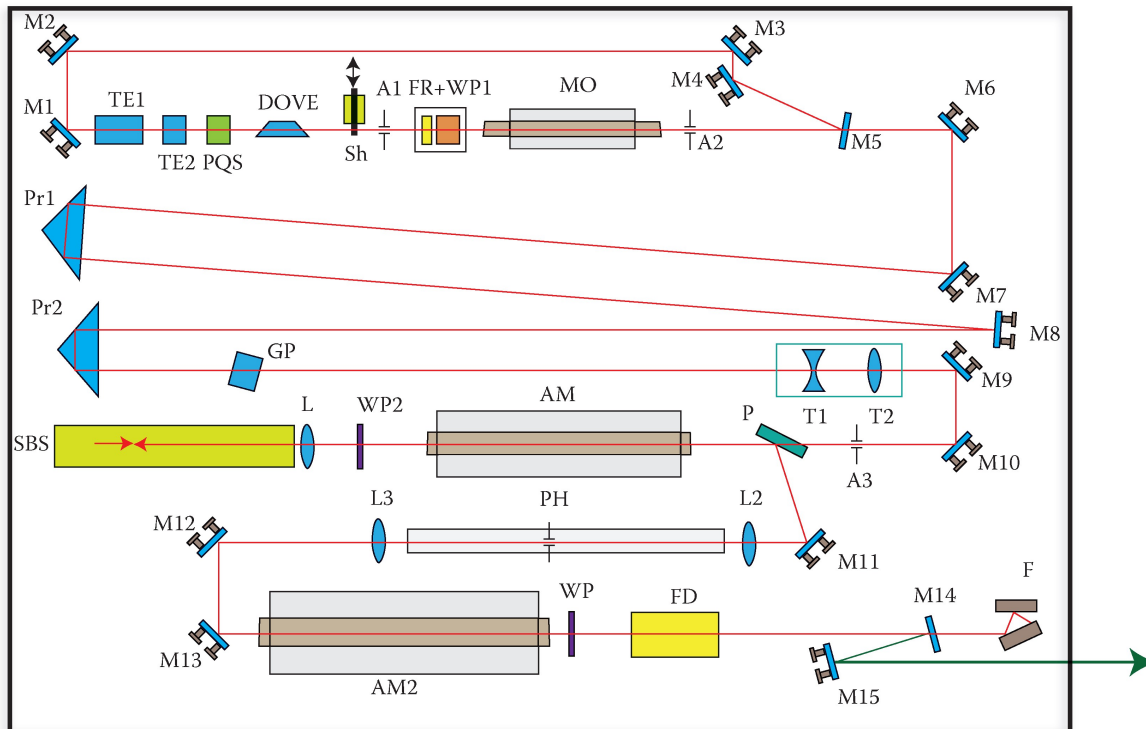


FIGURE 6.10 Optical schematic of the G5J Laser, a hybrid Nd:YLF/phosphate glass holography laser with an output of 5 J at 527 nm made by the Geola organisation.

efficiency to 526.5 nm of up to 60%. Harmonic separation is achieved by the pair of dichroic mirrors (M12 and M13), giving more than 99.7% separation. The residual part of the radiation at the basic harmonic wavelength is absorbed by two neutral density filters at the retroabsorption stage (F).

Figure 6.10 shows the optical scheme of a higher energy version of the laser capable of producing 5 J of output at 526.5 nm. This laser additionally uses a final stage large diameter Nd:phosphate glass amplifier ($\varnothing 20\text{ mm} \times 300\text{ mm}$) producing laser pulse amplification with almost complete stored-energy depletion. This amplifier is single pass and uses image plane translation lenses (L2 and L3) incorporating vacuum spatial filtering (PH). Vacuum filtering assures effective decoupling between amplifiers, thus preventing unwanted lasing, while also improving beam quality.

Two of the most important parameters for a holographic laser are beam distribution and coherence. The lasers described here have output pulse durations of approximately 35 ns with a coherence length of more than 3 m. The spatial profiles are quasi-Gaussian and have been optimised for holography.

6.3.5.3 Pump Electronics

The power supplies required for driving the flashlamps of the master oscillator and amplifiers each consist of a capacitor bank, a capacitor charging circuit, a trigger and pulse-forming module and a driving controller. The main capacitor bank is connected in series through an inductor directly to the flashlamp. The value of inductance essentially defines the characteristic pumping time. In the oscillator power supply, a high-frequency converter based on bipolar transistors with isolated input/output is used as the capacitor-charging unit. This unit has a power density of 0.3 W/cm^3 and presents a smooth noiseless load to the mains supply. The maximum output voltage is 1200 V with a stability of $\pm 0.15\%$. The charge rate of the module is 520 J/s. Typical capacitor bank and inductor values for the oscillator lamp are $100\text{ }\mu\text{F}$ and $100\text{ }\mu\text{H}$, respectively.

In the amplifier power supplies, a direct 50 Hz high-voltage network transformer incorporating rectifier, and driven by a thyristor switch, is used as the capacitor charging unit. Such an electronic system ensures ultrahigh reliability. The voltage stability is $\pm 0.2\%$. The amplifier in the G2J Laser uses a capacitor bank of $500\text{ }\mu\text{F}$ and an inductance of $100\text{ }\mu\text{H}$, whereas the second amplifier in the G5J laser uses



FIGURE 6.11 Photograph of the G5J Twin, a laser with two mutually coherent 5J outputs at 527 nm. (Courtesy of Geola Digital UAB.)

726 μF and 100 μH . Typical operating voltages of the two amplifiers are 1.7 kV (amp1) and 2.3 kV (amp2). Maximum stored energies are, respectively, 2.2 kJ (amp1) and 3.3 kJ (amp2).

The trigger modules of the various power supplies provide reliable operation of the commercially available flashlamps (INP5-75, INP13-250* and INP16-250). Series triggering is used for ignition of the flashlamps. The oscillator module provides an 18 kV triggering pulse for initial plasma creation—a “simmer” circuit then maintains ionisation; both amplifier modules provide a 25 kV triggering pulse. The pulse-forming modules are of a fixed pulsedwidth type. The modules consist of a capacitor bank, an inductor and a series-triggering transformer with driving circuits. The discharge pulse duration is optimised for two constraints: (i) optimal efficient performance, which is produced by matching the intrinsic fluorescence lifetime of the Nd:YLF crystal or of the Nd:phosphate glass rod, and (ii) maintaining a sufficient flashlamp lifetime, which usually equates to not pumping too quickly.

6.3.5.4 Cooling

The xenon flashlamps used to excite laser operation produce considerable heat. As with the ruby laser, this heat must be dissipated by a liquid cooling circuit. Both the G2J and G5J lasers use either the PS1222CO unit from the Lithuanian Company, Ekspla UAB or equivalent units made by the German Company, Termotek, AG for this purpose. This 2 kW water/water type heat exchangers provide excellent heat removal from the operating laser. A magnetic drive centrifugal pump is used for the circulation of the cooling liquid, which is usually a mixture of deionised water and ethanol. This pump provides noiseless operation. The cooling unit stabilises the temperature of the cooling liquid in the internal loop with an accuracy of 0.2°C.

6.3.6 Towards Even Higher Energy

Some advanced applications in holography require higher energy than the lasers described previously can provide. Although it is perfectly possible to make lasers with larger glass amplifiers, the cost can rapidly get out of hand. Often, the output laser beam in holography is split into a reference beam and several object beams. As a result, it turns out to be cheaper to produce lasers with multiple mutually coherent outputs. Such lasers can be constructed by using a single laser oscillator feeding one or more separate amplifier chains. Figure 6.11 shows an example of a commercial holography laser based on this principle. The laser produces a total of 10 J at 526.5 nm in two 5 J beams. The master oscillator is in fact an exact copy of the G2J/G5J oscillator. The output beam energy is then increased by a single-pass

* Note that the INP13-250 lamp is used without simmer.

Nd:YLF preamplifier before being split and fed into identical amplifier and frequency conversion chains. The amplifiers and frequency convertors are identical to those in the G5J laser discussed previously. Care must be taken to use the correct highly purified SBS fluid for the two-pass amplifiers to assure small and equal frequency shifts from the SBS cells. If this is not done, the mutual coherence of the beams can be compromised. The Geola G10J-Twin has an auto and mutual coherence of greater than 10 m. The concept can be extended to virtually any number of channels.

6.3.7 Applications

Geola has produced (and still produces) semiautomatic holographic portraiture systems based on its neodymium glass lasers [26–31] (Figure 6.12). These systems are able to generate both the transmission

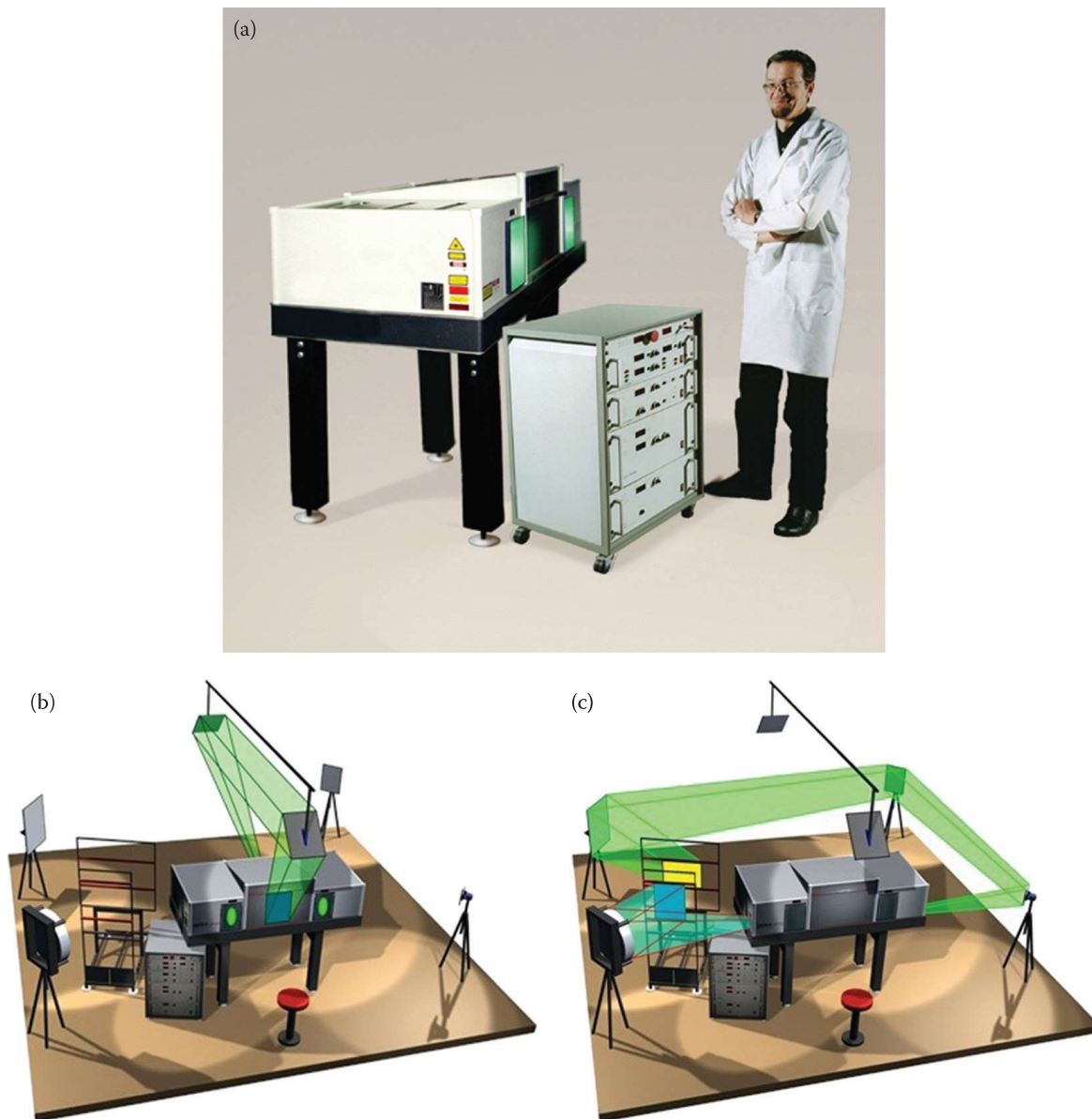


FIGURE 6.12 (a) Photograph of a commercial pulsed holographic portraiture system based on a 2 J Nd:YLF/glass laser; (b) mastering mode in which a pulsed H_1 transmission hologram is made; (c) copying mode, in which the H_1 hologram is transferred to a white light-viewable H_2 reflection hologram. The system automatically switches between modes (a) and (b), and sets all beam ratios and energies according to switch settings by the operator. Later models featured full computer control and automatic beam alignment. (Panel a, courtesy of Geola Digital UAB.)



FIGURE 6.13 Photograph of a portable pulsed holographic recording system based on a 2 J Nd:YLF/glass laser with special shutter allowing operation in ambient light. The system is designed for use in medical topometry, producing highly accurate three-dimensional computer models of patients' heads. (Courtesy of Geola Digital UAB).

master hologram and the final white light-viewable reflection copy. Options also allow rainbow holograms to be produced up to sizes larger than a square metre. The company has also worked with the Ceasar Institute in Germany to produce a medical topometry system that is portable and can be used in normal daylight [32,33] (Figure 6.13). The system works by recording a laser transmission hologram of a patient's head—the hologram is then scanned into a computer where an extremely accurate computer model of the head is generated. In effect, this application uses the ultra-realistic nature of holographic imaging to produce a three-dimensional computer model, which is rather more accurate than that available with other techniques.

6.4 High-Energy Two-Colour Emission: Stimulated Raman Amplification

A high-energy red beam at 674 nm may be efficiently produced by using the second harmonic output of a standard neodymium-pulsed laser to pump a simple laser based on stimulated Raman scattering (SRS) in pressurised hydrogen gas. In such a way, an intrinsically two-coloured red–green pulsed laser beam may be created far more economically than by mixing the beams of a ruby and a neodymium laser. It is worth pointing out that red–green holograms can sometimes give a very real impression of actually being full-colour holograms. Of course, this is not always the case, but given that the recording of a blue component is so much more problematic in pulsed holography due to the problem of Rayleigh scattering (which is present in all emulsions having a high enough sensitivity to avoid ocular damage to the human subject), there has been significant interest in such red–green concepts. Although present work has concentrated on SRS in hydrogen, replacement of the hydrogen with deuterium can be expected to produce a red-pulsed source of acceptable quality for holography at approximately 627 nm. Although in principle, anti-Stokes generation from a 527 nm pump can produce a blue signal, in practice, the quality of this beam has thus far been found insufficient for serious holographic applications.

SRS is well known as a simple and effective frequency conversion method. In its simplest form, a single cell known as an SRS-generator is filled with a compressed molecular gas such as hydrogen, and pump radiation from a Nd:YAG laser is then focussed to a point inside this cell. Under pumping by low-energy second harmonic (532 nm) pulses (pulse energy, $W_L < 50 \text{ mJ}$), an energy conversion efficiency

to Stokes radiation of up to 55% can be achieved in such simple schemes [34]. However, any further increase in the pumping energy leads to a decrease in the Stokes energy. Beyond a certain pumping threshold, any excess energy from the pump preferentially drives other competing non-linear processes in the SRS medium such as the generation of higher Stokes and anti-Stokes components, four-wave interactions and electro-optic breakdown. As the pump energy is increased, the probability of excitation of adjacent transverse SRS modes also increases.

The solution to producing a high-energy Stokes pulse suitable for holography is to use a more general scheme of SRS conversion incorporating the concept of a separate generator and amplifier [35]. In this case, a single mode Stokes seed with a smooth temporal shape is produced from a SRS generator cell by pumping just above the threshold. Further conversion then takes place in a separate Raman amplifier cell in which the collimated Stokes seed and the pump beam are collinearly mixed. To maintain a narrow spectral linewidth, compressed hydrogen is used as the SRS-active medium as this gas possesses the smallest known linewidth for spontaneous Raman scattering. Operation is in the collisional Dicke-narrowed region in which the spontaneous scattering linewidth can reach a value as low as 0.009 cm^{-1} (or 270 MHz) at a hydrogen pressure of only 3 to 4 atm. This linewidth can be additionally reduced during the SRS process by preferential amplification of the central spectral components.

If an optimised generation of Stokes radiation is to occur, the diameters of the interacting beams must be carefully chosen; in addition, the delay of the pump pulse relative to the Stokes seed must be optimised, and the hydrogen pressures in the generator and amplifier cells must be carefully equalised. Such optimisation allows conversion efficiencies close to the theoretical limit for the normal non-super-regenerative regime of Raman amplification. Practically, a maximum energy conversion efficiency to Stokes radiation of $\eta = 68\%$ has been attained to date. This is close to the theoretical limit of $\eta = 78\%$ given by the Manley–Rowe relation.

6.4.1 SRS Red–Green Pulsed Laser

We shall describe here a prototype SRS pulsed laser system, which was developed at Geola in the mid-1990s [35]. This laser was capable of producing 1 J of red radiation at 674 nm from a green pump pulse at 527 nm, at an efficiency of 68%.* Figure 6.14 shows the optical schematic of the system. A hybrid Nd:YLF/Nd:phosphate glass laser (a pre-commercial version of the Geola G5J model) is used as the pumping source for the forward Raman generator (RC1) and Raman amplifier (RC2). A pumping energy of $W_L \geq 5\text{ J}$ at a wavelength of 526.5 nm is available from the Nd:YLF laser. The temporal shape of a typical pump pulse is shown in Figure 6.15. The pulses are of a duration of 25 ns and exhibit a rather sharper leading edge and a rather more gently sloping tail due to the influence of amplification and Brillouin compression processes within the pump laser. The pump beam has a super-Gaussian intensity profile.

The output beam from the pump is divided into two parts by the polariser (P1). The ratio of the energy in the two beams is controlled precisely by the wave plate (WP1). The smaller of the two beams, after polarisation cleaning by the polarisers (P2–P4), is focussed by the lens (L1) to a point at the centre of Raman generator cell (RC1) which is filled with compressed hydrogen. The pressure in the Raman generator is 4 atm. Here, a single-mode Stokes seed is excited by pumping just over the threshold. This seed is then collimated by the lens (L2) and injected into the two-pass Raman amplifier (RC2) by the mirrors M1 and M2. The larger part of the second harmonic radiation serves as the pump for this amplifier. This part passes through the polariser (P1) and after restoration of its initial polarisation by the half-wave plate (WP2) passes through to the delay line M4 to M8. Image plane translation by the lenses L3, L4 and the pinhole (PH) is used to preserve the spatial distribution of the pump beam after several metres of optical delay. The collimated collinear pump and the Stokes beams are combined by the mirror (M3) and are directed into the forward Raman amplifier RC2 (1 m length). The windows of the RC2 cell are anti-reflection coated for both the wavelength of the pump and for the Stokes radiation at 674 nm. The exact alignment of the pump and seed Stokes beams must be performed using a He–Ne laser.

* We should mention that as early as in 1986, workers at Imperial College, in collaboration with Ilford, had succeeded in producing a small full-colour test hologram through Raman conversion of 532 nm radiation in high-pressure H_2 . However, the quality of the hologram was reported to be bad and the work was never published.

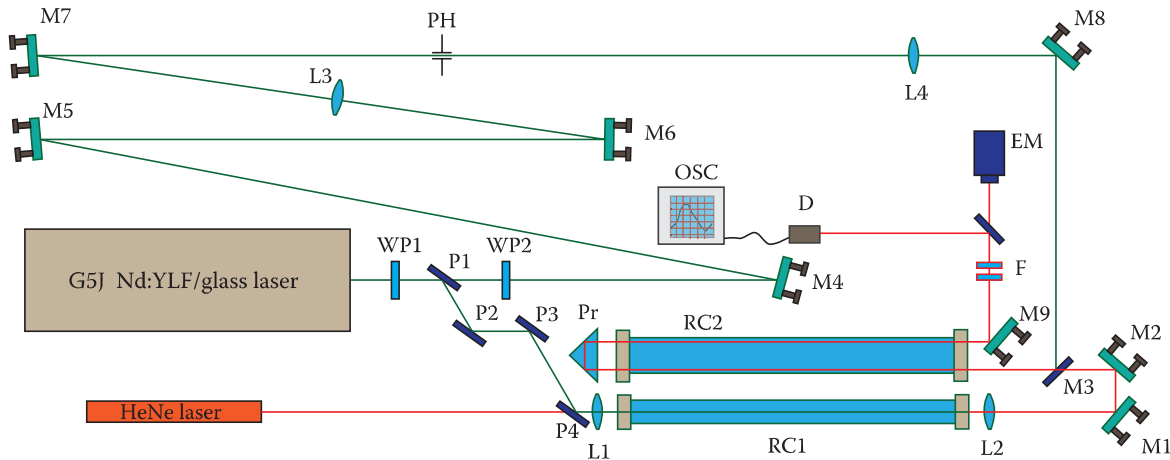


FIGURE 6.14 Optical schematic for forward Raman amplification of Stokes pulses in the Dicke-narrowed line of hydrogen.

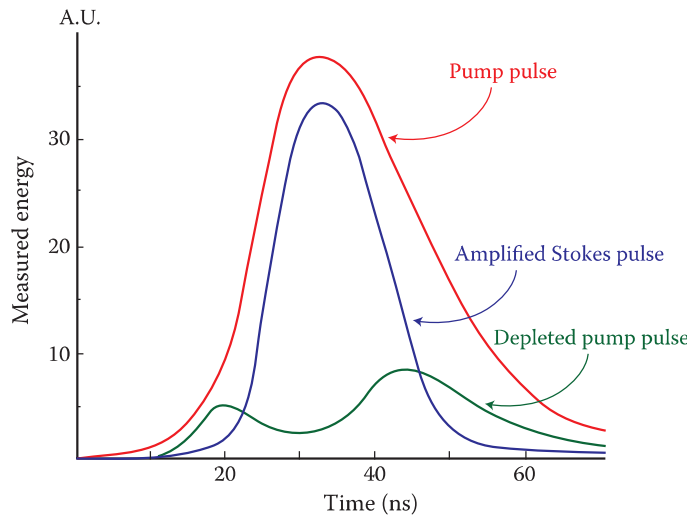


FIGURE 6.15 Typical temporal shapes of the pump pulse (red), the amplified Stokes pulse (blue) and the depleted pump pulse (green) for a conversion efficiency from 527 to 674 nm of greater than 55%.

After a first pass through the Raman amplifier, the transmitted beams are directed back into RC2 by the prism (Pr) for a second pass. M9 then directs the output beam, which consists of the depleted pump beam collinearly mixed with the Stokes beam, for analysis or use. The filters (F) weaken the output radiation and transmit either the Stokes or the depleted pump. The pulse energy is measured by an energy meter (EM). The temporal pulse shapes are measured by a fast oscilloscope (OSC) and a photodiode (D).

After optimisation of pump focussing in the generator cell (RC1) by selection of the lens (L1) and the optimal selection of input energy by rotation of the half-wave plate (WP1), a single-mode Stokes seed ($\lambda_{1S} = 674$ nm) with smooth temporal shape (Figure 6.16, blue curve) and Gaussian transverse beam profile is excited. The seed Stokes pulse typically has a rather sharper leading edge, a duration of approximately 10 to 15 ns (FWHM) and an energy of up to 1.5 mJ. The SRS generation threshold in the Raman generator should be exceeded by less than a factor of 1.4 to 1.7. Upon increasing the pumping to a factor of more than 2 over the threshold, deterioration of the temporal shape of the seed due to the onset of modulation typical of the transient SRS conversion regime is observed [34,36–38].

Due to the transient SRS conversion regime, the Raman amplification efficiency is strongly dependent on the delay between the pump pulses driving the amplifier RC2 and those driving the generator RC1. This delay is caused by the development of a phonon wave in the SRS-active medium provoked by the

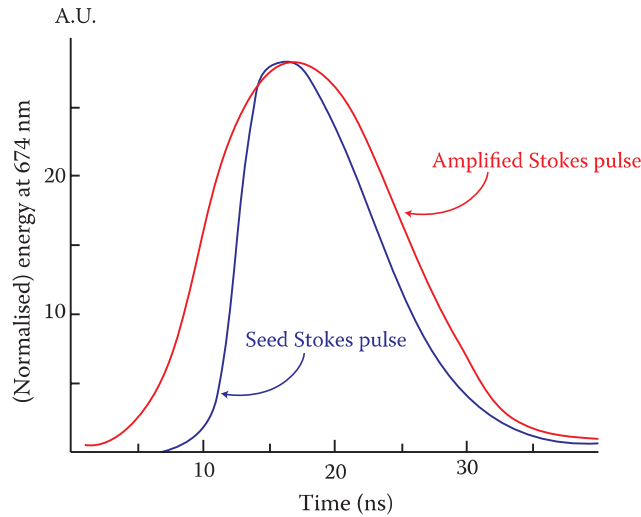


FIGURE 6.16 Temporal shapes of the seed Stokes pulse (blue) and the amplified Stokes pulse (red).

pump. Consequently, the Stokes pulse is emitted from the generator cell only at the end of the pumping pulse. In addition, the Raman amplification efficiency in the amplifier cell is maximal in the case that the seed Stokes pulse considerably precedes the instant corresponding to maximum pump intensity. Under a hydrogen pressure of 4 atm, the optimal delay amounts to approximately 20 ns. Detuning from this optimal delay of ± 4 ns leads to a 15% decrease in the Raman amplification efficiency. A similar strong dependence of the Raman amplification efficiency can be observed for a difference in the hydrogen pressures of the generator and amplifier cells. The Stokes shift, as well as the spontaneous Raman scattering linewidth, is hydrogen pressure-dependent [39]. A pressure disparity in the cells of only 1 atm leads to a detuning of the seed spectrum from the centre of the SRS amplification gain profile of one-half of this profile width. Under such detuning, the efficiency of Raman amplification is reduced by 20%. Hence, to achieve maximal efficiency, the pressure in the cells must be equalised exactly. This can be assured by using a flexible hose that effectively connects the generator (RC1) and amplifier (RC2) cells.

Figure 6.17 shows the typical experimental dependence of the energy conversion efficiency in the Raman amplifier on pump energy W_L . It can be seen that even under pump energies of $W_L > 0.7$ J, the conversion efficiency goes into saturation. In optimal conditions, using a pump energy of $W_L > 1$ J, a

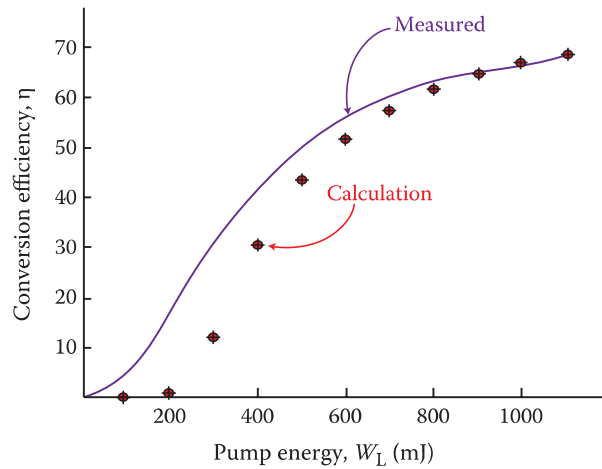


FIGURE 6.17 Typical experimental dependence of the energy conversion efficiency in the Raman amplifier with pump energy W_L for the case of a Raman seed energy of 1 mJ. The expected efficiencies as calculated from a three-dimensional computer simulation of forward transient SRS are also shown.

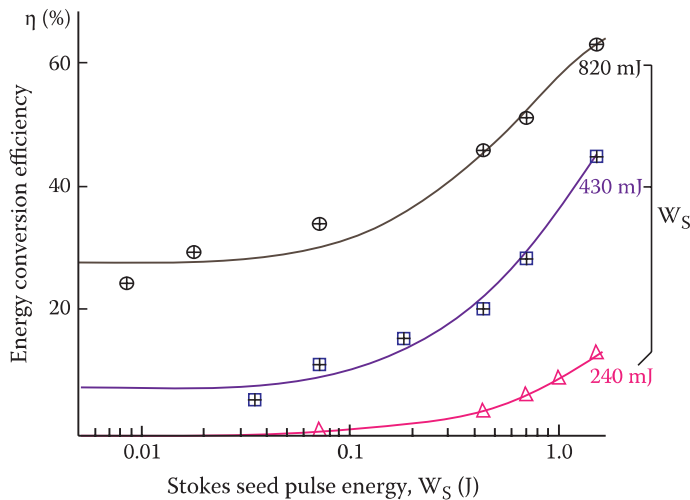


FIGURE 6.18 Dependence of Raman amplification efficiency versus injected seed energy measured for various values of the pump energy.

Stokes conversion with an efficiency of 68% can be expected. Self-excitation in the Raman amplifier at a pump energy of less than 1.1 J should not be observed in the absence of a Stokes seed pulse.

Figure 6.18 shows the dependence of the Raman amplification efficiency versus the injected seed energy measured under various values of the pump energy. As can be seen from these curves, the SRS conversion efficiency depends comparatively weakly on the energy of the injected seed over a wide range. The coherent properties of the radiation produced by the SRS converter are strongly controlled by the temporal shape of the pulses and their transverse beam profiles. Figure 6.15 shows typical shapes of the pump pulse (red curve), the amplified Stokes pulse (blue curve) and the depleted pump pulse (green curve) for a conversion efficiency of more than 55%. The amplified Stokes pulse has a smooth temporal shape and a duration of 18 ns, 30% lower than the pump pulse duration but 1.3 to 1.5 times higher than the seed Stokes pulse duration (Figure 6.16). The temporal shape of the Stokes pulses after amplification (Figure 6.16) becomes more symmetrical. The depleted pump pulses exhibit a large intensity hole close to the centre, which clearly demonstrates the high-energy conversion during Raman amplification. The transverse beam distribution of the amplified Stokes radiation generally mimics the pump beam distribution. When a pinhole is not used, diffraction rings on the pump beam are also seen on the amplified Stokes beam distribution.

Because the pump beam is severely depleted by the creation of the Stokes beam, it is usually necessary to dump this beam using a dichroic mirror and to then remix the Stokes beam with a clean collinear beam at 527 nm, again using dichroic mirrors. This assures a two-colour red–green beam of the correct spatial distribution for holography.

6.5 Pulsed RGB Lasers—Neodymium Lasers at 1.3 μm

Nd:YAG, Nd:YLF and Nd:YAP can all be made to produce laser action at 1.3 μm with the relatively strong $^4F_{3/2} \rightarrow ^4I_{3/2}$ transition. In YAG, there are two lines that have very similar cross-sections at room temperature. These are the $R_2 \rightarrow X_1$ transition at 1319 nm and the $R_2 \rightarrow X_3$ transition at 1338 nm. The cross-section of both these transitions is approximately three times smaller than the main $R_2 \rightarrow Y_3$ transition at 1064 nm. Frequency doubling and tripling allow conversion of the 1.3 μm emission to red and blue outputs. Workers at Geola in Lithuania were the first to demonstrate that the 1.3 μm transitions in neodymium could be used to make a pulsed RGB laser suitable for digital holography [6]. Later work by the same group showed that much higher energies could be obtained by amplification of the 1.3 μm line but that such higher energy lasers, having energies up to 1 J in the red, green and blue, would be rather

expensive due to the smaller gain available at $1.3\text{ }\mu\text{m}$. Here, we shall only briefly mention amplification strategies. We shall concentrate instead on the relatively low energy pulsed lasers that can be realised most easily and efficiently using the $1.3\text{ }\mu\text{m}$ line. The largest application for these lasers is in digital holographic printing, where they have been used very successfully.

6.5.1 Dual-Ring Cavity Pulsed RGB Nd:YLF/Nd:YAG Laser

Historically, the first true RGB pulsed holography laser was a laser based on two separate ring resonators (Figure 6.19). The first resonator comprised a standard ring cavity oscillator using Nd:YLF and passive Q-switching very similar to that described in Section 6.3.5.1. Frequency doubling was used to convert the infrared emission at 1053 nm to green at 526.5 nm . The second resonator was based on a Nd:YAG crystal lasing at 1319 nm . Passive Q-switching was accomplished by V:YAG, which, at the time, was an extremely rare crystal to find with the correct parameters. Frequency doubling and tripling of the $1.3\text{ }\mu\text{m}$ emission were organised by lithium triborate (LBO) crystals. The laser produced highly coherent red (659.5 nm), green (526.5 nm) and blue (439.6 nm) TEM₀₀-like emissions of 1.8 , 3.4 and 1.6 mJ , respectively, at pulsed durations of 45 ns (green) and 60 ns (red and blue). The laser maximum repetition rate was 15 Hz .

Figure 6.20 shows an optical schematic of the RGB laser. The first resonator, which is used for green light generation, is defined by the four rear high-reflection mirrors (M1g, M2g, M3g and M4g) and a meniscus output coupler (M5g). The active element (MOg) comprises a 4 mm diameter cylindrical Nd:YLF crystal that is 95 mm long with a 1% doping level, lasing at 1053 nm . The crystal is bevelled at each end at 3° to prevent reflection from these surfaces, creating an unwanted laser resonator. The crystal is pumped by a 75 mm xenon flashlamp, Samarium filters and ceramic reflectors housed in a custom pump chamber. Giant pulse operation is assured by a Cr:YAG passive Q-switch (Qg) with initial transmission of 47% . A 2.7 mm intracavity aperture (A1g) restricts lasing to TEM₀₀. A Dove prism (DPg) is likewise used to improve horizontal stabilisation of the vertical ring cavity. A Faraday rotator (FRg) and wave plate (WP1g) assure unidirectional lasing by introducing a direction-dependent loss. To achieve SLM operation, two air-spaced etalons are required: TE1g with a free spectral range of 3.26 GHz and

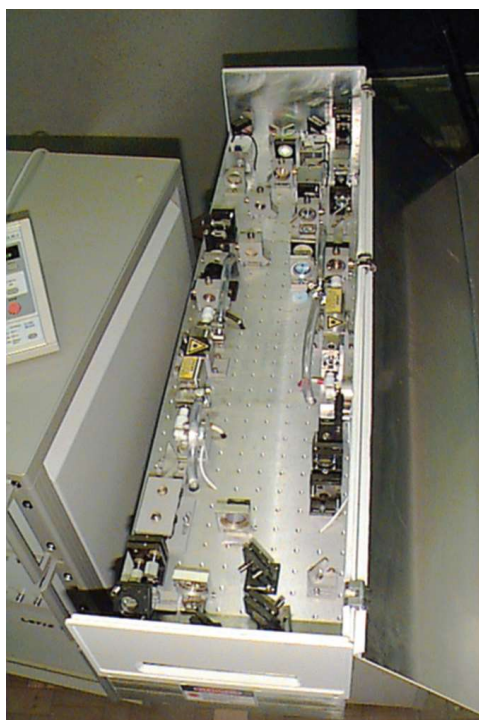


FIGURE 6.19 Original dual-ring cavity pulsed RGB holography laser from Geola (circa 2000).

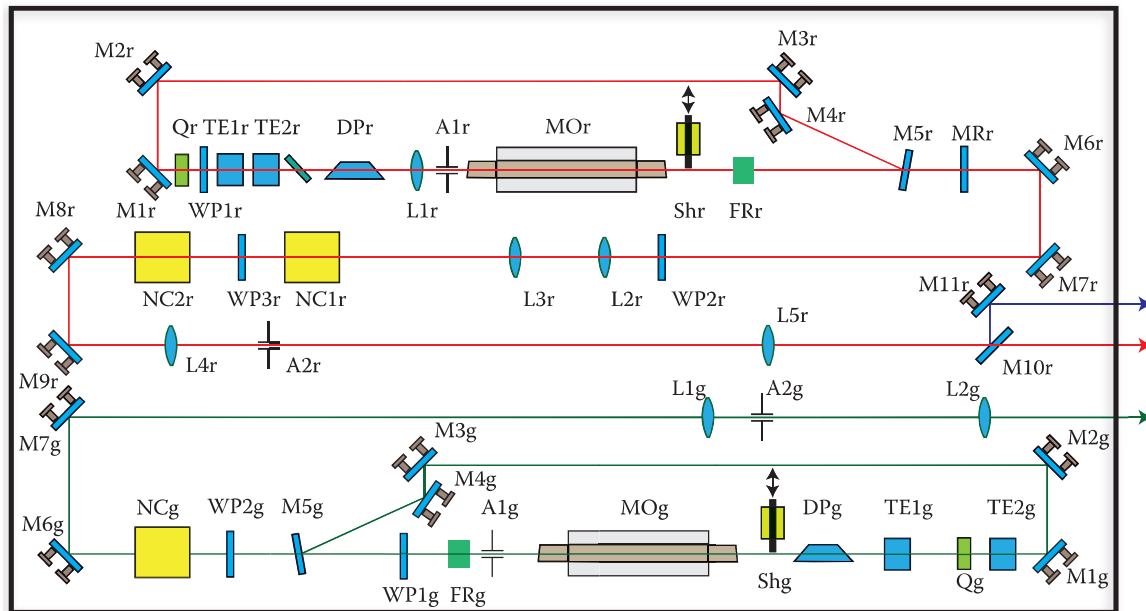


FIGURE 6.20 Optical schematic of the dual-ring cavity RGB pulsed holography laser.

TE2g with a free spectral range of 50 GHz. Frequency conversion to 526.5 nm is assured by an oven-mounted potassium dihydrogen phosphate (KTP) crystal (NCg) with wave plate (WP2g) as required for type II phase matching.

The second resonator, which is used for red and blue light generation, is defined by the four rear high-reflection mirrors (M1r, M2r, M3r and M4r) and a meniscus output coupler (M5r) having a small positive

TABLE 6.3

Parameters of First Commercial Dual-Ring Cavity RGB Pulsed Holography Laser

Parameter	Value
Master oscillator (1053 nm) flashlamp pump energy (threshold)	25 J
Measured master oscillator output energy (1053 nm)	27 mJ
Measured output energy (526.5 nm)	3.4 mJ
Energy stability of output pulses (526.5 nm) for 1200 pulses (σ)	$\pm 4\%$
Master oscillator (1319 nm) flashlamp pump energy (threshold)	28 J
Measured master oscillator output energy (1319 nm)	18 mJ
Measured output energy (659.5 nm)	1.8 mJ
Energy stability of output pulses (659.5 nm) for 1200 pulses (σ)	$\pm 4\%$
Measured output energy (439.7 nm)	1.6 mJ
Energy stability of output pulses (439.7 nm) for 1200 pulses (σ)	$\pm 8\%$
Coolant temperature setting	25°C
Coolant reservoir capacity:	4 L
External water temperature	<18°C
External water pressure	>150 kPa
Flow rate	<5 L/min
Cooling liquid type:	Ethanol 20% distilled water solution
Power consumption (220/240 V AC50/60 Hz, single phase):	<1250 W
Power supply PS-2241M:	<1000 W
Cooling unit PS1222CO:	2000 W
Grounding	<0.5 Ω

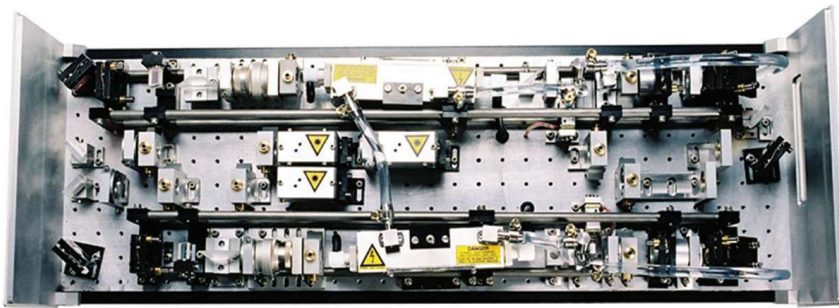


FIGURE 6.21 Later model dual-ring cavity pulsed holography RGB laser utilising super-invar resonators (circa 2002).

curvature. The active element (MOr) comprises a 4 mm diameter cylindrical Nd:YAG crystal that is 79 mm long with a 1% doping level, lasing at 1319 nm. As with the Nd:YLF crystal of the first resonator, the Nd:YAG crystal is bevelled at each end at 3° and is pumped by a 75 mm xenon flashlamp, Samarium filters and ceramic reflectors housed in a custom pump chamber. It is also antireflective (AR) coated for 1064 nm. Giant pulse operation is assured by a V:YAG passive Q-switch (Qr) with initial transmission of 53%. As above, TEM_{00} oscillation is arranged by a 2.7 mm intracavity aperture (A1r) and a Dove prism (DPr) is used to improve horizontal stabilisation. Unidirectional lasing is guaranteed by a return mirror (MRr) in addition to the Faraday rotator (FRr) and wave plate (WP1r). SLM operation requires, as with the green resonator, the use of two etalons: TE1r, a quartz etalon, and TE2g, an air-spaced etalon with a free spectral range of 96 GHz. The polariser (Pr) selects the correct cavity polarisation. Frequency conversion to 659.5 nm is assured by an oven-mounted KTP crystal (NC1r). The red and infrared signals are then combined in an LBO crystal (NC2r) where a third harmonic generation (THG) produces emission at 439.6 nm.

Table 6.3 lists the main parameters of the laser. To attain adequate stability for the intended application of digital holography, the resonators were mounted on a temperature-controlled aluminium breadboard. Later models (circa 2002) featured super-invar resonators (Figure 6.21).

6.5.2 Dual Linear-Cavity Pulsed RGB Nd:YAG Laser

To improve the stability and repetition rate of the pulsed RGB laser discussed in the previous section, the UK company, Geola Technologies Ltd., working in association with the Canadian company, XYZ Imaging Inc., produced a second-generation pulsed RGB laser in 2004 (Figure 6.22). This laser was based on twin linear Nd:YAG resonators, and replaced the passive Q-switching at 1.3 μm with the better-known crystal Co:MALO. Output was at 532 nm (6 mJ/35 ns), 659.5 nm (4 mJ/50 ns) and 438.6 nm (2.8 mJ/50 ns). The laser also incorporated electronic feedback of the cavity length to stabilise both

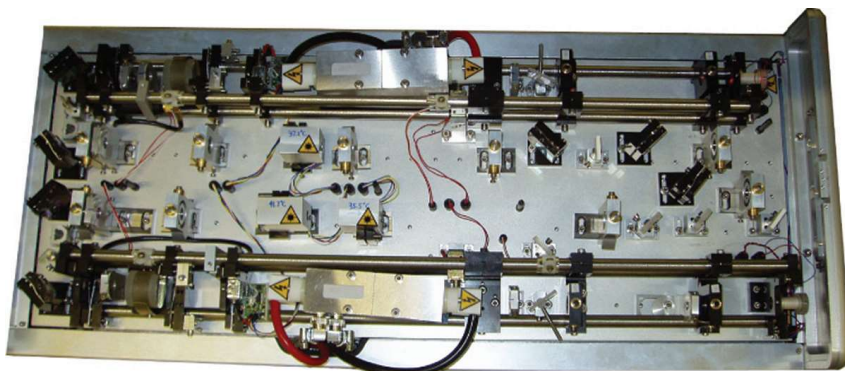


FIGURE 6.22 Photograph of the interior of a dual linear-cavity RGB pulsed holography laser manufactured by Geola Technologies (circa 2004).



FIGURE 6.23 Modern commercial RGB pulsed holography laser from Geola.

frequency and pulse energy output; this was a technique that made it realistically possible to avoid essentially any bad pulses [40] when using the laser to write composite reflection holograms comprising well over a million separate hogels (see Appendix 3).

Usual operation of these lasers is at 30 Hz, but stable operation has been tested to 50 Hz. With appropriate pump chambers, operation should be possible with the same design at up to 120 Hz. The company Geola Digital UAB currently offers various commercial laser models based on this design using Nd:YAG, Nd:YLF and Nd:YAP crystals (Figure 6.23). Table 6.4 lists the principal characteristic parameters of these commercial laser systems.* In 2009, workers at Geola also succeeded in producing an electro-optically Q-switched version of the 1.3 μm resonator for applications in which extremely accurate pulse triggering is required [41].

Figure 6.24 shows the optical scheme for the dual-channel 2004 Nd:YAG RGB pulsed laser of Figure 6.22. The laser consists of two channels. One channel (the “G channel”) generates 1064 nm laser light; green light (532 nm) is then achieved after frequency conversion. Another channel (the “R + B channel”) generates 1319 nm laser light; red (660 nm) and blue (440 nm) are then achieved after second harmonic generation (SHG) and third harmonic generation (THG).

The optical schemes of the 1064 nm channel and the 1319 nm channel are nearly identical to each other, except that the position of the passive Q-switch is different. For economy of space and time, we will describe only the 1319 nm channel in detail.

The linear cavity master oscillator of the 1319 nm channel is built using a two-mirror scheme comprising an output coupler (M1r) and high-reflectivity mirror (M2r). A 4 mm diameter Nd:YAG laser rod 95 mm long is mounted in a pump chamber with a close-coupled diffuse reflector and is pumped by a xenon-filled linear flashlamp (NL7054 from Heraeus Noblelight). The close-coupled diffuse reflector provides uniform rod pumping and UV filtration. Transverse mode selection and thermal lens compensation is provided by an intracavity telescope (lens L1r and L2r). This telescope also helps to shorten the cavity length and to increase the TEM_{00} mode size several times inside the Nd:YAG active rod (MOr), so that it can produce a high-output energy at low pumping level. SLM generation is achieved with the use of two etalons (etalon TE1r and etalon TE2r), a passive Q-switch (Q_r), which is placed between the intra-cavity telescope (while in the 1064 nm channel, the passive Q-switch is placed near the output coupler) and a rear cavity mirror operating with active feedback. To improve SLM stability, the etalon (TE2r) is placed in a temperature-controlled oven. In addition, two quarter-wave plates (WP1r and WP2r) are used to avoid spatial hole burning in the Nd:YAG laser rod and to improve the longitudinal mode selection.

* Very recent research at Geola has demonstrated that good lasing can be achieved at the Nd:YAG transition of 1356 nm using lamp pumping. Frequency doubling to 678 nm and tripling to 452 nm are possible.

TABLE 6.4

Specifications of Modern Commercial Pulsed RGB Holography Lasers from Geola Digital UAB

Nd:YLF	RGB-α-1353			RGB-α-1347		
Wavelength (nm)	657	527	438	657	524	438
Energy (mJ)	3.5	6.0	2.5	3.5	5.0	2.5
Pulse duration (ns)	35	35	30	35	35	30
Nd:YAP	RGB-α-1379			RGB-α-1379F		
Wavelength	671	540	447	1079	1341	
Energy	3.5	5.0	2.5	20	18	
Pulse duration	45	35	40	40	55	
Nd:YAG	RGB-α-1964			RGB-α-3864		
Wavelength	660	532	440	669	532	446
Energy	4.0	6.0	2.8	3.5	6.0	2.5
Pulse duration	50	35	50	50	35	50
Parameter	Value					
Typical energy stability (SD)	<3% over 10,000 pulses (without active stabilisation.)					
Beam divergence	Diffraction limited					
Linewidth	<0.003 cm ⁻¹					
Beam diameter (1/e ₂)	5...9 mm					
Beam profile	Near-Gaussian in near field, Gaussian in far field					
Repetition rate (Hz)	10/20/30/40/50					
Beam pointing stability (μ rad)	<150					
Polarisation	Horizontal or vertical >90%					
Q-Switching	Passive or electro-optical					
Jitter	5 μ s (passive Q-switching); 1 ns (EO Q-switching)					
Triggering	External/internal					
Laser head (L \times W \times H)	860 \times 360 \times 180 mm					
Power supply (L \times W \times H)	600 \times 550 \times 550 mm					

In the 1319 nm channel, the output energy and the pulse duration can be changed by moving the position of the Q-switch (Qr). The master oscillator generates horizontally polarised output pulses [determined by polariser (Pr) and the quarter-wave plates] with an energy of approximately 20 mJ and a pulse duration of approximately 70 ns, whereas in the G channel, fundamental output is approximately 13 mJ with pulse duration of approximately 45 ns. The beam shutter (SHTr) provides blocking of the laser beam on demand.

The output beam from the output coupler is reflected by a 45° mirror (M3r) before passing through an antireflection-coated window to reach another 45° mirror (M4r). A photodiode captures the reflected beam, providing information about pulse shape and output energy; these are used for active feedback of the cavity length through the piezo element PZTr and monitoring.

The half-wave plate after mirror (M4r) changes the horizontally polarised output beam by 45°, which is necessary for SHG conversion. The negative lens (L3r) and positive lens (L4r) together form a telescope for beam condensation, which allows high conversion efficiency in the SHG and THG crystals.

The SHG crystal is a type II [1319(e) + 1319(o)→660(e)], non-critical temperature phase-matching crystal, whose phase-matching temperature for 1319 nm is approximately 42°C. The crystal is cut along the z axis ($\theta = 0^\circ$, $\varphi = 0^\circ$). Because of the absence of walk-off effects in non-critical phase-matching, it is possible to use a longer crystal to achieve higher conversion efficiency. In this case, the crystal is purposely placed so that its SHG beam (660 nm) is horizontally polarised.

The THG crystal is a type I [1319(o) + 660(o)→440(e)], phase-matching crystal, whose phase-matching angle is $\theta = 90^\circ$, $\varphi = 21.1^\circ$. In this case, the THG beam (440 nm) is vertically polarised. The ratio of blue

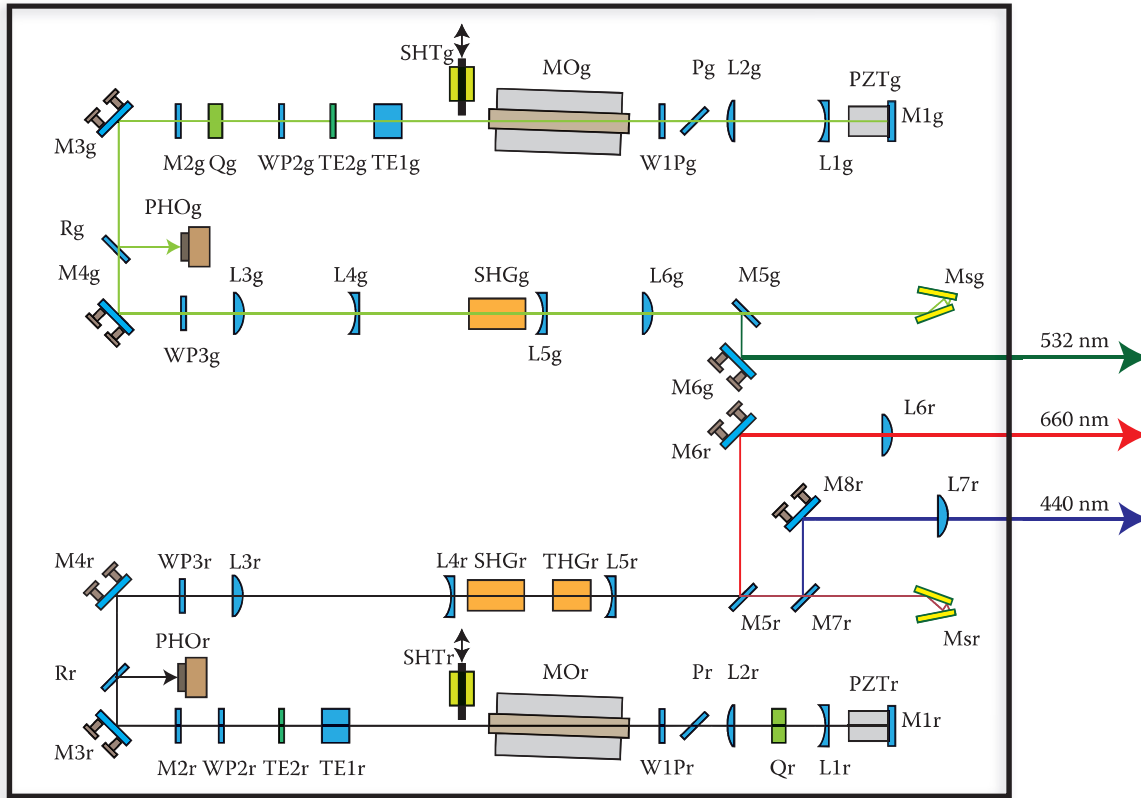


FIGURE 6.24 Optical schematic of the dual linear-cavity pulsed RGB holography laser in Figure 6.22.

(440 nm) and red (660 nm) beam output energy can be adjusted by slightly rotating the half-wave plate (WP3r).

Directly after the non-linear crystals, the fundamental beam, red beam and blue beam are collinear. The red beam is separated out and magnified by beam splitter M5r and M6r and telescope L5r/L6r, whereas the blue beam is treated by M7r and M8r, and L5r/L7r. The remaining fundamental beam is dumped to the beam diffuser (Msg).

The optical scheme of the G channel is almost the same as the R + B channel, except that, first, the position of passive Q-switch is different and, second, only one non-linear crystal is necessary for frequency conversion: a KTP type II phase-matching crystal is used to convert the 1064 nm infrared laser light into green light.

As with the dual-ring cavity laser, temperature stabilisation of the aluminium breadboard is vital for the type of stable output required for digital holography. This is arranged by a series of 27 small temperature controllers and heating pads capable of keeping every part of the breadboard at a constant temperature to within $\pm 0.02^\circ\text{C}$ (Figure 6.25). Both the linear resonators are also built using a construction employing three super-invar rods of ultra-low expansion coefficient. Final alignment of the laser must be done with its lid on such that the temperature stabilises around the resonators and is stable. This is accomplished via small holes in the lid and special tools.

The laser is able to operate at the same longitudinal mode at 1 μm and at 1.3 μm for a period of easily more than 30 min. However, after this period, mode-hops occur as the laser cavity length changes despite temperature control and the presence of super-invar resonators. This is usually caused by the efficiency of the flashlamp pumping changing in time as the lamp slowly degrades, producing different thermal loads on the active elements. Active stabilisation of the cavity lengths of both resonators proves extremely effective at stopping these mode-hops and allows continuous SLM operation at very stable energies for tens of millions of pulses. Cavity active stabilisation is covered in detail in Appendix 3. Very simply, it involves mounting the rear mirror on a piezo-crystal, or alternatively, inserting a thermally



FIGURE 6.25 Optical base of an RGB pulsed laser showing the mounting of multiple temperature controllers as well as liquid cooling and high-voltage connections.

controlled glass wedge within the cavity. The energy output from the cavity is then used to change the cavity length by either applying a voltage to the piezo-crystal or by heating the intracavity wedge. By using an algorithm that continuously optimises the output energy, the laser resonator is essentially always kept at its optimum position for oscillation at the incumbent longitudinal mode. The technique only fails when lamp degradation has continued to such an extent that the piezo or the wedge reaches their limit in producing a compensating cavity length change. Because one can tell when this is about to happen, it is possible to simply stop the laser and automatically recalibrate the active stabilisation system. Practically, when this happens, the optimal pumping voltage must be recalculated because the lasing threshold will have changed with lamp wear. Again, in modern commercial lasers, an automatic program takes care of these recalibrations.

6.5.3 Short-Cavity Pulsed RGB Lasers

All the lasers we have described previously have relatively large cavity lengths. As we have seen, one has to work hard to stabilise these lasers sufficiently for the testing application of digital holography. This is because long cavities are intrinsically unstable to thermal and mechanical stresses. One way forward is therefore to radically reduce the cavity length to produce what could be termed a short-cavity pulsed laser. At first sight, one might be tempted to raise two major objections to this idea. These are that a shorter cavity would be expected to naturally produce shorter pulse durations and also that a shorter cavity would have a smaller TEM₀₀ mode volume. A shorter pulse length is a potential problem as the most reliable photosensitive panchromatic silver halide materials tend to work only well above 30 ns. The smaller mode volume is also a potential problem because it can be expected to produce a lower energy pulse.

As it turns out, neither of the above problems are serious. By choosing the resonator parameters appropriately, and by employing passive Q-switches of an appropriate initial transmission, pulse lengths greater than 35 ns can be generated without problem. In addition, the output energy at 1 and 1.3 μm is still sufficient for many applications in digital holography [42].

6.5.3.1 Green Lasers

Figure 6.26 shows a schematic of a typical 1064 nm Nd:YAG short-cavity resonator. Photographs of the resonator are shown in Figure 6.27a to c. A rear cavity mirror and resonant output coupler are held in L-shaped steel tilted mirror holders and mounted on super-invar rods. The length of the linear cavity is 128 mm. Suspension of the cavity mirror holders using flat rigid springs on the rod structure allows precise X-Y alignment while isolating the sensitive resonator from baseplate temperature variations. A small stainless steel pump chamber (visible in Figure 6.27b) with diffuse ceramic reflector is mounted on

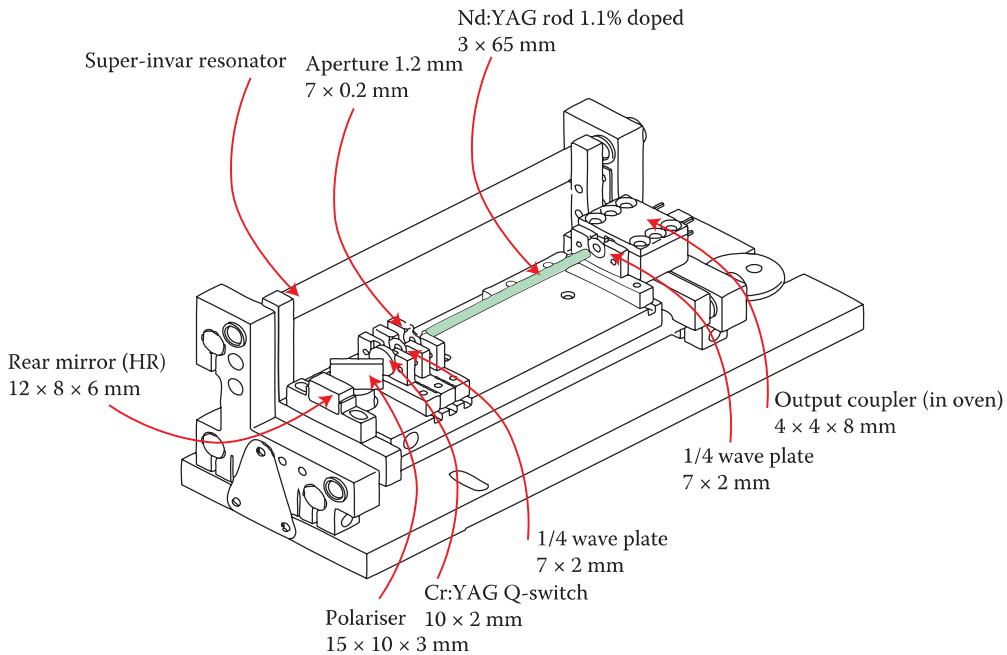


FIGURE 6.26 Short Nd:YAG resonant cavity oscillator ($l = 128$ mm).

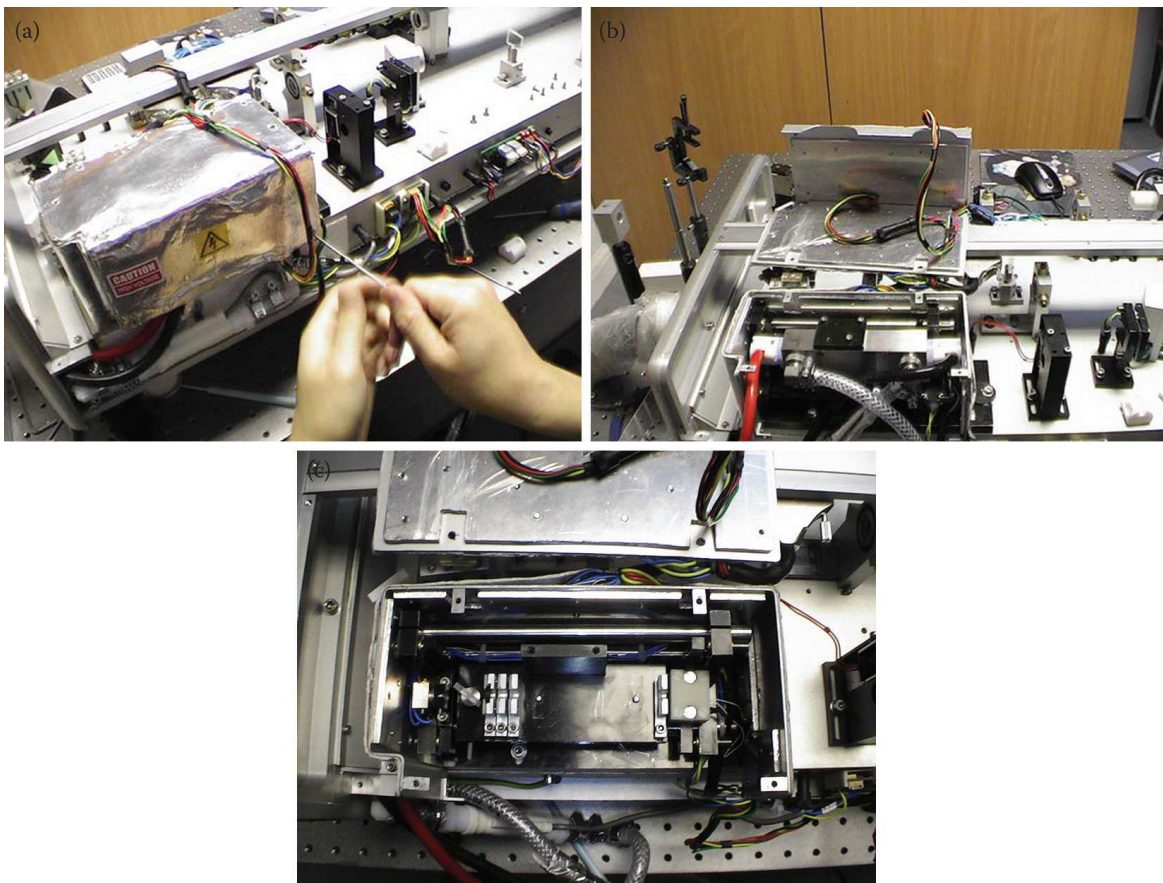


FIGURE 6.27 Three photographs of a short-cavity Nd:YAG oscillator. (a) View of external thermally stabilised cover; (b) cover removed showing stainless steel (lamp) pump chamber mounted within the super-invar resonator; (c) pump chamber removed exposing resonator and optics.

a steel baseplate in line with an intracavity aperture, a polariser, two quarter-wave plates and a Cr:YAG passive Q-switching crystal. The Nd:YAG active laser rod ($\varnothing 3\text{ mm} \times 65\text{ mm}$) was excited by a $\varnothing 5\text{ mm} \times 45\text{ mm}$ xenon-filled linear flashlamp with UV cut-off using Sm-doped glass. A laser power supply supplying pulses of up to 18 J at a repetition rate of up to 50 Hz is used to drive the pumping lamp. As usual, the function of the aperture is to restrict laser oscillation to TEM_{00} . The polariser likewise assures a single linear polarisation. The quarter-wave plates transform the cavity radiation to circular polarisation within the active element thus preventing spatial hole burning. The output coupler is usually made from an uncoated block of BK7 glass with parallel faces mounted in a temperature-controlled oven. This economical design allows frequency selection ensuring short-term SLM operation by acting as an etalon. It also allows cavity length control via computer adjustment of the oven temperature, which is required for long-term frequency and energy pulse stability.

By choosing a Cr:YAG Q-switch of an initial transmission of 76%, 43 ns pulses of SLM TEM_{00} linearly polarised radiation at 1064 nm can be generated at a lamp energy of 10 J per pulse. The energy from each pulse is approximately 1 mJ. Frequency conversion using a small reducing telescope and a type II oven-mounted KTP crystal (35.4°C) then produces stable pulses of 400 μJ at 532 nm. This is more than enough for modern panchromatic silver halide materials, which have a sensitivity of approximately 600 to 1500 $\mu\text{J}/\text{cm}^2$ depending on the exact type. For a hogel of 1 mm^2 , theoretically, one only then needs a pulse energy of 6 to 15 μJ . Of course, optical losses in the digital printer can increase this somewhat, but clearly, 400 μJ is far more than required.

For higher energy applications, more energy can be generated from the same laser resonator by using a Q-switch with lower initial transmission at the price of a reduced pulse duration (Figure 6.28). In addition, by placing the Q-switch between the two quarter-wave plates, greater pulse length can be attained for a given energy. In fact, pulse durations of up to 200 ns at output energies of 0.35 mJ can be attained in this way.

The short-cavity resonator is extremely stable when its temperature is properly stabilised. This is usually done by surrounding it in a metallic case that is kept at a uniform temperature by 10 or 20 individual thermocontrollers. The temperature of the output coupler is then fixed to an optimum level and this allows the resonator to produce tens of millions of pulses at the same longitudinal mode. Over 100 million pulses, it is usual to achieve a peak-to-peak energy stability of $\pm 3.5\%$.

Higher energy emission at arbitrary pulse duration requires amplification. Figure 6.29 shows an example of a commercial laser (model G-MINI-B10) made by Geola Technologies Ltd., which combines a short-cavity resonator as described here with a simple lamp-pumped one-pass Nd:YAG amplifier ($6\text{ mm} \times 100\text{ mm}$) giving more than 10 mJ at 532 nm with a pulsed length of approximately 12 ns. Typical output

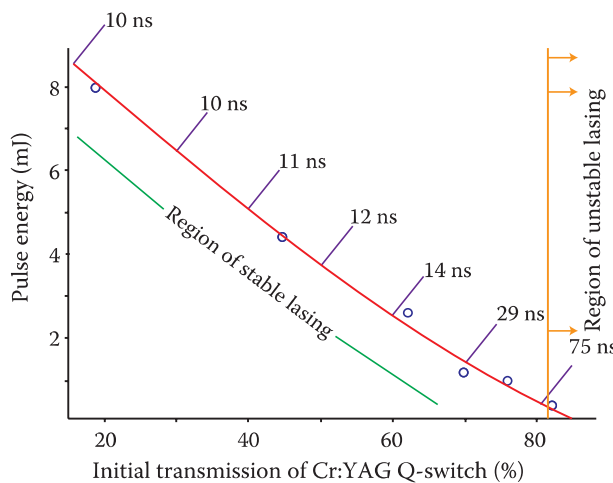


FIGURE 6.28 Pulse energy at 1064 nm versus initial transmission of the Cr:YAG Q-switch in a 128 mm short-cavity lamp-pumped Nd:YAG oscillator. Also shown are the corresponding pulse durations.



FIGURE 6.29 Commercial laser system based on the short-cavity oscillator concept designed for holography applications. The G-MINI-B10 shown here from Geola also incorporates a single-pass amplifier and frequency-doubling optics, producing an ultra-stable 532 nm output of >10 mJ per pulse at up to 10 Hz with a coherence length of >1 m.

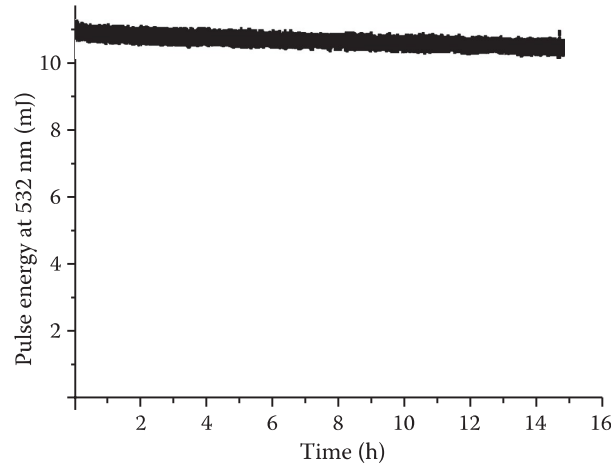


FIGURE 6.30 Typical plot of output pulse energy at 532 nm versus time of a G-MINI-B10 laser from Geola (all pulses plotted) showing ultra-stable operation. Note the gradual drop in energy due to wear of the amplifier flashlamp. Laser repetition rate is 10 Hz.

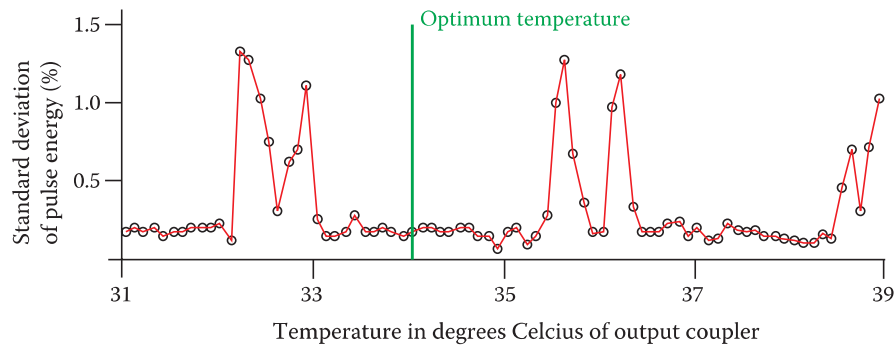


FIGURE 6.31 Computer scan of the output-coupler temperature of the short-cavity oscillator in a G-MINI-B10 showing stable and unstable regions. To guarantee long-term stability, the temperature must be set to the centre of the most stable region.

stability at 10 Hz is shown in Figure 6.30. To prevent mode-hops, the temperature of the output coupler must be set to an optimum level. This is determined by a computerised scan of oscillator output energy versus output coupler temperature (Figure 6.31).

6.5.3.2 Red and Blue Lasers

The short-cavity laser resonator described in Section 6.5.3.1 may be made to produce laser emission at 1.3 μm . Instead of the Cr:YAG Q-switch, a V:YAG or Co:MALO crystal is used. Because the gain at 1.3 μm is rather smaller than at 1 μm , a rather higher reflectivity must be used for the output coupler. Optics must be AR coated for 1064 nm as well as 1319 nm; otherwise, the stronger 1064 nm line will oscillate parasitically. The Nd:YAG rod must also be cut at 3° at both ends for the same reason. Finally, a rather longer excitation pulse must be used to excite the xenon lamp because too short a pulse will preferentially drive the 1338 nm line.

As with 1064 nm, the pulse duration of emission can be effectively tuned using the initial transmission of the passive Q-switch. For example, an energy of 1.2 mJ can be obtained at 45 ns. Typical energy stabilities for a resonator without active temperature stabilisation of the resonator cover or output coupler are 0.67% over 1000 pulses with a PTP stability of 3.7% [42]. With full temperature stabilisation, we again obtain single mode stable lasing for tens of millions of pulses.

To make a red laser emitting at 660 nm, a type II LBO crystal is used. Typical output characteristics are identical to the 532 nm laser. To make a blue laser emitting at 440 nm, however, the red 660 nm signal must be mixed with the 1319 nm signal in a type I LBO crystal using critical phase matching. The simplest way to organise this entails using two LBO crystals mounted very close to one another. Typical output characteristics for the blue laser are again very similar to the 660 nm laser except that a smaller conversion efficiency limits the energy to typically 300 μJ . Because a blue laser first entails the production of a red emission, and then mixing this signal with the infrared, a blue laser will always produce a residual red signal. By adjusting the incident polarisation to the non-linear conversion optics, a collinear red–blue laser may be made with a variable red–blue ratio.

6.5.4 Amplification at 1.3 μm : Higher Energy Emissions in the Red and Blue

Amplification at 1.3 μm is possible but quite inefficient using small seed energies. For example, starting with a 32 ns TEM₀₀ SLM pulse from a short-cavity oscillator at 1319 nm of 1.2 mJ, one can expect to obtain only 8.5 mJ after two-pass amplification using a 4 mm × 130 mm Nd:YAG 1.1% doped rod with standard lamp pumping [42]. Unfortunately, one cannot practically use an SBS mirror in the two-pass scheme as the one-pass energy is well below the threshold of any useful SBS liquid.

Luckily, amplification at higher seed energies is rather easier. For example, a long-cavity 1319 nm resonator as described in Section 6.5.2 produces 17 mJ TEM₀₀ SLM pulses of approximately 60 ns. These pulses may be amplified by a single 6 mm × 100 mm Nd:YAG 1.1% doped rod in a two-pass SBS scheme using SiCl₄ to produce 50 mJ. The SBS liquid mirror assures a good quality spatial distribution. This can be employed only because of the higher seed energy: typical one-pass gain is 2.4× and SBS reflectivity at 34 mJ is 60%. Using multiple amplifiers, energies up to 500 mJ and beyond should be easily attainable.

6.6 Pulsed Holography Lasers Based on Titanium Sapphire (Ti:Al₂O₃) and Cr:LiSAF

An alternative method to produce a blue-pulsed laser beam that is useful for holography is through the vibronic system of the titanium sapphire laser with amplification using Cr:LiSAF. This 860 nm laser can be frequency-doubled to produce a 430 nm blue beam.

Ti:Al₂O₃ laser crystals are grown using the Czochralski method and consist of sapphire doped with 0.1% Ti³⁺. The Ti³⁺ ions replace Al³⁺ ions. An energy level diagram of Ti:Al₂O₃ is shown in Figure 6.32. Laser transition occurs between the ²E excited state and the ²T₂ ground state. A large difference in the

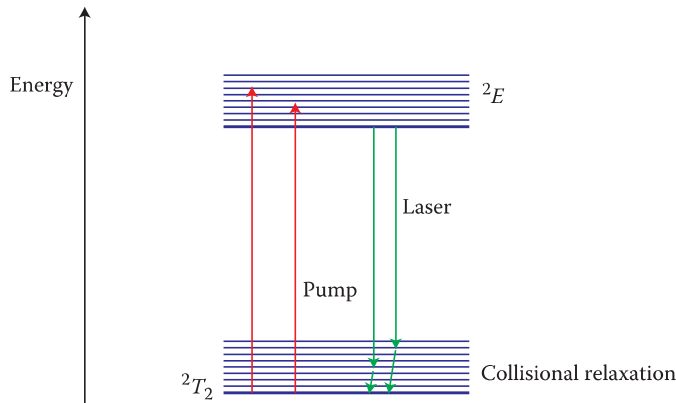


FIGURE 6.32 Energy level diagram for titanium sapphire ($\text{Ti:Al}_2\text{O}_3$).

electron energy distributions between these two levels and also the fact that there exists a strong interaction between the Ti atoms and the host crystal makes the transition fundamentally broad. Lasing is therefore possible over the wide band from 670 to 1070 nm, with fluorescence peaking at 780 nm. Although the material exhibits a large gain cross-section similar to Nd:YAG, it has a very small fluorescent lifetime (3.2 μs), making it rather inefficient for lamp pumping.

A similar vibronic laser to $\text{Ti:Al}_2\text{O}_3$ is the crystal Cr:LiSAF ($\text{Cr}^{3+}\text{LiSrAlF}_6$). This material has a much larger fluorescence lifetime of 67 μs , making it far more efficient for lamp pumping. Lasing is between the 4T_2 level and 4A_2 , giving rise to a peak emission at 830 nm. Cr:LiSAF has a cross-section of around eight times less than $\text{Ti:Al}_2\text{O}_3$. Nevertheless, this material can be made into very large crystals, making it rather suitable for use in lamp-pumped amplifiers.

In 1996, Lutz, Albe and Tribillon [43] produced a blue-pulsed laser suitable for holography* that was based on a $\text{Ti:Al}_2\text{O}_3$ oscillator and a Cr:LiSAF amplifier. The laser was lamp-pumped and produced an energy of 70 mJ at 430 nm, with a pulse duration of 110 ns. The coherence length of the laser was shown to be more than 1 m.

Figure 6.33 shows a diagram of the $\text{Ti:Al}_2\text{O}_3/\text{Cr:LiSAF}$ laser. The laser consists of three parts:

- A $\text{Ti:Al}_2\text{O}_3$ laser oscillator
- A Cr:LiSAF laser amplifier
- A frequency doubling system

The oscillator is of a linear type defined by mirrors M1 and M2, and has a cavity length of 1.45 m. The $\text{Ti:Al}_2\text{O}_3$ crystal is pumped by a flashlamp using single-pulse gain-switched operation. This simple mode does not require a Pockels cell; rather, the $\text{Ti:Al}_2\text{O}_3$ laser, when pumped by a single lamp pulse, simply produces a much shortened 110 ns laser pulse. Aperture A1 (2.5 mm) ensures that only the TEM_{00} mode oscillates. A SF4 Brewster-incident prism (P1) is used to select horizontal polarisation and to obtain a lasing wavelength of 830 nm. SLM operation is then obtained using the three etalons (ET1–ET3). The oscillator produces an energy of 4 mJ per pulse at 110 ns, an M^2 of 2.6 and a measured bandwidth of 250 MHz.

The amplifier is a simple three-pass design using a Cr:LiSAF crystal ($\varnothing 6\text{ mm} \times 101.6\text{ mm}$) doped with 0.8% Cr and mounted in a double-lamp pump chamber. A pump energy of 156 J is able to produce an amplified output pulse energy of 160 mJ at 860 nm.

After amplification, the beam is frequency-doubled using a crystal of KNbO_3 ($11.4\text{ mm} \times 10\text{ mm} \times 12\text{ mm}$) with AR coatings for both 860 nm and 430 nm. Type I phase matching allows an energy of 70 mJ

* Transmission and reflection holograms were produced using this laser on silver halide emulsions.

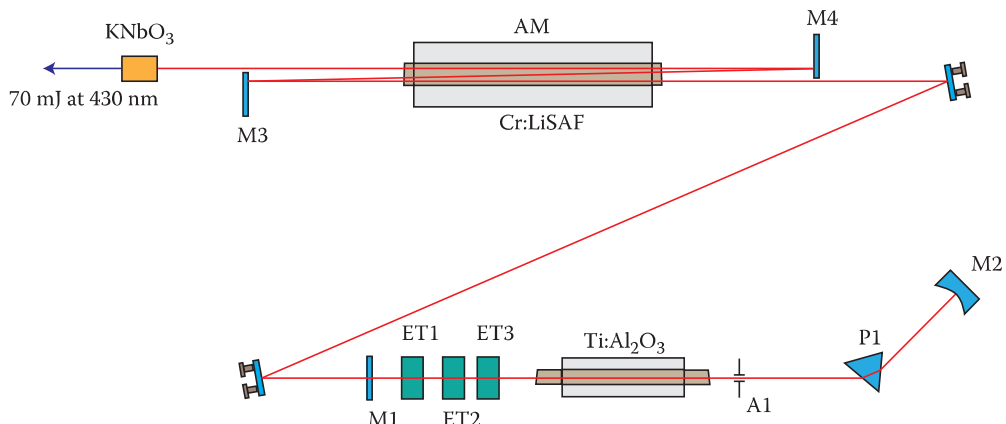


FIGURE 6.33 Optical scheme for a blue-pulsed laser based on a Ti:Al₂O₃ oscillator with amplification by Cr:LiSAF.

to be obtained at 430 nm. This type of laser should lend itself very easily to the production of the higher energies required for such applications as colour holographic portraiture.

6.7 Chromium Forsterite

Digital holographic printing is served extremely well by the neodymium lasers using the 1 and 1.3 μm transitions. However, the red radiation available from the best crystal hosts is still characterised by a rather large wavelength (657 nm). As we shall see in Chapter 13, modern red light-emitting diode illumination sources usually have wavelengths rather lower than this. As a result, for future digital printers, there is a desire to identify a laser solution having a wavelength of approximately 627 nm. One way to realise this is using the material chromium forsterite (Cr⁴⁺:Mg₂SiO₄). This is a vibronic system, like titanium sapphire, and possesses a wide band of laser transitions centred at approximately 1235 nm. Frequency doubling by KTP can be used to produce an emission of approximately 630 nm. By suitable design of the laser cavity and insertion of frequency-selective elements, a coherence length of several centimetres can be attained, which is sufficient for many applications in digital holography. This laser is usually gain-switched by pumping with a single pulse nanosecond Nd:YAG laser at either 1064 or 532 nm.

Figure 6.34 shows a simplified energy level diagram of the Cr⁴⁺ ion in forsterite. In the tetrahedral field of this crystal, the free ion ³F state is split into three states: ³A₂, ³T₂ and ³T₁ [44,45]. Lasing occurs through the ³T₂-³A₂ vibronic transition. The fluorescence lifetime of the ³T₂ state is 2.7 μs. Excited state absorption of pump and laser radiation occurs from ³T₂ to ³T₁; this is followed by fast relaxation back to the ³T₂ state. The main pumping bands are at 850 to 1200 nm, 600 to 850 nm and 350 to 550 nm.

A commercial system is currently available from the Byelorussian company LOTIS TII. This is the LT-2212G (Figure 6.35), which is designed to be pumped by the LS-2132 Nd:YAG laser. The system will produce several millijoules of useful energy in a 10 ns pulse at 627 nm (Figure 6.36). A linewidth of less than 0.01 nm is achieved by the use of a grating within the cavity. Unfortunately, a pulse duration of 10 ns can be rather short for exposing panchromatic silver halide materials.* In addition, initial unpublished tests done with the laser at the Centre for Laser Photonics in Wales in 2009 showed marginal shot-to-shot stability characteristics. As such more work needs to be done on this type of laser before it can be considered as a viable solution for digital holography.

* Double pulse pumping can be used to achieve longer output pulses.

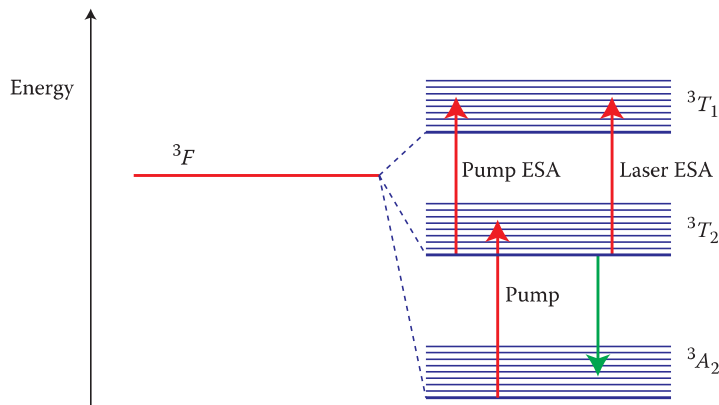


FIGURE 6.34 Simplified energy level diagram for $\text{Cr}^{4+}:\text{Mg}_2\text{SiO}_4$.



FIGURE 6.35 LT-2212G chromium forsterite laser from LOTIS TII.

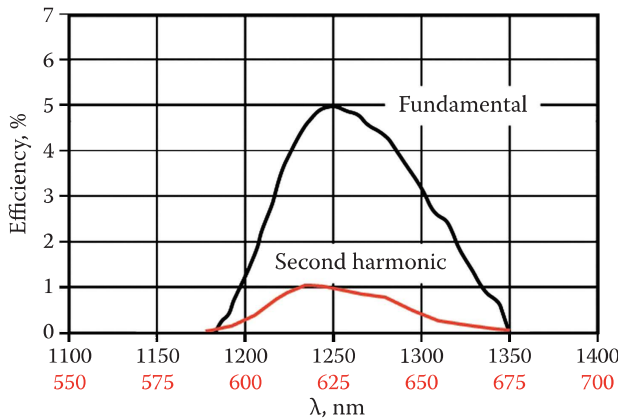


FIGURE 6.36 Tuning curve for the LT-2212G laser (pumped at 1064 nm with 150 mJ using a LOTIS TII LS-2132 Nd:YAG laser).

6.7.1 Injection Seeding

One strategy for improving both the linewidth and the stability of the $\text{Cr}^{4+}:\text{Mg}_2\text{SiO}_4$ laser may very possibly be through the use of injection seeding. Although no publications have appeared to date concerning such seeding in $\text{Cr}^{4+}:\text{Mg}_2\text{SiO}_4$, there has been clear success with the $\text{Ti}:\text{Al}_2\text{O}_3$ system and this is very similar to $\text{Cr}^{4+}:\text{Mg}_2\text{SiO}_4$ [46]. In particular, a simple injection-seeded $\text{Ti}:\text{Al}_2\text{O}_3$ pulsed laser has been demonstrated which produces 4 mJ of TEM_{00} SLM pulses of 30 ns duration at 780 nm using a CW diode laser as the seeder [46]. This laser does not require other frequency-selective elements (Figure 6.37).

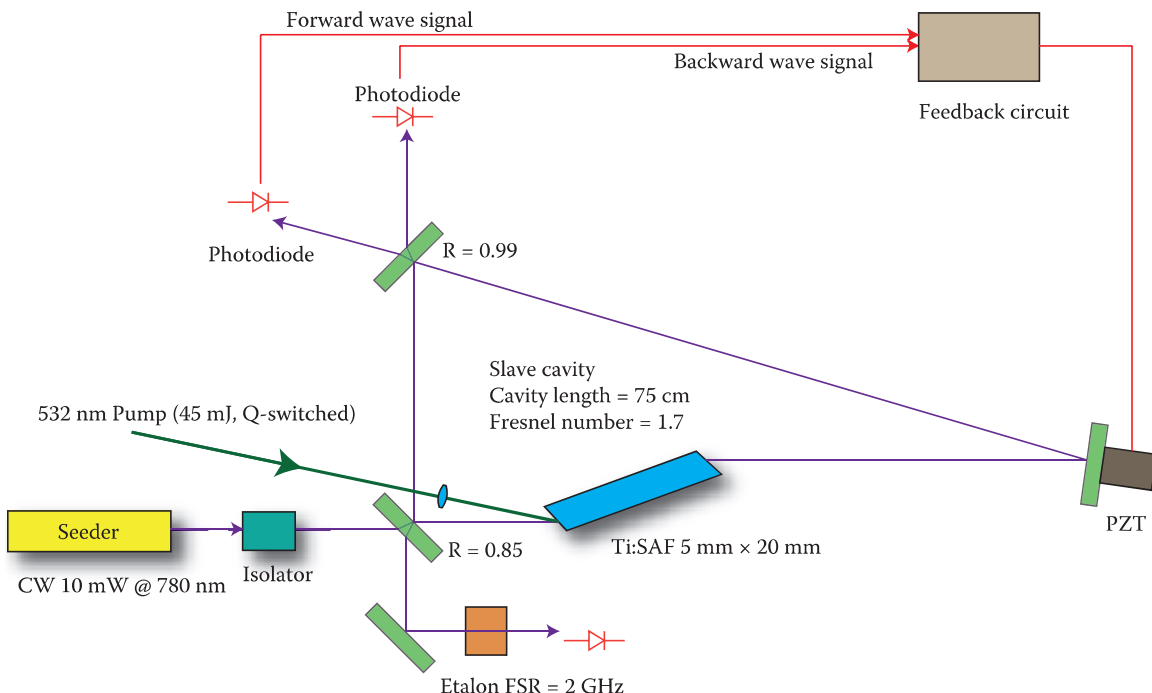


FIGURE 6.37 Optical scheme for a titanium sapphire diode injection-seeded SLM TEM00 pulsed laser pumped by a 532 nm Q-switched Nd:YAG laser. Two diodes measure the forward and backward cavity travelling waves and the piezo mirror (PZT), is used to optimise cavity length, guaranteeing SLM operation in the forward direction only. The authors suggest that this scheme might well be applied to Cr⁴⁺:Mg₂SiO₄.

6.8 Pulsed Diode-Pumped Lasers for Holography and the Future

All the lasers we have reviewed in this chapter have, up until now, either been lamp-pumped or must be pumped using another laser. There is a very good reason for this. Lamp pumping continues to offer the most economic and sensible pumping solution for high-energy nanosecond pulsed lasers. Even for the lower energies required in digital holographic printing applications, lamp pumping is still almost always the most economical means. Nevertheless, progress in digital holographic printing has meant that the repetition rates required in this sector are increasing and, at the same time, the energy requirement is actually decreasing.* At approximately more than 200 Hz,[†] it becomes impractical to use lamp pumping and diode pumping becomes necessary.

Single-shot high-energy pulsed lasers still continue to be required in holography and in other interferential applications. Today, lamp pumping remains the only viable solution to these needs. Xenon lamps produce much larger instantaneous powers than diodes. For example, the typical pump time of a xenon lamp in a Q-switched Nd:YAG laser, such as the G5J, which we reviewed previously (producing 10 J at 1053 nm), is 350 µs. Within this time, approximately 1 kJ is dumped into the lamp, giving an instantaneous power of nearly 3 MW. This is many orders of magnitude greater than current diodes are capable of generating.[‡] Diodes are of course much better matched to the absorption characteristics of many lasers. Their narrow band emissions can therefore be far more effective in pumping a population inversion than the brute force wide-spectrum lamp. However, this simply cannot compete with the huge advantage that large xenon lamps possess in peak power.

* We shall see in the next chapter that a higher resolution hologram with a smaller hogel leads to a smaller pulsed energy requirement.

[†] Often, the practical limit can be nearer to 100 Hz.

[‡] Diodes are often monolithically packaged into “bars” for efficient pumping—a 1 cm bar typically produces around 50 W/cm at an efficiency of 50% to 60%.

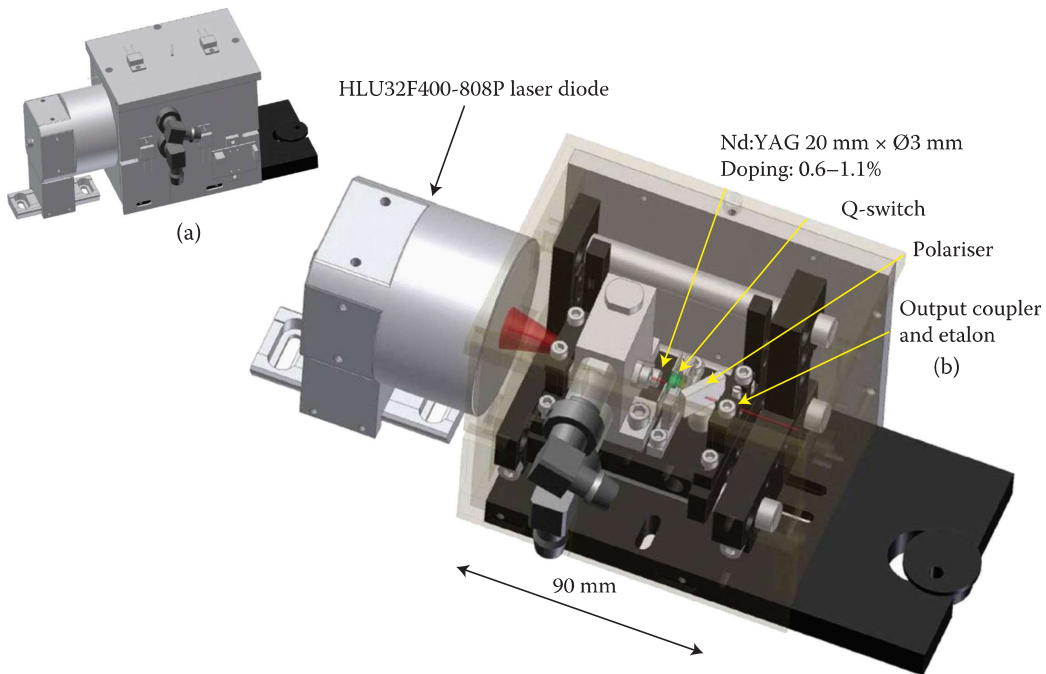


FIGURE 6.38 Prototype Nd:YAG pulsed DPSS laser pumped by a 40 W HLU32F400-808P laser diode driven by an LDD50 power supply (LIMO GmbH). Operation at both 1064 and 1319 nm was successfully achieved.

One sector that is attempting to change this equation is the inertial confinement nuclear fusion community. Current facilities, such as the National Ignition Facility (NIF), Laser Megajoule and Vulcan, use large neodymium glass lasers (essentially larger versions of the G5J) to achieve the enormous pulse energies (~2 MJ per pulse at the third harmonic of 1053 nm) required to heat a deuterium/tritium target to nuclear ignition. However, these lasers cannot be fired rapidly because of the thermal characteristics of the phosphate glass amplifiers; in addition, the laser wall-plug efficiency is extremely poor due to the intrinsic use of lamp pumping. The European project High Power Laser Energy Research (HiPER) Facility has identified key areas in the development of high-energy diode-pumped pulsed lasers. The eventual requirement is for a 200 kJ, 5 ns laser, but initially, the more moderate target of achieving a pulse energy of 10 kJ has been proposed. Currently, there are four such diode-pumped lasers worldwide that are capable of generating more than 100 J per pulse [17].

So in fact, it is possible today to use diode pumping in virtually all the holography lasers we have reviewed in this chapter. The reason this is generally not done is simply related to the cost of the diode stacks. However, as the price of diodes continues to fall, sooner or later we can expect high-energy diode-pumped solid-state (DPSS) lasers to replace most, if not all, of the current lamp-pumped solutions for holographic applications.

Some initial unpublished research into pulsed nanosecond DPSS RGB lasers for holography based on the 1 and 1.3 μm laser transitions in Nd:YAG was carried out in 2007 at the Centre for Laser Photonics in North Wales. Figure 6.38 shows a schematic diagram of the type of laser investigated. This was an end-pumped configuration using a 40 W, 808 nm diode source. TEM₀₀ SLM Q-switched pulses* were attained at both 1064 and 1319 nm, having durations from 6 to 10 ns and pulse energies up to 300 μJ . This work was not continued but showed that a small DPSS RGB holography laser suitable for digital holographic printing should be relatively easy to produce.

Perhaps the greatest advantage of diode pumping is that you do not end up injecting large quantities of unuseful energy into the active medium. In lamp pumping, most of the energy ends up heating the active crystal and, in the case of Nd:YAG, introducing stress birefringence. One has to work very hard to get rid of this extra energy and to stabilise the laser in order to achieve the required stability. Diode pumping

* Cr:YAG was used for 1064 nm and V:YAG for 1319 nm.

circumvents this problem by simply not injecting so much waste heat. As a result, lasing stability is naturally much better. Better values of M^2 can also be attained and lifetime is superior.

One final clear advantage that diodes hold over lamps is that some weaker transitions just cannot be pumped by lamps. The much narrower band of the diode can then be instrumental in pumping such lines. For example, the ${}^4F_{3/2} - {}^4I_{9/2}$ ($R_1 - Z_5$) transition at 946 nm in Nd:YAG [47] is interesting as a source of blue radiation for holography (946 nm/2 = 473 nm), but its cross-section is around six times lower than the main 1064 nm line. The lower laser level of the 946 nm system is only just above the ground state and it has a thermal population of nearly 1%. This thermal population increases the laser threshold significantly and the laser essentially becomes a quasi-three-level system.

Other examples are the 942 nm transition of Nd:GSAG [48,49] and, of particular interest, the 935 nm transition of Nd:YGG ($\text{Y}_3\text{Ga}_5\text{O}_{12}$) [50]. All these transitions may be doubled to achieve useful blue emissions suitable for holography. They are especially interesting too as they achieve a better match with current light-emitting diodes which are starting to become the solution of choice for illumination of holograms (see Chapter 13).

A material of particular interest for diode pumping is Nd:YVO₄ (neodymium-doped yttrium vanadate). It has a stimulated emission cross-section five times that of YAG at 1064 nm, and a strong broadband absorption at 809 nm (7 times higher than YAG in the π direction). Like the other neodymium-doped crystal hosts, it can also be used to generate 1.3 μm radiation. As such, this material would be a good choice for a next-generation pulsed DPSS RGB holography laser.

REFERENCES

1. M. Yamaguchi, T. Koyama, H. Endoh, N. Ohyama, S. Takahashi and F. Iwatali, "Development of full-parallax HoloPrinter," in *Practical Holography IX*, S. A. Benton ed., Proc. SPIE **2406**, 50–56 (1995).
2. M. Lucente, *Diffraction-Specific Fringe Computation for Electro-Holography*, Ph. D. Thesis, Dept. of Electrical Engineering and Computer Science, Massachusetts Institute of Technology, (1994).
3. D. Brotherton-Ratcliffe, F. M. Vergnes, A. Rodin and M. Grichine, *Method and Apparatus to Print Holograms*, Lithuanian Patent LT4842, (1999).
4. M. Klug, M. Holzbach and A. Ferdman, *Method and Apparatus for Recording 1-Step Full-Color Full-Parallax Holographic Stereograms*, US Patent 6,330,088 (filed 1998, granted 2001).
5. D. Brotherton-Ratcliffe, F. M. Vergnes, A. Rodin and M. Grichine, *Holographic Printer*, US Patent 7,800,803 (filed 1999, granted 2010).
6. A. Rodin F. M. Vergnes, D. Brotherton-Ratcliffe, *Pulsed Multiple Colour Laser*, EU Patent EPO 1236073 (2000).
7. A. Yariv, *Quantum Electronics*, 4th Edn., Wiley New York (1991).
8. A. E. Siegman, *Lasers*, University Science Books, Mill Valley CA (1986).
9. H. Haken, *Laser Theory*, Springer, Berlin Heidelberg (1984).
10. W. Koechner, *Solid State Engineering*, 6th Edn., Springer, Berlin Heidelberg (2006).
11. T. H. Maiman, "Stimulated optical radiation in ruby," *Nature* **187** (4736) 493–494 (1960).
12. H. Bingham, J. Lys, L. Verluyten, S. Willocq, J. Moreels, K. Geissler, G. Harigel, D. R. O. Morrison, F. Bellinger, H. I. Bjelkhagen, H. Carter, J. Ellermeier, J. Foglesong, J. Hawkins, J. Kilmer, T. Kovarik, W. Smart, J. Urbin, L. Voyvodic, E. Wesly, W. Williams, R. Cence, M. Peters, R. Burnstein, R. Naon, P. Nailor, M. Aderholz, G. Corrigan, R. Plano, R. L. Sekulin, S. Sewell, B. Brucker, H. Akbari, R. Milburn, D. Passmore, and J. Schneps, "Holography of particle tracks in the Fermilab 15-Foot Bubble Chamber," *Nucl. Instr. and Meth.* **A297**, 364–389 (1990).
13. H. Akbari and H. Bjelkhagen, "Pulsed holography for particle detection in bubble chambers," *Opt. Laser Technol.* **19**, 249–255 (1987).
14. R. Naon, H. Bjelkhagen, R. Burnstein and L. Voyvodic, "A system for viewing holograms," *Nucl. Instr. and Meth.* **A283**, 24–36 (1989).
15. G. Harigel, C. Baltay, M. Bregman, M. Hibbs, A. Schaffer, H. I. Bjelkhagen, J. Hawkins, W. Williams, P. Nailor, R. Michaels and H. Akbari, "Pulse Stretching in a Q-switched ruby laser for bubble chamber holography," *Appl. Opt.* **25**, 4102–4110 (1986).
16. V. A. Arsenev, I. N. Matveev and N. D. Ustinov, "Nanosecond and Microsecond pulse generation in solid-state lasers," *Soviet J. of Quantum Electron.* **7**, 1321 (1977).

17. N. Alexander, F. Amiranoff, P. Auger, S. Atzeni, H. Azechi, V. Bagnoud, P. Balcou, J. Badziak, D. Batani, C. Bellei, D. Besnard, R. Bingham, J. Breil, M. Borghesi, S. Borneis, A. Caruso, J. C. Chanteloup, R. J. Clarke, J. L. Collier, J. R. Davies, J.-P. Dufour, M. Dunne, P. Estrailleur, R. L. Evans, M. Fajardo, R. Fedosejevs, G. Figueria, J. Fils, J. L. Feugeas, M. Galimberti, J.-C. Gauthier, A. Giulietti, L. A. Gizzi, D. Goodin, G. Gregori, S. Gus'kov, L. Hallo, C. Hernandez-Gomez, D. Hoffman, J. Honrubia, S. Jacquemot, M. Key, J. Kilkenny, R. Kingham, M. Koenig, F. Kovacs, A. McEvoy, P. McKenna, J. T. Mendonca, J. Meyer-ter-Vehn, K. Mima, G. Morou, S. Moustazis, Z. Najmudin, P. Nickles, D. Neely, P. Norreys, M. Olazabal, A. Offenberger, N. Papodogianis, J. M. Perlado, J. Ramirez, R. Ramis, Y. Rhee, X. Ribeyre, A. Robinson, K. Rohlena, S. Rose, M. Roth, C. Rouyer, C. Rulliere, B. Rus, W. Sandner, A. Schiavi, G. Schurtz, A. Sergeev, M. Sherlock, L. Silva, R Smith, G. Sorasio, C. Strangio, H. Takabe, M. Tatarakis, V. Tikhonchuk, M. Tolley, M. Vaselli, P. Velarde, T. Winstone, K. Witte, J. Wolowski, N. Woolsey, B. Wyborn, M. Zepf and J. Zhang, "HiPER: The European high power laser energy research facility: technical background and conceptual design," DOI: *RAL Technical Reports*, RAL-TR-2007-008 (2007).
18. J. E. Bjorkholm and H. G. Danielmeyer, "Frequency control of a pulsed optical parametric oscillator by radiation injection," *Appl. Phys. Lett.* **15**, 171–174 (1969).
19. U. Ganiel, A. Hardy and D. Treves, "Analysis of injection locking in pulsed dye laser systems," *IEEE J. Quantum Electron.* **12**, 704–716 (1976).
20. N. P. Barnes, J. A. Williams, J. C. Barnes and G. E. Lockard, "A self injection locked, Q-switched, line-narrowed Ti:Al₂O₃ laser," *IEEE J. Quantum Electron.* **24**, 1021–1028 (1988).
21. S. Basu and R. L. Byr, "Short pulse injection seeding of Q-switched Nd:glass laser oscillators – theory and experiment," *IEEE J. Quantum Electron.* **26**, 149–157 (1990).
22. D. H. Barnhart, R. J. Adrian and G. C. Papen, "Phase conjugate holographic system for high resolution particle image velocimetry," *Appl. Opt.* **33**, 7159–7170 (1994).
23. A. M. Rodin and D. Brotherton-Ratcliffe, "Compact 16 Joule phase-conjugated SLM Nd:YLF/Nd:Phosphate glass laser," in *XIV Lithuanian-Byelorussian workshop on Lasers and Optical Nonlinearity*, Proc. Preila, Lithuania, (1999) pp. 51–52.
24. A. S. Dementjev, A. M. Rodin, M. V. Grichine and D. Brotherton-Ratcliffe, "High-energy phase-conjugated Nd:Glass laser for the pulsed holography," in *Spinduliuotes ir medziagos saveika, Konferencijos pranesimui medziaga, Kaunas, Technologija*, Proc. (1999) pp. 249–252.
25. M. V. Grichine, D. Brotherton-Ratcliffe and A. M. Rodin, "Design of a family of advanced Nd:YLF/Phosphate glass lasers for pulsed holography," in *Sixth Int'l Symposium on Display Holography*, T. H. Jeong and H. I. Bjelkhagen eds., Proc. SPIE **3358**, 194–202 (1998).
26. M. V. Grichine, D. Brotherton-Ratcliffe and G. R. Skokov, "An integrated pulsed-holography system for mastering and transferring onto AGFA or VR-P emulsions," in *Sixth Int'l Symposium on Display Holography*, T. H. Jeong and H. I. Bjelkhagen eds., Proc. SPIE **3358**, 203–210 (1998).
27. A. M. Rodin, D. Brotherton-Ratcliffe and G. R. Skokov, "An automated system for the production of image-planed white-light-viewable holograms by pulsed laser," in *Practical Holography XIII*, S. A. Benton ed., Proc. SPIE **3637**, 141–147 (1999).
28. D. Brotherton-Ratcliffe, A. M. Rodin and S. J. Zacharovas, "Evolution of automatic turn-key systems for the production of rainbow and reflection hologram runs by pulsed laser," in *Holography 2000*, T. H. Jeong and W. K. Sobotka eds., Proc. SPIE **4149**, 359–366 (2000).
29. A. M. Rodin, D. Brotherton-Ratcliffe and R. Rus, "Large-format automated pulsed holography camera system," in *Optical Organic and Inorganic Materials*, S. P. Asmontas and J. Gradauskas eds., Proc. SPIE **4415**, 39–43 (2001).
30. A. M. Rodin, D. Brotherton-Ratcliffe and R. Rus, "Large-format automated pulsed holography camera system," in *Abstracts of the 2nd International Conference Advanced Optical Materials and Devices*, Vilnius, Lithuania, (2000) p. 60.
31. A. M. Rodin, S. J. Zacharovas, D. Brotherton-Ratcliffe and F. R. Vergnes, "A mobile system for 3D capture of ultrafast events," in *High-Speed Imaging and Sequence Analysis III*, SPIE **4308**, (2001) Presented, but not published, can be obtained from: www.geola.com.
32. G. Gudaitis, S. J. Zacharovas, R. Bakanas, D. Brotherton-Ratcliffe, S. Hirsch, S. Frey, A. Thelen, L. Ladriere and P. Hering, "Portable holographic camera system HSF-MINI application for 3D measurement in medicine," in *2nd Int'l Conference "HOLOEXPO-2005, Science and Practice, Holography in Russia and Abroad*, Moscow, Russia (2005) pp. 27–29.

33. R. Bakanas, G. A. Gudaitis, S. J. Zacharovas, D. Brotherton-Ratcliffe, S. Hirsch, S. Frey, A. Thelen, N. Ladrière and P. Hering, "Using a portable holographic camera in cosmetology," *J. Opt. Technol.* **73**, 457–461 (2006).
34. P. A. Apanasevich, D. E. Gahovich, A. S. Grabchikov, Ju. J. Djakov, I. N. Zmakin, V. P. Kozich, G. G. Kot, S. Ju. Nikitin and V. A. Orlovich, "Backward SRS in the Conditions of Short Pump Focusing," *Izvestiya Akademii Nauk USSR, Seriya Fizicheskay*, **53** (6), 1031–1037 (1989).
35. A. M. Rodin, A. S. Dement'ev, M. V. Grichine and D. Brotherton-Ratcliffe, "High efficiency Raman Amplification in the Dicke Narrowed Line of Hydrogen," in *Lasers and Electro-Optics (CLEO/Europe'96) Technical Digest*, Hamburg, Germany, (1996) p. 155.
36. G. L. Kachen and W. H. Lowdermilk, "Self induced gain and loss modulation in coherent, transient Raman pulse propagation," *Phys. Rev. A*, **14**, 1472–1474 (1976).
37. V. G. Bespalov and D. I. Staselko, "The influence of stimulated Raman scattering on pump radiation coherency in the saturation regime," *Opt. and Spectrosc.* **61**, 153–158 (1986).
38. I. A. Kulagin and T. Usmanov, "Analysis of self-induced amplitude-phase wave modulation in the processes of transient amplification of the stokes component," *Opt. and Spectrosc.* **80**, 944–947 (1996).
39. W. K. Bischel and M. J. Dyer, "Wavelength dependence of the absolute raman gain coefficient for the Q(1) transition in H₂," *J. Opt. Soc. Am. B*, **3**, 677–682 (1986).
40. D. Brotherton-Ratcliffe, *Laser*; US Patent 7,852,887 (filed 2002, granted 2008).
41. R. Bakanas and J. Pileckas, "Frequency doubled pulsed single longitudinal mode Nd:YAG laser at 1319 nm with pulse build-up negative feedback controls," in *Solid State Lasers XIX: Technology and Device*, W. A. Clarkson, N. Hodgson and R. K. Shori eds., Proc. SPIE **7578** 75780V-1-6 (2010).
42. D. Brotherton-Ratcliffe, "Large format digital colour holograms using RGB pulsed laser technology," in *7th Int'l Symposium on Display Holography – Advances in Display Holography*, H. I Bjelkhagen ed., Proc., River Valley Press, Iowa City, IA (2006) pp. 200–208.
43. Y. Lutz, F. Albe and J.-L. Tribillon, "Etude et réalisation d'un laser à solide pulsé émettant dans le bleu pour l'holographie couleur d'objets dynamiques", *C.R. Acad. Sci. Paris*, t. **323**, Série Iib, 465–471, (1996).
44. W. Jia, H. Liu, S. Jaffe and W. M. Yen, "Spectroscopy of Cr³⁺ and Cr⁴⁺ ions in forsterite," *Phys. Rev. B*, **43**, 5234–5242 (1991).
45. T. S. Rose, R. A. Fields, M. H. Whitmore and D. J. Singel, "Optical Zeeman spectroscopy of the near-infrared lasing center in chromium:for-sterite," *J. Opt. Soc. Am. B* **11**, 428–435 (1994).
46. T. D. Raymond and A. V. Smith, "Injection-seeded Titanium doped Sapphire laser," *Opt. Lett.* **16**, 33–35 (1991).
47. T. J. Axenson, N. P. Barnes, D. J. Reichle and E. E. Köhler, "High-energy Q-switched 0.946 μm solid-state diode pumped laser," *J. Opt. Soc. Am. B* **19**, 1535–1538 (2002).
48. F. Kallmeyer, M. Dziedzina, X. Wang, H. J. Eichler, C. Czeranowsky, B. Ileri, K. Petermann and G. Huber, "Nd:GSAG-pulsed laser operation at 943 nm and crystal growth," *Appl. Phys. B* **89**, 305–310 (2007).
49. Z. Lin, X. Wang, F. Kallmeyer, H. J. Eichler, C. Gao, "Single-frequency operation of a tunable injection-seeded Nd:GSAG Q-switched laser around 942nm," *Opt. Expr.* **18**, 6131–6136 (2010).
50. J. Löhring, A. Meissner, D. Hoffmann, A. Fix, G. Ehret and M. Alpers, "Diode-pumped single-frequency-Nd:YGG-MOPA for water-vapor DIAL measurements: design, setup and performance," *Appl. Phys. B* **102**, 917–935 (2011).

7

Digital Colour Holography

7.1 Introduction

The earliest approach to “digital holography” sought to calculate numerically the complex wave front scattered by a virtual object [1,2]. By combining this wave front with a virtual reference beam, the resultant interference pattern could be calculated within a given medium. From the mid-1960s onwards, researchers used a combination of printing and photographic reduction methods to produce crude synthetic holograms from such calculated patterns. The technique of numerically synthesising and then physically encoding the interference pattern corresponding to a virtual object has today come to be known as computer-generated holography (CGH). The availability of comparatively cheap computational power has led to CGH now being used routinely to record high-quality transmission holographic gratings encoding either image or non-image data using electron beam lithography. Modern techniques allow the mass replication of such gratings for applications such as holographic security features and holographic optical elements (HOEs).

CGH is ideally suited to transmission holography because, in this case, the holographic information contained in the interference pattern is essentially two-dimensional (2D) in nature. In contrast, reflection holography intrinsically requires three-dimensional (3D) information; as such, no commercially realistic solution exists today for writing CGH data in the form of a reflection hologram. We have, however, seen in the preceding chapters that reflection holography is far more suited than transmission holography for the task of recording and playback of high-fidelity, distortion-free full-colour images. Historically, this led researchers to look for an alternative technique for digital holography: one that would be more naturally suited to the creation of reflection gratings.

7.2 Holographic Stereograms

As early as 1967, Pole [3] had been working on a technique that was rather different from CGH. In Pole’s experiments, he was able to create a crude reflection hologram based on multiple photographs. It was intrinsically a two-step process: first, a 2D matrix of small lenslets was used to image photographs of an object taken from many different horizontal and vertical perspectives. The second step was an optical transfer of the lenslet matrix to a reflection hologram. Upon viewing this reflection hologram, the eye coincided with a virtual image of the lenslets and a 3D effect was perceived. Pole reported that the resulting “holographic stereograms” exhibited full three-dimensionality, exactly like ordinary holograms, but that the large inactive area between the lenslets caused image degradation akin to viewing an ordinary hologram through a coarse grid structure. He concluded that the optimum lenslet size would be equal to the diameter of the human eye so as to best accommodate the compromise of sampling and depth of field inherent to the new display.

In 1969, DeBitetto [4] reported an alternative system in which a masked holographic plate was sequentially exposed to different perspective view images.* This solved the resolution problem inherent in Pole’s work, as with a contact aperture, the holographic exposures could be spaced with virtually no inactive area between them. Subsequent work by King et al. [5] reported the production of a white

* The images were projected with laser light onto a diffusive screen in front of the masked holographic plate.

light-viewable image plane hologram (an H_2) from a DeBitetto type (H_1) master. However, because the sequential exposure of the component holograms of a DeBitetto type H_1 required much more recording time than Pole's technique, the vertical parallax information was discarded, thus reducing the number of necessary exposures.

During the 1970s, Lloyd Cross [6] and others, inspired by the invention of the rainbow hologram [7], tackled the problem of generating holographic stereograms in yet another way. Here, transmission holography was used to produce bright rainbow holograms (without vertical parallax) using large cylindrical lenses for recording and cylindrical films for display. However, this type of system, although popular for a time, proved ultimately to be rather inferior to the DeBitetto/King approach.

By the early 1990s, most large stereograms had therefore started to be recorded as reflection holograms using the DeBitetto/King model. In 1991, Walter Spierings and his company, the Dutch Holographic Company B.V. introduced the first full-colour reflection stereograms [8] (see Chapter 1, Figure 1.45).^{*} Although impressive, these holograms were still derived from analogue photographic data. The transition to digital data, however, was already starting. Stephen Benton and his group at the Massachusetts Institute of Technology were probably the earliest workers in this field—and certainly the most influential. In 1991, Halle et al. [9] described the ultragram. The invention allowed one to record a two-step holographic stereogram with an arbitrary transfer distance. This was the first use of digital image distortion techniques and provided a clear reason for going “fully digital”. The advent of digital cameras and cheap spatial light modulators in recent years has only reinforced this doctrine. The original DeBitetto/King model is still used successfully today to produce full-colour horizontal parallax reflective holographic stereograms from digital camera or computer data.

7.3 One-Step Digital Holograms

With the advent of digital spatial light modulators (SLMs), a different avenue became available to create a high-resolution reflection hologram from computer or camera data. This was one-step or direct-write digital holography (DWDH). In analogue holography, an interference pattern is created by the superposition of the wave fronts of an object and reference wave within a photosensitive plate or film. CGH seeks to synthesise this pattern numerically. However, suppose that instead of calculating such a global interference pattern all at once, one breaks down the problem into writing only a small element of a hologram at a time. In other words, we consider the required hologram as being composed of a plurality of small microholograms arranged in the form of an (x, y) grid. The problem now reduces to writing sequentially each such microhologram. Of course, we could still calculate the interference pattern of each such microhologram via the methods of CGH and write them using electron beam lithography. However, with the advent of liquid crystal displays (LCDs), a far simpler solution became possible: a reference and object beam could be made to intersect at the surface of a photosensitive material to directly create the microhologram. The object beam is encoded with image data by being made to pass through a spatial light modulator such as a LCD and a lens system. A step-and-repeat mechanism then writes a plurality of juxtaposed microholograms (these came to be known as holographic pixels or hogels [10]).

There are many advantages to DWDH. The first and most evident is that, unlike CGH, it lends itself naturally to colour reflection holography; by using three or more laser wavelengths, full-colour reflective hogels can be written at the same physical location. The spatial frequencies within the hogels are indeed very large, but by using the natural interference process to generate each hogel, one is freed from having to use costly techniques such as electron beam lithography to attain the required high spatial resolution. Because the hogel is inevitably chosen to be small (usually in the range of 0.1 mm diameter to several millimetres) only small lasers are potentially required.

In fact, it turns out that depending on what image data is recorded, master holograms can also be generated in this fashion, hogel by hogel. These holograms can then be optically transferred to an H_2 . When this is done, the technique is known as master-write digital holography (MWDH). MWDH is effectively

^{*} These types of holograms were generated in a two-step $H_1:H_2$ process. The H_1 was made by laser projection of multiple analogue camera perspectives onto a diffusion screen—this process came to be known as MPGH.

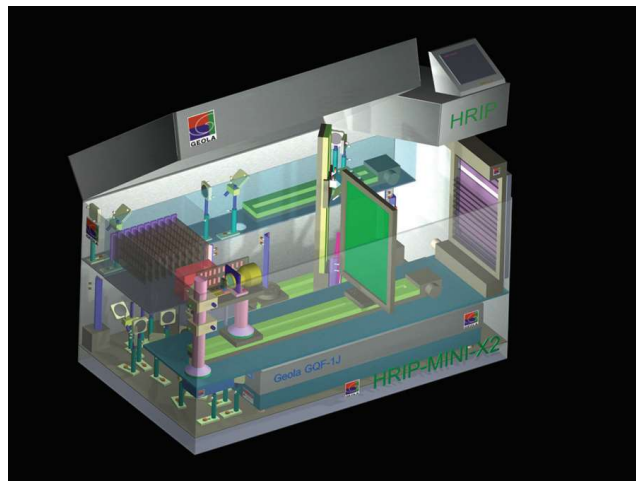


FIGURE 7.1 Early concept design (circa late 1990s) of a digital multiple photo-generated holography printer from Geola.

a DeBitetto/King full-parallax H_1 with a small square or hexagonal aperture. However, in modern systems, the aperture and the diffusion screen are usually replaced by a lens system.

In 1988, Yamaguchi et al. [11] became the first group to report experimental demonstration of DWDH. In their one-colour system, a 2D perspective sequence was generated. This was then image-processed to form an array of hogel mask frames, which were recorded on video tape and downloaded one-by-one to a twisted nematic LCD. A laser beam was used to illuminate the LCD and a lens system employed to record a volume reflection hologram of the Fourier transform of each mask. Each such hologram constituted a hogel and, by sequentially advancing the holographic plate between exposures, a matrix of abutting hogels was created. The resulting hologram reconstructed an accurate full-parallax view of the original scene. The process seemed promising, but the 320×240 hogel array required many hours to record.

In the late 1990s, Klug et al. [12], working at the US company Zebra Imaging Inc., extended the technique of Yamaguchi et al. to large-format, full-colour reflection holography. Zebra Imaging proved beyond a doubt that the DWDH technique was capable of generating large-format digital colour holograms of a quality never before imagined. In 1999, Brotherton-Ratcliffe et al. [13–16], working at the Lithuanian company Geola, subsequently demonstrated that the technique could be made to work much faster and more reliably using pulsed RGB lasers.

During the last decade, pulsed laser DWDH has been developed and used commercially by several companies, most notably Geola, XYZ Imaging Inc.* and Zebra Imaging. More recently, a dual-mode printer capable of writing holograms under both DWDH and CGH has been described by Kang et al. [17]. In 2009, a pulsed laser DWDH system was also developed, allowing the rapid generation of erasable digital holograms on photorefractive polymer [18].

7.4 A Simple DWDH Printer

7.4.1 Optical Scheme

Some early DWDH printers used a recording scheme very similar to the original DeBitetto scheme. A simplified diagram of such a printer is shown in Figure 7.2. A continuous wave (CW) laser is used to produce a reference and object beam through the use of a polarising beam splitter (PB). The reference to object ratio is controlled by the 1/2 wave plate (WPI) and the polarisations in the two beam paths are equalised by WP2. The object beam scheme basically consists of a projection system based on an

* More recently trading under the name Rabbitholes Media Inc.

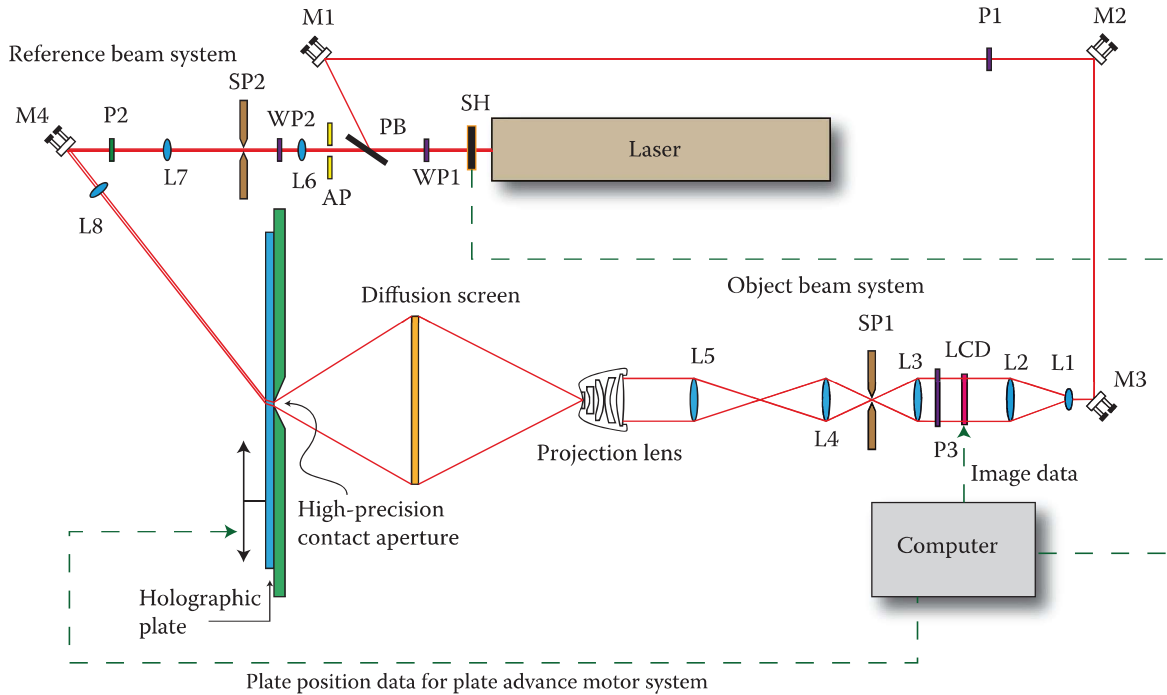


FIGURE 7.2 Simple DWDH monochromatic reflection hologram printer based on a CW laser. The object beam system comprises an LCD projector and a diffusing screen. A contact aperture is used to define the hogel. The device operates using a simple step-and-repeat sequence.

LCD panel. The beam polarisation is first cleaned up by the thin-film polariser (P1) before being collimated and expanded by the telescope (L1/L2). The LCD is a twisted nematic display, which modifies the polarisation of the radiation passing through it by its changeable birefringence. The polariser (P3) converts this polarisation change into an amplitude modulation. High-frequency noise is then removed from the transmitted object beam by the spatial filter (L3/SP1) and an image of the LCD is relayed to the projection lens (L4/L5). The projection lens then forms a high-quality distortion-free image of the LCD on the diffusion screen. Because the holographic plate is masked by a precision square contact aperture that defines the hogel, only the photosensitive emulsion directly within this hogel aperture can “see” the diffusing screen.

The reference beam system consists of three lenses: an aperture, a spatial filter and a polariser. The spatial filter (SP2) cleans out high-frequency structure in the beam and the polariser (P2) ensures a linear polarisation exactly matching the object beam. The lenses (L6–L8) and aperture (AP) define the shape of the collimated reference beam at the emulsion surface; this is usually chosen to be very close to the object beam hogel shape.

7.4.2 Speckle Blur

Because the object beam projection/diffusing system is a coherent system, it is subject to speckle. The speckle size will increase as the hogel size decreases, leading to a loss of angular resolution in the hologram. If unchecked, this will induce image blurring. Image blurring and speckle are treated in Chapter 11. The simplest solution to controlling speckle blurring is to incorporate an additional diffusing element upstream of the projection system.

7.4.3 Operation

The printer works by using a simple step-and-repeat procedure. The shutter (SH) is opened for a predetermined period of time and a hogel is written. The shutter is then closed and the holographic plate is

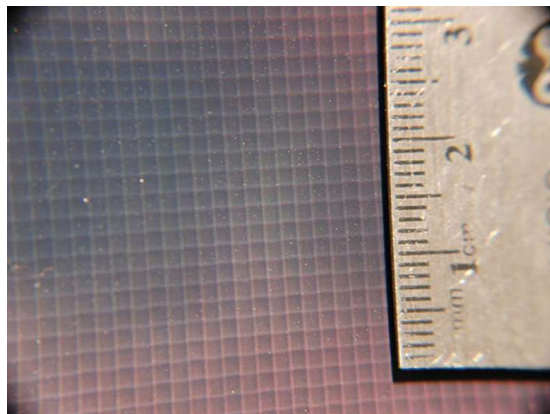


FIGURE 7.3 Magnified view of a small section of a DWDH hologram showing the matrix of hogels or elementary holograms (here, the hogels are 1.6 mm in diameter). Simple DWDH printers print one hogel at a time. At the end of each line, the printer drops to the next line and changes direction. Common hogel sizes range from just over 100 µm to several millimetres. It is also possible to print hexagonal hogels.

advanced. After a settling period, which is required for the system to reach interferometric stability, the shutter is again opened for the predetermined exposure time and the next hogel is written. The plate is moved one column at a time until a full line of hogels is finished. It then drops down a line and starts off in the other direction (Figure 7.3).

7.4.4 Image Data

The image data required by any DWDH printer can be derived from real-world images using devices such as holocams or structured light camera systems (Chapter 10). However, significant image processing needs to occur to get the data into a form ready for printing hogels. We shall discuss image-processing methods for both DWDH and MWDH in Chapters 8 and 9.

7.4.5 Deficiencies

There are several problems with this simple DWDH printer. First, the use of a contact aperture to define the hogel is difficult. Many emulsions are physically sensitive and the aperture must of course be in intimate contact with this sensitive surface. This usually means that an electromechanical system must lift the aperture away from the emulsion when the plate is moved and then gently push it back against the emulsion before exposure.* However, this takes a lot of time, and with the typical hogel size being less than 1 mm², even a 30 cm × 40 cm hologram can require 120,000 hogels. Another problem with contact apertures is that the final DWDH hologram can exhibit a clear grid-like structure. It can also be difficult to stop scattered light from actually recording a hologram of each aperture itself. Finally it can be difficult to guarantee exact alignment and proper contact at each exposure.

The use of a classic diffusing screen and an object beam projection system allows the recording of wide angle-of-view holograms with undistorted images. However, only an extremely small part of the object beam is actually used to expose the hogel! The result is that a large power laser is required and one ends up throwing away 99% of the power. Holographic diffusers can greatly improve this situation as they can diffuse the light into a small predetermined area that can be matched to the hogel. However, there is still a general problem with any type of diffusing system. This is the propensity of such systems to induce image blurring. The problem is that if the diffuser is too small and too close to the hogel, or if the hogel is too large, then the rays connecting a projected LCD pixel on the diffusing screen and any

* The commercial printer marketed by XYZ Imaging Inc. in 2005 actually used a system whereby the AgX film was sucked by a vacuum system onto an aperture in front of the writing optics. The function of the aperture was not to apodise the light beam in this printer but to ensure a flat film surface. There was indeed contact between the emulsion surface as it was dragged over the aperture and this caused many small scratches.

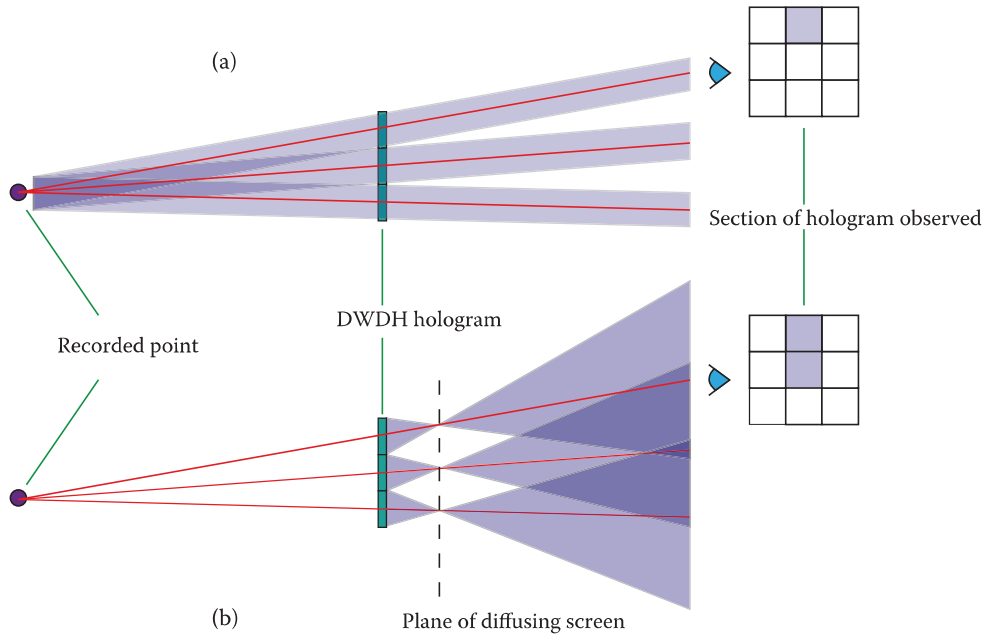


FIGURE 7.4 Diagram illustrating the induced blurring in a DWDH hologram, which occurs when too small a diffusion screen is used to write the hologram. Ideally, the ray bundles connecting a recording point with each hogel should be non-diverging as shown in (a). When too small a diffuser is used to record the hologram as in (b), the ray bundles become strongly diverging and, as a result, hogel bleeding occurs. The diagram only shows the central ray bundles for clarity—which is why there seem to be gaps in the viewing scenario in (a). In general, each hogel will be associated with just enough collimated ray bundles to fill these gaps, but then any divergence of the ray bundles in excess of the eye's angular resolution will lead to hogel bleeding as soon as the observation distance is greater than the diffuser distance.

hogel will, in general, form a cone with a relatively large angle—and the larger this angle, the greater the image blurring and the smaller the in-focus depth of the hologram (Figure 7.4). It can therefore be difficult to make compact printers capable of producing higher-resolution wide-angle holograms using diffusing screens.

A final problem with this simple printer is the time required to print a hologram. Interferometric stability must be present at each exposure. This translates into a long step-and-repeat time even when a high-power laser is used. With the added complication of a contact aperture, this can lead to print times of days for small holograms. Realistically, any small disturbance within this period of time is likely to create a badly exposed hogel and can effectively ruin the hologram.

7.5 Modern DWDH Printers

Modern DWDH printers use a number of major improvements over the simple system described in the previous section. First, and most importantly, small-pulsed lasers are often used to solve the stability problems inherent to the use of CW lasers. Second, the hogel is usually formed using an optical system rather than relying on an awkward contact aperture combined with a projection/diffusion scheme. This then allows the step-and-repeat plate movement system to be replaced by a constant velocity system.

7.5.1 Use of Pulsed Lasers

The use of nanosecond-pulsed lasers in DWDH printers can completely solve the problems of interferometric stability and low printing speed that plague CW laser printers. This is of fundamental importance because this means that small-power lasers may be used to print large holograms at reasonable times. With a pulsed laser, the holographic exposure is effectively done in such a small period of time that there is no need to let the system settle.

We shall see in the next section that the problematic contact apertures often used in early printers were quickly discarded and, as such, it became possible to simply move the holographic plate at a constant velocity while a constant repetition rate laser wrote sequential hogels. The maximum rate at which hogels can be written using this system is determined by the duration of the laser pulse, τ . If we demand that within this duration, the holographic plate may only move by one-tenth of a wavelength of light, then for a hogel of diameter, δ , the maximum hogel write rate is given by the simple formula

$$f = \frac{\lambda}{10\delta\tau} \quad (7.1)$$

For a pulse duration of 40 ns, which is typical of a Q-switched pulsed laser, and a hogel size of 0.5 mm, this equates to a rate of nearly 2.7 kHz at 532 nm! The pulse energy required to expose a single hogel is also extremely small. Taking a film sensitivity value of 2000 $\mu\text{J}/\text{cm}^2$, for example, one can see that the ballpark figure for the energy per hogel is approximately 10 μJ . This assumes, of course, that one has an optical system that (unlike the diffuser system described previously) does not waste energy. If one assumes a realistic hogel write rate of 100 Hz, then the power requirement on the pulsed laser is only 1 mW!

This calculation can be compared with a CW laser system, which also functions with a constant velocity plate displacement system at a hogel write rate of 100 Hz. Here, a laser shutter must constrain the exposure time so that movement of less than one-tenth of a wavelength occurs during the exposure. The exposure must thus be limited to approximately 1 μs . To get sufficient energy for the exposure, this then requires a laser having a CW power of 10 W—or 10,000 times more than that required of the pulsed laser!

7.5.1.1 Microsecond Pulsed Lasers

There is therefore an overwhelming case for the use of pulsed lasers in DWDH printers. Notwithstanding this, there is one major problem here! Some of the best photosensitive materials for colour holography are not properly sensitive to nanosecond laser pulses. For example, dichromated gelatin is a superb photosensitive material that can be used for colour holography—but it produces poor results with nanosecond pulses. Photopolymers, which are wonderfully convenient due to their freedom from wet chemical development, can also fall into this category.

One positive indication is that some of these materials, particularly photopolymers, can show good sensitivity to multiple nanosecond pulses. Therefore, future DWDH printers may well use pulsed lasers producing emissions of a few microseconds' duration—or nanosecond pulse trains with envelopes stretching to several microseconds. Although write rates somewhat lower than 100 Hz may be required, we shall see later that there are methods for writing multiple hogels with every laser pulse. However, microsecond lasers are unfortunately more complex to produce than nanosecond lasers and usually require complex fast-switching high-voltage electronics. We have already reviewed a simple version of a pulse stretcher as applied to a ruby laser in Chapter 6. Recent work at the Geola organisation has also tentatively demonstrated the feasibility of active Q-switching systems for microsecond RGB-pulsed lasers. To date, however, no prototype printer using these longer pulse-length lasers has been tested.

7.5.2 Lens-Based Printers

Special lens systems are frequently used to replace the contact aperture and projection/diffusion scheme described above. Such lens systems create the hogel optically by focussing the light transmitted by the spatial light modulator into a narrow waist. The light distribution at the hogel then effectively becomes the Fourier transform of the distribution at the SLM. Such lens systems can also create a greatly enlarged image of the SLM downstream of the Fourier plane (Figure 7.5).

The contact aperture and projection/diffusion system can therefore be conveniently replaced by a compact non-contact optical system. The exact shape of the hogel can be precisely defined by an aperture placed at any optical plane, which is conjugate to the Fourier plane of the main objective lens.

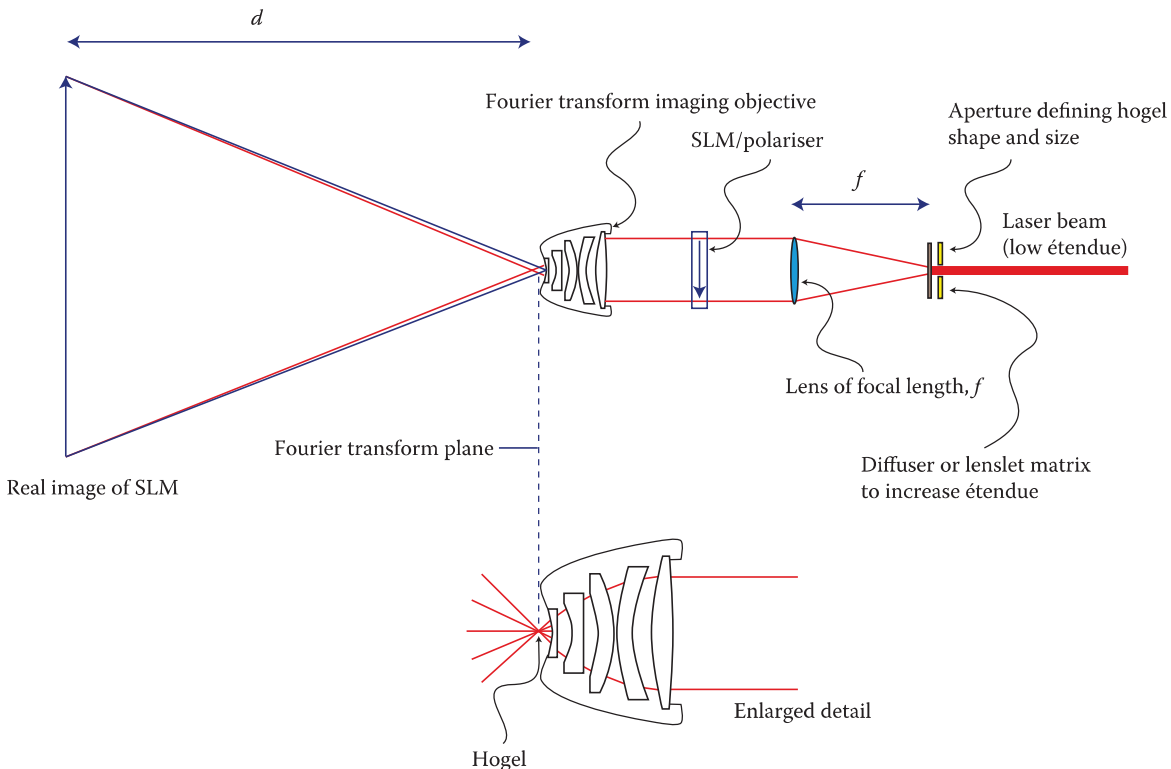


FIGURE 7.5 Lens-based hogel-forming system. Here, a Fourier transform imaging objective defines the hogel shape and also creates an image of the spatial light modulator downstream of the Fourier plane. The distance, d , should be large to avoid blurring of the hologram. The hogel shape may be conveniently defined by the shape of an aperture placed at a conjugate plane.

This type of system has great advantages. There is no need for any contact aperture and almost all the energy transmitted through the spatial light modulator is now used to record the hogel. The laser energy required is therefore extremely small. There are, however, two disadvantages we should mention. Both are related to the fact that it is difficult to design high-resolution Fourier transform imaging systems of high numerical aperture.

Unfortunately, the angular field of view of a DWDH hologram is defined by the conic angle of convergence of the focussed light forming the hogel. Usually, this angle must be large—in the order of 100° if the hologram is to be viewed from a variety of positions. This means that the numerical aperture of the Fourier transform optic must also be very large. However, as the numerical aperture increases, optical aberrations increase rapidly. These aberrations decrease the resolution of the optical system, which in turn induces image blurring in the final hologram.

It turns out that one can significantly increase the resolution of the optical system at high numerical apertures if one accepts a finite fifth coefficient (Barrel distortion) or, in other words, if one accepts that the image of the spatial light modulator produced by the optical system will become rather distorted (but not blurred). In Chapters 8 and 9, we shall discuss this problem, and in particular, we shall see how it can be dealt with in the context of image processing.

The second problem that arises through the need for a high numerical aperture system is related to the fact that higher resolution is always available from a monochromatic Fourier optical system as compared with that available from the corresponding apochromatic system. This usually results in three separate optical schemes being adopted in a DWDH printer, one for each primary colour. Such printers can be classified as triple-beam systems because they use three separate object/reference beam pairs to write three primary colour hogels in different physical locations of the holographic film. Of course, if large image depth or large fields of view are not required in a DWDH hologram, then it becomes possible to employ a single apochromatic optical system and to print single RGB hogels, one at a time.

7.5.3 Speckle in Lens-Based Printers

When a Fourier transform lens system is used in a DWDH printer, the hogel size must be controlled by the étendue of the object beam. An aperture in contact with a holographic diffuser and a Fourier transforming lens may therefore be conveniently used to define both the average étendue and the exact hogel shape. This system also provides ray averaging in that a single point at the image plane of the lens system is now connected to a single point on the spatial light modulator by multiple rays that travel different paths through the optical system. However, for small hogel sizes, too little averaging may be available due to the correspondingly small aperture size. In this case, speckle will appear at the real image of the spatial light modulator downstream of the lens system. Once again, this speckle can degrade the image by inducing image blur. Increasing the diffuser size, as can be done in a lensless printer (according to our previous discussions), is of course not an option here as the diffuser size is now directly coupled to the hogel size. One effective solution is to use a microlens array instead of a diffuser. By choosing the pitch of the lenslet matrix to be larger than a certain critical amount, lower spatial frequencies, which are predominantly responsible for the visible speckle and induced blurring, are eliminated. Of course, if too large a pitch is selected, then given that the area of the lenslet matrix is fixed by the hogel size, inefficient averaging will occur and again the image quality will be degraded. Nevertheless, for most hogel sizes, the lenslet matrix approach works well. An alternative solution that is sometimes adopted is the use of quasi-random phase plates, which are used to randomise the phase at the spatial light modulator.

7.5.4 Triple-Beam Printers

In its simplest form, an RGB triple-beam DWDH printer comprises three relatively identical optical channels—one for each of the three primary colours. Each optical channel comprises a laser emitting at a primary wavelength and an optical system for forming an object beam and a reference beam that are brought into physical coincidence at the surface of the photosensitive material where a hogel is formed.

7.5.4.1 Hogel-Writing Sequence

The hogel-writing sequence is illustrated in Figures 7.6 and 7.7. At first, the film or plate is moved at a constant speed and the lasers triggered at a constant interval such that a row of hogels is created for each of the three primary colours, each hogel being horizontally juxtaposed with respect to its neighbour. This is illustrated in Figure 7.6a.

Next, laser emission is blocked and the electromechanical system winds up the film or plate by an amount equal to the hogel diameter. The process described previously then restarts as the plate/film is moved to the right and a new line of hogels for each colour is formed under the previous line as shown in Figure 7.6b. The writing process continues in this way as illustrated in Figure 7.6c, d and e. Figure 7.6f shows the situation after the sixth line has been written.

The writing sequence continues in Figure 7.7. In Figure 7.7a, seven lines have been written. In Figure 7.7b, the eighth line of red hogels is seen to overprint the first line of green hogels. Similarly, the eighth line of green hogels overprints the first line of blue hogels. This overwriting process continues with further lines being overwritten until the blue hogels, which have already been overwritten by the green hogels, now start to be overwritten by the red hogels. As shown in Figure 7.7f, this process produces hogels that have all three primary colours.

There are several points to make about this writing procedure. Clearly, the distances between the centres of the writing locations for each colour channel have to be an integral multiple of the hogel diameter for the different colour hogels to coincide; this practically then leads to a constraint on the hogel diameter in a given printer. Typical hogel sizes are 1.6 and 0.8 mm. A typical distance between the red and green or green and blue writing locations in modern printers is 80 mm, corresponding to between 50 and 100 hogel diameters.*

* A distance between red and green writing locations of 7-hogel diameters was used for illustration purposes only in Figures 7.6 and 7.7. In modern printers, the figure is closer to 50 to 100.

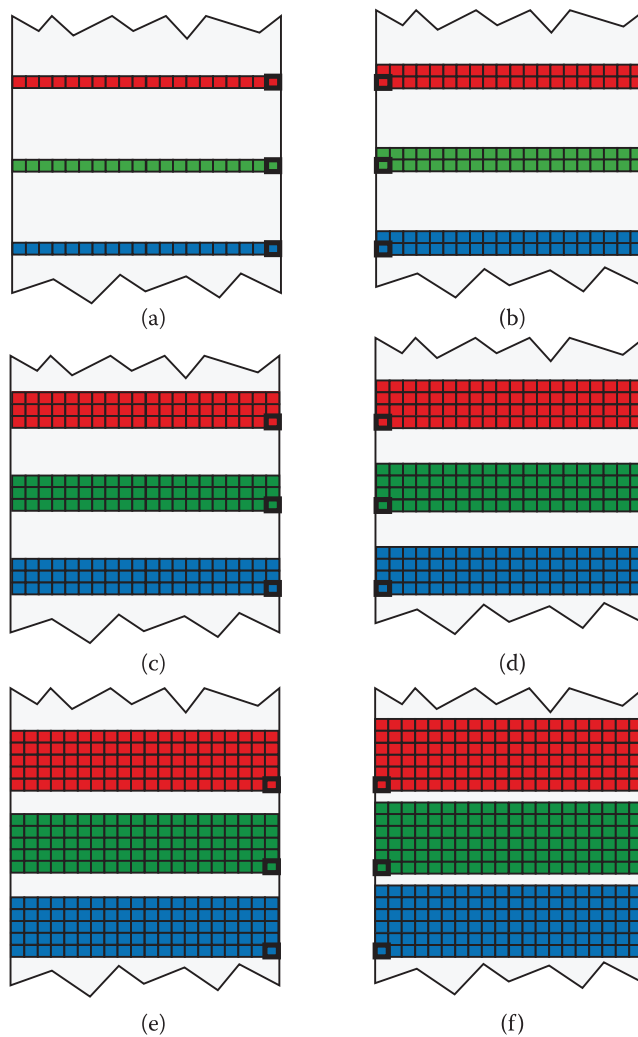


FIGURE 7.6 Hogel-writing sequence in a triple-beam DWDH printer. In (a) the photosensitive film has just been moved from right to left and a row of hogels written by each objective (the black square). In (b) the film has been moved up one step and then moved horizontally to the right while another line of hogels is written. The remaining figures show the progression of this process with three lines (c), four lines (d), five lines (e) and six lines (f) being written.

In practice, it is common for the writing process to start with the top of the photosensitive material directly under the bottom blue writing head. Writing starts only with the blue channel activated; only when the photosensitive material has moved up and the green head starts to overwrite the blue hogels is the green channel actually switched on. Likewise, the red channel is activated only when the red head actually starts to overwrite the blue/green hogels. At the end of the printing process, a similar inverse process is enacted whereby the blue and then the green heads are deactivated before the red head terminates the last line. In this way, all hogels printed contain the three primary colours.

7.5.4.2 Basic Systems in RGB-Pulsed Laser Triple-Beam Printers

Figure 7.8 shows a schematic optical and control diagram of a DWDH printer manufactured in 2001 by the Geola organisation for the production of large-format RGB horizontal parallax-only (HPO) reflection holograms (Figure 7.8). We will use this printer to illustrate how a modern pulsed laser triple-beam DWDH printer works before going on to discuss more complex variants. For clarity, Figure 7.8 shows only one colour channel. In the printer itself, there are three such colour channels (red, green and blue) which are schematically identical. The printer is designed to print reflection type hogels onto silver halide plates of a size up to 800 mm × 800 mm, using three pairs of object and reference beams powered

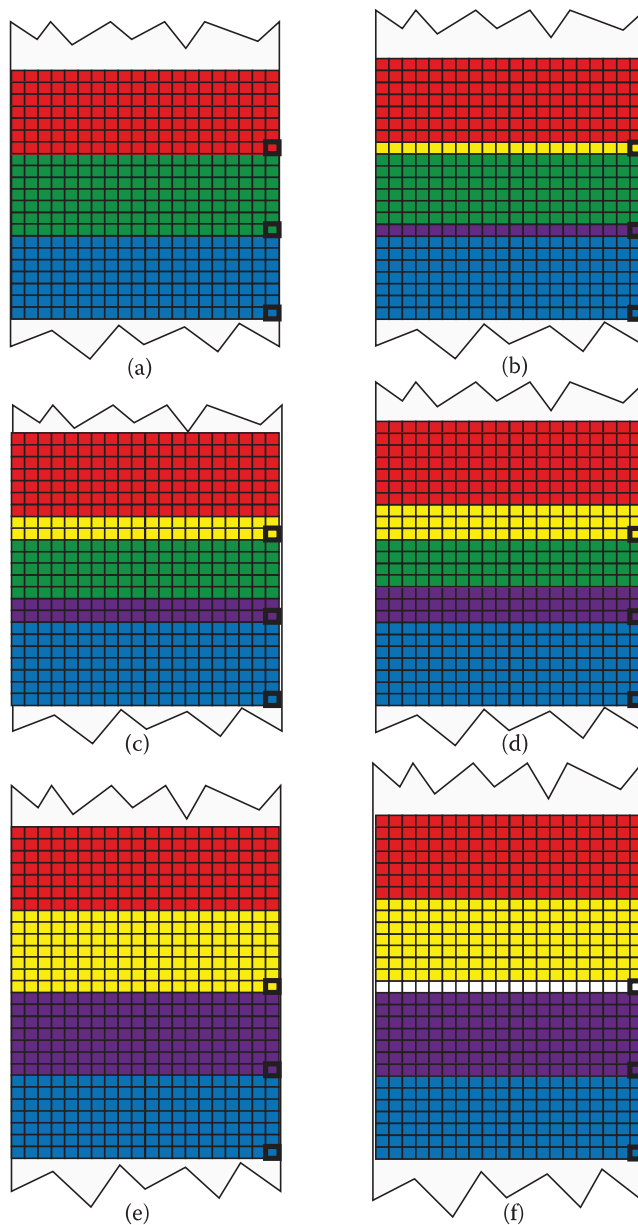


FIGURE 7.7 Hogel-writing sequence continued from Figure 7.6. In (a), seven lines of hogels have been written in each colour. In (b), the different colours start to overlap. Now a line of red hogels has been written over the green and a line of green hogels over the blue. By (e), additional lines have been written, and in (f), the first line of overlapping red, green and blue hogels (shown in white) is produced.

by an RGB-pulsed laser operating at 15 Hz. As with all triple-beam printers, each object and reference beam pair is made to intersect at a given location on the photosensitive film.

7.5.4.2.1 Control and Video Image Stream System

The printer is controlled by a DELL precision workstation 530 computer with twin Intel Xeon 1.4 GHz processors, Matrix Millennium G450 graphics card, an SCSI Raid HDD of 160 MB and an additional SCSI HDD of 73.4 GB and 1 GB of RDRAM running MS Windows 2000 Professional. An XVGA video signal connects the computer to a video splitter. This splitter drives a display monitor in addition to a CRI graphics controller card which feeds three Sony XGA1 1024 × 768 LCD panels for object beam data encoding. The printer includes many motorised microrotation and microtranslation stages for the

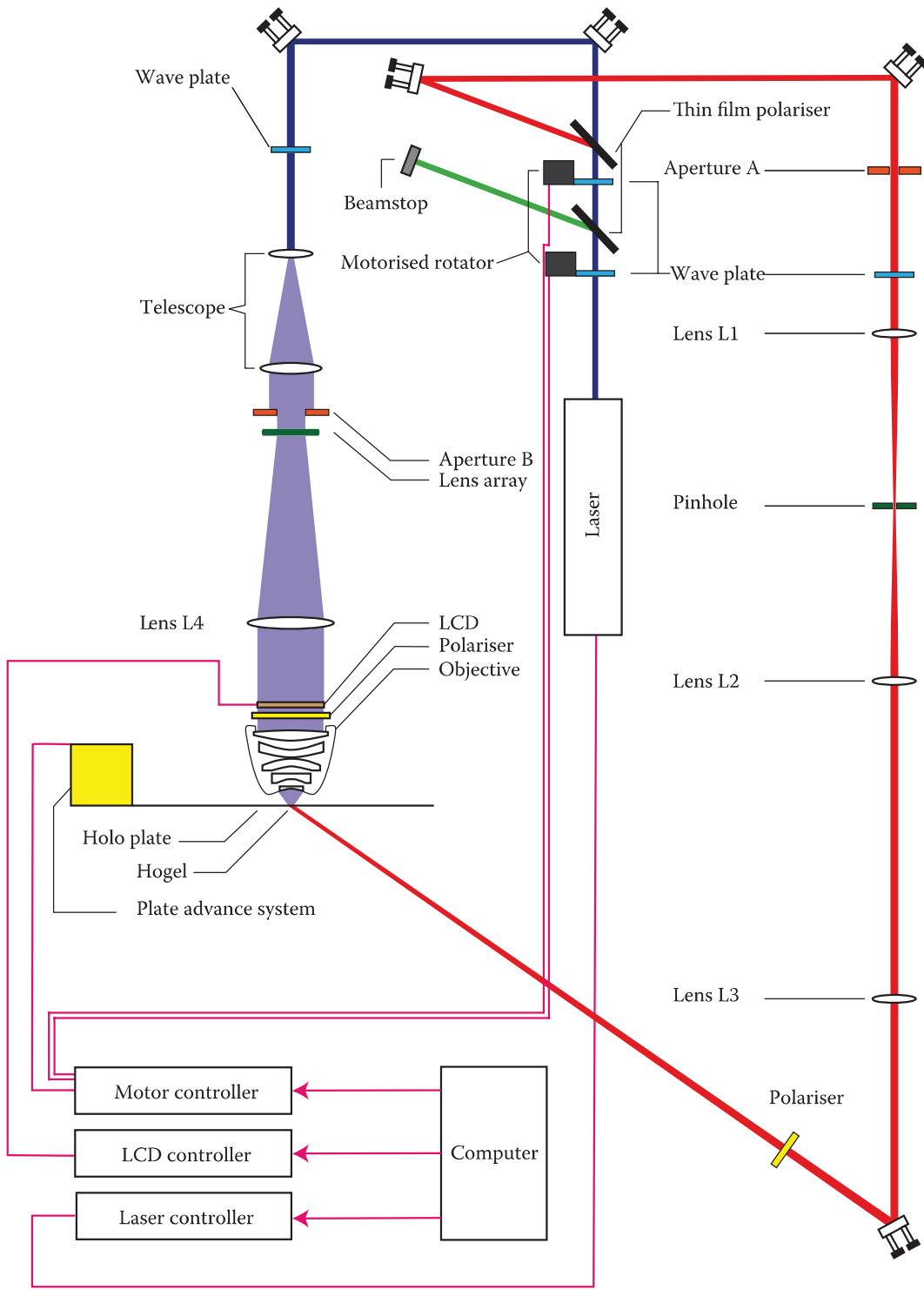


FIGURE 7.8 Optical and control schematic for the 2001 RGB-pulsed laser DWDH printer manufactured by Geola.

automatic adjustment of beam energies and ratios, in addition to electromechanical shutters. Controllers for these components are mounted with the main control computer in a large control rack (Figure 7.10).

7.5.4.2.2 Mechanical Plate Displacement System

The mechanical plate movement system comprises a vertical translator and a horizontal translator. The vertical translator consists of an LF6 200-mm width rail from the German Company Isel Germany AG

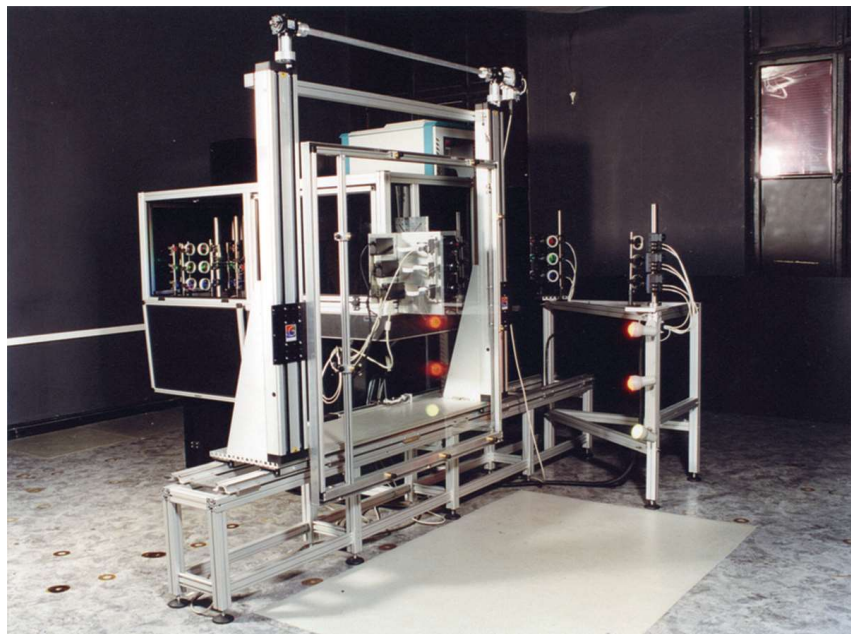


FIGURE 7.9 Photograph of the 2001 RGB-pulsed laser DWDH printer manufactured by Geola. Note the large plate-holder with 2D electromechanical displacement system in the foreground. To the right of the photograph can be seen the reference beam system. In the background are the main optical unit and laser (left) and the electronic control rack (right).

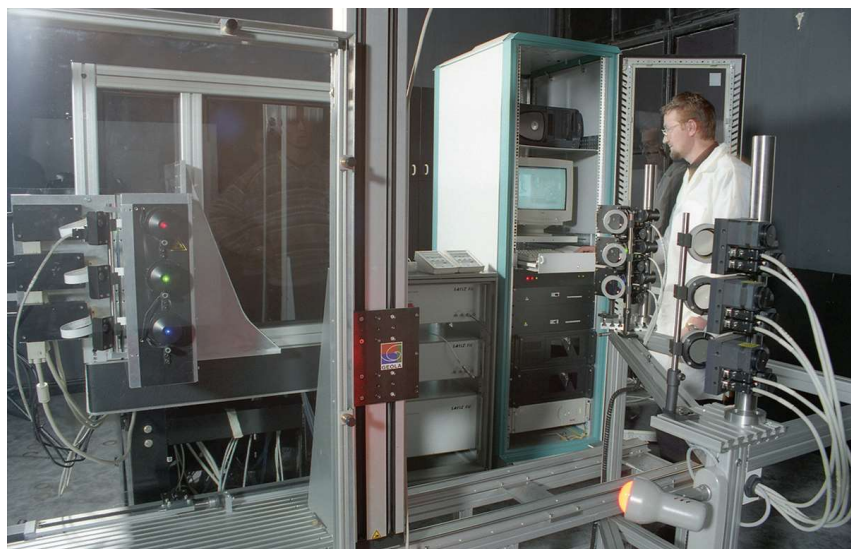


FIGURE 7.10 Photograph of the main control rack of the 2001 Geola printer showing the computer (top) and electronic controllers (bottom). To the left can be seen a separate smaller rack for the laser power supplies.

and a 16×5 ball screw spindle motor with gearbox (Shrittmotorantiesbstmodul 2430 Ncm, Amph Z-Achse, Dir. Antrieb m.Bef.Flan.ZF3 reicht). The horizontal translator comprises an Isel LF4 rail with 16×5 ball screw MS160 spindle motor. A master microprocessor-based controller (mounted in the main control rack) controls the triggering of both laser and stage motion.

7.5.4.2.3 System Architecture

The printer is limited to producing HPO holograms.* HPO holograms require much less memory storage and this allows a simplified computer system to be used, with image files being uploaded over a network.

* In later models, this was upgraded to also allow the creation of full-parallax holograms.

Holograms are created using perspective view information, which is generated either from a holocam (Chapter 10) or through commercially available computer modelling programs. The perspective information is uploaded to the control computer via a 1 GB intranet service where it is queued for processing. Computer software is based on a “.COM” architecture and comprises two main modules. The first module—the RFM—deals with the queuing of jobs for processing. It also undertakes the pixel swapping algorithms, optical distortion algorithms and gamma corrections required to convert the perspective view data to the actual data required by the LCDs. The output of the RFM is a folder containing the compressed LCD data files for each line in the hologram and a command sequence for every motor control required for the setup and printing of the hologram. The mathematical algorithms required for the distortion and pixel-swapping routines will be covered in Chapters 8 and 9. The second software module is the PMC, which controls printer operation, manages the print queue and prints each hologram using the data generated by the RFM.

7.5.4.2.4 Laser and Optical System

The optical system of the Geola printer is built around a dual ring-cavity neodymium RGB-pulsed laser emitting separate red, green and blue beams at wavelengths of 660, 526.5 and 439.5 nm. The pulse energies available are between 3 and 5 mJ at each colour and a repetition rate of 15 Hz is standard. We have already reviewed this laser in Section 6.5.1.

The laser beam is first attenuated to a desired level through a 1/2 wave plate and Brewster angle polariser pair. The wave plates for each colour channel are mounted in precision electromechanical rotation stages that are driven by stepper motors. These motors are controlled by standard motor controllers that are in turn connected to the printer’s dedicated control computer. Calibration tables are defined which allow the control computer to quickly select a given red, green or blue laser energy. Excess unwanted energy is absorbed in a beamstop.

A similar 1/2 wave plate and Brewster angle polariser pair is used to divide the main laser beam into a reference and object beam. In Figure 7.8, the reference beam is coloured red and the object beam is coloured blue. The wave plates are mounted as before in precision electromechanical rotation stages; with appropriate calibration, the control computer is then capable of commanding not only an exact laser energy for a given colour but now also an exact reference energy and an exact object energy. Two further fixed wave plates, one in the reference beam and the other in the object beam, are used to tune the polarisation to the desired direction. Figure 7.11 shows a photograph of the main optics unit of the Geola printer with the energy and ratio control system visible in the foreground to the left.

7.5.4.2.5 Object Beam Subsystem

A simple telescope (Figure 7.8) expands and collimates each laser beam. The beam then illuminates a microlens array that is apodised by the aperture (B). The function of the lens array is twofold. First, it creates a light source that has a larger étendue, which is directly controllable by the size of aperture (B). Second, it produces a clean approximately top hat spatial distribution. The focal length of the lenslets in the lens array is chosen to create a gradual expansion of the object beam and lens (L4) is positioned at a distance of approximately one focal length from the lens array. This ensures that in the case that aperture (B) is very small, the beam after (L4) is collimated.

The object beam now illuminates a Sony XGA1* twisted-nematic LCD panel where the digital image data are encoded onto the object beam. The LCD panel has an active area of 38.8 mm by 27.6 mm and a resolution of 1024×768 pixels. A polariser is required to convert the data, which is written initially by the LCD as changes in the polarisation vector, to amplitude modulation.

The final element in the object beam system is a high numerical aperture Fourier transforming objective lens system. This acts to strongly focus the object beam down to form the hogel and is a key part of the system. It must create a high-fidelity image of the LCD at a distance equal to or greater than the expected viewing distance of the final hologram and must have a Fourier plane at approximately 5 mm downstream of the lens. The conic angle of focus from the objective to the hogel is 105° in the Geola

* In later versions of the printer, the three XGA1 LCDs were updated to higher resolution Sony LCX028ALT panels. These were then mounted in ovens to assure operation at a higher hogel write rate of 30 Hz.



FIGURE 7.11 Photograph of the main optics unit of the 2001 Geola printer showing how the three colour channels are stacked one on top of the other. The laser is visible towards the rear left and the energy control systems are situated in the left foreground. Also visible to the right behind the large glass plate are the three hogel-writing optical objectives. The optics and motorised rotation stages visible to the left form part of the triple reference beam system.

printer and this fixes the intrinsic field of view of the hologram at 105° (Figure 7.12). For hogel sizes from 0.8 to 1.6 mm, the objective has a resolution capable of resolving the LCD pixels at all angles.

The footprint of the object beam at the surface of the photosensitive material is determined by the shape and size of the aperture (B). This is because aperture (B) is at essentially a plane conjugate to the emulsion plane. To see this, remember that the objective lens system produces a Fourier transform of the LCD plane at the emulsion plane. However, the Fourier plane of (L4) is at the lens array and so L4 approximately induces an inverse Fourier transform of the lens array plane at the LCD plane. The two transforms therefore cancel leading to the emulsion plane and the lens–array plane being conjugate. This is a useful feature in that aperture (B) can be controlled automatically to change the hogel size.

7.5.4.2.6 Reference Beam Subsystem

The function of the reference beam optical system in the Geola printer is to produce a clean collimated beam of the correct polarisation that illuminates the hogel from a given fixed angle with a defined spatial distribution. A 1/2 wave plate is used to rotate the polarisation to the desired angle, and a polariser is used to remove any elliptical component. Generally, one wants to minimise reflection from the photosensitive

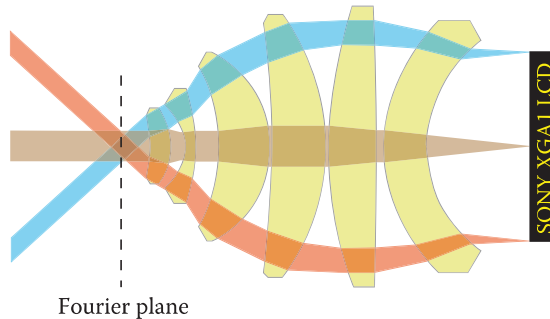


FIGURE 7.12 The 105° hogel-writing objective lens system used in the 2001 Geola printer. Note that the hogel is formed at the Fourier plane. Note also that the ray bundles emanating from a specific LCD pixel pass through the hogel as approximately collimated beams.

material or from the glass or film onto which it has been coated. The polarisation of the electric field is therefore usually chosen to be in the plane parallel to the photosensitive material. If Brewster's angle is chosen as the incidence angle, this then eliminates any unwanted reflections completely. The axial object polarisation must of course be tuned to exactly the same angle as the reference polarisation to achieve maximum interference.

The positive lenses L1 and L2 constitute a Kepler telescope. This telescope changes the diameter of the laser beam by a factor

$$M = f_2/f_1 \quad (7.2)$$

where f_1 and f_2 are the focal lengths of L1 and L2, respectively. The separation of L1 and L2 must be chosen as

$$s = f_1 + f_2 \quad (7.3)$$

to ensure beam collimation. By placing a pinhole at the focus of L1, the beam may be cleaned very effectively and higher spatial frequencies removed. In practice, the focal length f_1 is chosen to be 20 to 50 times larger than the laser beam diameter to minimise aberrations and also to avoid breakdown of the air at the pinhole due to the presence of a high electric field. The focal length of L2 is then determined by the required beam magnification and the separation (s) is fixed by beam collimation.

The function of the two remaining elements in the reference beam system, aperture A and lens L3, is to shape the footprint of the reference beam at the hogel to a desired form. Without these elements, the reference beam would strike the photosensitive material at the incidence angle, forming an elliptical shape, the eccentricity of which is determined by this angle. This is not what is required because, ideally, the reference beam footprint should be matched to that of the object beam. In practice, one actually wants to make the reference beam just a little larger so that the object beam never falls outside the reference footprint. For a 0.8 mm diameter hogel, the reference beam footprint is therefore chosen to be a circle of 0.9 mm diameter, which leads to a small bleed from hogel to hogel.

The desired reference beam footprint is accomplished by arranging lens L3 so that it forms an approximate image of aperture A at the surface of the photosensitive material. The shape of aperture A is then designed such that the required (usually square) distribution of light is obtained at the hogel.

The Kepler telescope relays an image of aperture A by a distance

$$R = -d + f_1(M+1) + \frac{f_1 M (f_1(M+1) - M d)}{f_1 + 2M(f_1 - d)} \quad (7.4)$$

where d is distance from aperture A to L1. By choosing d carefully, the relayed image of aperture A can easily be positioned to the right of the Kepler telescope. Then, it is simply a question of choosing the focal length (f_3) and position of the positive lens (L3) such that the relayed image is in turn imaged to a location approximately coincident with the hogel. To do this, one simply uses the Gaussian form of the thin lens equation

$$\frac{1}{t'} + \frac{1}{t} = \frac{1}{f_3} \quad (7.5)$$

where t and t' are, respectively, the (positive valued) separation between the relayed image and L3 and that between L3 and the hogel. If t and t' are chosen to be too large then diffraction will wash out the image at the hogel completely. On the other hand, if they are chosen too small, then the reference beam will not be sufficiently collimated.

Because the hogel is created by the coherent interference of the object and reference beams, it is important that the optical path lengths of both object and reference beams are as similar as possible. Although the intrinsic coherence length of the laser is theoretically greater than 1 m, any discrepancy in the path lengths will in practice tend to reduce the overall diffractive efficiency of the hogel.

7.5.4.2.7 Energy Requirements

The 2001 Geola printer required approximately 1 mJ of energy per pulse per primary colour channel to print 1.6 mm diameter hogels using a panchromatic silver halide material having a sensitivity of approximately 1000 $\mu\text{J}/\text{cm}^2$. This is, in fact, much bigger than the theoretically required energy of approximately 30 μJ —largely because many of the optical systems were simply not optimised.

7.5.4.2.8 Alignment

Triple-beam printers are fundamentally more difficult to align than apochromatic single-beam printers. The problem is that in triple-beam printers, the virtual image of the red, green and blue spatial light modulators, downstream of the writing objectives, are separated by the distance between the objectives. Although it is relatively easy to align the actual objectives in the x , y and z directions, it is rather more difficult to ensure the correct orientation of the emerging light.

An effective alignment process for triple-beam printers is to focus in the objectives to form an image of each SLM, for example at 50 cm from the Fourier plane. A graticule is then loaded onto each of the SLMs and a high-energy object beam is used to project an image of this graticule onto an exactly perpendicular target. By taking digital photographs of the target with the three projected graticules and analysing these using a computer, the optical system may be aligned very accurately. It is important to point out that it is not sufficient that the objectives alone point in the same direction. One must also ensure that the SLM is exactly centred with respect to the objective and is not at an angle. In the case that the alignment is not done properly, holograms will show misaligned red, green and blue images. Almost always, an iteration process is required to ascertain whether alignment has been successful. This entails recording a test hologram of a grid structure and analysing whether a given colour channel needs readjustment. In film printers, it is imperative that the normal vector of the emulsion surface at the red, green and blue hogel write locations be the same, otherwise even a perfectly aligned optical system will lead to displaced colours. Although it is possible to numerically recalibrate a physically misaligned optical system by predistorting the SLM image data, this generally introduces some noise into the final 3D image and, as such, it is always strongly recommended to properly align the optical system.

In apochromatic and monochromatic printers, alignment is much easier because there is only one hogel write location and one writing objective. One therefore only needs to verify that a good image is present downstream of the Fourier plane. Colour slip is immediately obvious and can be corrected for by looking at the projected image while adjusting the optics.

In addition to the alignment of the object beam system, in all DWDH printers, the footprint of each object beam must coincide with the corresponding reference beam footprint at the holographic film surface. If this does not occur, then at best, a full hogel will not be formed, and at worst, there will be no hologram at all. For small hogel sizes, it can be quite tricky to ensure proper object/reference alignment. The usual way of doing this is to replace the square aperture used in the printer object beam system (which produces a square hogel) with a very small circular aperture. This essentially forms a very dim “point hogel” which scatters on the emulsion surface (one usually uses old film or an old plate). By reducing the energy per pulse, it is safe for an observer to then look into the writing objective where a luminous point will appear at a certain location at the emulsion surface. This is the centre of the hogel. It is then relatively easy to align the reference beam such that the point appears exactly in the centre of the larger reference square. When glass plates are used, it is vital that the system be recalibrated for the exact thickness of the glass used. It is useless aligning the object and reference writing beams at one thickness and then recording with a slightly different thickness plate—Snell’s law will act to misalign the system and hogels will not be recorded properly.

7.5.4.2.9 Conjugate and Non-Conjugate Operation Geometries

Lens-based printers usually produce an image of each spatial light modulator downstream of the hogel. In contrast, diffusion screen systems always produce an image upstream. We have already discussed that a problem with diffusion screen systems is that the screen must be relatively large and at a good distance from the hogel if image blurring is not to result. In both lensless and lens-based hogel-forming systems, one has the choice of replaying the hologram with a conjugate or non-conjugate reference beam

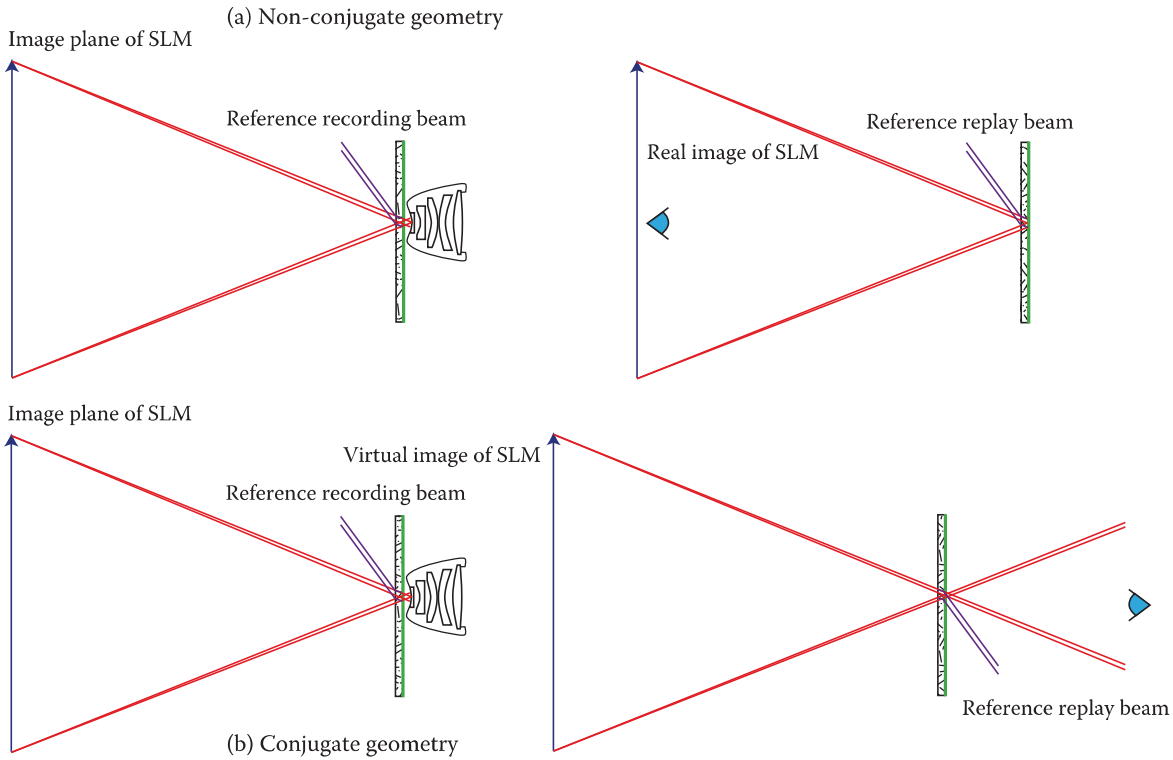


FIGURE 7.13 (a) Non-conjugate and (b) conjugate recording/replay geometries in a lens-based DWDH printer.

(Figure 7.13). If the image plane of the SLM is upstream* of the hogel at recording, then a non-conjugate reference beam at replay will produce a virtual image of the SLM behind the hologram. Likewise, a conjugate replay beam will produce a real image of the SLM, for each hogel, in front of the hologram.

The choice of which geometry to use is related to the printer construction. In the 2001 Geola printer, the glass holographic plates are always mounted with the emulsion facing towards the hogel-writing objectives. This is essentially a necessity, as the large plates are generally of a thickness that is greater than the distance between the physical end of the objectives and the Fourier plane. After processing, the sensitive emulsion surface must be at the rear of the hologram—blackening is then applied both to protect the emulsion and to improve the viewing characteristics of the hologram. This means that illumination of the hologram must be by a non-conjugate beam. When a diffusion screen system is employed, the same logic would dictate that a conjugate replay geometry be used.

If the image plane of the SLM is at a relatively small distance from the hologram and the hologram is to be viewed close-up, then it is generally better to ensure that a real image of the SLM is located on the viewing side of the hologram at replay. This will lead to the best image quality. However, it is often the case that the image plane distance can be made very large, and in this case, the choice of conjugate or non-conjugate replay geometries simply depends on the most convenient way to record and replay the hologram. In Chapters 8 and 9, we will see that the image transformations necessary to convert perspective view information into the SLM mask file information depend critically on whether the printer is designed for conjugate or non-conjugate operation.

7.5.4.2.10 Laser Stability Issues

By far the largest problem encountered with the 2001 Geola printer was related to the OEM RGB-pulsed laser. Although the laser's stability was relatively good from an absolute point of view, the occasional bad pulse often ruined a hologram after hours of writing—simply because a hologram could contain nearly one million hogels. For this reason, a new type of laser was developed by XYZ Imaging Inc. and Geola Technologies

* Note that Figure 7.13 shows the case of the image plane of the SLM being located downstream of the hogel.

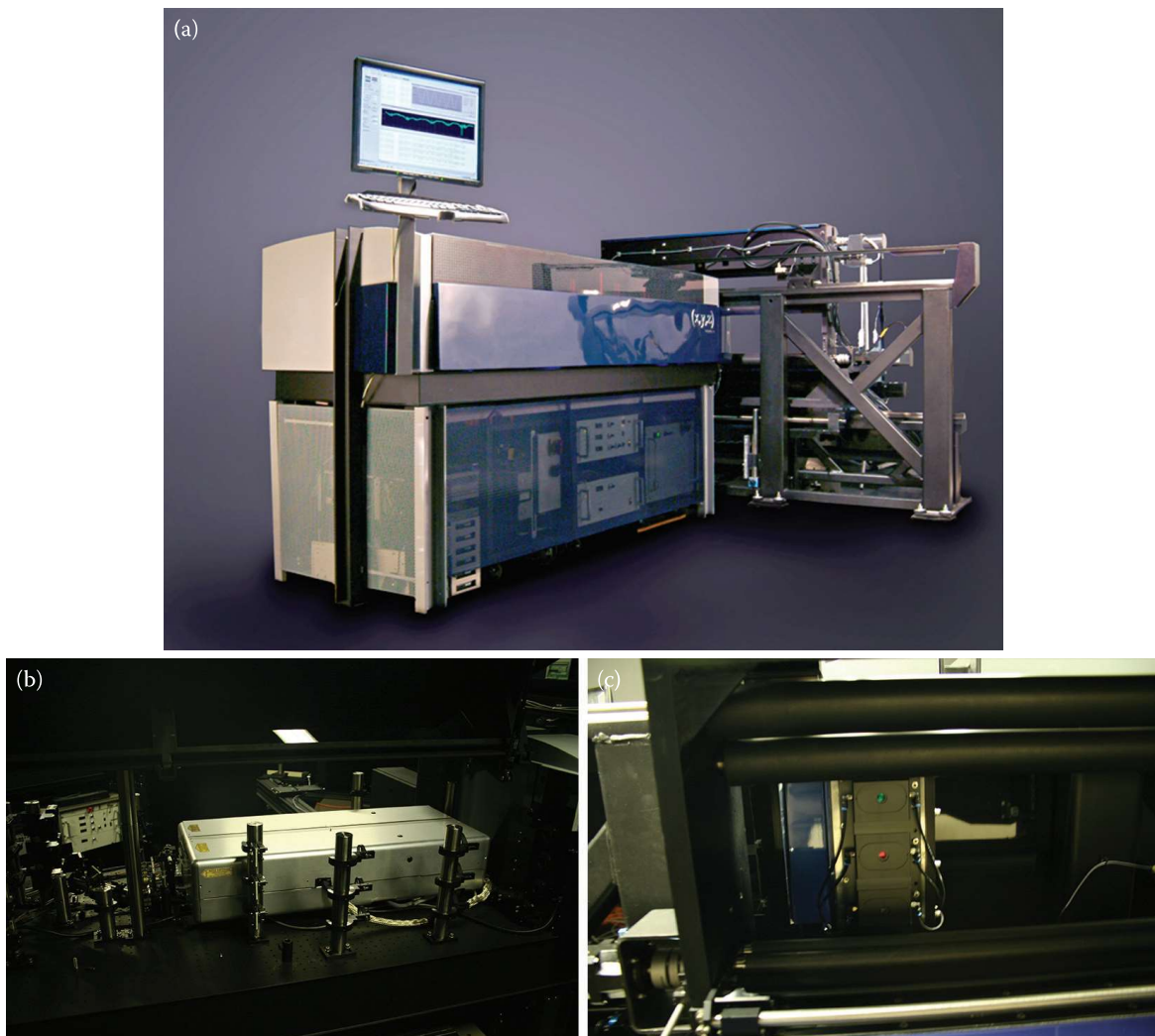


FIGURE 7.14 (a) Commercial DWDH triple-beam printer made by XYZ Imaging. (b) A shot of the interior showing the optics and the RGB-pulsed laser. (c) The three hogel-writing objectives, each surrounded by a vacuum unit, whose function is to pull the film flat at exactly the correct distance from the object. In practice, the optimum distance is a little downstream of the Fourier plane.

Ltd. This laser was built around twin linear telescopic cavities, rather than the initial ring cavity geometry. Another passive Q-switch, Cobalt MALO, was used in the 1319 nm channel and Nd:YLF was abandoned for Nd:YAG. This laser (see Section 6.5.2 in Chapter 6) was capable of operation at faster speeds—initially up to 30 Hz. The final piece of the puzzle was an active cavity length stabilisation scheme (see Appendix 3), which dramatically improved laser stability and allowed large DWDH holograms to be routinely produced.

7.5.4.2.11 Commercial DWDH Printers Based on 2001 Geola Printer

In 2004 to 2005, the company XYZ Imaging produced a commercial DWDH triple-beam printer based on the original Geola design (Figure 7.14). This was a film-based device* capable of writing DWDH holograms up to 1.1 m in width at hogel sizes of 0.8 or 1.6 mm. To keep the film at exactly the correct distance from the writing objectives, a vacuum system was used to suck the film onto a flat surface immediately in front of the three objectives (Figure 7.14c). XYZ Imaging also developed an automatic chemical processor. Photographs of holograms produced on the XYZ Imaging printer and on various other DWDH printers are shown in Chapters 10 and 14.

* The printer was designed to work with panchromatic silver halide film produced by the Russian Company Sfera-S.

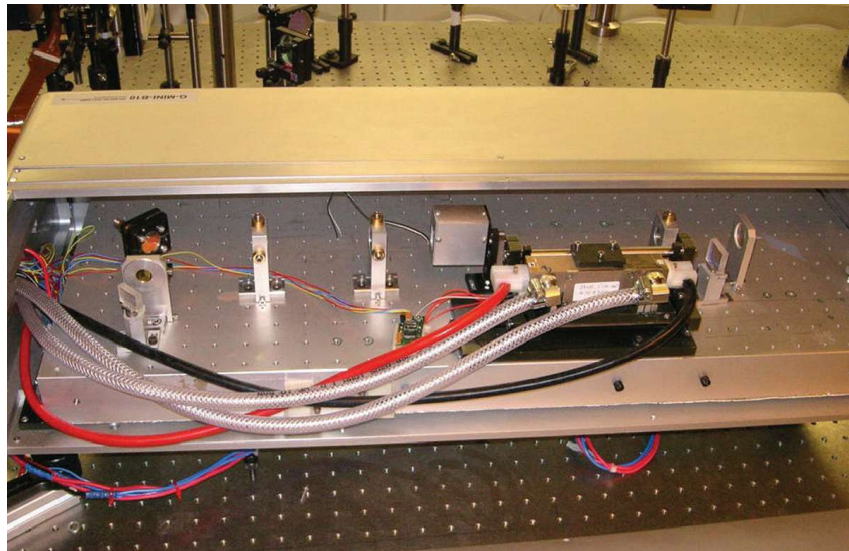


FIGURE 7.15 Short-cavity 532 nm Nd:YAG pulsed laser used in a 2006 prototype DWDH printer based on an LCOS display at Sussex University. The actual laser is visible in the centre of the picture. The optics in the larger laser case, are for frequency doubling and beam collimation. The main printer optics are visible in the background. The laser delivered stable pulses up to an energy of 1 mJ at a repetition rate of up to 50 Hz.

7.5.5 Printers Based on Liquid Crystal on Silicon Displays

John Tapsell [19], working at Sussex University in 2006, converted an old monochromatic DWDH printer supplied by Geola to work with a liquid crystal on silicon (LCOS) device. Marcin Lesniewski designed a telecentric afocal reversing system for the printer so that his 105° Fourier transform objective, which was used in the XYZ Imaging commercial printers, could be used with a BR768HC LCOS panel from Brillian. The printer used a short-cavity 532 nm, 30 ns pulsed Nd:YAG laser (Figure 7.15) of the type described in Section 6.5.3.1. The 768 × 1280 LCOS panel measured 17.91 mm diagonally and had a 12 µm pixel pitch. The fill factor was 92% with a reflectivity of 71% and a frame rate of 120 Hz. Small monochromatic DWDH reflection holograms were recorded with the system with a write rate of up to 40 Hz and a hogel size down to 300 µm. Very little energy was required and the 2000:1 contrast ratio available from the LCOS display produced a better quality image than available with comparative tests using an XGA1 Sony LCD panel. Figure 7.16 shows a diagram of the Sussex printer.

Geola Technologies Ltd used the experience gained from working on the LCOS printer at the engineering school of Sussex University in 2006 to come up with a concept design for a large-format RGB triple-beam DWDH LCOS printer. This design was subsequently used as the basis for the construction of a commercial printer built by the Centre for Laser Photonics in North Wales* for the production of metre-square full-colour reflection master holograms. Figure 7.17 shows a schematic of the design and Figure 7.18 shows a 3D visualisation.

The use of LCOS panels in DWDH printers is relatively simple. The slightly increased complexity of the object beam optical system is well merited due to the clear advantages offered by these panels in terms of higher switching speed (up to 200 Hz), better contrast (typically 2000:1) and superior efficiency (>70%). Table 7.1 lists the lenses used in the telecentric afocal reversing system and the Fourier transforming objective employed in the triple-beam printer.

* The Centre for Laser Photonics was a joint venture between Geola Technologies Ltd and Optopreneurs Ltd., which was operational between 2006 and 2010.

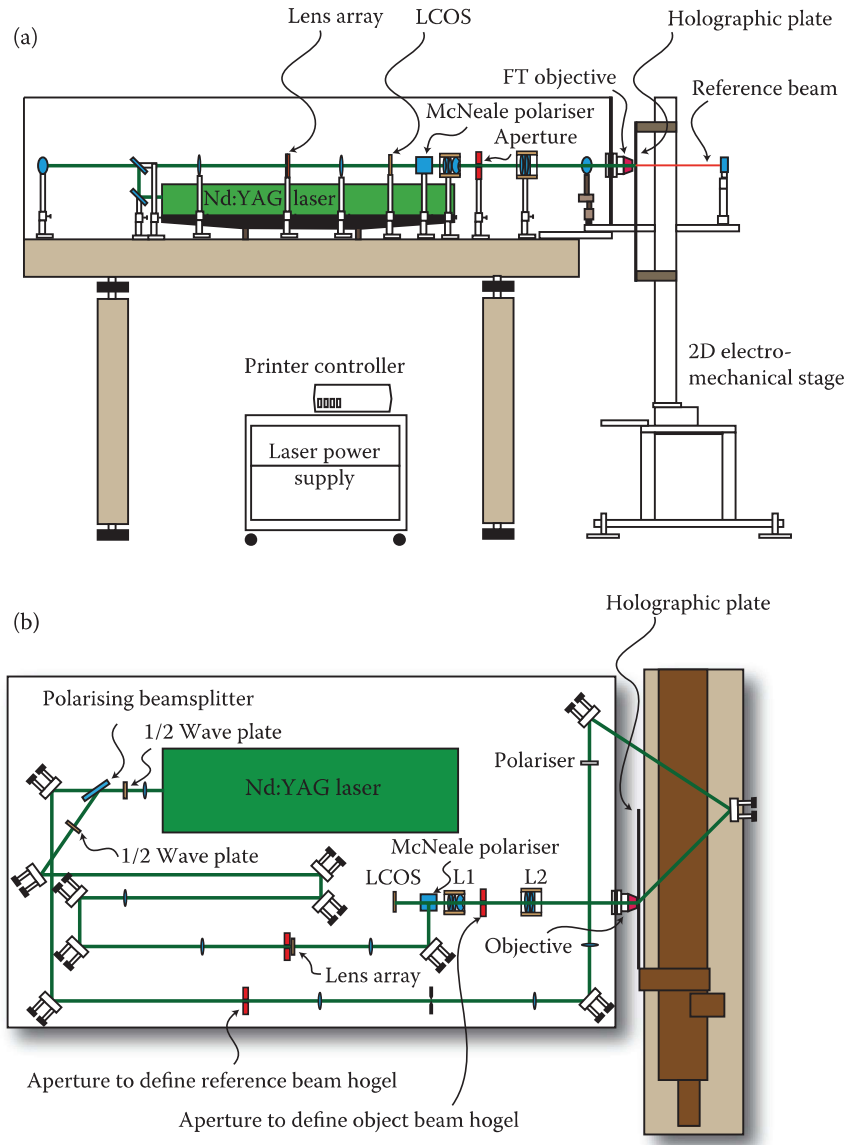


FIGURE 7.16 Sussex University LCOS printer. (a) Side view of the printer and (b) optical schematic. Note that the lens systems (L1 and L2), together with a meniscus field curvature correction lens next to the LCOS, form an afocal telecentric reversing system.

7.5.6 Printers Incorporating Variable Reference Beam Systems

All the printer schemes that we have reviewed above have used static reference beams. This is the simplest case to arrange optically. However, a static reference beam means that the written DWDH hologram must be replayed with a collimated light source if one is to avoid injecting any aberration into the hologram. However, this is rarely practical—in practice, the hologram must be illuminated by a point source relatively close to the display. One solution around this problem is to numerically predistort the image data to exactly counteract the induced aberration. We shall derive the equations needed for this purpose in Chapter 11 and discuss their solution in Appendix 4. For colour reflection holograms, both chromatic and geometric predistortion of the image data are required. Unfortunately, there is a rather strict limit on how much predistortion can be applied successfully and it gets more difficult the larger the hologram and the greater its field of view. Therefore, although numerical predistortion can certainly help, it is only very

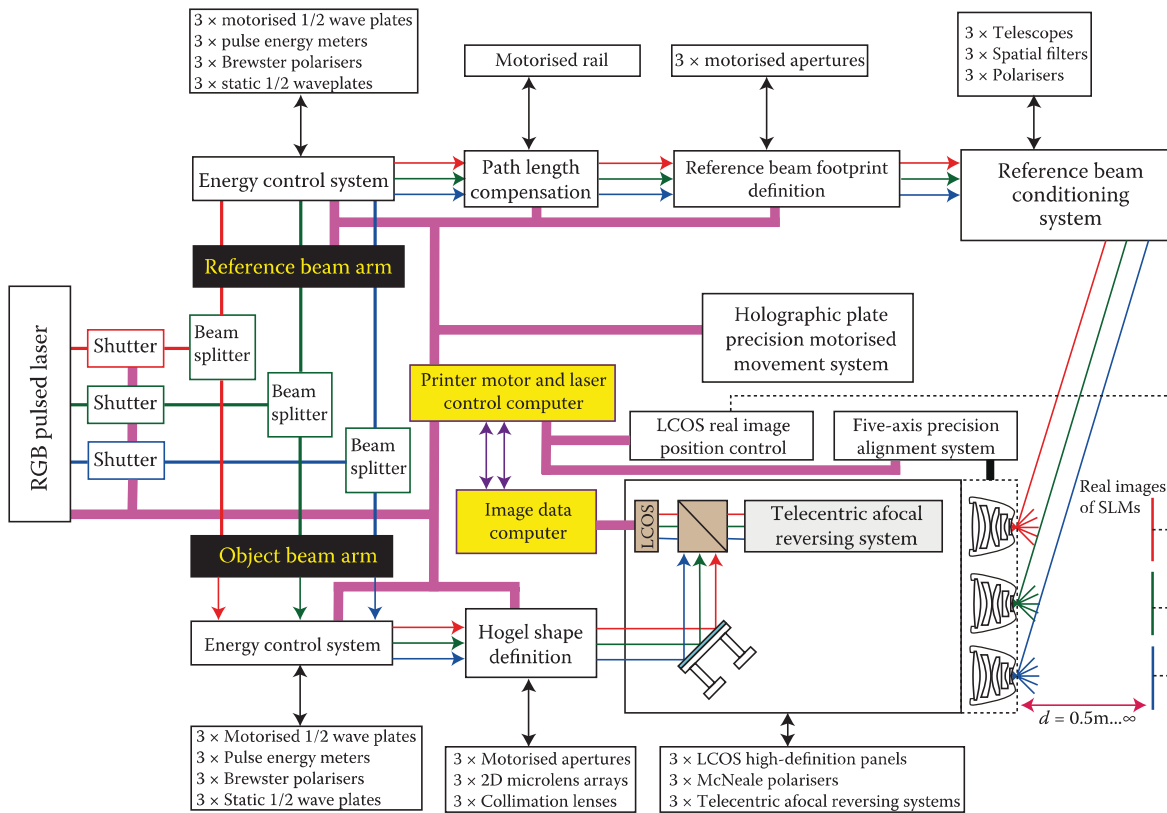


FIGURE 7.17 Systems schematic for a large, triple-beam DWDH LCOS printer that was built by the Centre for Laser Photonics in Wales. The design includes separate computers for image display and machine control for eventual operation at 120 Hz. The main trigger signal is originated by the LCOS controller and this is used to drive the main mechanical stage and the laser. A five-axis alignment system is used for easy alignment of the three objectives.

rarely capable of completely solving the problem of induced aberration due to a disparity in the reference recording and replay geometries.

The solution is to incorporate a variable-angle reference beam system into the printer. Each hogel can then be recorded using a software-selectable altitudinal and azimuthal angle. By choosing these angles carefully for each hogel, any type of macroscopic reference recording beam may be synthesised. In this way, a hologram may be produced so that it replays perfectly for a given location of the illuminating point source. In addition, under certain circumstances, small variations of the reference angle at each hogel may be combined favourably with numerical image predistortion to enhance the angle of view available from a given printer.

The downside to variable-angle reference beam systems is that they are rather more complex than static reference beam systems and can, if not designed properly, induce various problems including blurring and dimming into the hologram. The basic issue is that the object and reference beam footprints at the emulsion surface must overlap quite precisely. For small hogels (and they can go down to $<250\text{ }\mu\text{m}$), it can be a difficult enough task to arrange for proper footprint matching with a static reference beam, let alone for a 2D variable reference beam.

The simplest solution is to use a 2D-gimballed precision rotation stage to deflect the laser beam to a second 2D-gimballed rotation stage, itself mounted on a 2D translation stage. A computer then calculates the rotation angles and translation distances such that the reference beam strikes the hogel at given altitudinal and azimuthal angles. Of course, as the angles change, so the footprint at the emulsion surface also changes—this then needs to be compensated by the 2D rotation of a square aperture upstream of the hogel placed within a weak image-relaying system.* Figure 7.19 shows a schematic of this system.

* An LCD may also be used here as a programmable mask of variable shape.

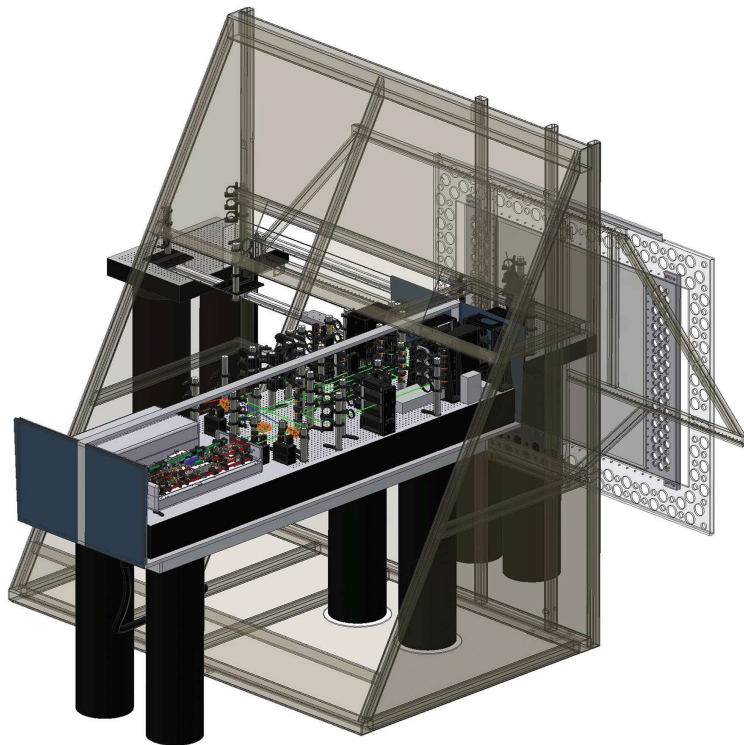


FIGURE 7.18 3D computer drawing of the large LCOS printer from Figure 7.17. Note the two lasers at the rear of the optical unit. The intention was to use a pulsed chromium forsterite laser for the red channel (627 nm) and to use an additional dual-channel 446 nm/532 nm pulsed Nd:YAG laser for the red and blue channels. In the actual printer, this design was modified to include only a single standard 440/532/660 nm RGB laser.

To work properly, this scheme must be very compact as the precision of the beam footprint alignment scales strongly with size.

Another type of variable reference beam system is based on a lens system and a single small-angle 2D-gimballed precision rotation stage as illustrated in Figure 7.20. Here, the centre of the reference beam is always aligned with the centre of the object beam and a small change in rotation angle produced by the rotation stage leads to a much larger change in angle at the hogel. The advantage of this type of system is that the footprint alignment is much more stable. The disadvantage is that if a large range of angles is required, then aberration in the lens system can induce blurring into the hologram. In addition, the footprint shape often changes in a non-linear way at large angles, requiring the use of an SLM as the apodising element. Figure 7.21 shows a photograph of a lens-based variable reference beam system in a recent triple-beam printer.

7.5.7 HPO Printers

The SLM mask file patterns used in triple-beam printers to print DWDH HPO holograms (ignoring numerical distortion correction for finite optical objective distortion and viewing window functions) are independent of the vertical coordinate. Horizontal information (as typified by the central row in the SLM) is essentially repeated in all rows within the viewing window. The vertical coordinate of the SLM is thus used in a very simplistic manner in these printers to induce a vertical divergence of rays at the hogel.* However, it is possible to use the vertical coordinate of the SLM to encode multiple hogels; to do

* Of course, when a full-parallax hologram (or indeed a rainbow hologram) is being written, this is not the case.

TABLE 7.1

Lens Parameters for the Telecentric Afocal Reversing System and Fourier Transform Objective Used in the Triple-Beam RGB DWDDH Printer Manufactured by the Centre for Laser Photonics in Wales (2009)

No.	Green Channel			EFL = -7.669			Red Channel			EFL = -7.671			Blue Channel			EFL = -7.716		
	Radius (mm)	Clear diameter (mm)	Separation (mm)	Material	Radius (mm)	Clear diameter (mm)	Separation (mm)	Material	Radius (mm)	Clear diameter (mm)	Separation (mm)	Material	Radius (mm)	Clear diameter (mm)	Separation (mm)	Material		
1	Plane	2.301	4	Air	Plane	2.301	4	Air	Plane	2.318	4	Air	Plane	2.318	4	Air		
2	-20.34	9.562	3.07	S-SF6	-19.476	9.563	3.15	S-SF6	-21.69849	9.627	3.05	S-SF6						
3	-9.616	11.63	1.93	Air	-9.3	11.678	1.8	Air	-10.03	11.678	2	Air						
4	-7.6	12.36	1.45	S-SF6	-7.465	12.309	1.54	S-SF6	-7.852	12.474	1.45	S-SF6						
5	-26.03	17.598	3.45	Air	-25.54	17.781	3.36	Air	-29.51541	17.734	3.45	Air						
6	-25.027	24.134	7.45	S-SF6	-25.36	24.173	7.5	S-SF6	-27.31236	24.774	7.53	S-SF6						
7	-16.144	28.39	0.3	Air	-16.144	28.396	0.3	Air	-16.707	28.995	0.3	Air						
8	-201.01914	37.924	7.8	S-SF6	-131.52	37.312	7.64	S-SF6	-142.99318	38.172	7.87	S-SF6						
9	-35.57	39.759	0.3	Air	-34.04	39.35	0.3	Air	-34.95308	40.243	0.3	Air						
10	59.7	42.1	7.03	S-SF6	60.9	42.341	7.16	S-SF6	63.76992	42.852	6.83	S-SF6						
11	1310.14201	41.384	1.27	Air	-568.9	41.829	1.28	Air	-1469.7998	42.281	1.3	Air						
12	27.27	38.142	6.15	S-SF6	27.27	38.281	6.15	S-SF6	27.29649	38.636	6.15	S-SF6						
13	20.51	32.078	14.72777	Air	20.51	32.205	14.82	Air	20.51	32.379	15.27	Air						
14	Plane	46	246.59396	Air	Plane	64	246.59396	Air	Plane	64	246.59396	Air	Plane	64	246.59396	Air	S-SF5	
15	693	64	4.33	S-SF5	693	64	4.33	S-SF5	693	64	4.33	S-SF5						

16	224.9	64	7.33	S-BK7	224.9	64	7.5	Air	224.9	64	7.33	S-BK7
17	-304.8	64	0.5	Air					-304.8	64	0.5	Air
18	693	64	4.33	S-SF5	693	64	4.33	S-SF5	693	64	4.33	S-SF5
19	224.9	64	7.33	S-BK7	224.9	64	7.33	S-BK7	224.9	64	7.33	S-BK7
20	-304.8	64	250.1	Air	-304.8	64	250.1	Air	-304.8	64	250.1	Air
21	Plane	50.895	73.58	Air	Plane	50.895	73.58	Air	Plane	50.895	73.58	Air
22	-29.51	35.98	15.2	J-BAF7	-29.51	35.98	15.2	J-BAF7	-29.51	35.98	15.2	J-BAF7
23	-37.1	45.5	0.4	Air	-37.1	45.5	0.4	Air	-37.1	45.5	0.4	Air
24	483.10001	47	6.4	J-SK4	483.10001	47	6.4	J-SK4	483.10001	47	6.4	J-SK4
25	-110.15	47	0.2	Air	-110.15	47	0.2	Air	-110.15	47	0.2	Air
26	129.42	47	9.8	J-SK12	129.42	47	9.8	J-SK12	129.42	47	9.8	J-SK12
27	-80.91	47	4	J-SF14	-80.91	47	4	J-SF14	-80.91	47	4	J-SF14
28	Plane	47	50	Air	Plane	47	50	Air	Plane	47	50	Air
29	Plane	30	30	S-BK7	Plane	30	30	S-BK7	Plane	30	30	S-BK7
30	Plane	30	36.68504	Air	Plane	30	36.68504	Air	Plane	30	36.68504	Air
31	-65.845	30	2	S-SF5	-65.845	30	2	S-SF5	-65.845	30	2	S-SF5
32	Plane	30	1.15834	Air	Plane	30	1.23033	Air	Plane	30	1.67108	Air
	Thickness	807.707		Thickness	807.779			Thickness	808.279			

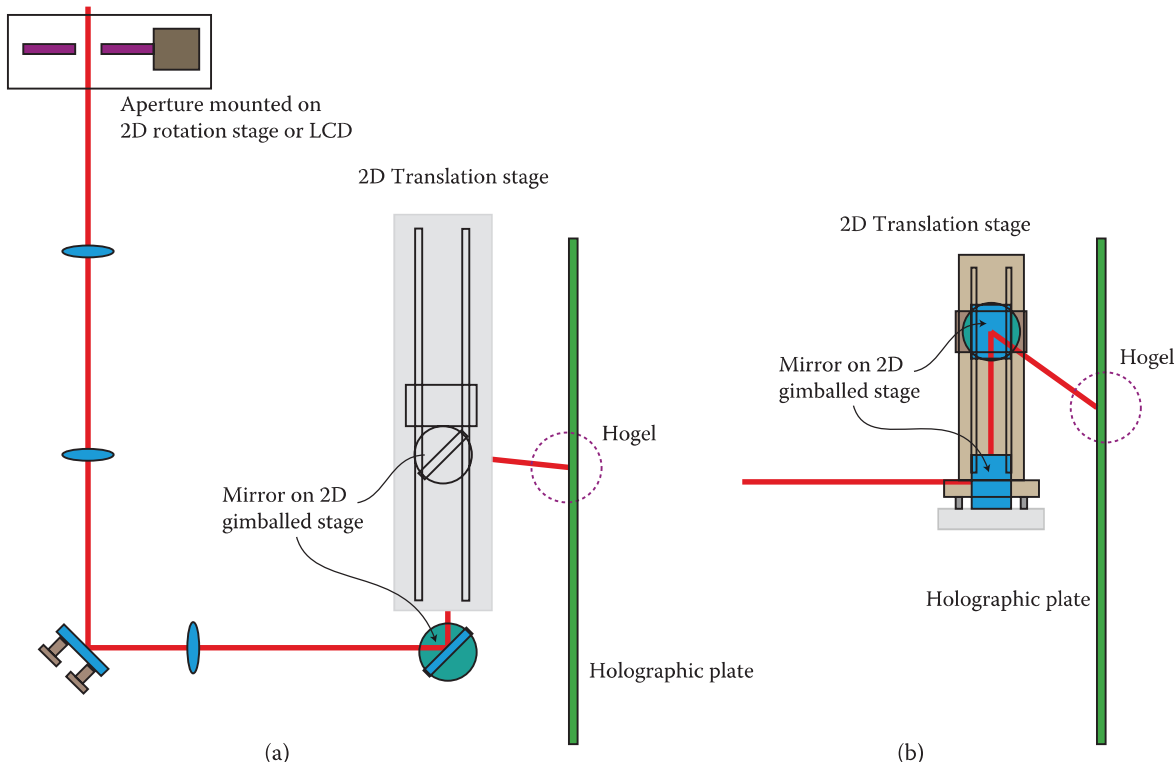


FIGURE 7.19 Simple optical scheme for automatically changing the reference beam angle (altitude and azimuth) at each hogel—view from the top (a) and from the side (b). Note that for fast printing, each motor controller must be preprogrammed with exact position data versus time. Before hogel-writing commences, the motors will need to backtrack a little and then start an acceleration sequence. Thereafter, the velocity of each stage will, in general, be a non-linear but smooth function of time. This ensures that the reference beam attains the correct angles and proper footprint alignment at each hogel at just the correct time without introducing mechanical transients into the system.

this, one must delegate the job of creating a vertical divergence of rays at the hogel to another system. The Fourier transforming objective then becomes a cylindrical lens system and the form of the hogel becomes an elongated column, the length of which, in the simplest variant, is equal to the SLM panel height, although a telescope may easily be used to modify this. A vertical diffusing element must be used in contact with the holographic emulsion and a modified “elongated column” reference beam must be employed. Klug and Kihara [20] described a variant of this system in 1995.

In 1998, Shirakura et al. [21], working at Sony Corporation, designed and built an integrated one-step CW laser HPO DWDH monochrome reflection hologram portraiture printer using this concept (Figure 7.22). The system consisted of a charge-coupled device (CCD) camera for image capture, a high-speed image processing device and a desktop DWDH HPO digital holographic printer. The portraits were delivered as an HPO 3D image ($78 \text{ mm} \times 59 \text{ mm}$) and recorded on DuPont photopolymer film (HRF700XO71-20). The CCD camera unit moved along a straight track from right to left, driven by a stepping motor. There was another stepping motor in the camera unit to move a $2/3$ in. CCD unit anti-parallel to the direction in which the camera moved; these two motors were synchronised so that the optical axis was always pointing directly at the object.

The hologram was recorded by projection of the digital images through a 510-K pixel thin-film transistor monochrome LCD using one-dimensional image compression with a cylindrical lens. The images displayed on the LCD were calculated from the perspective images available from the camera. The CCD camera recorded 295 2D images (640 pixels by 480 pixels) which were captured in 7.5 s of shooting (30 frames/s). A 400 mW frequency-doubled CW Nd:YAG laser of 532 nm was used as the recording light source in the tabletop printer, which measured only $1100 \text{ mm} \times 700 \text{ mm} \times 300 \text{ mm}$. Each column hogel ($0.2 \text{ mm} \times 78 \text{ mm}$) was exposed onto the photopolymer in 0.25 s. A diffuser was attached to the LCD to

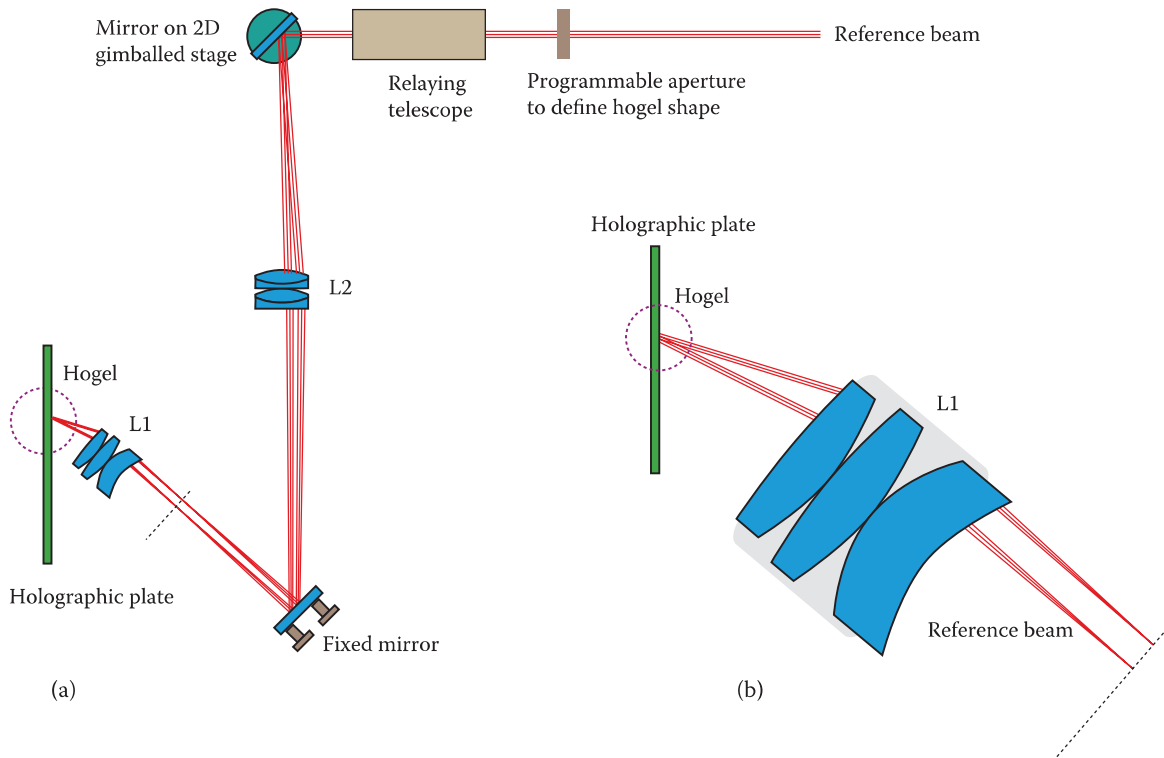


FIGURE 7.20 Lens-based optical scheme (a) for automatically changing the reference beam angle (in altitude and azimuth). Details of the main reference objective and the rays affecting the hogel under two different angles of incidence are shown (b). A typical system may be able to achieve a variation $\pm 25^\circ$ at the hogel (in both vertical and horizontal angles) for an angular variation at the gimballed rotation stage of $\pm 1.5^\circ$. Due to intrinsic aberration of systems that can cope with large angle variations, a programmable aperture such as an LCD may be used in junction with a relaying telescope to ensure a proper hogel shape at all times.

make the beam intensity more uniform within the width of an elemental hologram and a slit, placed at an optical plane conjugate to the film plane, was used to form the hogel. The cylindrical focussing lens gave the holograms a horizontal field of view of 57° . A vertical diffuser in contact with the film likewise ensured a vertical viewing angle of 40° . The entire printing time of the 295 column hogels took only 147 s.

Clearly, a triple-beam pulsed laser DWDH printer designed using this concept could be expected to print HPO holograms much faster than the type of DWDH printers we have been discussing up until now. Nevertheless, in practice, it can be difficult to stop the hologram from looking “banded” and there are issues associated with the use of a contact diffuser.

7.5.8 Single-Beam RGB Printers

Single-beam DWDH printers can be constructed using apochromatic lens systems if resolution or angle of view can be sacrificed. Often, source size and chromatic blurring significantly limit the available depth in a display hologram. One may not then need the increased resolution available from a monochromatic system, and as such, it makes sense to design the printer using a single hogel write head. As we have discussed previously, this enormously simplifies the task of aligning the component colours.

7.5.8.1 Screen-Based Hogel Formation Systems

When limited depth in a hologram is acceptable, a lensless solution forming a single RGB hogel can also be used. In fact, we began our discussion of DWDH printers by presenting just such a system, based on a diffusion screen (Figure 7.2). We did, however, mention that there were several problems associated



FIGURE 7.21 Photograph of a lens-based variable reference beam system in a modern large-format DWDH printer. To the left of the plate carrier (just visible) are two of the three object beam Fourier transform lenses. To the right of the plate carrier are the three lens systems for the reference beam angle control.

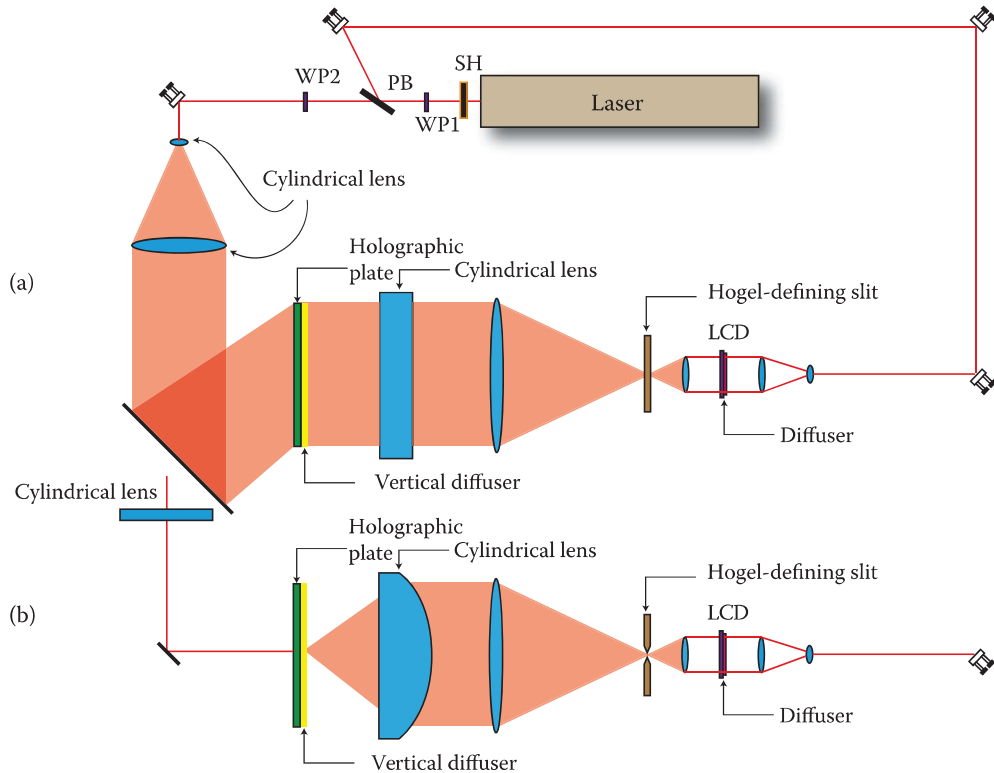


FIGURE 7.22 Simplified optical schematic of the 1998 Sony Corporation portrait printer, which printed small monochrome DWDH HPO reflection holograms as elongated “column” hogels using a 400 mW CW Nd:YAG laser in under three minutes. (a) Side view and (b) overhead view.

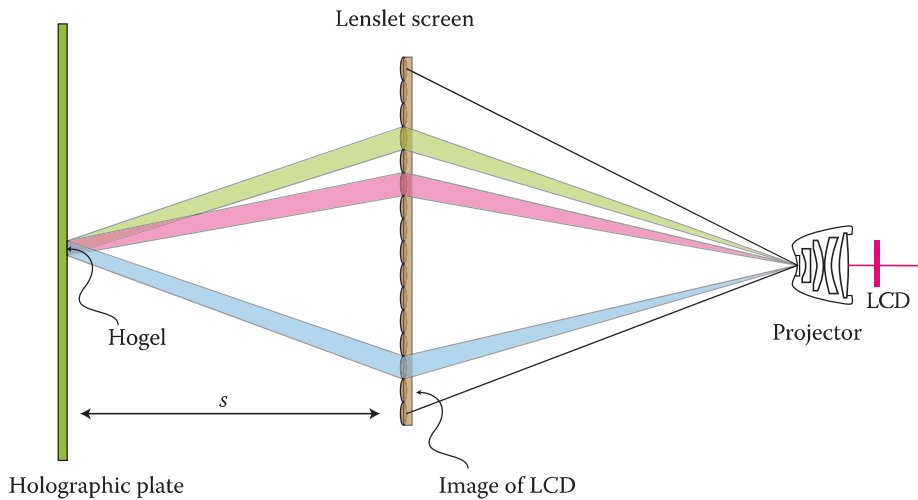


FIGURE 7.23 Diagram of an object beam hogel formation system based on a lenslet array. The size of the lenslets is greatly exaggerated.

with the simple diffusing screen. In particular, one needs a contact aperture to form the hogel; also, the energy efficiency is extremely poor. However, both these issues can be resolved by using a lenslet matrix to focus a 2D real image into a hogel (Figure 7.23). Nevertheless, there are two remaining problems. The first is illustrated in Figure 7.24. If the lenslet screen is too close and the lenslets are too large, then there will be viewing zones with no images. This produces the effect of image points flickering as an observer walks past the hologram. To avoid this, the lenslet size must be reduced, but this introduces a divergence into the ray bundles connecting each lenslet to each hogel. Any such divergence of a large enough magnitude will introduce blurring into points within the hologram beyond a certain depth. As we shall study in Chapter 11, a general paraxial formula for the critical depth, beyond which (interior) blurring occurs due to any form of ray bundle divergence is given by

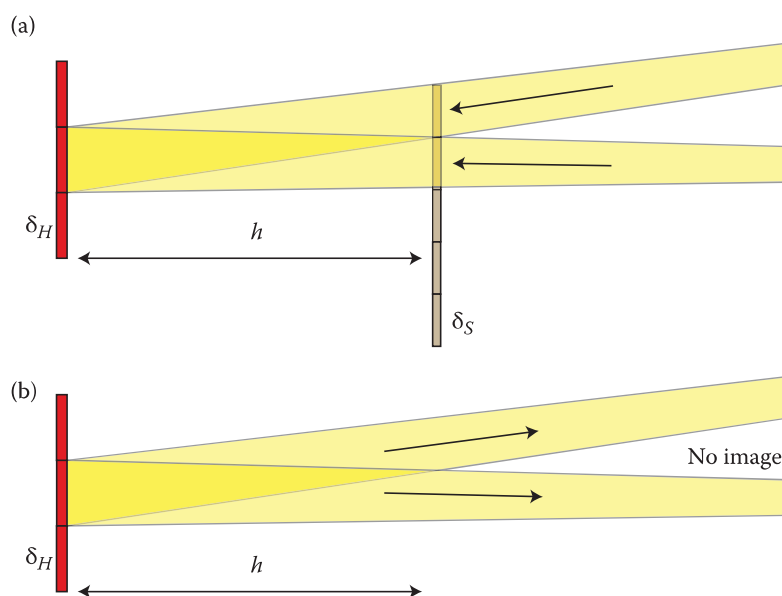


FIGURE 7.24 Diagram illustrating (a) the recording and (b) playback of a hogel using a lenslet screen. If the lenslet screen is too close, and the lenslets are too large, then there will be viewing zones with no images.

$$d \sim \frac{h\delta\theta_{\text{Eye}}}{\delta\varphi - \delta\theta_{\text{Eye}}} \quad \forall \delta\varphi > \delta\theta_{\text{Eye}}$$

$$\sim \infty \quad \forall \delta\varphi \leq \delta\theta_{\text{Eye}}$$
(7.6)

where h is the viewing distance from the eye to the hogel, $\delta\varphi$ is the ray bundle divergence and $\delta\theta_{\text{Eye}}$ is the angular resolution of the human eye. In the limit that the lenslet size is much smaller than the hogel size, which will usually be correct for a close screen, the ray bundle divergence induced in the present case is simply $\delta\varphi = \delta_H/s$, where s is the screen to hogel distance.

As an example, let us take a hogel diameter of 0.5 mm. Then, if we place the screen at a distance of $s = 5$ cm from the hogel, at a viewing distance of $h = 0.5$ m, we will observe blurring at a distance of $d = 6$ cm into the hologram. This is clearly not very acceptable. At a distance of $s = 15$ cm, things are rather better. Resolvable image blurring then starts at approximately $d = 22$ cm for $h = 0.5$ m. Decreasing the hogel size makes things even better. If one goes to a hogel size of 250 μm , then a screen placed at 15 cm will only induce image burring at a depth of more than 75 cm for $h = 0.5$ m. However, we must be careful here because decreasing the hogel size will induce a second type of blurring—digital diffractive blurring. The critical distance at which digital diffractive blurring operates (for wavelengths, λ) is given by

$$d \sim \frac{h\delta\theta_{\text{Eye}}}{\lambda/\delta_H - \delta\theta_{\text{Eye}}} \quad \forall \lambda/\delta_H > \delta\theta_{\text{Eye}}$$

$$\sim \infty \quad \forall \lambda/\delta_H \leq \delta\theta_{\text{Eye}}$$
(7.7)

We shall discuss this type of blurring in Chapter 11—but basically, it is caused by the innate diffractive property of a small source (the hogel). Plugging in the numbers for the case of interest, we obtain a value for d of 44 cm for $h = 0.5$ m.* Therefore, for a 250 μm hogel, digital diffractive blurring is more limiting at $h = 0.5$ m than the blurring induced by a close recording screen. In fact, digital diffractive blurring gets worse as you get closer to the hologram, and thus, one wants to avoid using too small a hogel. By ensuring that the hogel size is greater than or equal to 0.5 mm, this type of blurring is eliminated for the human observer with normal eyesight.

As long as the field of view of the hologram is not too great, it can therefore be feasible to use a lenslet screen to form the hogel. Good quality small-hogel (albeit relatively shallow) holograms can be made in this way within the design remit of a compact printer. However, we will now illustrate why this technique is not so appropriate for the case of ultra-realistic holograms of great depth and field of view. Let us again take a hogel diameter of 0.5 mm; anyhow, we cannot use a smaller diameter without incurring digital diffractive blurring. We now demand no induced blurring from any viewing distance. However, to guarantee this, we need to place the screen at a distance of at least 500 mm from the hogel. At a field of view of 130°, this leads to a screen that is more than 2 m wide!

Holographic diffusers and holographic optical elements may also be employed usefully as hogel-forming devices. These elements are usually used as a more convenient form of the lenslet matrix screen. Most screen-based hogel production techniques have two main potential advantages. The first is that they can usually be used in an apochromatic or single-beam printing system. The second is that, even for high fields of view, they have the potential of not inducing any image distortion into the hogel. In high-numerical aperture, lens-based systems, one must inevitably tolerate such induced distortion, which is caused by a finite fifth Seidel coefficient.

7.5.9 Ultra-Realistic Printers

Ultra-realistic printers are DWDH printers capable of producing full-colour high virtual volume (HVV) displays. HVV holograms are digital full-colour reflection holograms which, when illuminated correctly,

* We assume that the average human eye can resolve 1 mm separations at a distance of 1 m.

exhibit essentially no perceivable image blurring or distortion. For a printer to be capable of writing HVV displays, it must have the following characteristics:

- Rigid high-precision printing medium such as photosensitive glass plates
- High-precision 2D electromechanical plate translation stage
- Holog-writing SLMs with a sufficiently high pixel count
- Holog-forming optical system with a sufficiently high resolution and sufficiently high numerical aperture
- Reference beam system with a sufficiently low divergence

In addition to these constraints, the photosensitive material must be capable of supporting a high spatial frequency, of not changing its physical size upon processing* and of producing a good diffractive response—this is especially needed if the field of view at replay is required to be large as in the case of holographic window-type displays. The image data and image processing must also be able to produce a data set that either matches the optical resolution of the printer or better than that of the human eye. For an HVV hologram to actually generate a proper “HVV” image, the hologram must be illuminated properly. This means that the diameter of the illuminating source must be smaller than 1 mm for every 1 m that the source is diagonally distant from the hologram. The spectral width of each colour illuminating the hologram should also be less than 1 nm. Any larger than this and there will be induced chromatic aberration (unless Bragg selection is able to mitigate this—which is unlikely). However, much below 2 nm, speckle blur becomes a concern. We shall see in Chapter 13 that speckle may be essentially eliminated using devices that induce a fast temporal modulation in the phase of the illuminating light.

The 2001 Geola printer, which we described previously, is not an ultra-realistic printer. It uses an LCD having a horizontal pixel count of 1024 and a paraxial field of view of 86° (note that the non-paraxial field of view is nearly 105° due to a finite fifth coefficient at large angles). This endows each hologram written with an angular resolution of approximately $\delta\varphi = 1.8 \text{ mrad}$ —which is nearly two times the human eye resolution. Following Equation 7.6, the maximum clear depth that the holograms can display is given by the paraxial rule

$$d \sim \frac{h\delta\theta_{\text{Eye}}}{\delta\varphi - \delta\theta_{\text{Eye}}} \quad (7.8)$$

which, for a viewing distance of $h = 1 \text{ m}$, comes out at approximately 1.25 m.

The 2001 Geola printer could be potentially modified by replacing the 1024×768 LCD display with a 1080p panel. This would solve the SLM insufficiency problem for paraxial viewing because the resolution of the Fourier lens system is easily sufficient to resolve the 1080p panel. However, at higher angles, the resolution falls below the pixel size and again blurring due to insufficient objective resolution is injected into the hologram, fundamentally limiting the virtual volume.

In thinking about the design of the ultra-realistic DWDH printer, we come up against two conflicting processes. On the one hand, we generally wish to increase the field of view of the hologram. This is certainly the case for “holographic window”-type displays in which the idea is to mimic a window. To do this, we are obliged to use a higher numerical aperture objective. However, on the other hand, we must now increase the resolution of the objective to be able to resolve more SLM pixels. Further work needs to be done in investigating how far both conditions may be satisfied in a single compound lens system. Current objectives made at Geola use SF6 glass. It is possible that by using higher index glasses, a higher numerical aperture might be attained at sufficiently high resolution.

However, even if this were the case, current HD SLMs do not have the pixel counts required for large fields of view. We shall see in Section 14.4.1 of Chapter 14, that at least four 1080p panels are required to write an HDD hologram with a field of view of $100^\circ \times 120^\circ$. Although it is possible to tile these displays together using prisms and a variant of the telecentric afocal reversing system described previously, the

* Although a physical change in the thickness of the emulsion and a change in the refractive index on processing can be compensated for using numerical image processing algorithms, this inevitably leads to the introduction of some noise.

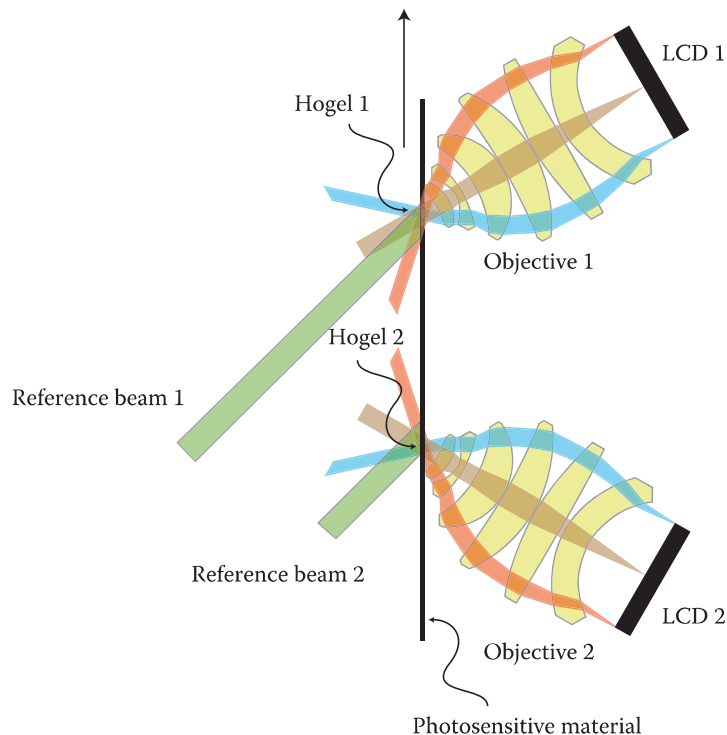


FIGURE 7.25 Writing a very-wide angle hologram using multiple objectives. Objective 1 writes hogel 1 and objective 2 writes hogel 2. Then, as the film advances, hogel 2 is overwritten by objective 1 again. In this way, hogels can be built up in several steps.

proposed UHDTV 4320p standard, which has a pixel count of 7680×4320 , would certainly make the optics rather simpler.

7.5.9.1 3N-Objective Printers

Beyond a certain field of view, it becomes impractical to write HVV holograms using single compound lenses for each primary colour. With a sufficient index modulation in the photosensitive material (see Chapters 11 and 12 for the theory behind this), one can, however, envisage writing hogels in angular segments as illustrated in Figure 7.25. The idea is basically an extension of the RGB triple-beam printer concept—except that here, one would use, in the simplest variant, an array of 2×3 objectives, two for each colour. These two objectives would be angled such that, together, a greater horizontal field of view could be covered. Special care is needed with the numerical image processing in the overlapping regions, as the rays from the two SLM/objective systems do not of course align. In some cases, it may therefore be better to use a 3×3 system (or a $3^2 \times 3$ system in the case of 2D angle extension) rather than a 2×3 system.

7.5.10 DWDH Transmission Hologram Printers

Geola has run a number of research projects using DWDH transmission printers since 1999. All these devices have been monochromatic pulsed laser printers operating at either 532 or 440 nm. The optical schematic is just the same as in Figure 7.8, with the single exception that now the reference beam impinges onto the hogel from the same side as the object beam. It can often be a little tricky getting the reference beam in, as there is not much space between the physical end of the objective and the photosensitive plate. For wide-angle objectives, one usually uses an angle of incidence that is a little larger to cope with this. Alternatively, the reference beam can be brought in through the main objective as shown in Figure 7.26.

The main interest in DWDH transmission holograms is that full-colour rainbow, achromatic and mixed rainbow–achromatic holograms may be generated from digital data in a single printing step using

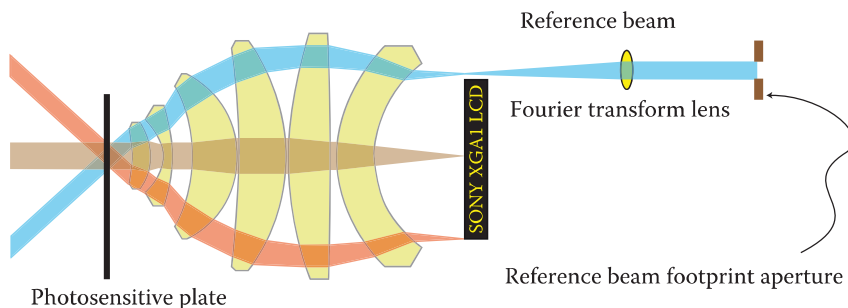


FIGURE 7.26 DWDH transmission hologram hogel formation. Here, the reference beam is actually brought in through the Fourier transform objective.

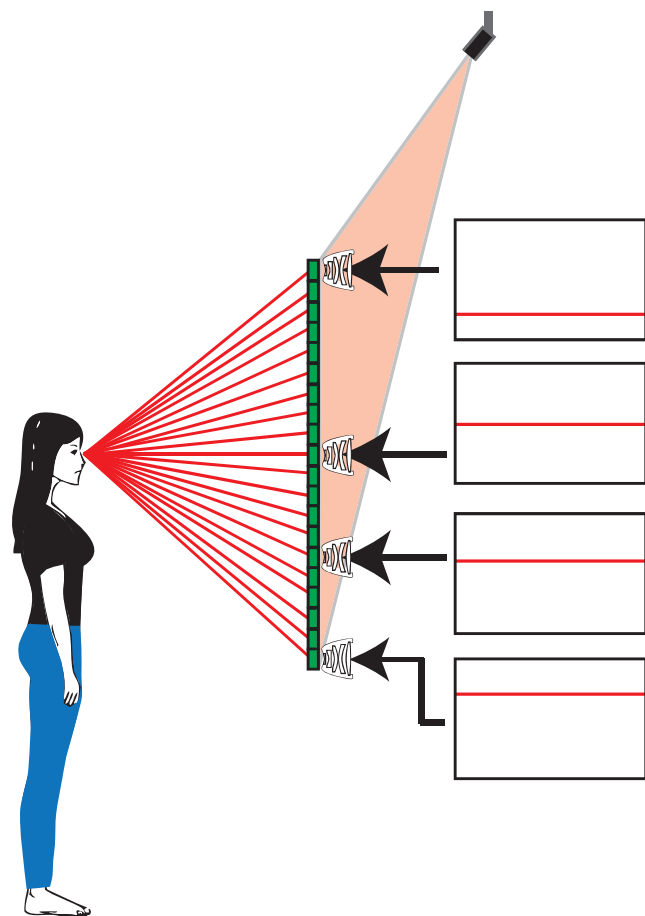


FIGURE 7.27 A 1-slit DWDH rainbow transmission hologram is seen here illuminated by light of only one colour. The observer, as positioned, sees a monochromatic holographic image. On illumination by white light, this image is available at different heights where it replays now with different colours. The four rectangles to the right of the diagram illustrate the data displayed on the printer LCD when the indicated hogels are written. The LCD data for each hogel is in the form of a line which is modulated by image data specific to that hogel. The vertical height of a given line on the LCD is determined by the vertical height of the hogel in the hologram in such a way that a rainbow viewing slit is synthesised as shown. The technique can be extended to any number of rainbow slits (using only a single colour laser) to produce full-colour DWDH rainbow transmission or achromatic transmission holograms.

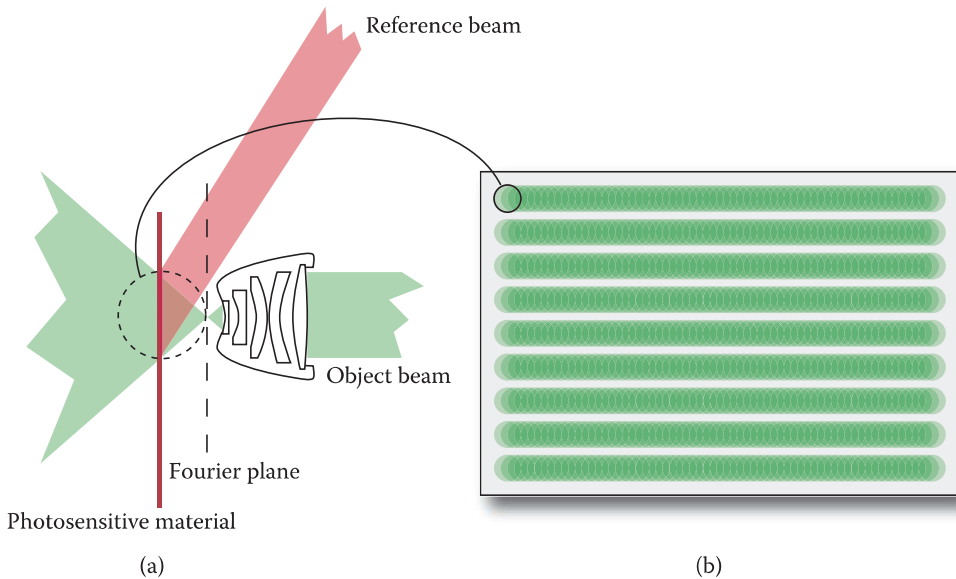


FIGURE 7.28 MWDH often uses overlapping hogels away from the Fourier plan (a). Typical hogel footprints, (b), are shown here for an MWDH transmission H_1 hologram designed for transfer to a HPO reflection H_2 to be illuminated by broadband illumination. Note the distance between hogel lines—dispersion in the vertical direction makes the gaps invisible in the final H_2 . Note also the circular hogel shape—in MWDH one is not constrained to use a square or hexagonal footprint.

only a single-colour laser (see Figure 7.27). In principle, these printers are much simpler than the triple-beam reflection hologram printers. By introducing the reference beam into the writing objective, one essentially only has optics on one side of the photosensitive material—and by only needing one laser, the optical scheme can be made very small. Alignment of the reference and object beam is also much easier. Variable reference beam systems can also be incorporated with relative ease. Very compact printers, the size of normal photocopiers, should be achievable using this technique if processing-free materials, such as monochromatic photopolymers, are used. In Chapter 8, we shall study the image-processing algorithms required to write full-colour rainbow and achromatic (i.e., black-and-white) holograms.

Small transmission rainbow and achromatic DWDH holograms have applications in document security. The Geola organisation is currently able to produce such holograms using a 440 nm pulsed laser at a hogel size of 250 μm . The holograms are then transferred to photoresist to make the embossed shims.

Large transmission rainbow and achromatic DWDH holograms have potential applications in advertising and display. They are particularly useful as shop window displays as the images can project outside the shop and into the street. With reflection holograms, a light is needed on the same side as the viewer so this is not possible.

Finally, it is possible to write full-colour, full-parallax transmission holograms using either a single-colour laser or by using three lasers in a triple-beam configuration. However, such holograms must be illuminated by three different colours from substantially different angles to eliminate the cross-talk images. As we shall see in Chapter 11, the volume transmission hologram has greater angle selectivity than the corresponding reflection hologram, allowing angle discrimination to be used more easily.

7.6 MWDH Printers

MWDH is the technique of writing first an H_1 hologram using digital image data and then optically transferring the H_1 to a white light-viewable H_2 . In many ways, MWDH is similar to the technique of multiple photo-generated holography pioneered by Spierings and van Nuland [8]. However, no diffusion screen is used, hogels are written as spots rather than long, thin rectangles and digital data replace the photographs. MWDH can also be used to create full-parallax holograms of great depth, which is difficult to arrange using multiple photo-generated holography.

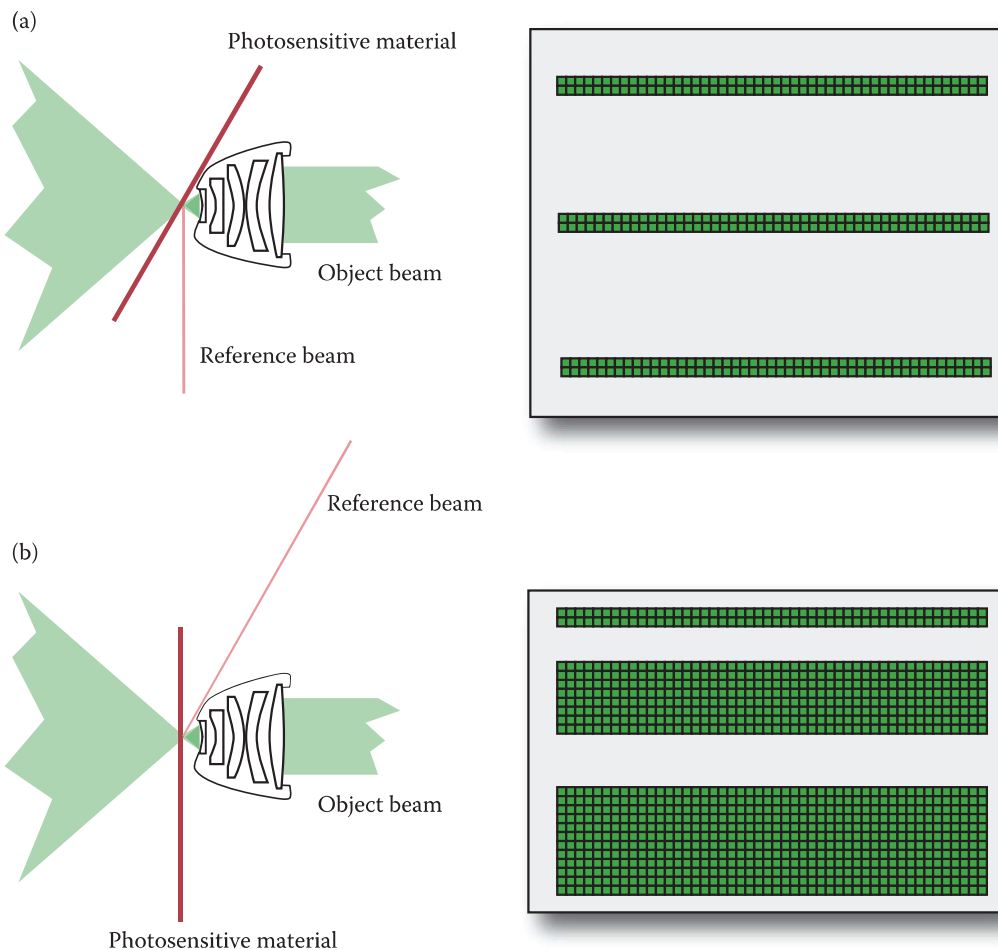


FIGURE 7.29 Writing an MWDH transmission H_1 rainbow master hologram with a monochromatic laser using a plate holder tilted at the achromatic angle (a) and a standard perpendicular plate-holder (b). In (a), the red, green and blue “slits” are the same width because the H_1 is tilted at the achromatic angle. In (b), two of the slits are much thicker as multiple rows of hogels are used to synthesise virtual slits at the correct distance behind the plate. When viewed under laser light, these wider bands would therefore seem to contain an image of a slit behind the hologram. Note of course that the size of the hologram has been greatly exaggerated in the diagram.

From an optical point of view, an MWDH printer is virtually the same as a DWDH printer. The major difference is therefore in the image data. Often, the data required by the SLM(s) in an MWDH printer are just the perspective view data available from a tracking camera. In a DWDH printer, the hogel data must be calculated from the perspective view data by a mathematical algorithm that changes the optical plane. The optical transfer from H_1 to H_2 fulfils this role in MWDH.

Basically, any type of hologram may be made using MWDH or DWDH. The decision as to which technique to use usually comes down to the speed of printing and the ease of copying. A 0.5 mm hogel DWDH hologram, 1 m \times 1 m, takes 11 hours to write at a hogel write speed of 100 RGB hogels per second, but if the hologram is an HPO hologram, then the corresponding H_1 hologram can take only a very small fraction of this time to write. This is because an HPO hologram does not usually require such a high vertical hogel density.*

Copying of DWDH holograms is usually done through a contact-copy method. However, with this method, it is not possible to adjust the ratio of the object and reference beams at the copy—as this is defined by the diffractive response of the master hologram. However, certain materials may require a

* This is the case when a broadband illumination source is used.

higher modulation to record a proper copy hologram. The H_1/H_2 distance transfer process solves this problem completely, making it more suitable sometimes for the rapid production of copies. The disadvantage of course is that a full-aperture transfer requires a lot of energy, whereas the contact scheme can be accomplished by line-scanning using a small laser.

In general, MWDH and DWDH are complementary techniques. With full-parallax data, it is possible to transform a full set of perspective view data to any optical plane. In this way, computational and optical image-plane transformations can be combined as desired. This can be useful, for example, to optimise a copy geometry. By using an optical image plane transformation rather than an entirely computational one as in DWDH, the pattern of hogels on the physical plate becomes defocussed and the quality of the hologram can be increased.

Another technique used in MWDH is to write overlapping hogels downstream of the Fourier plane (shown in Figure 7.28). Because an optical transfer will be used to convert the H_1 to an H_2 , the loss of diffractive efficiency caused by this overlap does not really matter. The quality of the final H_2 holograms can be somewhat increased using this technique. Another advantage is that for transmission systems, where it is not possible to bring the reference beam through the writing objective, there is now extra space to accomplish this.

Like DWDH printers, MWDH printers can produce either transmission or reflection holograms. Most often, MWDH is most appropriate for transmission holograms written using a monochromatic laser. Here, full-colour rainbow and achromatic holograms can easily be produced using a plate holder that is tilted at the achromatic angle (Figure 7.29). Alternatively, a standard perpendicular plate holder may be used if special image processing transformations are employed. Geola makes commercial H_1/H_2 transfer systems using green-pulsed lasers for formats up to $1\text{ m} \times 1.5\text{ m}$ (Figure 6.12). One should also note that full-colour transmission or achromatic holograms can be produced using only a single “slit” with MWDH if an RGB laser is used in place of the monochromatic laser.

7.7 Copying Full-Colour DWDH Holograms

As we have already mentioned, printing full-parallax, ultra-realistic DWDH holograms is slow! For the technology to become commercially interesting, either the laser and print speed must be increased dramatically or one needs to develop a technique to copy the DWDH holograms produced. Certainly, print speed may realistically be increased by a certain amount. Current pulsed laser systems can be redesigned to work at up to 120 Hz with flash pumping. Beyond this, diode-pumped laser solutions may be expected to produce repetition rates that can be actually as high as required. However, no SLM technology exists at this moment to practically produce a printer with a repetition rate of greater than 200 hogels per second. To go faster than this requires multiple write heads that, although possible, will increase the price point of any printer rather dramatically.

Here, we present the results of recent experiments (2006–2010) carried out by the Geola organisation to produce high-quality holographic copies of digital master holograms written with a DWDH printer [22]. A standard RGB-pulsed laser (the same as that used to record the DWDH master holograms) was used in the line-scanning contact copying system. Figure 7.30 shows a simplified optical scheme of the experimental setup.

So that a good quality copy may be produced from a reflection master, it is vital that the DWDH master hologram replays at exactly its recording wavelengths. To ensure this, the emulsion must be processed in a special way and care must be taken with regard to ambient humidity and temperature during the entire process.

With reference to Figure 7.30, each of the laser beams (11) passes through computer-controlled wave plates (12) and polarisers (13). By rotating the wave plates (12), the colour balance of the hologram copy may be adjusted. The beams are now cleaned by spatial filters (14) and a proper polarisation is ensured by polarisation correctors (15). The beams are then directed by mirrors (16) to a three-colour combiner-deflector system (17), after which they are shaped by a shaping/deflection system (18) into a narrow elongated and slightly oval achromatic slit. This achromatic beam is then reflected by the flat mirror (22) to illuminate the non-exposed photosensitive material (1) as a reference beam. Part of the achromatic beam

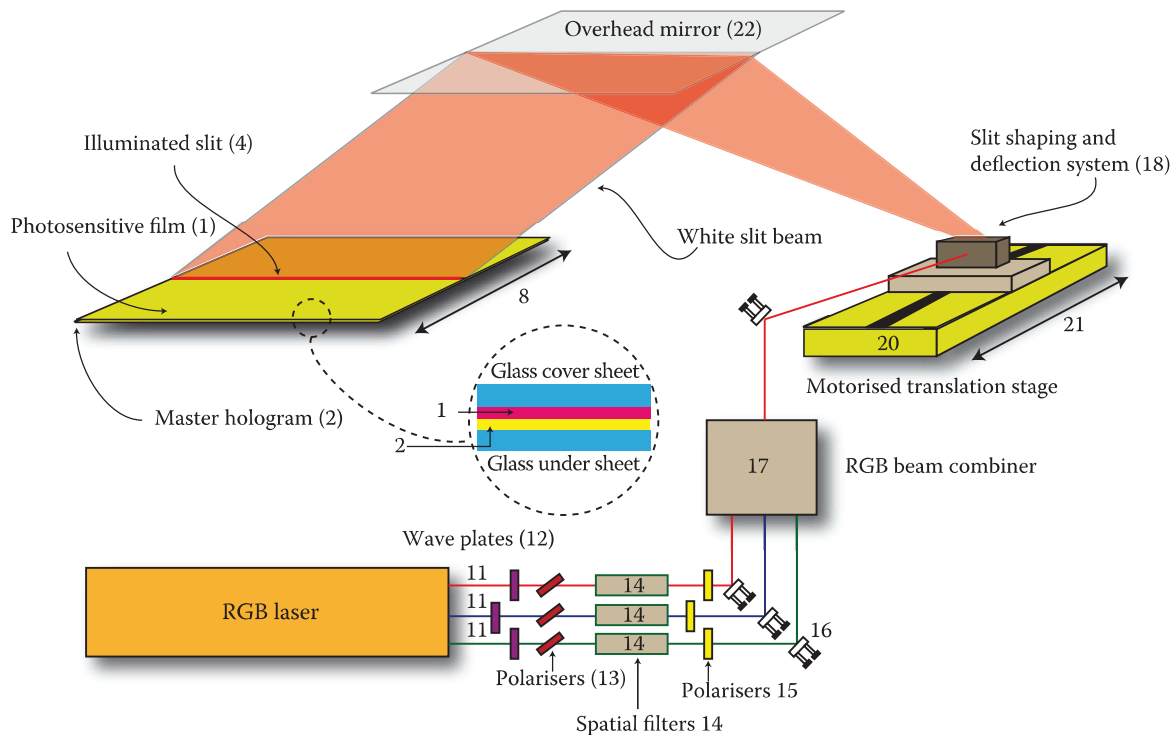


FIGURE 7.30 Simplified optical scheme of a line-scanning RGB film hologram contact copier. The system, which uses multiple pulses from an RGB-pulsed laser, produces RGB reflection film copies from a DWDH master (film) reflection hologram.



FIGURE 7.31 (a) Master DWDH hologram, 0.8 mm hogel, 20 × 30 cm; (b) three-colour copy on PFG03CN silver halide; (c) three-colour copy on Bayer Photopolymer. (Hologram image designed in 3D StudioMax. Courtesy of Razvan Maftei, 2005.)

is, however, transmitted through the photosensitive material and onto the master hologram (2) where it generates a diffractive reflection forming the object beam.

The zone illuminated by the laser slit beam (4) is transverse to the scanning movement of the slit. The laser radiation shaping/deflection system (18) is fixed onto the computer-controlled linear translation stage (20) to ensure an even movement in direction (21). At the same time, the linear translation stage (20) ensures movement of the light slit in direction (8), which is perpendicular to the longitudinal axis of the illumination slit. This ensures an even exposure of both the non-exposed photosensitive material and of the master hologram, giving, in turn, an even recording of the reconstructed master hologram.

Experimental results showed that existing silver halide photoemulsions (Geola tried both PFG-03CN from Sfera-S and the SilverCross emulsion) do not allow the production of full-colour contact copies having a diffraction efficiency greater than the diffraction efficiency of the master hologram. The best result that Geola was able to achieve was a colour copy with a relative diffraction efficiency (as a percentage of the master diffraction efficiency) of 100% in red and green and 50% in blue. Despite the less than perfect result in blue, the quality and brightness obtained were still judged adequate for commercialisation. An interesting observation is that if the copy is made with only two colours, its diffraction efficiency can reach 150% of the master hologram efficiency (using AgX).

A panchromatic photopolymer material from Bayer was also used to record high-quality copy holograms. Here, relative diffraction efficiencies in the red and green of well over 100% were obtained. Figure 7.31a, b and c show the experimental results for both AgX and photopolymer. All of Geola's work has thus far concentrated on AgX film masters. The use of glass-plate masters should, of course, substantially improve the image quality. Additionally, the use of SHSG processing could significantly improve copy efficiency.

REFERENCES

1. B. R. Brown and A. W. Lohmann, "Complex spatial filtering with binary masks," *Appl. Opt.* **5**, 967–969 (1966).
2. L. B. Lesem, P. M. Hirsch and J. A. Jordan, "Scientific applications: Computer synthesis of holograms for 3-D display," *Commun. ACM* **11**, 661–674 (1968).
3. R. V. Pole, "3-D imagery and holograms of objects illuminated in white light," *Appl. Phys. Lett.* **10** (1), 20–22 (1967).
4. D. J. DeBitetto, "Holographic panoramic stereograms synthesized from white light recordings," *Appl. Opt.* **8**, 1740–1741 (1969).
5. M. King, A. Noll and D. Berry, "A new approach to computer-generated holography," *Appl. Opt.* **9**, 471–475 (1970).
6. L. Cross, "The Multiplex technique for cylindrical holographic stereograms," in SPIE San Diego August Seminar (1977) [Presented but not published].
7. S. A. Benton, "Hologram reconstructions with extended incoherent sources," *J. Opt. Soc. Am.* **59**, 1545–1546A (1969).
8. W. Spierings and E. van Nuland, "Calculating the right perspectives for multiple photo-generated holograms," in *Int'l Symposium on Display Holography*, T .H. Jeong ed., Proc. SPIE **1600**, 96–108 (1992).
9. M. Halle, S. Benton, M. Klug and J. Underkoffler, "The Ultragram: A generalized holographic stereogram," in *Practical Holography V*, S. A. Benton ed., Proc. SPIE **1461**, 142–155 (1991).
10. M. Lucente, "Diffraction-Specific Fringe Computation for Electro-Holography", Ph. D. Thesis, Dept. of Electrical Engineering and Computer Science, MIT, (1994).
11. M. Yamaguchi, N. Ohyama and T. Honda, "Holographic 3-D printer," in *Practical Holography IV*, S. A. Benton ed., Proc. SPIE **1212**, 84–92 (1990).
12. M. Klug, M. Holzbach and A. Ferdman, *Method and apparatus for recording 1-step full-color full-parallax holographic stereograms*, US Patent 6,330,088 (filed 1998, granted 2001).
13. D. Brotherton-Ratcliffe, S. J. Zacharovas, R. J. Bakanas, J. Pileckas, A. Nikolskij and J. Kuchin, "Digital holographic printing using pulsed RGB lasers," *Opt. Eng.* **50**, 091307-1-9 (2011).
14. D. Brotherton-Ratcliffe, F. M. Vergnes, A. Rodin and M. Grichine M, *Method and apparatus to print Holograms*, Lithuanian Patent LT4842 (1999).

15. D. Brotherton-Ratcliffe, F. M. Vergnes, A. Rodin and M. Grichine, *Holographic printer*, US Patent 7,800,803 (filed 1999, granted 2010).
16. A. Rodin, F. M. Vergnes and D. Brotherton-Ratcliffe, *Pulsed multiple colour laser*, EU Patent EPO 1236073 (2001).
17. D.-K. Kang, M. A. Rivera and M. L. Cruz-López, “New fully functioning digital hologram recording system and its applications” *Opt. Eng.* **49**, 105802-1-9 (2010).
18. P.-A. Blanche, A. Bablumian, R. Voorakaranam, C. Christenson, W. Lin, T. Gu, D. Flores, P. Wang, W.-Y. Hsieh, M. Kathaperumal, B. Rachwal, O. Siddiqui, J. Thomas, R. A. Norwood, M. Yamamoto and N. Peyghambarian, “Holographic three-dimensional telepresence using large-area photorefractive polymer,” *Nature* **468**, 80–83, (4 Nov. 2010).
19. J. Tapsell, “*Direct-write digital holography*”, PhD Thesis, Univ. of Sussex, UK (2008).
20. M. Klug and N. Kihara, “Reseau full-colour one-step holographic stereograms,” in *Fifth Int'l Symposium on Display Holography*, T. H. Jeong ed., Proc. SPIE **2333**, 411–417 (1995).
21. A. Shirakura, N. Kihara and S. Baba, “Instant Holographic Portrait Printing System,” in *Practical Holography XII*, S. A. Benton ed., Proc. SPIE **3293**, 248-255 (1998).
22. I. Lancaster, “Geola builds holographic copier,” *Holography News*, Vol. **23**, (3) 4, (2009).

8

Digital Holographic Printing: Data Preparation, Theory and Algorithms

8.1 Introduction

In the last chapter, we have seen how digital holographic printers are physically put together from the points of view of optical schemes, mechanical design and laser choice. In this chapter, we will concentrate on the subject of digital data processing. In general, we will start with digital image data that is derived from either a computer model or from a large array (or matrix) of digital cameras. We must then transform this data into a form suitable for actually printing a hologram [1,2].

Most of this chapter and the next describe a system for keeping track of and manipulating image data. More often than not, we actually start with the data we need! Unfortunately, this data is often in the wrong order and, as such, needs reordering and rescaling before a hologram can be written. From an absolute point of view, the algorithms and mathematics required to do this are extremely simple. However, we will need to keep track of many pointers in a fashion dictated by an accurate analysis of the ray geometries of the image model and the hologram, and this may well give the impression that things are more complicated than they actually are!

Because there is such a large difference between the cases of horizontal parallax-only (HPO) holograms and full-parallax holograms—not only in their optical properties and applications but also in the computational algorithms required to generate the printer write-data—we shall concentrate mostly on HPO holograms in this chapter, leaving a proper discussion of the full-parallax case to Chapter 9.

8.2 Basic Considerations

Every hologram seeks to display an image of a three-dimensional object, which is defined within a certain three-dimensional space. This is illustrated in Figure 8.1a. This figure may be interpreted in two different ways. In the first interpretation, object \mathcal{A} is placed behind a glass window \mathcal{H} . In the second interpretation, \mathcal{H} is a hologram and \mathcal{A} is the holographic reproduction of the object of the first interpretation. In either case, assuming that the hologram is recorded and illuminated in a perfect fashion, an observer would find it hard to distinguish between the two interpretations, as the radiation field emanating from plane \mathcal{H} must be ostensibly identical in both cases.

A well-known principle of optics is Huygens' principle [e.g., 3]. Formally, this principle, which can be directly derived from the Maxwell equations, can be used to analyse Figure 8.1. Huygens' principle tells us that to completely define the radiation field over \mathcal{H} , which emanates from region \mathcal{A} , knowledge of its distribution is sufficient at any plane ($\mathcal{P}_1, \mathcal{P}_2, \mathcal{P}_3$, etc.). We therefore envisage the situation depicted in Figure 8.1b, in which a real object (\mathcal{O}) appears located behind plane \mathcal{H} . We would like to create a hologram that reproduces the radiation field passing through \mathcal{H} . Although we could just measure the radiation field at \mathcal{H} , it is more useful to consider measuring the field on a different plane. We therefore imagine an additional plane (\mathcal{C}) located in front of and perpendicular to \mathcal{H} . To measure the radiation field at \mathcal{C} , we imagine this plane to be covered with a matrix of perfect “pinhole” cameras all orthogonally directed with respect to plane \mathcal{C} ; each camera records the luminous intensity it receives as a function of vertical

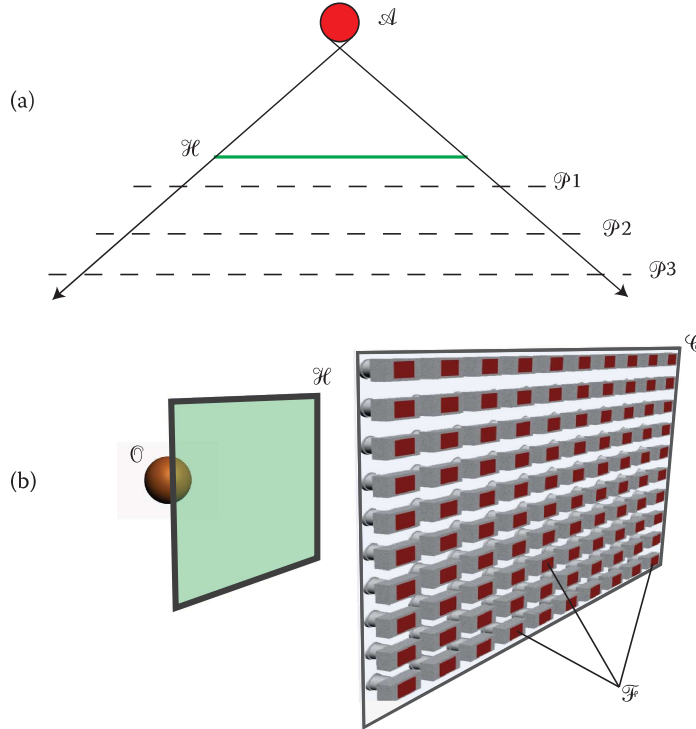


FIGURE 8.1 (a) In one interpretation of this diagram \mathcal{A} may be regarded as an object and \mathcal{H} as a glass window. In an alternative interpretation \mathcal{A} is a holographic image and \mathcal{H} is a hologram. The light-field at \mathcal{H} due to \mathcal{A} is the same in both cases. If we have a full knowledge of the light-field on any of the planes (\mathcal{P}_1 , \mathcal{P}_2 or \mathcal{P}_3) then the distribution of light at \mathcal{H} is uniquely defined. (b) We can define the (incoherent) light-field produced by a hologram or object by arranging a matrix of idealised closely-spaced cameras on plane \mathcal{C} .

and horizontal angles. This information will then be encoded onto each of the planes (\mathcal{F}_{ξ}), which are none other than the planes of the film from each camera.

Following this logic, the optical information represented by the recorded light intensity distributions present on the totality of the planes (\mathcal{F}_{ξ}) formally represents all the information we need to reconstruct the (incoherent) radiation field produced by the original object passing through the hologram plane \mathcal{H} . Whether we use a real object and take a matrix of real photographs or whether we take a virtual object in a computer and take “virtual” photographs does not change the mathematics required.

In the following sections, we will formulate mathematically how the camera information from the totality of the planes (\mathcal{F}_{ξ}) may be used to calculate the optical information required by a digital holographic printer to print a hologram which reproduces a given radiation field.

8.3 Coordinate Systems

To record any type of digital hologram, we must consider an image acquisition scheme and a writing scheme. This is illustrated in Figure 8.2. For simplicity, we consider a pinhole model for both the recording camera(s) and for the printer’s optical writing head. This is equivalent to using a geometric optics approximation with the assumption of a small-aperture camera and a “point” hogel. Figure 8.2a depicts a generic image acquisition system consisting of a large matrix of parallel forward-facing identical cameras distributed evenly over plane \mathcal{C} situated at some distance from the object to be recorded. Associated with each camera is a film plane (\mathcal{F}), which is the plane where the camera produces a focussed image of

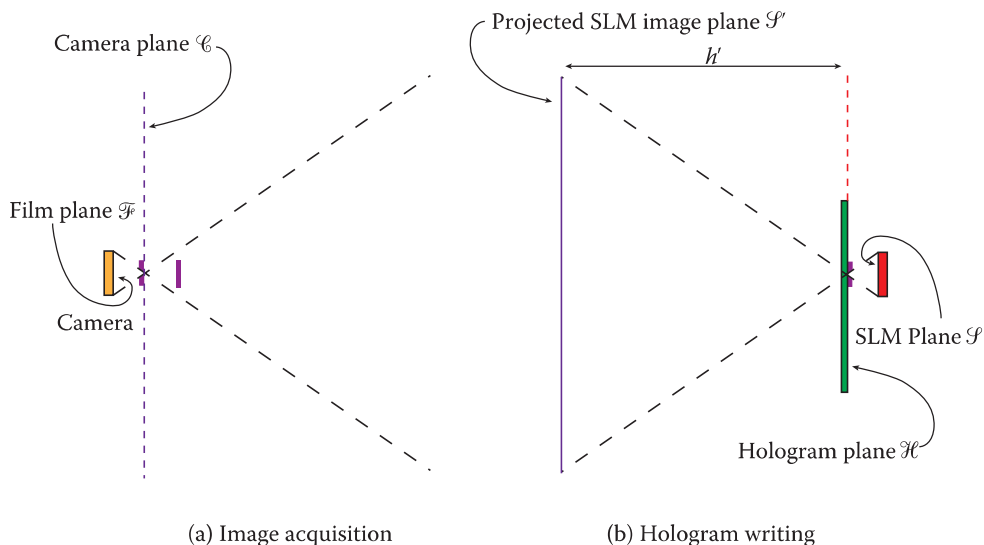


FIGURE 8.2 Generic image acquisition (a) and hologram-writing (b) geometries.

the object. We will also define the paraxially projected image plane of \mathcal{F} , which we shall label \mathcal{F}' . The film plane is assumed to be rectangular as in a usual camera and, accordingly, we associate a horizontal and vertical field of view with each of the cameras.

Figure 8.2b depicts a generic hologram-writing scenario in which, as mentioned previously, we have replaced the complex optical system of the printer with a simple pinhole located at the hologram plane. In addition to the hologram plane, we identify two additional planes; these are the spatial light modulator (SLM) plane, \mathcal{S} , where data are placed to encode the writing laser beam with the required information to form the hologram, and the projected image plane of the SLM, \mathcal{S}' , which is a plane at some distance downstream or upstream of the hogel. In general, the image transformation from \mathcal{S} to \mathcal{S}' will be non-paraxial. However, we shall limit all our discussions to the paraxial case until we introduce non-paraxial printer optics in the last part of this chapter. As with the cameras, we assume a rectangular SLM and, accordingly, we are able to associate with the printer writing system both a horizontal and vertical field of view.

Most of what follows in this chapter and in Chapter 9 is concerned with the computational techniques of converting camera information to the data required by the printer SLM to generate the various types of holograms. In the generic image acquisition and writing scenarios described previously, we have identified six principal planes: these are the hologram plane, the SLM plane, the projected SLM image plane, the camera plane, the film plane and the paraxially projected film plane. To discuss data processing, we must first characterise these planes.

We will start with the three principal planes involved in image acquisition (Figure 8.3). We let the camera plane (\mathcal{C}) be parameterised by the Cartesian coordinate system (ξ, ζ) . The origin of this and all other Cartesian planes used in this book is taken to be located at the lower left-hand corner of the plane as we view the plane from the right-hand side. The dimensions of plane \mathcal{C} are defined as $D_\xi \times D_\zeta$. We let each of the film planes (\mathcal{F}) be defined by the Cartesian coordinate system (x, y) ; the dimensions of \mathcal{F} are taken to be $D_x \times D_y$. Likewise, \mathcal{F}' will be described by the Cartesian coordinate system (x', y') and the dimensions of \mathcal{F}' are taken to be $D'_x \times D'_y$.

We now treat the three principal planes involved with the process of writing the hologram (Figure 8.4). We describe the hologram plane \mathcal{H} by a Cartesian coordinate system (X, Y) having dimensions $D_X \times D_Y$. The SLM plane \mathcal{S} is likewise described by the Cartesian system (U, V) with dimensions $\Pi \times \Sigma$. The projected SLM plane \mathcal{S}' is defined by the Cartesian system (U', V') with dimensions $\Pi' \times \Sigma'$.

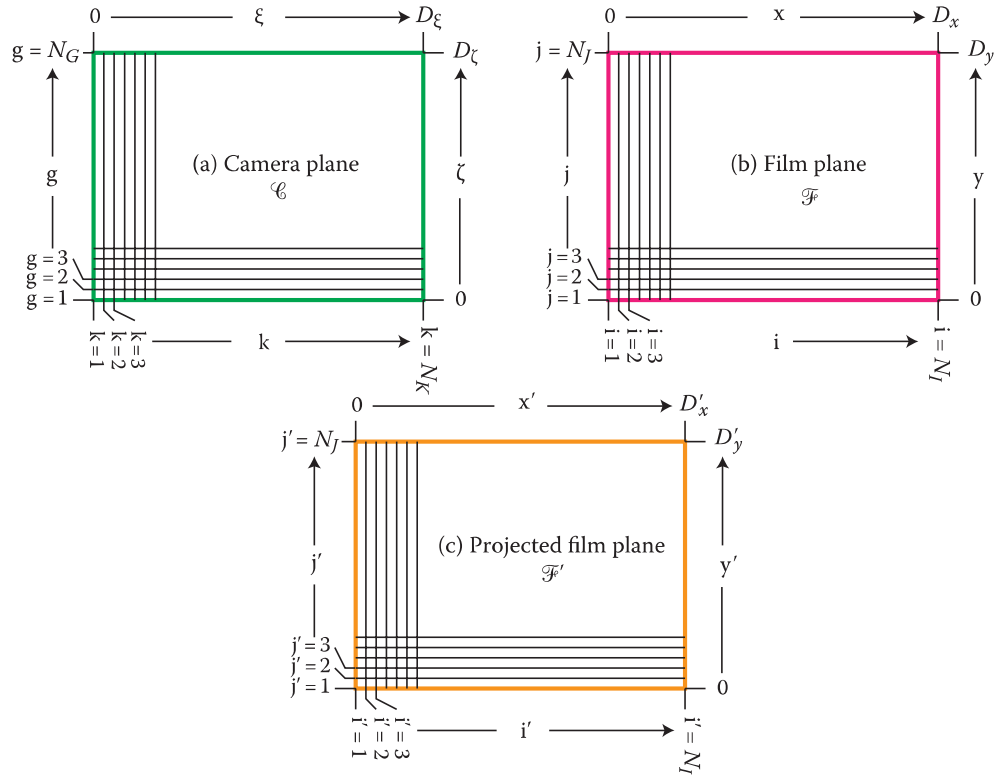


FIGURE 8.3 Characterisation of the principal image acquisition planes: (a) camera plane, (b) film plane and (c) projected film plane.

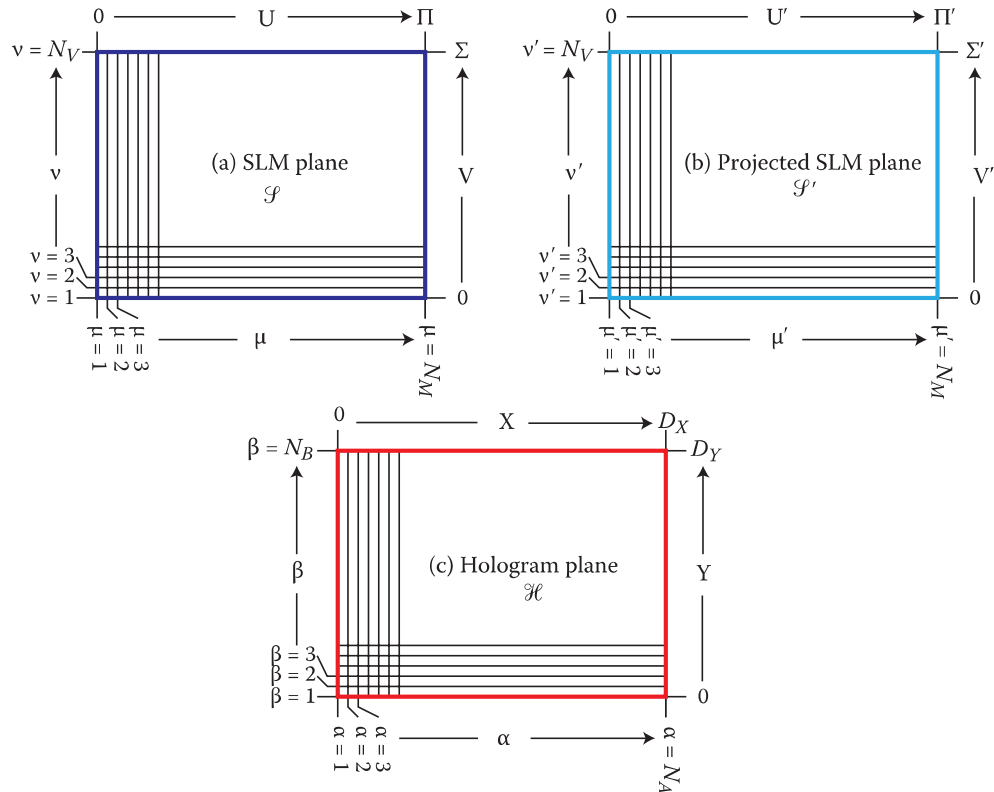


FIGURE 8.4 Characterisation of the principal hologram-writing planes: (a) SLM plane, (b) projected SLM plane and (c) hologram plane.

8.4 Coordinate Meshes

Having set up the coordinate systems, we must now discretise these systems because we wish to consider the case of writing a hologram, which is built up of digital hogels, and because plane \mathcal{C} is populated with a finite number of digital cameras.

Starting with the camera plane (\mathcal{C}), we discretise the coordinates (ξ, ζ) in terms of positive integers k and g :

$$\xi = \frac{(k-1)D_\xi}{N_K - 1} \quad k = 1, 2, 3, \dots, N_K \quad (8.1)$$

$$\zeta = \frac{(g-1)D_\zeta}{N_G - 1} \quad g = 1, 2, 3, \dots, N_G \quad (8.2)$$

The parameters (k, g) then effectively describe a set of discrete positions in which a camera may be placed on the camera plane.

Likewise, we discretise the film plane coordinates (x, y) in terms of positive integers i and j :

$$x = \frac{(i-1)D_x}{N_I - 1} \quad i = 1, 2, 3, \dots, N_I \quad (8.3)$$

$$y = \frac{(j-1)D_y}{N_J - 1} \quad j = 1, 2, 3, \dots, N_J \quad (8.4)$$

In exactly the same manner as before, the parameters (i, j) divide up the film plane into discrete locations. Finally, we discretise the projected film plane coordinates (x', y') in terms of positive integers i' and j' :

$$x' = \frac{(i'-1)D'_x}{N_I - 1} \quad i' = 1, 2, 3, \dots, N_I \quad (8.5)$$

$$y' = \frac{(j'-1)D'_y}{N_J - 1} \quad j' = 1, 2, 3, \dots, N_J \quad (8.6)$$

Turning now to the principal writing planes, we introduce discretised coordinates, α and β , to describe the location of each hogel on the hologram plane in terms of the continuous hologram coordinates (X, Y) :

$$X = \frac{(\alpha-1)D_X}{N_A - 1} \quad \alpha = 1, 2, 3, \dots, N_A \quad (8.7)$$

$$Y = \frac{(\beta-1)D_Y}{N_B - 1} \quad \beta = 1, 2, 3, \dots, N_B \quad (8.8)$$

The SLM plane is parameterised by the integers (μ, ν) and by the continuous coordinates (U, V) :

$$U = \frac{(\mu-1)\Pi}{N_M - 1} \quad \mu = 1, 2, 3, \dots, N_M \quad (8.9)$$

$$V = \frac{(\nu-1)\Sigma}{N_V - 1} \quad \nu = 1, 2, 3, \dots, N_V \quad (8.10)$$

The projected image plane, \mathcal{S}' , is likewise parameterised by

$$U' = \frac{(\mu' - 1)\Pi'}{N_M - 1} \quad \mu' = 1, 2, 3, \dots, N_M \quad (8.11)$$

$$V' = \frac{(v' - 1)\Sigma'}{N_V - 1} \quad v' = 1, 2, 3, \dots, N_V \quad (8.12)$$

The parameters Π' and Σ' effectively define, respectively, the horizontal and vertical fields of view of the printer writing head. The optical objective in the printer writing head is usually circularly symmetric, but when it is combined with a rectangular SLM, one obtains a different field of view in the horizontal and vertical directions. We may therefore write Π' and Σ' in terms of these angles:

$$\Pi' = 2h' \tan\left(\frac{\Psi_{PH}}{2}\right) \quad (8.13)$$

$$\Sigma' = 2h' \tan\left(\frac{\Psi_{PV}}{2}\right), \quad (8.14)$$

where h' is the distance from the hologram plane, \mathcal{H} , to the projected SLM image plane, \mathcal{S}' .

For each primary colour, we may define the totality of optical information measured by the cameras by the optical intensity (\mathbf{I}) of each of the pixels on each of the camera film planes. \mathbf{I} is a four-dimensional object as it is a function of the integer parameters k , g , i and j . We will therefore write it as ${}^{kg}\mathbf{I}_{ij}$.

We may also define the totality of optical information for a given primary colour that we wish to write to the hologram as the optical intensity (\mathbf{S}) of each of the SLM pixels required to write each of the hogels. Like \mathbf{I} , \mathbf{S} is a four-dimensional object as it is a function of the integer parameters μ , v , α and β . We will therefore write it as ${}^{\mu v}\mathbf{S}_{\alpha\beta}$. The question is now simple: how can we best calculate \mathbf{S} from \mathbf{I} ?

8.5 Independent Primary Colours

As we have seen in Chapter 7, most current holographic printers use three primary colours to generate full-colour reflection holograms. Some types of holograms, such as full-colour rainbow holograms, require only a single-colour writing laser but nevertheless require image data in three or more primary colours. We have also mentioned in Chapter 5 that the use of more than three primary colours in any type of full-colour hologram can be beneficial in producing a better spectral replay. In the following sections, we shall treat each individual primary colour separately. In many cases, we will then simply be able to apply the same algorithms to each primary colour. Of course, separate γ corrections will need to be applied for proper colour balance, but this is trivial. In some cases, however, cross-coupling occurs between the colour data, for example, when the primary hologram recording and replay wavelengths differ, when the recording reference beam geometry does not match the replay illumination geometry, or when the holographic photosensitive material changes its properties after writing. We will return to such cross-coupling a little later.

8.6 Viewing Plane

To write a digital hologram, a data set for each of the primary colours needs to be calculated for every hogel. This data set populates the writing SLM at the moment that the hogel is written. Clearly, we wish to calculate this data set from camera data (${}^{kg}\mathbf{I}_{ij}$). However, before we can do this, we must consider

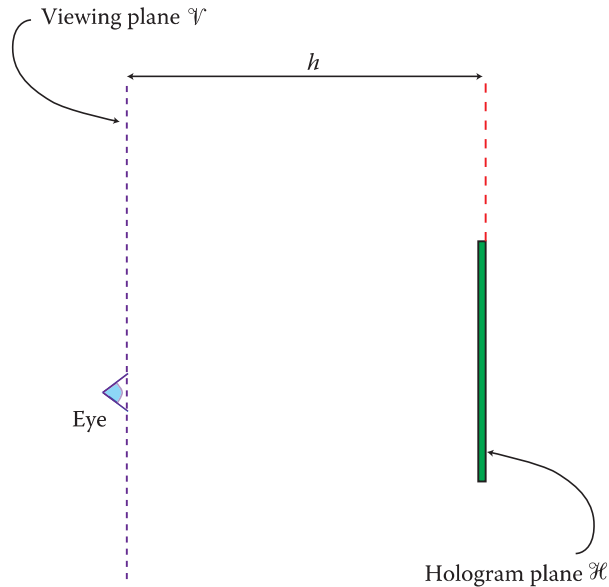


FIGURE 8.5 Hologram viewing geometry.

how we are going to view the final hologram. Figure 8.5 shows a simplified diagram of the viewing process. In particular, we consider a plane (\mathcal{V}), parallel to \mathcal{S} and \mathcal{S}' , situated a distance h away from \mathcal{H} at which we want to observe the hologram. It is important to realise that for HPO holograms, there is a unique viewing distance. Only at this distance does the viewer observe an undistorted image. For full-parallax holograms, a viewer may, in general, observe the undistorted hologram from any point in space. However, even here, it is extremely useful to define a specific viewing plane as we can then seek to match the radiation field characteristic of the acquired image data and the field produced by the hologram at replay at this plane. The mathematical operation of matching the fields in this way essentially defines the data required to write the hologram. In the case of a full-parallax hologram, this process then assures the matching of the light-field at all other planes automatically as required by Huygens' principle.

8.7 Simple Cases

There are two simple cases in which \mathbf{S} may be trivially derived from \mathbf{I} . The first is the case of a direct-write digital holography (DWDH) analogue of a Denisyuk reflection hologram and the second is the case of master-write digital holography (MWDH), where a master H_I hologram is written. In both cases, we will assume that the printer optical objective is paraxial. We shall discuss non-paraxial objectives in Section 8.10.

8.7.1 Full-Parallax DWDH “Denisyuk” Reflection Hologram

First, we arrange for the camera or cameras, which acquire the image data, to have identical horizontal and vertical fields of view as those possessed by the printer writing head and for the SLM and charge-coupled device (CCD) dimensions to correspond, that is

$$\begin{aligned} \Psi_{CH} &= \Psi_{PH} \equiv \Psi_H \\ \Psi_{CV} &= \Psi_{PV} \equiv \Psi_V \\ N_M &= N_I \\ N_V &= N_J \end{aligned} \tag{8.15}$$

Generally, we must collect image data by either arranging a large matrix of cameras situated on the camera plane or by using a single camera, which we move in such a fashion that it takes sequential pictures from all locations on the defined integer grid at the camera plane. Of course, if the three-dimensional object that we want to digitise is not static, then it is difficult to use the latter choice. We shall discuss image acquisition in greater detail in Chapter 10, but for now, we should keep in mind that the single camera may be either a real camera or a virtual camera within a computer-aided design (CAD) program.

We now seek to superimpose the various planes involved in image acquisition, hologram writing and hologram viewing with the intention of matching, at the viewing plane, the light-field emanating from the original object, the light-field used to write the hologram and the light-field observed upon viewing the hologram. This amounts to superimposing the diagrams of Figure 8.2a and b and Figure 8.5. This is shown in Figure 8.6. Note that we have chosen to collocate the camera plane (\mathcal{C}) with the hologram plane (\mathcal{H}). In addition, the projected SLM plane \mathcal{S}' , the projected film plane \mathcal{F}' and the viewing plane (\mathcal{V}) have been collocated and we have taken $h' = h$. This choice of collocation means that the camera pinhole and the hogel are also collocated.

Having chosen to configure the various principal planes in this fashion, we see that a test ray emanating from the object, which passes through a given point on \mathcal{H} , will intersect exactly the same pixel address on the projected film plane as on the projected SLM plane or, in other words, for the viewer to see a light-field exactly reproducing the acquired light-field that emanated from the original object in plane \mathcal{V} , the data in \mathcal{S}' must correspond exactly with the camera data recorded on \mathcal{F}' . More specifically

$${}^{\mu\nu'} \mathbf{S}'_{\alpha\beta} = {}^{\alpha\beta} \mathbf{I}'_{\mu\nu'} \quad (8.16)$$

where, as previously,

$$\begin{aligned} \mu' &= 1, 2, 3, \dots, N_M & v' &= 1, 2, 3, \dots, N_V \\ \alpha &= 1, 2, 3, \dots, N_A & \beta &= 1, 2, 3, \dots, N_B \end{aligned} \quad (8.17)$$

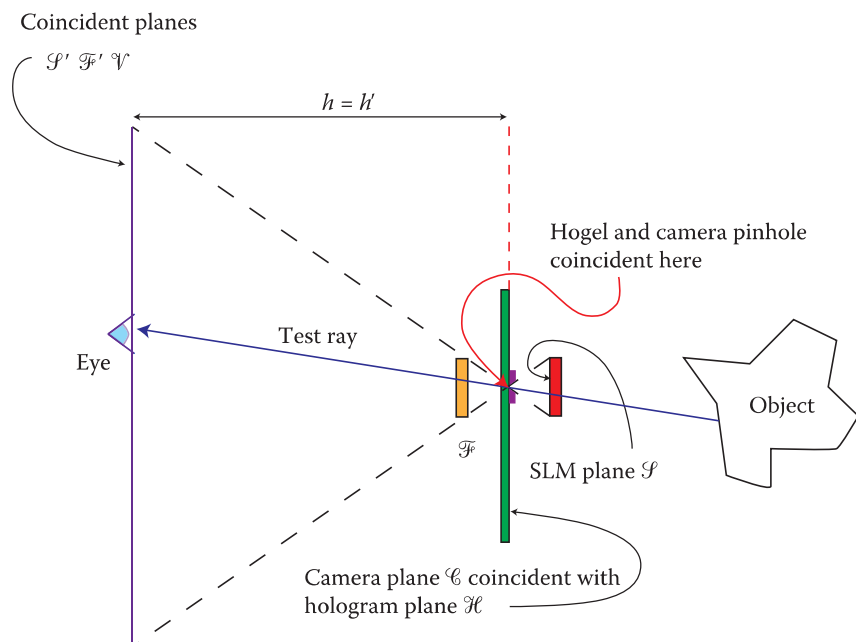


FIGURE 8.6 Writing a DWDH Denisyuk hologram.

Then, because \mathcal{F}' , \mathcal{S}' and \mathcal{F} are downstream of the hogel and camera pinhole, whereas \mathcal{S} is located upstream, this leads to the following transformation rule between \mathbf{I} and \mathbf{S} :

$${}^{\mu\nu}\mathbf{S}_{\alpha\beta} = {}^{\alpha\beta}\mathbf{I}_{N_M-l-\mu, N_V-l-\nu} \quad (8.18)$$

This transformation describes the SLM data for each primary colour required to write a full-parallax reflection hologram, which is a direct analogue to the Denisyuk type of analogue reflection hologram. The image appears entirely behind the hologram plane as with the Denisyuk hologram and is visible at any angle within the field of view of the recording camera. Note that if a real camera is used with a finite aperture, then blurring will occur because any real camera will only focus a certain range of depths properly onto its film plane. In CAD programs, one usually uses a camera of effectively zero aperture, which gives infinite depth. Nevertheless, just like a real Denisyuk hologram, the final digital hologram will be subject to inherent image blurring if it is illuminated by a source of spatially or temporally incoherent radiation (i.e., a normal white-light source). By reducing the hogel size to submillimetre dimensions, it can be difficult to tell this type of digital hologram from a true Denisyuk hologram.

8.7.2 MWDH Master Hologram

The second simple case we will examine is that of a master (MWDH) hologram. This is essentially the analogue of the H_1 hologram of classical analogue holography [4]. This hologram can be HPO or full-parallax, and it can be of transmission or reflection type. If the hologram is HPO, it will generally be in the form of a slit, which is recorded at a distance from the object that corresponds to the viewing distance of the hologram. In the full-parallax case, the recording distance is chosen so that subsequent optical transfer to an H_2 hologram can provide a final image that appears partly in front of the holographic plate. By writing a reflection master, several primary colours may be encoded onto the same plate and a full-colour H_2 hologram produced using well-known techniques. For the purposes of this section, we shall treat the case of a full-parallax master H_1 hologram and derive the trivial transformations between the acquired image data \mathbf{I} and the hologram write-data \mathbf{S} .

As before we must arrange for the acquisition camera to have an identical horizontal and vertical field of view as those possessed by the printer writing head (i.e., Equation 8.15 applies). We then associate the various principal planes of acquisition, writing and viewing. This is a little more complex this time, as we must consider the $H_1:H_2$ transfer process as well. Figure 8.7a illustrates the writing of the H_1 reflection hologram. Figure 8.7b then illustrates the $H_1:H_2$ transfer. Finally, Figure 8.7c illustrates the viewing of the H_2 reflection hologram. From these figures, it can be seen that both the camera plane (\mathcal{C}) and the viewing plane (\mathcal{V}) are collocated with the hologram plane which we can now label \mathcal{H}_1 for clarity. This means that we must take $h = 0$ of course. The transfer process is completely standard and upon viewing, a faithful reproduction of the original object is viewable at \mathcal{V} in the case of an HPO hologram or at any location within the camera field of view in the full-parallax case.

Clearly, the geometry of Figure 8.7 implies that the light-fields emitted by object and hologram at, respectively, \mathcal{F}' and \mathcal{S}' are the same and accordingly the transformation between \mathbf{S}' and \mathbf{I}' is:

$${}^{\mu'\nu'}\mathbf{S}'_{\alpha\beta} = {}^{\alpha\beta}\mathbf{I}'_{\mu'\nu'} \quad (8.19)$$

Because \mathcal{F} and \mathcal{S} are collocated, this then gives simply

$${}^{\mu\nu}\mathbf{S}_{\alpha\beta} = {}^{\alpha\beta}\mathbf{I}_{\mu\nu}. \quad (8.20)$$

8.8 Image-Planned DWDH HPO Holograms

We will now turn our attention to the less trivial case of the \mathbf{I} -to- \mathbf{S} transformations describing DWDH HPO reflection holograms. These types of holograms are characterised by the assumption that the camera and viewing planes must coincide such that $h = h'$. This allows all the optical write data for

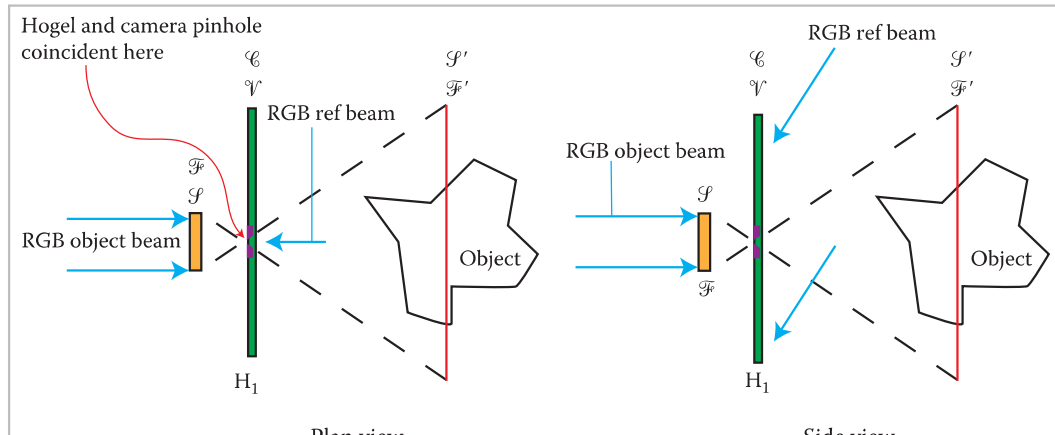
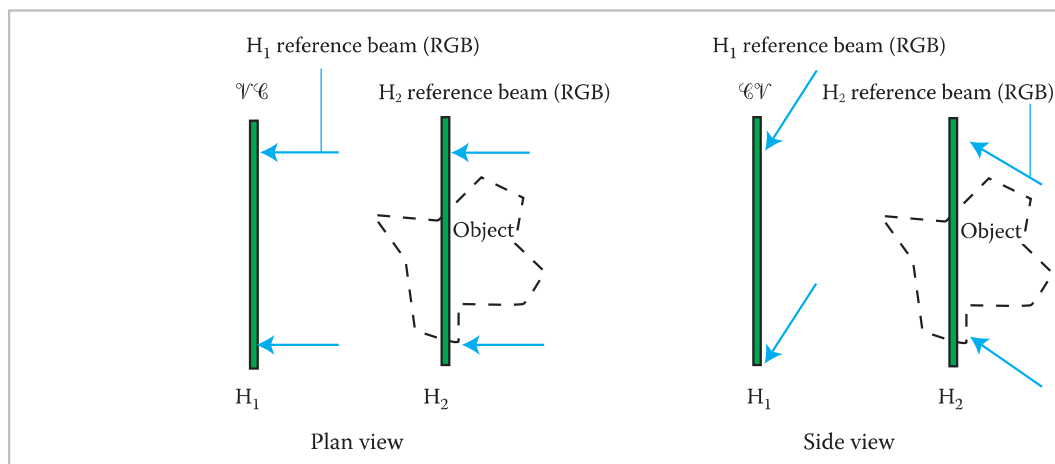
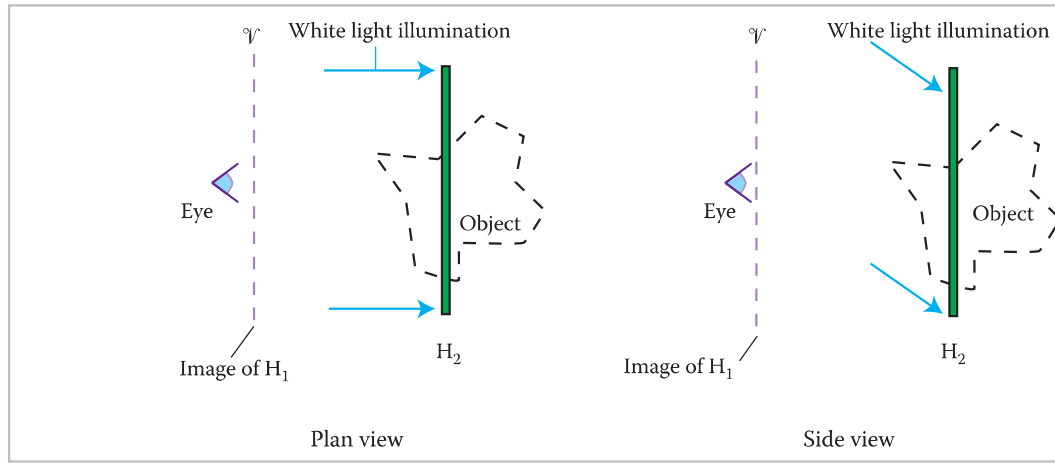
(a) Creation of H_1 hologram(b) $H_1:H_2$ transfer process(c) Viewing the H_2

FIGURE 8.7 Writing an MWDH H_1 reflection master hologram: (a) writing the H_1 hologram, (b) $H_1:H_2$ transfer process and (c) viewing the H_2 reflection hologram.

the hologram to be calculated using only a linear array of cameras instead of a two-dimensional matrix, which is required in the full-parallax case. The camera data required for an HPO hologram is therefore associated with a three-dimensional object (${}^k\mathbf{I}_{ij}$) rather than the four-dimensional object (${}^{kg}\mathbf{I}_{ij}$), which we have introduced above and which is required for the general full-parallax case. In addition, we shall see that the form of ${}^{uv}\mathbf{S}_{\alpha\beta}$ also essentially becomes three-dimensional in the HPO case.

In terms of computer memory requirements, HPO represents a considerable saving. Take for example the case of a $1\text{ m} \times 1\text{ m}$ DWDH full-parallax colour reflection hologram, which might typically require an array of 1000×1000 cameras, each of a resolution of 1024×768 . The total uncompressed information in \mathbf{I} is approximately 2.4 TB. For the HPO case, this information decreases by a factor of 1000 to 2.4 GB!

We must remember, however, that there is a price to pay for such a spectacular reduction in information. An HPO hologram only replays a non-distorted image when the viewer's eyes coincide geometrically with the linear array of cameras. As the viewer approaches and withdraws from the hologram, the image becomes distorted, and as the viewer moves his or her head up and down, instead of seeing over and underneath an object, the object just appears to rotate such that it always presents the same orientation to the viewer. If the camera distance (h) is large enough, there nevertheless exists a significant viewing region around this distance where distortion is difficult to notice. In general, because the distortion becomes increasingly difficult to perceive as the observation distance is increased, it is normally possible to achieve practical distortion-free viewing from the camera plane to infinity if h is rather larger than the characteristic hologram dimension.

In addition, there are two significant further advantages inherent to reflection HPO holograms when illuminated by usual broadband sources. The first is that very large image depths may be recorded and replayed using such holograms, making them an obvious choice for large-format display applications. This is not usually the case for modern full-parallax reflection holograms, which must be recorded onto an emulsion of finite thickness and are usually illuminated by broadband sources; here, as we shall discuss in Chapters 9 and 11, chromatic blurring can severely limit the clear image depth. The second advantage is that multiple broadband illumination sources may be used to illuminate an HPO reflection hologram without introducing image blurring. We shall discuss this aspect in detail in Chapter 13.

We should also mention that one can indeed discuss curved camera trajectories instead of linear ones. After all, initial work on stereograms [5] used a fixed camera and a rotating object—although most often the final stereogram was itself actually curved. Nevertheless, we find little benefit in an HPO hologram that has a curved optimum viewing plane in place of a linear one. In the case of full-parallax holograms, however, the camera plane is essentially independent of the viewing plane and the hologram can (ideally) be viewed without distortion at any location; in Chapter 10, we shall see how the results of this chapter can then be usefully extended to the cases of cylindrical and spherical camera surfaces.

8.8.1 Printer, Camera and Viewing Window Options

There are several choices as to how a single parallax DWDH hologram may be physically written. First, we may decide to keep the SLM static or we may use an objective with a larger entrance pupil and opt to move the SLM within this pupil. Second, various formats of computer data, which effectively correspond to different camera geometries, may be used. A simple translating camera (for example, a real physical camera) will produce, in general, a different ${}^k\mathbf{I}_{ij}$ data set than a specially programmed virtual camera. Either a real or a virtual camera may rotate as it translates, and this too produces a different ${}^k\mathbf{I}_{ij}$. Finally, different viewing window geometries may be selected. If we elect to use the full field of view of the printer optical objective when writing each hogel, then we will have a different result than if we constrain our viewing window to a well-defined rectangle at the viewing plane.

All the above choices must be made according to the specific application at hand. In the following sections, we will treat the most important major cases and derive for each geometry the transformations necessary to convert the single parallax camera data, ${}^k\mathbf{I}_{ij}$, into the SLM data, ${}^{uv}\mathbf{S}_{\alpha\beta}$. We will only treat the

case of a static SLM in this book because the historical motivation for moving the SLM has largely been overtaken by modern advances in high-definition SLM technology.

8.8.2 General Rectangular Viewing Window

8.8.2.1 Simple Translating Camera

In this section, a specific image data model, ${}^k\mathbf{I}_{ij}$, will be assumed. This model relates to a simple translating camera that follows a horizontal trajectory through the midpoint of the hologram viewing plane. Figure 8.8 shows a side (a) and plan (b) view of the geometry. The viewing zone of the hologram is defined (at \mathcal{V}) to be a rectangle having horizontal dimension W and vertical dimension H . This means that $D_\xi = W$.

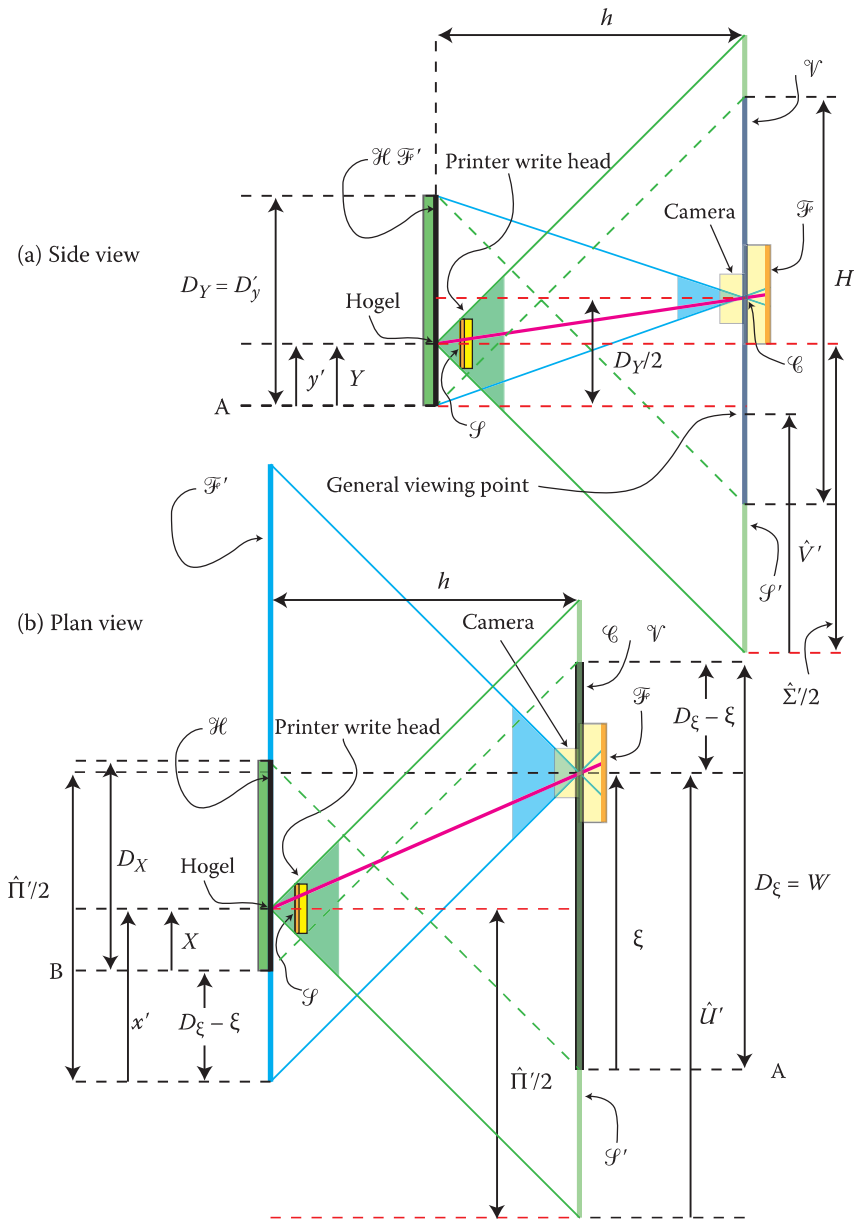


FIGURE 8.8 Writing a DWDH HPO reflection hologram. Ray geometry for (a) side view and (b) plan view. Note the conjugate SLM position.

To simplify the geometry of Figure 8.8, we chose to illustrate a (symmetrically) restricted field of view of the printer's optical objective. We define the horizontal and vertical components of this restricted field of view as

$$\begin{aligned} \tan\left(\frac{\hat{\Psi}_{\text{PH}}}{2}\right) &= \frac{\hat{\Pi}'}{2h} = \frac{W + D_x}{2h} \\ \tan\left(\frac{\hat{\Psi}_{\text{PV}}}{2}\right) &= \frac{\hat{\Sigma}'}{2h} = \frac{H + D_y}{2h} \end{aligned} \quad (8.21)$$

Of course, we are implicitly assuming here that $\Psi_{\text{PH}} \geq \hat{\Psi}_{\text{PH}}$ and $\Psi_{\text{PV}} \geq \hat{\Psi}_{\text{PV}}$ because, clearly, one cannot restrict an angle to a larger angle! For clarity, we shall label the SLM data, when we calculate it using restricted fields of view, as $\hat{\mathbf{S}}$ to distinguish it from \mathbf{S} , which refers to data corresponding to the full field of view of the printer. Likewise, we will introduce \hat{N}_M and \hat{N}_V as the reduced SLM integer dimensions and \hat{U}' and \hat{V}' as the restricted real dimensions of the projected SLM. Finally, we introduce the restricted integer coordinates of the SLM, $\hat{\mu}'$ and $\hat{\nu}'$:

$$\hat{U}' = \frac{(\hat{\mu}' - 1)\hat{\Pi}'}{\hat{N}_M - 1} \quad \hat{\mu}' = 1, 2, 3, \dots, \hat{N}_M \quad (8.22)$$

$$\hat{V}' = \frac{(\hat{\nu}' - 1)\hat{\Sigma}'}{\hat{N}_V - 1} \quad \hat{\nu}' = 1, 2, 3, \dots, \hat{N}_V \quad (8.23)$$

We choose a camera whose horizontal field of view exactly matches the restricted horizontal field of view of the printer so that $\Psi_{\text{CH}} = \hat{\Psi}_{\text{PH}}$. If we were to use a larger camera angle, we would simply end up collecting image data that we did not need! Using the same philosophy, we use a vertical camera field of view that is defined as

$$\tan\left(\frac{\Psi_{\text{CV}}}{2}\right) = \frac{D_y}{2h}. \quad (8.24)$$

The difference in the choice between horizontal and vertical angles is because we are considering an HPO hologram and so the camera always stays vertically at the midpoint height of the hologram. This is in contrast with the horizontal behaviour of the camera, which consists of linear tracking and therefore requires a larger field of view.

We are now ready to examine Figure 8.8 in detail. Let us look at the side view in (a) to start with. Here, we have superimposed the hologram, the printer SLM and the camera. The camera is fixed at a height corresponding to the centre of the hologram and points straight forward. Its field of view is illustrated in blue and can be seen to just cover the hologram plane—that is, vertically, the projected film plane (\mathcal{F}') is perfectly coincident with \mathcal{H} . In the plan view of (b), \mathcal{F}' can be seen to be much larger than \mathcal{H} , as the camera, when on one extreme end of its track, must still cover all of \mathcal{H} . This is a characteristic of a simple translating camera and one can immediately see that this type of camera is inefficient, as it produces data that falls outside the field of \mathcal{H} —such data is, of course, useless.

We consider an arbitrary hogel on the hologram plane. The diagrams illustrate (in green) the field of view of the SLM and the printer objective during the printing process of this hogel. By considering the projected SLM plane \mathcal{S}' located at the camera distance (h), one can see that each hogel clearly has the capacity to deliver radiation to every point within the viewing zone. The magenta line connecting the hogel with the camera is a test ray. We will use this test ray to match the radiation fields at the viewing line (\mathcal{V}) during image acquisition and during hologram writing to relate camera data to SLM data. Specifically, we will demand that the angle and position of this arbitrary test ray at the viewing line (\mathcal{V}) be exactly the same for the case of image acquisition and for the case of writing the hologram. This then makes sure that the hologram replays an identical copy of the light-field emitted by the original object.

In fact, we will cheat a little and not match angles and positions at \mathcal{V} . Instead, we will opt for the equivalent process of matching positional coordinates (only) at two planes, \mathcal{H} and \mathcal{V} . Because we are considering an HPO hologram, we must seek to match acquisition plane coordinates and hologram-writing coordinates at the hogel location, both horizontally and vertically. In addition, we must match acquisition plane horizontal coordinates and hologram-writing horizontal coordinates at the camera location. These three matching operations will define the three freedoms implicit in the transformation between the two three-dimensional objects (\mathbf{I} and $\hat{\mathbf{S}}$).

The simplest matching operation is that of the vertical (\mathcal{F}') coordinate at the hogel with that of \mathcal{H} . This gives

$$y' = Y, \quad (8.25)$$

which leads to the index law through Equations 8.4 and 8.8

$$j' = \left\lceil \frac{(\beta - 1)(N_J - 1)}{N_B - 1} \right\rceil + 1 \quad (8.26)$$

Note that we use the notation of two sets of double lines enclosing a real expression to indicate the nearest integer operation—that is, in terms of the floor function $\|x\| \equiv \lfloor x + 1/2 \rfloor$. Now, because we have chosen to place \mathcal{F}' downstream of the camera pinhole, the \mathcal{F} coordinates are related to their primed counterparts by the simple relation

$$\begin{pmatrix} i \\ j \end{pmatrix} = \begin{pmatrix} N_I - i' + 1 \\ N_J - j' + 1 \end{pmatrix} \quad (8.27)$$

We can therefore use this to convert Equation 8.26 to the more useful form:

$$j = N_J - \left\lceil \frac{(\beta - 1)(N_J - 1)}{N_B - 1} \right\rceil \quad (8.28)$$

Of course, Equation 8.27 assumes that we start with data from a normal inverting camera. This is not always the case as both virtual cameras in CAD programs and modern digital cameras are fundamentally non-inverting. In such a case, Equation 8.27 must be replaced by

$$\begin{pmatrix} i \\ j \end{pmatrix} = \begin{pmatrix} i' \\ j' \end{pmatrix} \quad (8.29)$$

and Equation 8.28 becomes

$$j = \left\lceil \frac{(\beta - 1)(N_J - 1)}{N_B - 1} \right\rceil + 1 \quad (8.30)$$

Nevertheless, we shall continue with the case of an inverting camera and use Equations 8.27 and 8.28 in the following sections. Two further matching laws are then clear from Figure 8.8b.

$$X = x' - (W - \xi). \quad (8.31)$$

$$\hat{U}' - \xi = D_X - X \quad (8.32)$$

These are best combined to give

$$\xi = \hat{U}' - D_X + X \quad (8.33)$$

and

$$x' = W + D_X - \hat{U}' \quad (8.34)$$

We can then derive the corresponding index transformations using Equations 8.1, 8.5, 8.7 and 8.22:

$$\begin{aligned} k &= 1 + \left\lceil \frac{(N_K - 1)}{W} D_X \left[\frac{(\hat{\mu}' - 1)}{(\hat{N}_M - 1)} \frac{\hat{\Pi}'}{D_X} - 1 + \frac{(\alpha - 1)}{(N_A - 1)} \right] \right\rceil \\ &= 1 + \left\lceil \frac{(N_K - 1)}{W} D_X \left[\frac{(\hat{\mu} - 1)}{(\hat{N}_M - 1)} \left(\frac{W}{D_X} + 1 \right) + \frac{(\alpha - N_A)}{(N_A - 1)} \right] \right\rceil \end{aligned} \quad (8.35)$$

$$\begin{aligned} i' &= 1 + \left\lceil \frac{(N_I - 1)}{D_x} \left(W + D_X - \frac{(\hat{\mu}' - 1)\hat{\Pi}'}{(\hat{N}_M - 1)} \right) \right\rceil \\ &= 1 + \left\lceil \frac{(N_I - 1)(\hat{N}_M - \hat{\mu})}{(\hat{N}_M - 1)} \right\rceil \end{aligned} \quad (8.36)$$

We have used the fact that $\hat{\mu} = \hat{\mu}'$ in the second line of both Equations 8.35 and 8.36. This comes from the choice of locating both \mathcal{S} and \mathcal{S}' upstream of the hogel (we refer to this as the “conjugate SLM position”). Again, we should comment on this as positioning the SLM to the right of the hologram is simply a choice. The alternative (“the non-conjugate SLM position”) is to position the SLM to the left (with both the recording and replay reference beams from the right), in which case the coordinates of \mathcal{S} and \mathcal{S}' are related by

$$\begin{pmatrix} \hat{\mu} \\ \hat{v} \end{pmatrix} = \begin{pmatrix} \hat{N}_M - \hat{\mu}' + 1 \\ \hat{N}_V - \hat{v}' + 1 \end{pmatrix} \quad (8.37)$$

This is illustrated in Figure 8.9. As discussed in Chapter 7, the choice of a conjugate or non-conjugate SLM position depends largely on the optical design of the printer. When using a non-collimated reference beam (i.e., one which is characterised by different azimuthal and altitudinal reference angles for each hogel), one must be careful in the conjugate SLM case that the reconstruction reference geometry is geometrically conjugate to the recording geometry. In this case, the recording beam is from the left with

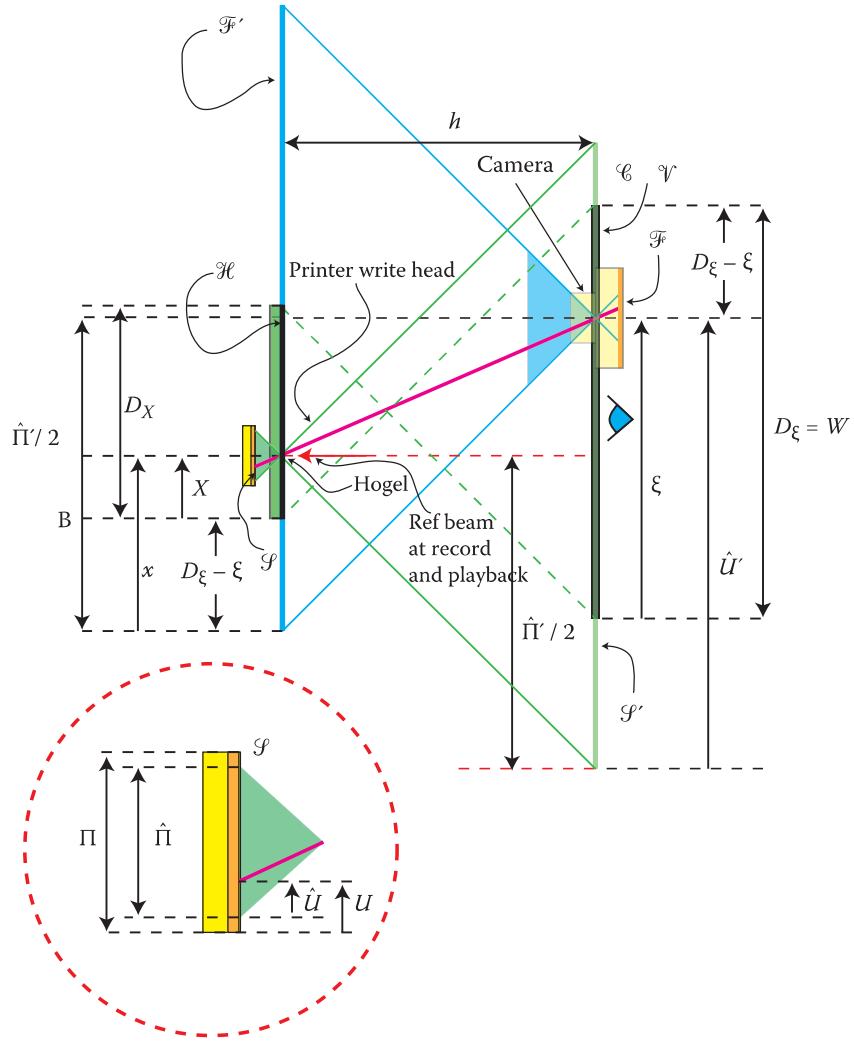


FIGURE 8.9 Writing a DWDH HPO reflection hologram with a non-conjugate SLM position—side view.

replay from the right. In the non-conjugate case, the recording reference beam and the replay reference beam are identical and both illuminate the hogel from the right.

We now use Equation 8.27, which describes an inverting camera to arrive at the unprimed version of Equation 8.36:

$$i = N_I - \left\| \frac{(N_I - 1)(\hat{N}_M - \hat{\mu})}{(\hat{N}_M - 1)} \right\| \quad (8.38)$$

Equations 8.28, 8.35 and 8.38 provide us with the necessary rules to calculate $\hat{\mathbf{S}}$ at the viewing line. This corresponds to knowing $\hat{\mathbf{S}}_{\alpha\beta}$ for only a single value of the index \hat{v} . Because we are seeking to construct an HPO hologram, we can simply copy this information for all other values of \hat{v} . This will mean that each hogel emits a light field that uniformly sweeps the vertical direction—which is precisely what we mean by an HPO hologram. If we wish to limit the vertical field of view of the hologram as a function of the hogel coordinate Y such as to create a viewing window of height H then we can impose the condition that

$$\begin{aligned} \hat{\mathbf{S}}_{\alpha\beta} &= k \mathbf{I}_{ij} \quad \forall \{ \hat{V}' \in \mathbb{R} \mid D_Y - Y \leq \hat{V}' \leq D_Y - Y + H \} \\ &= 0 \quad \text{otherwise} \end{aligned} \quad (8.39)$$

This condition on \hat{V}' translates into the following condition on \hat{v} :

$$\left\| \frac{D_Y}{D_Y + H} \frac{(\hat{N}_V - 1)(N_B - \beta)}{(N_B - 1)} \right\| + 1 \leq \hat{v} \leq 1 + \left\| \frac{D_Y}{D_Y + H} (\hat{N}_V - 1) \left\{ \frac{N_B - \beta}{N_B - 1} + \frac{H}{D_Y} \right\} \right\| \quad (8.40)$$

If we do not impose this condition, then we will generate a rolling vertical window. This has the effect that at the optimum viewing distance, there will be positions where we see only half the hologram and that as we change the position of our head up and down, so we will see more or less of the hologram. Of course, even with Condition 8.40, when the observer is significantly further away from the hologram than V , he will observe such a rolling window. However, the important point to understand is that HPO holograms are designed to be viewed from (approximately at least) a given distance and as such it makes good sense to create a proper rectangular window at this distance. The perceived brightness of a hogel is after all a direct function of its solid angle of emittance and it makes little sense to therefore put energy and brightness into angular emission zones where only a proportion of the hologram is visible—often, it is therefore much better to maximise the brightness in a clearly defined viewing zone.

We must also be attentive to the horizontal coordinates of the viewing window boundary. In general, Equation 8.35 can produce values of k outside the lower limit of 1 and the upper limit of N_K . To constrain k properly and to assure the proper horizontal definition of the viewing window, we must use a condition exactly similar to Equation 8.40. This condition can of course simply be derived by setting $k = 1$ and $k = N_K$ in Equation 8.35:

$$\left\| \frac{D_X}{D_X + W} \frac{(\hat{N}_M - 1)(N_A - \alpha)}{(N_A - 1)} \right\| + 1 \leq \hat{\mu} \leq 1 + \left\| \frac{D_X}{D_X + W} (\hat{N}_M - 1) \left\{ \frac{N_A - \alpha}{N_A - 1} + \frac{W}{D_X} \right\} \right\| \quad (8.41)$$

We are now in a position to write down the full \mathbf{I} -to- $\hat{\mathbf{S}}$ transformation for a monochromatic DWDH HPO reflection hologram for the case of a simple translating camera and a paraxial printer objective:

$$\begin{aligned} \hat{\mu} \hat{v} \hat{\mathbf{S}}_{\alpha\beta} &= {}^k \mathbf{I}_{ij} \quad \forall \hat{v} \in \mathbb{N} \left\| \frac{D_Y}{D_Y + H} \frac{(\hat{N}_V - 1)(N_B - \beta)}{(N_B - 1)} \right\| + 1 \leq \hat{v} \leq 1 + \left\| \frac{D_Y}{D_Y + H} (\hat{N}_V - 1) \left\{ \frac{N_B - \beta}{N_B - 1} + \frac{H}{D_Y} \right\} \right\| \\ &\quad \forall \hat{\mu} \left\{ \hat{\mu} \in \mathbb{N} \left\| \frac{D_X}{D_X + W} \frac{(\hat{N}_M - 1)(N_A - \alpha)}{(N_A - 1)} \right\| + 1 \leq \hat{\mu} \leq 1 + \left\| \frac{D_X}{D_X + W} (\hat{N}_M - 1) \left\{ \frac{N_A - \alpha}{N_A - 1} + \frac{W}{D_X} \right\} \right\| \right\} \\ &\quad \forall \alpha \left\{ \alpha \in \mathbb{N} \mid \alpha \leq N_A \right\} \quad \forall \beta \left\{ \beta \in \mathbb{N} \mid \beta \leq N_B \right\} \\ &= 0 \quad \text{otherwise} \end{aligned} \quad (8.42)$$

where

$$\begin{aligned} i &= N_I - \left\| \frac{(N_I - 1)(\hat{N}_M - \hat{\mu})}{(\hat{N}_M - 1)} \right\| \quad j = N_J - \left\| \frac{(\beta - 1)(N_J - 1)}{N_B - 1} \right\| \\ k &= 1 + \left\| \frac{(N_K - 1)}{W} D_X \left[\frac{(\hat{\mu} - 1)}{(\hat{N}_M - 1)} \left(\frac{W}{D_X} + 1 \right) + \frac{(\alpha - N_A)}{(N_A - 1)} \right] \right\| \end{aligned} \quad (8.43)$$

Remember that this transformation is valid for an inverting camera and a conjugate SLM position; it is also valid for the restricted field of view of the printer, not the actual field of view. To formulate the

transformation for \mathbf{S} rather than for $\hat{\mathbf{S}}$, we write the projected SLM coordinates in terms of their restricted counterparts (Figure 8.10):

$$\begin{aligned} U' &= \hat{U}' + \frac{1}{2}(\Pi' - \hat{\Pi}') \\ V' &= \hat{V}' + \frac{1}{2}(\Sigma' - \hat{\Sigma}') \end{aligned} \quad (8.44)$$

We then use Equations 8.11, 8.12, 8.22 and 8.23 to arrive at the transformation rules between μ and $\hat{\mu}$ and between ν and $\hat{\nu}$:

$$\begin{aligned} \hat{\mu} = \hat{\mu}' &= \left\| \frac{(\hat{N}_M + 1)}{2} + \frac{h(\hat{N}_M - 1)\tan\left(\frac{\Psi_{\text{PH}}}{2}\right)}{(D_X + W)(N_M - 1)}(2\mu - N_M - 1) \right\| \\ \hat{\nu} = \hat{\nu}' &= \left\| \frac{(\hat{N}_V + 1)}{2} + \frac{h(\hat{N}_V - 1)\tan\left(\frac{\Psi_{\text{PV}}}{2}\right)}{(D_Y + H)(N_V - 1)}(2\nu - N_V - 1) \right\| \end{aligned} \quad (8.45)$$

The values of $\hat{\mu}$ and $\hat{\nu}$ must, however, be between 1 and \hat{N}_M and \hat{N}_V , respectively. This means that there are minimum and maximum values for μ and ν outside which $\mathbf{S} = 0$ (this was after all why we introduced these restricted values!). If we denote the minimum index value by a subscript 1 and the maximum by 2, we can write expressions for these minimum and maximum values:

$$\mu_1 = \left\| \frac{N_M + 1}{2} - \frac{(D_X + W)(N_M - 1)}{4h\tan\left(\frac{\Psi_{\text{PH}}}{2}\right)} \right\| \quad \mu_2 = \left\| \frac{N_M + 1}{2} + \frac{(D_X + W)(N_M - 1)}{4h\tan\left(\frac{\Psi_{\text{PH}}}{2}\right)} \right\| \quad (8.46)$$

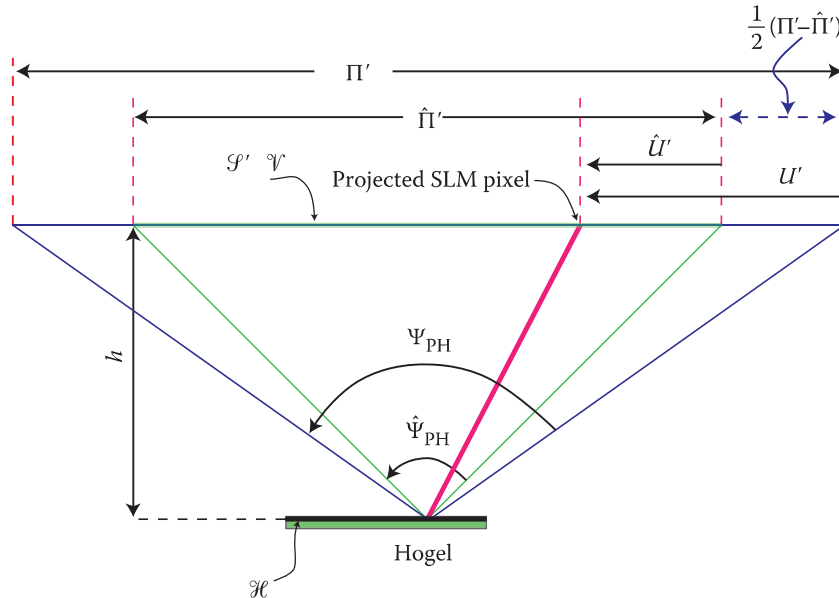


FIGURE 8.10 Plan view of the hologram showing the relationship between restricted and unrestricted SLM coordinate systems.

and

$$v_1 = \left\| \frac{N_V + 1}{2} - \frac{(D_Y + H)(N_V - 1)}{4h \tan\left(\frac{\Psi_{PV}}{2}\right)} \right\| \quad v_2 = \left\| \frac{N_V + 1}{2} + \frac{(D_Y + H)(N_V - 1)}{4h \tan\left(\frac{\Psi_{PV}}{2}\right)} \right\| \quad (8.47)$$

Of course, the viewing window constraints (Equations 8.40 and 8.41) must always constitute more constraining conditions than the conditions $\mu_1 \leq \mu \leq \mu_2$ and $v_1 \leq v \leq v_2$; the viewing window conditions can be written in terms of (μ, v) by the use of Equation 8.45 in Equations 8.40 and 8.41, giving

$$\begin{aligned} N_{U1} &\leq \mu \leq N_{U2} \\ N_{V1} &\leq v \leq N_{V2} \end{aligned} \quad (8.48)$$

where

$$\begin{aligned} N_{U1}(\alpha) &= \left\| \frac{N_M + 1}{2} + \frac{(N_M - 1)}{2h \tan\left(\frac{\Psi_{PH}}{2}\right)} \left\{ D_X \frac{(N_A - \alpha)}{N_A - 1} - \frac{(D_X + W)}{2} \right\} \right\| \\ N_{U2}(\alpha) &= \left\| \frac{N_M + 1}{2} + \frac{(N_M - 1)}{2h \tan\left(\frac{\Psi_{PH}}{2}\right)} \left\{ D_X \left\{ \frac{(N_A - \alpha)}{N_A - 1} + \frac{W}{D_X} \right\} - \frac{(D_X + W)}{2} \right\} \right\| \end{aligned} \quad (8.49)$$

and

$$\begin{aligned} N_{V1}(\beta) &= \left\| \frac{N_V + 1}{2} + \frac{(N_V - 1)}{2h \tan\left(\frac{\Psi_{PV}}{2}\right)} \left\{ D_Y \frac{(N_B - \beta)}{N_B - 1} - \frac{(D_Y + H)}{2} \right\} \right\| \\ N_{V2}(\beta) &= \left\| \frac{N_V + 1}{2} + \frac{(N_V - 1)}{2h \tan\left(\frac{\Psi_{PV}}{2}\right)} \left\{ D_Y \left\{ \frac{(N_B - \beta)}{N_B - 1} + \frac{H}{D_Y} \right\} - \frac{(D_Y + H)}{2} \right\} \right\| \end{aligned} \quad (8.50)$$

From a practical point of view, these (or equivalently, Equations 8.40 and 8.41) are the constraints we will need. Nevertheless, Equations 8.46 and 8.47 can be useful when using restricted variables as offset indices to address S directly.*

* In this case, it is good practice to fine-tune W and H such that the offset indices are integers.

We can now define \mathbf{S} in terms of $\hat{\mathbf{S}}$:

$$\begin{aligned} {}^{\mu\nu}\mathbf{S}_{\alpha\beta} &= {}^{\hat{\mu}\hat{\nu}}\hat{\mathbf{S}}_{\alpha\beta} \quad \forall \alpha \left\{ \alpha \in \mathbb{N} \mid \alpha \leq N_A \right\} \quad \forall \beta \left\{ \beta \in \mathbb{N} \mid \beta \leq N_B \right\} \\ &\quad \forall \mu \left\{ \mu \in \mathbb{N} \mid N_{U1}(\alpha) \leq \mu \leq N_{U2}(\alpha) \right\} \quad \forall \nu \left\{ \nu \in \mathbb{N} \mid N_{V1}(\beta) \leq \nu \leq N_{V2}(\beta) \right\} \\ &= 0 \quad \text{otherwise} \end{aligned} \quad (8.51)$$

where $\hat{\mu}$ and $\hat{\nu}$ are given by Equation 8.45. Alternatively, we can substitute Equation 8.45 into Equations 8.42 and 8.43 to give the direct **I**-to-**S** transformation:

$$\begin{aligned} {}^{\mu\nu}\mathbf{S}_{\alpha\beta} &= {}^k\mathbf{I}_y \quad \forall \mu \left\{ \mu \in \mathbb{N} \mid N_{U1}(\alpha) \leq \mu \leq N_{U2}(\alpha) \right\} \quad \forall \nu \left\{ \nu \in \mathbb{N} \mid N_{V1}(\beta) \leq \nu \leq N_{V2}(\beta) \right\} \\ &\quad \forall \alpha \left\{ \alpha \in \mathbb{N} \mid \alpha \leq N_A \right\} \quad \forall \beta \left\{ \beta \in \mathbb{N} \mid \beta \leq N_B \right\} \\ &= 0 \quad \text{otherwise} \end{aligned} \quad (8.52)$$

where

$$i = N_I - \left\| \left(N_I - 1 \right) \left\{ \frac{1}{2} - \frac{h(2\mu - N_M - 1)}{(D_x + W)(N_M - 1)} \tan\left(\frac{\Psi_{PH}}{2}\right) \right\} \right\| \quad (8.53)$$

$$j = N_J - \left\| \frac{(\beta - 1)(N_J - 1)}{N_B - 1} \right\| \quad (8.54)$$

$$k = 1 + \left\| \frac{(N_K - 1)(W + D_x)}{W} \left\{ \frac{1}{2} + \frac{h(2\mu - N_M - 1)}{(D_x + W)(N_M - 1)} \tan\left(\frac{\Psi_{PH}}{2}\right) + \frac{D_x(\alpha - N_A)}{(W + D_x)(N_A - 1)} \right\} \right\| \quad (8.55)$$

You will notice that all mention of restricted values has now disappeared from this transformation. These values might therefore be regarded as simply a useful tool to arrive at the general **I**-to-**S** transformation. However, very often it is more efficient to calculate $\hat{\mathbf{S}}$, as \mathbf{S} usually contains a high percentage of constantly zero elements (often $>70\%$). Computationally, it can therefore make better sense to calculate only $\hat{\mathbf{S}}$ for each hogel and to then only update these elements on the SLM. This is particularly true when HPO SLM data is calculated from camera data in real time between successive hogel-write operations; one then has very limited time available to calculate the data.*

8.8.3 Centred Camera Configuration

It will be clear from Figure 8.8b that most of the camera film plane is not actually used in computing the SLM data, as much of the projected film plane, \mathcal{F}' , falls outside the hologram plane \mathcal{H} . This is the major disadvantage of the simple translating camera configuration. We shall see in Chapter 10 how a combination of translation and rotation of the camera can be used in real-world image acquisition systems to

* We shall introduce shortly an even more efficient system known as the centred SLM coordinate system. However, this system has variable rather than fixed offset indices and this can induce digital noise—more on this later.

improve this situation dramatically—but at a cost. Here, we shall describe a much simpler technique which is available for use with most virtual cameras within CAD software and which has essentially no disadvantages. This is the centred camera configuration. In Chapter 10, we shall also look at how this configuration can be programmed under the 3D Studio Max software platform.

The centred camera configuration is essentially an idealised camera with a translating film plane. In the case of an HPO reflection hologram with a fixed rectangular viewing box located at distance h from the hologram, this consists of a camera whose field of view is chosen to be

$$\begin{aligned}\Psi_{\text{CH}} &= 2 \tan^{-1} \left(\frac{D_x + W}{2h} \right) \\ \Psi_{\text{CV}} &= 2 \tan^{-1} \left(\frac{D_y}{2h} \right)\end{aligned}\quad (8.56)$$

This is of course exactly the same as the restricted field of view that we introduced in the last section for a simple translating camera. The camera is, however, now chosen to have a (horizontally) smaller film plane, which we shall label, $\hat{\mathcal{F}}$, such that not all the light gathered by the camera falls on this plane. The horizontal dimensions of $\hat{\mathcal{F}}$ are chosen such that when positioned in front of the hologram at the centre of the camera track, an image of the hologram just fills $\hat{\mathcal{F}}$. As the camera is moved either to the right or to the left of this position, $\hat{\mathcal{F}}$ is automatically shifted horizontally such that the image of the hologram always exactly fills $\hat{\mathcal{F}}$. In this way, $\hat{\mathcal{F}}$ is always exactly collocated with \mathcal{H} .

Mathematically, we may describe the centred camera configuration for HPO holograms by a requirement on the size of $\hat{\mathcal{F}}$ within \mathcal{F} and by the required horizontal translation of $\hat{\mathcal{F}}$ in terms of the usual x coordinate of \mathcal{F} . Mathematically, this may be expressed as

$$\begin{aligned}x_1 &= W - \xi \\ x_2 &= W - \xi + D_x\end{aligned}\quad (8.57)$$

where the subscript 1 indicates where $\hat{\mathcal{F}}$ starts and the subscript 2 indicates where $\hat{\mathcal{F}}$ stops. We shall come back to this in Chapter 10 when we discuss how to program a centred camera configuration. For our present purposes, however, we will simply assume that we are given \mathbf{I} in terms of $\hat{\mathcal{F}}$ rather than in terms of \mathcal{F} . We shall then use the coordinates x and y (and their corresponding integer partners i and j) simply to refer to $\hat{\mathcal{F}}$ rather than to \mathcal{F} . Accordingly, we shall put $D_x = D_X$ in addition to the condition $D_y = D_Y$, which we have used throughout our discussion of HPO holograms. It is important to understand that in the HPO simple translating camera configuration, D_x is uniquely defined by the horizontal field of view of the camera, Ψ_{CH} , whereas in the HPO centred camera configuration, the relation $D_x = D_X$ defines a subset of the total horizontal optical field defined by Ψ_{CH} .

The centred camera configuration simplifies the horizontal geometry (the plan view) significantly; the vertical geometry (the side view) remains identical to the case of the HPO simple translating camera (Figure 8.8a). Figure 8.11 shows a plan view of the geometry for the centred camera configuration. As previously, we use a test ray (shown in magenta) to identify rays of \mathbf{I} and \mathbf{S} and to match the light-fields at the viewing plane. We do this by matching \mathbf{I} and \mathbf{S} at the indicated hogel on $\mathcal{H}/\hat{\mathcal{F}}$ and at the indicated camera position on \mathcal{C}/\mathcal{S}' , which is equivalent to matching direction and angle of all rays on \mathcal{V} .

The matching conditions at the hogel give the trivial relations

$$X = x' ; Y = y' \quad (8.58)$$

The conditions at the camera pinhole (Equation 8.32) remain unchanged:

$$\hat{U}' - \xi = D_X - X \quad (8.59)$$

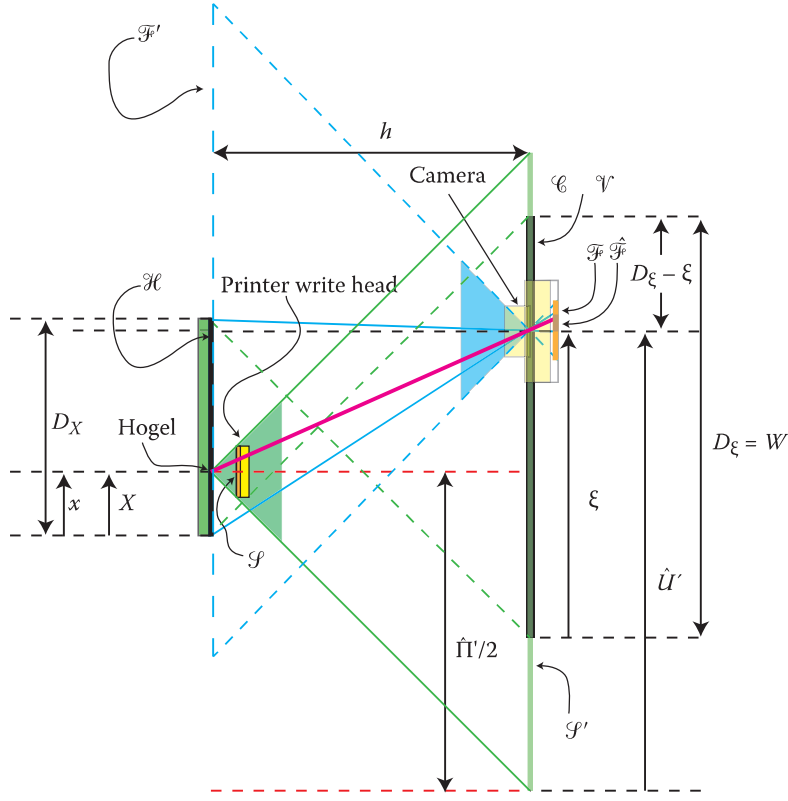


FIGURE 8.11 Plan view of ray geometry for a centred camera.

The corresponding index transformations are then derived using Equations 8.1, 8.5, 8.7, 8.8, 8.22 and 8.27:

$$\begin{aligned}
 i &= N_I - \left\| \frac{(\alpha-1)(N_I-1)}{(N_A-1)} \right\|, \quad j = N_J - \left\| \frac{(\beta-1)(N_J-1)}{(N_B-1)} \right\| \\
 k &= 1 + \left\| \frac{(N_K-1)}{W} D_X \left[\frac{(\hat{\mu}-1)}{(\hat{N}_M-1)} \left(\frac{W}{D_X} + 1 \right) + \frac{(\alpha-N_A)}{(N_A-1)} \right] \right\|
 \end{aligned} \tag{8.60}$$

The paraxial \mathbf{I} -to- $\hat{\mathbf{S}}$ transformation for a monochromatic DWDH HPO reflection hologram for the case of the centred camera configuration and a general rectangular window can therefore be written:

$$\begin{aligned}
 \hat{\mu}\hat{v}\hat{\mathbf{S}}_{\alpha\beta} &= {}^k\mathbf{I}_j \quad \forall \hat{v} \in \mathbb{N} \left\| \frac{D_Y}{D_Y+H} \frac{(\hat{N}_V-1)(N_B-\beta)}{(N_B-1)} \right\| + 1 \leq \hat{v} \leq 1 + \left\| \frac{D_Y}{D_Y+H} (\hat{N}_V-1) \left\{ \frac{N_B-\beta}{N_B-1} + \frac{H}{D_Y} \right\} \right\| \\
 \forall \hat{\mu} &\left\{ \hat{\mu} \in \mathbb{N} \left\| \frac{D_X}{D_X+W} \frac{(\hat{N}_M-1)(N_A-\alpha)}{(N_A-1)} \right\| + 1 \leq \hat{\mu} \leq 1 + \left\| \frac{D_X}{D_X+W} (\hat{N}_M-1) \left\{ \frac{N_A-\alpha}{N_A-1} + \frac{W}{D_X} \right\} \right\| \right\} \\
 \forall \alpha &\left\{ \alpha \in \mathbb{N} \mid \alpha \leq N_A \right\} \quad \forall \beta &\left\{ \beta \in \mathbb{N} \mid \beta \leq N_B \right\} \\
 &= 0 \quad \text{otherwise}
 \end{aligned} \tag{8.61}$$

where i, j and k are given by Equation 8.60. We can also use Equation 8.45 in Equation 8.60 to arrive at the corresponding direct **I**-to-**S** transformation:

$$\begin{aligned} {}^{\mu\nu} \mathbf{S}_{\alpha\beta} &= {}^k \mathbf{I}_j & \forall \alpha \left\{ \alpha \in \mathbb{N} \mid \alpha \leq N_A \right\} & \forall \beta \left\{ \beta \in \mathbb{N} \mid \beta \leq N_B \right\} \\ & \forall \mu \left\{ \mu \in \mathbb{N} \mid N_{U1}(\alpha) \leq \mu \leq N_{U2}(\alpha) \right\} & \forall v \left\{ v \in \mathbb{N} \mid N_{V1}(\beta) \leq v \leq N_{V2}(\beta) \right\} \\ &= 0 & \text{otherwise} \end{aligned} \quad (8.62)$$

where

$$\begin{aligned} i &= N_I - \left\| \frac{(\alpha-1)(N_I-1)}{N_A-1} \right\|, & j &= N_J - \left\| \frac{(\beta-1)(N_J-1)}{N_B-1} \right\| \\ k &= 1 + \left\| \frac{(N_K-1)}{W} \left\{ \frac{D_x+W}{2} + \frac{h(2\mu-N_M-1)}{(N_M-1)} \tan\left(\frac{\Psi_{PH}}{2}\right) + \frac{(\alpha-N_A)D_x}{N_A-1} \right\} \right\| \end{aligned} \quad (8.63)$$

and where N_{U1} , N_{U2} , N_{V1} and N_{V2} are given by Equations 8.49 and 8.50. This transformation is the main result of the present section. Again, as with all the transformations described here, it pertains to the case of an inverting camera and to a conjugate SLM position.

Before terminating our discussion on centred cameras, we will, for completeness, show how camera data from a simple translating camera can be converted to the data from a centred camera. To do this, we will introduce new x' and i' coordinates for the centred camera plane, $\hat{\mathcal{F}'}$

$$\hat{x}' = \frac{(\hat{i}'-1)}{(\hat{N}_I-1)} D_x \quad (8.64)$$

We will keep the original coordinates (x', i') for the simple translating camera plane \mathcal{F}' . Comparing Figure 8.8b and Figure 8.11, one can easily see that

$$\hat{x}' = x' - (W - \xi) \quad (8.65)$$

Equations 8.5, 8.64 and 8.65 then tell us that

$$i' = 1 + \left\| \frac{(N_I-1)W}{W+D_x} \left\{ \frac{(\hat{i}'-1)}{(\hat{N}_I-1)} D_x + \frac{(N_K-k)}{(N_K-1)} \right\} \right\| \quad (8.66)$$

or equivalently,

$$i = N_I - \left\| \frac{(N_I-1)W}{W+D_x} \left\{ \frac{(\hat{N}_I-\hat{i})}{(\hat{N}_I-1)} D_x + \frac{(N_K-k)}{(N_K-1)} \right\} \right\| \quad (8.67)$$

Usually, one would also try and choose

$$\frac{\hat{N}_I-1}{N_I-1} = \frac{D_x}{W+D_x} \quad (8.68)$$

for obvious reasons. If we now denote \mathbf{I} as the camera data for the simple translating camera, and $\hat{\mathbf{I}}$ for corresponding data pertaining to a centred camera, then we can define $\hat{\mathbf{I}}$ in terms of \mathbf{I} as follows:

$$\begin{aligned} {}^k\hat{\mathbf{I}}_{ij} &= {}^k\mathbf{I}_{ij} \quad \forall i \left\{ i \in \mathbb{N} \mid i \leq N_I \right\} \\ &\quad \forall j \left\{ j \in \mathbb{N} \mid j \leq N_J \right\} \\ &\quad \forall k \left\{ k \in \mathbb{N} \mid k \leq N_K \right\} \end{aligned} \quad (8.69)$$

where i is given by Equation 8.67.

8.8.4 Centred SLM Configuration

We mentioned in previous sections that the system of restricted SLM coordinates allowed us to economise memory and processing time by not bothering to calculate and store image data that were always going to be zero-valued. The SLM was then updated using the restricted data set $\hat{\mathbf{S}}$ together with constant offset relations that defined which subsection of the SLM address space $\hat{\mathbf{S}}$ pertained. We can actually extend this logic one step further and define projected centred SLM coordinates (\bar{U}', \bar{V}') as illustrated in Figure 8.12. The centred SLM geometry corresponds exactly to the centred camera geometry; the coordinates now only span the camera plane. In this way, absolutely no non-zero values are stored. The only disadvantage is that the required offset relations are now not constant but change with the hogel being printed. It is therefore necessary to calculate these offset relations in real time or to keep a record of them before printing. The choice of whether to use restricted SLM coordinates or centred SLM coordinates usually comes down to the design of the SLM electronics. Restricted coordinates allow the exterior

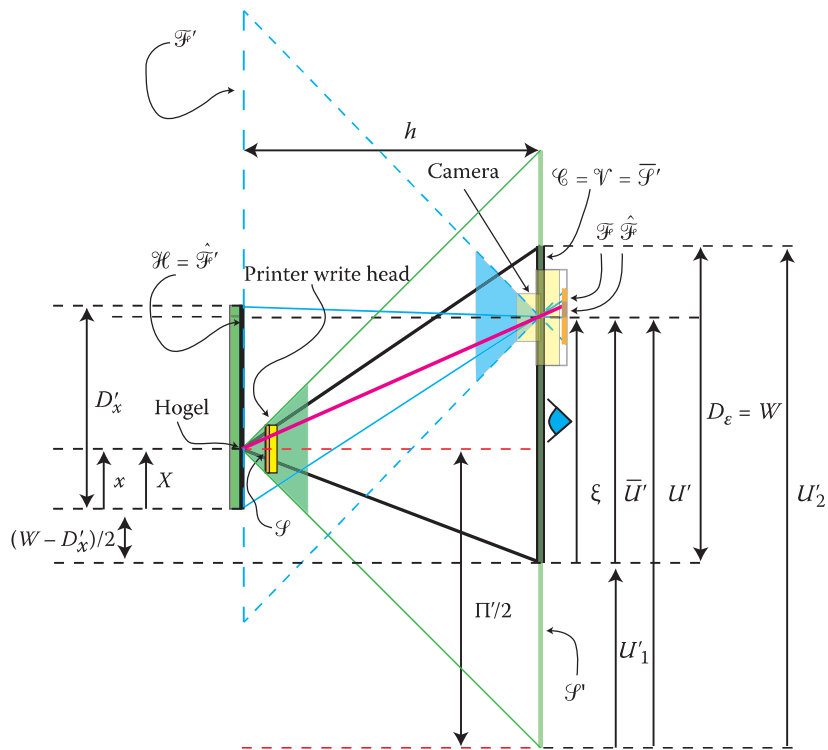


FIGURE 8.12 Plan view of ray geometry for a centred camera and centred SLM.

region of the SLM to be cleared and then only the fixed interior region updated from hogel to hogel. Centred coordinates require the SLM to be cleared before writing the data set. We shall see in Chapter 9 that the centred SLM geometry is particularly useful in the context of full-parallax holograms.

The centred SLM coordinates are defined by the simple relation

$$\bar{U}' = \xi \quad (8.70)$$

Extending our standard notation, this leads to the integer rule

$$k = 1 + \left\| \frac{\Pi'(N_K - 1)}{W(N_M - 1)} (\bar{\mu}' - 1) \right\| \quad (8.71)$$

which, in turn, leads to the following paraxial \mathbf{I} -to- $\bar{\mathbf{S}}$ transformation valid for a centred inverting camera and a conjugate SLM position

$$\begin{aligned} {}^{\bar{\mu}\bar{v}}\bar{\mathbf{S}}_{\alpha\beta} &= {}^k\mathbf{I}_{\bar{j}} & \forall \bar{v} \left\{ \bar{v} \in \mathbb{N} \mid 1 \leq \bar{v} \leq 1 + \left\| \frac{H(N_V - 1)}{\Sigma'} \right\| \right\} \\ & & \forall \bar{\mu} \left\{ \bar{\mu} \in \mathbb{N} \mid 1 \leq \bar{\mu} \leq 1 + \left\| \frac{W(N_M - 1)}{\Pi'} \right\| \right\} \\ & & \forall \alpha \left\{ \alpha \in \mathbb{N} \mid \alpha \leq N_A \right\} \\ & & \forall \beta \left\{ \beta \in \mathbb{N} \mid \beta \leq N_B \right\} \\ & = 0 & \text{otherwise} \end{aligned} \quad (8.72)$$

where

$$\begin{aligned} i &= N_I - \left\| \frac{(\alpha - 1)(N_I - 1)}{(N_A - 1)} \right\| \\ j &= N_J - \left\| \frac{(\beta - 1)(N_J - 1)}{(N_B - 1)} \right\| \\ k &= 1 + \left\| \frac{\Pi'(N_K - 1)}{W(N_M - 1)} (\bar{\mu}' - 1) \right\| \end{aligned} \quad (8.73)$$

Under special circumstances, we can sometimes arrange that

$$\frac{\Pi'}{W} = \frac{(N_M - 1)}{(N_K - 1)} \quad (8.74)$$

in which case for a non-inverting camera, the transformation simplifies dramatically to

$$\begin{aligned}
 {}^{\bar{\mu}\bar{v}}\bar{\mathbf{S}}_{\alpha\beta} &= {}^k\mathbf{I}_{ij} & \forall \bar{v} \left\{ \bar{v} \in \mathbb{N} \mid 1 \leq \bar{v} \leq 1 + \left\lceil \frac{H(N_V - 1)}{\Sigma'} \right\rceil \right\} \\
 && \forall \bar{\mu} \left\{ \bar{\mu} \in \mathbb{N} \mid 1 \leq \bar{\mu} = k \leq N_K \right\} \\
 && \forall \alpha \left\{ \alpha \in \mathbb{N} \mid \alpha = i \leq N_A \right\} \\
 && \forall \beta \left\{ \beta \in \mathbb{N} \mid \beta = j \leq N_B \right\} \\
 &= 0 & \text{otherwise}
 \end{aligned} \tag{8.75}$$

In other words, ${}^{\bar{\mu}\bar{v}}\bar{\mathbf{S}}_{\alpha\beta}$ is identical to ${}^k\mathbf{I}_{ij}$! The conditions required for this are that the integer coordinate meshes at recording and hologram-writing line up. We shall discuss this problem of coordinate line-up at length in the next section, but for now, we should just note that such a line-up occurs more easily in the context of full-parallax holograms as we shall see in Chapter 9.

The centred SLM transformation needs to be used with offset relations so that we can relate the actual SLM memory map \mathbf{S} to the centred data set $\bar{\mathbf{S}}$. We can work out these offset relations by relating U' to \bar{U}' with the help of Figure 8.12:

$$U' = \bar{U}' + U'_1 = \bar{U}' + \Pi'/2 - X - W/2 + D_x/2 \tag{8.76}$$

Or, in terms of integer coordinates

$$\mu = \bar{\mu}' + \left\lceil \frac{1}{2}(N_M - 1) \left(1 + \frac{D_x - W}{\Pi'} \right) - \frac{(\alpha - 1)D_x(N_M - 1)}{\Pi'(N_A - 1)} \right\rceil \tag{8.77}$$

Then, the offset coordinates, which tell us which indices μ_1 and μ_2 in \mathbf{S} correspond, respectively, to the indices $\bar{\mu}' = 1$ and $\bar{\mu}' = \left\lceil W(N_M - 1)/\Pi' \right\rceil + 1$ in $\bar{\mathbf{S}}$, are defined as

$$\begin{aligned}
 \mu_1 &= 1 + \left\lceil \frac{1}{2}(N_M - 1) \left(1 + \frac{D_x - W}{\Pi'} \right) - \frac{(\alpha - 1)D_x(N_M - 1)}{\Pi'(N_A - 1)} \right\rceil \\
 \mu_2 &= 1 + \left\lceil \frac{W}{\Pi'}(N_M - 1) + \frac{1}{2}(N_M - 1) \left(1 + \frac{D_x - W}{\Pi'} \right) - \frac{(\alpha - 1)D_x(N_M - 1)}{\Pi'(N_A - 1)} \right\rceil
 \end{aligned} \tag{8.78}$$

In an exactly similar fashion, the vertical offset coordinates are given by

$$\begin{aligned}
 v_1 &= 1 + \left\lceil \frac{1}{2}(N_V - 1) \left(1 + \frac{D_y - H}{\Sigma'} \right) - \frac{(\beta - 1)D_y(N_V - 1)}{\Sigma'(N_B - 1)} \right\rceil \\
 v_2 &= 1 + \left\lceil \frac{H}{\Sigma'}(N_V - 1) + \frac{1}{2}(N_V - 1) \left(1 + \frac{D_y - H}{\Sigma'} \right) - \frac{(\beta - 1)D_y(N_V - 1)}{\Sigma'(N_B - 1)} \right\rceil
 \end{aligned} \tag{8.79}$$

We can now appreciate a weakness of the centred SLM coordinate system. The offset index relations contain a truncation error, which will change from hogel to hogel. Because, in general, the \mathbf{I} -to- \mathbf{S} transformation itself also contains an interpolation error, we see that with the centred SLM coordinate

system, we can end up with two sequential errors. The index relations (Equations 8.46 and 8.47), which are relevant to restricted SLM coordinates, are invariant under a change of hogel coordinates; more importantly, they can also easily be made free of truncation error by choosing W and H appropriately.*

8.8.5 Fundamental Integer Constraints

Let us review the simple procedure that we have used to derive the **I-to-S** transformations in the previous sections. We started by defining various planes—the camera plane, the viewing plane, the hologram plane, etc.—we then described the general positions on these planes using two sets of coordinates. The first set is real and the second set is composed of integers. Of course, we want to define integer coordinates because our data is in digital form. The SLM is a digital device, as is the CCD detector of a digital camera; we divide the hologram into digital “hogels” and we move the camera from one discrete location to another. However, nothing says that the digital data of the acquisition system must line up and coincide exactly with the digital data that must be written to the hologram. Such lining up of the digital data is actually a powerful constraint that we may or may not be able to impose on a real printer. The fact that, in general, the digitisation of camera data (\mathcal{C} and \mathcal{F}) does not line up with the digitisation of hologram data (\mathcal{H} and \mathcal{S}') creates optical noise in the hologram. In the case of HPO holograms, this optical noise is most evident as dark vertical lines traversing the hologram. We will have more to say about such interpolation noise a little later.

Before embarking on a discussion of how we might force our digital data to line up, it is worth pointing out that most digital holographic printers do not have paraxial optical objectives. This means that the projection of the SLM, more often than not, takes the form of an intrinsically curvilinear coordinate system. From a practical point of view, this means that one simply cannot make the Cartesian integer coordinates of the SLM line up with the camera coordinates. In Section 8.10 and in the next chapter, we will discuss the non-paraxial projections of \mathcal{S} to \mathcal{S}' caused by objective distortion and holographic aberrations, and we will derive practical **I-to-S** transformations that reduce interpolation noise. We shall see that the main idea is to incorporate the inherent optical aberrations directly into the **I-to-S** transformations and to perform a single nearest integer operation rather than performing successive nearest integer operations.

In the case that there are no aberrations in the printer and in the hologram, it makes sense to impose conditions on the **I-to-S** transformation such that the various integer coordinate meshes line up. There are basically three conditions that lead to a quantisation of the distance, h , in terms of the (integer) quantum number, n . These rules are best understood from Figures 8.13 and 8.14, where a simple case is examined for, respectively, $n = 1$ and $n = 2$. The diagrams are plan views of the hologram and viewing/camera planes for a centred camera configuration using restricted angles of view.

The first condition is that the camera spacing must be equal to the hologram pitch. This can be written as

$$\frac{W}{N_K - 1} = \frac{D_X}{N_A - 1} \quad (8.80)$$

The second condition is that the (horizontal) pitch of the projected camera film plane at the hologram surface must equal an integer multiple of the hogel pitch (note that the centred camera condition has been applied here) or

$$\begin{aligned} \frac{D_X - m_X \delta}{N_I - 1} &= n \delta \\ \frac{D_Y}{N_J - 1} &= \delta \end{aligned} \quad (8.81)$$

* If N_M and N_V are large, which is of course always the case, then Equations 8.46 and 8.47 act to introduce a fine-scale quantisation into W and H . Thus, one does not have to change the window by much to ensure that the index laws for conversion of $\hat{\mathbf{S}}$ to \mathbf{S} are exact.

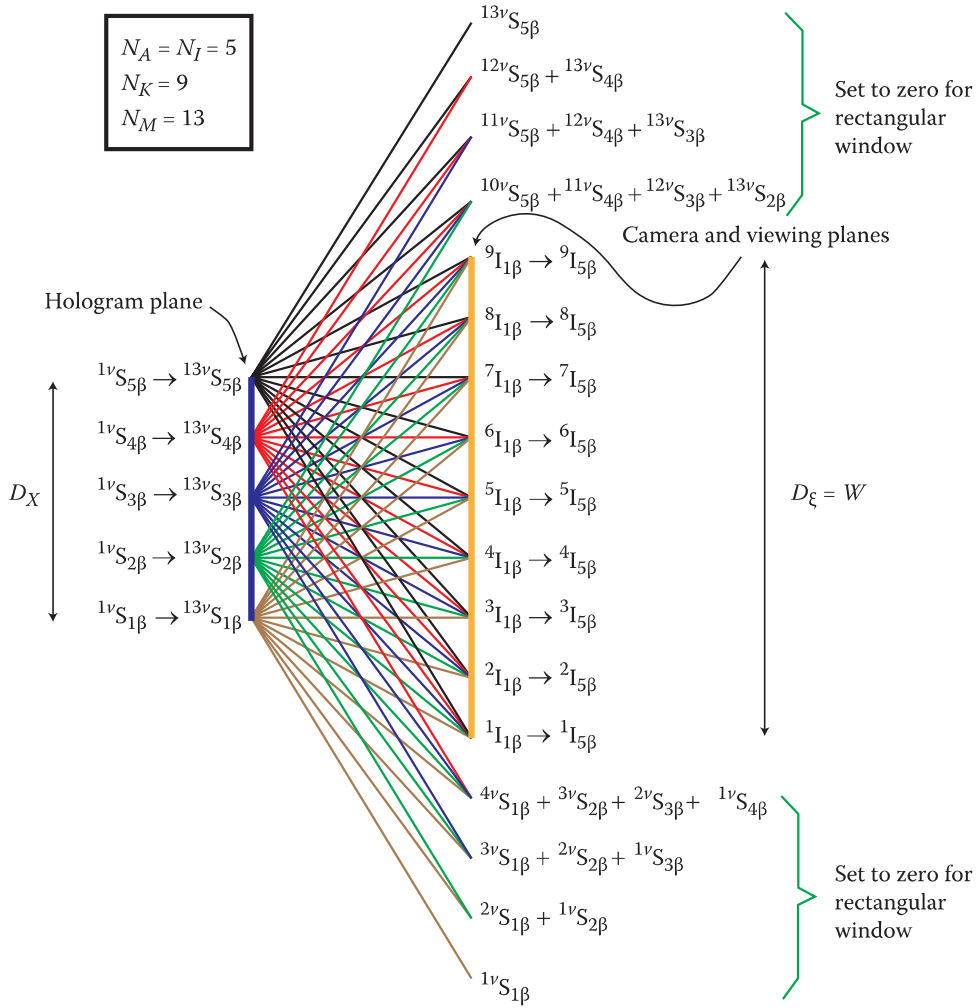


FIGURE 8.13 Illustration of exact ray correspondence between **I** and **S** for the simplified case of five hogels with a quantum number of $n = 1$.

where n is an integer greater or equal to 1 and δ is the hogel diameter defined as

$$\delta = \frac{D_x}{N_A - 1} = \frac{D_y}{N_B - 1} \quad (8.82)$$

The m parameter reflects the fact that camera data is not required in all cases at those film plane pixels corresponding to the last $n - 1$ hogels closest to the hologram boundary. This is just modular arithmetic; imagine that you want to divide a series of seven points/hogels into a line of points having twice the spacing. If you want to make the second series line up with the first, then there are just two principal ways of doing this which together use up all the points. We could choose points 1, 3, 5 and 7 for our second series or we could choose the series 2, 4 and 6. Both series have double the spacing of the original series, but the dimension of the new series is 4 in the first case and 3 in the second case. This is what happens with the projected film mesh—this mesh often finishes at $n - 1$ or fewer pixels from the edge of the hologram mesh. If you spend a little time with a pen and paper, you will be able to see that*

$$m_x = N_A - 1 - \left\lfloor \frac{N_A - k}{n} \right\rfloor n - \left\lfloor \frac{k-1}{n} \right\rfloor n \quad (8.83)$$

* We have assumed that both N_A and N_M are odd here.

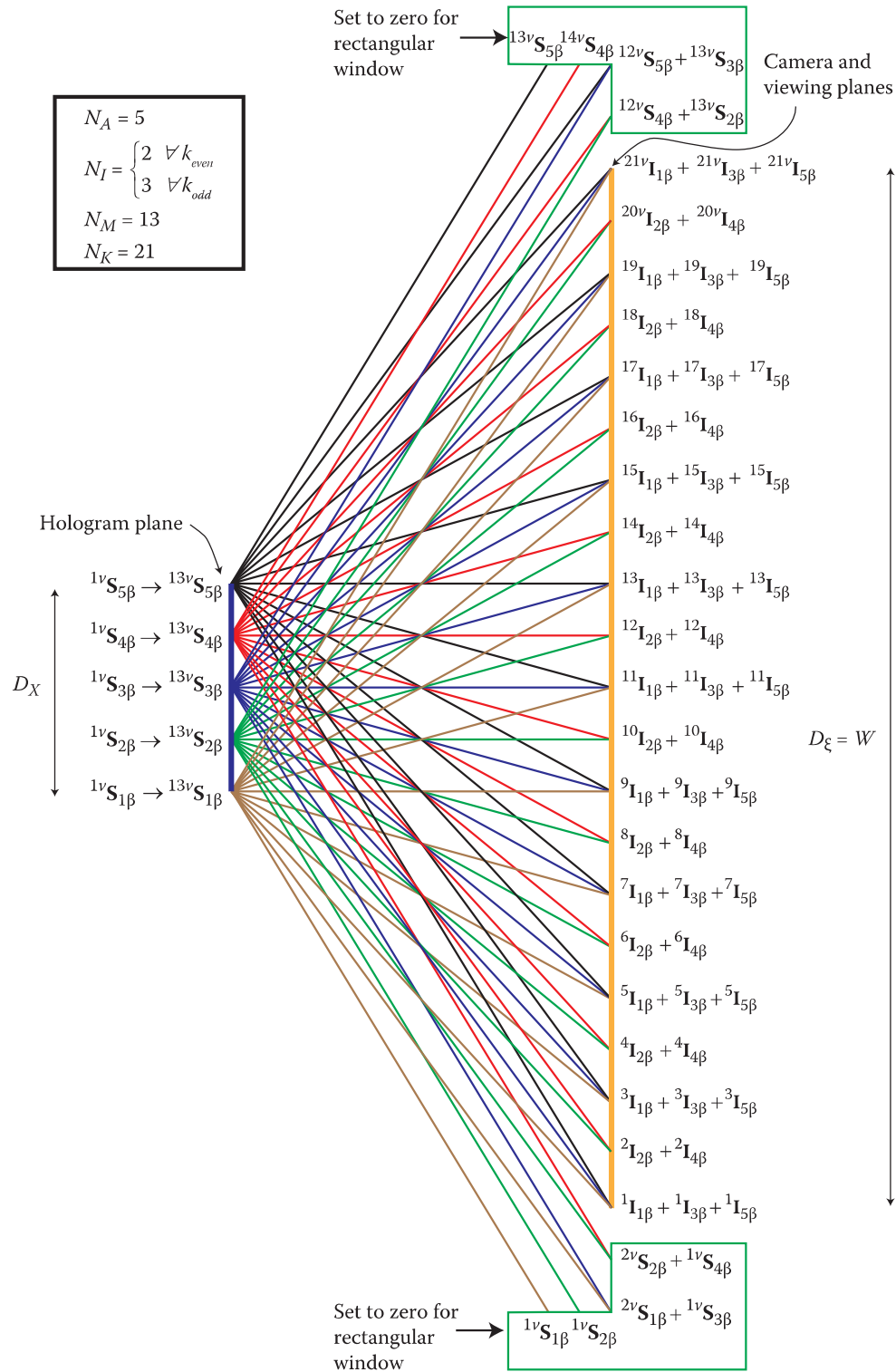


FIGURE 8.14 Illustration of exact ray correspondence between \mathbf{I} and \mathbf{S} for the simplified case of five hogels with a quantum number of $n = 2$.

This has the interesting consequence that N_I becomes a function of k . Equation 8.81 tells us that

$$N_I = 1 + \left\lfloor \frac{N_A - k}{n} \right\rfloor + \left\lfloor \frac{k-1}{n} \right\rfloor \quad (8.84)$$

$$N_J = N_B$$

By comparing Figures 8.13 and 8.14, you can see how this works. In the $n = 1$ case of Figure 8.13, each camera position is connected to all five hogels. However, in the $n = 2$ case of Figure 8.14 each camera position is connected by either two (even k) or three (odd k) rays to every other hogel. The odd values of k correspond to a film plane size equal to the entire hologram dimension, but the even k values correspond to only 1/2 the hologram dimension.

The third and final condition is that the pitch of the projected SLM plane at the camera plane must be equal to the same integral multiple, n of the camera spacing or

$$\frac{\Pi'}{N_M - 1} = \frac{\hat{\Pi}'}{\hat{N}_M - 1} = n \frac{W}{N_K - 1} \quad (8.85)$$

To see how these conditions work, we must think which parameters are fixed by their absolute nature and which may be changed to accommodate the conditions. In general, we start with a knowledge of N_M and N_V as these numbers are determined by the printer SLM. We will also know the desired hologram size, defined by D_X and D_Y , and the hogel diameter, δ . This then defines the number of hogels horizontally, N_A , and the number of hogels vertically, N_B . We regard all these numbers as being fixed in an absolute way. Condition 8.80 then tells us that we must choose the viewing window width, W , such that the quantity W/δ is an exact integer. This is usually a very acceptable constraint because adjusting the viewing width by a very minimal amount is, for almost all applications, simply without consequence.

Having now chosen W , D_X and N_A , we define N_K (using Equation 8.80) as

$$N_K = 1 + \frac{W}{\delta} = \frac{W}{D_X} (N_A - 1) + 1 \quad (8.86)$$

Condition 8.81 then tells us the values of N_I (for each value of k) and N_J . With a numerical camera within a CAD program, a camera can usually be configured in a very flexible fashion, and so again, this step is not a problem. We shall discuss real cameras in Chapter 10.

Finally, we come to Condition 8.85, which represents by far the most stringent condition and effectively defines a unique value of h for each n :

$$h = \frac{(N_M - 1)}{(N_A - 1)} \frac{n D_X}{2 \tan\left(\frac{\Psi_{PH}}{2}\right)} \quad (8.87)$$

Table 8.1 shows how this works for a typical printer in two cases. The first case is a 600 mm \times 400 mm landscape format hologram having a hogel diameter of 1 mm. The second case pertains to the same format but with a hogel size of 0.5 mm. Note that the values of D_X and D_Y are always a hogel less than the full-hologram size as the D values measure distance between hogel centres rather than hogel edges. The table shows clearly how the value of the integer parameter n quantises the viewing distance h . The bottom line is that forcing the integer coordinates of our camera acquisition and hologram recording planes to align has a significant price. This is the quantisation of the camera/viewing distance. For large hogel

TABLE 8.1
Table Showing the Quantised Distance, h , for Two HPO Holograms with Different Quantum Numbers, n

N_M	N_V	D_X	D_Y	Ψ_{PH}	Ψ_{PV}	W	N_A	N_B	n	N_K	$N_I(k=1)$	N_J	h	$N_I N_J N_K \cdot 10^9$
1280	1024	599	399	105.2	92.6	800	600	400	1	801	600	400	488.9355	192
1280	1024	599	399	105.2	92.6	2199	600	400	2	2200	300	400	977.8709	264
1280	1024	599	399	105.2	92.6	3598	600	400	3	3599	200	400	1466.806	288
1280	1024	599	399	105.2	92.6	4997	600	400	4	4998	150	400	1955.742	300
1280	1024	599.5	399.5	105.2	92.6	800	1200	800	1	1601	1200	800	244.4677	1537
1280	1024	599.5	399.5	105.2	92.6	2200	1200	800	2	4400	600	800	488.9355	2112
1280	1024	599.5	399.5	105.2	92.6	4999	1200	800	4	9998	300	800	977.8709	2400
1280	1024	599.5	399.5	105.2	92.6	6398	1200	800	5	12797	240	800	1222.339	2457
1280	1024	599.5	399.5	105.2	92.6	7798	1200	800	6	15596	200	800	1466.806	2495
1280	1024	599.5	399.5	105.2	92.6	9197	1200	800	7	18395	172	800	1711.274	2531
1280	1024	599.5	399.5	105.2	92.6	10597	1200	800	8	21194	150	800	1955.742	2544

Note: The holograms are both 600×400 mm. The first has a hogel size of 1 mm (first 4 lines of table). The second has a hogel size of 0.5 mm (remaining eight lines of table). Note that angles are in degrees and dimensional distances in mm.

sizes, the spacing between the various “ n ” quantum levels can be large, making it difficult to use this procedure. However, as can be seen from Table 8.1, for smaller hogel sizes, the situation does improve. Of course, the great advantage of using lined-up coordinate meshes is that one escapes completely from injecting interpolation noise into the hologram. We shall see later that the most common aberrations vanish when a hogel is viewed perpendicularly to the hologram surface; by using the procedure outlined here, we can then often, even for a real printer and a real hologram, effectively abolish interpolation noise in the central (and most visually obvious) zone of the hologram’s light emission cone.

Finally, we should note that when $n > 1$, the camera data is effectively squashed by a factor n in the horizontal direction. Indeed the information content of a single frame, \mathbf{I}_{ij} , is reduced by a factor of n . However the centred camera frame essentially dithers as k changes and this means that both the angular resolution and spatial resolution of the hologram are independent of n . Note that for full parallax holograms, the aspect ratio of the camera data is unchanged for any n .

8.9 Rainbow and Achromatic Transmission Holograms

Rainbow [6] and achromatic [7] holograms can both be generated using the two-step MWDH method or directly using one-step DWDH. Because these holograms are single-parallax holograms, there is a large potential advantage in using MWDH to generate the H_1 hologram (which is simply a one-dimensional “slit” hologram in the rainbow case) and then producing the H_2 by traditional optical transfer. The total information printed using this technique can be many orders of magnitude less than DWDH.

8.9.1 MWDH

The most obvious way to produce full-colour analogue rainbow holograms is by using a single on-axis RGB slit reflection H_1 using three (R, G and B) lasers. An RGB transfer process of this single slit H_1 then produces a full-colour transmission rainbow H_2 hologram. In digital holography, however, we are free to use another method that requires a single laser only. In this variant, three (or more) slit masters are recorded (usually transmission holograms) using specially processed RGB image data from a simple translating (or translating/rotating) camera which moves on a rail in front of the real or virtual object. A single-wavelength transfer is then made in which the three H_1 masters are geometrically staggered according to their desired replay colour and aligned on a plane that is tilted vertically at the achromatic angle with respect to the H_2 normal. This well-known technique was first practised using analogue film cameras and by projecting laser light through the diapositive sequence obtained onto a diffusing screen which was then holographed [8]. In Chapter 7, we described how the more modern MWDH technique naturally lends itself to the production of H_1 holograms required for the generation of full-colour rainbow H_2 holograms. In particular, we saw how this could be arranged, from an optics point of view, through the generation of a single RGB H_1 or via multiple component-colour H_1 holograms (see Figure 7.29). In Chapter 7, however, we did not discuss the image data transformations required; we shall study this aspect now. Before starting this discussion, we should note in passing that the technique of using a single laser can indeed be applied in analogue holography as well, but here, it can be difficult to optically introduce the required image transformations into each of the off-axis H_1 masters—and this usually leads to image deregistration between colours.

8.9.1.1 Vertically Aligned RGB H_1 Master

We will consider first the case of using three or more lasers each operating at a different primary wavelength and writing a single RGB reflection H_1 hologram suitable for RGB transfer with the same wavelengths to a final H_2 transmission rainbow hologram. This is a simple task, but it will serve to set the stage for the more complicated case of component-colour H_1 holograms and will also serve to set up the required notation. Plan and side views of the three critical stages—writing the H_1 , producing the H_2 and viewing the H_2 —are shown in Figure 8.15. Because the rainbow hologram is intrinsically an HPO hologram, we must generate the \mathbf{I} data along a camera track, which is placed at a distance from the (virtual or real) object that is

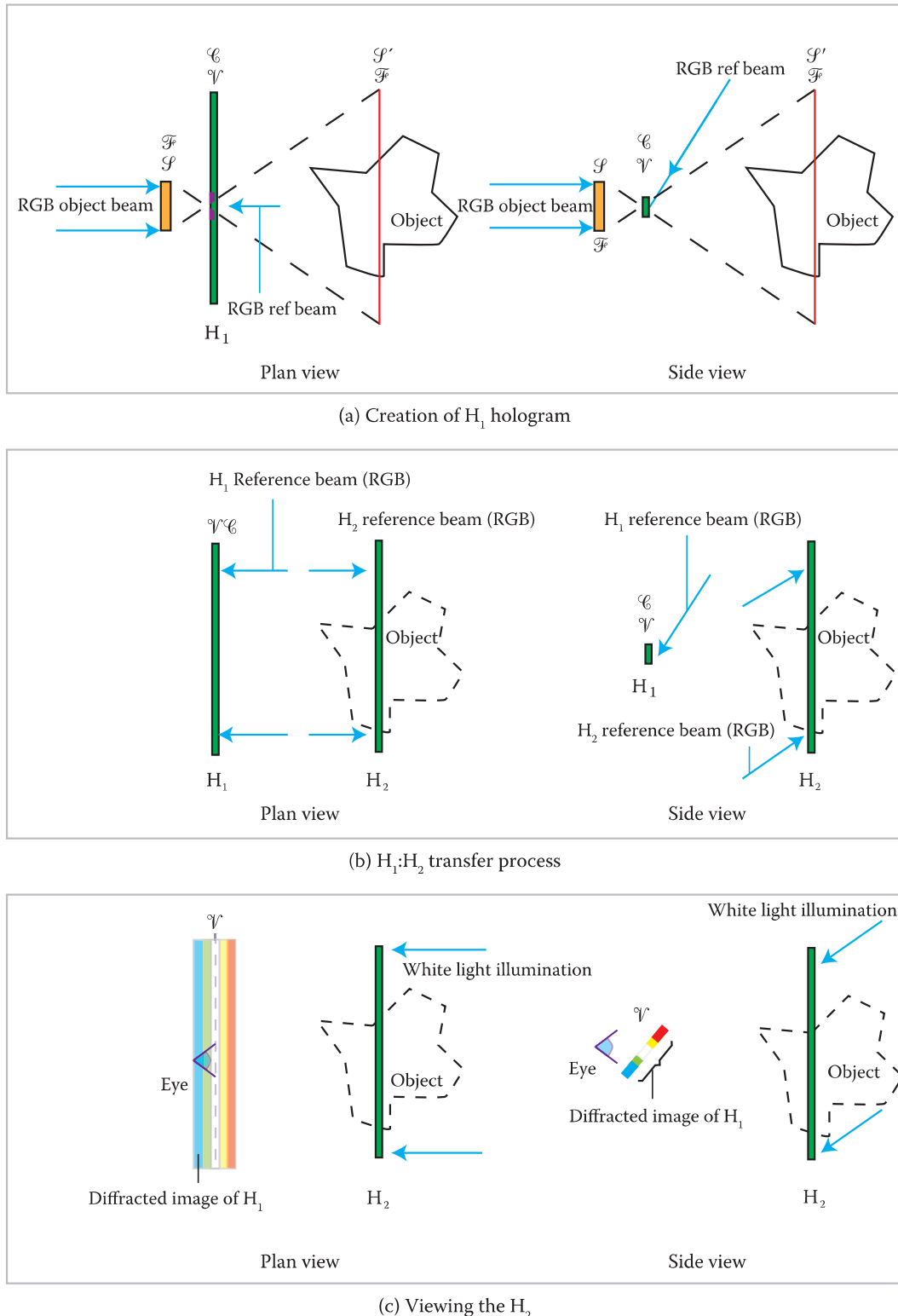


FIGURE 8.15 The creation of an MWDH rainbow master hologram using red, green and blue lasers: (a) the creation of the RGB H_1 reflection hologram, (b) the $H_1:H_2$ transfer using an RGB laser, and (c) viewing the final H_2 rainbow transmission hologram.

equal to the distance of the intended viewing plane from the holographic image of the object in the final H_2 . This is similar to the situation we discussed in Section 8.7.2, except that there, we were considering a two-dimensional grid of camera positions. We will use the integer coordinates (i, j, k) to describe such a simple one-dimensional (forward facing) translating camera with inverted image and we will denote ${}^k\mathbf{I}_{ij}^R$, ${}^k\mathbf{I}_{ij}^G$ and ${}^k\mathbf{I}_{ij}^B$ as the red, green and blue primary-colour component data produced by it. As in Section 8.7.2, we shall assume that the horizontal and vertical fields of view of the camera are identical to those of the printer and that the number of pixels on the printer SLM and on the camera CCD is identical or

$$\begin{aligned}\Psi_{CH} &= \Psi_{PH} \equiv \Psi_H \\ \Psi_{CV} &= \Psi_{PV} \equiv \Psi_V \\ N_M &= N_I \\ N_V &= N_J\end{aligned}\tag{8.88}$$

We shall describe the red, green and blue SLM data as, respectively, ${}^{\mu\nu}\mathbf{S}_{\alpha\beta}^R$, ${}^{\mu\nu}\mathbf{S}_{\alpha\beta}^G$ and ${}^{\mu\nu}\mathbf{S}_{\alpha\beta}^B$ and we shall assume a non-conjugate SLM configuration. Then we may define the SLM data using the following trivial transformation:

$$\begin{aligned}{}^{\mu\nu}\mathbf{S}_{\alpha\beta}^C &= {}^\alpha\mathbf{I}_{\mu j}^C \quad \forall \beta \left\{ \beta \in \mathbb{N} \mid 1 \leq \beta \leq N_B \right\} \\ &\quad \forall \mu \left\{ \mu \in \mathbb{N} \mid \mu \leq N_M \right\} \quad \forall \alpha \left\{ \alpha \in \mathbb{N} \mid \alpha \leq N_A \right\} \\ &\quad \forall v \left\{ v \in \mathbb{N} \mid v \leq N_V \right\} \quad \forall C \left\{ C \in \{R, G, B\} \right\} \\ &= 0 \quad \text{otherwise}\end{aligned}\tag{8.89}$$

where

$$j = v + \left\| \left(\beta - \left\{ \frac{N_B + 1}{2} \right\} \right) (N_J - 1) \frac{\delta}{2h \tan \left(\frac{\Psi_V}{2} \right)} \right\| \tag{8.90}$$

and the integer parameter $N_B \geq 1$ controls the vertical size of the H_1 slit. The last term in Equation 8.90 essentially shifts the camera image up or down for slits below or above the camera rail, thus ensuring that each such shifted slit hologram projects a real image of exactly the same camera data onto the H_2 plane in perfect alignment (see Figure 8.16, from which it is evident that $V' + Y - Y_C = y'$, which implies the integer rule if we assume a symmetric hogel). As discussed in Chapter 7, the plane of recording of the H_1 hologram may be somewhat displaced from the Fourier plane of the printer objective in MWDH and, in this case, small values of N_B close or equal to 1 may be employed. Alternatively, the printer may be operated with the Fourier plane of the objective/SLM being coincident with the hologram plane, in which case, larger values of N_B can be used. The larger the value of N_B , the greater will be the colour desaturation observed in the final H_2 and the lower will be the intrinsic image noise. However, the price to pay for this is that chromatic blurring increases with N_B . As with usual analogue rainbow holograms, a compromise must therefore be adopted and a practical value for N_B chosen for each situation. This is because we have considered the case of the H_1 hologram being perpendicular to the optical axis of the printer writing head; this is, after all, the most usual case for an RGB printer. You may remember that we discussed in Chapter 7 that an alternative existed and that was to tilt the H_1 plate at the achromatic angle as defined by Equation 8.92 below. This allows us to potentially decouple chromatic blurring from saturation and can lead to a better hologram when large image depths are required. To be in a position to write down the transformation for this case, we will first study the case of using only a single wavelength to record three H_1 slit masters.

Figure 8.17 shows the three critical steps involved: (a) writing the three H_1 holograms on a single tilted plate, (b) transferring the H_1 holograms to an H_2 rainbow hologram and (c) viewing. We shall assume

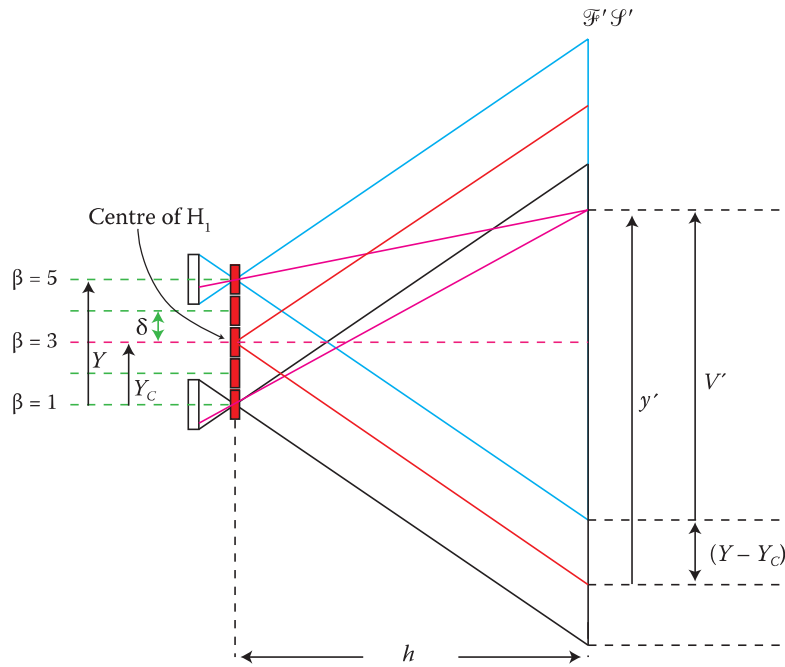


FIGURE 8.16 Side view of the vertically aligned H_1 showing its individual hogels and the light cones generated by the writing process. The central light cone must coincide with the camera light cone. All light cones must project an image at \mathcal{F}' that exactly corresponds to the image produced by the central light cone.

that the RGB image data is collected, as in our previous discussions, by a simply translating rail-mounted camera. This data is then colour-separated and each of the component colours is processed and used to generate a slit master. The image processing is chosen such that a given slit master, if illuminated under the transfer geometry of Figure 8.17b and by its designed replay wavelength, will produce a real image of the aperture of the slit-master at \mathcal{V} coincident with the camera track and further, each hogel of this master will project a focussed image of the original camera data onto the H_2 plane. The image processing must above all ensure that each of the processed R, G and B component-colour images, corresponding to a given camera position and as projected by the corresponding $3N_B$ hogels associated with this camera position, align precisely at the H_2 plane.

8.9.1.2 Component-Colour H_1 Masters

To understand how to write down the I-to-S transformations for three-component colour H_1 holograms, we must use results from the paraxial hologram theory that is described in Chapter 11. This theory describes how an object point, holographically recorded at a first wavelength, maps to an image point when the hologram is replayed at a second wavelength. Figure 8.17a shows the geometry we need to consider. The three H_1 slits are located at coordinates (y_B, z_B) , (y_G, z_G) and (y_R, z_R) with the H_2 plane (which is coincident with \mathcal{S}' and \mathcal{F}' in all cases) being at $z = 0$. The centre of the H_2 is taken as $(0,0)$ meaning that all z values of interest are negative; positive y means that the point is above the H_2 mid-plane.

Each of the slit holograms is recorded using light at a wavelength of λ_W . We wish to arrange that, when we illuminate the recorded red H_1 with light at λ_R , the image of the red slit will move onto the axis at $z = -h$. Likewise, when we illuminate the recorded green or blue H_1 with light at, respectively, λ_G or λ_B , the image of the green or blue slit must also move onto the axis at $z = -h$. Note also that any ray intersecting a given point on a given H_1 must always intersect with the image of the H_1 at the same relative position along the horizontal or x dimension of the H_1 when this H_1 is replayed at its design wavelength.

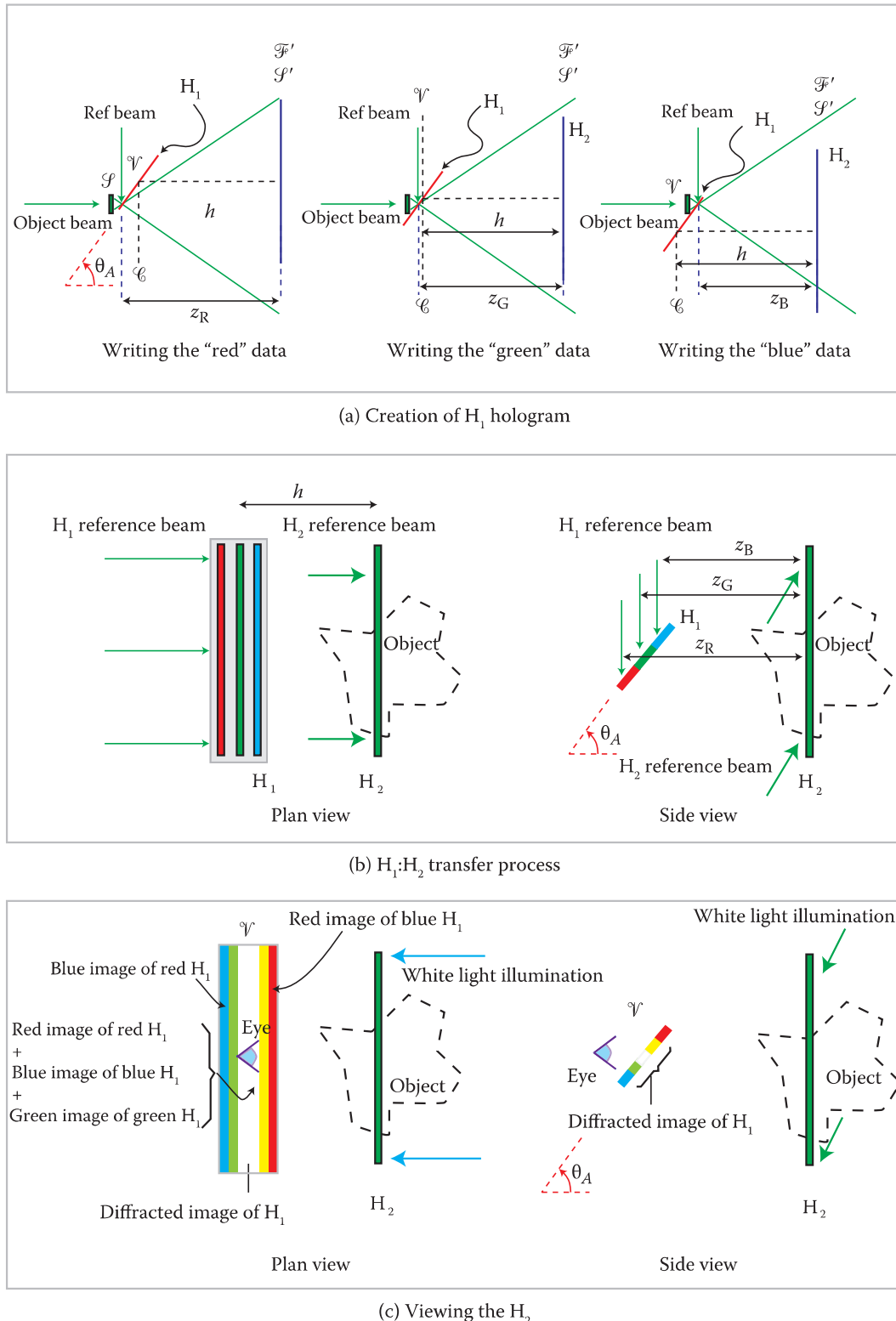


FIGURE 8.17 The creation of an MWDH rainbow master hologram using a single laser: (a) creation of the red, green and blue H_1 holograms, (b) the $H_1:H_2$ transfer using a single colour laser, and (c) viewing the final H_2 rainbow transmission hologram. Note the inverting camera and the non-conjugate SLM configuration.

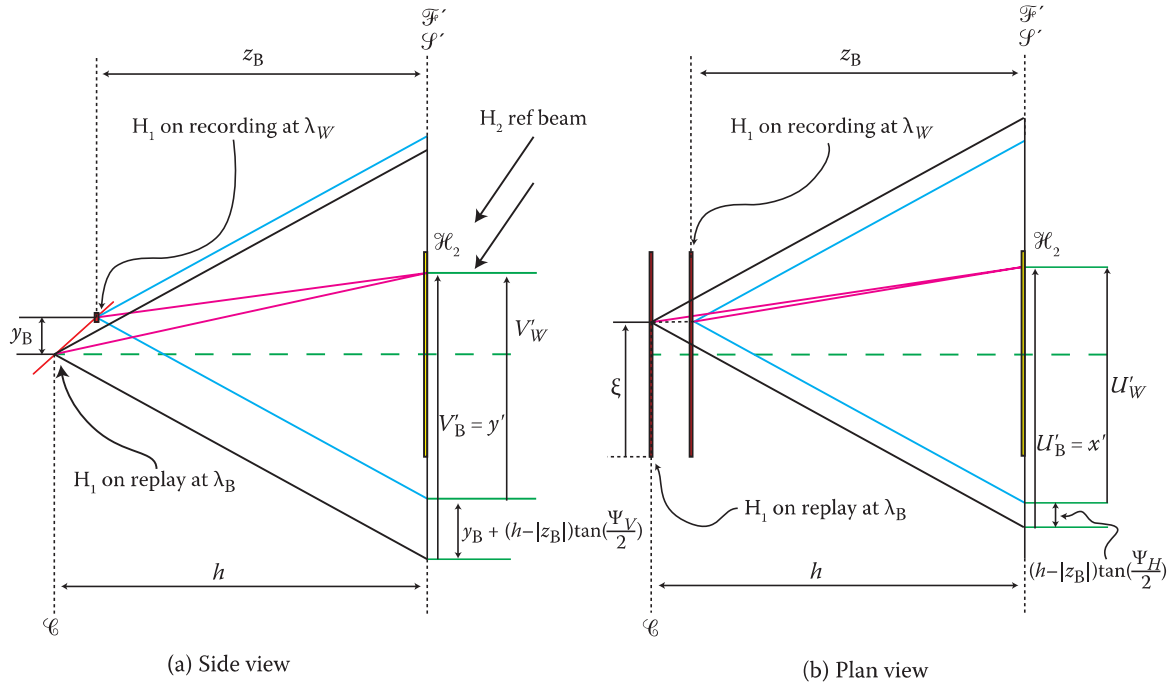


FIGURE 8.18 Coordinate systems (U'_W, V'_W) and (U'_B, V'_B) characterising the projected SLM plane showing rays at off-axis recording (λ_W) and on-axis replay (λ_B) for (a) side view and (b) plan view.

Using the results from Chapter 11 (Equation 11.20)* and taking h to be a positive value, we can see that the first condition described above is satisfied (in terms of the following 3×2 matrices) when

$$\begin{pmatrix} y_R & z_R \\ y_G & z_G \\ y_B & z_B \end{pmatrix} = -\frac{h}{\lambda_W} \begin{pmatrix} (\lambda_R - \lambda_W) \sin \theta & \lambda_R \\ (\lambda_G - \lambda_W) \sin \theta & \lambda_G \\ (\lambda_B - \lambda_W) \sin \theta & \lambda_B \end{pmatrix} \quad (8.91)$$

This implies that the R, G and B H_1 holograms are aligned at an angle equal to the achromatic angle defined as

$$\theta_A = \tan^{-1}(\sin \theta) \quad (8.92)$$

where θ represents the angle of reference (and illumination) incidence. To understand the image processing required, we consider two cases: (i) writing the blue H_1 at λ_W and (ii) how this H_1 replays at λ_B . With this in view, we set up separate real Cartesian coordinate systems (U'_W, V'_W) and (U'_B, V'_B) , respectively, for the projected SLM plane \mathcal{S}' in both cases as illustrated in Figure 8.18. For a test ray written at λ_W off-axis to then replay at λ_B the correct camera data on-axis, we require that

$$\begin{aligned} U'_W &= x' - (h - |z_B|) \tan\left(\frac{\Psi_H}{2}\right) \\ V'_W &= y' - y_B - (h - |z_B|) \tan\left(\frac{\Psi_V}{2}\right) \end{aligned} \quad (8.93)$$

* Note that we have transformed to the coordinates we are using here which are different from those used in Equation 11.20.

We must then be careful to discretise the (U'_w, V'_w) system in the following way:

$$\begin{aligned} U'_w &= \frac{2|z_B|(\mu' - 1)}{N_M - 1} \tan\left(\frac{\Psi_H}{2}\right) \\ V'_w &= \frac{2|z_B|(\nu' - 1)}{N_V - 1} \tan\left(\frac{\Psi_V}{2}\right) \end{aligned} \quad (8.94)$$

This takes into account the fact that the effective field of view of the printer objective is decreased on replay due to the change in wavelength. This then leads us, with the help of Equations 8.88 and 8.91, to the index rules between (i', j') and (μ', ν') :

$$\begin{aligned} i' &= 1 + \left\| \frac{\lambda_B}{\lambda_w} (\mu' - 1) + \frac{(N_M - 1)(\lambda_w - \lambda_B)}{2\lambda_w} \right\| \\ j' &= 1 + \left\| \frac{\lambda_B}{\lambda_w} (\nu' - 1) + \frac{(N_V - 1)(\lambda_w - \lambda_B)}{2\lambda_w} \left(1 + \sin \theta \cot\left(\frac{\Psi_V}{2}\right) \right) \right\| \end{aligned} \quad (8.95)$$

We may now convert these equations to relations for the un-primed integers (i, j, μ, ν) by application of the inverting camera Equation 8.27 and the corresponding relations for a non-conjugate SLM— $\mu' = N_M - \mu + 1$ and $\nu' = N_V - \nu + 1$. Finally we can use these index laws and Equation 8.89 with $NB = 1$ to arrive at the following transformation:

$$\begin{aligned} {}^{\mu\nu} \mathbf{S}_\alpha^C &= {}^\alpha \mathbf{I}_{ij}^C & \forall \mu \{ \mu \in \mathbb{N} | \mu \leq N_M \} & \forall \alpha \{ \alpha \in \mathbb{N} | \alpha \leq N_A \} \\ & & \forall \nu \{ \nu \in \mathbb{N} | \nu \leq N_V \} & \forall C \{ C \in \{R, G, B\} \} \\ &= 0 & \text{otherwise} & \end{aligned} \quad (8.96)$$

where

$$\begin{aligned} i &= N_M - \left\| \frac{\lambda_C}{\lambda_w} (N_M - \mu) + \frac{(N_M - 1)(\lambda_w - \lambda_C)}{2\lambda_w} \right\| \\ j &= N_V - \left\| \frac{\lambda_C}{\lambda_w} (N_V - \nu) + \frac{(N_V - 1)(\lambda_w - \lambda_C)}{2\lambda_w} \left(1 + \sin \theta \cot\left(\frac{\Psi_V}{2}\right) \right) \right\| \end{aligned} \quad (8.97)$$

We have omitted the subscript β from \mathbf{S} on purpose, as this transformation describes R, G and B H_1 slit holograms only one hogel high. This is the case of maximum possible saturation. To reduce saturation and to increase image fidelity without introducing chromatic blurring, we must write each H_1 with N_B rows of hogels. In general, we may choose the row-to-row spacing to be different from the hogel diameter as in the final H_2 the pattern of hogels will be located on the viewing plane. The smaller the row-to-row separation, the greater the overlap of the hogels will be. This will decrease diffractive efficiency of the H_1 somewhat but will also tend to smooth out the “hogelisation”. The final choice of the number of rows N_B to print and the row-to-row spacing must be made according to the requirements of image fidelity, required final image saturation and image clarity.

We should note also that Equation 8.97 may lead to values of i and j greater than the maximum, or less than the minimum permitted values if $\lambda_C > \lambda_R$. This is because the effective field of view changes with wavelength.

8.9.1.3 Achromatically Tilted Component-Colour H_1 Masters

Because we have assumed that the photosensitive plate is tilted at the achromatic angle to the optical axis of the printer writing head, we characterise the row-to-row separation by a quantity δ_V . At $\beta = 1$ with $N_B = 1$ we have seen above that the blue H_1 slit must be located at coordinates (y_B, z_B) . At a general value of β when $N_B \neq 1$, these coordinates will change to

$$\begin{pmatrix} y_B(\beta) \\ z_B(\beta) \end{pmatrix} = \begin{pmatrix} y_B(\phi) + \left(\beta - \frac{N_B+1}{2} \right) \delta_V \sin \theta_A \\ z_B(\phi) + \left(\beta - \frac{N_B+1}{2} \right) \delta_V \cos \theta_A \end{pmatrix} = \begin{pmatrix} -\frac{h}{\lambda_w} (\lambda_B - \lambda_w) \sin \theta + \left(\beta - \frac{N_B+1}{2} \right) \delta_V \sin \theta_A \\ -\frac{h \lambda_B}{\lambda_w} + \left(\beta - \frac{N_B+1}{2} \right) \delta_V \cos \theta_A \end{pmatrix} \quad (8.98)$$

where $(y_B(\phi), z_B(\phi))$ locates the centre of the blue slit and where we have used Equation 8.91 to deduce the second step. We can now proceed in the same way and use these expressions in Equation 8.93 to obtain

$$i' = \left\| \left\{ \frac{\lambda_B}{\lambda_w} - \left(\beta - \frac{N_B+1}{2} \right) \frac{\delta_V}{h} \cos \theta_A \right\} \left\{ \mu' - \frac{N_M+1}{2} \right\} + \frac{N_M+1}{2} \right\|$$

$$j' = 1 + \left\| \left\{ \frac{\lambda_B}{\lambda_w} - \left(\beta - \frac{N_B+1}{2} \right) \frac{\delta_V}{h} \cos \theta_A \right\} \left\{ v' - \frac{N_V+1}{2} \right\} \right.$$

$$\left. + \frac{(N_V-1)}{2} \left\{ \left[\frac{\lambda_w - \lambda_B}{\lambda_w} \sin \theta + \left(\beta - \frac{N_B+1}{2} \right) \frac{\delta_V}{h} \sin \theta_A \right] \cot \left(\frac{\Psi_V}{2} \right) + 1 \right\} \right\| \quad (8.99)$$

The **I**-to-**S** transformation for the MWDH achromatically tilted H_1 rainbow hologram with a thick slit of N_B hogels high and a row-to-row spacing of δ_V is then

$$\begin{aligned} {}^{\mu\nu} \mathbf{S}_{\alpha\beta}^C &= {}^\alpha \mathbf{I}_{ij}^C \quad \forall \mu \{ \mu \in \mathbb{N} | \mu \leq N_M \} \quad \forall \alpha \{ \alpha \in \mathbb{N} | \alpha \leq N_A \} \\ &\quad \forall v \{ v \in \mathbb{N} | v \leq N_V \} \quad \forall C \{ C \in \{R, G, B\} \} \\ &\quad \forall \beta \{ \beta \in \mathbb{N} | \beta \leq N_B \} \\ &= 0 \quad \text{otherwise} \end{aligned} \quad (8.100)$$

where

$$i = \left\| \left\{ \frac{\lambda_C}{\lambda_w} - \left(\beta - \frac{N_B+1}{2} \right) \frac{\delta_V}{h} \cos \theta_A \right\} \left\{ \mu - \frac{N_M+1}{2} \right\} + \frac{N_M+1}{2} \right\|$$

$$j = \left\| \left\{ \frac{\lambda_C}{\lambda_w} - \left(\beta - \frac{N_B+1}{2} \right) \frac{\delta_V}{h} \cos \theta_A \right\} \left\{ v - \frac{N_V+1}{2} \right\} + \frac{N_V+1}{2} \right. \\ \left. - \frac{(N_V-1)}{2} \left\{ \left[\frac{\lambda_w - \lambda_C}{\lambda_w} \sin \theta + \left(\beta - \frac{N_B+1}{2} \right) \frac{\delta_V}{h} \sin \theta_A \right] \cot \left(\frac{\Psi_V}{2} \right) \right\} \right\| \quad (8.101)$$

The positional coordinates of the three slits during the H_2 transfer are defined by Equation 8.91.

8.9.1.4 Achromatically Tilted RGB H₁ Master

We can now return to the MWDH case of writing a single H₁ with red, green and blue lasers. We discussed this case previously in the context of the photosensitive plate being aligned perpendicular to the optical axis of the printer writing head. We noted that in this case, when we wrote more than one row of hogels, then inevitably we would increase chromatic blurring. By tilting the photosensitive plate at the achromatic angle, we can largely avoid this. We can see immediately how to write the I-to-S transformation for this case from Equation 8.101 by simply putting λ_w = λ_c:

$$\begin{aligned} {}^{\mu\nu}\mathbf{S}_{\alpha\beta}^C &= {}^\alpha\mathbf{I}_{ij}^C \quad \forall \mu \left\{ \mu \in \mathbb{N} \mid \mu \leq N_M \right\} \quad \forall \alpha \left\{ \alpha \in \mathbb{N} \mid \alpha \leq N_A \right\} \\ &\quad \forall v \left\{ v \in \mathbb{N} \mid v \leq N_V \right\} \quad \forall C \left\{ C \in \{R, G, B\} \right\} \\ &\quad \forall \beta \left\{ \beta \in \mathbb{N} \mid \beta \leq N_B \right\} \\ &= 0 \quad \text{otherwise} \end{aligned} \tag{8.102}$$

where

$$i = \left\| \left\{ 1 - \left(\beta - \frac{N_B + 1}{2} \right) \frac{\delta_v}{h} \cos \theta_A \right\} \left\{ \mu - \frac{N_M + 1}{2} \right\} + \frac{N_M + 1}{2} \right\| \tag{8.103}$$

$$j = \left\| \begin{aligned} &\left\{ 1 - \left(\beta - \frac{N_B + 1}{2} \right) \frac{\delta_v}{h} \cos \theta_A \right\} \left\{ v - \frac{N_V + 1}{2} \right\} \\ &- \frac{(N_V - 1)}{2} \left\{ \left(\beta - \frac{N_B + 1}{2} \right) \frac{\delta_v}{h} \sin \theta_A \cot \left(\frac{\Psi_v}{2} \right) - 1 \right\} \end{aligned} \right\| \tag{8.104}$$

Note that by assuming a symmetric hogel—that is, if δ_v = δ—and by taking θ_A = π/2, we retrieve, as expected, the transformation of Equation 8.89 and Equation 8.90, which is pertinent to the case of RGB vertically tilted slits.

8.9.2 MWDH Achromats

By using achromatic camera data and a single achromatically tilted H₁ with a very large value of δ_v, extreme desaturation may be achieved. This then changes the nature of the final transmission H₂ to that of an achromatic hologram. The hologram no longer changes colour as the observer moves his head up and down; rather, it appears uniformly achromatic with only the extreme ends of the vertical viewing window being coloured. This type of hologram can be produced using the transformation of Equations 8.102 to 8.104, with one writing laser wavelength and one achromatic camera data set.

8.9.3 DWDH

Writing digital rainbow and achromat holograms using MWDH is a good idea when large quantities of such holograms are required and the substantial extra cost of the transfer apparatus is merited. For small quantities, however, DWDH offers a cheaper alternative that can generate the final rainbow or achromatic hologram in a single step and without any transfer apparatus at all! In Section 7.5.10, we discussed briefly how a digital printer must be set up to create this type of hologram—we saw that, essentially, the only substantial detail was that the reference beam had to be made to be incident to the hogel on the same side of the photosensitive substrate; this is because we wish to produce a transmission hologram. As with full-colour reflection holograms, the photoplate is mounted in a normal fashion, orthogonal to

the optical axis. The technique then consists of writing hogel by hogel and generating the entire rainbow hologram as a two-dimensional grid.

As with MWDH, there is a basic choice of using either one laser wavelength for the recording or using three laser wavelengths. The physics is exactly the same as with the MWDH case, but with DWDH, we simply seek to computationally synthesise the three viewing slits of a rainbow hologram by numerical image processing of the camera data instead of doing this by physically creating three H_1 holograms and then optically changing the image plane through a transfer process. Essentially, the process then splits into two geometries: the vertical geometry, which defines the slits, and the horizontal geometry, which defines the image transformations of the camera data. The horizontal geometry for both the one wavelength and the three wavelength cases is identical to MWDH. This is obvious because the physical slit H_1 holograms of MWDH are identical to the “slits” of DWDH and the same information must therefore be recorded. However, the vertical geometry of the DWDH technique needs to be derived specifically.

8.9.3.1 Synthesis of the Vertical Slit

We will start by calculating how to define a general virtual viewing slit located on an achromatically tilted plane centred on the camera rail. We will need this information for both the one wavelength and the three wavelength cases. Figure 8.19 shows a diagram of the vertical geometry. We consider two hogels and the ray intersections connecting their SLM planes with the desired slit location. Clearly, a viewing slit is created by only writing lines of information to the SLM at each hogel and by changing the height of the line according to a special rule. Thicker slits can then be built up by superposition in a trivial way. We can find this special rule by considering the projection of the rays emanating from the slit onto the SLM plane associated with each hogel and writing down the corresponding V' coordinate on \mathcal{S}' :

$$\begin{aligned} V'(y_s, z_s) &= \frac{\Sigma'}{2} + \frac{h}{z_s} \left(y_s + \frac{D_Y}{2} - Y \right) \\ &= h \tan\left(\frac{\Psi_{PV}}{2}\right) + \frac{h}{z_s} \left(y_s + \frac{D_Y}{2} - Y \right) \end{aligned} \quad (8.105)$$

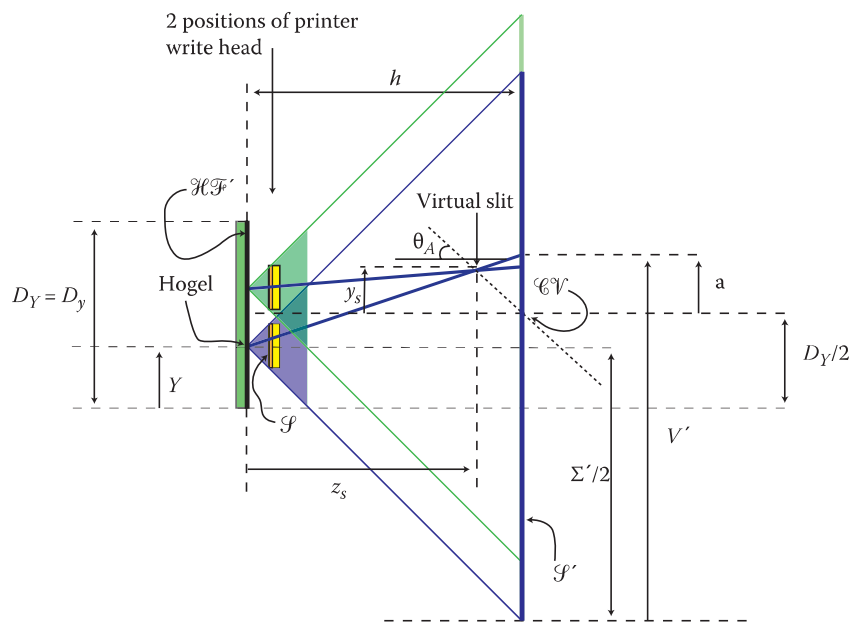


FIGURE 8.19 Vertical geometry of a DWDH transmission rainbow hologram: this diagram shows how a virtual slit is synthesised.

This then leads to the general integer coordinate rule

$$v_s(\beta) = v' = \left\| \frac{N_V + 1}{2} + \frac{(N_V - 1)}{2z_s \tan\left(\frac{\Psi_{PV}}{2}\right)} \left\{ y_s + \frac{D_Y}{2(N_B - 1)} (N_B - 2\beta + 1) \right\} \right\| \quad (8.106)$$

This tells us that to create a viewing slit of unit size at the location (y_s, z_s) , we need to write image information to the SLM corresponding to each hogel in the form of a single line of unit height and at the pixel height location given by Equation 8.106. Each such line will, of course, be modulated by the camera information so as to create the actual image.

We must now extend this rule to the case of a broad slit of width δ_s centred on $(\langle y_s \rangle, \langle z_s \rangle)$ and composed of points (y_s, z_s) . Instead of drawing a one pixel-high line on each SLM exposure, we will now have to draw a rectangular region composed of a number of abutting lines, each of which will be modulated with differently processed camera data in the horizontal dimension. The first task is therefore to determine the maximum (N_2) and minimum (N_1) values of v that determine the top and bottom boundaries of the rectangular region. These are given by simply putting

$$\begin{pmatrix} y_s \\ z_s \end{pmatrix} \rightarrow \begin{pmatrix} y_s \pm \frac{\delta_s}{2} \sin(\theta_A) \\ z_s \mp \frac{\delta_s}{2} \cos(\theta_A) \end{pmatrix} \quad (8.107)$$

in Equation 8.106 giving,

$$\begin{aligned} N_1(\beta) &= \left\| \frac{N_V + 1}{2} + \frac{(N_V - 1)}{2 \left\{ \langle z_s \rangle + \frac{\delta_s}{2} \cos(\theta_A) \right\} \tan\left(\frac{\Psi_{PV}}{2}\right)} \left\{ \langle y_s \rangle - \frac{\delta_s}{2} \sin(\theta_A) + \frac{D_Y}{2(N_B - 1)} (N_B - 2\beta + 1) \right\} \right\| \\ N_2(\beta) &= \left\| \frac{N_V + 1}{2} + \frac{(N_V - 1)}{2 \left\{ \langle z_s \rangle - \frac{\delta_s}{2} \cos(\theta_A) \right\} \tan\left(\frac{\Psi_{PV}}{2}\right)} \left\{ \langle y_s \rangle + \frac{\delta_s}{2} \sin(\theta_A) + \frac{D_Y}{2(N_B - 1)} (N_B - 2\beta + 1) \right\} \right\| \end{aligned} \quad (8.108)$$

This tells us that the SLM region of $N_1 \leq v \leq N_2$ for each hogel must be filled with the processed image data that we wish to view within the finite slit centred at $(\langle y_s \rangle, \langle z_s \rangle)$. This now brings us to the image information required. We shall deal first with the case of writing a rainbow hologram with three laser wavelengths. As with the corresponding case in MWDH, we shall assume that all three slits are designed to play back on-axis and, as such, we consider three superimposed slits (R, G and B) of width δ_s centred on $(\langle y_s \rangle, \langle z_s \rangle) = (0, h)$. Each slit is then recorded and viewed at its own wavelength. The fact that the slits are wide simply decreases saturation.

8.9.3.2 Transformations Required When Using an RGB Laser

The I-to-S transformation required here is similar to the HPO reflection hologram case. If we take a centred camera configuration, we must simply take into consideration the fact that any and all slits are characterised by the locus of points (y_s, z_s) in the $y-z$ plane such that

$$\frac{dy_s}{dz_s} = -\sin \theta = -\tan \theta_A \quad (8.109)$$

Note that this equation differs from Equation 8.92 by a minus sign as we are considering here the geometry of Figure 8.20, in which the viewing slit is located to the right of the coordinate origin at a positive z value. The rays emanating from different (y_s, z_s) points (but having equal horizontal coordinates along the slit) must then all be associated with the same camera position and be characterised by the equations $x = X$ and $y = Y$. This can be understood in several ways. The first is that diffraction occurs at the hologram surface (i.e., at each hogel) on replay and acts paraxially to induce a rotation of rays about the x axis of the hogel. This rotation brings rays from one (y_s, z_s) point to another in the achromatic plane. It is therefore clear that image registration in a direction perpendicular to the parallax direction can only be assured if rays connecting a given hogel with both (y_s, z_s) points at recording correspond to exactly the same camera position and exactly the same camera film plane coordinates. An alternative way of looking at this is to think of the analogy with writing an achromatically tilted H_1 using the old method of projecting camera data (usually diapositives) onto a diffusion screen using a laser object beam (Figure 8.21). Here, the tilted H_1 is placed in front of the diffusion screen. It is immediately clear that any two vertically separated points on the tilted H_1 will then see the same image displayed on the diffusion screen.

The one thing we need to be careful about is that when calculating the SLM data for a hogel corresponding to a certain slit location (y_s, z_s) , we must replace h in Equation 8.63 by z_s . This is because the slit is physically at this distance on writing even if at replay diffraction refocusses it to a distance of h . Accordingly, we can write down the \mathbf{I} -to- \mathbf{S} transformation for the generation of a general achromatically tilted slit of width δ_s centred at $(\langle y_s \rangle, \langle z_s \rangle)$ on recording. This is

$$\begin{aligned} {}^{\mu\nu} \mathbf{S}_{\alpha\beta} &= {}^k \mathbf{I}_{ij} & \forall \mu \in \mathbb{N} | N_{U1}(\alpha) \leq \mu \leq N_{U2}(\alpha) \quad & \forall v \in \mathbb{N} | N_1(\beta) \leq v \leq N_2(\beta) \\ & \forall \alpha \{ \alpha \in \mathbb{N} | \alpha \leq N_A \} & & \forall \beta \{ \beta \in \mathbb{N} | \beta \leq N_B \} \\ &= 0 & \text{otherwise} & \end{aligned} \quad (8.110)$$

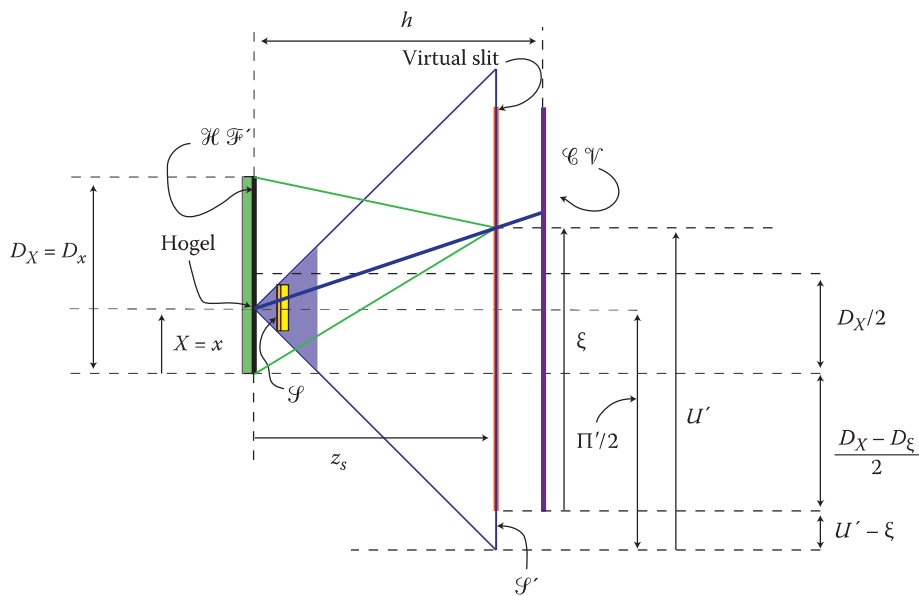


FIGURE 8.20 Horizontal geometry of a DWDH rainbow transmission hologram made with a single-colour laser. The rays intersecting a given point (y_s, z_s) on the virtual slit (on writing and replay) must be characterised by the equations $x = X$ and $y = Y$. In addition, the k equation is given by replacing h by z_s in Equation 8.63.

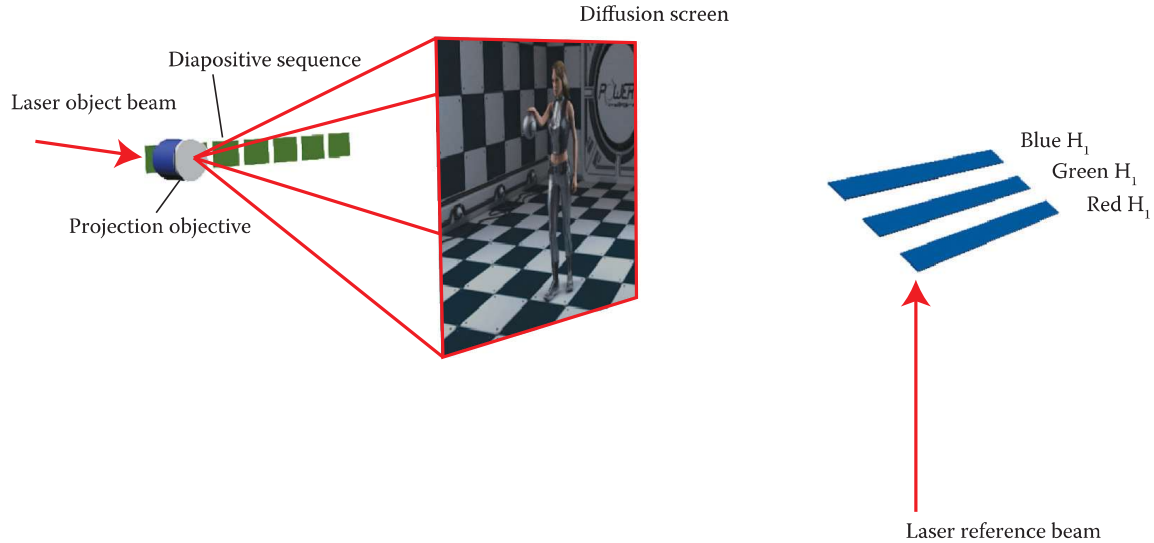


FIGURE 8.21 Original technique of writing a transmission rainbow hologram based on data from diapositives. The single-colour laser beam is split into reference and object beams. The object beam is used to project the image of a diapositive onto the diffusion screen and the three slit masters in turn record the red, green and blue information as different black and white slides are selected. All three slits see colour-separated but registered images on the diffusion screen.

where

$$i = 1 + \left\| \frac{(\alpha - 1)(N_I - 1)}{N_A - 1} \right\| \quad j = 1 + \left\| \frac{(\beta - 1)(N_J - 1)}{N_B - 1} \right\| \quad (8.111)$$

$$k = 1 + \left\| \frac{(N_K - 1)}{W} \left\{ \frac{D_X + W}{2} + \frac{z_s(2\mu - N_M - 1)}{(N_M - 1)} \tan\left(\frac{\Psi_{PH}}{2}\right) + \frac{(\alpha - N_A)D_X}{N_A - 1} \right\} \right\| \quad (8.112)$$

$$z_s = \begin{cases} \frac{D_Y(N_B - 2\beta + 1)}{2(N_B - 1)} + \langle y_s \rangle + \tan \theta_A \langle z_s \rangle \\ \frac{\tan\left(\frac{\Psi_{PV}}{2}\right)(2\nu - 1 - N_V)}{(N_V - 1)} + \tan \theta_A \end{cases} \quad (8.113)$$

and where

$$N_1(\beta) = \left\| \frac{N_V + 1}{2} + \frac{(N_V - 1)}{\{2\langle z_s \rangle + \delta_s \cos(\theta_A)\} \tan\left(\frac{\Psi_{PV}}{2}\right)} \left\{ \langle y_s \rangle - \frac{\delta_s}{2} \sin(\theta_A) + \frac{D_Y}{2(N_B - 1)} (N_B - 2\beta + 1) \right\} \right\| \quad (8.114)$$

$$N_2(\beta) = \left\| \frac{N_V + 1}{2} + \frac{(N_V - 1)}{\left\{ 2\langle z_s \rangle - \delta_s \cos(\theta_A) \right\} \tan\left(\frac{\Psi_{PV}}{2}\right)} \left\{ \langle y_s \rangle + \frac{\delta_s}{2} \sin(\theta_A) + \frac{D_Y}{2(N_B - 1)} (N_B - 2\beta + 1) \right\} \right\| \quad (8.115)$$

$$N_{U1}(\alpha) = \left\| \frac{N_M + 1}{2} + \frac{(N_M - 1)}{2z_s \tan\left(\frac{\Psi_{PH}}{2}\right)} \left\{ D_X \frac{(N_A - \alpha)}{N_A - 1} - \frac{(D_X + W)}{2} \right\} \right\| \quad (8.116)$$

$$N_{U2}(\alpha) = \left\| \frac{N_M + 1}{2} + \frac{(N_M - 1)}{2z_s \tan\left(\frac{\Psi_{PH}}{2}\right)} \left\{ D_X \left\{ \frac{(N_A - \alpha)}{N_A - 1} + \frac{W}{D_X} \right\} - \frac{(D_X + W)}{2} \right\} \right\| \quad (8.117)$$

Here, we have obtained Equation 8.113 by using Equation 8.106 and the equation of the achromatic plane $y_s = -\tan\theta_A z_s + \langle y_s \rangle + \tan\theta_A \langle z_s \rangle$ to solve for z_s . The parameters N_{U1} and N_{U2} are derived from Equation 8.50 by replacing h with z_s .

This transformation is the basis of DWDH rainbow and achromatic holography. By setting $\langle y_s \rangle = 0$ and $\langle z_s \rangle = h$, we arrive directly at the case of a DWDH rainbow hologram written by three R, G and B lasers. Each of the three primary colour channels has an identical transformation. By using only a single wavelength and a single achromatic data set, and also using $\langle y_s \rangle = 0$ and $\langle z_s \rangle = h$, we obtain, if δ_s is large, the transformation describing an achromatic hologram.

8.9.3.3 Transformations for One-Colour Laser

We can also use the general transformation above to discuss the case of the generation of the three slits required to create a full-colour rainbow hologram with only one laser wavelength. Here, we write the three slits, each of width, δ_s , on the achromatic plane intersecting $(y_s, z_s) = (0, h)$ at wavelength λ_w . The central coordinates of each of these slits are $(\langle y_R \rangle, \langle z_R \rangle), (\langle y_G \rangle, \langle z_G \rangle)$ and $(\langle y_B \rangle, \langle z_B \rangle)$. On replay, each of the slits is designed to diffract, respectively, onto axis at the wavelengths $(\lambda_R, \lambda_G, \lambda_B)$. We should therefore be able to use Equation 8.91 to calculate the required central slit positions which, upon substitution in Equation 8.113, should lead us to the required transformation for the full-colour three-slit rainbow hologram recorded at a single wavelength. We must, however, be careful that in the present geometry z_s is positive and so the appropriate form of Equation 8.91 is actually

$$\begin{pmatrix} y_R & z_R \\ y_G & z_G \\ y_B & z_B \end{pmatrix} = \frac{h}{\lambda_w} \begin{pmatrix} (\lambda_w - \lambda_R) \sin\theta & \lambda_R \\ (\lambda_w - \lambda_G) \sin\theta & \lambda_G \\ (\lambda_w - \lambda_B) \sin\theta & \lambda_B \end{pmatrix} \quad (8.118)$$

Using this in Equation 8.113 to define $\langle y_s \rangle$ and $\langle z_s \rangle$, we arrive at the required transformation:

$${}^{\mu\nu} \mathbf{S}_{\alpha\beta} = \sum_C {}^{\mu\nu C} \mathbf{S}_{\alpha\beta}^C \quad (8.119)$$

where

$$\begin{aligned} {}^{\mu v_C} \mathbf{S}_{\alpha \beta}^C &= {}^k \mathbf{I}_{ij}^C \quad \forall \mu \left\{ \mu \in \mathbb{N} \mid N_{U1}(\alpha) \leq \mu \leq N_{U2}(\alpha) \right\} \quad \forall v_C \left\{ v_C \in \mathbb{N} \mid N_1^C(\beta) \leq v_C \leq N_2^C(\beta) \right\} \\ &\quad \forall \alpha \left\{ \alpha \in \mathbb{N} \mid \alpha \leq N_A \right\} \quad \forall \beta \left\{ \beta \in \mathbb{N} \mid \beta \leq N_B \right\} \quad \forall C \left\{ C \in \{R, G, B\} \right\} \\ &= 0 \quad \text{otherwise} \end{aligned} \quad (8.120)$$

and where

$$i = 1 + \left\| \frac{(\alpha - 1)(N_I - 1)}{N_A - 1} \right\|, \quad j = 1 + \left\| \frac{(\beta - 1)(N_J - 1)}{N_B - 1} \right\| \quad (8.121)$$

$$k = 1 + \left\| \frac{(N_K - 1)}{W} \left\{ D_x + W \frac{2\mu - N_M - 1}{2} + z_C \frac{\tan\left(\frac{\Psi_{PH}}{2}\right)}{(N_M - 1)} + \frac{(\alpha - N_A)D_x}{N_A - 1} \right\} \right\| \quad (8.122)$$

$$z_C = \left\{ \frac{\frac{D_Y(N_B - 2\beta + 1)}{2(N_B - 1)} + \langle y_C \rangle + \tan\theta_A \langle z_C \rangle}{\tan\left(\frac{\Psi_{PV}}{2}\right)(2v_C - 1 - N_V)} \right\} \quad (8.123)$$

$$N_1^C(\beta) = \left\| \frac{N_V + 1}{2} + \frac{(N_V - 1)}{\{2\langle z_C \rangle + \delta_s \cos(\theta_A)\} \tan\left(\frac{\Psi_{PV}}{2}\right)} \left\{ \langle y_C \rangle - \frac{\delta_s}{2} \sin(\theta_A) + \frac{D_Y}{2(N_B - 1)} (N_B - 2\beta + 1) \right\} \right\| \quad (8.124)$$

$$N_2^C(\beta) = \left\| \frac{N_V + 1}{2} + \frac{(N_V - 1)}{\{2\langle z_C \rangle - \delta_s \cos(\theta_A)\} \tan\left(\frac{\Psi_{PV}}{2}\right)} \left\{ \langle y_C \rangle + \frac{\delta_s}{2} \sin(\theta_A) + \frac{D_Y}{2(N_B - 1)} (N_B - 2\beta + 1) \right\} \right\| \quad (8.125)$$

$$N_{U1}(\alpha) = \left\| \frac{N_M + 1}{2} + \frac{(N_M - 1)}{2z_C \tan\left(\frac{\Psi_{PH}}{2}\right)} \left\{ D_x \frac{(N_A - \alpha)}{N_A - 1} - \frac{(D_x + W)}{2} \right\} \right\| \quad (8.126)$$

$$N_{U2}(\alpha) = \left\| \frac{N_M + 1}{2} + \frac{(N_M - 1)}{2z_C \tan\left(\frac{\Psi_{PH}}{2}\right)} \left\{ D_x \left\{ \frac{(N_A - \alpha)}{N_A - 1} + \frac{W}{D_x} \right\} - \frac{(D_x + W)}{2} \right\} \right\| \quad (8.127)$$

with

$$\begin{aligned}\langle y_c \rangle &= \frac{h}{\lambda_w} (\lambda_w - \lambda_c) \tan \theta_A \\ \langle z_c \rangle &= \frac{h \lambda_c}{\lambda_w}\end{aligned}\tag{8.128}$$

Note that this transformation is only valid when δ_s is small enough such that none of the slits overlap.

8.10 Correcting for Inherent Distortion in Printer Optical Objectives

Up until now, we have discussed **I-to-S** transformations pertinent to the case of a printer with a paraxial optical system and a perfect aberration-free system of recording, processing and playback of the hologram. In some cases, this approximation is genuinely all one needs—particularly when the angles of view are small. However, in many cases, fundamental aberrations are present and these must be taken into account. The most basic of these is the distortion induced by a printer objective having a high numerical aperture and a finite fifth Siedel coefficient. Such objectives allow extremely high resolution at the same time as affording a large angle of view. As such, they are fairly fundamental to printer design. As we have already mentioned, interpolation error is a significant worry in formulating the **I-to-S** transformation as generally the various integer coordinate meshes associated with image acquisition and hologram writing do not line up. The naïve scheme of using a paraxial **I-to-S** transformation and then predistorting each SLM frame to correct for a finite fifth coefficient often ends up by introducing interpolation noise two times over. It therefore turns out to be much more efficient to combine the predistortion of data with the paraxial **I-to-S** transformation to create a single non-paraxial transformation. In Appendix 4, we discuss how this idea can be extended to all holographic aberrations including those induced by the processing chemistry.

8.10.1 Setting up the Formalism

We will start by setting up some coordinate systems. Let (ρ, θ) represent right-handed cylindrical polar coordinates of a pixel on the SLM with origin at the centre of the SLM. Laser light traversing the SLM is focussed by the optical objective to form an image downstream of the hogel position on a plane whose normal vector is parallel to the axial propagation vector. Let (r, ϑ) be right-handed cylindrical polar coordinates describing the position of the pixel on this image plane with $r = 0$ representing the optical axis. The objective distortion may then be characterised by the following relation

$$\begin{aligned}\rho &= r \{1 - \mathcal{D}(r)\} \\ \theta &= \vartheta + \pi\end{aligned}\tag{8.129}$$

Alternatively, an inverse formalism can be used

$$\begin{aligned}r &= \rho \{1 - \mathcal{G}(\rho)\} \\ \vartheta &= \theta + \pi\end{aligned}\tag{8.130}$$

Now, we define x and y to be the right-handed Cartesian coordinates of a pixel on the SLM. As before, we take the origin to be at the centre of the SLM. Likewise, we introduce x' and y' as the Cartesian coordinates of the projected image plane with origin as the optical axis.

We define the aspect ratio of the SLM as its useful height divided by its useful width. In general, the rectangular SLM will either underfill or overfill the circular aperture of the objective. Here we will assume that there is an overfill in the horizontal direction leading to “dead” areas of the SLM (Figure 8.22). We label the absolute width and height of the SLM by w_s and h_s where $w_s > h_s$. We will assume of course that the SLM is mounted symmetrically with respect to the objective. We then label the length of the dead zone to one side of the SLM as x_d . Using these labels, we may write the following simple expression for the SLM aspect ratio:

$$a_s = \frac{h_s}{w_s - 2x_d}. \quad (8.131)$$

It is useful to now introduce non-dimensional coordinates for both the SLM plane and the projected SLM image plane. On the SLM plane, we introduce the coordinates (\hat{x}, \hat{y}) , which are defined as

$$\begin{aligned} \hat{x} &\equiv \frac{2a_s x}{h_s} \\ \hat{y} &\equiv \frac{2a_s y}{h_s} \end{aligned} \quad (8.132)$$

On the projected SLM image plane, we introduce the coordinates (\hat{x}', \hat{y}') , which are likewise defined as

$$\begin{aligned} \hat{x}' &\equiv \frac{2a_s x'}{h_s [1 - \mathcal{G}(w_s/2 - x_d)]} \\ \hat{y}' &\equiv \frac{2a_s y'}{h_s [1 - \mathcal{G}(w_s/2 - x_d)]} \end{aligned} \quad (8.133)$$

Figure 8.23 shows a diagram of the projected image plane of the SLM (a) and the SLM plane (b). To use the maximum field of view of the printer, we must specify the image data over a grid within the red rectangle shown in (a). This image data must then be distorted using an inverse transform such that we write data to the SLM that will then be transformed to form effectively undistorted data. The red contour in (b) shows the effect of such predistortion on the contour of the outer data rectangle of (a). Note that the aspect ratio of the image data in (a) is equal to that of the SLM as the distortion transformation does not affect angle.

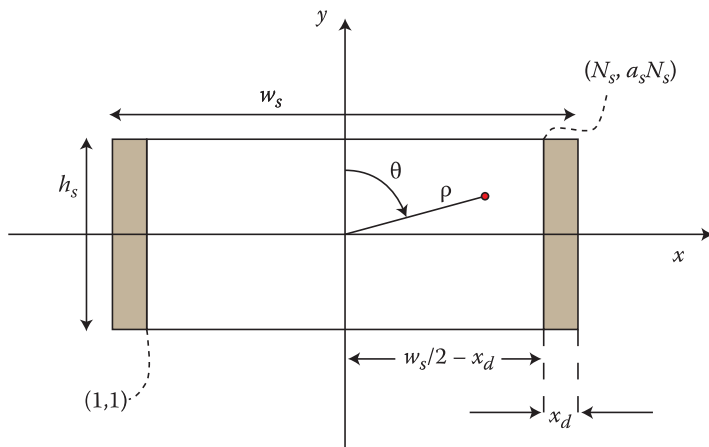


FIGURE 8.22 The printer SLM and the parameters that describe it. The physical SLM has height, h_s and width, w_s . However we envisage the SLM overfilling the aperture of the objective giving rise to two dead zones of length x_d .

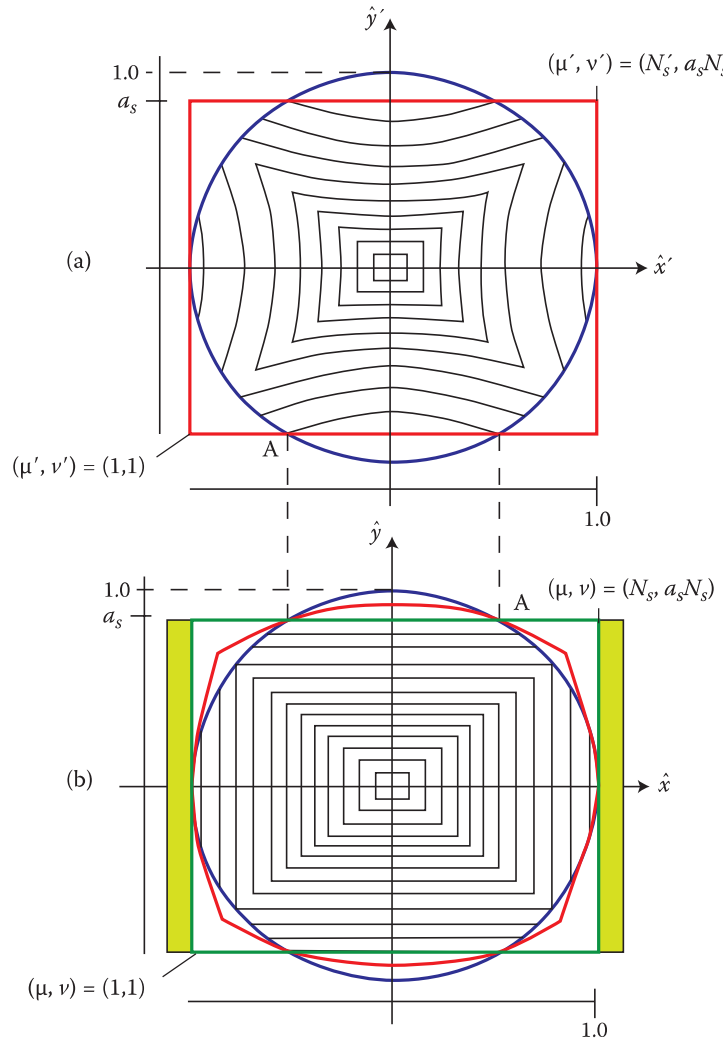


FIGURE 8.23 Coordinate systems of (a) the projected image plane of the SLM and (b) the SLM plane.

8.10.2 Data Predistortion

Data predistortion seeks to introduce an inverse distortion into the input image data such that the optical distortion introduced by the objective exactly cancels this out. The result is therefore that the objective appears completely paraxial. To formalise the predistortion process, we must introduce two coordinate systems. These describe image data on the SLM and on the projected plane of the SLM downstream of the hogel.

Image data must be known over the red rectangular region of Figure 8.23a. We therefore divide up this region of the projected image plane using a uniform (x,y) Cartesian grid of integer dimensions $(N'_s, a_s N'_s)$ and denote the irradiance distribution over this grid by $\mathbf{S}'_{\mu'\nu'}$, where

$$\begin{aligned}\hat{x}' &= \frac{2(\mu'-1)}{N'_s-1} - 1 \quad \forall \mu' = 1, 2, 3, \dots, N'_s \\ \hat{y}' &= \frac{2a_s(\nu'-1)}{a_s N'_s - 1} - a_s \quad \forall \nu' = 1, 2, 3, \dots, a_s N'_s\end{aligned}\tag{8.134}$$

The point $(\mu'\nu') = (1,1)$ is taken to be the bottom left-hand corner of the rectangle in Figure 8.23a and the point $(\mu'\nu') = (N'_s, a_s N'_s)$ corresponds to the top right-hand-corner.

In an exactly similar manner to above, we discretise the useful aperture of the SLM plane as defined by the green rectangle in Figure 8.23b. We denote the irradiance distribution over this grid by $\mathbf{S}_{\mu\nu}$ where

$$\begin{aligned}\hat{x} &= \frac{2(\mu-1)}{N_s-1} - 1 \quad \forall \mu = 1, 2, 3, \dots, N_s \\ \hat{y} &= \frac{2a_s(v-1)}{a_s N_s - 1} - a_s \quad \forall v = 1, 2, 3, \dots, a_s N_s\end{aligned}\tag{8.135}$$

Following our convention, we take the point $(\mu, v) = (1, 1)$ to be the bottom left-hand corner of the green rectangle in Figure 8.23b and the point $(\mu, v) = (N_s, a_s N_s)$ to correspond to the top right-hand-corner.

Now, in the case that the objective was perfectly paraxial, we would have for $N'_s = N_s$

$$\mathbf{S}_{\mu\nu} = \mathbf{S}'_{\mu'\nu'} \quad \forall \left\{ \mu' \in \mathbb{N} \mid \mu' \leq N_s, v' \leq a_s N_s \right\} \tag{8.136}$$

where

$$\begin{aligned}\mu' &= N_s + 1 - \mu \\ v' &= aN_s + 1 - v\end{aligned}\tag{8.137}$$

Equation 8.137 just describes an image inversion from the primed to the unprimed plane as the primed and unprimed planes have been assumed to be on opposite sides of the hogel—this is just because we have chosen to study the case in which the SLM is in the non-conjugate position. Of course, in the case that the primed and unprimed planes are on the same side as the hogel, as in the case of Figure 8.19, for example (the conjugate SLM position), then Equation 8.137 must be replaced by the simpler relation

$$\begin{aligned}\mu' &= \mu \\ v' &= v\end{aligned}\tag{8.138}$$

Anyhow, in the non-paraxial case (and for the non-conjugate SLM position), a point (\hat{x}, \hat{y}) on the SLM is related to a point (\hat{x}', \hat{y}') on the projected image plane by

$$\begin{aligned}\hat{x}' &= -\hat{x} \frac{1 - \mathcal{G}(\rho)}{1 - \mathcal{G}(w_s/2 - x_d)} \\ \hat{y}' &= -\hat{y} \frac{1 - \mathcal{G}(\rho)}{1 - \mathcal{G}(w_s/2 - x_d)}\end{aligned}\tag{8.139}$$

or in terms of the discrete coordinates

$$\begin{aligned}\mu' &= \frac{N'_s + 1}{2} + \left(\frac{N_s + 1}{2} - \mu \right) \left\{ \frac{N'_s - 1}{N_s - 1} \right\} \frac{1 - \mathcal{G}(\rho)}{1 - \mathcal{G}(w_s/2 - x_d)} \\ v' &= \frac{a_s N'_s + 1}{2} + \left(\frac{a_s N_s + 1}{2} - v \right) \left\{ \frac{N'_s - 1}{N_s - 1} \right\} \frac{1 - \mathcal{G}(\rho)}{1 - \mathcal{G}(w_s/2 - x_d)}\end{aligned}\tag{8.140}$$

It is usually more convenient at this point to introduce a non-dimensional radius

$$\hat{\rho} \equiv \frac{2a_s}{h_s} \rho \tag{8.141}$$

and an alternative normalised distortion function

$$\mathcal{K}(\hat{\rho}) \equiv \frac{1 - \mathcal{G}(\rho)}{1 - \mathcal{G}(w_s/2 - x_d)}. \quad (8.142)$$

This function can be easily generated using ray tracing of the printer optical system and may then be conveniently expanded using a least-squares fit as a truncated one-dimensional power series

$$\mathcal{K}(\hat{\rho}) \equiv \sum_{\sigma=0}^{N_E} k_{\sigma} \hat{\rho}^{\sigma}. \quad (8.143)$$

A typical example of this distortion function is shown in Figure 8.24. Note that by a sensible choice of N'_s and N_s the coordinate systems (μ, ν) and (μ', ν') may be made to line up in the central field where $\mathcal{K}(\rho) \sim 0$. To achieve an undistorted data set at the projected image plane, we must then load our SLM with information $\mathbf{S}_{\mu\nu}$, which is calculated by the transformation

$$\begin{aligned} \mathbf{S}_{\mu\nu} &= \mathbf{S}'_{\mu'\nu'} & \forall \left\{ \mu, \nu, \mu', \nu' \in \mathbb{N} \mid \mu, \mu' \leq N_s; \nu, \nu' \leq a_s N_s \right\} \\ &= 0 & \forall \left\{ \mu, \nu, \mu', \nu' \in \mathbb{N} \mid \mu \leq N_s; \nu \leq a_s N_s; \mu' > N_s \right\} \\ &= 0 & \forall \left\{ \mu, \nu, \mu', \nu' \in \mathbb{N} \mid \mu \leq N_s; \nu \leq a_s N_s; \nu' > a_s N_s \right\} \end{aligned} \quad (8.144)$$

where

$$\begin{aligned} \mu' &= \left\| \frac{N'_s + 1}{2} + \left(\frac{N_s + 1}{2} - \mu \right) \left\{ \frac{N'_s - 1}{N_s - 1} \right\} \mathcal{K}(\hat{\rho}) \right\| \\ \nu' &= \left\| \frac{a_s N'_s + 1}{2} + \left(\frac{a_s N_s + 1}{2} - \nu \right) \left\{ \frac{N'_s - 1}{N_s - 1} \right\} \mathcal{K}(\hat{\rho}) \right\| \\ \hat{\rho} &= \left\{ \left[2 \frac{(\mu - 1)}{N_s - 1} - 1 \right]^2 + a_s^2 \left[2 \frac{(\nu - 1)}{a_s N_s - 1} - 1 \right]^2 \right\}^{1/2} \end{aligned} \quad (8.145)$$

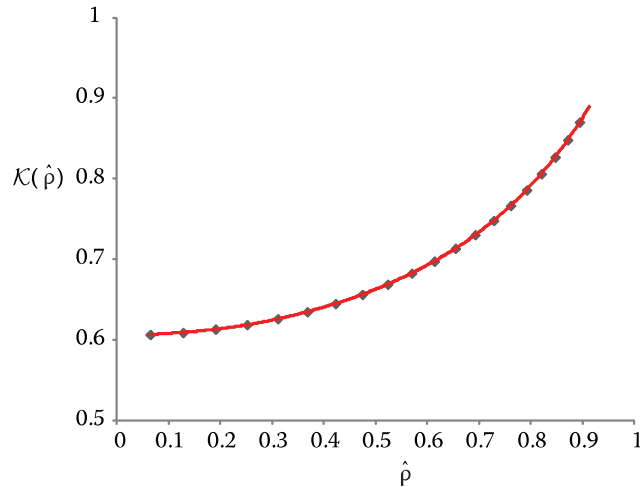


FIGURE 8.24 Example of the measured distortion function of a typical printer objective along with a 6th order power law fit. The data are from a GEOLA blue (437.7 nm) objective apodised by a sony XGA1 LCD with horizontal paraxial field of view of 85 degrees. The function $\mathcal{K}(\hat{\rho})/\mathcal{K}(0)$ essentially measures the change in effective pitch of paraxial and non-paraxial integer coordinate systems at \mathcal{S}' .

Setting $\mathcal{K}(\hat{\rho}) = 1$ and $N'_s = N_s$, we retrieve the paraxial case of Equations 8.136 and 8.137. For a conjugate SLM position, the first two relations of Equation 8.145 must be replaced by

$$\begin{aligned}\mu' &= \left\| \frac{N'_s + 1}{2} + \left(\mu - \frac{N_s + 1}{2} \right) \left\{ \frac{N'_s - 1}{N_s - 1} \right\} \mathcal{K}(\hat{\rho}) \right\| \\ v' &= \left\| \frac{a_s N'_s + 1}{2} + \left(v - \frac{a_s N_s + 1}{2} \right) \left\{ \frac{N'_s - 1}{N_s - 1} \right\} \mathcal{K}(\hat{\rho}) \right\|\end{aligned}\quad (8.146)$$

when $\mathcal{K}(\hat{\rho}) = 1$ and $N'_s = N_s$, this then leads to Equation 8.138 as expected.

The transformation of Equations 8.144 and 8.145 allow us to use a paraxial transformation on \mathbf{I} to arrive at \mathbf{S}' and then from \mathbf{S}' to calculate the required SLM data \mathbf{S} . As we have already discussed, however, this procedure often introduces interpolation errors two times over. The exception is if we specifically align our various integer coordinate meshes and choose a specific quantised value of h such that \mathbf{S}' is free of interpolation error as described in Section 8.8.5. In this case, Equation 8.144 can be implemented in a real-time fashion within the printing process itself. As a result, from the point of view of data preparation, the task then becomes simply the generation of paraxial SLM data. One should note that Equation 8.144 is intrinsically two-dimensional and as written, uses nearest-neighbour interpolation. This transformation may be rewritten using bilinear and bicubic interpolation.* These more advanced types of interpolation can often still be used in real-time within the printer writing software and act to lessen the introduced interpolation noise, particularly at high spatial frequencies.

In many cases, one simply cannot fulfil the requirements necessary to abolish interpolation error in the calculation of the paraxial SLM data and, in this case, it makes good sense to formulate a single non-paraxial \mathbf{I} -to- \mathbf{S} transformation. We cannot avoid the introduction of interpolation noise on the application of this transformation, but we will always introduce less noise in a single nearest-neighbour transform than if we use two sequential transforms; that is, if g and α are integers and f_1 and f_2 are arbitrary but well-behaved real functions, then generally, $g = \|f_1(\|f_2(\alpha)\|)\|$ can be a poor approximation to $g = \|f_1(f_2(\alpha))\|$. One might have thought that replacing the nearest-neighbour interpolation in an \mathbf{I} -to- \mathbf{S} transformation with a higher order interpolation could offer a good alternative approach. However, HPO holograms practically require three-dimensional interpolation schemes and full-parallax holograms, four-dimensional schemes. As such, they are difficult to implement, extremely time-consuming with current computing technology and of questionable advantage for the moment.

8.10.3 Non-Paraxial I-to-S Transformations

Any of the previous paraxial transformations that we have introduced giving \mathbf{S}' in terms of \mathbf{I} may be trivially combined with Equations 8.144 to 8.146, to give a single non-paraxial transformation by simple substitution. For example, the transformation of Equation 8.62 and Equation 8.63 can be written in terms of (μ', v') in the following trivial way:

$$\begin{aligned}{}^{\mu'\nu'} \mathbf{S}'_{\alpha\beta} &= {}^k \mathbf{I}_{ij} \quad \forall \mu' \left\{ \mu' \in \mathbb{N} \mid N_{U1}(\alpha) \leq \mu' \leq N_{U2}(\alpha) \right\} \\ &\quad \forall v' \left\{ v' \in \mathbb{N} \mid N_{V1}(\beta) \leq v' \leq N_{V2}(\beta) \right\} \\ &\quad \forall \alpha \left\{ \alpha \in \mathbb{N} \mid \alpha \leq N_A \right\} \\ &\quad \forall \beta \left\{ \beta \in \mathbb{N} \mid \beta \leq N_B \right\} \\ &= 0 \quad \text{otherwise}\end{aligned}\quad (8.147)$$

* We discuss higher order interpolation in Chapter 9 and in Appendix 7.

where

$$i = N_I - \left\| \frac{(\alpha-1)(N_I-1)}{N_A-1} \right\|, \quad j = N_J - \left\| \frac{(\beta-1)(N_J-1)}{N_B-1} \right\| \quad (8.148)$$

$$k = 1 + \left\| \frac{(N_K-1)}{W} \left\{ \frac{D_X+W}{2} + \frac{h(2\mu'-N_M-1)}{(N_M-1)} \tan\left(\frac{\Psi'_{\text{PH}}}{2}\right) + \frac{(\alpha-N_A)D_X}{N_A-1} \right\} \right\| \quad (8.149)$$

and where N_{U1} , N_{U2} , N_{V1} and N_{V2} are given by Equations 8.49 and 8.50. The parameter Ψ'_{PH} is the non-paraxial field of view and is defined as

$$\tan\left(\frac{\Psi'_{\text{PH}}}{2}\right) = \frac{1}{K(0)} \tan\left(\frac{\Psi_{\text{PH}}}{2}\right) \quad (8.150)$$

Using a conjugate SLM position, we then simply substitute Equation 8.146 into Equation 8.149 with $N_s = N'_s = N_M$ to give

$$k = 1 + \left\| \frac{(N_K-1)}{W} \left\{ \frac{D_X+W}{2} + \frac{(2\mu-N_M-1)\mathcal{K}(\hat{\rho})}{(N_M-1)} h \tan\left(\frac{\Psi'_{\text{PH}}}{2}\right) + \frac{(\alpha-N_A)D_X}{N_A-1} \right\} \right\| \quad (8.151)$$

where

$$\hat{\rho} = \left\{ \left[2 \frac{(\mu-1)}{N_M-1} - 1 \right]^2 + a_s^2 \left[2 \frac{(v-1)}{a_s N_M-1} - 1 \right]^2 \right\}^{1/2} \quad (8.152)$$

and

$$a_s N_M = N_V \quad (8.153)$$

Now, it is usual that the non-paraxial distortion is not greater than about 20%. If this is the case, we can usually ignore its effect on the viewing window boundary and write the full non-paraxial transformation as

$$\begin{aligned} {}^{\mu\nu} \mathbf{S}_{\alpha\beta} &= {}^k \mathbf{I}_{ij} & \forall \mu \left\{ \mu \in \mathbb{N} \mid N_{U1}(\alpha) \leq \mu \leq N_{U2}(\alpha) \right\} \\ && \forall v \left\{ v \in \mathbb{N} \mid N_{V1}(\beta) \leq v \leq N_{V2}(\beta) \right\} \\ && \forall \alpha \left\{ \alpha \in \mathbb{N} \mid \alpha \leq N_A \right\} \\ && \forall \beta \left\{ \beta \in \mathbb{N} \mid \beta \leq N_B \right\} \\ &= 0 & \text{otherwise} \end{aligned} \quad (8.154)$$

where

$$i = N_I - \left\| \frac{(\alpha-1)(N_I-1)}{N_A-1} \right\|, \quad j = N_J - \left\| \frac{(\beta-1)(N_J-1)}{N_B-1} \right\| \quad (8.155)$$

$$k = 1 + \left\| \frac{(N_K-1)}{W} \left\{ \frac{D_X+W}{2} + \frac{(2\mu-N_M-1)\mathcal{K}(\hat{\rho})}{(N_M-1)} h \tan\left(\frac{\Psi'_{\text{PH}}}{2}\right) + \frac{(\alpha-N_A)D_X}{N_A-1} \right\} \right\| \quad (8.156)$$

In the central paraxial region where $\hat{\rho}$ is small this equation is identical to the paraxial equation but clearly as $\hat{\rho}$ increases the rule between k and μ is now modified. This transformation will, however, yield a viewing window that is a distorted rectangle. To arrive at a transform with a perfectly rectangular window, we must transform the (μ', v') inequality of Equation 8.147. To transform this inequality, one must solve a number of non-linear equations to determine the viewing boundary in terms of (μ, v) for each hogel. Because of the form of Equation 8.130, for a given v , there will always be either 0, 1 or 2 values of μ . We therefore adopt the strategy of determining the topmost and bottommost values of v on the window boundary; we then calculate pairs of μ values for all rows between these two extremes. This allows us to perform the calculation of \mathbf{S} on a row-by-row basis.

The first step is then to calculate the topmost and bottommost values of v on the boundary. To do this, we start with coordinates of the top left-hand corner:

$$\mu = N_{U1}; \quad v = N_{V2} \quad (8.157)$$

and the top right-hand corner

$$\mu = N_{U2}; \quad v = N_{V2} \quad (8.158)$$

where N_{U1} , N_{U2} and N_{V2} are defined by Equations 8.49 and 8.50 but with non-paraxial angles (e.g., Equation 8.150) replacing paraxial angles. Then, we solve the following $N_{U2} - N_{U1} + 1$ non-linear equations to give the v coordinates of the top window boundary:

$$N'_{VT}(\mu) = \|v\| \quad \forall \mu \left\{ \mu \in \mathbb{N} \mid N_{U1} \leq \mu \leq N_{U2} \right\}$$

where

$$N_{V2} = \frac{N_V + 1}{2} + \left(v - \frac{N_V + 1}{2} \right) \mathcal{K} \left(\left\{ \left[2 \frac{(\mu - 1)}{N_M - 1} - 1 \right]^2 + a_s^2 \left[2 \frac{(v - 1)}{N_V - 1} - 1 \right]^2 \right\}^{1/2} \right) \quad (8.159)$$

We then calculate the maximum value of $N'_{VT}(\mu)$, which is the topmost v coordinate of the viewing window:

$$N'_{V2}(\alpha, \beta) \equiv \max \left\{ N'_{VT}(\mu = N_{U1}), N'_{VT}(\mu = N_{U1} + 1), \dots, N'_{VT}(\mu = N_{U2}) \right\} \quad (8.160)$$

A similar procedure then defines the minimum value of $N'_{VB}(\mu)$, which is the bottommost v coordinate of the viewing window:

$$N'_{V1}(\alpha, \beta) \equiv \min \left\{ N'_{VB}(\mu = N_{U1}), N'_{VB}(\mu = N_{U1} + 1), \dots, N'_{VB}(\mu = N_{U2}) \right\} \quad (8.161)$$

Equation 8.159 and its partner, which defines $N'_{VB}(\mu)$, are typically solved computationally using a Newton–Raphson iteration. Note that we have deleted the nearest integer operators so that the equations are well behaved—this just means that we treat v as real for the purpose of solving the equation and then we simply use $\|v\|$.

We now solve a further $(N_{V2} - N_{V1} + 1)$ equations for the left-hand μ coordinate of each row of the viewing window and a similar number for the right-hand coordinate. These are, respectively

$$(i) \quad N'_{V1}(v) = \|\mu\| \quad \forall v \left\{ v \in \mathbb{N} \mid N'_{V1} \leq v \leq N'_{V2} \right\} \text{ where}$$

$$N_{U1} = \frac{N_M + 1}{2} + \left(\mu - \frac{N_M + 1}{2} \right) \mathcal{K} \left(\left\{ \left[2 \frac{(\mu - 1)}{N_M - 1} - 1 \right]^2 + a_s^2 \left[2 \frac{(v - 1)}{N_V - 1} - 1 \right]^2 \right\}^{1/2} \right) \quad (8.162)$$

(ii) $N'_{U2}(v) = \|\mu\| \forall v \{ v \in \mathbb{N} | N'_{V1} \leq v \leq N'_{V2} \}$ where

$$N_{U2} = \frac{N_M + 1}{2} + \left(\mu - \frac{N_M + 1}{2} \right) \mathcal{K} \left(\left\{ \left[2 \frac{(\mu - 1)}{N_M - 1} - 1 \right]^2 + a_s^2 \left[2 \frac{(v - 1)}{N_V - 1} - 1 \right]^2 \right\}^{1/2} \right) \quad (8.163)$$

The exact **I-to-S** transformation can then be formulated in the following way:

$$\begin{aligned} {}^{\mu\nu} \mathbf{S}_{\alpha\beta} &= {}^k \mathbf{I}_{ij} & \forall \mu \{ \mu \in \mathbb{N} | N'_{U1}(\alpha, v) \leq \mu \leq N'_{U2}(\alpha, v) \} \\ & \forall v \{ v \in \mathbb{N} | N'_{V1}(\alpha, \beta) \leq v \leq N'_{V2}(\alpha, \beta) \} \\ & \forall \alpha \{ \alpha \in \mathbb{N} | \alpha \leq N_A \} \\ & \forall \beta \{ \beta \in \mathbb{N} | \beta \leq N_B \} \\ & \forall k \{ k \in \mathbb{N} | k \leq N_K \} \\ &= 0 & \text{otherwise} \end{aligned} \quad (8.164)$$

where

$$i = N_I - \left\| \frac{(\alpha - 1)(N_I - 1)}{N_A - 1} \right\|, \quad j = N_J - \left\| \frac{(\beta - 1)(N_J - 1)}{N_B - 1} \right\| \quad (8.165)$$

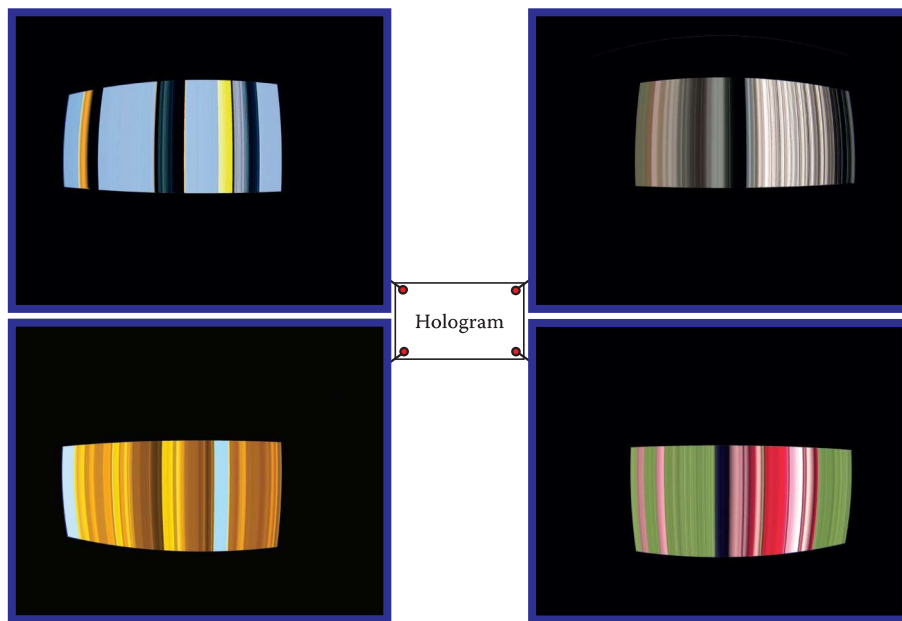


FIGURE 8.25 Typical SLM data, prepared using a non-paraxial transformation, pertaining to the four extreme corner hogels of an HPO reflection hologram with a rectangular viewing window. Note that the SLM is in the non-conjugate position here.

$$k = 1 + \left\| \frac{(N_K - 1)}{W} \left\{ \frac{D_X + W}{2} + \frac{(2\mu - N_M - 1)\mathcal{K}(\hat{\rho})}{(N_M - 1)} h \tan\left(\frac{\Psi'_{\text{PH}}}{2}\right) + \frac{(\alpha - N_A)D_X}{N_A - 1} \right\} \right\| \quad (8.166)$$

A different technique which can be used to define an exactly rectangular viewing window is, for each hogel, to calculate (μ', ν') for every (μ, ν) on the SLM using Equation 8.146. By testing (μ', ν') against the required rectangle, the parameters $N'_{V1}(\alpha, \beta), N'_{V2}(\alpha, \beta), N'_{U1}(\alpha, \nu), N'_{U2}(\alpha, \nu)$ can once again be defined. Precalculation of these boundary functions is often advantageous and can be performed with either technique. Figure 8.25 shows typical SLM data pertaining to the four extreme corner hogels of an HPO reflection hologram with a rectangular viewing window. The distortion function used is that of Figure 8.24.

REFERENCES

1. D. Brotherton-Ratcliffe and A. Rodin, *Holographic printer*, US patent 7,161,722 (filed 2002, granted 2007).
2. D. Brotherton-Ratcliffe, A. Rodin and L. Hryniw, *Method of writing a composite 1-step hologram*, US patent 7,333,252 (filed 2002, granted 2008).
3. R. Guenther, *Modern Optics*, John Wiley & Sons, New York (1990).
4. G. Saxby, *Practical Holography*, 3rd Edn, IOP Publishing Ltd., London, UK (2004).
5. L. Cross, “The multiplex technique for cylindrical holographic stereograms,” in SPIE San Diego August Seminar (1977). [Presented, but not published]
6. S. A. Benton, “Hologram reconstructions with extended incoherent sources,” *J. Opt. Soc. Am.* **59**, 1545–1546A (1969).
7. S. A. Benton, “Achromatic images from white light transmission holograms,” *J. Opt. Soc. Am.* **68**, 1441A (1978).
8. K. Ohnuma and F. Iwata, “Color rainbow hologram and color reproduction,” *Appl. Opt.* **27**, 3859–3863 (1988).

9

Digital Holographic Printing: Computational Methods for Full-Parallax Holograms

9.1 Introduction

In Chapter 8, we presented a detailed discussion of the typical image-processing algorithms which are required for the conversion of raw camera data into a form suitable for the generation of both direct-write and master-write (DWDH and MWDH) digital holograms. We paid particular attention to horizontal parallax-only (HPO) holograms. The algorithms for this type of hologram can all be implemented on a single PC with several gigabytes of memory. In all but the largest DWDH HPO holograms, all data can be read directly, and in its entirety, into the computer's memory and the transformations applied. One therefore only needs to read the raw camera data one time, process it, and then write it out one time. With the advent of 64-bit PCs, high-resolution DWDH HPO holograms of even many tens of square metres in size present no particular difficulty in such an implementation.

In contrast to HPO holograms, even small full-parallax holograms can require just too much image data for all the data to be loaded at one time into main memory. For example, a 40 cm × 30 cm RGB DWDH full-parallax reflection hologram with a maximal viewing window, good angular resolution and a 0.5 mm-diameter hogel can be expected to require approximately 1 to 2 TB of memory storage when used with a printer spatial light modulator (SLM) of 1024 × 1280. This is beyond the practical main memory limitations of modern PCs. As a result, it is not possible to read all image data into main memory, apply the appropriate image processing transformation and then write the data out. Rather if one follows the techniques used in HPO holography directly, one ends up reading and writing data to and from the disk many times. This then leads to enormous inefficiency and prohibitively long processing times.

The intrinsically large image data set characteristic of full-parallax display holograms leads to various problems. In Chapter 10, we shall discuss how one copes with generating such large data sets in typical computer modelling programs and how one collects such data from real-world objects. The sheer size of the data can present transport and storage problems for companies which print digital holograms. The image data for even large HPO holograms can be compressed and sent over the Internet without any problem. In contrast, at the time of writing, even small full-parallax data sets can rarely be sent electronically. Archiving customer data effectively often requires petabyte storage facilities.

There are various strategies one can apply to circumvent the issue of image processing of intrinsically large data sets. Perhaps the most obvious is the use of MWDH in place of DWDH. Here, an H_1 master is written using the direct camera data. In Chapter 8, we derived the **I-to-S** transformation required (Equation 8.20). Another strategy is to write a DWDH Denisyuk hologram according to Section 8.7.1. Again, this only requires raw camera data. Both these techniques have their applications and merits. RGB DWDH reflection Denisyuk holograms are an excellent choice when no image projection in front of the hologram plane is required. MWDH is particularly suited for medium-sized holograms—but if the final H_2 hologram is too small, then one runs into resolution and aberration problems with the printer write-head.* At the other end of the scale, one ends up requiring an extremely large RGB laser to achieve the optical $H_1;H_2$ transfer.

* Essentially, one can end up requiring a very high resolution SLM and then only using a small fraction of it.

At the end of the day, many full-parallax holograms require fundamental image data reorganisation. This is because the raw image data is inevitably available at one plane and we would simply like to write a hologram at another plane. The most usual reason for this situation is apparent from analogue holography. Here, an H_1 hologram is made and then optically transferred to an H_2 hologram, thereby effectively changing the image plane. As a result of this procedure, the image of the final H_2 hologram can be made to bisect the physical hologram surface. With digital holograms, we have just the same problem. To end up with an image that bisects the physical hologram plane, we must apply an image-planing transformation to our raw camera data, the only difference being that, in this case, the transformation is mathematical and not optical.

One rather different way around the data reorganisation problem is available when special computer modelling software is used to generate the three-dimensional (3D) model. Most commercially available modelling software programs generate conventional camera image data only. They do this by calculating the intensity values of many light rays emanating from the 3D model given various assumptions about the optical properties of the model. Groups of rays are then calculated to define a camera image. From an absolute point of view, one can imagine using this same model to calculate the intensity of all those rays required to directly define a hogel. This comes down to simply asking the software to work in a different order in calculating rays. There is, however, a sizeable problem here as most current commercial software packages are configured and optimised to calculate rays in the groups associated with normal cameras rather than with hogels. The result is that either the software works many hundreds of times slower when forced to calculate hogels directly or it simply cannot be configured in this fashion. Nevertheless, software packages that are able to calculate hogel data directly from a 3D computer model have been written and, although not commercially available, are in use today by some groups working in digital holography. The technology behind this type of software is outside the scope of this book, and the interested reader is referred to the published literature [1–5]. The advantage of this technique is that it enables one to directly calculate the required rendered images for each hogel from a compact 3D computer model. In addition, such software can, in principle, correct for many aberrations including optical aberration in the writing objective. In this light, and from a truly absolute point of view, it must be regarded theoretically as the best solution for generating virtual data sets for full-parallax holograms. However, from a practical point of view, the number of people needing this type of special modelling program is relatively small. As such, the more standard commercially available programs for 3D computer modelling, although they lack the facility to generate direct hogel data, inevitably provide a better solution for the generation of state-of-the-art render data today. This is the approach we take in this book; it is also the approach that companies such as Geola Digital UAB have taken since the early days of digital display holography.

9.2 Practical Strategies for Changing the Image Plane

In Chapter 8, we discussed the alignment of the integer coordinate meshes concerned with data acquisition and hologram writing. We saw how, in the context of HPO holograms, the viewing distance became quantised when one demanded that these coordinate meshes lined up. From a practical point of view, given the specifications of a printer and the specifications of a desired HPO hologram, the most common situation we encounter is that such quantisation is unacceptable.* In other words, we find ourselves wanting to define a viewing plane distance that inevitably leads to a non-integer mapping between indices representing acquisition and writing coordinate systems. This is perhaps inevitable in the context of HPO holography because the optimal viewing distance at observation time is equal to the camera distance at acquisition time. With full-parallax digital holography, however, we are in a much better position due to Huygens' principle; here, we can view the hologram where we like and we can put the camera plane where we like. Of course, we may find ourselves in a situation in which we have image data from a physical camera (as opposed to a virtual camera) at a fixed plane and in this case we have to either adapt

* We should make the point that in the case that the write-head of a digital printer is designed to function for only a selected set of specific hologram formats, it may be possible to design it such that the rules of quantisation are acceptable for this restricted set. This solution trades flexibility for a reduction in interpolation noise.

the hologram parameters so that the camera distance obeys the quantisation rules or use more advanced interpolation mathematics - or accept a certain amount of interpolation noise.

9.2.1 Camera Definition

In the case of a virtual camera, by far the best and most practical solution for generating a full-parallax hologram is to prepare the data set at the first quantised value of the camera distance (i.e., in the language of Section 8.8.5, at a value of h corresponding to $n = 1$). At this distance, the size of a projected SLM pixel is the same as the hogel diameter and assuming a centered camera configuration

$$\begin{aligned} N_I &= N_A \\ N_J &= N_B \end{aligned} \quad (9.1)$$

We must further arrange that the camera spacing is equal to the hogel diameter according to Equation 8.80. This amounts to the minor restriction of the window width W being an integer multiple of the hogel diameter. Similarly, we need to add a vertical constraint

$$\frac{H}{N_G - 1} = \frac{D_Y}{N_B - 1} \quad (9.2)$$

which then leads to a corresponding constraint on the window height, H . With these constraints, one has all one needs to define the camera and its animation under a centred camera configuration for a hologram of size $(D_X \times D_Y) = (N_A - 1)\delta \times (N_B - 1)\delta$. The relevant camera parameters are

$$h = \frac{\delta}{2}(N_M - 1)\cot(\Psi_{PH}/2) = \frac{\delta}{2}(N_V - 1)\cot(\Psi_{PV}/2) \quad (9.3)$$

$$N_I = N_A; \quad N_J = N_B \quad (9.4)$$

$$N_K = 1 + \frac{W}{\delta}; \quad N_G = 1 + \frac{H}{\delta} \quad (9.5)$$

where δ represents the hogel diameter and the camera/viewing window is defined by

$$W \equiv m_1\delta \leq \delta(N_M - N_A); \quad H = m_2\delta \leq \delta(N_V - N_B) \quad (9.6)$$

with m_1 and m_2 non-zero positive integers. The parameters Ψ_{PH} and Ψ_{PV} are defined by the printer writing objective and N_M and N_V by the printer SLM. The first-quantised h value given in Equation 9.3 is then seen to be an intrinsic property of the printer for a given hogel diameter.

The above camera definition produces a single-colour image data set ${}^{kg}\mathbf{I}_{ij}$ for $1 \leq k \leq N_K$, $1 \leq g \leq N_G$, $1 \leq i \leq N_I$ and $1 \leq j \leq N_J$. To illustrate this, let us use the example of the 40 cm \times 30 cm, 0.5 mm-hogel hologram we discussed in Section 9.1. Here, $(D_X, D_Y) = (399.5, 299.5$ mm) as we always calculate distances from hogel centre to hogel centre. This then gives $N_A = 800$ and $N_B = 600$. With a horizontal printer field of view (FOV) of 85° and a printer SLM with pixel dimensions of 1280 \times 1024, the $n = 1$ h value is 348.95 mm. If we choose a window size at this distance of 50 cm \times 40 cm, then we must use $N_K = 1001$ and $N_G = 801$. Using Equation 9.4, we can calculate the memory requirement for the combined red, green and blue component image data (${}^{kg}\mathbf{I}_{ij}$). This is simply

$$M = 3N_A N_B N_K N_G \quad (9.7)$$

which works out at just over 1 TB. In Chapter 10, we shall look at how to generate this data using computer modelling software. We shall also see how it may be best derived from physical camera data. For now, however, we shall simply assume that we have this data on disk and we will direct our attention to the problem of changing the image plane—that is, we will examine how this data can be used to calculate a new data set corresponding to a camera position defined by $h = 0$.

9.2.2 Changing the Image Plane—Two-Step I-to-S Transformations

As we have discussed in the previous section, the size of ${}^{kg}\mathbf{I}_{ij}$ makes it practically impossible to read into memory at one time. The data is organised in $N_K \times N_G$ files each of size $3N_A N_B$. Each hogel requires just one RGB irradiance value from each of these 800,000 odd files. Opening 800,000 files and closing them each time we want to define a hogel is of course not an option. So converting the data to the form wanted in one step seems impossible. However, not all is lost, as we can do the next best thing: convert the data in two steps. This turns out to be actually very efficient, as we shall see.

The idea is as follows: we start with our data (${}^{kg}\mathbf{I}_{ij}$) arranged in $N_K \times N_G$ RGB disk files. Let us denote this data as ${}^{kg}\mathbf{I}_{[ij]}$ to emphasise that the object is divided into files and that each file has an i and a j index. The first step is for each index $k = \bar{k}$ to read into main memory the N_G files described by ${}^{kg}\mathbf{I}_{[\bar{k}j]}$. The memory load for each such operation is just a little under 1.2 GB. Then, we simply reorganise the data and write it out into files described not by i and j but now by i and g . In other words, we make the transformation:

$${}^{\bar{k}}\mathbf{I}_{[\bar{k}j]} \rightarrow {}^{\bar{k}}\left[{}^g\mathbf{I}_i \right]_j \quad \forall \bar{k} \left\{ \bar{k} \in \mathbb{N} \mid \bar{k} \leq N_K \right\} \quad (9.8)$$

This then gives us $N_K \times N_J$ files, each of which we denote by ${}^g\mathbf{I}_i$. Taking a typical SATA 3 drive speed of 300 MB/s, we can see that at the time of writing, a fairly standard PC is able to perform this transformation in somewhat less than 3 h.

Having arranged our data in this new form, we will see that the required **I-to-S** transformation becomes much easier to implement. At this stage, we need to go back to our derivation of the paraxial **I-to-S** transformation for the monochromatic HPO DWDH reflection hologram with a centred camera configuration and written in restricted coordinates (see Equations 8.60 and 8.61). We can generalise this transformation to the full-parallax case and our specific (non-inverting) camera configuration fairly simply*:

$$\begin{aligned} {}^{\hat{v}}\hat{\mathbf{S}}_{\alpha\beta} &= {}^k\left[{}^g\mathbf{I}_i \right]_j \quad \forall \hat{v} \left\{ \hat{v} \in \mathbb{N} \mid N_B - \beta + 1 \leq \hat{v} \leq N_B - \beta + N_G \right\} \\ &\quad \forall \hat{\mu} \left\{ \hat{\mu} \in \mathbb{N} \mid N_A - \alpha + 1 \leq \hat{\mu} \leq N_A - \alpha + N_K \right\} \\ &\quad \forall \alpha \left\{ \alpha \in \mathbb{N} \mid \alpha \leq N_A \right\} \quad \forall \beta \left\{ \beta \in \mathbb{N} \mid \beta \leq N_B \right\} \\ &= 0 \quad \text{otherwise} \end{aligned} \quad (9.9)$$

where

$$i = \alpha \quad j = \beta \quad k = \hat{\mu} + \alpha - N_A \quad g = \hat{v} + \beta - N_B \quad (9.10)$$

Given ${}^k\left[{}^g\mathbf{I}_i \right]_j$ instead of ${}^{kg}\mathbf{I}_{ij}$, it should be immediately obvious that we can now perform this transformation one β value at a time. In other words, we can work out the required hogel write data one hologram line at a time. Thus, for $\beta = 1$ we read into main memory the N_K RGB files ${}^k\left[{}^g\mathbf{I}_i \right]_1$. In our example, these files will take up a memory space of approximately 1.9 GB. We can then perform the transformation (Equations 9.9 and 9.10) in main memory and write out a whole line of hogel data, ${}^{\hat{v}}\hat{\mathbf{S}}_{\alpha 1}$. We then proceed to $j = \beta = 2$ to write out the second line and so forth. Each line of hogels can be expected to take approximately 6 s to calculate with modern SATA disk drives. This means that for RGB hogel write speeds of less than 100 Hz, a single PC is able to cope with performing the required **I-to-S** transformation on the image data and in writing the processed data to the printer SLM.

You will note that we have used restricted coordinates to characterise the SLM plane \mathcal{S} as we wish to minimise memory load as much as possible. Anyway, all values of μ and v outside their restricted limits are zero all the time, so it makes little sense to allow space for them in our calculation. Instead, we use the fixed offset expressions (Equations 8.46 and 8.47) as pointers to our SLM memory map and then employ directly ${}^{\hat{v}}\hat{\mathbf{S}}_{\alpha\beta}$ to update the SLM. Figure 9.1 provides a summary of the two-step **I-to-S** transformation and hogel-writing sequence using restricted coordinates.

* This transformation is valid for a conjugate SLM position. See Section 8.8.2.1.

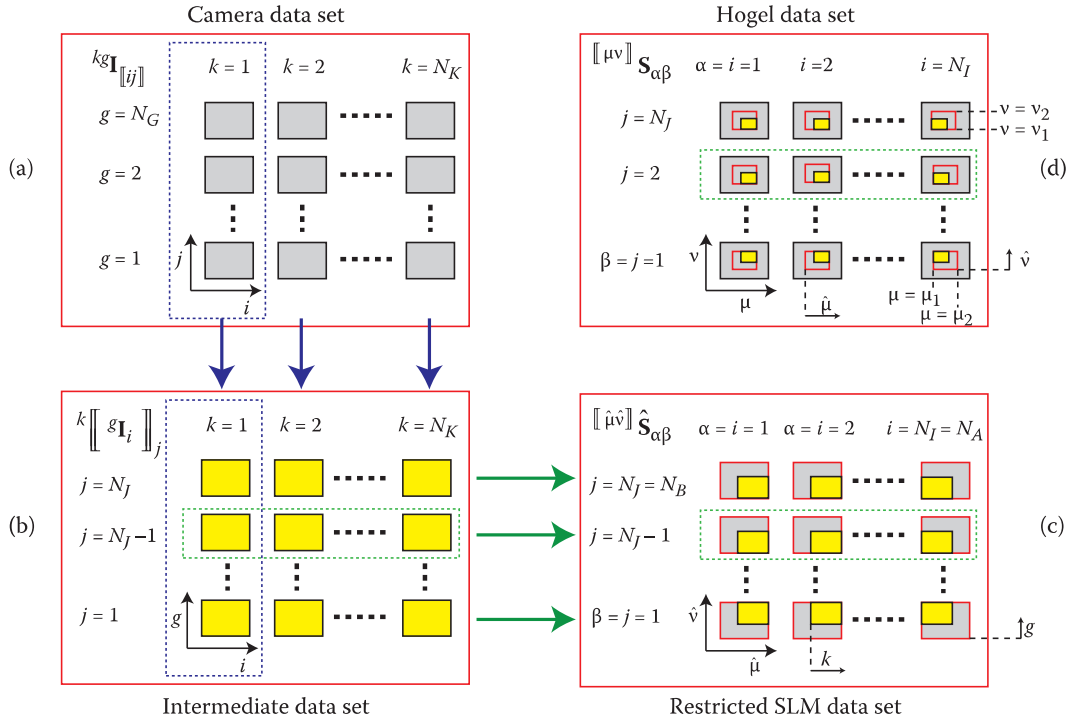


FIGURE 9.1 Illustration of the two-step paraxial objective **I**-to-**S** transformation described by Equations 9.8 and 9.9 using restricted SLM coordinates. This transformation converts camera image data corresponding to a given primary colour to the hogel data required to write a DWDH full-parallax, full-colour reflection hologram. The initial camera data (a) is composed of an $N_K \times N_G$ matrix of standard camera image files, each of dimensions $N_I \times N_J$ collected at the special $n = 1$ plane. The first step in the processing sequence is to load each column of this matrix into main memory and then to write it out to disk in the form of N_J files, each of dimensions $N_I \times N_G$. This process occurs for each of the N_K matrix columns leading to the intermediate $N_K \times N_J$ matrix of files shown in (b). Each file is of dimensions $N_I \times N_G$. The second step is to read each row of the intermediate matrix into main memory. Equations 9.9 and 9.10, with index rules, can then be used simply to populate $\llbracket \hat{\mu} \hat{v} \rrbracket \hat{\mathbf{S}}_{\alpha\beta}$ row by row (c). The SLM defining each hogel can finally be updated (d) using the corresponding file in the restricted SLM data set with the offset rules from Equations 8.46 and 8.47.

In Chapter 8, we introduced a system of coordinates that was even more efficient than the restricted SLM coordinates—this was the centred SLM configuration with its associated data set $\bar{\mathbf{S}}$. To use the data set $\bar{\mathbf{S}}$ to update the real SLM data, \mathbf{S} , we need to use variable index offset relations that change from hogel to hogel. As we saw in Chapter 8, it is not usually possible in HPO holography to achieve an alignment of the coordinate meshes, and as such, the centred SLM configuration can reduce image fidelity through the introduction of extra interpolation noise.

In full-parallax holography, the viewing plane is not collocated with the camera plane and as discussed previously, we can usually achieve a coordinate alignment. This makes the centred SLM configuration especially useful as it provides the greatest economy in memory. In its simplest form, we can simply replace Equation 9.9 by a step exactly analogous to Equation 9.8:

$${}^k \llbracket {}^g \mathbf{I}_i \rrbracket_j \rightarrow {}^{[kg]} \mathbf{I}_{ij} \quad (9.11)$$

In other words, we simply read in for $j = 1$ the N_K files ${}^k \llbracket {}^g \mathbf{I}_i \rrbracket_1$ and then write out the N_I files ${}^{[kg]} \mathbf{I}_{ii}$. We then repeat this exercise for all j . The final data set ${}^{[kg]} \mathbf{I}_{ij}$ is then actually identical to $\bar{\mathbf{S}}$ —that is,

$$\llbracket \bar{\mu} \bar{v} \rrbracket \mathbf{S}_{\alpha\beta} = {}^{kg} \mathbf{I}_{ij} \quad \forall \bar{\mu} = k, \bar{v} = g, \alpha = i, \beta = j \quad (9.12)$$

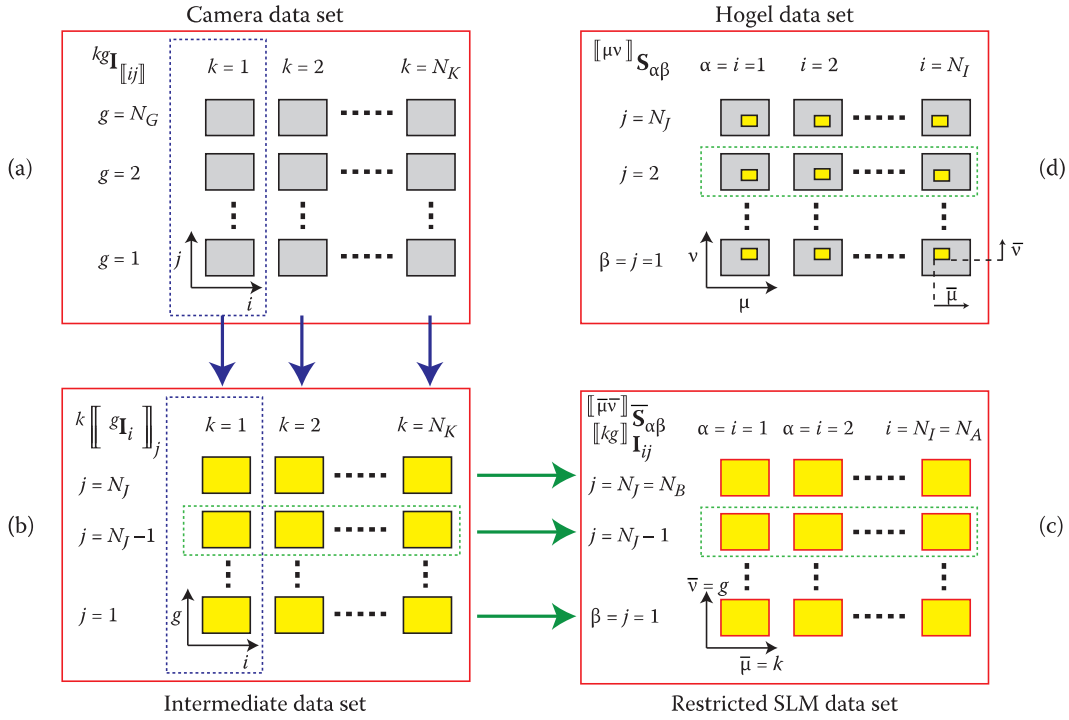


FIGURE 9.2 Illustration of the two-step paraxial objective \mathbf{I} -to- \mathbf{S} transformation described by Equations 9.8, 9.11, 9.12 and 9.13 using centred SLM coordinates. This transformation converts camera image data corresponding to a given primary colour to the hogel data required to write a DWDH full-parallax, full-colour reflection hologram. The initial camera data (a) is composed of an $N_K \times N_G$ matrix of standard camera image files, each of dimensions $N_I \times N_J$ collected at the special $n = 1$ plane. The first step in the processing sequence is to load each column of this matrix into main memory and then to write it out to disk in the form of N_I files, each of dimensions $N_I \times N_G$. This process occurs for each of the N_K matrix columns leading to the intermediate $N_K \times N_J$ matrix of files shown in (b). Each file is of dimensions $N_I \times N_G$. The second step is to read each row of the intermediate matrix into main memory and to write it out to disk in the form of $N_J = N_B$ files of dimensions $N_K \times N_G$. This process occurs for each of the $N_J = N_B$ matrix rows leading to the new $N_A \times N_B$ matrix of files ($[\bar{\mathbf{S}}_{\alpha\beta}]_{ij} = [kg\mathbf{I}_{ij}]$) shown in (c). Each file is of dimensions $N_K \times N_G$. The SLM defining each hogel can finally be updated (d) using the corresponding file in the centred SLM data set with the variables offset rules from Equation 9.13.

Therefore, to calculate $\bar{\mathbf{S}}$, all we need to do is to essentially swap two indices of the object \mathbf{I} —this is done by the two independent transforms (Equations 9.8 and 9.11).

The index relations required to compute \mathbf{S} from $\bar{\mathbf{S}}$ are those of Equations 8.78 and 8.79. Under the $n = 1$ quantum conditions, these reduce to

$$\begin{aligned} \mu_1 &= 2 - \alpha + \left\| \frac{1}{2} (N_A - N_K + N_M - 1) \right\| & \mu_2 &= N_K + 1 - \alpha + \left\| \frac{1}{2} (N_A - N_K + N_M - 1) \right\| \\ v_1 &= 2 - \beta + \left\| \frac{1}{2} (N_B - N_G + N_V - 1) \right\| & v_2 &= N_G + 1 - \beta + \left\| \frac{1}{2} (N_B - N_G + N_V - 1) \right\| \end{aligned} \quad (9.13)$$

To avoid truncation errors, one should further ensure that $N_A - N_K + N_M$ and $N_B - N_G + N_V$ are odd numbers. Figure 9.2 illustrates the processing sequence when using the centred SLM configuration.

9.2.3 General Full-Parallax Paraxial Objective Transformations

In cases in which the available camera data does not coincide with any of the quantised values of h , we must use a direct generalisation of the HPO transformations reviewed in Chapter 8. The two-stage

process described above can of course be used in this case, only that the second stage transformation is modified from that of Equations 9.9 and 9.10. In terms of restricted SLM coordinates, the appropriate monochromatic **I**-to-**S** DWDH transformation for a centred camera can be written as follows:

$$\begin{aligned}
 \hat{\mathbf{S}}_{\alpha\beta} &= {}^{kg}\mathbf{I}_{\hat{j}} \quad \forall \hat{v} \in \mathbb{N} \left\{ \hat{v} \in \mathbb{N} \left| \frac{D_Y(\hat{N}_V - 1)(N_B - \beta)}{(D_Y + H)(N_B - 1)} + 1 \leq \hat{v} \leq 1 + \frac{D_Y(\hat{N}_V - 1)}{D_Y + H} \left\{ \frac{N_B - \beta}{N_B - 1} + \frac{H}{D_Y} \right\} \right. \right\} \right\} \\
 &\quad \forall \hat{\mu} \left\{ \hat{\mu} \in \mathbb{N} \left| \frac{D_X(\hat{N}_M - 1)(N_A - \alpha)}{(D_X + W)(N_A - 1)} + 1 \leq \hat{\mu} \leq 1 + \frac{D_X(\hat{N}_M - 1)}{D_X + W} \left\{ \frac{N_A - \alpha}{N_A - 1} + \frac{W}{D_X} \right\} \right. \right\} \right\} \\
 &\quad \forall \alpha \left\{ \alpha \in \mathbb{N} \mid \alpha \leq N_A \right\} \quad \forall \beta \left\{ \beta \in \mathbb{N} \mid \beta \leq N_B \right\} \\
 &= 0 \quad \text{otherwise}
 \end{aligned} \tag{9.14}$$

where

$$i = N_I - \left\lceil \frac{(\alpha - 1)(N_I - 1)}{(N_A - 1)} \right\rceil \tag{9.15}$$

$$j = N_B - \left\lceil \frac{(\beta - 1)(N_J - 1)}{(N_B - 1)} \right\rceil \tag{9.16}$$

$$k = 1 + \left\lceil \frac{(N_K - 1)}{W} D_X \left[\frac{(\hat{\mu} - 1)}{(\hat{N}_M - 1)} \left(\frac{W}{D_X} + 1 \right) + \frac{(\alpha - N_A)}{(N_A - 1)} \right] \right\rceil \tag{9.17}$$

$$g = 1 + \left\lceil \frac{(N_G - 1)}{H} D_Y \left[\frac{(\hat{v} - 1)}{(\hat{N}_V - 1)} \left(\frac{H}{D_Y} + 1 \right) + \frac{(\beta - N_B)}{(N_B - 1)} \right] \right\rceil \tag{9.18}$$

This transformation is valid for an inverted camera and a conjugate SLM position and should be used in conjunction with the previous offset Equations 8.46 and 8.47. Using centred SLM coordinates, the corresponding transformation (also pertaining to an inverting camera and a conjugate SLM position) can be written*

$$\begin{aligned}
 \bar{\mathbf{S}}_{\alpha\beta} &= {}^{kg}\mathbf{I}_{\bar{j}} \quad \forall \bar{v} \in \mathbb{N} \left\{ \bar{v} \in \mathbb{N} \left| 1 \leq \bar{v} \leq 1 + \left\lceil \frac{H(N_V - 1)}{\Sigma'} \right\rceil \right. \right\} \\
 &\quad \forall \bar{\mu} \left\{ \bar{\mu} \in \mathbb{N} \left| 1 \leq \bar{\mu} \leq 1 + \left\lceil \frac{W(N_M - 1)}{\Pi'} \right\rceil \right. \right\} \\
 &\quad \forall \alpha \left\{ \alpha \in \mathbb{N} \mid \alpha \leq N_A \right\} \\
 &\quad \forall \beta \left\{ \beta \in \mathbb{N} \mid \beta \leq N_B \right\} \\
 &= 0 \quad \text{otherwise}
 \end{aligned} \tag{9.19}$$

* Here we have assumed that $\Pi'/(N_M - 1) = \bar{\Pi}'/(\bar{N}_M - 1)$ and that $\Sigma'/(N_V - 1) = \bar{\Sigma}'/(\bar{N}_V - 1)$.

where

$$\begin{aligned} i &= N_I - \left\| \frac{(\alpha-1)(N_I-1)}{(N_A-1)} \right\| & j &= N_J - \left\| \frac{(\beta-1)(N_J-1)}{(N_B-1)} \right\| \\ k &= 1 + \left\| \frac{\Pi'(N_K-1)}{W(N_M-1)} (\bar{\mu}-1) \right\| & g &= 1 + \left\| \frac{\Sigma'(N_G-1)}{H(N_V-1)} (\bar{v}-1) \right\| \end{aligned} \quad (9.20)$$

Once again, the offset index relations required to compute \mathbf{S} from $\bar{\mathbf{S}}$ are those of Equations 8.78 and 8.79.

9.2.4 Non-Paraxial Printer Objectives

By using an intrinsically two-step process, we have seen how a single PC can calculate exact $h = 0$ camera data from a given data set characteristic of a first quantised camera distance. This data can then be naturally adjusted to compensate for the fifth Seidel aberration of a non-paraxial objective using bilinear or bicubic interpolation before writing to the printer SLM. This process allows low-noise digital holograms to be produced efficiently, having an image projection up to a value equal to the first quantised value of h . If larger image projections are required, then one can either decide to go to $n = 2$ or increase the hogel size. Alternatively, one may simply decide to use a non-paraxial general transformation as mentioned in Section 8.10. For example, Expressions 8.154 to 8.156 may be generalised to the full-parallax case by rewriting Equation 8.154 as

$$\begin{aligned} {}^{\mu\nu}\mathbf{S}_{\alpha\beta} &= {}^{kg}\mathbf{I}_g \quad \forall \mu \in \mathbb{N} | N_{U1}(\alpha) \leq \mu \leq N_{U2}(\alpha) \quad \forall \alpha \in \mathbb{N} | \alpha \leq N_A \\ &\quad \forall v \in \mathbb{N} | N_{V1}(\beta) \leq v \leq N_{V2}(\beta) \quad \forall \beta \in \mathbb{N} | \beta \leq N_B \\ &= 0 \quad \text{otherwise} \end{aligned} \quad (9.21)$$

and introducing another “ g ” equation:

$$g = 1 + \left\| \frac{(N_G-1)}{H} \left\{ \frac{D_Y+H}{2} + \frac{(2v-N_V-1)\mathcal{K}(\hat{\rho})}{(N_V-1)} h \tan\left(\frac{\Psi_{PV}}{2}\right) + \frac{(\beta-N_B)D_Y}{N_B-1} \right\} \right\| \quad (9.22)$$

As before, the two-step method then applies. We shall see in Chapter 10 that even physical camera data can nearly always be processed to produce the required data set defined in Section 9.2.1. As we have already mentioned, a great advantage of exact transformations such as Equations 9.9 and 9.10, or their higher-order equivalents is that each file ${}^{[\bar{\mu}\bar{v}]}\hat{\mathbf{S}}$ can be corrected efficiently for printer objective distortion using bilinear or bicubic interpolation.

9.2.5 Larger Holograms

The two-step process that we have described above for generating the image data required for DWDH full-parallax holograms can be applied to holograms of reasonable size. As we have seen, a high-resolution (0.5 mm-hogel) 40 cm \times 30 cm DWDH hologram with a typical window requires around a 3 h preprocessing cycle and a 1.5 h write cycle. A 64-bit PC with approximately 6 GB of main memory would be recommended for this type of task. Larger DWDH holograms can increase the memory requirement quite fast however. For example, a 1 m \times 1 m, 0.5 mm-hogel DWDH three-colour reflection hologram with a maximum (unapodised) window assuming a horizontal printer FOV of 85° and a printer SLM with pixel dimensions of 1280 \times 1024 would entail loading *step 1* files into the main memory amounting to a total size of around 15 GB. The *step 2* files would also be approximately of this

size. Although it is just about possible for 64-bit PCs to cope with these numbers, the disk read times do become rather long.

For larger holograms, it therefore makes sense to divide the hologram into smaller zones and to calculate the data required for each zone separately. The simplest way to do this is to divide the hologram into several vertical slices. Because the two-stage calculation process that we have described works by hologram lines, the size of the *step 1* files (assuming an $n = 1$ camera distance) is $3N_A N_B N_G$ and the size of the *step 2* files is likewise $3N_A N_G N_K$.^{*} By reducing N_A , we therefore reduce both the *step 1* and *step 2* file sizes. Of course, we are at liberty to define a two-step process which works by columns rather than lines; in this case, we would then seek to reduce N_B rather than N_A . In either case, each slice of the hologram can now be calculated by a different PC. Not only is the memory requirement of that PC reduced linearly with the number of slices employed, but also the total time taken to calculate the data is also reduced linearly. There are two relatively minor complications to this method. The first is that the original data set must be made available to all PCs, and the second is that once each PC has calculated its slice of the hologram, these slices usually have to be integrated so that the printer is able to print a full line of hogels.

For extremely large and wide-angle full-parallax holograms with small hogel sizes, the sliced two-step technique that we have just described may nevertheless become inadequate. In this case, we must adopt the technique of dividing both *the hologram and its viewing window* into individual equal areas. As before, the original data must now be distributed to all PCs in the network and each PC is then responsible for calculating its own partial hogel set using the standard line-based two-step technique described in Section 9.2.2. After calculation, a given PC will contain partial hogel data for a section of the hologram and corresponding only to a certain viewing zone. The data from the different PCs must therefore be integrated by the printer before hogel lines may be printed.

9.2.6 Rectangular Viewing Windows

We saw in Chapter 8 that writing an HPO digital hologram with a well-defined rectangular viewing window made good sense for a variety of reasons. The most important of these reasons is that an HPO hologram has, by definition, a preferred viewing distance as the camera plane and viewing plane are collocated. Only at this plane will the hologram look truly “right”. It therefore makes sense to define a rectangular window at this unique distance such that an observer here will see the whole image or nothing—depending on whether he or she is laterally in or out of the defined viewing zone. This is just good sense as any hologram that emits over a wide solid angle will be dimmer than one of similar diffractive properties but which focusses the light into a well-defined rectangular window.

With full-parallax holograms, this logic remains only partly valid. Certainly, if we spread the diffracted light too widely over a solid angle, we are still going to end up with a dim hologram. However, defining a window at a certain fixed distance from the hologram can lead to problems with viewing. This is illustrated in Figure 9.3, in which it is clear that there are zones where only a partial image of the hologram is available. In HPO holography, one is always near the special camera/viewing plane and so these partial image zones are not so important: you just cannot go up to a 1 m × 1 m HPO hologram and look at it at a 30 cm distance when it has been written for viewing at 1 m. Because of the lack of a vertical parallax, the image simply appears to disintegrate. However, this is just the advantage of the full-parallax hologram! The image is designed for viewing over a wide range of distances.

The upshot of all this is that one has to be more careful with window definitions in full-parallax display holography than with HPO holography. It can therefore be desirable to use a rectangular window at a distance that is relatively large compared with the hologram size. If we elect not to use a window at all and simply use the full SLM field for every hogel, then this is equivalent to a rectangular window at infinity. However, this will often produce too dim a hologram[†] and we need to at least restrict the vertical

* This is true even for the case of an unrestricted viewing window where we use all the printer SLM—in this case, however, the files $k^g I_{[ij]}$ are not all the same size and in general N_i and N_j become functions of k and g .

[†] This depends on the type of photosensitive material used and the type of illumination.

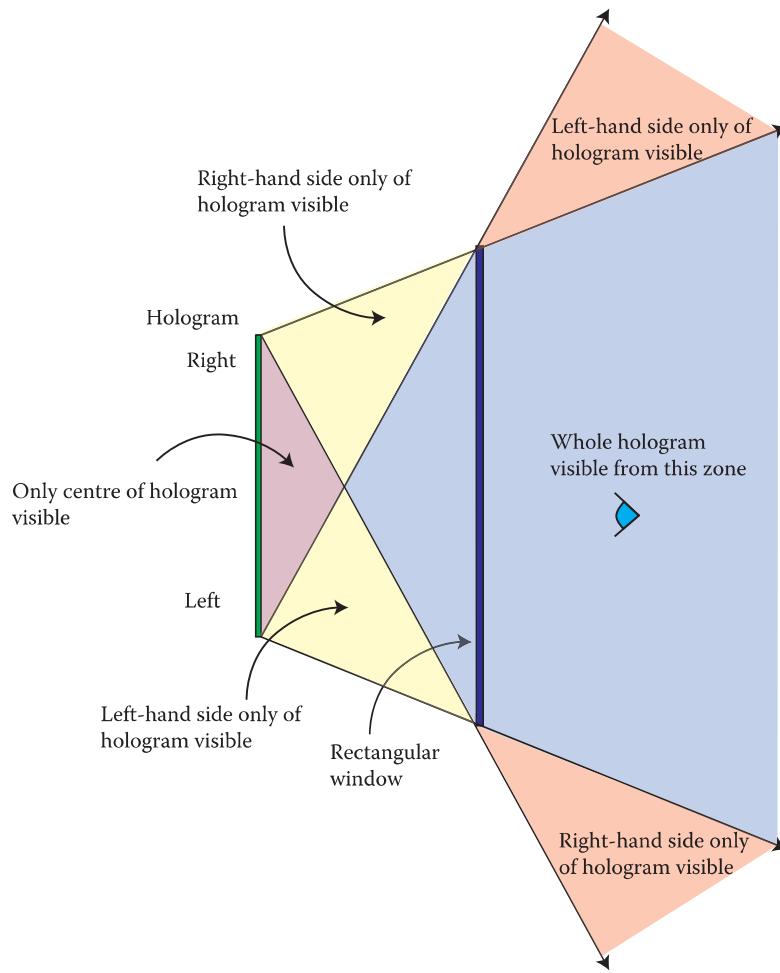


FIGURE 9.3 Plan view of a hologram made with a defined rectangular window. Note that an observer who is not at the same distance as the window location can find himself or herself in a zone where only part of the holographic image is visible.

field. We may therefore sometimes wish to use an astigmatic window in which the horizontal focus is at a greater distance than the vertical focus.

Another very important point to remember is that we do not always require the window distance in full-parallax holography to coincide with the camera plane. The most usual reason for this is that if one is forced to use a small camera distance by the quantisation rules, then the window will be just too close to the hologram. In fact, this is frequently the case with full-parallax digital holograms.

An alternative to using the entire SLM for each hogel is to use only a constant restricted area in its centre. Figure 9.4 illustrates the viewing geometry for this case. Mathematically, this case is equivalent to the largest possible infinitely distant rectangular window we could generate using the restricted field of view corresponding to the restricted SLM area.

9.2.6.1 General Astigmatic Rectangular Viewing Window

We shall now discuss how to define a general astigmatic rectangular viewing window situated at a distance that is greater than the camera plane. As we mentioned previously, this is frequently the most desired method to compensate for a small camera distance imposed by quantisation. Figure 9.5 shows a plan view of the ray geometry for a DWDH hologram with a centred camera and centred SLM

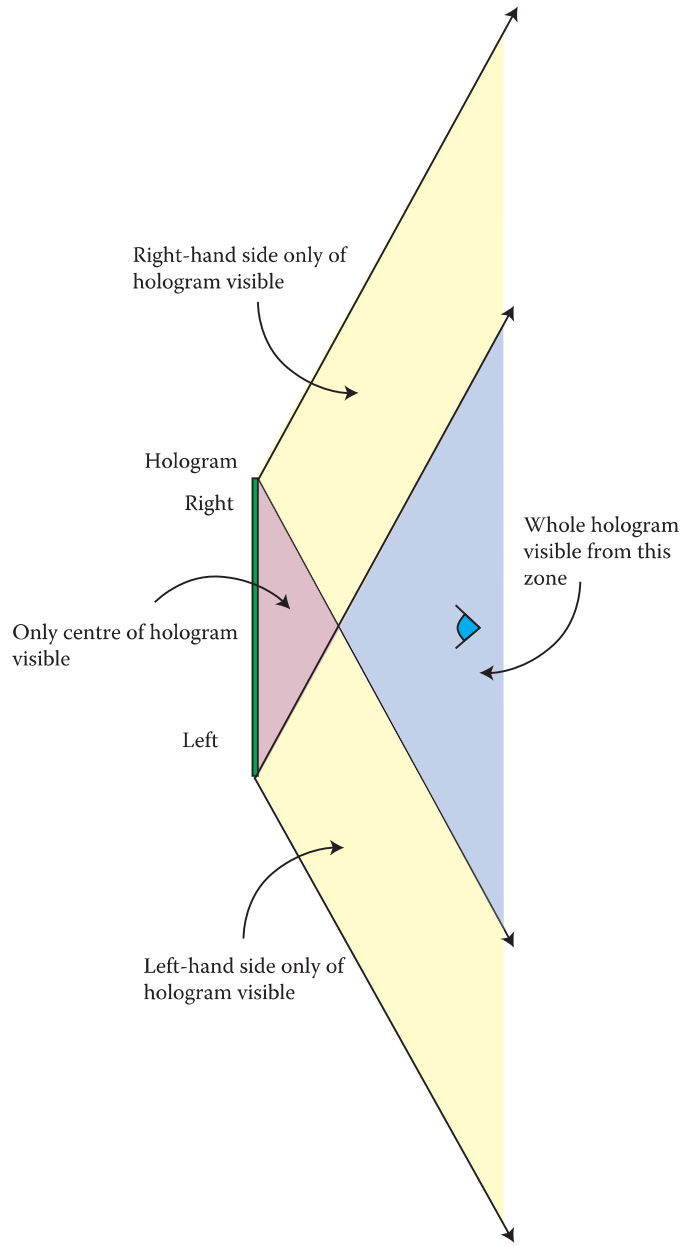


FIGURE 9.4 Plan view of a hologram with an unrestricted viewing angle. Note that an observer can still find himself or herself in a zone where only part of the holographic image is available.

configuration incorporating a rectangular viewing window at a distance $h_{w1} \neq h$. As in Chapter 8, the coordinates ξ and \bar{U}' can be defined to be the same as long as we choose

$$D_\xi = W \frac{h}{h_{w1}} + D_X \left(1 - \frac{h}{h_{w1}} \right) \quad (9.23)$$

Likewise, if we define the vertical window distance as h_{w2} , then the corresponding vertical coordinates ζ and \bar{V}' can be defined to be the same as long as

$$D_\zeta = H \frac{h}{h_{w2}} + D_Y \left(1 - \frac{h}{h_{w2}} \right) \quad (9.24)$$

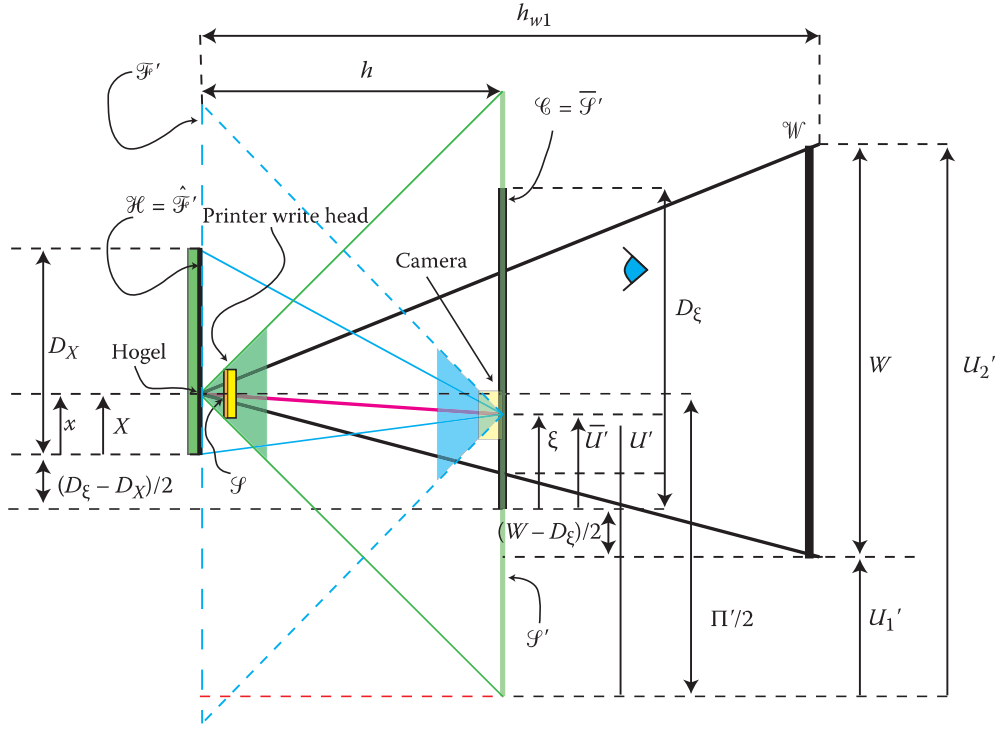


FIGURE 9.5 Plan view of ray geometry showing the writing of a DWDH hologram with a rectangular window at a distance $h_{w1} > h$. Coordinates corresponding to a centred camera ($x = X$) and to a centred SLM ($\xi = \bar{U}'$) are used.

There is, however, a sizeable difference to the transformation of Equations 9.19 and 9.20. Defining

$$\begin{aligned} {}^1D_\xi &\equiv D_\xi/2 - (W + D_X)h/(2h_{w1}) + D_X/2 \\ {}^2D_\xi &\equiv D_\xi/2 + (W + D_X)h/(2h_{w1}) - D_X/2 \\ {}^1D_\zeta &\equiv D_\zeta/2 - (H + D_Y)h/(2h_{w2}) + D_Y/2 \\ {}^2D_\zeta &\equiv D_\zeta/2 + (H + D_Y)h/(2h_{w2}) - D_Y/2 \end{aligned} \quad (9.25)$$

then only within the limits

$$\begin{aligned} {}^1D_\xi &\leq \bar{U}' \leq {}^2D_\xi \\ {}^1D_\zeta &\leq \bar{V}' \leq {}^2D_\zeta \end{aligned} \quad (9.26)$$

will the projected centred film plane, $\hat{\mathcal{F}'}$, be congruent to the hologram plane, \mathcal{H} . In other words, only in this region is $D_x = D_X$ and $D_y = D_Y$. Outside this region, either $D_x < D_X$, $D_y < D_Y$ or both. In fact, the camera plane is, in general, split up into nine different zones as illustrated in Figure 9.6.

There are two ways to proceed with calculating ${}^{\mu\nu}\bar{\mathbf{S}}_{\alpha\beta}$ from ${}^{kg}\mathbf{I}_{ij}$. The first is a simple brute force method where we use a data set ${}^{kg}\mathbf{I}_{[ij]}$ in which the files $\mathbf{I}_{[ij]}$ all have dimensions of $N_i \times N_j$ and all follow the usual definition of a centred camera, which states that the film plane $\hat{\mathcal{F}'}$ is congruent to \mathcal{H} . We then impose the following window limits on $\bar{\mu}$ and \bar{v} :*

$$\bar{\mu}_1 = 1 + \left\| \frac{(N_M - 1)}{\Pi'} \left\{ \left(\frac{h_{w1} - h}{h_{w1}} \right) \left[\frac{\alpha - 1}{N_A - 1} D_X + \frac{W - D_X}{2} \right] - \frac{(W - D_\xi)}{2} \right\} \right\| \quad (9.27)$$

* Here we have assumed that $\Pi'/(N_M - 1) = \bar{\Pi}'/(\bar{N}_M - 1)$ and that $\Sigma'/(N_V - 1) = \bar{\Sigma}'/(\bar{N}_V - 1)$.

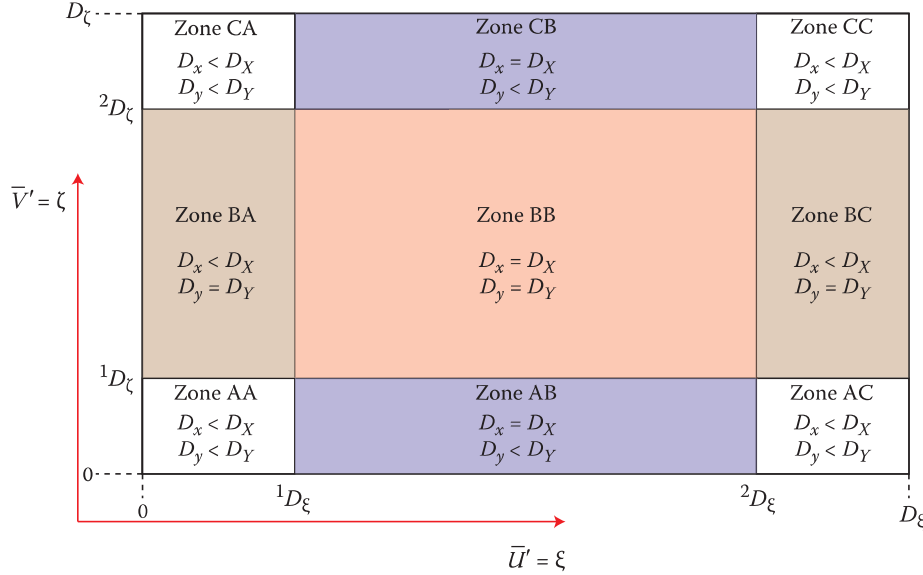


FIGURE 9.6 The camera plane divides into nine zones when a rectangular viewing window is not in the same plane. A camera in zone BB is required to define (projected) image data over the entire hologram surface. However, a camera in the other eight zones is only required to define image data over a partial region.

$$\bar{\mu}_2 = 1 + \left\| \frac{(N_M - 1)}{\Pi'} \left\{ \left(\frac{h_{w1} - h}{h_{w1}} \right) \left[\frac{\alpha - 1}{N_A - 1} D_X - \frac{W + D_X}{2} \right] + \frac{(W + D_\zeta)}{2} \right\} \right\| \quad (9.28)$$

$$\bar{v}_1 = 1 + \left\| \frac{(N_V - 1)}{\Sigma'} \left\{ \left(\frac{h_{w2} - h}{h_{w2}} \right) \left[\frac{\beta - 1}{N_B - 1} D_Y + \frac{H - D_Y}{2} \right] - \frac{(H - D_\zeta)}{2} \right\} \right\| \quad (9.29)$$

$$\bar{v}_2 = 1 + \left\| \frac{(N_V - 1)}{\Sigma'} \left\{ \left(\frac{h_{w2} - h}{h_{w2}} \right) \left[\frac{\beta - 1}{N_B - 1} D_Y - \frac{H + D_Y}{2} \right] + \frac{(H + D_\zeta)}{2} \right\} \right\| \quad (9.30)$$

We can therefore write the **I**-to-**S** transformation between **S̄** and **I** as

$$\begin{aligned} \bar{\mu}^{\bar{v}} \bar{S}_{\alpha\beta} &= {}^{kg} \mathbf{I}_{\bar{j}} & \forall \bar{\mu} \left\{ \bar{\mu} \in \mathbb{N} \mid \bar{\mu}_1 \leq \bar{\mu} \leq \bar{\mu}_2 \right\} & \forall \alpha \left\{ \alpha \in \mathbb{N} \mid \alpha \leq N_A \right\} \\ &\quad \forall \bar{v} \left\{ \bar{v} \in \mathbb{N} \mid \bar{v}_1 \leq \bar{v} \leq \bar{v}_2 \right\} & \forall \beta \left\{ \beta \in \mathbb{N} \mid \beta \leq N_B \right\} \\ &= 0 & \text{otherwise} \end{aligned} \quad (9.31)$$

where $\bar{\mu}_1$, $\bar{\mu}_2$, \bar{v}_1 and \bar{v}_2 are given by Equations 9.27 to 9.30 and where (for the case of an inverting camera and conjugate SLM position)

$$\begin{aligned} i &= N_I - \left\| \frac{(\alpha - 1)(N_I - 1)}{(N_A - 1)} \right\| & j &= N_J - \left\| \frac{(\beta - 1)(N_J - 1)}{(N_B - 1)} \right\| \\ k &= 1 + \left\| \frac{\Pi'(N_K - 1)}{W(N_M - 1)} (\bar{\mu} - 1) \right\| & g &= 1 + \left\| \frac{\Sigma'(N_G - 1)}{H(N_V - 1)} (\bar{v} - 1) \right\| \end{aligned} \quad (9.32)$$

Before updating the SLM with $\bar{\mathbf{S}}$, and prior to a hogel-write operation, the index rules (Equations 8.78 and 8.79) must be used. Additionally, the elements of \mathbf{S} outside the area specified by these indices must be blanked. If we use the $n = 1$ camera plane (and assuming a non-inverting camera and $N_I = N_A$ and $N_J = N_B$), then Equation 9.32 is reduced to the trivial form

$$i = \alpha \quad j = \beta \quad k = \bar{\mu}' \quad g = \bar{v}' \quad (9.33)$$

The disadvantage of this scheme is that we end up using more camera data than we actually need. This is because only in zone “BB” of Figure 9.6 do we actually require the full film-plane data. Not surprisingly, the memory and processing load can be significantly reduced if we only process the strict minimum of camera data required. What this amounts to is starting with different-sized files ${}^{kg}\mathbf{I}_{[ij]}$ for each k and g . When we apply the first step of the general two-step \mathbf{I} -to- \mathbf{S} transformation as illustrated in Figure 9.2, we then end up with an intermediate data set that now also contains files of differing sizes as its matrix elements. This process continues to the final calculated data set, ${}^{kg}\mathbf{I}_{ij} = [{}^{\mu\nu}] \bar{\mathbf{S}}_{\alpha\beta}$, where the size of each file depends on α and β . Of course, using Equation 9.31 directly gets one to the same result by calculating and then just ignoring the redundant data.

We shall now describe briefly the steps required in an optimised algorithm. As before, we use a centred camera and centred SLM. We use a camera distance, h , given by the $n = 1$ constraints. The camera plane is defined by Equation 9.23 and 9.24 in terms of the desired astigmatic window $W \times H$. Assuming that we are going to generate the required 3D image data using a computer modelling program, our very first step must be to define the camera geometry. In zone BB of Figure 9.6, the camera constitutes a completely standard centred configuration for $h_{n=1}$ as summarised in Section 9.2.1. In particular, $\hat{\mathcal{F}}$ is congruent to the hologram plane, \mathcal{H} , and each rendered film frame must be of integer dimensions $N_I = N_A$ and $N_J = N_B$. In this way, each film frame pixel corresponds to a partner hogel.

In zones other than zone BB, only a subset of the film plane needs be populated with image data. The reason for this is apparent from Figure 9.5, in which it can be seen that from certain camera positions, there are simply no rays connecting the camera to some portions of the hologram plane. Figure 9.7 shows a labelling scheme for the image subset characteristic of the nine camera plane zones. For a general zone ZZ, we require image data only in the region

$$\begin{aligned} {}^{1ZZ}N_I &\geq i' \geq {}^{2ZZ}N_I \\ {}^{1ZZ}N_J &\geq j' \geq {}^{2ZZ}N_J \end{aligned} \quad (9.34)$$

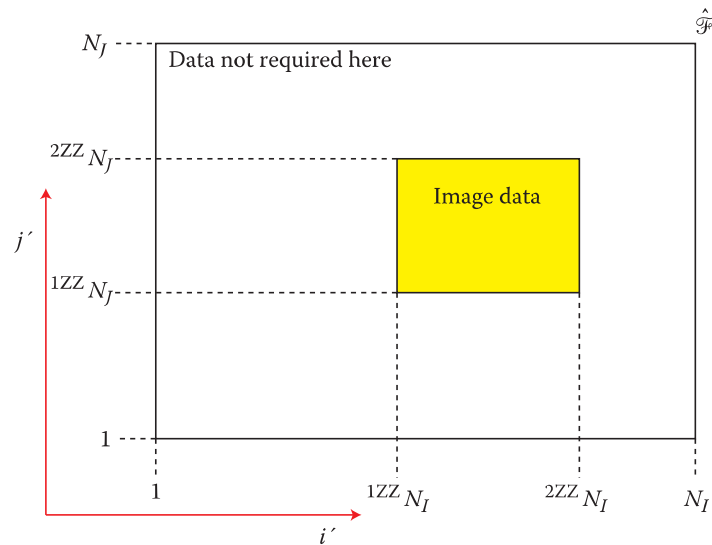


FIGURE 9.7 This diagram shows the centred film plane, $\hat{\mathcal{F}}$, corresponding to a camera located within a general zone, ZZ, of Figure 9.6. The yellow rectangle indicates the required subsection of $\hat{\mathcal{F}}$ that is required to be populated with image data. The white region of $\hat{\mathcal{F}}$ is not required and so does not need to be stored on disk.